Quantitative fluorescence microscopy methods to investigate molecular interactions and dynamics in living cells

KUMULATIVE DISSERTATION

zur Erlangung des akademischen Grades

Doctor rerum naturalium (Dr. rer. nat.)

in der Wissenschaftsdisziplin Molekularbiologie

eingereicht an der

Mathematisch-Naturwissenschaftlichen Fakultät der Universität Potsdam

Institut für Biologie und Biochemie

von

Annett Petrich, M.Sc.

17. August 2023

Zusammenfassung

Biomoleküle wie Proteine und Lipide spielen eine wichtige Rolle bei zahlreichen Zellfunktionen, darunter Biomolekültransport, Proteinfunktionen, zelluläre Homöostase und Biomembranintegrität. Traditionelle biochemische Methoden liefern keine Informationen über die Verteilung und das Verhalten zellulärer Biomolekülen unter natürlichen Bedingungen, da sie nicht auf lebende Zellproben übertragbar sind. Folglich kann dies zu Ungenauigkeiten bei der Quantifizierung von Biomolekülinteraktionen führen und potenzielle Komplexitäten der Heterogenität nativer Biomembranen übersehen. Um diese Einschränkungen zu überwinden, wurden minimalinvasive mikroskopische Techniken wie die Fluoreszenzfluktuationsspektroskopie (FFS) in Kombination mit Fluoreszenzproteinen (FPs) und Fluoreszenzlipidanaloga entwickelt. FFS-Techniken und Membraneigenschaftssensoren ermöglichen die Quantifizierung verschiedener Parameter, einschließlich Konzentration, Dynamik, Oligomerisierung und Wechselwirkung von Biomolekülen in lebenden Zellproben.

In dieser Arbeit wurden mehrere FFS-Ansätze und Sensoren für Membraneigenschaften implementiert und eingesetzt, um biologische Prozesse in verschiedenen Zusammenhängen zu untersuchen. Die Mehrfarben-Scanning-Fluoreszenzfluktuationsspektroskopie (sFCS) wurde zur Untersuchung von Protein-Oligomerisierung, Protein-Protein-Wechselwirkungen (PPIs) und Proteindynamik an der zellulären Plasmamembran (PM) eingesetzt. Zusätzlich wurde die Zweifarben-Analyse von Anzahl und Helligkeit (N&B) mit der Kreuzkorrelationsanalyse erweitert, um Hetero-Interaktionen von Proteinen in der PM mit sehr langsamer Dynamik zu quantifizieren, die mit sFCS aufgrund starker anfänglicher Bleiche der Fluorophore nicht zugänglich wären. Darüber hinaus wurden zwei halbautomatische Analysepipelines entwickelt: die spektrale Förster-Resonanz-Energie-Transfer (FRET)-Analyse zur Untersuchung von Änderungen der Membranladung auf der Innenseite der PM und die spektrale generalisierte Polarisation (GP)-Bildgebung sowie die spektrale Phasor-Analyse zur Überwachung von Änderungen der Membranfluidität und -ordnung.

Ein wichtiger Parameter zur Untersuchung von PPIs ist die molekulare Helligkeit, die die Oligomerisierung direkt bestimmt und aus FFS daten extrahiert werden kann. Allerdings weisen FPs häufig komplexe photophysikalische Übergänge auf, einschließlich nichtfluoreszierender Zustände. Daher ist es von entscheidender Bedeutung, FPs hinsichtlich ihrer dunklen Zustände zu charakterisieren, um zuverlässige Oligomerisierungsmessungen sicherzustellen. In dieser Studie wurden N&B- und sFCS-Analysen angewendet, um die photophysikalischen Eigenschaften neuartiger grüner FPs unter verschiedenen Bedingungen (d. h. Anregungsleistung und pH-Wert) in lebenden Zellen zu bestimmen. Die Ergebnisse zeigten, dass die neuen FPs mGreenLantern (mGL) und Gamillus die höchste molekulare Helligkeit aufwiesen, allerdings auf Kosten einer geringeren Photostabilität. Das etablierte mEGFP blieb die beste Option, um PPIs bei niedrigerem pH-Wert zu untersuchen, während mGL am besten für neutralen pH-Wert und Gamillus für hohen pH-Wert geeignet war. Diese Ergebnisse bieten Orientierung für die Auswahl eines geeigneten FP zur Quantifizierung von PPIs über FFS unter verschiedenen Umgebungsbedingungen.

Als nächstes wurden mehrere biophysikalische Fluoreszenzmikroskopie-Ansätze (z. B. sFCS, GP-Bildgebung, Membranladung-FRET) eingesetzt, um Veränderungen in der Lipid-Lipid-Packung in Biomembranen in verschiedenen biologischen Kontexten zu überwachen. Es ist bekannt, dass der Lipidstoffwechsel in Krebszellen die schnelle Vermehrung und Metastasierung fördert. Daher ist die gezielte Beeinflussung der Lipidsynthese oder der Membranintegrität eine vielversprechende Strategie zur Krebsbekämpfung. Der Wirkungsmechanismus des neuartigen Wirkstoffs Erufosin (EPC3) auf die Membranstabilität ist nicht vollständig geklärt. Die vorliegende Arbeit ergab, dass EPC3 die Lipidpackung und -zusammensetzung reduziert sowie die Fluidität und Dynamik der Membran erhöht und somit die Lipid-Lipid-Wechselwirkung verändert. Diese Auswirkungen auf die Membranintegrität wurden wahrscheinlich durch Modulationen des Lipidstoffwechsels und der Membranorganisation ausgelöst. Im Falle einer Infektion mit dem Influenza-A-Virus (IAV) ist die Regulierung des Lipidstoffwechsels für mehrere Schritte der IAV-Replikation von entscheidender Bedeutung und hängt mit der Pathogenität von IAV zusammen. Hier wird zum ersten Mal gezeigt, dass eine IAV-Infektion eine lokale Anreicherung negativ geladener Lipide an der Innenseite der PM auslöst, die Fluidität und Dynamik der Membran verringert und die Lipidpackung an der Assemblierungsstelle in lebenden Zellen erhöht. Dies legt nahe, dass IAV die Lipid-Lipid-Wechselwirkungen und die Organisation am PM verändert. Insgesamt unterstreicht diese Arbeit das Potenzial biophysikalischer Techniken als Screening-Plattform zur Untersuchung von Membraneigenschaften in lebenden Zellen auf Einzelzellebene.

Abschließend ging diese Studie auf verbleibende Fragen zur frühen Phase der IAV-Assemblierung ein. Die Rekrutierung von Matrixprotein 1 (M1) und seine Wechselwirkung mit anderen viralen Oberflächenproteinen, Hämagglutinin (HA), Neuraminidase (NA) und Matrixprotein 2 (M2), war aufgrund widersprüchlicher Ergebnisse Gegenstand von Debatten. In dieser Studie wurden verschiedene FFS-Ansätze in transfizierten Zellen durchgeführt, um Wechselwirkungen zwischen IAV-Proteinen untereinander und Wirtsfaktoren an der PM zu untersuchen. FFS-Messungen ergaben, dass M2 stark mit M1 interagiert, was zur Translokation von M1 zur PM führt. Diese Interaktion fand wahrscheinlich entlang des nichtkanonischen Weges statt, was durch den Nachweis einer Interaktion zwischen M2 und dem Wirtsfaktor LC3-II belegt wurde, die zur Rekrutierung von LC3-II zur PM führte. Darüber hinaus wurde eine schwächere Wechselwirkung zwischen HA und membrangebundenem M1 beobachtet und keine Wechselwirkung zwischen NA und M1. Interessanterweise waren höhere oligomere Zustände von M1 nur in infizierten Zellen nachweisbar. Diese Ergebnisse deuten darauf hin, dass M2 den Zusammenbau von Virionen initiiert, indem es M1 zur PM rekrutiert, welches als Plattform für weitere Interaktionen mit viralen Proteinen und Wirtsfaktoren dienen könnte.

Abstract

Biomolecules such as proteins and lipids have vital roles in numerous cellular functions, including biomolecule transport, protein functions, cellular homeostasis and biomembrane integrity. Traditional biochemistry methods do not provide precise information about cellular biomolecule distribution and behavior under native environmental conditions since they are not transferable to live cell samples. Consequently, this can lead to inaccuracies in quantifying biomolecule interactions due to potential complexities arising from the heterogeneity of native biomembranes. To overcome these limitations, minimal invasive microscopic techniques, such as fluorescence fluctuation spectroscopy (FFS) in combination with fluorescence proteins (FPs) and fluorescence lipid analogs, have been developed. FFS techniques and membrane property sensors enable the quantification of various parameters, including concentration, dynamics, oligomerization, and interaction of biomolecules in live cell samples.

In this work, several FFS approaches and membrane property sensors were implemented and employed to examine biological processes of diverse context. Multi-color scanning fluorescence fluctuation spectroscopy (sFCS) was used the examine protein oligomerization, protein-protein interactions (PPIs) and protein dynamics at the cellular plasma membrane (PM). Additionally, two-color number and brightness (N&B) analysis was extended with the cross-correlation analysis in order to quantify hetero-interactions of proteins in the PM with very slow motion, which would not accessible with sFCS due strong initial photobleaching. Furthermore, two semi-automatic analysis pipelines were designed: spectral Förster resonance energy transfer (FRET) analysis to study changes in membrane charge at the inner leaflet of the PM, and spectral generalized polarization (GP) imaging and spectral phasor analysis to monitor changes in membrane fluidity and order.

An important parameter for studying PPIs is molecular brightness, which directly determines oligomerization and can be extracted from FFS data. However, FPs often display complex photophysical transitions, including dark states. Therefore, it is crucial to characterize FPs for their dark-states to ensure reliable oligomerization measurements. In this study, N&B and sFCS analysis were applied to determine photophysical properties of novel green FPs under different conditions (i.e., excitation power and pH) in living cells. The results showed that the new FPs, mGreenLantern (mGL) and Gamillus, exhibited the highest molecular brightness at the cost of lower photostability. The well-established monomeric enhanced green fluorescent protein (mEGFP) remained the best option to investigate PPIs at lower pH, while mGL was best suited for neutral pH, and Gamillus for high pH. These findings provide guidance for selecting an appropriate FP to quantify PPIs via FFS under different environmental conditions.

Next, several biophysical fluorescence microscopy approaches (i.e., sFCS, GP imaging, membrane charge FRET) were employed to monitor changes in lipid-lipid-packing in biomembranes in different biological context. Lipid metabolism in cancer cells is known to support rapid proliferation and metastasis. Therefore, targeting lipid synthesis or membrane integrity holds immense promise as an anticancer strategy. However, the mechanism of action of the novel agent erufosine (EPC3) on membrane stability is not fully under-

stood. The present work revealed that EPC3 reduces lipid packing and composition as well as increased membrane fluidity and dynamic, hence, modifies lipid-lipid-interaction. These effects on membrane integrity were likely triggered by modulations in lipid metabolism and membrane organization. In the case of influenza A virus (IAV) infection, regulation of lipid metabolism is crucial for multiple steps in IAV replication and is related to the pathogenicity of IAV. Here, it is shown for the first time that IAV infection triggers a local enrichment of negatively charged lipids at the inner leaflet of the PM, which decreases membrane fluidity and dynamic, as well as increases lipid packing at the assembly site in living cells. This suggests that IAV alters lipid-lipid interactions and organization at the PM. Overall, this work highlights the potential of biophysical techniques as a screening platform for studying membrane properties in living cells at the single-cell level.

Finally, this study addressed remaining questions about the early stage of IAV assembly. The recruitment of matrix protein 1 (M1) and its interaction with other viral surface proteins, hemagglutinin (HA), neuraminidase (NA), and matrix protein 2 (M2), has been a subject of debate due to conflicting results. In this study, different FFS approaches were performed in transfected cells to investigate interactions between IAV proteins themselves and host factors at the PM. FFS measurements revealed that M2 interacts strongly with M1, leading to the translocation of M1 to the PM. This interaction likely took place along the non-canonical pathway, as evidenced by the detection of an interaction between M2 and the host factor LC3-II, leading to the recruitment of LC3-II to the PM. Moreover, weaker interaction was observed between HA and membrane-bound M1, and no interaction between NA and M1. Interestingly, higher oligomeric states of M1 were only detectable in infected cells. These results indicate that M2 initiates virion assembly by recruiting M1 to the PM, which may serve as a platform for further interactions with viral proteins and host factors.

List of Abbreviations

ACF	autocorrelation function
APL	alkylphospholipid
BiFC	bimolecular fluorescence complementation
CCF	cross-correlation function
cRNA	complementary vRNA
EPC3	erufosine
ER	endoplasmic reticulum
F(C)CS	fluorescence (cross-)correlation spectroscopy
F(S)FS	fluorescence (spectral) fluctuation spectroscopy
FP	fluorescence protein
FRAP	fluorescence recovery after photobleaching
(sm)FRET	(single-molecule) Förster resonance energy transfer
FWHM	full width at half maximum
GG	geranylgeranyl
GP	generalized polarization
GPI	glycosylphosphatidylinositol
GPL	glycerophospholipid
GPMV	giant plasma membrane vesicle
GUV	giant unilamellar vesicle
HA	hemagglutinin
HIV	human immunodeficiency virus
IAV	influenza A virus
mEGFP	monomeric enhanced green fluorescent protein
mGL	mGreenLantern
LC3-II	PS-conjugated microtubule-associated protein 1 light chain 3 protein
L_d/L_o	liquid disorder/ liquid orderd
M1	matrix protein 1
M2	matrix protein 2
MALDI-MS	matrix-assisted laser desorption/ionization)-mass spectrometry
MbCD	methyl-ß-cyclodextrin

MDR	multidrug-resistant
mp	myristoyl/palmitoyl
NA	neuraminidase
nanoSIMS	nano secondary ion mass spectrometry
(cc)N&B	(cross-correlation) number and brightness
NEP	nuclear export protein
NP	nucleoprotein
NS1	non-structural protein 1
pFCS	point fluorescence correlation spectroscopy
PA	polymerase acidic protein
PALM	photoactivation localization microscopy
PB1	polymerase basic protein 1
PB2	polymerase basic protein 2
PC	phosphatidylcholine
PE	phosphoethanolamine
p_f	fluorescence probability
PI	phosphatidylinositol
PIP2	phosphatidylinositol 4,5-biphosphate
PM	plasma membrane
PPI	protein-protein interaction
PS	phosphatidylserine
PSF	point spread function
RdRp	RNA-dependent RNA polymerase
R(S)ICS	raster scanning (spectral) image correlation spectroscopy
SBL	supported lipid bilayer
SUV	small unilamellar vesicle
sF(S)CS	scanning fluorescence spectral correlation spectroscopy
SMLM	single molecule localization microscopy
STED	stimulated emission depletion microscopy
TIRF	total internal reflection fluorescence
v(m)RNA	viral (m)RNA

vRNP   viral ribonucleoprotein

VP40   viral protein 40

Contents

1   Introduction

Proteins dictate the outcome of cellular processes by forming dynamic macromolecular complexes with other proteins and lipids that are vital for cell signaling, enzymatic activity, protein localization, membrane dynamics and cellular organization (1-3). These dynamic interactions are influenced by factors such as protein concentration, lipid composition and organization. Quantitative analysis methods are necessary to comprehend the mechanisms and dynamics of these interactions. While several biochemical and biophysical methods are utilized in such investigations, only a few permit the monitoring of proteins and lipids in living cells (1-3). Particularly, fluorescence microscopy and spectroscopy techniques enable the direct observation of biological processes in real-time at the cellular or molecular level and provide valuable quantitative information such as the concentration and stoichiometry of protein complexes (1-5). Pathogens exploit various biological processes and compartments within infected host cells throughout their lifecycle (6, 7). By utilizing quantitative parameters, a comprehensive understanding of the mechanisms employed by pathogenic proteins during infection can be achieved (7). This understanding enables the identification of crucial factors that can be targeted for the development of novel therapeutic approaches (7).

1.1   Fluorescence Fluctuation Spectroscopy

Fluorescence fluctuation spectroscopy (FFS) is a powerful quantitative method that utilizes statistical analysis of fluorescent signal fluctuations within a prescribed detection volume (4, 5). By analyzing these fluctuations, FFS enables the precise determination of kinetic parameters of fluorescent molecules and thereby molecular interactions (4, 5). Significant advancements in microscopy techniques, including the implementation of confocal illumination schemes, lasers with high temporal stability, objectives with high numerical aperture, and sensitive single-photon counting detectors, have enabled FFS measurements with time resolutions in nanoseconds and sub-femtoliter focal volumes (5, 8, 9). These technical breakthroughs have revolutionized FFS, allowing minimally invasive spatio-temporal measurements at the single-molecule level in living systems. The most prominent FFS approaches in cell biology are fluorescence correlation spectroscopy (FCS) variants, raster scanning image correlation spectroscopy (RICS) and number and brightness analysis (N&B) (5, 9, 10).

1.1.1   Basic principle of fluorescence (cross)correlation spectroscopy

FCS was initially developed in 1972 to study binding dynamics of ethidium bromide to DNA (11). Subsequently, it was successfully employed to monitor the lateral diffusion of concanavalin A receptors and lipid analogues in the plasma membrane (PM) of myoblast cells (12, 13) as well as lipid analogues in planar lipid bilayers (14). To obtain quantitative information

from fluctuations, a high numerical aperture objective focuses the excitation laser into the cell (i.e, for point FCS (pFCS): single spot is positioned in the cytosol) (Figure 1) (9, 15, 16).
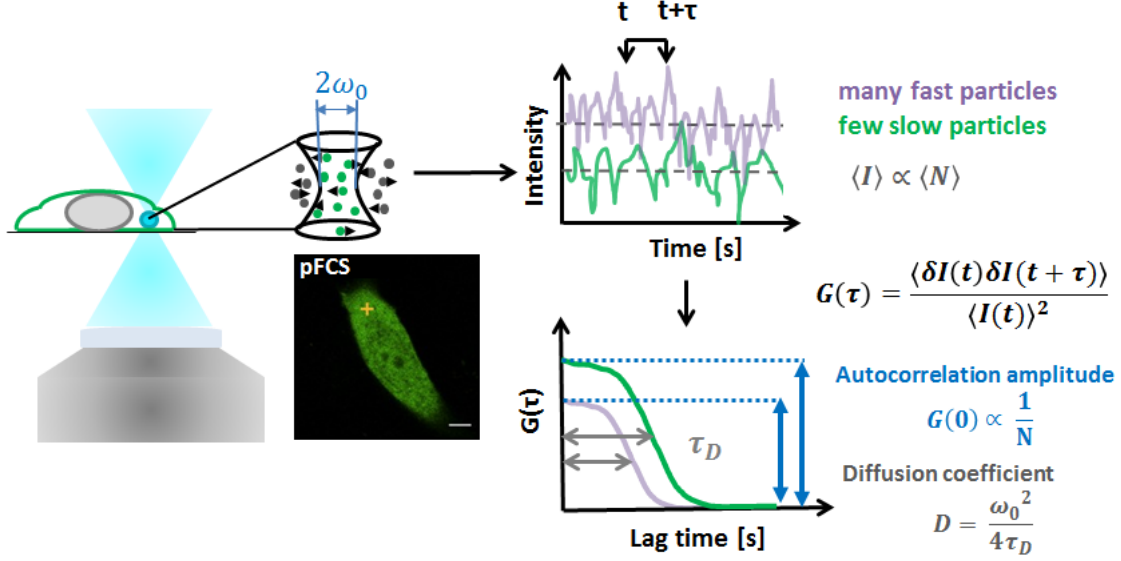
Figure 1 Schematic principle of confocal point fluorescence correlation spectroscopy (pFCS). The focused laser beam scans a single point in the cytosol of the cell, where green fluorescent proteins (FPs) diffuse in and out through the confocal volume causing a rise to fluorescence fluctuations. The mean intensity and fluctuation frequency of a system tend to increase with the presence of numerous fast-moving objects, while the opposite is observed with the presence of a small number of slow-moving particles. From the resulting intensity trace, the autocorrelation function ($G(\tau)$), which represents the self-similarity of the signal, is calculated and fitted to a two-dimensional diffusion model in order to obtain diffusion time (τ_D, half-maximum decay of $G(\tau)$) and the concentration of the diffusing particles (N, from the $G(\tau)$ at time zero). An increase of τ_D is associated with slower motion and a decrease of the $G(\tau)$ amplitude corresponds to an increase of N. Adapted from (5).

A burst of photons are emitted when fluorescent particles pass through the observation volume, which are recorded over time. The resulting fluctuating intensity traces contain valuable information about photophysical processes (i.e., photobleaching, triple state formation and blinking) and variation in the particle number due to their Brownian motion (9, 15, 16). The average fluctuation provides the fluorophore concentration, while the average burst frequency reflects the diffusion time of the fluorophores (9, 15, 16). The latter parameter can be influenced by multiple factors such as the molecular mass/ hydrodynamic size of the particle, viscosity of the system and temperature (9, 15, 16). From the intensity trace, the autocorrelation function (ACF) can be calculated by comparing the fluctuating signal at time t and at time $t + \tau$, which is proceed with multiple lag times τ (8, 9, 15, 16). The product is averaged over all times and divided by square of their average fluorescent signal $\langle I(t) \rangle$ (8, 9, 15, 16). Therefore, the ACF measures the self-resemblance of a signal over time and can be written as:

$$G(\tau) = \frac{\langle \delta I(t) \delta I(t+\tau) \rangle}{\langle I(t) \rangle^2}, \qquad (1)$$

where the fluorescence fluctuations $\delta I(t)$ are defined as the deviations of the fluorescent signal $I(t)$ from the temporal mean fluorescence $\langle I(t) \rangle$ (8, 9, 15, 16):

$$\delta I(t) = I(t) - \langle I(t) \rangle. \qquad (2)$$

In case of short lag times, fluorophores within the observation volume do not undergone substantial movement, resulting in minimal changes in the intensity signal (8, 17). Consequently, the intensity trace exhibits a high degree of self-similarity, and the ACF yields a large sum and high amplitude for small lag times (8, 17). As lag time intervals increases, fluorophores tend to diffuse beyond the boundaries of the detection volume (8, 17). Consequently, the self-similarity of the intensity trace diminishes, leading to a gradual decay in the ACF towards zero (8, 17). The decay time determined from the inflection point of the ACF, known as the diffusion time (τ_D), serves as a measure of the diffusion coefficient D of the fluorophores (8, 17). Therefore, the width of the ACF is inversely proportional to the diffusion coefficient (8, 17, 18). The diffusion coefficient D is also related to the beam waist ω_0 of the excitation light and is defined as:

$$D = \frac{\omega_0^2}{4\tau_D},\qquad(3)$$

where the beam waist ω_0 is the ratio between the axial dimension z_0 and the shape factor of the confocal volume S (8, 18).

Assuming that (i) the number of particles N within the detection volume follows Poisson distribution, where the mean and the variance of the fluctuating molecules are equal, and (ii) the intensity is proportional to the number of molecules in the detection volume, the zero-lag amplitude $G(0)$ of the ACF provides an estimate of the average number of the observed particles and can be mathematically expressed as follows (17):

$$G(0) = \frac{\langle \delta I^2 \rangle}{\langle I \rangle^2} = \frac{\langle \delta N^2 \rangle}{\langle N \rangle^2} = \frac{1}{\langle N \rangle}.\qquad(4)$$

Consequently, the number of molecules is inversely proportional to the amplitude of the ACF (17). This implies, a higher amplitude corresponds to a smaller number of observed molecules, while a lower amplitude indicates a larger number of molecules being sampled.

The commonly used method, pFCS, is effective for measuring fluorescence fluctuations in homogeneous solutions and the cytosol (5, 18). However, it does have limitations. One major drawback is the lack of spatial information, as pFCS measures fluctuations in a small volume at a specific position within the cell (5, 18). Another limitation is the significant photobleaching that can occur in systems with slow dynamics, such as biomembranes, due to continuous illumination (5, 18). To overcome these limitations, alternative FCS modalities, such as scanning FCS (sFCS), have been developed (5, 18-21). In sFCS, the observation volume is moved through the sample at a controlled speed and frequency (i.e., performed as a linear scan perpendicular to the cellular membrane), providing both spatial and temporal information about intensity fluctuations (5, 18). This approach enables the correction of lateral movement of cells and allows for extended acquisition times required for investigating slow diffusion dynamics (5, 18, 21).

FCS holds tremendous potential for analyzing the dynamics and concentrations of labeled molecules both *in vitro* and *in vivo* (5). However, to observe interactions between different molecular partners, a significant difference in mass is required to detect interactions of two or more molecules (5). This gap has been bridged by the advancement of FCS to include multi-

ple spectral channels, leading to the development of fluorescence cross-correlation spectros-copy (FCCS) by Schwille et al. in 1997 (22). In two-color FCCS, fluorescence fluctuations from two spectrally separated observation volumes are recorded and analyzed using their ACFs and cross-correlation function (CCF) (Figure 2) (5, 8, 16).
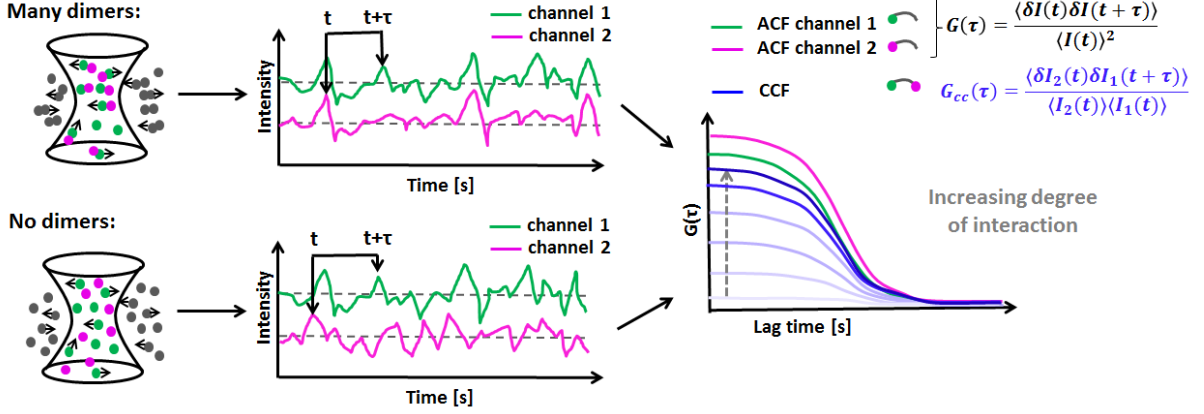
Figure 2 Schematic principle of two-color confocal fluorescence cross-correlation spectroscopy (FCCS). In FCCS analysis, two different FPs with distinct spectra, such as green and magenta, are employed to represent the presence and the absence of dimerization. Each FP will produce fluctuating signals and their autocorrelation function (ACF) will be calculated as shown in Figure 1. The interaction between two different FPs is determined by calculating the cross-correlation function (CCF) between the two intensity traces, which represents the similarity between the two signals. The CCF fitted to a two-dimensional diffusion model (represented in blue). The amplitude of the CCF will rise then many molecules interact (many dimers: dark blue), while the opposite is observed for non-interacting molecules (no-dimer: light blue). Adapted from (16, 23).

In spectral cross-correlation analysis, the focus is on analyzing the similarity between fluctu-ating signals from each fluorophore, I_1 and I_2, rather than examining the self-similarity of the fluctuation signals from a single fluorescent species (5, 8, 16). Therefore, the CCF is calculat-ed analogously to ACF:

$$G_{cc}(\tau) = \frac{\langle \delta I_2(t)\delta I_1(t+\tau)\rangle}{\langle I_2(t)\rangle\langle I_1(t)\rangle}. \tag{5}$$

The resulting function gives information about the similarity of the two signals at different time delays. If the two fluorophores are linked or interacting, their signals will show a positive cross-correlation, indicating that they are moving together through the detection volume (17, 23). On the other hand, if there is no interaction or correlation between the two fluorophores, the cross-correlation curve will be close to zero (17, 23). The ratio of the amplitude of the cross-correlation curve to that of the autocorrelation curves can be used as a measure of the binding affinity between the two fluorophores (17, 23). A higher ratio indicates a stronger interaction or binding between the two species (17, 23).

Overall, these advancements in FCCS offer enhanced capabilities for studying of hetero-molecular interactions and movements (5, 16, 18). Therefore, this technique provides valuable information about the behavior and binding properties of different fluorophores, thereby ena-bling a deeper understanding of complex biological processes. The implementation of genet-

ically encoded fluorescent proteins (FPs) as protein tags has played a crucial role in advancing the field of FCCS studies. This combination has enabled the direct quantification of bio-molecular interactions within living cells. Compared to other techniques like fluorescence recovery after photobleaching (FRAP), F(C)CS has gained popularity in cellular applications due to its ability to operate at low, sub-micromolar concentrations (15, 18). These concentrations align with the endogenous levels of many cellular molecules, minimizing perturbations and ensuring compatibility with delicate systems such as lipid membranes (15, 18). Additionally, the use of lower excitation power further reduces potential disturbances, such as fluorescence contamination or laser-induced heating (15, 18). The principles underlying FCCS can be extended to other FFS techniques, including two-color RICS and two-color N&B analysis (15, 18).

### *1.1.2 Basic principle of image based fluctuation spectroscopy analysis*

RICS is a technique that falls under the category of image correlation spectroscopy (ICS), where spatial autocorrelations are obtained from time-series image data (8, 10, 18, 24). RICS takes advantage of the hidden temporal structure within a single frame obtained via raster scanning to determine fast transport dynamics (Figure 3) (10, 18). The RICS correlation function is calculated by comparing the intensity fluctuations at different positions within the image frame (10, 18, 24). This is done by analyzing the temporal correlation between adjacent pixels in a line and successive lines (10, 24). While the position along the horizontal direction changes linearly with time at a constant speed (typically at a μs time scale), the vertical motion is adjusted according to the line time (normally at ms time scale) (10, 18). The scanning beam introduces spatial correlation, which can be utilized to generate diffusion and concentration maps over the cell (18, 24). This is a key advantage of RICS over traditional FCS techniques.

In RICS, the concept of spatial autocorrelation is akin to the time-dependent ACFs obtained from FCS analysis, but it focuses on correlations between different spatial points within the image data (8, 18). The fluctuations in fluorescence intensity at each pixel are analyzed using the spatial ACF, that correlates the intensity fluctuations at each pixel with the intensity fluctuations at a shifted point in the same image (8, 10, 18, 24).

The spatial ACF is defined as

$$G(\xi,\psi) = \frac{\langle \delta I(x,y)\delta I(x+\xi,y+\psi)\rangle}{\langle I(x,y)\rangle^2}, \tag{6}$$

where $I(x,y)$ is the fluorescence intensity of an image at the pixel position xy, the fluorescence fluctuations $\delta I(x,y)$ is deviation of the local fluorescence intensity $I(x,y)$ and the spatial average $< I(x,y) >$, ξ and ψ represent the spatial increments in the x and y space and can be characterized as the fast and slow direction, respectively (8, 10, 24). The angle brackets indicate an averaging over all coordinates of one image (8, 10, 24). The amplitude of the ACF reflects the similarity of fluorescence signals over different shifts data (10, 25, 26).
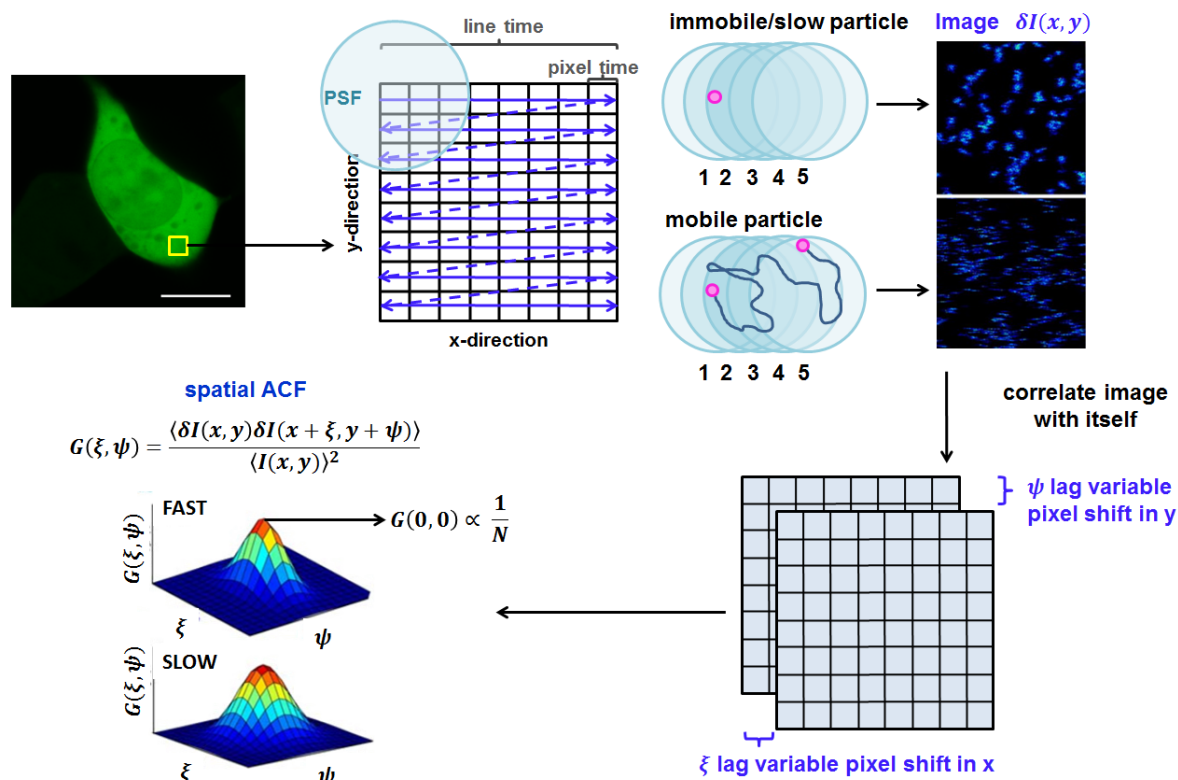
Figure 3 Schematic principle of raster scanning image correlation spectroscopy (RICS). In RICS, the intensity data from an intracellular area is collected as sequence of neighboring pixels. The graphical representation of a raster image comprises also temporal information due to the pixel-by-pixel and line-by-line scanning. As particles move and pixel positions change, only those molecules capable of sufficient speed will be observed at a distant pixel within the same image frame. For example, immobile or slowly moving objects will be only detected at position 1 to 3 during the scan. For faster moving particles, it is likely to record also signals at position 4 and 5. The spatial autocorrelation function $G(\xi, \psi)$ is calculated from the image by applying a multiplying-shift operation to the image, which analyses the fluctuating signals at each pixel and correlate them with the obtained values from a shifted pixel in the same pixel. The autocorrelation function represents the self-similarity of an image. Similar to FCS (Figure 1), a rise in the zero-shift amplitude of the RICS autocorrelation is reciprocal to the number of particles N. A higher width of the RICS autocorrelation corresponds to slower motion. Adapted from (26, 27).

A high amplitude indicates that the signals are relatively similar for short shifts, while a decrease in amplitude indicates dissimilarity for larger shifts (10, 25, 26). Similar to FCS, the zero-shift amplitude $G(0,0)$ of the ACF provides information about the average number of particles (N) within the observation volume (point spread function, PSF) and can also reveal details about fluorescent molecule concentrations and brightness (10, 18). For immobile or slowly moving particles, there is a superposition of the PSF between adjacent points, leading in a correlation of intensities at those points (25-27). For example, in Figure 3, signal can be detected in the PSF 1-3 but not 4-5, leading to a high similarity between PSF 1 to 3 and low at PSF 4 and 5. In the case of fast-moving particles, if the distance between points is smaller than the PSF width, there may still be some correlation due to diffusion of the particles to adjacent points (25-27). Consequently, random diffusion and longer time intervals decrease correlation at shorter spatial scales but increase correlation at distant pixels (25-27). Therefore, the spatial correlation of particles reflects the extent of PSF superposition and molecular

diffusion to nearby points (10, 18, 25, 26). Notable, the horizontal ACF captures pixel-pixel correlation, which is sensitive to fast moving particles, but less responsive to slow moving objects conversely to the vertical ACF, which provides line-to-line correlation (25, 27).

The N&B analysis is widely employed to determine the oligomerization state of proteins and protein concentration within a cell, including its sub-compartments (18). Unlike other techniques mentioned earlier, N&B does not provide information about the diffusion properties of the system (9). This method relies on the moment analysis of the fluorescence intensity distribution (Figure 4) (18). By calculating the first two moments, referred to as the average intensity and variance of the intensity distribution at each pixel from a time-series of images, a spatial map illustrating the distribution of protein oligomerization and aggregates as well as number of particles is generated (9, 18). The average fluorescence intensities $\langle I \rangle$ and variance σ^2 at each pixel in a time series of K are determined and used to calculate the average apparent brightness B and apparent number of emitting molecules N (28, 29). Assuming that the occupation number follows Poisson distribution, the average fluorescence intensity $\langle I \rangle$ is equal to the product of the average number of emitting particles n and their molecular brightness ε (28, 29). These can be expressed as follows:

$$\langle I \rangle = \frac{\sum_i I_i}{K} \qquad (7) \qquad\qquad \sigma^2 = \frac{\sum_i (I_i - \langle I \rangle)^2}{K} \qquad (8)$$

$$B = \frac{\sigma^2}{\langle I \rangle} = \varepsilon + 1 \qquad (9) \qquad\qquad N = \frac{\langle I \rangle^2}{\sigma^2} = \frac{\varepsilon n}{\varepsilon + 1} \qquad (10)$$

Here, the brightness provides information about the property of each fluorophore whereas the intensity is the sum of all contributions overall fluorophores (29). Additional, the apparent brightness B is related to the molecular brightness ε, but is independent from the number of molecules n (28). The same relationship to the molecular brightness can be also applied to the previous mentioned methods, FCS and RICS, in order to gain information about protein-protein interactions (18).

Information about the oligomeric state of a protein of interest can be achieved by calculating the ratio of the obtained molecular brightness ε_n of the protein and the molecular brightness ε_1 of the monomeric reference protein (18). Considering that not all FPs emit light simultaneously due to various photophysical processes, such as long-lived dark states, FP maturation time, and folding prone intermediates, the molecular brightness has to be corrected by these factors (32). All the artefacts are summarized in on single parameter, referred as apparent fluorescence probability p_f, and used as correction factor (32). Consequently, the effective measured brightness for an oligomer of size η can be calculated as follows:

$$\eta = 1 + \frac{\frac{\varepsilon_\eta}{\varepsilon_1} - 1}{p_f}. \qquad (11)$$

In contrast to fluorescence-based techniques like Förster resonance energy transfer (FRET) or bimolecular fluorescence complementation (BiFC), fluorescence fluctuation spectroscopy

offers the advantage of providing information about the size of the complex (23). Additionally, it is less reliant on the precise labeling position of the fluorophores (23).
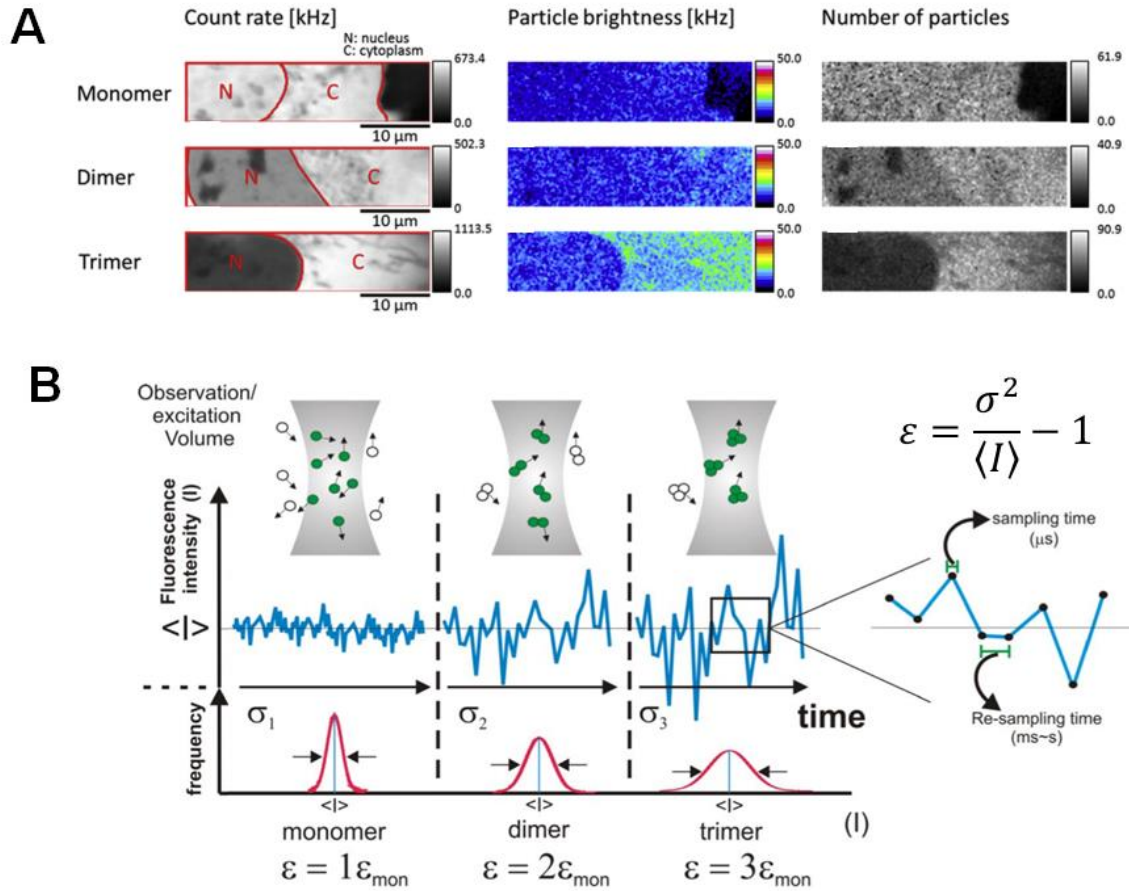
Figure 4 Schematic principle of number and brightness (N&B) analysis. (A) Shows obtained maps from the N&B analysis of green FP oligomers in living cells: The intensity map (left panel), the molecular brightness map (middle panel) and the concentration map (right panel). The intensity and the number of particles are proportional, while the molecular brightness remains independent from the particle number. Specifically, high intensity values and particle numbers do not necessarily lead to higher brightness values (see maps for the dimer). The brightness provides information about the property of each fluorophore and will, therefore rise with the oligomeric state of a protein. Higher oligomeric protein states are excluded from the nucleus. N: nucleus; C: cytoplasm. Adapted from (30). (B) Schematic principle of the molecular brightness analysis to extract information about protein oligomerization. From top to bottom: observation volume with diffusing green fluorescent protein oligomers, corresponding intensity and intensity distribution. A similar number of molecules in the observation volume are illustrated for all oligomeric states, which results in the same average intensity for variants but they differ in their variance. Monomers exhibit minor fluctuations over time, while broader fluctuations are observed as molecules undergo oligomerization. Signal intensity changes in a monomer are solely influenced by individual molecules diffusing through the observation volume. For higher oligomers, multiple molecules simultaneously diffuse through the observation volume, leading to stronger fluctuations in signal intensity compared to the average intensity. Consequently, the variance or strength of these fluctuations provides valuable information about the number of fluorescent units in an oligomer. As molecules continue to oligomerize and fluctuations further broaden, the brightness increases proportionally to the level of oligomerization. For example, the average brightness of a dimer will be twice that of a monomer, and the average brightness of trimer will be tripled and so on. Adapted from Adapted from (31).

1.2 Fluorescence microscopy techniques to study membrane heterogeneity

Biological cells are enclosed by lipid membranes that separate them from the external environment (33-36). These membranes are highly complex, consisting of various lipids and proteins that play crucial roles in cellular functions such as adhesion, ion conductivity, and cell signaling (33-36). Membranes are not just passive barriers but also active participants in cellular processes (34). A high majority of proteins are embedded in membranes or associated with membranes through various interactions (i.e. lipid-protein and protein-protein interactions) (34). The physicochemical features of the lipid bilayer, such as viscosity and permeability, are essential for proper cellular function (34).

Biomembranes exhibit lateral heterogeneity at the submicrometer scale, with specific lipids driving the formation of functionally important membrane regions known as lipid rafts (Figure 5) (34-36). These rafts are ordered domains, enriched in cholesterol, saturated lipids, and glycosylated lipids, that exist in both the inner and outer leaflets of the asymmetric cell membrane (34-36). These domains are believed to be coupled across the leaflets (35). Experimental evidence using model membrane systems, such as supported lipid bilayers (SBLs) and giant unilamellar vesicles (GUVs), has supported the existence of these domains and their roles in cellular processes such as fluidity, permeability, curvature, and lateral compartmentalization (34, 35). In particular, these studies demonstrated the separation of membranes into distinct liquid phases, with one phase enriched in saturated lipids, cholesterol, and glycosylated lipids, and the other phase enriched in unsaturated lipids, known as the fluid liquid disorder (L_d) phase (35, 36). The tightly packed phase enriched in saturated lipids and cholesterol, known as the liquid ordered (L_o) phase, is considered to be the model for lipid rafts (35, 36). This phase separation is driven by lipid-lipid and lipid-protein interactions, which contribute to the formation of lipid raft domains (35, 36). However, studying natural systems like biological membranes presents challenges due to their complexity (35).

One approach to studying membrane dynamics and lipid phase separation in a more physiologically relevant system is the use of giant plasma membrane vesicles (GPMVs) (35, 36). GPMVs are derived from PM of cells and preserving to a great extent the compositional lipid and protein diversity of the native cell membranes (35, 40, 41). They have shown to be an effective model to provide insights into the molecular details of lipid rafts formation (35, 41). However, direct microscopic detection of lipid rafts in live cells remains a challenging due to spatial and time resolution limits (35, 41).

Over the last years, advanced fluorescence microscopy and spectroscopy have revolutionized the study of lipids and membranes. Techniques such as confocal microscopy, FRAP, FCS, FRET, and total internal reflection fluorescence (TIRF) have enabled the investigation of lipid dynamics on various timescales (36, 42, 43). These techniques have revealed the formation of nanoscale clusters and dynamic domains of lipid-modified proteins (36). FPs have further enhanced the study of membranes, allowing visualization of proteins in their native environment (35).
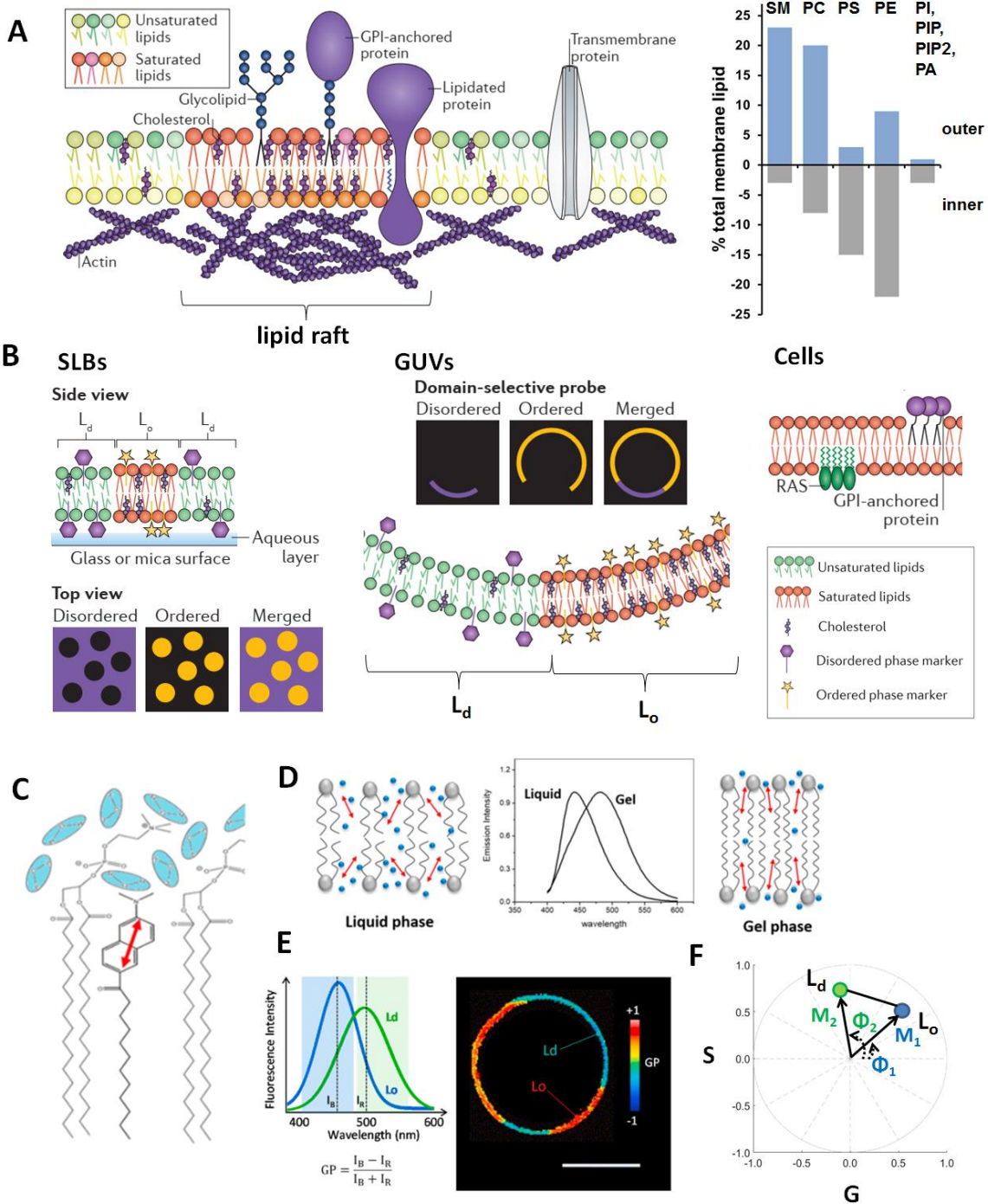
Figure 5 Overview of the plasma membrane organization and compostion, model membrane systems and fluorescent reporter molecules. (A) Schematic representation of lateral lipid membrane heterogeneity. Lipid rafts are tightly packed, highly ordered plasma membrane (PM) regions, which are enriched with saturated phospholipids, nonglyceride lipds (steroids and sphingolipids), glycolipids, lipidated and GPI-anchored proteins. Lipids in the PM are asymmetric organized in both, inner and outer leaflet, which is depicted in the plot. Sphingomyelin (SM) and phosphocholine (PC) species are mainly in the outer leaflet, whereas phosphatidylserine (PS) and phosphoethanolamine (PE) most common in the inner leaflet. Other phospholipids, such as phosphatidic acid (PA) and phosphatidylinositol (PI) species, were present in minor quantities on both sides of the membrane. Adapted from (35, 37) (B) Model membrane systems and fluorescent sensors used to investigate membrane heterogeneity and dynamics. Model systems usually used to visualize lipid phases include supported lipid bilayers (SLBs), giant unilamellar vesicles (GUVs) or whole cells. SLBs (left panel) are adsorbed on a solid planar surface, which provides mechanical stability and two-dimensional lateral fluidity.

Figure 5 (continued) Bias caused by the solid support in SLBs can be avoided by using stand-alone membranes such as GUVs. They are often used to study effects of membrane curvature and crowding. Both artificial membrane systems are preferred for phase separation studies. More physiological relevant are measurements in whole cells. All membrane model systems can be labelled with L_o and L_d-specific fluorescent lipid probes, phase sensing probes or FP sensors (i.e. GPI-anchored proteins for the outer leaflet and Ras proteins for the inner leaflet). These probes allow a mapping of lipid membranes and a quantification of local membrane dynamics. Adapted from (35). (C) Incorporation of the solvatochromic lipid probe Laurdan into the membrane interphase. Red arrow represents the orientation of the fluorophore. Taken from (38). (D) Orientation of Laurdan inside L_d phase (= liquid phase) and L_o phase (= gel phase), depicted as red arrows, surrounded by water molecules (blue spheres). Spectrum shift is introduced by the reorientation of the water molecules. Taken from (38). (E-F) Phase separation studies are analyzed either via generalized polarization (GP) approach (E) or spectral phasor plot (F). Fluorescence spectra can be separated into two single wavelength or wavelength ranges (L_o shown in blue and L_d in green) for determine the ratiometric GP value, here represented in phase separated GUVs, or the entire spectra is used to generate a spectral phasor plot. The latter is represented as vectors of length (=modulus [M]) and phase angle (ϕ), which are correspond to the spectrum width and the maximum emission wavelength. For example, phase moves counterclockwise upon red-shift (ϕ increases) and closer to plot center then the width increases (M decreases). Taken from (39) and modified from (38).

The use of membrane-associated fluorescent peptides has revolutionized the field of cell biology, enabling researchers to study various aspects of membrane dynamics, lipid-lipid packing, and interleaflet coupling. Membrane markers, such as myristoyl/palmitoyl (mp)- and geranyl-geranyl (GG)-lipid chain peptides, as well as glycosylphosphosphatidylinositol (GPI)-anchors, have been extensively utilized in FFS to investigate the behavior of the inner and outer leaflets of the PM. The mp- and GG-lipid modification on peptides enabled the visualization of protein localization and quantification of protein dynamics within specific PM regions of the inner leaflet (20, 35, 44, 45). Similarly, the GPI-anchor is another marker frequently employed to study lateral organization of lipids in the outer leaflet of the PM (35, 45). By utilizing FFS techniques, they observed changes in protein diffusion coefficients, indicating alterations in membrane fluidity and lipid packing. Therefore, they can serve as reliable markers to probe lipid-lipid interactions, lipid domain formation and lipid-driven interleaflet coupling (35, 45). However, the use of FPs enhanced our knowledge of membrane protein dynamics, but lacking direct information of functional lipid dynamics (35, 42). Therefore, several fluorescent probes, including phase-specific and phase-sensitive lipid analogs, have been engineered in the past few years to study lipid dynamics using fluorescence-based methods (35, 38, 39).

The photophysical behavior of phase-specific analogs is determined by their preference for one domain over another (42). Organic dyes are linked to lipids, such as cholesterol, and phospholipids, and then incorporated into cell membranes (42). The majority of such dyes have a higher quantum efficiency and brightness compared to FPs (42). The reliability of the lipid analogs heavily relies on the selection of both the lipid species and the fluorescent dye (35, 42). The wide range of membrane compositions and physical properties observed in various cell types as well as during physiological process indicates the existence of diverse packing states within living cells (35, 42). To quantify this lipid packing, phase-sensitive lipid analogs, such as Laurdan and Di-4-ANEPPDHQ, can be employed (35, 38, 39, 42). These analogs exhibit changes in their photophysical properties depending on the lipid environment they are in (35, 38, 39, 42). They have the ability to effectively penetrate lipid membranes and provide insights into various physical properties, such as lipid phase order, lipid packing,

membrane tension and hydration (35, 42, 46-49). Upon internalization into the lipid order region, both Laurdan and Di-4-ANEPPDHQ experience a spectral shift due to changes in their local environment (35, 38, 39, 42). In particular, the shift is attributed to the reorientation of water molecules surrounding the dyes within the L_d phase. This reorientation alters the dye's electronic environment, resulting in a shift towards longer wavelengths, known as a red shift (35, 38, 39, 42). On the contrary, when polar-sensitive dyes are internalized into L_o phases, they exhibit a blue-shift in their emission spectra (38, 39, 42). These spectral shifts are usually quantified by a generalized polarization (GP) approach (Figure 5E). The GP values are calculated by using the fluorescence intensities I of dye-specific wavelengths λ or wavelength ranges, which represent the two lipid phases (42, 50, 51). Equation for the single wavelength (Equation 12) and spectral range (Equation. 13) analysis are:

$$GP = \frac{I_{\lambda L_o} - I_{\lambda L_d}}{I_{\lambda L_o} + I_{\lambda L_d}} \qquad (12) \qquad GP = \frac{\sum_{\lambda_{min}}^{\lambda_{max}} I_{\lambda_i L_o} - \sum_{\lambda_{min}}^{\lambda_{max}} I_{\lambda_i L_d}}{\sum_{\lambda_{min}}^{\lambda_{max}} I_{\lambda_i L_o} + \sum_{\lambda_{min}}^{\lambda_{max}} I_{\lambda_i L_d}} \qquad (13)$$

The spectral imaging approach and detection in the photon-counting mode were shown to provide more information and to improve the accuracy and sensitivity of the measurements (52, 53). Moreover, determination of membrane fluidity via spectral acquisition allows spectral phasor analysis and has some advantages over the GP approach. Spectral phasor analysis is a fit-free model that uses the entire spectrum, rather than using a pre-defined single wavelength or small range, and transfers the spectral information to the Fourier space (Figure 5F) (38, 54). The fluorescence emission spectra from each pixel within spectral images were transformed into the phasor coordinates ($G(\lambda)$ and $S(\lambda)$) as following:

$$x \; coordinate = G(\lambda) = \frac{\sum_\lambda I(\lambda) \cos(\frac{2\pi n(\lambda - \lambda_{min})}{\lambda_{max} - \lambda_{min}})}{\sum_\lambda I(\lambda)} \qquad (14)$$

$$y \; coordinate = S(\lambda) = \frac{\sum_\lambda I(\lambda) \sin(\frac{2\pi n(\lambda - \lambda_{min})}{\lambda_{max} - \lambda_{min}})}{\sum_\lambda I(\lambda)} \qquad (15)$$

The coordinates $G(\lambda)$ and $S(\lambda)$ represent the real and imaginary component of the Fourier transformation, respectively. $I(\lambda)$ is the intensity for each wavelength and n is the harmonic number (38, 54, 55). The first harmonic is preferred for interpreting phasor locations and visual characteristics when the spectral contribution spans the full wavelength range and the spectral components have distinct emission wavelengths (55). However, at the shortest wavelengths, phasors can become distorted due to the limited data points in that region (55). On the other hand, the second harmonic is useful for decomposing spectral species with narrowly spaced emission wavelengths, and is less susceptible to bias at the shortest wavelengths (55). However, when the spectral components are far apart across the wavelength range, visual interpretation of the data can be more challenging due to the "wrap-around" effect in the phasor plot (55).

The x- and y-coordinates were then plotted in the four-quadrant spectral phasor plot as previously described (38, 54, 55). The coordinates G(λ) and S(λ) take values between 1 to -1. Their angular position in the phasor plot is proportional to the center of mass and the phasor radius is inversely proportional to the full width at half maximum (FWHM) of the emission spec-

trum (55). For instance, one spectrum has the same FWHM but is blue-shifted, meaning it has a different center of mass (55). Then, the position of the points will be rotated anti-clockwise toward the coordinates (1,0) in the same circle of the phasor plot, meaning the phasor angle will decrease (55). On the other hand, the radial position depends on the FWHM of the spectrum (55). Has a spectrum a broader width but the same center of mass, then, the points will move closer to the center of the phasor plot, meaning the modulus is decreasing (55).

In conclusion, fluorescent reporter molecules and biophysical fluorescence microscope approaches can increase our understanding of lipid phase separation and its potential roles in various cellular processes such as virus entry and assembly, tumorigenesis, and membrane trafficking.
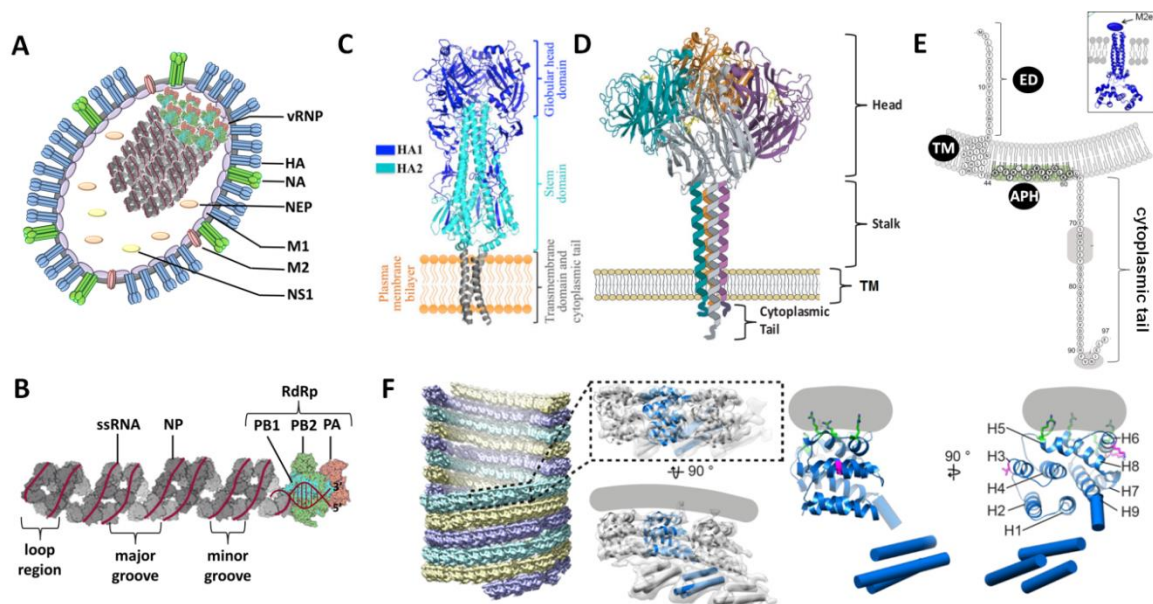
1.3 Influenza A virus

Influenza, caused by different types of influenza viruses, is a highly infectious disease that ranges from mild illness to severe complications and death (56-60). Each year, influenza epidemics cause hundreds of thousands of deaths worldwide (61, 62). Influenza A and B viruses cause yearly epidemics with significant morbidity, mortality, and economic losses (57, 59, 63, 64). Influenza C viruses cause milder respiratory disease (57, 65). Certain populations, such as those with underlying health conditions and the elderly, are at higher risk for severe complications (56, 58, 66). The clinical outcome of an infection depends on both the intrinsic properties of the virus and the pre-existing immunity of the infected individual (56, 58, 67). Influenza A viruses (IAVs) are of particular concern as they circulate in both humans and animals, leading to frequent epidemics and occasional pandemics (64, 68). Novel zoonotic IAVs periodically emerge from animals, such as swine or birds, through genetic reassortment (64, 68-70). These outbreaks can lead to unpredictable pandemics with increased infection and mortality rates (62, 64, 67-71). Vaccination and antiviral drugs are used for prevention and control influenza infections, but influenza viruses can evolve and develop resistance (61, 71, 72). Antigenic drift and shift allow the viruses to escape control measures (61, 64, 71, 72). As a result, the annual vaccine needs to be updated to match the circulating strains (61, 64, 71, 72). While the annual influenza vaccine is the most effective, new therapeutic strategies are needed (61, 64, 71, 72). Current antiviral drugs have limitations due to the emergence of drug-resistant strains (61, 64, 71, 72). Therefore, finding new approaches and understanding viral control mechanisms are crucial in combating influenza. Biophysical and molecular biology methods promise substantial progress in the discovery of intracellular mechanisms of influenza virus replication and assembly.

1.3.1 Structure and components of Influenza A virus

IAVs belong to the family of the *Orthomyxoviridae* and are pleomorphic, as they show spherical as well as filamentous shapes (6, 73, 74). IAV is enveloped with a lipid bilayer that is derived from the host cell membrane, in which two transmembrane glycoprotein spikes (he-

magglutinin, HA, and neuraminidase, NA) and a proton channel (matrix protein, M2) are incorporated (Figure 6) (6, 71, 73, 75). The major surface protein of IAV is homotrimeric HA with an abundance of approximately 80 % followed by homotetrameric NA (up to 17 %) (71, 73, 76).

Figure 6 Structure of Influenza A viruses (IAV) and of the viral proteins. (A) Schematic representation of an IAV particle. IAV is enveloped by a host‑derived PM containing two transmembrane glycoproteins (hemagglutinin (HA), neuraminidase (NA)) and one proton channel protein (matrix protein 2 (M2)). Beneath the lipid layer forms matrix protein 1 (M1) a tight layer, which connects the viral envelop with the eight vRNPs. Furthermore, the virion core consists a small amount of two other viral proteins: nuclear export protein (NEP) and non-structural protein 1 (NS1). (B) Enlargement of a vRNP segment from (A). Each vRNP contains a negative-sense, single-stranded RNA, which is covered with multiple copies of the nucleoprotein (NP), and a single heterotrimeric RNA dependent RNA polymerase (RdRp) complex (composed of PB1, PB2 and PA), which is associated to the panhandle structure at the 3'- and 5' termini of the RNA. The vRNPs forms a antiparallel double-helical structure, with a loop at one end (modified image from (54). (C) Schematic representation of the structural features of the trimeric HA within a membrane bilayer (PDB code: 3LZG). The trimer contains the N-terminal HA1 globular head group (colored in blue) with the receptor-binding site, the HA2 stem region (colored in turquoise) with the fusion peptide, the transmembrane domain and the C-terminal short cytoplasmic tail (~ 12 aa). Taken from (78). (D) Schematic representation of the structural organization of the tetrameric NA within a membrane bilayer. The individual monomers of NA are shown in pseudocolor. The monomer is composed of four unique structural domains, namely the C-terminal catalytic head, the stalk, the transmembrane region (TM), and the very short N-terminal cytoplasmic tail (~ 5 aa). To this date, only the head domain of NA has been structurally resolved (PDB code: 4GZX), while the remaining portions are represented as alpha-helices in depictions. Modified from (79). (E) Structural arrangement of M2 within a membrane bilayer. Schematic representation of the different domains of a monomeric M2 shows the short N-terminal ectodomain (ED, ~25 aa) and transmembrane domain (TM, ~18 aa) as well as the long C-terminal domain (~ 57 aa) including the membrane-interacting amphipathic helix (APH). Regions which are suggested to play for the interaction with M1 (residues 71-76) and LC3 (residues 91-94) are indicated with gray shading. The section on the upper right shows a structural model of a tetrameric M2. Modified from (80, 81). (F) Structural organization of M1 within filamentous influenza virus like particles (VLPs) obtained from electron cryotomography analysis. M1 is tightly packed and forms a helix array which arranged into three parallel strands (shown in pseudocolor). The enlarged section shows that the M1 protein layer forms a two-lobed structure and is tightly attached to the inner leaflet of the membrane bilayer (grey). The model of the M1 monomer shows the arrangement of the alpha-helices (H) and the interaction of the positively charged residues (green) inside the N-terminal domain (located in H5, H6 and H8) with negatively charged phospholipids at the inner leaflet. Residues at the inter-strand interface which can alter the virion morphology are shown in magenta. Taken from (82).

Additionally, only a small amount of homotetrameric M2 is embedded in the envelope (approximately 16 to 20 molecules) (76). HA plays a major role in viral entry by mediating the attachment of the virus to cell surface sialic acid molecules, membrane fusion after internalization, and the release of viral genome into target cells (6, 64, 73, 76, 77). Whereas NA facilitates the release and spread of the newly synthesized virus particles from the PM by enzymatic cleavage of the cell surface receptor sialic acid molecules, and prevents rebinding of virions through HA and virion aggregation (6, 64, 75, 76). Lastly, M2 is critically involved in entry and budding processes of IAV, and controls the pH of the viral interior during virus genome uncoating (6, 73, 75, 76). The luminal side of the viral envelope is coated with the matrix protein 1 (M1), which forms the viral capsid in close contact to the lipid membrane and interacts with the viral genome (6, 73, 75, 76). Furthermore, M1 is important for multiple processes during viral replication including the regulation of disassembly, nuclear import and export of viral ribonucleoproteins (vRNPs), transcription and replication of viral RNA (vRNA), and, finally, transport and assembly of newly formed vRNPs, virus budding and morphogenesis (6, 75, 76). M1 is the most abundant protein within virus particles and stabilizes the 3D structure of the virus envelope (74). The viral core beneath the matrix layer contains the segmented viral genome, which is organized in eight vRNPs, and a small number of the viral nuclear export protein (NEP, also known as non-structural protein 2 (NS2)) as well as non-structural protein 1 (NS1), and some host proteins (6, 64, 73, 76). NEP mediates the export of the newly assembled vRNPs from the cell nucleus (6, 76). NS1 has multiple functions, including interaction with several host proteins, blocking host mRNA production, suppression of the host immune response, and a modulating effect on viral transcription and translation processes (6, 64, 76). Each vRNP comprises a single-stranded, negatively oriented vRNA, which is covered by several copies of nucleoproteins (NP) over their entire length, and organized in a rod-shaped structure (6, 76, 83). An additional component of the vRNP is the viral RNA-dependent RNA polymerase (RdRp) with three subunits (polymerase basic protein 1 (PB1), polymerase basic protein 2 (PB2) and polymerase acidic protein (PA)), and is associated to the partially double-stranded 5' and 3' ends of each vRNA segment (6, 76, 84).

1.3.2   Life cycle of Influenza A virus

At the initiation of infection in mammals, IAV infects epithelial cells throughout the tracheo-bronchial tree (66, 68, 73, 85). Unusual for an RNA virus, IAV replication occurs in the nucleus of their host cells, thus, vRNPs have to overcome different host cell barriers (86, 87). The replication cycle of IAV is a multistage process, which occurs in the following manner: (1) virus adsorption to the host cell, (2) internalization by receptor-mediated endocytosis, (3) endocytic transport and fusion, (4) uncoating and release of vRNPs to the cytoplasm, (5) access of vRNPs into the nucleus, (6) genome transcription and translation of viral proteins, (7) replication of the viral genome, (8) export of the vRNPs from the nucleus, (9) viral assembly, (10) viral budding at the host cell PM, and release of progeny virions (Figure 7). A large number of these processes are depending on the viral interaction with cellular factors and signaling pathways to accomplish replication (6, 76, 84, 88, 89). Interactions with the host fac-

tors exert a high selection pressure on influenza viruses, and offers targets for the development of antiviral drugs.

The infection process of IAV begins with the attachment of the virus to host cells through viral transmembrane protein HA. The receptor binding domain of HA recognizes and binds to the terminal galactose-conjugated N-acetylneuraminic acids (also called as sialic acids) of cellular glycoproteins or glycolipids on the apical surface of respiratory epithelial cells (6, 73, 76, 84). Each host species has different types of sialic acids-galactose linkages with altered structural conformations, which determine the species specificity of IAV (6, 73, 76, 84). Avian influenza viruses preferentially bind to α-2,3-linked sialic acids, human seasonal IAV with α-2,6-linked sialic acids and IAV subtypes emerged from swine attach to both sialic acid-linkages (6, 73, 76, 84, 85). After binding to the host cell, the virus is internalized through receptor-mediated endocytosis (6, 76, 84). The internalized virus is transported through the endocytic pathway to acidic, late endosomes (6, 73, 76, 84). The low pH of the late endosomes triggers a conformational change in HA, exposing the fusion peptide and allowing the fusion of the viral envelope with the endosomal membrane (6, 73, 76, 84). The acidification of the late endosomes also activates the M2 ion channel, which acidifies the virus interior and triggers the disassociation of the matrix layer from the viral genome complex (6, 73, 76, 84). This allows the release of the viral genome into the host cytoplasm through HA-mediated fusion pores (6, 73, 76, 84). Interaction of several host factors and M1 trigger the removal of M1 from the viral genome, which results in a dissociation of the vRNP complex (6, 84, 86, 90). To enter the nucleus, the unbundled vRNPs require active, energy-driven transport mechanisms mediated by nuclear transport receptors (86, 90). Through the interaction of NP and importin proteins, unbundled vRNPs are imported into the nucleus through nuclear pore complexes (6, 84, 86, 90). Once inside the nucleus, the vRNPs are dispersed throughout the nucleoplasm (91). The exact mechanism of vRNP import, whether as separate entities or subcomplexes, is still under debate (86, 90, 91).

Viral genome replication and transcription occur in the nucleoplasm, involving host cell factors and the viral RdRp (6, 76, 84, 86, 90-92). Each parental vRNP acts as a template for viral mRNA synthesis and replication of progeny vRNPs (6, 76, 84, 86, 90-92). vmRNA synthesis relies on a cap-snatching mechanism by the RdRp, where PB2 binds to small host mRNA, PA cleaves downstream the cap, generating short RNA fragments that serve as primers (6, 76, 84, 86, 90-92). PB1 then elongates the capped primer, creating a positive strand of vmRNA (6, 76, 84, 86, 90-92). Transcription continues until a uridine sequence near the vRNAs 5' end induces PB1 stuttering, generating a polyadenylated (polyA) tail (6, 76, 84, 86, 90-92). Mature vmRNAs dissociate, splice, and bind to cellular cap-binding proteins to form vmRNPs, which move to the cytoplasm for translation (6, 76, 84, 86, 90-92). Protein synthesis occurs in early, intermediate, and late phases based on infection stage (6, 73, 93). The viral polymerase subunit proteins, NP, and NS1 are the first proteins synthesized on cytoplasmic ribosomes and then re-translocate into the nucleus, where they promote further viral transcription and replication, neutralize cellular immune responses, and induce host shut-off (6, 64, 73, 76, 93, 94). Noteworthy, previous reports suggested that PA and PB1 forming heterodimers in the cytosol and transported together into the nucleus where they interact with PB2 to form the heterotri-

meric polymerase complex (6, 95, 96). However, this hypothesis based on classic biochemical approaches and two-color FCS analysis, and the detailed mechanism behind the nuclear import remains unclear.
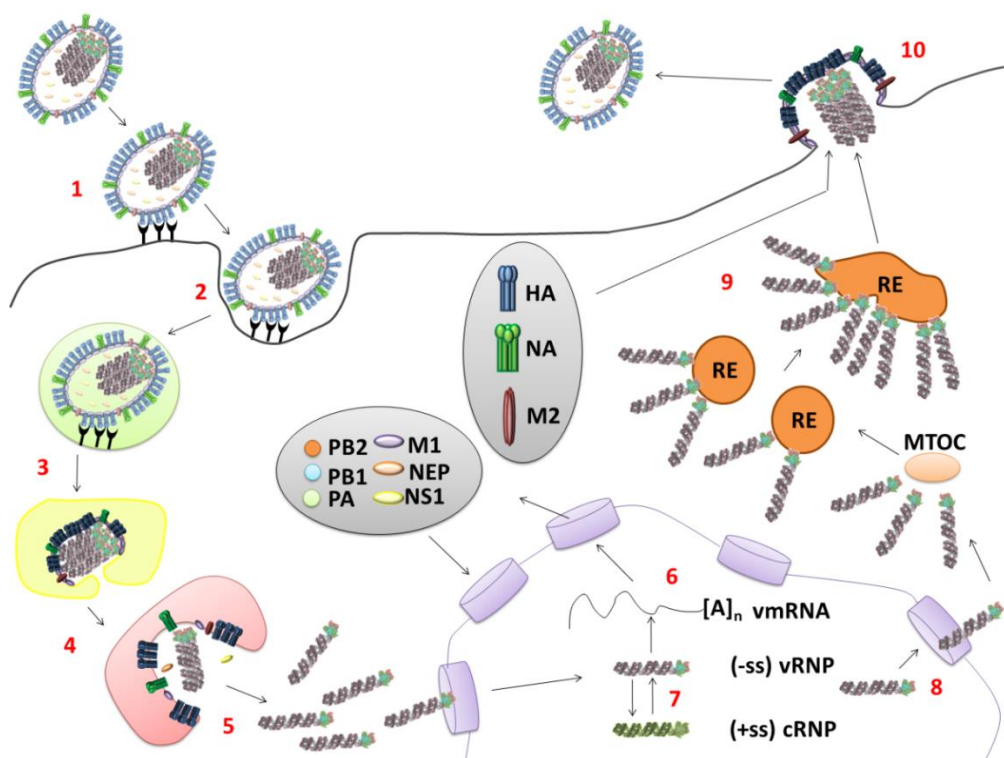

Figure 7 Scheme of the classical IAV replication cycle. (1) Cell entry of influenza virions is initiated by binding of HA to sialic acid residues on the cell surface. (2) After virus adsorption to the host cell receptor, virions internalize into the host cells mainly by clathrin-mediated endocytosis. (3) During transport of virus particles within endosomes along microtubules, the declining, luminal pH mediates conformational change in HA, which induce fusion of viral and endosomal membrane. (4) Activation of the M2 proton channel leads to a proton influx into the viral core, thus causes an acidification of the virus interior, which promotes a disassembly of M1 thereby destabilization of the viral core and dissociation of M1 from the viral genome (also known as uncoating). Furthermore, HA forms fusion pores, which is used for the vRNP release into the cytosol nearby the perinuclear region. (5) Viral genome segments enter the nucleus through nuclear pore complexes by hijacking the cellular importin-α-importin-β1-pathway. (6) Once in the nucleus, primary transcription of vRNAs results into production of vmRNAs, thus are transported into the cytosol where protein translation takes place. Early and intermediate proteins (PB1, PB2, PA, NS1, NP, M1, NEP) are synthesized on cytoplasmic ribosomes whereas late proteins (HA, NA, M2) are translated on ribosomes of the endoplasmic reticulum (ER). Early and intermediate proteins are transported back into the nucleus where they facilitate transcription, replication, formation of progeny vRNPs, and nuclear export of vRNP. (7) After an accumulation of re-imported, early proteins, transcription switches to replication. Therefore, negative-sense vRNAs are transcribed into positive-sense complimentary RNAs (cRNAs) thus are used as template for the replication of vRNAs. Both RNA species are associated with a RdRp complex and multiple copies of NP to form cRNPs and vRNPs. (8) Intermediate proteins (M1 and NEP) incorporate with newly-synthesized vRNPs to promote the recruitment of CRM1, which induces the nucleocytoplasmic transport of vRNPs through the NPC to the microtubule organizing center (MTOC). (9) Subsequently, vRNPs are transported to the apical PM on Rab11-associated recycling endosomes (RE) in a microtubule-dependent manner. Rab11-positive vesicles might be serving as a platform for vRNP packaging. Simultaneously, late proteins (HA, NA, M2) are modified and folded on the ER and trans-Golgi network, and subsequently transported to the budding sites on the cell surface by using the secretory pathway. (10) After the initialization of budding by viral transmembrane proteins, multiple segment complexes with eight unique vRNPs incorporate into emerging virions. Afterwards, M2 promotes membrane scission followed by the NA-mediated release of progeny virions from the host cell membrane.

Secondly, M1 and NEP are translated on cytoplasmic ribosomes and imported back to the nucleus to regulate RdRp activity and induce nucleocytoplasmic transport of progeny vRNPs (6, 76, 84, 90, 91, 93, 97, 98). Lastly, viral transmembrane proteins are synthesized on membrane-bound ribosomes of the endoplasmic reticulum (ER) and modified in the Golgi apparatus (6, 73, 85, 93, 99). After transcription, viral genome replication occurs in two steps. First, complementary vRNA (cRNA) is synthesized without a cap or poly(A) tail (6, 84, 85, 90, 91). These replicative intermediates are then used as templates to produce new vRNAs (6, 84, 85, 90, 91). Both cRNA and vRNA are encapsidated by NP, and associate with RdRp (6, 84, 85, 90, 91). RdRp initiates *de novo* synthesis of the first nucleotides, which are then elongated (6, 84, 85, 90, 91). The switch between viral transcription and replication is still a topic of debate. Finally, newly synthesized vRNAs are bound by NP and RdRp to form new vRNPs (6, 84, 85, 90, 91). The exact mechanism of cooperation between RdRp, NP molecules, and vRNA to achieve the final vRNP structure is still unclear.

During the late infection phase of influenza virus, newly synthesized vRNPs accumulate in the nucleus and are then exported into the cytoplasm. This export process of the vRNPs is facilitated by its interaction with several host factors, M1 and NEP (6, 84, 90, 91, 100). The nuclear export of vRNPs occurs in three stages: the release of vRNPs from chromatin, the formation of the transport complex vRNP-M1-NEP-CRM1-RAN-GTP and their translocation across the nuclear pore (6, 84, 90, 91, 100). The apoptotic pathway activation during the late infection phase enhances the diffusion capacity of the nuclear pores, promoting RNP export (100). It is still unclear whether vRNPs are translocated individually or as multiple segment complexes (MSCs) into the cytosol (100). Two models for cytoplasmic vRNP transport are described: active microtubule-dependent transport through the cytosol by Rab11a-associated recycling endosomes (RE) and transport by Rab11-positive endocytic recycling compartment (ERC) derived from modified ER tubules (6, 100, 101). On the PM, Rab11 is not detectable in progeny virions, indicating that vRNPs dissociate from Rab11 before they are transferred into the virions (90). This dissociation might be supported by interactions between vRNP components and other viral proteins (6, 90, 100, 102).

The final step in intracellular IAV infection is the assembly and budding of progeny virions (Figure 7 and 8). The assembly and budding processes are dependent on viral envelope proteins (HA, NA and M2), M1 and vRNPs, but the exact molecular mechanism is still poorly understood and subject to debate (6, 75, 90, 91, 100, 102). Budding of progeny virions occurs at the apical PM of polarized cells, necessitating the transport of viral proteins to the PM prior to assembly (6, 75, 76, 84, 91, 99, 100, 103). The viral envelope proteins (HA, NA, M2) entering the secretory pathway to the cell periphery, after their maturation in the ER and Golgi apparatus (6, 99, 100, 103). During their passage through the rough ER and trans-Golgi network, viral transmembrane proteins undergo glycosylation (HA and NA) and/or palmitoylation (HA and M2) (6, 99, 100, 103). The final structure of the envelope proteins is achieved through the oligomerization of independently folded monomers or pre-formed dimers, which likely form co-clusters for transport to the PM (99, 104, 105). Previous studies suggested that M2 is transported to the apical PM independently from HA and NA through its interaction with the PS-conjugated microtubule-associated protein 1 light chain 3 protein (LC3-II) (99, 106). Moreover, it has been proposed that NA are processed along the same

intracellular route as HA (ER-Golgi-apical PM) via cholesterol-/sphingomyelin-rich vesicles (103, 107, 108). Evidence suggests that several host factors support the apical transport of viral transmembrane proteins (6, 99, 100, 108, 109). As the infection progresses, the apical cell surface becomes enriched with viral proteins, which span the PM (6, 75, 100, 102, 109). Specifically, glycoproteins HA and NA are believed to accumulate in lipid raft microdomains, while ion channel protein M2 localizes to the periphery of these domains (6, 75, 100, 102, 109), which is under debate since recent reports could not confirm this observation (110-116). Nevertheless, this distinct sorting of glycoproteins to the PM is likely due to lipid modifications of the C-terminal cysteine (HA) or the C-terminus of the TMD (NA) that occur in the trans-Golgi network (75, 103, 109). Additionally, HA possess multiple basic residues at its cytoplasmic tail, which play a role in phosphoinositide interactions to modulate HA clustering in the PM and its membrane association and might be responsible for the re-localization of PIP2 to the center of the HA cluster (43, 103, 117-120). It was suggested that the accumulation of HA and NA molecules in the PM initiates the budding process of progeny virions by inducing signal transduction events that lead to curvature of the membrane (6, 75, 100, 102, 109). Nevertheless, M1 and vRNPs are also required for virus budding in infected cells (6, 75, 100, 102, 109). Notable, the membrane localization of M1 is believed to occur through piggy-back transport with HA, NA, M2, or vRNPs since M1 lacks an apical transport signal (6, 75, 84, 91, 100, 121, 122). Some studies suggest that M1 associates with the cytoplasmic tails of HA, NA, and M2 during their transport, but these interactions are still debated due to conflicting data reports (123-127). Therefore, cytosolic protein M1 and vRNPs have been proposed to accumulate in the budding site by interacting with the cytoplasmic tails of the transmembrane proteins HA, NA, and M2 (6, 75, 100, 102, 109, 121, 125, 128) as well as anionic lipids of the inner leaflet (129-132). With a sufficient amount of viral envelope proteins, vRNPs, and M1 on the cell periphery, particle assembly continues with the formation of a bud by an outward curvature of the PM (6, 75, 100, 102, 109, 121, 125). This extension occurs while the vRNP segment bundles incorporated perpendicular to the budding tip (6, 75, 100, 102, 109, 121, 125). The virus core is formed by the oligomerization of M1 (6, 75, 84, 91, 100, 121, 122). After budding, the ion channel M2 concentrates at the outer periphery of the budding site, at the neck of the progeny virion. This concentration induces strong, negative Gaussian membrane curvature and scission of virions by incorporating its amphipathic α-helix (6, 75, 99, 100, 102, 109, 121, 125). Moreover, the intercalation also facilitates viral particle release and promotes filamentous particle formation (6, 75, 99, 100, 102, 109, 121). The matrix protein M1 might also influence membrane curvature at the budding site and the filamentous phenotype (6, 75, 84, 91, 100, 121, 122, 125). Eventually, NA of budded virions catalyzes the hydrolysis of the glycosidic linkage of sialic acids on the PM to ensure the final release of emerging virions. This process prevents the retention of newly formed virus particles to the already infected cell and the self-aggregation of progeny virions (6, 75, 100, 102, 109, 121). In addition to viral factors, only a few cellular host factors have been suggested to be involved in the budding and release mechanism. Tetraspanins are probably needed in the membrane scission process and is retained in the emerging virion (100). However, multiple cell factors have also been reported to play a role in the budding process (91, 99, 100, 102, 109, 121).
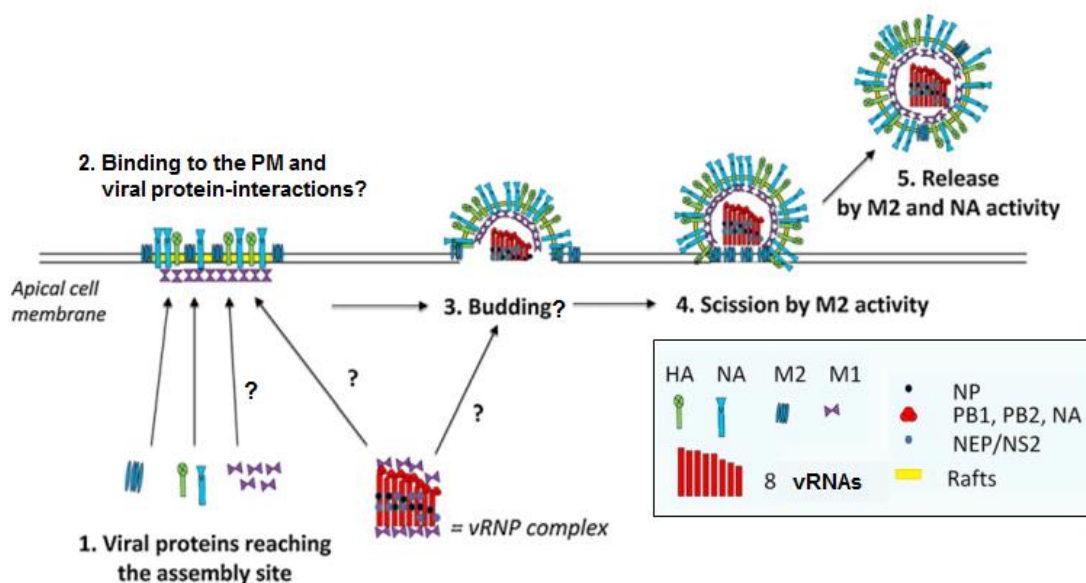
Figure 8 Model for IAV assembly and budding inside lipid rafts of the apical PM. It is hypothesized that the virus assembly and egress occurs in lipid rafts zone, which are membrane domains with a higher thickness and enriched with cholesterol and sphingomyelin. However, contrary results were obtained in recent studies. (1) The viral membrane proteins (HA, NA and M2) are transported to the lipid raft domains at the apical PM via secretory pathways. Notable, recent studies showed that they are also targeted to non-raft domain. Various models have been proposed to explain the transport of M1 and the vRNPs to the budding site, and are still under debate. (2) The viral envelope proteins cluster inside the PM and M1 starts to oligomerize at the inner leaflet of the PM. The exact mechanisms behind these are still not fully understood. (3) The budding process is initialized by multiple factors, such as vRNP recruitment, and "pushing" and "pulling" forces through M1 oligomerization and HA clustering, respectively. Little is known concerning the lipid composition and organization at the assembly and budding site. (4) Fission of viral particles is initialized by recruitment of M2 to the periphery of the lipid rafts. (5) Release of progeny virions is facilitated by the activation of NA. Adapted from (102).

2 Research objectives

This study primarily focused on two main objectives. The first objective was to evaluate and implement FFS techniques and membrane property sensors for conducting *in cellula* measurements of molecular interactions and dynamics as well as PM lipid alterations. The second objective was to utilize these optimized techniques to address complex biological inquiries: (i) investigating the impact of the antineoplastic drug erufosine (EPC3) on lipid-lipid interactions in the PM of breast cancer cells, (ii) examining the effect of avian and human IAV infections on lipid composition and lipid-lipid interactions at the assembly site of different cell lines, and (iii) understanding how interactions of viral proteins contribute to the recruitment of M1 to the PM and viral protein assembly. In order to address these questions, a variety of biophysical fluorescence microscope techniques were employed, including sFCS, N&B and RICS in both one-color and cross-correlation mode, FRET, and generalized polarization (GP) imaging. The goals of this study are detailed in the following subsections.

2.1 Systematic evaluation of green fluorescent proteins for molecular brightness analysis

PPIs are crucial for various cellular functions, including biomolecule transport and ion channel activity (133-135). However, traditional methods like co-immunoprecipitation (co-IP) lack information about intracellular protein distribution, are not compatible with live-cell samples, and cannot account for variations in concentrations between different cells (18, 136). As a result, these methods may lead to inaccuracies in quantifying PPIs (23, 136). Conventional optical microscopy can visualize protein localization, but its resolution is limited (32, 136). Therefore, non-invasive *in cellula* techniques like FFS offer valuable insights into complex biological processes at the single-cell level (18, 32, 136). FFS utilizes the parameter of molecular brightness to determine the oligomeric state of proteins by fusing them with FPs (18, 32). However, the accuracy of FFS measurements and quantified parameters heavily rely on the fluorescence properties of the FPs used to tag proteins of interest (18, 32). The fluorescence behavior of FPs is affected by multiple factors such as instrumental settings (e.g., excitation power, duration of illumination), sample environment like pH, and photophysical processes like photobleaching and non-fluorescent states, leading to an underestimation of protein oligomerization (18, 20, 32, 137-141). One commonly used FP in FFS is the monomeric enhanced green fluorescence protein (mEGFP), which has shown a decrease in the p_f value under acidic pH conditions, likely due to an increase in proteins in the dark state (138, 141). Thus, researchers have engineered novel green FPs in recent years with improved intensity, folding efficiency, photostability, and pH stability, which can enhance the quality of FFS measurements (138, 140, 142-145). In complex live cell experiments, FPs may encounter different environments and pH conditions (e.g., acidic pH in lysosomes, neutral pH in the cytoplasm, high pH in mitochondria) (144, 146). Therefore, it is important to systematically analyze the properties of the novel FPs compared to the standard mEGFP to select the appropriate

fluorescent tag for live cell imaging applications and accurately quantify PPIs in diverse intra-cellular environments. To this aim, FFS measurements on cytosolic and membrane-associated FP monomers and homodimers are performed and factors (e.g. excitation power and pH) that influence their photostability and brightness were investigated. The work is presented in chapter 3.1.

2.2 Characterization of membrane diffusion dynamics and fluidity in cancer cells and IAV infected cells

Lipids are a diverse group of biomolecules that play essential roles in biological membranes, cellular structures, energy storage, and cell signaling (147, 148). They are grouped into fatty acids, glycerides (neutral glycerides and phosphoglycerides), nonglyceride lipids (steroids and sphingolipids), and lipoproteins (147, 148). Lipid metabolism, including uptake, synthesis, and hydrolysis, is crucial for maintaining cellular homeostasis (147, 148). Alterations in lipid metabolism can affect cell function and contribute to diseases such as cancer and viral infections (147-150).

In cancer cells, lipid metabolism is utilized to support rapid proliferation, survival, and metastasis (147, 148). Blocking lipid uptake and utilization have been proposed as potential approaches to inhibit tumor growth (147, 148). Cholesterol is an essential component of biological membranes and inhibiting its synthesis has shown promise as an anticancer strategy (147, 148). However, the efficacy of cholesterol synthesis inhibitors, such as statins, in cancer treatment remains inconclusive (147, 148). Finding substances that target lipid metabolism in cancer cells without causing toxic effects in normal cells is a major challenge. New potential anticancer agents, such as EPC3 and other alkylphospholipids (APLs), have shown promising results in inhibiting tumor growth (151). Little is known about the molecular mechanism behind the antineoplastic activity of EPC3 on cell membrane integrity and lipid organization. To address this, different fluorescence imaging techniques were employed to investigate the effect of EPC3 on physical properties of the PM, such as sFCS to quantify membrane protein dynamics in adherent cancer cells and cell-derived GPMVs. The work is presented in chapter 3.2.

In the context of viral infections, IAV has been found to alter lipid metabolism in host organisms, potentially contributing to the pathogenicity of the virus (149, 150). The lipid metabolism of the host cell is involved in various stages of the IAV life cycle, including virus-host receptor interaction, membrane fusion, nuclear transport, virion assembly, and budding (75, 107, 121, 152, 153). To this date, investigation about the effect of IAV proteins on host cells are inconclusive, and limited studies analyzing the lipidome of whole infected cells have shown marginal effects on lipid metabolism (43, 117, 154). Virus assembly and egress occur mainly in certain PM regions, the so-called lipid rafts (75, 107, 121). Whole cell analysis could therefore obscure the impact of infection on PM properties. Nevertheless, previous findings emphasize a crucial role of a well-regulated lipid metabolism for IAV replication, which

seemed to be influenced by both host and virus origin. Therefore, understanding the connection between lipid metabolism and IAV infection is crucial for developing targeted antiviral treatments. In order to enhance our understanding of how IAV infection affects membrane properties during assembly and egress, as well as the impact of the host environment and IAV strain origin, it is crucial to conduct comprehensive studies on the membrane properties of infected cells. Hence, biophysical fluorescence imaging approaches were employed, for the first time, to provide detailed insights into the molecular mechanisms involved. A semi-automatic spectral FRET analysis was implemented to monitor membrane charge changes at the inner leaflet of the PM. Changes in membrane fluidity was quantified via a new semi-automatic spectral GP and Phasor analysis. The impact on membrane protein dynamics was investigated via sFCS. The work is presented in chapter 3.3.

2.3 Implementation of fluorescence fluctuation spectroscopy to quantify protein-protein interactions between IAV proteins and host factors

The assembly of IAV begins when HA and NA arrive at the PM through secretory pathways (6, 103, 107, 108). It was suggested that the translocation of M2 to the membrane is facilitated by Rab11-positive and LC3-II-positive vesicles (99). There are different hypotheses regarding the transport of M1 to the membrane. Some studies propose that M1 associates with vRNPs or the cytoplasmic tails of viral envelope proteins (HA, NA, and M2) during transport, but conflicting data reports have led to ongoing debates about these interactions (123-127). Previous reports have shown that M1 can directly bind to anionic lipids of artificial membranes and initiate oligomerization (129-132). However, when M1 is expressed alone in mammalian cells, none of these observations are made (129). Therefore, the molecular mechanisms underlying M1-driven IAV assembly remain not fully understood, and the specific interactions between M1 and other viral envelope proteins have not been directly quantified *in cellula*. To gain insight into the initial stages of IAV assembly, several FFS techniques were employed to quantify the oligomeric state, concentration, and diffusion dynamics of viral surface proteins (HA, NA, M2) and M1. These techniques were applied to co-transfected cells as well as infected cells to obtain quantitative information on protein-protein interactions in their native cellular environment. The work is presented in chapter 3.4.

Most FFS interaction studies are limited to two-color fluorophore species, which is insufficient for studying signal transduction in biological systems and viral assembly that depend on specific interactions among multiple biomolecules. Therefore, more versatile FFS techniques are needed to address this limitation. In this work, two spectral FFS approaches were applied to investigate the oligomerization, diffusion, and cross-correlation of three- and four-spectrally overlapping FPs at the PM and in the nucleus. To demonstrate the potential applications of these techniques, two biological examples were chosen. Firstly, scanning fluorescence spectral correlation spectroscopy (SFSCS) was used to quantify the hetero-interactions and oligomerization of the IAV protein M2 with two host factors, the autophagy marker protein LC3-II and the tetraspanin CD9, at the PM. It was observed that LC3-II is recruited to the PM in IAV-infected cells, possibly facilitated by its interaction with M2 (99). Additionally,

tetraspanins have been shown to be incorporated into IAV virions and are believed to play a functional role in the assembly process (91, 100). Secondly, raster spectral image correlation spectroscopy (RSICS) was employed to gain insights into molecular interactions, diffusion, molecular brightness, and stoichiometry of the IAV polymerase complex (PC) in the nucleus. Previous studies have proposed that an interaction between the three viral polymerases (PB1, PB2, and PA) occurs in the nucleus, and that two hetero-trimers are interact to initiate vRNA synthesis during infection (6, 92, 95, 96). However, the previous analysis was limited to studying interactions between only two of the three subunits simultaneously, and the stoichiometry of the complex was only reported for the dimerization of the PA protein. Therefore, this new technique could provide valuable information on the dynamics and organization of the viral polymerase complex within the nuclear environment. The work is presented in chapter 3.5.

2.4 Publications

The following manuscripts constitute the main part of this cumulative dissertation:

Publication I: Benchmarking of novel green fluorescent proteins for the quantification of protein oligomerization in living cells

Authors: **Annett Petrich**, Amit Koikkarah Aji, Valentin Dunsing, Salvatore Chiantia
Journal: PloSOne || published on 03.08.2023 || doi: 10.1371/journal.pone.0285486

Author contributions: Annett Petrich, Amit Koikkarah Aji and Salvatore Chiantia conceived the work. Annett Petrich and Amit Koikkarah Aji were involved in the experimental design and performed the experiments. In particular, Amit Koikkarah Aji performed the N&B experiments and Annett Petrich the cloning work, N&B and sFCS experiments. Annett Petrich, Valentin Dunsing and Salvatore Chiantia wrote the analysis software. Annett Petrich and Amit Koikkarah Aji analysed the data. Annett Petrich visualized the data and wrote the origin manuscript. Amit Koikkarah Aji, Valentin Dunsing and Salvatore Chiantia reviewed and edited the manuscript. Annett Petrich and Salvatore Chiantia were involved in the revision process.

Approved: ————————————
        Prof. Dr. Salvatore Chiantia

Publication II: Effect of Erufosine on Membrane Lipid Order in Breast Cancer Cell Models

Authors: Rumiana Tzoneva, Tihomira Stoyanova, **Annett Petrich**, Desislava Popova, Veselina Uzunova, Albena Momchilova, Salvatore Chiantia
Journal: Biomolecules || published on 22.05.2020 || doi: 10.3390/biom10050802

Author contributions: Rumiana Tzoneva and Salvatore Chiantia conceived the work. Rumiana Tzoneva, Tihomira Stoyanova, Annett Petrich, Desislava Popova and Veselina Uzunova performed the experiments. In particular, Rumiana Tzoneva and Veselina Uzunova performed the TLC and gas chromatography experiments, Desislava Popova the RICS experiments on SLBs, Tihomira Stoyanova the membrane fluidity measurements in cells and Annett Petrich the cloning work and sFCS experiments. Salvatore Chiantia wrote the analysis software. Rumiana Tzoneva, Tihomira Stoyanova, Annett Petrich, Desislava Popova, Veselina Uzunova and Salvatore Chiantia analysed the data. Rumiana Tzoneva, Salvatore Chiantia and Annett Petrich visualized the data. Rumiana Tzoneva and Salvatore Chiantia wrote the origin manuscript. Annett Petrich and Albena Momchilova reviewed and edited the manuscript. Annett Petrich, Rumiana Tzoneva and Salvatore Chiantia were involved in the revision process.

Approved: ————————————
        Prof. Dr. Salvatore Chiantia

Publication III: Influenza A virus infection alters lipid packing and surface electrostatic potential of the host plasma membrane

Authors: **Annett Petrich**, Salvatore Chiantia
Journal: Viruses || submitted on 07.08.2023 || peer-review (manuscript ID: viruses-2573699)

Author contributions: Annett Petrich and Salvatore Chiantia conceived the work. Annett Petrich was involved in the experimental design and performed the experiments. Annett Petrich and Salvatore Chiantia wrote the analysis software. Annett Petrich analysed and visualized the data. Annett Petrich wrote the manuscript with editing by Salvatore Chiantia.

Approved: ─────────────────────
Prof. Dr. Salvatore Chiantia

Publication IV: Influenza A M2 recruits M1 to the plasma membrane: A fluorescence fluctuation microscopy study

Authors: **Annett Petrich**, Valentin Dunsing, Sara Bobone, Salvatore Chiantia
Journal: BiophysJ || published on 11.12.2021 || doi: 10.1016/j.bpj.2021.11.023

Author contributions: Annett Petrich and Salvatore Chiantia conceived the work. Annett Petrich was involved in the experimental design and performed the experiments. Annett Petrich, Valentin Dunsing and Salvatore Chiantia wrote the analysis software. Annett Petrich analysed and visualized the data. Annett Petrich wrote the origin manuscript. Sara Bobone, Valentin Dunsing and Salvatore Chiantia reviewed and edited the manuscript. Annett Petrich and Salvatore Chiantia were involved in the revision process.

Approved: ─────────────────────
Prof. Dr. Salvatore Chiantia

Publication V: Multicolor fluorescence fluctuation spectroscopy in living cells via spectral detection

Authors: Valentin Dunsing, **Annett Petrich**, Salvatore Chiantia
Journal: Elife || published on 08.09.2021 || doi: 10.7554/eLife.69687

Author contributions: Valentin Dunsing, Annett Petrich and Salvatore Chiantia conceived the work. Valentin Dunsing and Annett Petrich were involved in the experimental design and performed the experiments. In particular, Valentin Dunsing performed most of the microscopic experiments with the support of Annett Petrich. Additionally, Annett Petrich did the cloning work and cell preparation. Valentin Dunsing and Salvatore Chiantia wrote the analysis software. Valentin Dunsing and Salvatore Chiantia analysed and visualized the data. Valentin Dunsing and Salvatore Chiantia wrote the origin manuscript. Annett Petrich reviewed and edited the manuscript. Valentin Dunsing and Salvatore Chiantia were involved in the revision process.

Approved: ─────────────────────
Prof. Dr. Salvatore Chiantia

In addition, the author contributed to the following publications:

Petrich A, Chiantia S. Influence of host cell type and influenza A virus strain origin on M2-mediated recruitment of M1 to the plasma membrane and its oligomerization. (manuscript in preparation)

Petrich A, Chiantia S. Interaction of the influenza A virus matrix protein 2 with other viral proteins and host factors. (manuscript in preparation)

Dahmani I, **Petrich A**, Ludwig K, Chiantia S. Inhibition of Virus Entry: Harnessing the potential of cationic lipids for preventing spike protein binding to host cell receptors. (manuscript in preparation)

Dunsing-Eichenauer V, **Petrich A**, Schreiber G, Luckner M, Chiantia S, Klipp E. Ribosome numbers, inheritance and volume occupancy in bakers yeast revisited by quantitative microscopy techniques. (manuscript in preparation)

Schwarzer-Sperber HS, **Petrich A**, Schade M, Nilson N, Lehmann MJ, Witkowski PT, Krueger D, Herrmann A, Schwarzer R. Investigation of Orthohantavirus replication by single molecule fluorescence in situ hybridization. (manuscript in preparation)

Ziegeler MJ, Yserentant K, Dunsing V, Middel V, Gralak AJ, Pakari K, Bargstedt J, Kern C, **Petrich A**, Chiantia S, Strähle U, Herten D-P, Wombacher R (2022) Mandipropamid as a chemical inducer of proximity for in vivo applications. Nat Chem Biol. 18:64-69.

Bauherr S, Larsberg F, **Petrich A**, Sperper HS, Klose-Grzelka V, Luckner M, Azab W, Schade M, Höfer CT, Lehmann MJ, Witkowski PT, Krüger DH, Herrmann A, Schwarzer R (2020): Macropinocytosis and Clathrin-Dependent Endocytosis Play Pivotal Roles for the Infectious Entry of Puumala Virus. J. Virol. 94: e00184-20.

Berrin Y, Kikhney J, Musci M**, Petrich A**, Schulze J, Sutrave S, Wießner A, Falk V, Moter A (2020) Aerococcus urinae – a potent biofilmer in endocarditis. PLoS One. 15:e0231827.

Sutrave S, Kikhney, J, Schmidt J, **Petrich A**, Wiessner A, Kursawe L, Gebhardt M, Kertzscher U, Gabel G, Goubergrits L, Affeld K, Moter A (2019) Effect of daptomycin and vancomycin on Staphylococcus epidermidis biofilms: An in vitro assessment using fluorescence in situ hybridization. PLoS One. 14: e0221786.

Rojas P, **Petrich A**, Schulze J, Wiessner A, Loddenkemper C, Epple HJ, Sterlacci W, Vieth M, Kikhney J, Moter A. (2017) Distribution and phylogeny of Brachyspira spp. in human intestinal spirochetosis revealed by FISH and 16S rRNA-gene analysis. Anaerobe. 47:25-32.

Kikhney J, von Schöning D, Steding I, Schulze J, **Petrich A**, Reischl U, Moter A, Thomas A (2016) Is Ureaplasma spp. the leading causative agent of acute chorioamnionitis in women with preterm birth? Clin Microbiol Infect. pii: S1198-743X(16)30480-3.

Petrich A, Rojas P, Schulze J, Loddenkemper C, Giacani L, Schneider T, Hertel M, Kikhney J, Moter A (2015) Fluorescence in situ hybridization for the identification of Treponema pallidum in tissue sections. Int J Med Microbiol. 305(7):709-18.

Schmiedel D; Kikhney J; Masseck J; Rojas Mencias P; Schulze J; **Petrich A**; Thomas A; Henrich W; Moter A (2014) Fluorescence in situ hybridization for identification of microorganisms in acute chorioamnionitis. J Clin Microbiol. 20(9):O538-41.

Moter A, Schmiedel D, **Petrich A**, Wiessner A, Kikhney J, Schneider T, Moos V, Göbel UB, Reischl U. (2013) Validation of an rpoB gene PCR assay for detection of Tropheryma whipplei: Ten years experience in a national reference laboratory. J Clin Microbiol. 51(11): 3858-61.

Schillinger C*, **Petrich A***, Lux R, Riep B, Kikhney J, Friedmann A, Wolinsky LE, Göbel UB, Daims H, Moter A. (2012) Co-localized or randomly distributed? Pair cross correlation of in vivo grown subgingival biofilm bacteria quantified by digital image analysis. PLoS One. 7:e37583.

Drescher J, Schlafer S, Schaudinn C, Riep B, Neumann K, Friedmann A, **Petrich A**, Göbel UB, Moter A. (2010): Molecular epidemiology and spatial distribution of Selenomonas spp. in subgingival biofilms. Eur J Oral Sci. 118(5):466-74.

Schlafer S, Riep B, Griffen AL, **Petrich A**, Hübner J, Berning M, Friedmann A, Göbel UB, Moter A. (2010): Filifactor alocis-involvement in periodontal biofilms. BMC Microbiol. 10:66.

Benoit VM, **Petrich A**, Alugupalli KR, Marty-Roix R, Moter A, Leong JM, Boyartchuk VL. (2010): Genetic control of the innate immune response to Borrelia hermsii influences the course of relapsing fever in inbred strains of mice. Infect Immun. 78(2):586-94.

Mallmann C, Siemoneit S, Schmiedel D, **Petrich A**, Gescher DM, Halle E, Musci M, Hetzer R, Göbel UB, Moter A. (2010): Fluorescence in situ hybridization to improve the diagnosis of endocarditis: a pilot study. Clin Microbiol Infect. 16(6):767-73.

Schmiedel D, Epple HJ, Loddenkemper C, Ignatius R, Wagner J, Hammer B, **Petrich A**, Stein H, Göbel UB, Schneider T, Moter A. (2009): Rapid and accurate diagnosis of human intestinal spirochetosis by fluorescence in situ hybridization. J Clin Microbiol. 47(5):1393-401.

Schweickert B, Goldenberg O, Richter E, Göbel UB, **Petrich A**, Buchholz P, Moter A. (2008): Occurrence and clinical relevance of Mycobacterium chimaera sp. nov., Germany. Emerg Infect Dis. 14(9):1443-6.

Schlafer S, Nordhoff M, Wyss C, Strub S, Hübner J, Gescher DM, **Petrich A**, Göbel UB, Moter A. (2008): Involvement of Guggenheimella bovis in digital dermatitis lesions of dairy cows. Vet Microbiol. 128(1-2):118-25.

* Authors contributed equally to the work.

3 Results

3.1 Publication I: Benchmarking of novel green fluorescent proteins for the quantification of protein oligomerization in living cells

RESEARCH ARTICLE

Benchmarking of novel green fluorescent proteins for the quantification of protein oligomerization in living cells

Annett Petrich[1], Amit Koikkarah Aji[1], Valentin Dunsing[1,2], Salvatore Chiantia⬡[1] *

1 University of Potsdam, Institute of Biochemistry and Biology, Potsdam, Germany, **2** Aix-Marseille University, CNRS, UMR 7288, IBDM, Turing Center for Living Systems, Marseille, France

* chiantia@uni-potsdam.de

Abstract

Protein-protein-interactions play an important role in many cellular functions. Quantitative non-invasive techniques are applied in living cells to evaluate such interactions, thereby providing a broader understanding of complex biological processes. Fluorescence fluctuation spectroscopy describes a group of quantitative microscopy approaches for the characterization of molecular interactions at single cell resolution. Through the obtained molecular brightness, it is possible to determine the oligomeric state of proteins. This is usually achieved by fusing fluorescent proteins (FPs) to the protein of interest. Recently, the number of novel green FPs has increased, with consequent improvements to the quality of fluctuation-based measurements. The photophysical behavior of FPs is influenced by multiple factors (including photobleaching, protonation-induced "blinking" and long-lived dark states). Assessing these factors is critical for selecting the appropriate fluorescent tag for live cell imaging applications. In this work, we focus on novel green FPs that are extensively used in live cell imaging. A systematic performance comparison of several green FPs in living cells under different pH conditions using Number & Brightness (N&B) analysis and scanning fluorescence correlation spectroscopy was performed. Our results show that the new FP Gamillus exhibits higher brightness at the cost of lower photostability and fluorescence probability (*pf*), especially at lower pH. mGreenLantern, on the other hand, thanks to a very high *pf*, is best suited for multimerization quantification at neutral pH. At lower pH, mEGFP remains apparently the best choice for multimerization investigation. These guidelines provide the information needed to plan quantitative fluorescence microscopy involving these FPs, both for general imaging or for protein-protein-interactions quantification via fluorescence fluctuation-based methods.

Introduction

A multitude of cellular processes, such as biomolecule transport, ion channel activity, cell-cell adhesion and communication are regulated by protein-protein-interactions (PPIs) [1–3]. "Classical" bulk biochemical *in vitro* methods that are used to quantify PPIs (e.g., co-

immunoprecipitation (co-IP), pull-down assays and western blotting) cannot be used to obtain information about intracellular protein distribution in live-cell samples or to monitor the effects of variations in concentrations between different cells [4, 5]. Conventional optical microscopy can visualize the localization of proteins, but its resolution is limited [4, 6]. More complex approaches, such as fluorescence fluctuation spectroscopy (FFS), can assess the interactions between molecules in complexes and obtain insights into cellular pathways and assembly processes [4–8]. FFS provides information about dynamics through the analysis of signal fluctuations from fluorescently labeled molecules [6, 7, 9]. Additionally, the magnitude of such fluctuations can be used to derive quantitative information about the multimerization state (i.e., number of monomers in a multimer) of the protein of interest [7–10].

A common strategy to investigate PPIs *in cellula* via FFS is the fusion of a fluorescent protein (FP) to the protein of interest [7–9, 11]. By comparing the brightness of protein multimers tagged with FPs to the brightness of a monomeric reference, it is possible to quantify the number of FP monomers in the complex and, thus, the oligomerization state of the protein of interest [5, 7, 12]. A major problem for several FFS applications that rely on FPs, though, is the presence of non-emitting "dark" proteins, which can be quantified through the so-called fluorescence probability (*pf*) [7, 13]. It is sometime assumed that FPs have a *pf* value of 1 meaning that, for example, a trimer containing three FPs emits in average a three-fold higher signal than a monomer labelled with one FP [5, 7]. Instead, *pf* values of e.g. green emitting FPs have been reported in the range between 0.5 and 0.8 [1, 2, 7, 13–19]. Recently, we have systematically quantified the *pf* of several FPs, focusing mainly on proteins emitting in the red part of the visible spectrum [7]. In summary, since high *pf* values are required for increased sensitivity, not all FPs are equally suitable for oligomerization studies [7]. Because of the presence of non-emitting FPs (i.e., *pf* lower than 1), FFS approaches might underestimate the amount of FPs and therefore, the oligomeric state of the protein of interest.

Some of the most used FPs are the green fluorescent protein (GFP) and its mutants, such as the monomeric enhanced GFP (mEGFP) [5, 20]. This FP has a high quantum yield (QY), enhanced photostability, and minimal interference with the cellular machinery [20]. Of note, several variants have been engineered over the past few years (e.g. mNeonGreen (mNG), mGreenLantern (mGL), and Gamillus) in an effort to optimize molecular brightness, folding efficiency, photostability, and pH stability of the fluorescent probe (Table 1) [21–24].

In the context of complex experiments in living cells, a FP might encounter different environments and pH conditions (e.g. acidic pH in lysosomes, secretory granule and endosomes; neutral pH in the nucleus, cytoplasm and endoplasmic reticulum (ER); basic pH in mitochondria and a pH gradient in the Golgi network) [22, 25]. Measurements of GFP at acidic pH have shown a decrease of the *pf* value, possibly due to an increase of proteins in the dark-state [22, 26–28]. Consequently, it would be useful to systematically analyze the properties of the above-

Table 1. Photophysical characteristics of the fluorescence proteins (FPs). QY, Quantum yield; norm., normalized.

FP	λ_{ex} [nm]	λ_{em} [nm]	QY	Brightness*	cellular norm. <I>	pK_a	maturation [min]	Reference
mEGFP	488	507	0.71	38.0	1.0[#,†]	6.0	28.0	[21]
mNG	506	516	0.78	90.0	3.3[#]	5.7	18.0	[21]
mGL	503	514	0.72	74.0	6.3[#]	5.6	14.0	[21]
Gamillus	504	519	0.90	74.7	0.5[†]	3.4	8.0	[24]

* (extinction coefficient × QY)/1,000, where QY and extinction coefficients are measured at the absorbance peak (λ_{ex} ± 2 nm)

[#] Average intensity in FP-expressing BE (2)-M17 human neuroblastoma cells, relative to EGFP, using the P2A quantitative co-expression system

[†] Average intensity in FP-expressing HeLa cells, relative to EGFP

https://doi.org/10.1371/journal.pone.0285486.t001

31

mentioned novel FPs, in order to perform an exact quantification of PPIs, also in different intra-cellular environments.

Here, we benchmarked the performance of novel green FPs (mGL and Gamillus) against the well-established mEGFP and mNG. The presence of non-fluorescent states and photo-stability under different pH conditions were measured using Number & Brightness (N&B) and scanning fluorescence correlation spectroscopy (sFCS) analysis [5]. Our results indicate that some of the observed proteins are brighter, although unstable under longer/stronger illumination. Furthermore, we identify which proteins are more suitable for multimerization quantification, rather than "simple" imaging, also at different pH conditions.

Materials and methods

Fluorescent protein constructs

A description of the cloning procedure for all constructs can be found in the Supporting Information. All plasmids generated for this work will be available on Addgene (https://www. addgene.org/). A schematic overview of the intracellular localization of the constructs is provided in S1A Fig in S1 File and an overview of the linker sequences within the FP structures is provided in S1 Table in S1 File.

Cell culture

Human embryonic kidney cells from the 293T line (HEK293T, CRL-3216[TM]) and Chinese hamster ovary cells (CHO-K1, CCL-61™) were purchased from ATCC (Kielpin Lomianki, Poland). Both cell lines were maintained in phenol red-free Dulbecco's modified Eagle's medium (DMEM) supplemented with 10% fetal bovine serum, 2 mM L-glutamine, 100 U/mL penicillin, and 100 μg/mL streptomycin in a humidified incubator with 5% CO_2 at 37˚C. Cells were passaged every 2–3 days after reaching ca. 80% confluence in tissue culture flask, for a maximum of 15 passages. All solutions, buffers, and media used for cell culture were purchased from PAN-Biotech (Aidenbach, Germany).

Preparation for microscopy experiments

For microscopy, 6×10^5 (HEK293T) or 4×10^5 (CHO-K1) cells were plated in 35 mm dishes (CellVis, Mountain View, CA, USA) with optical glass bottom (#1.5 glass, 0.16–0.19 mm), 24 h before transfection. HEK293T cells are more suitable for sFCS measurements since they are relatively thick and therefore preferable for sFCS acquisition perpendicular to the PM. CHO-K1 cells are rather flat and therefore more suitable for N&B measurements in the cytoplasm. Cells (40–50% confluency) were transfected 16–24 h before imaging using 200 ng plasmid DNA per dish with Turbofect (Thermo Fisher Scientific, Waltham, MA, USA) according to the manufacturer's instructions. For measurements under different pH conditions, the culture medium was exchanged with buffer containing 140 mM NaCl, 2.5 mM KCl, 1.8 mM CaCl₂, 1.0 mM MgCl₂, and 20 mM HEPES with a pH value of 5.6, 7.4 or 9.2, and incubated for 5 minutes.

Confocal microscopy system and setup calibration for fluorescence fluctuation spectroscopy

All measurements were performed on a Zeiss LSM780 microscope (Carl Zeiss Microscopy GmbH, Oberkochen, Germany) using a Plan-Apochromat 40×/1.2 Korr DIC M27 water immersion objective and a 32-channel GaAsP detector. FPs were excited with a 488 nm Argon laser (488 nm dichroic mirror) and the fluorescence signal was collected in the range of 498 to

606 nm in photon-counting mode. For the spectral analysis under different pH conditions, fluorescence was detected in spectral channels of 8.9 nm width (23 channels between 491 nm and 690 nm). To decrease out-of-focus light, a one airy unit pinhole was used. All measurements were performed at $22 \pm 1°$C. Cells were incubated for 5 min at room temperature before each measurement.

The confocal volume was calibrated daily by performing point FCS measurements with Alexa Fluor® 488 (AF488, Thermo Fischer, Waltham, MA, USA) in water at 30 nM, with the same laser power and beam path used for N&B and sFCS measurements. Prior to that, the signal was maximized adjusting the collar ring of the objective and the pinhole position. Then, five measurements were performed, each consisting of 15 acquisitions of 10 s, and the data was fitted using a three-dimensional diffusion model including a triplet contribution. The structure parameter S (i.e., the ratio between the vertical and lateral dimension of the confocal volume) was typically around 5 to 9, and the diffusion time τ_d around 30 to 35 μs.

N&B measurements

N&B analysis was performed as previously described [7, 10] with few modifications: 100 frames were acquired as 128x 128 pixel images with pixel dimensions of 400 nm and pixel dwell time of 50 μs. The time-stacks were analyzed using a custom MATLAB code (The MathWorks, Natick, MA, USA). The MATLAB algorithm calculates the molecular brightness and number as a function of pixel position, as described by Digman *et al.* [11]. Bleaching and minor cell movements are partially corrected using a boxcar-filter with an 8-frame window applied pixel-wise, as previously described [7, 29, 30]. Final brightness values were calculated by extrapolating the partial brightness values (i.e., calculated within each 8-frame window) to the earliest time point. Detector saturation was avoided by excluding pixels with photon-counting rates exceeding 1 MHz. A schematic overview of the N&B analysis is provided in S1C Fig in S1 File.

sFCS measurements

Scanning FCS experiments were performed as previously described [7, 31]. Briefly, a line scan of 256×1 pixels (pixel size $\approx$80 nm) was performed perpendicular to the membrane, using a 472.73 μs scan time. 400,000 lines were acquired (total scan time $\approx$3 min) in photon counting mode. Laser power values were typically between $\approx$1.5 μW (brightness analysis) and $\approx$6 μW (photobleaching analysis). Measurements were exported as TIFF files and analyzed in MATLAB (The MathWorks, Natick, MA, USA) using a custom-written script as previously described [7, 31, 32]. The obtained autocorrelation curves $G(\tau)$ were analyzed using a two-dimensional Brownian diffusion model [33]: $\frac{1}{N}\left(1 + \frac{\tau}{\tau_d}\right)^{-1/2}\left(1 + \frac{\tau}{\tau_d S^2}\right)^{-1/2}$, where S is the structure parameter, τ_d is the diffusion time and N is the amount of fluorescent particles in the detection volume. The average molecular brightness is then calculated as the ratio between the average fluorescence intensity $<I>$ and the particle number N. A schematic overview of the sFCS analysis is provided in S1D Fig in S1 File.

Brightness calibration and fluorophore maturation

The molecular brightness, i.e. the average amount of photons emitted by a molecule in the unit of time, is directly connected to the oligomeric state of protein complexes. This is based on the typical premise that all fluorophores within an oligomer are fluorescent. However, FPs can be in a non-mature state, undergo dark state transitions or, in general, be non-fluorescent [8]. We characterize all the processes leading to non-fluorescent FPs using a single parameter, the

apparent fluorescence probability (*pf*), i.e. the probability of a FP to emit a fluorescence signal. The determination of the *pf* value from apparent brightness values was performed as previously described [7, 32]. Shortly, for each sample and each experiment day, the average brightness for a monomeric construct was determined from multiple cells (see e.g. Figs 2A and 3A). Then, measurements were performed in several cells expressing the dimer constructs (S2 Fig in S1 File) and, from each of these measurements and the average monomer brightness obtained before, one *pf* value was calculated using the formula $pf = {}^{Brightness_{dimer}}/_{Brightness_{monomer}} - 1$ [7, 32]. The final *pf* value was calculated as mean of such a set of measurements (see Figs 2B and 3B).

Statistical analysis

Results from at least three independent measurements were pooled and visualized using GraphPad Prism ver. 9.0.0 (GraphPad Software, LCC, San Diego, CA, USA). All results are displayed as box plots with each point corresponding to a measurement in a single cell or as mean ± standard error of the mean (SEM) plots. Median values and whiskers indicating minimum and maximum values are displayed in the box plots. The mean, median, interquartile range (IQR) are indicated in each graph together with the sample size. Significance values are given in each graph and figure captions, respectively. Statistical significance was tested by using D'Agostino-Pearson normality test followed by one-way ANOVA analysis and the Tukey's or Fishers Least Significant Difference (LSD) multiple comparisons test.

Results

mGL and Gamillus are less photostable than mEGFP or mNG

All monomeric FPs were evaluated for photostability at different laser powers using confocal microscopy, in the context of a typical N&B experiment performed in CHO-K1 cells. Such an approach simply consists of a time-series acquisition with continuous scanning over ca. two minutes. mGL and Gamillus displayed higher photobleaching, both in the cytosol and at the PM, in comparison to mEGFP and mNG (Fig 1A and 1B, S2 Table in S1 File). For example, ≈30% of the total mGL was bleached after a ca. two-minute of continuous scanning, using 2.4 μW excitation power. At the same time, N&B analysis provided the brightness of each FP, as a function of the laser power. Although an accurate analysis should be performed at an excitation power causing as low as possible bleaching (see next paragraph), Fig 1C and 1D confirm that the observed brightness predictably increases roughly linearly with the laser power. As expected, due to the detection geometry, a higher signal is observed for molecules restricted to the PM [34]. Finally, Gamillus shows generally a higher brightness, as especially noticeable for measurements at the PM or at higher excitation powers.

Gamillus exhibits high brightness but low fluorescence probability

To compare the brightness effectively observed in a typical confocal microscopy setup and, specifically, in the context of FFS experiments, we have performed in-depth N&B analysis of FP monomer and dimer constructs. In order to maintain bleaching below ≈15%, we have excited the fluorophores with a laser power of 1.2 μW. CHO-K1 cells were transfected with the required plasmids and observed after 16 h. Fig 2A shows the brightness values measured for the different FP monomer constructs, either in the cytosol or at the PM. The results follow, as expected, the general trend described above (Fig 1C and 1D). No significant difference can be observed between mean brightness values at this low laser power, with the exception of mp-Gamillus displaying a higher mean brightness than the other membrane-associated constructs.

34
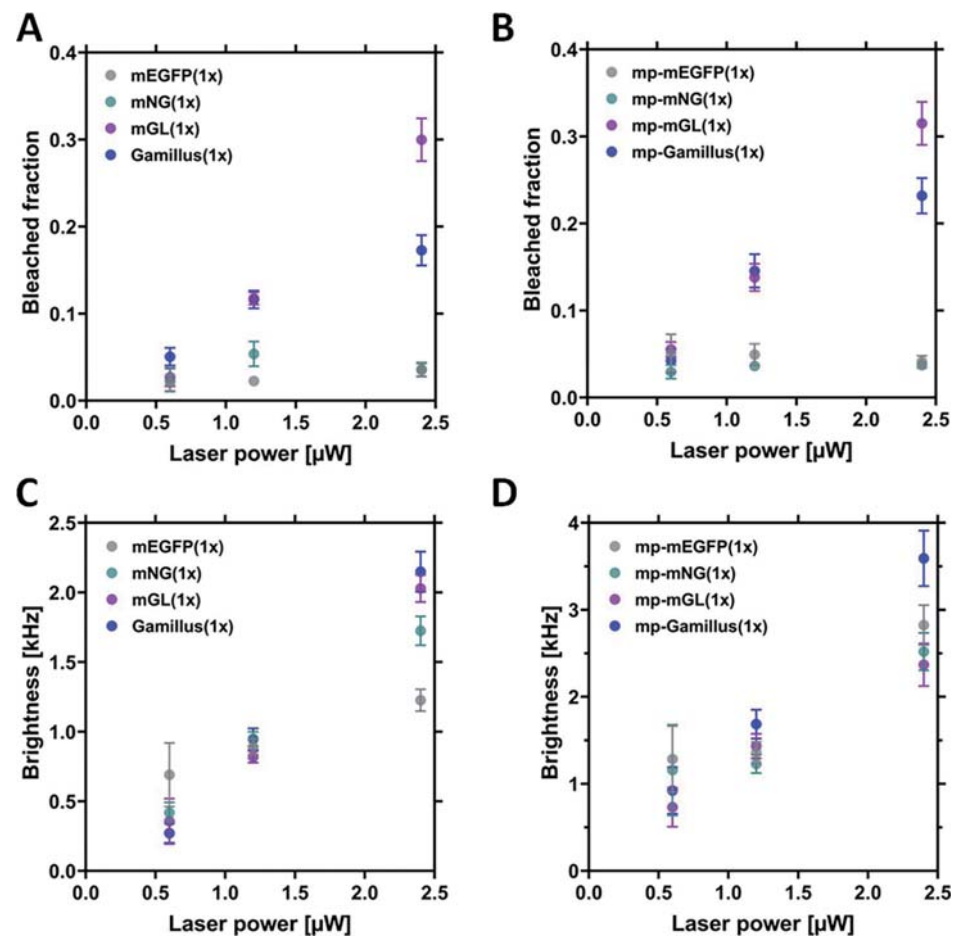
Fig 1. Comparison of the molecular brightness and bleached fraction for the monomeric FPs, as obtained from N&B measurements in CHO-K1 cells. CHO-K1 cells were transfected with plasmids coding for the monomeric cytosolic FPs (mEGFP(1x), mNeonGreen(1x) (here, called mNG(1x)), mGreenLantern(1x) (here called mGL(1x)) and Gamillus(1x)) or with membrane-anchored FPs. The latter are anchored to the inner leaflet of the PM via a myristoylated and palmitoylated (mp) peptide (mp-mEGFP(1x), mp-mNG(1x), mp-mGL(1x) or mp-Gamillus(1x)). N&B measurements were performed ≈16 h after transfection with a laser power of 0.6 μW, 1.2 μW and 2.4 μW. (A-B): Mean bleached fractions measured for cytosolic FPs (A) and for PM-anchored FPs (B), as a function of laser power. The bleached fraction indicates the amount of fluorescence signal lost after a N&B measurement. Error bars indicate the standard error of the mean (SEM). (C-D): Mean brightness values measured for cytosolic FPs (C) and for PM-anchored FPs (D), as a function of laser power. Error bars represent the SEM. Exact values and sample sizes are summarized in S2 Table in S1 File.

https://doi.org/10.1371/journal.pone.0285486.g001

Next, we have performed similar experiments on dimer constructs of the same FPs (S2A Fig and S3 Table in S1 File), in order to calculate the *pf*, as shown in Fig 2B. All *pf* values are in the expected range, around 0.7, and no large difference can be observed between the different fluorophores in general. Noticeably though, mp-Gamillus exhibits *pf* values lower than those of the other FPs (in particular, significantly lower than mp-mGL, ca. 0.6 vs. ca. 0.9).

Performance comparison of FPs at different pH values

The fluorescence emission intensity of some FPs often decreases at low pH values due to protonation of the chromophore [22, 24, 26]. Protonation can induce the transition to dark states and, therefore, negatively affect the accuracy of molecular brightness measurements [28].
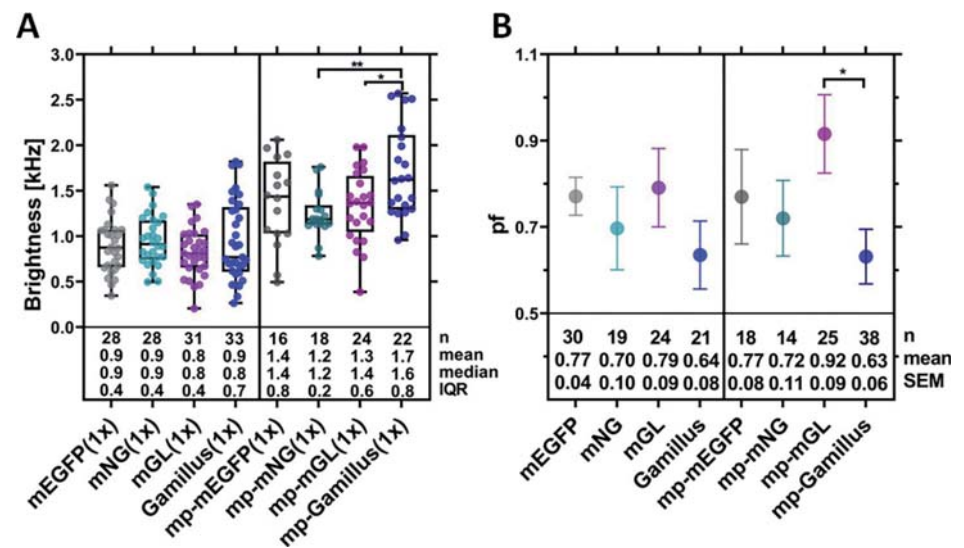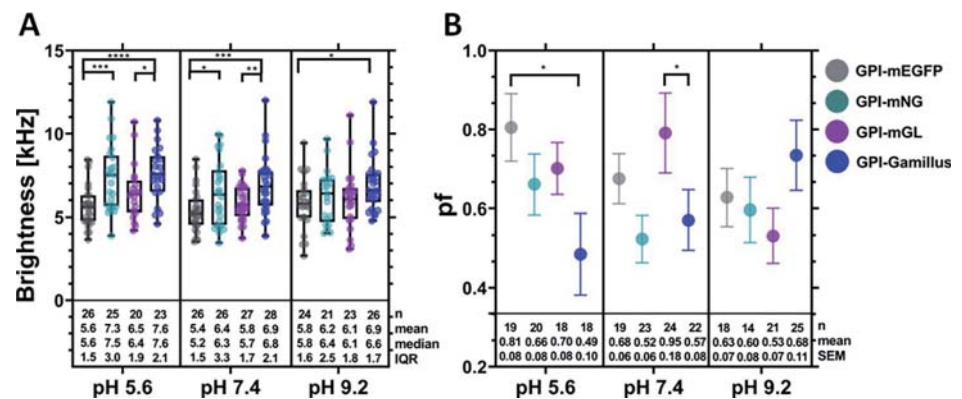
Fig 2. Comparison of brightness and fluorescence probability (*pf*) for the examined green FPs, as obtained from N&B measurements in CHO-K1 cells. N&B measurements were performed ≈16 h after transfection, using a laser power of 1.2 µW. (A): Box plot of the molecular brightness for the examined cytosolic and membrane-anchored FPs (i.e., mp-FP). Each point represents the average value measured in a single cell, from three independent experiments. Median values and whiskers ranging from minimum to maximum values are displayed. (B): Mean *pf* values calculated for the cytosolic and membrane-anchored FPs, using the brightness values measured for the corresponding FP dimers (S2A Fig in S1 File). Data were collected from three independent experiments. The error bars represent the SEM. Sample size, mean/median, and interquartile range (IQR)/SEM are indicated below the graph. Statistical significance within both plots for selected sample pairs were determined using one-way ANOVA Tukey´s multiple comparison test (* p < 0.05, ** p < 0.005).

https://doi.org/10.1371/journal.pone.0285486.g002

Here, the pH-dependent fluorescence of the FPs was analyzed via confocal microscopy in the pH range from 5.6 to 9.2 in HEK293T cells using constructs associated to the outer side of the PM via a glycosylphosphatidylinositol (GPI) anchor. The fluorescence emission spectra of the different FPs did not change considerably in the assessed pH range and no photoconversion was observed (S3 Fig in S1 File). Also, the photostability of the FP variants at different pH conditions was qualitatively compared (S4 Fig in S1 File) using an excitation power of 6 µW, on a specific position of the PM, for ca. three minutes. This configuration is usually employed for FCS measurements at the PM and is different from the N&B whole-frame scanning approach used for the experiments described in the previous paragraphs [10]. GPI-mEGFP showed a good photostability at all pH conditions, with the fluorescence signal decreasing by only ca. 20% (S4A and S5 Figs in S1 File). GPI-mNG(1x) exhibited fast initial photobleaching, particularly at pH values 5.6 and 9.2, down to ca. 50% of the original signal. At neutral pH, bleaching of GPI-mNG was only slightly higher than that of GPI-mEGFP (S4B and S5 Figs in S1 File). A fast and substantial photobleaching, especially at neutral and low pH was observed for GPI-mGL (S4C and S5 Figs in S1 File). Finally, as shown in S4D and S5 Figs in S1 File, a strong pH-dependency of photostability was observed for GPI-Gamillus: at the highest pH the bleaching was minor (i.e., ca. 20%, similar to GPI-mEGFP), while at neutral and low pH the emission signal dramatically decreased (i.e., to ca. 40% and 10% at pH 7.4 and 5.6, respectively). Overall, mEGFP showed the highest photostability for all pH conditions followed by mNG and then Gamillus (pH < 9.2) and mGL, in agreement with the results from N&B analysis (Fig 1B).

Additionally, the molecular brightness of the different FPs under various pH conditions was evaluated for monomer and dimer membrane-associated GPI-anchored constructs, and the corresponding *pf* values were determined (Fig 3, S2B Fig and S4 Table in S1 File). To

36

Fig 3. Comparison of brightness and *pf* values for the examined FPs, as obtained from scanning fluorescence correlation spectroscopy (sFCS) measurements in HEK293T cells, under different pH conditions (pH 5.6, pH 7.4, and pH 9.2). sFCS measurements were performed ≈16 h after transfection, using a laser power of 1.5 μW. (A): Box plots of the molecular brightness for the membrane-anchored FPs GPI-mEGFP, GPI-mNG, GPI-mGL and GPI-Gamillus, for three different pH conditions. Each point represents the average value measured in single cells, from three independent experiments. Median values and whiskers ranging from minimum to maximum values are displayed. (B): Average *pf* values calculated using the brightness values measured for the corresponding FP dimers (S2B Fig in S1 File), for three different pH conditions. Data were collected from three independent experiments. The error bars represent the SEM. Statistical significance was determined for selected sample pairs in both plots using one-way ANOVA Fishers Least Significant Difference (LSD) multiple comparison test (* $p < 0.05$, ** $p < 0.005$, *** $p < 0.0005$, **** $p < 0.0001$).

https://doi.org/10.1371/journal.pone.0285486.g003

complement the previous experiments, we used an alternative FFS approach (i.e., sFCS [33]) and an alternative live-cell model (i.e., HEK293T) for this set of experiments. sFCS experiments result in fluorescence autocorrelation curves which can be analyzed to extract parameters such as diffusion coefficients of the labelled proteins, concentration and molecular brightness (see S6 Fig in S1 File for representative examples). As shown in Fig 3A, the results obtained at pH 7.4 corroborate what was observed also via N&B (Figs 1D and 2A), i.e. that Gamillus overall exhibits a higher brightness compared to the other FPs. This observation holds true for all the tested pH conditions. In general, the observed brightness values did not differ much among each other (being all within a ca. 15% variation interval) and we did not observe an effect of pH, at least at the low laser powers used here.

More marked differences were observed, however, for the *pf* values. In general, this parameter showed a negative correlation with increasing pH for GPI-mEGFP and a positive correlation for GPI-Gamillus. No strong correlation was observed instead for GPI-mGL or GPI-mNG. At pH 5.6, the *pf* of GPI-Gamillus was significantly lower than that of GPI-mEGFP and, overall, the lowest among all investigated proteins. At neutral pH, GPI-mGL showed the best performance, in agreement with what we observed for mp-mGL via N&B (Fig 2B). At pH 9.2, no strong differences were observed in general among all FPs, although GPI-Gamillus displayed by trend the highest *pf* value. Notably, we did not observe pH-induced changes in the autocorrelation functions (indicating e.g. significant alterations in the triplet state fraction) for any FP at this low excitation power (S6 Fig in S1 File). An in-depth study of fluorescence intensity dynamics faster than ca. 1 ms would require, in general, approaches with higher temporal resolution.

Discussion

PPIs and, specifically, homo-multimerization can be quantified directly in living cells using quantitative fluorescence microscopy approaches based on FFS (e.g., sFCS and N&B) [6–8].

37

The molecular brightness (i.e., photon count rate per molecule) derived from such experiments allows the determination of the oligomeric state of FP-tagged protein complexes [7, 8, 10]. The reliability of such approaches is influenced by the photophysical behavior of the FPs, which can be summed up by the *pf* parameter [7]. The *pf* is determined by the specific experimental conditions (e.g. excitation wavelength and power, duration of illumination, geometry of the detection volume), sample environment (pH, ion composition, etc.), intracellular biochemical processes (e.g. maturation time and folding efficiency) and photophysical processes (photobleaching, quantum yield, triplet state formation, protonation- or light-induced "blinking", long-lived dark states, etc.) [9, 20, 26–28, 33, 35–40]. Therefore, three requisites should be ideally met by FPs used in typical FFS studies: i) high molecular brightness, required to achieve sufficient signal-to-noise ratio to detect single molecule fluctuations, ii) high photostability, essential to allow prolonged imaging and iii) a high *pf*, crucial for a large dynamic range and accuracy of oligomerization measurements. In this study, we present a systematic analysis of novel GFP variants (mGL and Gamillus) and discuss their suitability in the context of brightness-based oligomerization studies. Both proteins were reported to mature remarkably quickly and to possess a high brightness and medium-low acid sensitivity compared to mEGFP (see Table 1) [21, 24], thus suggesting that they are promising candidates for quantitative FFS studies. These features are, at least partially, shared also by the established GFP variant mNG [23], which is therefore also included in this study.

Previous studies have characterized these FPs and compared them to e.g. mEGFP as standard (see e.g. [41]). Nevertheless, it must be noted that essential parameters, such as brightness, pH sensitivity or photostability, are often measured with different methods and the outcome might depend on the specific setup [23, 24, 41–43]. Thus, it is reasonable to compare the FPs systematically using specific conditions and approaches resembling those of actual FFS experiments. Following this logic, we used typical FFS approaches (i.e., N&B and sFCS) to quantify the stability, brightness, pH sensitivity and *pf* of mEGFP, mNG, Gamillus and mNG.

A first unexpected result is that, in general, we do not observe strikingly different brightness values between each FP. While this observation can likely be explained by the distinctive experimental setup (e.g. very low excitation power, longer acquisition times, specific intra-cellular localization [21, 42, 44]), it is nevertheless relevant for users planning similar FFS-based investigations. Furthermore, the brightness measured via FFS is an average value derived from a statistical analysis of single molecule fluctuations. Such analysis is different from bulk methods that measure the fluorescence emission in a whole cell as a readout of brightness. While remaining both valid, the different approaches might provide information about different aspects of the fluorescent system. Finally, in our experimental conditions, Gamillus displayed a higher brightness compared to the other FPs, at least when located at the PM or while using higher laser powers. This observation was independently confirmed via both sFCS and N&B analysis.

Both techniques also indicate that the higher brightness of Gamillus is counterbalanced by a stronger tendency to photobleach, at least in the conditions used in our experiments (e.g., pH 7.4). A similarly low photostability was observed also for mGL, while mNG and mEGFP proved to be remarkably stable under continuous irradiation. Of interest, the contrast with reports indicating a strong photostability of mGL and Gamillus might be only apparent. A general comparison of these observations with previous studies is complicated by the fact that, often, different conditions and experimental setups result in different apparent photochemical behavior. For example, mEGFP was shown to be less stable than mNG under widefield illumination, more stable under laser illumination [23] and similarly stable using a spinning disk confocal microscope [42]. Nevertheless, the photostability observed here at pH 7.4 for mEGFP is in the same range as previously reported [23, 45]. Also, mGL was reported to be less

38

photostable than Clover that, in turn, is less photostable than mEGFP [21, 45], in agreement with our observations. On the other hand, in contrast to our observation, Shinoda *et al.* showed that Gamillus has a 2-fold higher photostability than mEGFP under widefield illumination and acidic conditions [24]. Once more, a possible explanation for such discrepancies might reside in the considerably different experimental conditions which, in this case, might be specifically relevant for FFS-based multimerization studies.

Next, we have measured the *pf* values for the different FPs, since this is a parameter of fundamental importance for quantitative multimerization studies. Our results indicate that, in general, all the examined FPs perform relatively well (i.e., *pf* ca. 0.7) and definitely better than most red or blue FPs [7, 19]. In particular, mGL excels in this context, with a *pf* value of 0.8 and above, as confirmed by both N&B and sFCS in different cell models. This might be due to its fast maturation rate [21].

In the second part of our work, we compared the FPs under different pH conditions. This is relevant for live-cell studies with FPs targeting e.g. acidic organelles, such as endosomes, secretory granules, lysosomes, and Golgi-Network (pH range ca. 4.7–8 [46]), which play a role for the sorting, transport and degradation of proteins [24, 25]. In general, mNG and mGL did not exhibit a special sensitivity to changes in pH values between 5.6 and 9.2. Neither of the monitored parameters (photostability, brightness or *pf*) displayed a significant correlation with pH values.

In contrast, mEGFP showed an increase of *pf* at acidic pH, with this value being significantly higher than that of Gamillus. We did not observe a strong decrease in mEGFP brightness at low pH values, as it was instead previously reported [26, 28, 43, 44]. This might be due to the low laser powers employed in our studies, since a control experiment performed at a ca. four-fold higher laser power resulted in a decrease in mEGFP brightness of ca. 40% (S7 Fig in S1 File). Apart from light-induced photochemical effect, it might also be possible that the data spread obtained at lower excitation power could partially mask a decrease in brightness. In any case, our data show that the brightness of mEGFP at pH 5.6 is indeed slightly lower than that of the other FPs.

Also, Gamillus was influenced by changes in pH value. First, we observed that its brightness remained higher than that of mEGFP, especially at low pH values. Interestingly, the photostability and the *pf* decreased dramatically as a function of decreasing pH values. In contrast with the idea of Gamillus being a FP particularly useful under acidic conditions [24], our data indicate that this fluorophore might perform best in basic environments in the context of FFS measurements. It is possible that strong differences between Gamillus and, e.g., mEGFP might be observed instead at pH values below those explored in this work (i.e. pH <5.5).

In conclusion, our results indicate that mEGFP is in general a very good choice for the quantification of multimerization via FFS, also at pH values between 5.6 and 7.4. Although its brightness is lower than other examined FPs, its remarkable photostability would allow using higher excitation powers (thus increasing its brightness). Bright FPs, such as Gamillus, could be efficiently used for e.g. qualitative imaging with short acquisition times and low excitation powers. At neutral pH conditions, a remarkably high *pf* was observed for mGL, although care should be taken in experiments in which photobleaching might represent an issue. Finally, at basic pH conditions (e.g., up to 9.2), Gamillus represents an optimal choice based on a good photostability, high *pf* and brightness.

Supporting information

S1 File. Supporting materials and methods, supporting tables and supporting figures.
(DOCX)

39

S1 Data.

(XLSX)

Acknowledgments

Author Contributions

References

1. Arant RJ, Ulbrich MH. Deciphering the subunit composition of multimeric proteins by counting photo-bleaching steps. Chemphyschem. 2014; 15(4):600–5. https://doi.org/10.1002/cphc.201301092 PMID: 24481650

2. Hillesheim LN, Chen Y, Müller JD. Dual-color photon counting histogram analysis of mRFP1 and EGFP in living cells. Biophysical journal. 2006; 91(11):4273–84. https://doi.org/10.1529/biophysj.106.085845 PMID: 16980358

3. Kuzmanov U, Emili A. Protein-protein interaction networks: probing disease mechanisms using model systems. Genome Medicine. 2013; 5(4):37. https://doi.org/10.1186/gm441 PMID: 23635424

4. Godin AG, Rappaz B, Potvin-Trottier L, Kennedy TE, De Koninck Y, Wiseman PW. Spatial Intensity Distribution Analysis Reveals Abnormal Oligomerization of Proteins in Single Cells. Biophys J. 2015; 109 (4):710–21. https://doi.org/10.1016/j.bpj.2015.06.068 PMID: 26287623

5. Petazzi RA, Aji AK, Chiantia S. Fluorescence microscopy methods for the study of protein oligomerization. Prog Mol Biol Transl Sci. 2020; 169:1–41. https://doi.org/10.1016/bs.pmbts.2019.12.001 PMID: 31952683

6. Bacia K, Kim SA, Schwille P. Fluorescence cross-correlation spectroscopy in living cells. Nature Methods. 2006; 3(2):83–9. https://doi.org/10.1038/nmeth822 PMID: 16432516

7. Dunsing V, Luckner M, Zühlke B, Petazzi RA, Herrmann A, Chiantia S. Optimal fluorescent protein tags for quantifying protein oligomerization in living cells. Sci Rep. 2018; 8(1):10634. https://doi.org/10.1038/s41598-018-28858-0 PMID: 30006597

8. Chen Y, Johnson J, Macdonald P, Wu B, Mueller JD. Observing protein interactions and their stoichiometry in living cells by brightness analysis of fluorescence fluctuation experiments. Methods Enzymol. 2010; 472:345–63. https://doi.org/10.1016/S0076-6879(10)72026-7 PMID: 20580971

9. Chen Y, Wei LN, Müller JD. Probing protein oligomerization in living cells with fluorescence fluctuation spectroscopy. Proc Natl Acad Sci U S A. 2003; 100(26):15492–7. https://doi.org/10.1073/pnas.2533045100 PMID: 14673112

10. Dunsing V, Chiantia S. A Fluorescence Fluctuation Spectroscopy Assay of Protein-Protein Interactions at Cell-Cell Contacts. J Vis Exp. 2018(142). https://doi.org/10.3791/58582 PMID: 30582596

11. Digman MA, Dalal R, Horwitz AF, Gratton E. Mapping the number of molecules and brightness in the laser scanning microscope. Biophys J. 2008; 94(6):2320–32. https://doi.org/10.1529/biophysj.107.114645 PMID: 18096627

40

12. Dunsing V, Petrich A, Chiantia S. Multicolor fluorescence fluctuation spectroscopy in living cells via spectral detection. Elife. 2021;10. https://doi.org/10.7554/eLife.69687 PMID: 34494547

13. Heesink G, Caron C, van Leijenhorst-Groener K, Molenaar R, Gadella TWJ, Claessens MMAE, et al. Quantification of Dark Protein Populations in Fluorescent Proteins by Two-Color Coincidence Detection and Nanophotonic Manipulation. The Journal of Physical Chemistry B. 2022. https://doi.org/10.1021/acs.jpcb.2c04627 PMID: 36190918

14. Foo YH, Naredi-Rainer N, Lamb DC, Ahmed S, Wohland T. Factors affecting the quantification of bio-molecular interactions by fluorescence cross-correlation spectroscopy. Biophys J. 2012; 102(5):1174–83. https://doi.org/10.1016/j.bpj.2012.01.040 PMID: 22404940

15. Liebsch F, Aurousseau MRP, Bethge T, McGuire H, Scolari S, Herrmann A, et al. Full-length cellular β-secretase has a trimeric subunit stoichiometry, and its sulfur-rich transmembrane interaction site modulates cytosolic copper compartmentalization. J Biol Chem. 2017; 292(32):13258–70.

16. McGuire H, Aurousseau MR, Bowie D, Blunck R. Automating single subunit counting of membrane proteins in mammalian cells. J Biol Chem. 2012; 287(43):35912–21. https://doi.org/10.1074/jbc.M112.402057 PMID: 22930752

17. Ulbrich MH, Isacoff EY. Subunit counting in membrane-bound proteins. Nat Methods. 2007; 4(4):319–21. https://doi.org/10.1038/nmeth1024 PMID: 17369835

18. Wu B, Chen Y, Müller JD. Fluorescence fluctuation spectroscopy of mCherry in living cells. Biophys J. 2009; 96(6):2391–404. https://doi.org/10.1016/j.bpj.2008.12.3902 PMID: 19289064

19. Balasubramanian H, Sankaran J, Goh CJH, Wohland T. The dependence of EGFR oligomerization on environment and structure: A camera-based N&B study. Biophysical Journal. 2022; 121:4452–66.

20. Schwille P, Kummer S, Heikal AA, Moerner WE, Webb WW. Fluorescence correlation spectroscopy reveals fast optical excitation-driven intramolecular dynamics of yellow fluorescent proteins. Proc Natl Acad Sci U S A. 2000; 97(1):151–6. https://doi.org/10.1073/pnas.97.1.151 PMID: 10618386

21. Campbell BC, Nabel EM, Murdock MH, Lao-Peregrin C, Tsoulfas P, Blackmore MG, et al. mGreenLantern: a bright monomeric fluorescent protein with rapid expression and cell filling properties for neuronal imaging. Proceedings of the National Academy of Sciences. 2020; 117(48):30710. https://doi.org/10.1073/pnas.2000942117 PMID: 33208539

22. Costantini LM, Baloban M, Markwardt ML, Rizzo M, Guo F, Verkhusha VV, et al. A palette of fluorescent proteins optimized for diverse cellular environments. Nat Commun. 2015; 6:7670. https://doi.org/10.1038/ncomms8670 PMID: 26158227

23. Shaner NC, Lambert GG, Chammas A, Ni Y, Cranfill PJ, Baird MA, et al. A bright monomeric green fluorescent protein derived from Branchiostoma lanceolatum. Nat Methods. 2013; 10(5):407–9. https://doi.org/10.1038/nmeth.2413 PMID: 23524392

24. Shinoda H, Ma Y, Nakashima R, Sakurai K, Matsuda T, Nagai T. Acid-Tolerant Monomeric GFP from Olindias formosa. Cell Chemical Biology. 2018; 25(3):330–8.e7. https://doi.org/10.1016/j.chembiol.2017.12.005 PMID: 29290624

25. Casey JR, Grinstein S, Orlowski J. Sensors and regulators of intracellular pH. Nat Rev Mol Cell Biol. 2010; 11(1):50–61. https://doi.org/10.1038/nrm2820 PMID: 19997129

26. Haupts U, Maiti S, Schwille P, Webb WW. Dynamics of fluorescence fluctuations in green fluorescent protein observed by fluorescence correlation spectroscopy. Proc Natl Acad Sci U S A. 1998; 95 (23):13573–8. https://doi.org/10.1073/pnas.95.23.13573 PMID: 9811841

27. Widengren J, Mets Ü, Rigler R. Photodynamic properties of green fluorescent proteins investigated by fluorescence correlation spectroscopy. Chemical Physics. 1999; 250(2):171–86.

28. Vámosi G, Mücke N, Müller G, Krieger JW, Curth U, Langowski J, et al. EGFP oligomers as natural fluorescence and hydrodynamic standards. Sci Rep. 2016; 6:33022. https://doi.org/10.1038/srep33022 PMID: 27622431

29. Dunsing V, Mayer M, Liebsch F, Multhaup G, Chiantia S. Direct evidence of amyloid precursor-like protein 1 trans interactions in cell-cell adhesion platforms investigated via fluorescence fluctuation spectroscopy. Mol Biol Cell. 2017; 28(25):3609–20. https://doi.org/10.1091/mbc.E17-07-0459 PMID: 29021345

30. Sperber HS, Welke RW, Petazzi RA, Bergmann R, Schade M, Shai Y, et al. Self-association and sub-cellular localization of Puumala hantavirus envelope proteins. Sci Rep. 2019; 9(1):707. https://doi.org/10.1038/s41598-018-36879-y PMID: 30679542

31. Tzoneva R, Stoyanova T, Petrich A, Popova D, Uzunova V, Momchilova A, et al. Effect of Erufosine on Membrane Lipid Order in Breast Cancer Cell Models. Biomolecules. 2020; 10(5). https://doi.org/10.3390/biom10050802 PMID: 32455962

41

32. Petrich A, Dunsing V, Bobone S, Chiantia S. Influenza A M2 recruits M1 to the plasma membrane: A fluorescence fluctuation microscopy study. Biophys J. 2021; 120(24):5478–90. https://doi.org/10.1016/j.bpj.2021.11.023 PMID: 34808098

33. Ries J, Schwille P. Studying slow membrane dynamics with continuous wave scanning fluorescence correlation spectroscopy. Biophys J. 2006; 91(5):1915–24. https://doi.org/10.1529/biophysj.106.082297 PMID: 16782786

34. Smith EM, Macdonald PJ, Chen Y, Mueller JD. Quantifying protein-protein interactions of peripheral membrane proteins by fluorescence brightness analysis. Biophys J. 2014; 107(1):66–75. https://doi.org/10.1016/j.bpj.2014.04.055 PMID: 24988342

35. Balleza E, Kim JM, Cluzel P. Systematic characterization of maturation time of fluorescent proteins in living cells. Nat Methods. 2018; 15(1):47–51. https://doi.org/10.1038/nmeth.4509 PMID: 29320486

36. Hendrix J, Flors C, Dedecker P, Hofkens J, Engelborghs Y. Dark states in monomeric red fluorescent proteins studied by fluorescence correlation and single molecule spectroscopy. Biophys J. 2008; 94 (10):4103–13. https://doi.org/10.1529/biophysj.107.123596 PMID: 18234806

37. Hur KH, Macdonald PJ, Berk S, Angert CI, Chen Y, Mueller JD. Quantitative measurement of brightness from living cells in the presence of photodepletion. PLoS One. 2014; 9(5):e97440. https://doi.org/10.1371/journal.pone.0097440 PMID: 24820174

38. Ries J, Chiantia S, Schwille P. Accurate determination of membrane dynamics with line-scan FCS. Biophysical journal. 2009; 96(5):1999–2008. https://doi.org/10.1016/j.bpj.2008.12.3888 PMID: 19254560

39. Schenk A, Ivanchenko S, Röcker C, Wiedenmann J, Nienhaus GU. Photodynamics of red fluorescent proteins studied by fluorescence correlation spectroscopy. Biophys J. 2004; 86(1 Pt 1):384–94. https://doi.org/10.1016/S0006-3495(04)74114-4 PMID: 14695280

40. Shaner NC, Steinbach PA, Tsien RY. A guide to choosing fluorescent proteins. Nat Methods. 2005; 2 (12):905–9. https://doi.org/10.1038/nmeth819 PMID: 16299475

41. Cranfill PJ, Sell BR, Baird MA, Allen JR, Lavagnino Z, de Gruiter HM, et al. Quantitative assessment of fluorescent proteins. Nat Methods. 2016; 13(7):557–62. https://doi.org/10.1038/nmeth.3891 PMID: 27240257

42. Heppert JK, Dickinson DJ, Pani AM, Higgins CD, Steward A, Ahringer J, et al. Comparative assessment of fluorescent proteins for in vivo imaging in an animal model system. Mol Biol Cell. 2016; 27(22):3385–94. https://doi.org/10.1091/mbc.E16-01-0063 PMID: 27385332

43. Liu Y, Kim HR, Heikal AA. Structural basis of fluorescence fluctuation dynamics of green fluorescent proteins in acidic environments. J Phys Chem B. 2006; 110(47):24138–46. https://doi.org/10.1021/jp062164t PMID: 17125385

44. Steiert F, Petrov EP, Schultz P, Schwille P, Weidemann T. Photophysical Behavior of mNeonGreen, an Evolutionarily Distant Green Fluorescent Protein. Biophys J. 2018; 114(10):2419–31. https://doi.org/10.1016/j.bpj.2018.04.013 PMID: 29706225

45. Lam AJ, St-Pierre F, Gong Y, Marshall JD, Cranfill PJ, Baird MA, et al. Improving FRET dynamic range with bright green and red fluorescent proteins. Nat Methods. 2012; 9(10):1005–12. https://doi.org/10.1038/nmeth.2171 PMID: 22961245

46. Theillet FX, Binolfi A, Frembgen-Kesner T, Hingorani K, Sarkar M, Kyne C, et al. Physicochemical properties of cells and their effects on intrinsically disordered proteins (IDPs). Chem Rev. 2014; 114 (13):6661–714. https://doi.org/10.1021/cr400695p PMID: 24901537

42

Supporting Information

Benchmarking of novel green fluorescent proteins for the quantification of protein oligomerization in living cells

Annett Petrich[1], Amit Koikkarah Aji[1], Valentin Dunsing[1,2], Salvatore Chiantia[1,‡]

Supporting Materials and Methods

Fluorescent protein constructs

For the cloning of all constructs, standard PCRs with custom-designed primers were performed, followed by digestion with FastDigest restriction enzymes and ligation with T4-DNA-Ligase according to the manufacturer's instructions. All enzymes and reagents were purchased from Thermo Fisher Scientific (Waltham, MA, USA) and primers were acquired from Sigma Aldrich trademark of Merck KGaA (Darmstadt, Germany). Each construct was verified by Sanger sequencing (LGC Genomics GmbH, Berlin, Germany).

The plasmids encoding the monomeric and dimeric fluorescence protein (FP) mEGFP for i) cytoplasmic expression (mEGFP(1x) and mEGFP(2x)), ii) inner leaflet plasma membrane (PM) localization (FP linked to a myristoylated and palmitoylated (mp) peptide, mp-mEGFP(1x) and mp-mEGFP(2x)) and iii) outer leaflet PM localization (FP linked to a glycosylphosphatidylinositol (GPI)-anchor, GPI-mEGFP(1x)) were previously described [1, 2]. GPI-mEGFP(2x) was cloned by amplifying the GPI signal peptide (GPI$_{sp}$) linked to mEGFP from the GPI-mEGFP(1x) plasmid and inserting it into mp-EGFP(1x), using digestion with HindIII and NotI. Afterwards, the GPI-anchor C-terminally linked to mEGFP was amplified from GPI-mEGFP(1x) and cloned into the GPI$_{sp}$-mEGFP construct, using digestion with MluI and NotI.

The plasmids encoding the monomeric and dimeric FP mGreenLantern (mGL) for i) cytoplasmic expression (mGL(1x) and mGL (2x)), ii) inner leaflet PM localization (FP linked to a mp peptide, mp-mGL(1x) and mp-mGL(2x)) and iii) outer leaflet PM localization (FP linked to a GPI-anchor, GPI-mGL(1x) and GPI-mGL(2x)) were created by cloning of the monomeric mGL cassette from mGreenLantern_pcDNA3.1, a gift from Benjamin C. Campell (Helen and Robert Appel Alzheimer's Disease Research Institute, Weill Cornell Medicine, New York; Addgene plasmid #161912). To obtain all constructs in the same vector backbone, mGL was amplified from the mGreenLantern_pcDNA3.1 vector with and without a N-terminal linked mp peptide and cloned into the mEGFP-C1 (gift from Michael Davidson, Addgene plasmid #54759) by digestion with AgeI and Kpn21 or NheI and Kpn21, respectively. Subsequently, an additional amplified monomeric cassette from the mGreenLantern_pcDNA3.1 vector was ligated into mGL(1x) and mp-mGL(1x) by digestion with BglII and Kpn21 to generate mGL(2x) and mp-mGL(2x). Next, mp-mGL(1x) was digested with AgeI and BsrGI and cloned into GPI-mEGFP(1x) to generate GPI-mGL(1x). To generate the GPI dimer construct, mGL from the GPI-mGL(1x) construct was ligated into the GPI$_{sp}$-mEGFP plasmid by digestion with HindIII and BsrGI to generate the GPI$_{sp}$-mGL construct. Finally, the GPI-anchor C-terminally linked to mGL was amplified from the GPI-mGL(1x) plasmid and cloned into the GPI$_{sp}$-mGL construct, using digestion with MluI and NotI.

The plasmids encoding the monomeric and dimeric FP mNeonGreen (mNG) for i) cytoplasmic expression (mNG(1x) and mNG(2x)), ii) inner leaflet PM localization (FP linked to a mp peptide, mp-mNG (1x) and mp-mNG (2x)) and iii) outer leaflet PM localization (FP linked to a GPI-anchor, GPI-mNG(1x) and GPI-mNG(2x)) were created by cloning of the monomeric mNG cassette from pHAGE mNeonGreen-Core (HBc from HBV) IRES puro, a gift from Raphael Gaudin (Addgene plasmid #122202). To have all constructs in the same vector backbone, mNG was amplified from the pHAGE mNeonGreen-Core (HBc from HBV) IRES puro vector and cloned into mEGFP-C1 (gift from Michael Davidson, Addgene plasmid #54759) by digestion with AgeI and Kpn21 to generate mNG(1x). To obtain mNG(2x), mNG was amplified from mNG(1x) and the PCR product inserted into mNG(1x) by digestion with KpnI and EcoRI. Mp-mNG(1x) was generated by a ligation of the digest product of mNG(1x) with AgeI and BsrGI into the mp-mEGFP(1x) plasmid. Afterwards, the monomeric mNG cassette was amplified from the mp-NG(1x) construct and cloned into the mNG(2x) by digestion with NheI and BsrGI to obtain the mp-mNG(2x) plasmid. To generate GPI-mNG(1x), mp-mNG(1x) was digested with AgeI and BsrGI and cloned into GPI-mEGFP(1x) to generate GPI-mNG(1x). To obtain GPI-mNG(2x), mNG from the GPI-mNG(1x) construct was ligated into the GPI$_{sp}$-mEGFP plasmid after digestion with HindIII and BsrGI to generate the GPI$_{sp}$-mNG construct. Subsequently, the GPI-anchor C-terminal linked to mNG was amplified from the GPI-mNG(1x) plasmid and cloned into the GPI$_{sp}$-mNG construct, using digestion with MluI and NotI.

The plasmids encoding the monomeric and dimeric FP Gamillus for i) cytoplasmic expression (Gamillus(1x) and Gamillus(2x)), ii) inner leaflet PM localization (FP linked to a mp peptide, mp-Gamillus(1x) and mp-Gamillus(2x)) and iii) outer leaflet PM localization (FP linked to a GPI-anchor, GPI-Gamillus(1x) and GPI-Gamillus(2x)) were created by cloning of the monomeric Gamillus cassette from Gamillus/pcDNA3, a gift from Takeharu Nagai (Addgene plasmid #124837). To obtain all constructs in the same vector backbone, Gamillus was amplified from Gamillus/pcDNA3 and inserted into mEGFP-C1 (gift from Michael Davidson, Addgene plasmid #54759) by digestion with AgeI and Kpn21 to generate Gamillus(1x). To obtain Gamillus(2x), Gamillus was additionally amplified from Gamillus/pcDNA3 and cloned into Gamillus(1x) by digestion with Kpn21 and BglIII. The mp-Gamillus(1x) construct was generated by cloning the monomeric Gamillus cassette from Gamillus(1x) into mp-mEGFP(1x) after digestion with AgeI and BsrGI. The mp-Gamillus(2x) construct was obtained by a stepwise cloning. First, monomeric Gamillus cassette was amplified from Gamillus/pcDNA3 and cloned into mp-mNG(2x) by digestion with AgeI and BglII. Finally, the Gamillus cassette was additionally amplified from the Gamillus/pcDNA3 vector and inserted into the mp-Gamillus-mNG construct after digestion with BglII and EcoRI. Next, mp-mGamillus(1x) was digested with AgeI and BsrGI and cloned into GPI-mEGFP(1x) to generate GPI-mGamillus(1x). To generate the GPI dimer construct, the Gamillus cassette from the GPI-Gamillus(1x) construct was ligated into the GPI$_{sp}$-mEGFP plasmid by digestion with HindIII and BsrGI to generate the GPI$_{sp}$-Gamillus construct. Subsequently, the GPI-anchor C-terminal linked to mGamillus was amplified from the GPI-Gamillus(1x) plasmid and cloned into the GPI$_{sp}$-Gamillus construct, using digestion with MluI and NotI.

An overview of the linker sequences between the FPs is provided in Table S1.

Supporting Tables

Table S1: Overview of the linker sequences of the homo-dimers for the different fluorescence protein (FP) constructs used in this study. mp: myristoylated and palmitoylated peptide, GPI: glycosylphosphatidylinositol anchor. In previous work, we have shown that already a flexible 7 aa linker is sufficient to avoid significant energy transfer in a homo-oligomer and artifacts in brightness measurements [2]. The energy transfer efficiency might be even lower for linkers without glycines [3, 4]. Therefore, in general, long (i.e., ≥ 7 aa) linkers were used for the constructs in this study. For constructs which are already characterized and available (e.g., mEGFP constructs), the long flexible linkers were not modified. For newly produced constructs, when possible, 7-10 aa long rigid linkers (i.e., prolin-rich linkers containing the sequence PPAAPP) were introduced.

Construct	Linker length between FPs	Linker sequence between FPs
mEGFP(2x)	7 aa	SGLRSRG
mp-mEGFP(2x)	7 aa	SGLRSRG
GPI-mEGFP(2x)	12 aa	CTSRLPLHLRNA
mGL(2x)	10 aa	SGPPAAAPPV
mp-mGL(2x)	10 aa	SGPPAAAPPV
GPI-mGL(2x)	10 aa	PPAAAPPERV
mNG(2x)	10 aa	SGLRSRAQAS
mp-mNG(2x)	7 aa	RSRAQAS
GPI-mNG(2x)	10 aa	PPAAAPPERV
Gamillus(2x)	10 aa	SGPPAAAPPV
mp-Gamillus(2x)	10 aa	RSPPAAAPPV
GPI-Gamillus(2x)	10 aa	PPAAAPPERV

Table S2: Overview of molecular brightness and bleached fraction values measured via number and brightness (N&B) analysis for monomeric FPs in the cytosol and at the plasma membrane (PM), for different laser powers. Data correspond to Fig 1 of the main manuscript.

| Construct	Laser power [µW]	Bleached fraction		Brightness [kHz]		n
		mean	SEM	mean	SEM	
mEGFP(1x)	0.6	0.020	0.009	0.69	0.23	3
	1.2	0.023	0.004	0.89	0.06	28
	2.4	0.036	0.008	1.23	0.08	21
mNG(1x)	0.6	0.024	0.013	0.42	0.07	7
	1.2	0.054	0.014	0.95	0.05	28
	2.4	0.036	0.007	1.73	0.10	24
mGL(1x)	0.6	0.027	0.011	0.36	0.16	3
	1.2	0.117	0.007	0.82	0.04	25
	2.4	0.300	0.025	2.03	0.10	26
Gamillus(1x)	0.6	0.051	0.010	0.27	0.07	8
	1.2	0.116	0.010	0.95	0.08	33
	2.4	0.173	0.018	2.15	0.14	32
mp-mEGFP(1x)	0.6	0.051	0.022	1.30	0.40	4
	1.2	0.049	0.013	1.36	0.13	14
	2.4	0.041	0.007	2.82	0.23	29
mp-mNG(1x)	0.6	0.030	0.008	1.20	0.50	6
	1.2	0.036	0.006	1.23	0.11	17
	2.4	0.037	0.005	2.52	0.22	30
mp-mGL(1x)	0.6	0.056	0.009	0.73	0.23	6
	1.2	0.138	0.016	1.43	0.14	22
	2.4	0.315	0.025	2.37	0.25	8
mp-Gamillus(1x)	0.6	0.042	0.014	0.92	0.27	8
	1.2	0.146	0.019	1.69	0.17	22
	2.4	0.232	0.020	3.60	0.30	37

4

Table S3: Overview of average molecular brightness and fluorescence probability (*pf*) values from N&B analysis with a laser power of 1.2 µW for all FPs measured in the cytosol and at the PM. Data correspond to Figure 2 and Figure S2A.

	Brightness		pf		Brightness		pf
	mean ± SD	median ± IQR	mean ± SEM		mean ± SD	median ± IQR	mean ± SEM
mEGFP	0.9 ± 0.3	0.9 ± 0.4	0.77 ± 0.04	mp-mEGFP	1.4 ± 0.5	1.4 ± 0.8	0.77 ± 0.08
mEGFP(2x)	1.6 ± 0.2	1.5 ± 0.3		mp-mEGFP(2x)	2.5 ± 0.7	2.6 ± 1.2	
mNG	0.9 ± 0.3	0.9 ± 0.4	0.70 ± 0.10	mp-mNG	1.2 ± 0.2	1.2 ± 0.2	0.72 ± 0.11
mNG(2x)	1.6 ± 0.4	1.6 ± 0.7		mp-mNG(2x)	2.0 ± 0.4	2.0 ± 0.6	
mGL	0.8 ± 0.3	0.8 ± 0.4	0.79 ± 0.09	mp-mGL	1.3 ± 0.4	1.4 ± 0.6	0.92 ± 0.09
mGL(2x)	1.4 ± 0.4	1.4 ± 0.7		mp-mGL(2x)	2.7 ± 0.6	2.6 ± 1.1	
Gamillus	0.9 ± 0.4	0.8 ± 0.7	0.64 ± 0.08	mp-Gamillus	1.7 ± 0.5	1.6 ± 0.8	0.63 ± 0.06
Gamillus(2x)	1.6 ± 0.3	1.5 ± 0.6		mp-Gamillus(2x)	3.0 ± 0.8	3.1 ± 1.3	

Table S4: Overview of average molecular brightness and fluorescence probability (*pf*) values from scanning fluorescence correlation spectroscopy (sFCS) analysis with a laser power of 1.5 µW for all FPs measured at the PM under different pH conditions. Data correspond to Figure 3 and Figure S2B.

	pH 5.6			pH 7.4			pH 9.2		
	Brightness		pf	Brightness		pf	Brightness		pf
	mean ± SD	median ± IQR	mean ± SEM	mean ± SD	median ± IQR	mean ± SEM	mean ± SD	median ± IQR	mean ± SEM
GPI-mEGFP	5.6 ± 1.3	5.6 ± 1.5	0.81 ± 0.08	5.4 ± 1.3	5.2 ± 1.5	0.68 ± 0.06	5.8 ± 1.6	5.8 ± 1.6	0.63 ± 0.07
GPI-mEGFP(2x)	9.9 ± 2.0	9.4 ± 3.6		8.6 ± 1.6	8.0 ± 3.2		9.0 ± 1.8	8.7 ± 2.0	
GPI-mNG	7.3 ± 2.0	7.5 ± 3.0	0.66 ± 0.08	6.4 ± 2.0	6.3 ± 3.3	0.52 ± 0.06	6.2 ± 1.6	6.4 ± 2.5	0.60 ± 0.08
GPI-mNG(2x)	12.4 ± 2.8	12.2 ± 4.5		9.8 ± 2.6	9.4 ± 3.5		10.0 ± 1.8	10.1 ± 3.4	
GPI-mGL	6.5 ± 1.7	6.4 ± 1.9	0.70 ± 0.08	5.8 ± 1.0	5.7 ± 1.7	0.95 ± 0.18	6.1 ± 1.8	6.1 ± 1.8	0.53 ± 0.07
GPI-mGL(2x)	10.0 ± 2.0	10.3 ± 3.1		10.1 ± 2.8	9.4 ± 3.4		8.8 ± 2.0	8.1 ± 2.4	
GPI-Gamillus	7.6 ± 1.6	7.6 ± 2.1	0.49 ± 0.10	6.9 ± 1.8	6.8 ± 2.1	0.57 ± 0.08	6.9 ± 1.6	6.9 ± 1.7	0.68 ± 0.11
GPI-Gamillus(2x)	11.5 ± 3.4	10.7 ± 4.7		10.8 ± 2.5	11.0 ± 3.5		11.5 ± 2.9	10.9 ± 3.9	

Supporting Figures
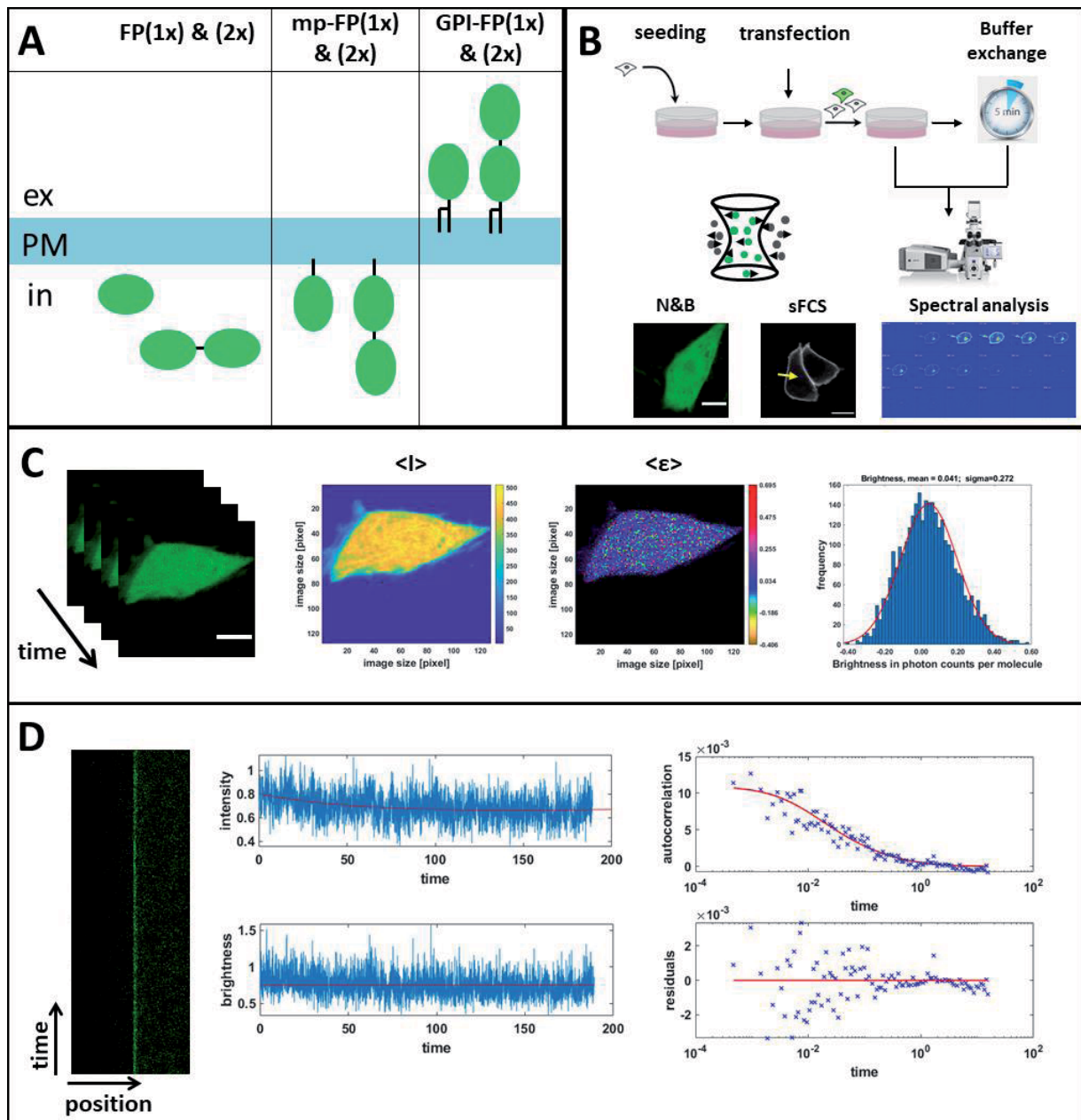
Fig S1: Schematic overview of the experimental setup. (A) Overview of the different fluorescent proteins (FPs) used in this study: cytosolic/soluble FPs, membrane associated constructs with the myristoylated and palmitoylated (mp) peptide and glycosylphosphatidylinositol (GPI)-anchor linked to the FP as a monomer or homo-dimer. The FPs used in this study were mEGFP, mNeonGreen (mNG), mGreenLantern (mGL) and Gamillus. PM: plasma membrane, ex: extracellular side, in: intracellular side. (B) Overview of the experimental procedure. One day after seeding, cells are transfected. The day after, cells are directly used for Number and Brightness (N&B) measurements or are washed and equilibrated in HEPES-Buffer with the appropriate pH before each measurement for scanning fluorescence correlation spectroscopy (sFCS) and spectral analysis. (C) N&B acquisition results in a three-dimensional (x-y-time) image stack. A ROI is selected around a cell or membrane region. Then, brightness (ε) values are calculated in each pixel. The results are then visualized as average intensity (<I>) map, brightness (<ε>) map or a brightness histogram with e.g. a superimposed Gaussian fit model. (D) sFCS measurements are performed perpendicular to the plasma membrane (PM), as also shown in panel (B). Scan lines (represented as kymographs) are aligned and the intensity at PM is integrated. The thus obtained fluorescence as a function of time is shown in the middle panels. Intensity variations on a long-time scale are corrected via subtraction of e.g. an exponential function (red line, upper panel), to obtain a final intensity trace (lower panel). Then, the autocorrelation function is calculated from the intensity trace and analyzed with a two-dimensional diffusion model (see S6 Fig for examples). This analysis provides, among other parameters, the average number of particles in the detection volume *N* and the average intensity <I>. The ratio between *N* and <I> is used to calculate the average molecular brightness.

7
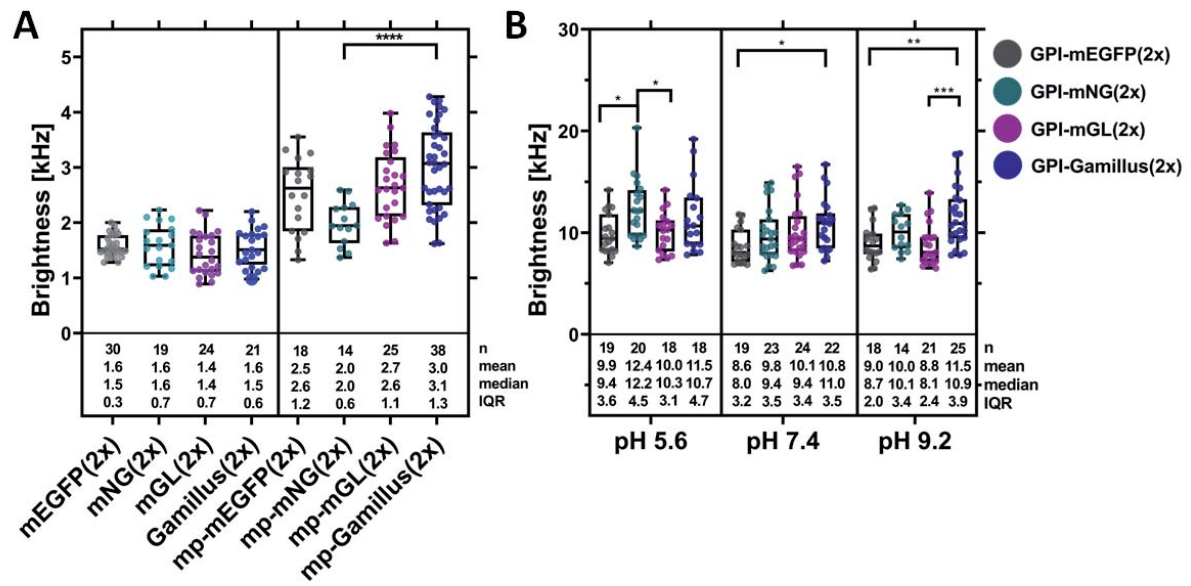
Fig S2: Brightness comparison for different green FP homo-dimers. (A): N&B measurements were performed ≈16 h after transfection in CHO-K1 cells, using a laser power of 1.2 µW. Box plot of the molecular brightness in kHz for the examined cytosolic and membrane-anchored FP (i.e., mp-FP) homo-dimers. Each point represents the average value measured in a single cell, pooled from three independent experiments. (B): sFCS measurements were performed in HEK293T cells for different pH conditions (pH 5.6, pH 7.4, and pH 9.2) ≈16 h after transfection, with a laser power of 1.5 µW. Box plots with single data points from three independent experiments show the molecular brightness in kHz for the homo-dimers of GPI-mEGFP , GPI-mNG , GPI-mGL and GPI-Gamillus. Median values and whiskers ranging from minimum to maximum values are displayed. Sample size, mean, median, and interquartile range (IQR) are indicated in the graph. Statistical significance was determined for both plots using one-way ANOVA Tukey´s multiple comparison test; * $p < 0.05$, ** $p < 0.005$, ***$p < 0.0005$, ****$p < 0.0001$.
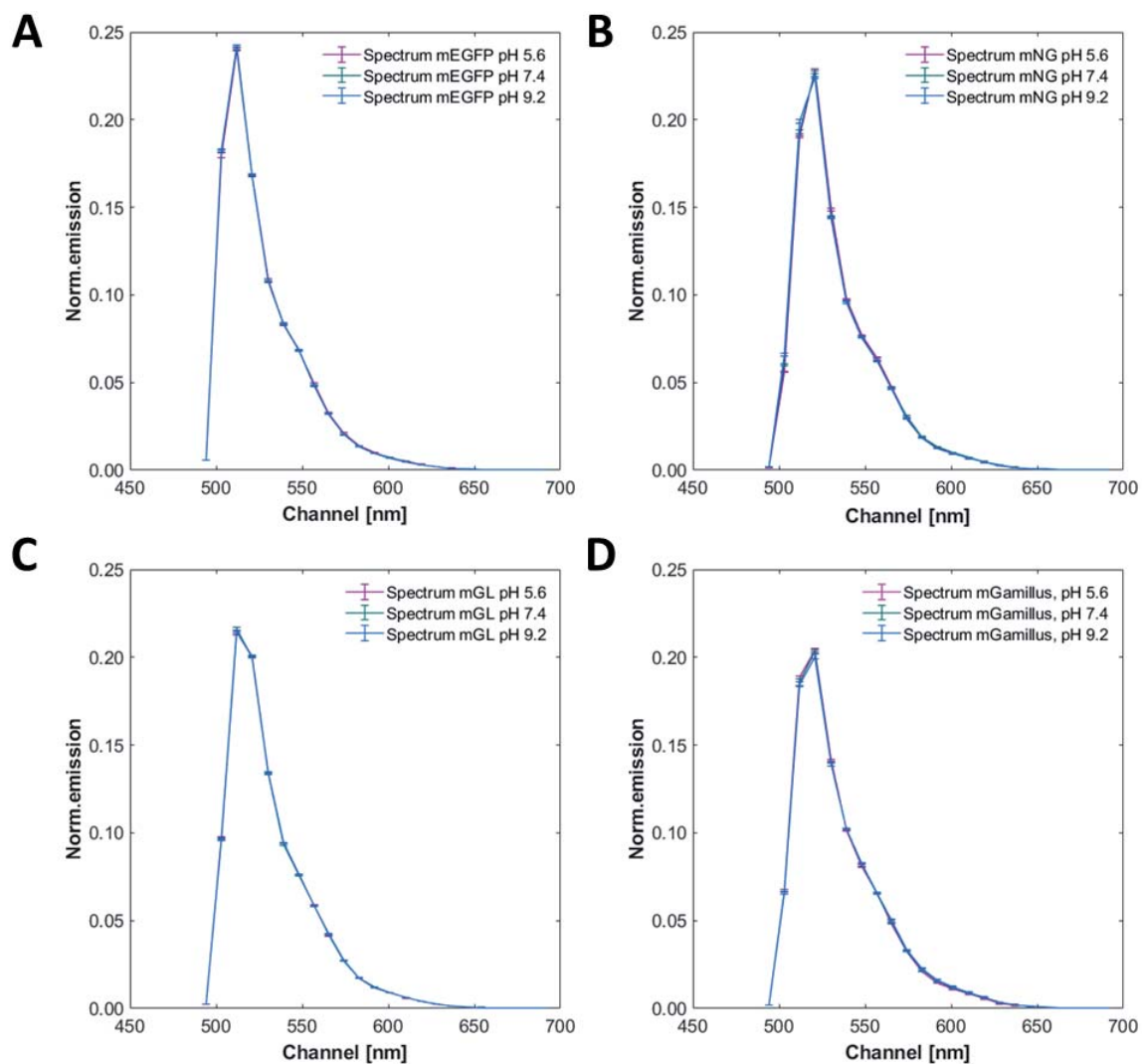
Fig S3: Normalized FP emission spectra at different pH values. Average emission spectra of GPI-mEGFP (A), GPI-mNG (B), GPI-mGL (C), and GPI-Gamillus (D) measured via spectral imaging (23 spectral channels from 491 nm to 695 nm) using 488 nm excitation on HEK 293T cells supplemented with buffer at different pH values (5.6, 7.4 and 9.2). At each pH value, ca. 10 cells were imaged, acquiring ten frames. To obtain the average emission spectra, pixels corresponding to the PM were semi-manually segmented (manual selection followed by removal of pixels with intensities below 25% of the maximum pixel intensity in the selected region) and detected spectra averaged over all pixels and cells measured at each pH.
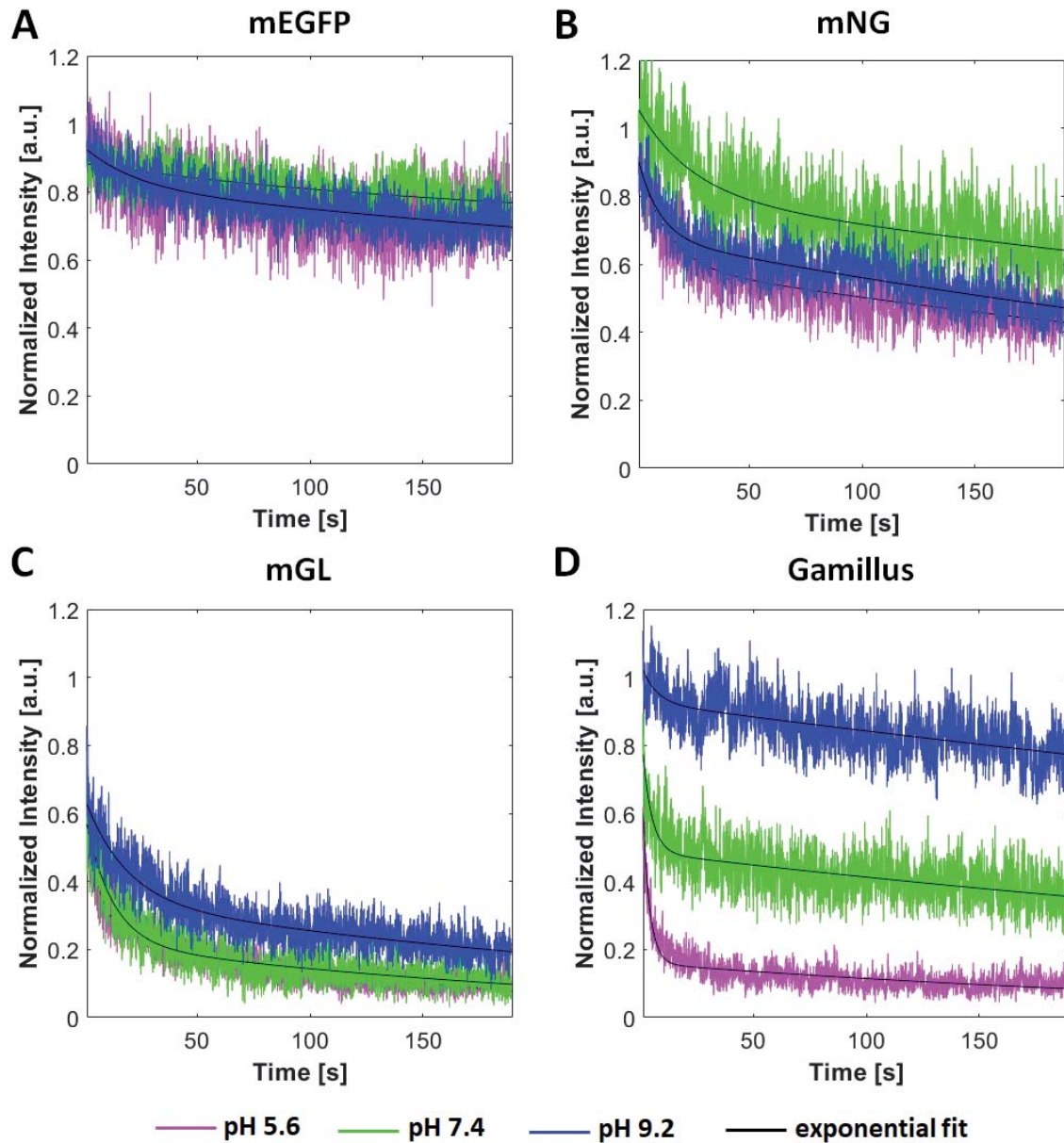
Fig S4: Comparison of photostability for different monomeric green FPs under different pH conditions via sFCS measurements. HEK293T cells were transfected with the appropriate FP construct, washed on the next day with HEPES buffer with the corresponding pH (pH 5.2 (magenta), pH 7.4 (green), and pH 9.2 (blue)) and then measured with a laser power of 6 μW, which is 4-fold higher than that used for standard sFCS measurements. The emission intensities were normalized to the initial values. Representative photobleaching curves are shown for GPI-mEGFP (A), GPI-mNG (B), GPI-mGL (C) and GPI-Gamillus (D). Solid line represents a double exponential fit, as guide to the eye.
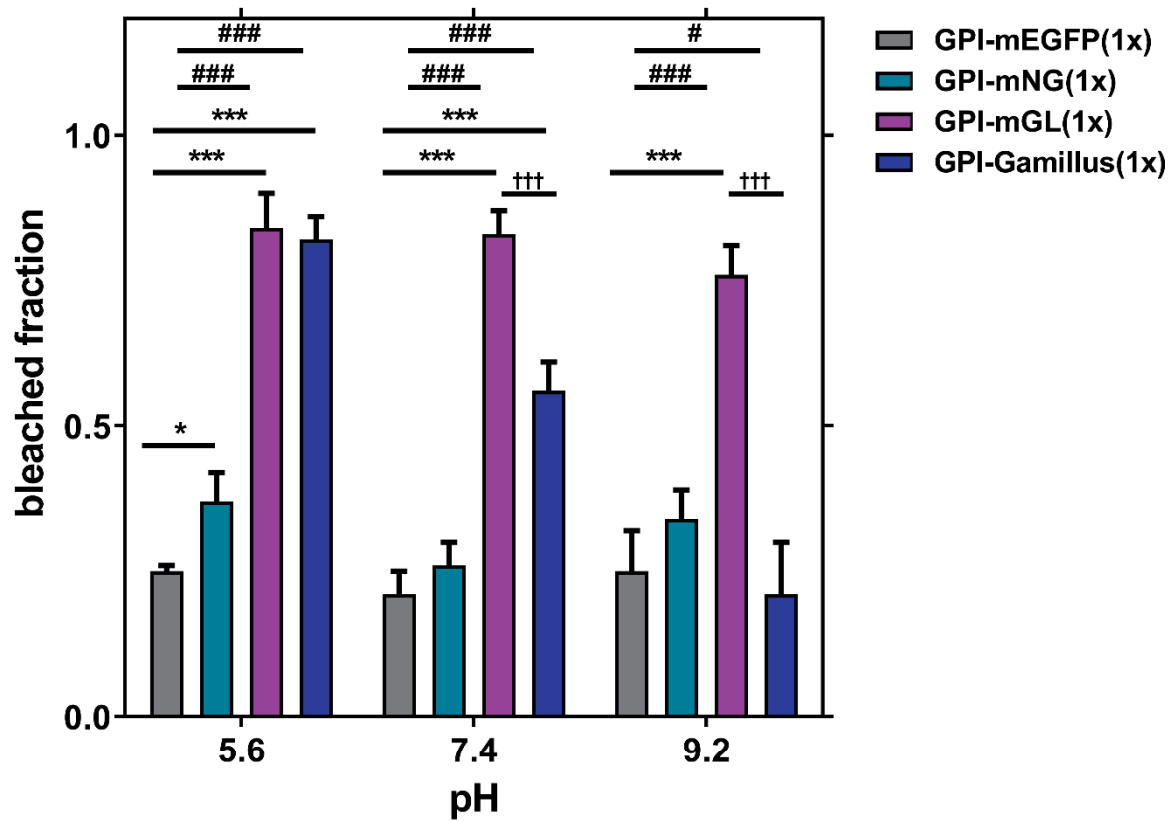
Fig S5: Comparison of bleached fractions for the examined monomeric FPs, at different pH values. The decrease of the fluorescence signal has been quantified after a 180 s sFCS measurement, as exemplified in Fig S4. For each FP, between 12 and 15 measurements from 3 independent samples were performed. Statistical significance was determined using one-way ANOVA Tukey´s multiple comparison test; * $p < 0.05$, ** $p < 0.005$, ***$p < 0.0005$. Different symbols refer to comparisons to GPI-mEGFP (*), GPI-mNG (#), GPI-mGL (†).
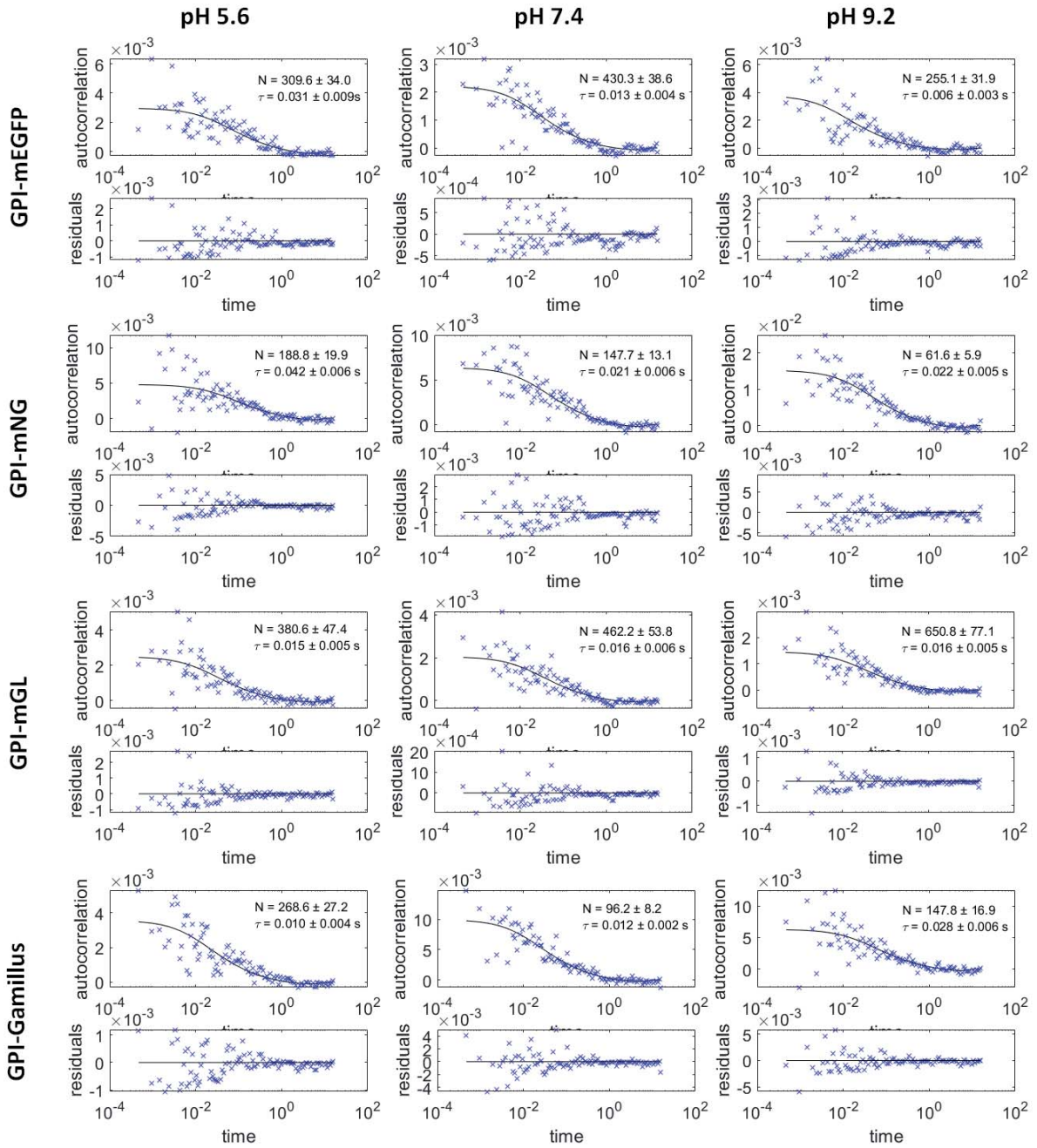
Fig S6: Representative sFCS autocorrelation functions and fit curves obtained for cells expressing GPI-FPs, under different pH conditions. Fit curves (solid line) were obtained by fitting with a two-dimensional Brownian diffusion model [5]: $\frac{1}{N}\left(1+\frac{\tau}{\tau_d}\right)^{-1/2}\left(1+\frac{\tau}{\tau_d S^2}\right)^{-1/2}$, where S is the structure parameter, τ_d is the diffusion time and N is the amount of fluorescent particles in the detection volume. The brightness parameter is calculated as ratio between the average detected signal $<I>$ and N. It is worth noting that, in order to compare different FP with varying photostability, generally low excitation powers had to be used to minimize bleaching, thus resulting in sub-optimal signal-to-noise ratio for some autocorrelation curves.

12

54
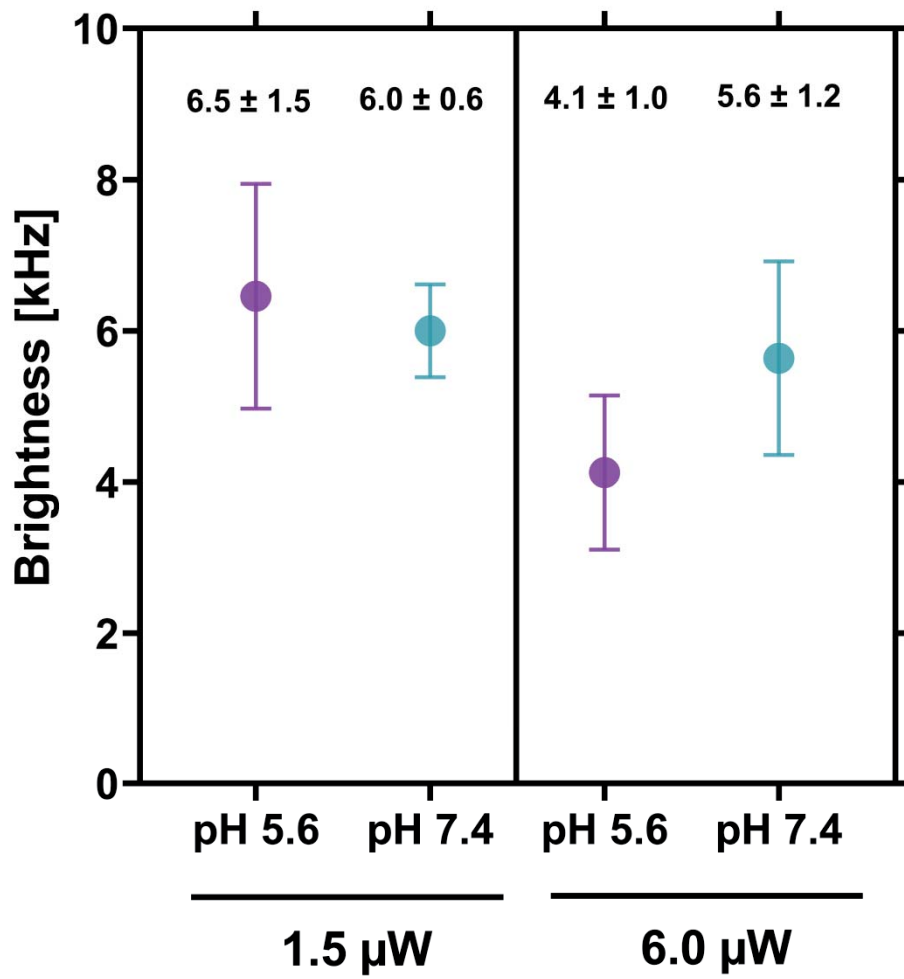
Fig S7: Comparison of brightness for the monomeric GPI-mEGFP at different pH values and laser powers. sFCS measurements were performed ≈16 h after transfection in HEK293T cells under different pH conditions (pH 5.6 and pH 7.4), using a laser power of 1.5 µW or 6 µW. The figure shows the mean brightness values from the monomeric GPI-mEGFP with the SD as error bar.

13

Supporting References

1. Dunsing, V., A. Petrich, and S. Chiantia, *Multicolor fluorescence fluctuation spectroscopy in living cells via spectral detection.* Elife, 2021. **10**.
2. Dunsing, V., et al., *Optimal fluorescent protein tags for quantifying protein oligomerization in living cells.* Sci Rep, 2018. **8**(1): p. 10634.
3. van Rosmalen, M., M. Krom, and M. Merkx, *Tuning the Flexibility of Glycine-Serine Linkers To Allow Rational Design of Multidomain Proteins.* Biochemistry, 2017. **56**(50): p. 6565-6574.
4. Arai, R., et al., *Design of the linkers which effectively separate domains of a bifunctional fusion protein.* Protein Eng, 2001. **14**(8): p. 529-32.
5. Ries, J. and P. Schwille, *Studying slow membrane dynamics with continuous wave scanning fluorescence correlation spectroscopy.* Biophys J, 2006. **91**(5): p. 1915-24.

3.2 Publication II: Effect of Erufosine on Membrane Lipid Order in Breast Cancer Cell Models

Effect of Erufosine on Membrane Lipid Order in Breast Cancer Cell Models

Rumiana Tzoneva [1],[†], **Tihomira Stoyanova** [1],[†], **Annett Petrich** [2], **Desislava Popova** [1], **Veselina Uzunova** [1] , **Albena Momchilova** [1] **and Salvatore Chiantia** [2],*

[1]   Bulgarian Academy of Sciences, Institute of Biophysics and Biomedical Engineering, 1113 Sofia, Bulgaria; tzoneva@bio21.bas.bg (R.T.); tihomira_stoyanova@abv.bg (T.S.); desislava.popova94@abv.bg (D.P.); vesi.uzunova@abv.bg (V.U.); albena_momchilova@abv.bg (A.M.)
[2]   Institute of Biochemistry and Biology, University of Potsdam, Karl-Liebknecht-Street 24-25, 14476 Potsdam, Germany; apetrich@gmx.net
*   Correspondence: chiantia@uni-potsdam.de; Tel.: +49-331-9775872
†   These author contribute equally to this work.

Abstract: Alkylphospholipids are a novel class of antineoplastic drugs showing remarkable therapeutic potential. Among them, erufosine (EPC3) is a promising drug for the treatment of several types of tumors. While EPC3 is supposed to exert its function by interacting with lipid membranes, the exact molecular mechanisms involved are not known yet. In this work, we applied a combination of several fluorescence microscopy and analytical chemistry approaches (i.e., scanning fluorescence correlation spectroscopy, line-scan fluorescence correlation spectroscopy, generalized polarization imaging, as well as thin layer and gas chromatography) to quantify the effect of EPC3 in biophysical models of the plasma membrane, as well as in cancer cell lines. Our results indicate that EPC3 affects lipid–lipid interactions in cellular membranes by decreasing lipid packing and increasing membrane disorder and fluidity. As a consequence of these alterations in the lateral organization of lipid bilayers, the diffusive dynamics of membrane proteins are also significantly increased. Taken together, these findings suggest that the mechanism of action of EPC3 could be linked to its effects on fundamental biophysical properties of lipid membranes, as well as on lipid metabolism in cancer cells.

Keywords: alkylphospholipids; fluorescence microscopy; fluorescence correlation spectroscopy; lipids; plasma membrane; cancer; lipid–lipid interactions; membrane microdomains; membrane biophysics

1. Introduction

Erufosine (EPC3) is a novel derivate of erucylphosphocholine that belongs to a group of antineoplastic drugs based on alkyl ether lipids [1]. EPC3 can effectively be applied intravenously, can cross the blood-brain barrier, and shows antitumor activity in the μM range [1,2]. For these reasons, EPC3 is a promising drug for treatment of several types of tumors, including human urinary bladder carcinoma, breast carcinoma, glioblastoma, and multiple myeloma [2]. On the one hand, due to its hydrophobic nature, this molecule is supposed to interact with cellular membranes, but detailed information regarding its molecular mechanism of action is scarce. On the other hand, other alkylphospholipids (APL) have been characterized in more detail. For example, it was shown that edelfosine, which was one of the first characterized APLs, induced apoptosis in cancer cells via interactions with lipid rafts [1], i.e., lipid-protein domains of the plasma membrane (PM) which are enriched in sphingolipids and cholesterol [3–5] and are involved in several cellular functions (see e.g., [6,7]). Such domains can also be characterized in protein-free model membrane systems

(e.g., lipid vesicles) constituted of typical PM lipids (e.g., saturated sphingomyelin (SM), unsaturated phosphatidylcholine (PC), and cholesterol). It was shown in fact that these model membranes displayed a phase separation into a liquid-ordered (L_o) and a liquid-disordered (L_d) phase [8]. The L_o phase was enriched in saturated lipids and cholesterol, and therefore provided a simple physical model to study raft-like domains [9,10]. In this context, it was shown that APLs partitioned into lipid bilayers and directly interacted with L_o domains [11]. The observed effects varied depending on lipid composition and the investigated APL (e.g., edelfosine or miltefosine) and included: disorganization of L_o domains [11], moderate to significant increase of membrane fluidity [12,13], and stabilization of SM/cholesterol domains [14]. More specifically, studies on erucylphosphocholine (which is more similar to EPC3, due to the shared unsaturated acyl chain structure) have indicated that this APL increases the fluidity of both cellular and model membranes [12], while weakening SM–cholesterol interactions [15].

So far, studies regarding the molecular mechanisms connected to the antitumor activity of EPC3 have been limited. Recently, using spectroscopic ellipsometry as a novel technique to study solid-supported lipid model systems, we have shown that treatment of lipid films composed of PC, SM, and cholesterol with EPC3 induced an increase in monolayer thickness [16].

In this work, we employed several methods based on fluorescence microscopy and analytical chemistry to investigate, for the first time, how EPC3 affected the physical properties of the PM.

First, we applied line-scan fluorescence correlation spectroscopy (lsFCS) [17,18] and scanning fluorescence correlation spectroscopy (sFCS) [19–21] to monitor the dynamics of membrane lipids and proteins, both in simple artificial membranes and directly in the PM of living cells. These methods belong to the family of fluorescence fluctuation techniques and have been effectively used in the past to quantify membrane dynamics (and, indirectly, membrane order) [22]. Furthermore, supported lipid bilayers (SLBs) as membrane models were used to study lipid–lipid interactions in a controlled environment and in specific relation to the precise lipid composition of the bilayer [23,24].

Second, using thin layer chromatography and gas chromatography, we evaluated the changes occurring in phospholipid and cholesterol amounts in the membranes of EPC3-treated cancer cells.

Finally, we quantified the influence of EPC3 on membrane order for the PM of cancer cell models using polarity-sensitive fluorescent probes [25]. In more detail, we investigated the spectral properties of two membrane probes (Laurdan and Di-4-ANEPPDHQ) which were shown to be influenced by lipid packing, membrane hydration, and composition to different extents [25,26].

Our results indicate that EPC3 modulates the PM lipid composition of cancer cells. Furthermore, it affects lipid–lipid interactions both in lipid membrane models and cellular membranes. Such alterations in membrane order appear to have a direct effect on membrane protein dynamics.

2. Materials and Methods

2.1. Chemicals

Erufosine (EPC3) was synthesized in the Max Planck Institute for Biophysical Chemistry, Göttingen, Germany, and was most graciously provided by Prof. Martin R. Berger. It was dissolved in a PBS (phosphate buffer saline, 137 mM NaCl, 2.7 mM KCl, 8 mM Na_2HPO_4, and 2 mM KH_2PO_4, pH 7.4) in 10 mM stock solution and kept at 4 °C. Di-4-ANEPPDHQ and Laurdan (6-dodecanyl-2-dimethylaminonaphtalene) were from Molecular Probes (Eugene, OR, USA). L-α-phosphatidylcholine from chicken egg (eggPC), cholesterol from ovine wool (Chol), sphingomyelin from porcine brain (bSM), 23-(dipyrrometheneboron difluoride)-24-norcholesterol (TF-Chol) and 1,2-dioleoyl-sn-glycero-3-phosphoethanolamine-N-(lissamine rhodamine B sulfonyl) (Rhod–DOPE) were purchased from Avanti Polar Lipids, Inc. (Alabaster, AL, USA).

2.2. Cell Culture

MDA-MB-231 highly invasive breast cancer cells and MCF-7 epithelial cancer cells were acquired from the American Type Culture Collection (ATCC, Kielpin Lomianki, Poland). Both cell lines are derived from breast adenocarcinoma, with MCF-7 cells retaining some characteristics of the differentiated mammary epithelium. All cell lines were incubated in phenol red-free DMEM culture medium with 10% fetal bovine serum, 2 mM L-glutamine, and 100 U/mL penicillin and 100 µg/mL streptomycin at 37 °C and 5% CO_2. Cells were passaged every 3–5 days, no more than 15 times. All solutions, buffers, and media used for cell culture were purchased from PAN-Biotech (Aidenbach, Germany).

2.3. Plasmids

The plasmid coding for human EGFR tagged with EGFP (hEGFR-EGFP) was a kind gift from Alexander Sorkin (Addgene plasmid #32751) [27]. To replace EGFP with mEGFP, both plasmids hEGFR-EGFP and mEGFP-N1 (gift from Michael Davidson, Addgene plasmid #54767) were digested with AgeI and NotI (New England Biolabs GmbH, Ipswich, MA, USA). The hemagglutinin (HA) gene from influenza virus strain A/FPV/Rostock/34 (H7N1) tagged with mEGFP at the C-terminus (FPV-HA-mEGFP) was cloned based on the previously described FPV-HA-mEYFP (gift from Andreas Herrmann, Humboldt University Berlin) [28]. Briefly, FPV-HA-mEYFP was digested using BglII and SacII (New England Biolabs GmbH, Ipswich, MA, USA), and the obtained HA-insert was ligated into mEGFP-N1. This plasmid is available on Addgene (#127810).

2.4. Supported Lipid Bilayers

Supported lipid bilayers (SLBs) were prepared as previously described [29,30]. Briefly, lipids were mixed in chloroform at the desired concentrations and dried on the walls of a glass vial. Then, the lipid film was rehydrated in PBS pH 7.4 and, after vigorous vortexing, sonicated to clarity in a bath sonicator. Typical concentrations during sonication were ~5–10 µM. Then, the obtained small unilamellar vesicle suspension was diluted ca. 10-fold and 100 µL were deposited on a small thin piece (~10 mm^2) of freshly cleaved mica glued to the surface of a glass coverslip (thickness #1). The mica and the vesicles suspension were confined using a 7 mm plastic cylinder, also glued to the glass surface. Vesicle fusion and bilayer formation were induced by addition of 3 mM $CaCl_2$. The volume was adjusted to 300 µL and the suspension was incubated for 10 min. Unfused vesicles were removed by addition and removal of 500 µL PBS, performed 10 times. The treatment with EPC3 was performed by adding the drug at the desired concentration in PBS directly on top of the SLB and waiting ca. 30 min before performing fluorescence measurements.

2.5. Line-Scan Fluorescence Correlation Spectroscopy on SLBs

The line-scan FCS (lsFCS) measurements on SLBs were performed as previously described [17]. Briefly, data were acquired by repeatedly scanning the focal volume in a linear fashion in the plane of the membrane. Line scans of ca. 5–10 µm length were chosen so that both bilayer phases (L_d and L_o) were scanned through. We typically acquired 2.5×10^5 lines, each divided in 256 pixels, with a pixel time of 1.27 µs (line time 763 ms). The intensity values were correlated along each line and between different lines, calculating the full spatiotemporal autocorrelation $G(\xi, \tau_i)$. To account for photobleaching, a mathematical correction was applied [17]. Data analysis was performed with a custom-written script in Matlab, by fitting $G(\xi, \tau_i)$ using a weighted nonlinear least-squares fitting algorithm and a mathematical model taking into account the linear scanning and two-dimensional (2D) Brownian diffusion. To capture the statistical information at larger lag times, we also included in the evaluation (via global fitting) the analysis of the temporal autocorrelation curve $G(0, \tau_i)$, calculated on a logarithmic scale with a multiple τ-algorithm [17]. Thus, we could obtain estimates for the waist ω_0 and the diffusion coefficient D for a fluorescent lipid analogue (TF-Chol, 0.01 mol%) added to

the examined SLBs. The autocorrelation curves were calculated independently for the different lipid phases, which could be identified due to the distinct affinity of a fluorescent dye (i.e., Rhod-DOPE, 0.1 mol%) to the L_o- and the L_d-phases. Line scans were performed using the same setup described above for sFCS, using a 488 nm argon laser (ca. 1.5 µW) for the excitation of TF-Chol. The signal originating from the Rhod-DOPE (excitation 561 nm, 561/488 dichroic mirror, emission collected between 571 and 650 nm) was collected only in order to distinguish the lipid phases, but not used further for lsFCS analysis. The reported D values for TF-Chol were calculated as an average of ca. 10 measurements for each EPC3 concentration, from three independent experiments, performed in different days. The D values in the L_o and L_d phase of SLB in the absence of EPC3 were used as a normalization reference for the D values measured in the presence of EPC3, in order to emphasize the relative effect of the drug rather than, for example, day-to-day variations in sample properties.

2.6. Lipid Extraction and Analysis of Phospholipids

MCF-7 and MDA-MB-231 cells were seeded in 25 cm^2 cell culture flasks at a density of 1.5×10^5 cells/mL. After a 24 h incubation, cells were treated with IC_{50} and IC_{75} amounts of EPC3 [31] and further incubated for 24 h. The extraction of membrane lipids (including internal membranes) was performed as described previously [32] with chloroform/methanol, according to the method of Bligh and Dyer [33]. Briefly, the organic phase obtained after extraction was concentrated and analyzed by thin layer chromatography. The individual phospholipid fractions were separated on silica gel G 60 plates (20 × 20 cm, Merck, Darmstadt, Germany) in a solvent system containing chloroform/methanol/acetic acid/water (70:35:8:4, *v/v*). The location of the separated fractions was visualized by iodine staining. The spots were scraped and quantified by estimation of inorganic phosphorus [34].

2.7. Determination of Cholesterol by Gas Chromatography

The cholesterol content in the membranes of EPC3-treated breast cancer cells (as described above) was determined using gas chromatography [35] using Carlo Erba gas-chromatography equipped with a flame-ionization detector isothermally at 190 °C and with a 2 m column coated with 10% DEGS on Chromosorb W60/80 mesh (Pharmacia Fine Chemicals Inc., Piscataway, NJ, USA), with nitrogen as the gas carrier.

2.8. Confocal Microscopy Imaging Using Di-4-ANEPPDQ and Laurdan

The cells were seeded in 35 mm microscopy dishes (CellVis, Mountain View, CA, USA) with an optical glass bottom (#1.5 glass, 0.16–0.19 mm) at a density of 5×10^4 cells/well for MDA-MB 231 and 1×10^5 cells/well for MCF-7. After an ~12 h incubation, the MDA-MB-231 cells were treated with a 20 (or 30) µM EPC3 solution in culture medium, corresponding to the previously measured IC_{50} and IC_{75} values [31]. The MCF-7 cells were treated with a 40 (or 60) µM EPC3 solution (corresponding to IC_{50} and IC_{75} values, Tzoneva R., unpublished data) in culture medium. In both cases, the treatment lasted for 24, 48, or 72 h. Control cells were incubated just with culture medium, following the same protocols. After the incubation period, the cell medium was removed. Then, the cells were washed twice with PBS, pH 7.4. Afterwards, 2 mL of serum-free and phenol red-free DMEM, and fluorescent dye (with final concentration of 1 µM for Di-4-ANEPPHQ or 5 µM for Laurdan) were added to the cell dish. The cells were further incubated for 30 min at 37 °C.

A Zeiss LSM 780 system (Carl Zeiss, Oberkochen, Germany) was used to acquire the confocal images, with a pixel size of ca. 200 nm (512 × 512 pixels). Samples were imaged using a Plan-Apochromat 40×/1.2 Korr DIC M27 water immersion objective. The excitation sources were a 488 nm argon laser (for Di-4-ANEPPDQ) or a 405 nm diode laser (for Laurdan). Fluorescence was detected between 498–579 nm (Channel 1) and 620–750 nm (Channel 2) for Di-4-ANEPPDQ, after passing through a 488 nm dichroic mirror, using a gallium arsenide phosphide (GaAsP) detector. Fluorescence of Laurdan was detected in the spectral ranges 410–463 nm (Channel 1) and 472–543 nm (Channel 2), after passing

through a 405/565 nm dichroic mirror. Out-of-plane fluorescence was reduced by using a 42.4 μm pinhole in front of the detector.

Confocal images were analyzed as previously described [25,26]. Briefly, for each experimental condition, ca. 5–10 confocal images of treated cells were acquired. In each fluorescence intensity image, several regions of interest (ROIs) were selected in correspondence of the PM of different cells. Due to the effect to the EPC3 treatment, some cells displayed significant morphological alterations, while undergoing apoptosis. We focused our analysis instead on pre-apoptotic cells, i.e., morphologically comparable to untreated cells. In these cells, ROIs could be chosen so to include portions of the PM clearly recognizable as ~0.5 μm thick bright lines (see Figure S1 for examples). Experiments were performed as independent duplicates on different days so that, for each EPC3 concentration and each time point, at least 50 cells were analyzed in total. All the pixels from ROIs collected within equivalent samples (i.e., same EPC3 concentration and same time point) were pooled together. For each pixel, the generalized polarization (GP) value was calculated as defined in [26], using a custom-written Matlab (The MathWorks, Natick, MA, USA) script and setting the calibration factor G = 1. The obtained results are shown as normalized occurrence histograms of all selected pixels.

2.9. Scanning Fluorescence Correlation Spectroscopy (sFCS) in Living Cells

For one-color sFCS experiments, 8×10^4 MDA-MB-231 cells were seeded in 35 mm dishes (CellVis, Mountain View, CA, USA) with optical glass bottoms (#1.5 thickness, 0.16–0.19 mm). After 24 h, cells were treated with medium containing 30 μM EPC3. After an additional incubation for 24 h, cells were transfected by using 200 ng (mp-mEGFP and mp-mEGFP(2×)) or 600 ng (hEGFR-EGFP or A/FPV-HA-mEGFP) plasmid DNA per dish with Lipofectamine™ 3000 according to the manufacturer's instructions (Thermo Fisher Scientific, Waltham, MA, USA). Plasmids were incubated for 15 min with 2 μL P3000 per μg plasmid and 2 μL Lipofectamine™ 3000 diluted in 50 μL serum-free medium, and then added dropwise to the cells.

After 24 h incubation, scanning fluorescence correlation spectroscopy (sFCS) measurements were carried out on a Zeiss LSM 780 system, equipped with a Plan-Apochromat 40×/1.2 Korr DIC M27 water immersion objective. Samples were excited with a 488 nm argon laser and the fluorescence was detected between 499 and 597 nm, after passing through a 488 nm dichroic mirror, using a GaAsP detector. To decrease out-of-focus light, a pinhole size of one airy unit (~39 μm) was used. To keep photobleaching below 20%, a laser power of 1.2 μW was chosen. For cell measurements, a line-scan of 256×1 pixel (pixel size 80 nm) was performed perpendicular to (i.e., across) the PM with a 403.20 μs scan time (0.67 μs pixel dwell time). For each measurement, 4×10^5 lines were acquired in photon counting mode, and the total scan time was around 3 min per measurement. Scanning data were exported as TIFF files. At the beginning of each measurement day, the signal was optimized by adjusting the collar ring of the objective to the maximal count rate for an Alexa Fluor® 488 (AF488, Thermo Fischer, Waltham, MA, USA) solution (50 μM dissolved in water) excited at the same laser power. For the focal volume calibration, a series of point FCS measurements was performed (ten measurements at different locations, each consisting of 15 repetitions of 10 s), and the data were fitted with a three-dimensional model including a triplet contribution. The structure parameter was typically around 6 to 9, and the diffusion time around 35 to 40 μs. The waist ω_0 was calculated from the measured average diffusion time ($\tau_{d,AF488}$) and previously determined diffusion coefficient of the used dye at room temperature ($D_{AF488} = 435$ μm^{2}s^{-1}) [36], according to the following Equation (1):

$$\omega_0 = \sqrt{4\tau_{d,AF488}D_{AF488}} \tag{1}$$

Typical values were 200–250 nm. All measurements were performed at room temperature.

The sFCS analysis followed the procedure described previously [19,21,37]. Briefly, the TIFF files were imported and analyzed in Matlab using a custom-written code. All scanning lines were aligned as kymographs and divided in blocks of 1000 lines. In each block, lines were column-wise summed

and the x position with maximum fluorescence was determined by fitting with a Gaussian function. This algorithm finds the position of the PM in each block and is used to align all lines to a common origin. The pixels corresponding to the membrane were defined as pixels which are within ±2.5 σ of the peak. In each line, these pixels were integrated, providing the membrane fluorescence time series F(t). A background correction was applied by subtracting the average pixel fluorescence value on the inner side of the membrane multiplied by 2.5 σ (in pixel units) from the membrane fluorescence, in blocks of 1000 lines [38]. In order to correct for depletion due to photobleaching, the fluorescence time series was fitted with a two-component exponential function and a mathematical correction was applied [17]. Finally, the normalized ACF was calculated according to Equations (2) and (3):

$$G(\tau) = \frac{\langle \delta F(t)\delta F(t-\tau)\rangle}{\langle F(t)\rangle^2} \tag{2}$$

where

$$\delta F = F(t) - \langle F(t)\rangle \tag{3}$$

To avoid artefacts that can be caused by long-term instabilities of the system or single bright events, correlation functions were first calculated segment wise (10 segments per time trace), and segments with distortions were manually removed before averaging the correlation functions. Eventually, a model for two-dimensional diffusion in the membrane and a Gaussian focal volume geometry [37] was fitted to the ACF, as described in Equation (4):

$$G(\tau) = \frac{1}{N}(1 + \frac{\tau}{\tau_D})^{-1/2}(1 + \frac{\tau}{\tau_D S^2})^{-1/2} \tag{4}$$

where τ_D denotes the diffusion time, and N the number of particles. The structure parameter S was fixed to the value of the daily based calibration measurement. Diffusion coefficients (D) were calculated using the calibrated waist ω_0 of the focal volume: $D = \omega_0^2/4\tau_D$.

All resulting data were analyzed using GraphPad Prism 5.0 (GraphPad Software Inc., San Diego, CA, USA), and were displayed as box plots indicating the median values and with Tukey whiskers. Quantities in the main text are expressed as mean ± SD. Sample sizes and *p*-values are indicated in figure captions. Statistically significant differences between control and test samples were determined using one-way ANOVA analysis followed by the Bonferroni's multiple comparisons test. A *p*-value < 0.01 was considered indicative of statistical significance.

3. Results and Discussion

3.1. EPC3 Increases Membrane Fluidity in Lipid Bilayer Models

In order to assess the influence of EPC3 on lipid–lipid interactions, first, we investigated its effects on controlled membrane models. In more detail, we prepared SLBs mimicking the general composition of the outer leaflet of the PM. These bilayers were composed of a natural mixture of PC (i.e., eggPC), sphingomyelin (bSM), and cholesterol (4/4/2 molar ratio). Such ternary lipids mixtures are known to separate into a liquid disordered (L_d) and a liquid-ordered phase (L_o), thus, providing a simple model for the study of phase separation occurring at the PM of living cells [22,39,40].

In this experiment, first, we observed the effect of EPC3 on the general appearance of the L_o/L_d phase separation in SLBs, via confocal fluorescence microscopy. For this purpose, SLBs were labeled with an unsaturated fluorescent lipid (Rhod-DOPE) which readily partitions in the L_d phase [41]. As apparent in Figure 1A, SLBs show bright patches enriched in Rhod-DOPE (i.e., L_d phase) and dark regions devoid of Rhod-DOPE (i.e., L_o phase). In the presence of increasing amounts of EPC3 in solution, the surface occupied by the L_d phase increases (Figure 1B–D, Figure S2). At the highest EPC3 concentration (i.e., 10 μM, Figure 1D), only small patches of L_o phase are still visible. These

results indicate that EPC3 can effectively insert into the bilayer and destabilize the L_o phase. A similar induction of lipid mixing was also observed for other APLs in giant unilamellar vesicles [42].
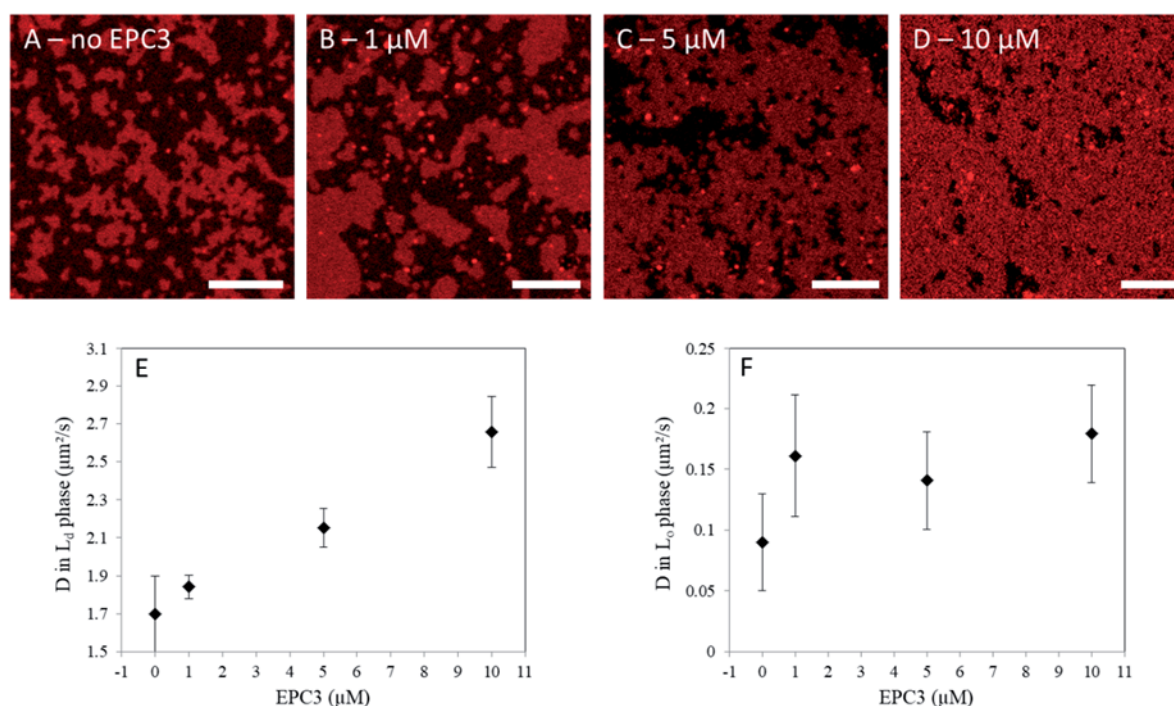
Figure 1. Effect of erufosine (EPC3) on phase-separating model membranes. (**A–D**) Representative confocal fluorescence microscopy images of eggPC/bSM/Chol 4/4/2 molar ratio supported lipid bilayers (SLBs) in the presence of 0, 1, 5, and 10 µM EPC3, respectively. The bilayers were labeled with 0.1 mol% Rhod-DOPE. Darker zones (devoid of Rhod-DOPE) indicate L_o regions of the SLB. Images were acquired at RT. Scale bars are 10 µm; (**E–F**) Values of the diffusion coefficients D measured via line-scan fluorescence correlation spectroscopy (lsFCS) in the L_d, (**E**) and L_o phase (**F**) of eggPC/bSM/Chol 4/4/2 molar ratio SLBs in the presence of EPC3. The reported values refer to the diffusion of a fluorescent cholesterol analogue (TF-Chol, 0.01 mol%). Independent experiments were repeated in triplicate and averaged after normalization (see Materials and Methods). Error bars represent standard deviations.

Next, we characterized the degree of order of the lipid bilayer, in each phase. To this aim, we quantified the diffusion coefficient (D) of a fluorescent membrane probe (TF-Chol) both in the L_o and L_d phases. Lipid dynamics are, in general, connected with membrane order, with lower D values associated with tighter lipid packing and stronger lipid–lipid interactions [22]. Using lsFCS, we measured D for TF-Chol in the L_d (Figure 1E) and L_o phases (Figure 1F), in the presence of increasing concentrations of EPC3. In the absence of the drug, D was ca. 0.1 µm²/s in the ordered phase and ca. 20-fold higher in the disordered phase, as expected from previous experiments [39]. In the presence of EPC3, we observed a ca. 60% increase in lipid diffusion dynamics in the L_d phase. For the L_o phase, we observed a similar increase in D, although the data spread was larger in this case. On the one hand, these results clearly suggest that EPC3 has a fluidizing effect on the lipid bilayer that leads to a significant increase of the diffusion of membrane components. On the other hand, it is not possible to determine from these data whether EPC3 interacts preferentially with (and inserts in the bilayer through) the L_o or the L_d phase. Interestingly, saturated alkylphospholipids were suggested to partition at the boundary between L_o and L_d phases [42].

3.2. EPC3 Treatment Alters Phospholipid and Cholesterol Contents in Cell Membranes

To monitor the influence of EPC3 on the concentrations of the major phospholipid components and cholesterol in cell membranes (i.e., PM and internal membranes), we characterized the following

two breast cancer cell models: the high-invasive MDA-MB-231 cell line and the low-invasive MCF-7 cell line. Both cell types were treated with EPC3 (IC_{50} and IC_{75}) for 24 h and lipid amounts were measured by means of TLC and gas chromatography.

Some APLs are known to inhibit the synthesis of key phospholipids such as PC and SM [43–46]. Accordingly, we observed a similar effect in EPC3-treated MCF-7 and MDA-MB-231 cells (Figure 2A,B, respectively). The SM content significantly decreased with increasing concentration of EPC3 in both cell lines. For instance, the decrease of SM content after treatment with IC_{75} EPC3 was ~24% for MCF-7 cells and ~16% for MDA-MB-231 cells as compared with the control samples. This finding is in line with the observations of Marco and coworkers [47] who showed that treatment of human hepatoma HepG2 cell line with Miltefosine led to inhibition of SM metabolism. Disturbances in SM synthesis could cause the accumulation of ceramide and sphingosine, which regulate cellular functions such as proliferation, gene expression, differentiation, mitosis, cell survival, and apoptosis. For example, sphingosine and ceramide can induce apoptosis via the intrinsic apoptotic pathway by modulating the permeability of the mitochondrial membrane, thereby releasing proteins such as cytochrome C [48].
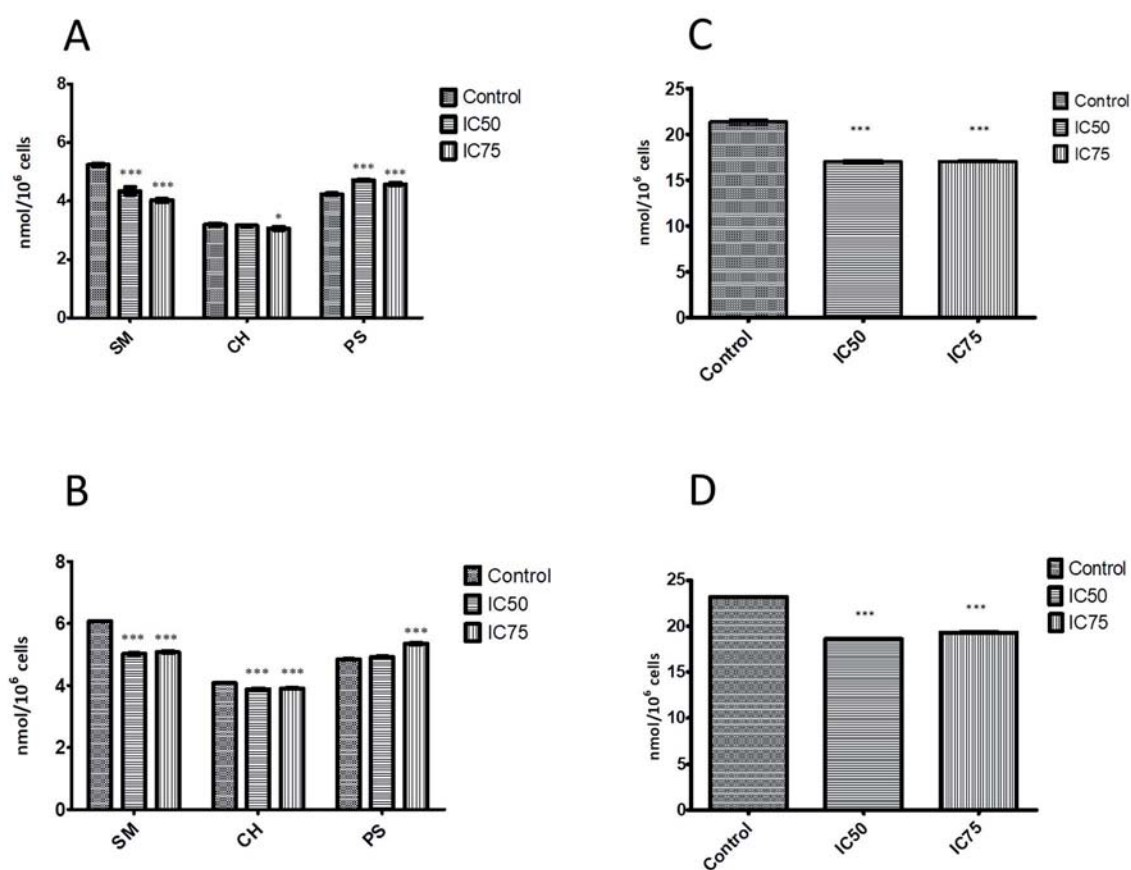
Figure 2. Effect of EPC3 on the level of sphingomyelin, cholesterol, phosphatidylserine, and phosphatidylcholine in cell membranes. (**A**) Amounts of sphingomyelin (SM), cholesterol (CH), and phosphatidylserine (PS) in MCF-7 cells treated with EPC3 for 24 h; (**B**) Amounts of sphingomyelin (SM), cholesterol (CH), phosphatidylserine (PS) in MDA-MB-231 cells treated with EPC3 for 24 h; (**C**) Amounts of phosphatidylcholine (PC) in MCF-7 cells treated with EPC3 for 24 h; (**D**) Amounts of phosphatidylcholine (PC) in MDA-MB-231 cells treated with EPC3 for 24 h. Data are obtained as means of three independent experiments. Error bars represent the standard deviations. Statistical significance is calculated against controls in each group using ANOVA one-way test and Bonferroni post-test. * $p < 0.01$ and *** $p < 0.0001$.

Furthermore, our results show an EPC3-induced reduction of PC amount. The effect was observed in both cancer cell lines (Figure 2C,D). In the MCF-7 cells treated with IC_{75} EPC3, the PC decrease was

20% as compared with the control samples. In the MDA-MB-231 cells, we observed a 17% decrease. Interestingly, one of the pathways for inducing apoptosis in cells treated with APLs is thought to be indeed the inhibition of PC synthesis. Our results support this hypothesis, as they show statistically significant reductions in PC levels at both EPC3 concentrations. Previous studies have demonstrated that Miltefosine also inhibited PC synthesis [44].

In contrast, the PS levels in the membranes of both treated cell lines appear to slightly increase (Figure 2A,B). Increased PS levels have also been previously observed in cancer cells as a response to chemotherapy or radiation treatment [49].

As shown in Figure 2A,B, treatment with EPC3 also resulted in a slight decrease in cholesterol levels. The membranes of the highly invasive cell line MDA-MB-231 were found to initially contain more cholesterol than those of the MCF-7 cells. These results are consistent with the hypothesis that high cholesterol levels in cell membranes can enhance cell migration in cancer models, including MDA-MB-231 cells [50–52]. Our data further show a reduction in cholesterol levels after treatment with EPC3 cells that is correlated with reduced cell survival, as we have previously observed [31]. Recent studies have indicated that the administration of membrane-active APLs such as edelfosine, erucylphosphocholine, and perifosine reduces the proliferation of HepG2 cells, disrupting cholesterol trafficking from the PM to intracellular membranes and decreasing the esterification of cholesterol [53]. Our data show that treatment of both MCF-7 and MDA-MB-231 cells with highly cytotoxic concentrations of EPC3 (IC$_{75}$, [31]) resulted in a small but reproducible reduction in cholesterol levels (i.e., ~5%). The molar ratio of phospholipid-to-cholesterol content of low invasive untreated MCF-7 cells was ~9.7. After treatment with EPC3 (IC$_{75}$), the ratio decreased to ~8.4 (unpaired t-test, $p < 0.0004$). The high-metastatic cell line MDA-MB-231 showed an average phospholipid-to-cholesterol ratio of ~8.4, which decreased to 7.6 upon treatment with IC$_{75}$ EPC3 (unpaired t-test, $p < 0.0002$). Altered levels of (intra-)cellular lipids and cholesterol are linked to cancer aggressiveness [54–56]. More specifically, saturated lipids were suggested to reduce the fluidity and dynamics of the membrane and to increase resistance to conventional chemotherapy [57]. The presence and amounts of saturated sphingolipids (e.g., SM) are linked to the physical properties of ordered PM domains (e.g., raft domains) [58]. In addition, reducing cholesterol content with membrane-depleting agents or inhibitors of cholesterol synthesis (e.g., statins) was suggested to alter the structure of lipid rafts [57]. The consequent raft destabilization could, in turn, interfere with the proliferation and migration of tumor cells [59,60]. EPC3 treatment of both cancer cell lines induces a significant decrease in the amounts of specific cellular lipids, such as SM and cholesterol, as well as alterations in their relative molar ratios. Therefore, we argue that the cytotoxic effects of EPC3 could be linked to alterations in the lateral organization of cellular membranes and, in particular, to a decreased stability or amount of ordered lipid domains.

3.3. EPC3 Alters the Fluidity of the Plasma Membrane of Living Cells

In order to investigate the effects of EPC3 directly in the PM of living cells, we applied an approach based on the spectroscopic properties of two fluorescent molecules (i.e., Di-4-ANEPPDHQ and Laurdan) which are strongly sensitive to membrane order and lipid packing [25,26]. In the context of studies regarding the effect of APLs on lipid bilayers, Laurdan was used to detect and increase in the fluidity of model membranes induced by Miltefosine [61]. In this experiment, we directly characterized the PM of both MDA-MB-231 and MCF-7 breast cancer cell models. In previous studies, we observed that EPC3 caused increased cytotoxicity, apoptosis, and cytoskeleton reorganization especially in highly invasive MDA-MB-231 cells as compared with MCF-7 samples [62,63]. In addition, MDA-MB-231 cells showed cell cycle arrest after treatment with EPC3 [63].

The mechanism by which Laurdan and Di-4-ANEPPDHQ detect changes in the local membrane environment is similar for the two molecules, i.e., the less polar environment of the ordered bilayer phase (e.g., L$_o$ phase or a raft-like domain in the PM) induces a blue shift in the emission maxima of both fluorescent probes. This shift can be quantified by calculating a ratiometric measurement of the fluorescence intensity observed in two spectral regions (or channels), known as a GP value. Higher GP

values correspond to a relatively higher fluorescence emission in the shorter-wavelength spectral region, and therefore a higher degree of membrane order and tighter lipid packing [26].

The MDA-MB-231 and MCF-7 cells were treated with the corresponding IC_{50} and IC_{75} EPC3 concentrations and were observed via confocal fluorescence microscopy after 24, 48, and 72 h. The EPC3 treatment induced, in general, decreased cell viability, accompanied by morphological changes which, eventually, led to apoptosis [31]. Next, we focused our analysis on early apoptotic cells, i.e., cells which do not yet appear morphologically significantly different from those in the control samples. For such cells, it was possible to clearly identify the PM and perform a GP analysis of the fluorescence signal (Figure S1).

Figure 3 shows normalized histograms for Di-4-ANEPPDQH GP values measured in MDA-MB-231 cells, in the presence of 20 µM or 30 µM EPC3. In all cases, the PM region of several cells was manually selected and the GP values for each pixel within these ROIs were calculated, as described in the Materials and Methods section and Figure S3A–D.
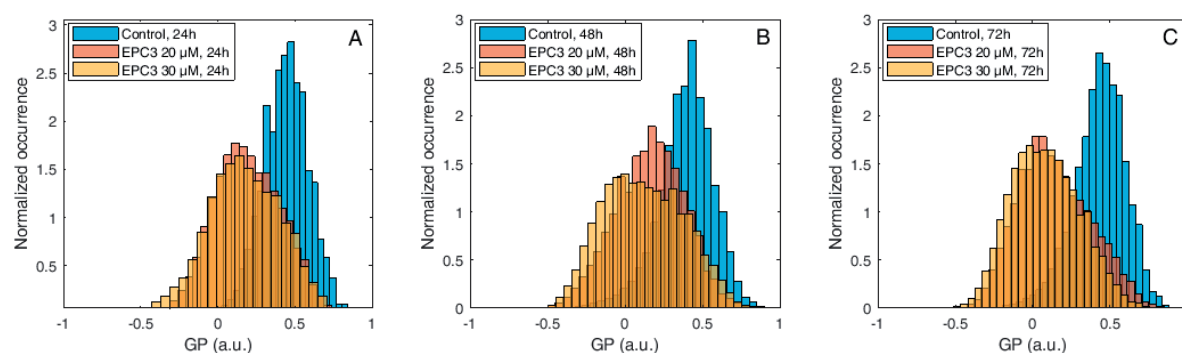
Figure 3. Di-4-ANEPPDQH generalized polarization (GP) values measured at the plasma membrane (PM) of MDA-MB-231 cells after EPC3 treatment. Normalized histograms of GP values measured in pixels belonging to the PM of MDA-MB-231 cells labeled with Di-4-ANEPPDQH. Cells were treated with 20 µM (orange bars) or 30 µM (yellow bars) EPC3. GP values measured in cells not treated with EPC3 are shown as blue bars. Fluorescence intensity values were acquired 24 h (**A**), 48 h (**B**), and 72 h (**C**) after the addition of EPC3. For each condition, GP values were pooled from ca. 50 ROIs selected at the PM of distinct cells, in two independent experiments. The total number of calculated GP values (and measured pixels) for each experimental condition was between ca. 10,000 and 40,000. Measurements were performed at RT. Representative images of treated cells and ROIs are shown in Figures S1 and S3.

As shown in Figure 3, Figure S3, and Table S1, the fluorescence emission of Di-4-ANEPPDQH indicates that EPC3 treatment of cancerous cells induces a time-dependent increase of PM disorder. Only minor differences were observed between IC_{50} and IC_{75} EPC3 concentrations (i.e., 20 and 30 µM for MDA-MB-231 cells, respectively). Performing the same experiment using MCF-7 cells (Figure 4, Figure S4, and Table S2), we observed that EPC3-induced membrane order alterations are stronger and occur faster in MDA-MB-231 cells.

In the case of MCF-7 cells, in fact, no significant alteration in membrane order was observed after 24 h of treatment, both at IC_{50} and IC_{75} EPC3 concentrations (i.e., 40 and 60 µM for MCF-7 cells, respectively). After 48 and 72 h, however, the GP distribution appeared significantly shifted to lower values, independently from the EPC3 concentration (Figure 4B–C, Figure S4, and Table S2).

Next, we employed a complementary assay quantifying the GP parameter, following analogous treatment of MDA-MB-231 and MCF-7 cells, using Laurdan as the fluorescent probe instead of Di-4-ANEPPDHQ (Figures S1I,L and S5).

The results shown in Figure 5, Figure S5, and Table S3 indicate the presence of a concentration-dependent decrease in membrane order after 48 and 72 h treatment with EPC3. We did not observe prominent alterations of the cell membrane order after 24 h treatment. These observations are qualitatively similar to those performed using Di-4-ANEPPDQH as the fluorescent probe. In addition,

in analogy to the results shown in Figure 4 (i.e., labeling of MCF-7 cells with Di-4-ANEPPDQH), the observed changes in lipid packing were larger in MDA-MB-231 than in MCF-7 cells (Figures S6 and S7, and Table S4).
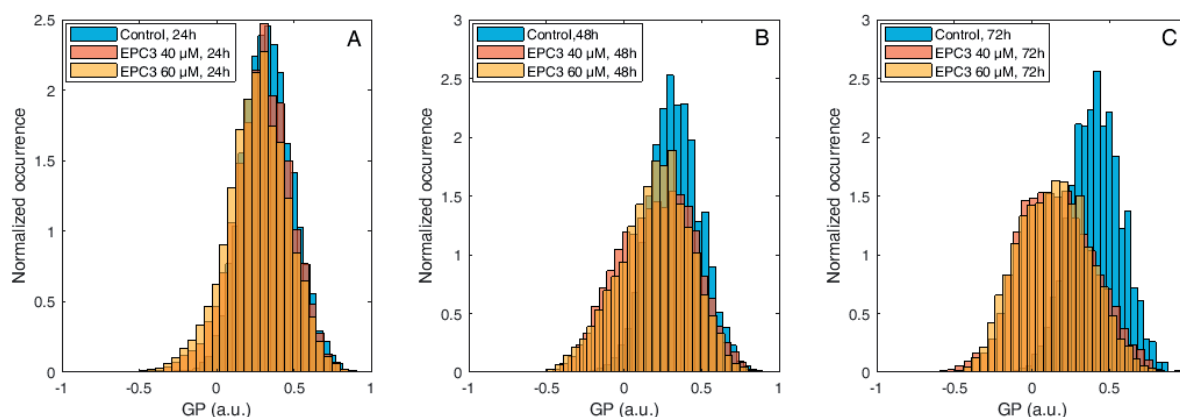
Figure 4. Di-4-ANEPPDQH GP values measured at the PM of MCF-7 cells after EPC3 treatment. Normalized histograms of GP values measured in pixels belonging to the PM of MCF-7 cells labeled with Di-4-ANEPPDQH. Cells were treated with 40 μM (orange bars) or 60 μM (yellow bars) EPC3. GP values measured in cells not treated with EPC3 are shown as blue bars. Fluorescence intensity values were acquired 24 h (**A**), 48 h (**B**), and 72 h (**C**) after the addition of EPC3. For each condition, GP values were pooled from ca. 50 ROIs selected at the PM of distinct cells, in two independent experiments. The total number of calculated GP values (and measured pixels) for each experimental condition was between ca. 10,000 and 30,000. Measurements were performed at RT. Representative images of treated cells and ROIs are shown in Figures S1 and S4.

Figure 5. Laurdan GP values measured at the PM of MDA-MB-231 cells after EPC3 treatment. Normalized histograms of GP values measured in pixels belonging to the PM of MDA-MB-231 cells labeled with Laurdan. Cells were treated with 20 μM (orange bars) or 30 μM (yellow bars) EPC3. GP values measured in cells not treated with EPC3 are shown as blue bars. Fluorescence intensity values were acquired 24 h (**A**), 48 h (**B**), and 72 h (**C**) after the addition of EPC3. For each condition, GP values were pooled from ca. 50 ROIs selected at the PM of distinct cells, in two independent experiments. The total number of calculated GP values (and measured pixels) for each experimental condition was between ca. 10,000 and 40,000. Measurements were performed at RT. Representative images of treated cells and ROIs are shown in Figures S1 and S5.

In summary, fluorescence microscopy measurements based on both Laurdan and Di-4-ANEPPDQH labeling indicate a decrease in PM lipid packing and order induced by EPC3, especially in the case of MDA-MB-231 cells. It is worth noting that, since the GP analysis was performed on early apoptotic cells (i.e., morphologically still comparable to untreated cells), the actual decrease in average membrane order

for the whole cell population could be even more significant than what was suggested by our results. Additionally, the observed effects were much more noticeable when Di-4-ANEPPDHQ was used, instead of Laurdan. This difference could stem from two different factors. First, on the one hand, as previously described [64], Di-4-ANEPPDQH is more effective in specifically labeling the PM. Laurdan, on the other hand, penetrates more easily into the cytosol and labels also intracellular structures (see Figure S1), thus making ROI selections more difficult and less precise, while generally increasing the spread in observed GP values. Second, Di-4-ANEPPDQH and Laurdan are sensitive to different properties of the lipid bilayer [25]. While Laurdan is sensitive to lipid packing, the spectroscopic properties of Di-4-ANEPPDQH are influenced by other factors, such as cholesterol content of the membrane or internal electric dipole potential of the bilayer. Therefore, it is tempting to assume that the changes in membrane order (observed by using Di-4-ANEPPDQH rather than Laurdan) could be connected to specific alterations in membrane compositions brought about by EPC3. This hypothesis is in agreement with our observation that EPC3 alters the concentration of key lipid components of the PM (e.g., cholesterol and SM) which play an important role in membrane lateral organization (Figure 2). Similarly, it has been previously shown that other APLs could influence lipid metabolism and lipid-mediated signaling cascades. However, our experiments on model membranes clearly indicate that EPC3 can also directly influence lipid–lipid interactions and membrane fluidity, even in the absence of any alteration in membrane composition (Figure 1). Therefore, we conclude that EPC3 modulates the physical properties of the PM, for example, by directly influencing the interactions between cholesterol and other lipids or altering the internal electric dipole potential of the bilayer. Additional effects due to alterations in lipid metabolism and PM composition could also be involved in vivo.

3.4. EPC3 Increases Diffusion Dynamics of Trans-Membrane Proteins in the PM

We next investigated whether the alterations in lipid–lipid interactions, as well as lipid composition caused by EPC3 treatment discussed in the previous paragraphs can have a specific influence on the behavior of membrane proteins. Therefore, we investigated the diffusive dynamics of two illustrative transmembrane proteins, namely the human EGF receptor (hEGFR) and the hemagglutinin receptor from influenza A FP virus (FPV-HA), in MDA-MB-231 cells treated with 30 μM EPC3 (IC_{75}). The hEGFR is a well-characterized membrane protein which partitions in lipid domains of the PM [65]. The transmembrane glycoprotein HA of the influenza A virus is known to form trimers at the PM, where it localizes in raft domains [66,67].

As shown in the previous paragraph, EPC3 (in this case, 30 μM in MDA-MB-231 cells) strongly influences the physical state of the PM, as reported by Di-4-ANEPPDQH. The two examined proteins were labeled with a fluorescent protein (GFP) and visualized via confocal fluorescence microscopy. As shown in Figure 6A, EPC3 does not significantly alter the localization of either protein at the PM. Then, we applied sFCS to quantify the diffusion dynamics of the two fluorescently labeled proteins. Figure 6B shows representative autocorrelation curves for the fluorescence signal recorded for hEGFR (upper panel) and FPV-HA (lower panel), also in the presence of EPC3.

Both membrane proteins diffuse in the PM of untreated cells with a diffusion coefficient D ~0.2 μm^2/s, as expected from previous experiments [19–21]. In the presence of EPC3, we observed an average ~5-fold increase in diffusion dynamics, both for hEGFR and FPV-HA (Figure 6C). This appears to be due to a direct EPC3-lipid bilayer interaction (rather than, e.g., cytoskeleton reorganization), as suggested by measurements in PM-derived giant lipid vesicles (Figure S8 and Table S5). In fact, a moderate increase in FPV-HA-EGFP dynamics can be observed already 1 h after EPC3 treatment. Then, the diffusion coefficient D increases further during the course of 48 h treatment, both for proteins at the PM and in GPMVs (Figure S8 and Table S5). Changes in protein diffusion were previously observed as a consequence of alterations in lipid–lipid and lipid–protein interactions. For example, it was shown that hEGFR and HA diffusion coefficients increase as a result of alterations in membrane composition or protein dissociation from membrane domains [28,65,68]. Our data suggest that EPC3 could alter the

physical properties of the PM through two different processes. Initially, EPC3 modifies lipid–lipid interactions, as seen in model membranes (Part 3.1) and in cell models 1 h after EPC3 treatment. Later on, alterations in lipid metabolism and membrane composition also induced by EPC3 (Part 3.2) could further increase membrane fluidity and dynamics, acting in synergy with the initial effect.
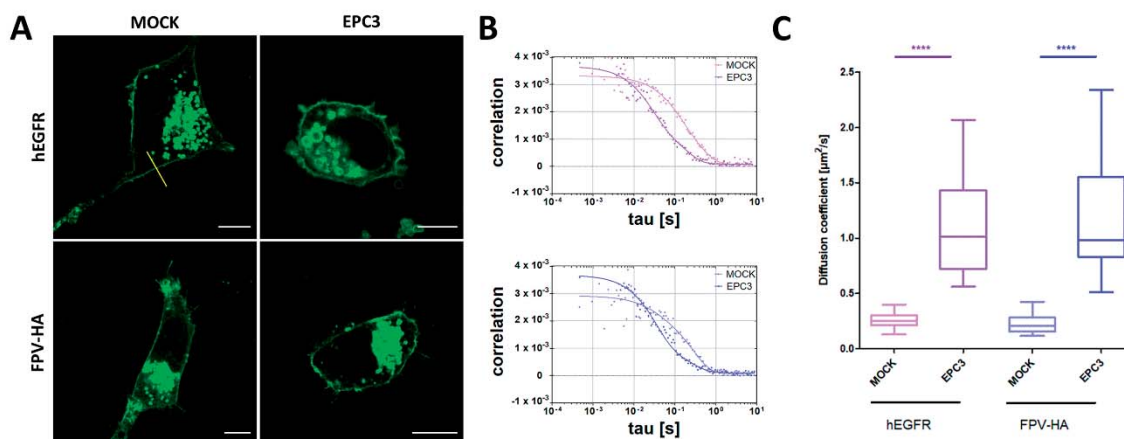
Figure 6. Quantification of protein diffusion in EPC3-treated cells via scanning fluorescence correlation spectroscopy (sFCS). (**A**) Representative confocal fluorescence microscopy images of MDA-MB-231 cells expressing hEGFR-EGFP (upper row), and FPV-HA-EGFP (lower row), in the absence of EPC3 or after 48 h incubation with EPC3. The yellow line in (**A**) represents an example of scanning path used for sFCS measurements. Scale bars are 10 μm; (**B**) Representative sFCS autocorrelation functions and fit curves obtained for cells expressing hEGFR-EGFP (upper graph) and FPV-HA-mEGFP (lower graph), in the absence of EPC3, or after 48 h incubation with EPC3. Fit curves (solid line) were obtained by fitting a two-dimensional diffusion model to the data, as described in the Methods section; (**C**) Shows box plots of diffusion coefficients calculated from sFCS diffusion times, pooled from three independent experiments (each consisting of measurements on 20 cells). The value of diffusion coefficient D for hEGFR-EGFP significantly increased from 0.26 ± 0.08 to 1.1 ± 0.5 μm^{2}s^{-1} after EPC3 treatment. The value of diffusion coefficient D for FPV-HA-mEGFP significantly increased from 0.22 ± 0.08 to 1.2 ± 0.5 μm^{2}s^{-1} after EPC3 treatment. All measurements were performed at RT. **** $p < 0.0001$.

4. Conclusions

The increased amount of saturated lipids and ordered lipid domains in tumor cells (as compared with healthy cells) [69] correlates with a reduction in membrane fluidity/dynamics and an increase in chemotherapy resistance [57,70]. In cancer cells, a wide range of signaling proteins and receptors regulating pro-oncogenic and apoptotic pathways are localized in ordered lipid domains (e.g., raft domains) [6]. It is now accepted that APLs exert their effect by interacting with such domains, due to their participation in the regulation of cell survival and cell death pathways [71]. In this context, we show, for the first time, that EPC3 causes alterations in cellular lipid composition and a significant increase in PM disorder through, at least, two separate mechanisms. These effects appear to be stronger in the high-invasive cancer cell line MDA-MB 231 and to have a direct effect on the dynamics of membrane components, as demonstrated by our measurements of membrane protein diffusion. Increased protein diffusion dynamics likely affects the likelihood of protein–protein interactions, and therefore could modulate signaling pathways involved in cell survival. Furthermore, it is possible that the decrease in lipid packing corresponds to a higher permeability of the PM, and thus an increased intake of EPC3 or other drugs through the cell membrane.

PM of MCF-7, Figure S5: Analysis of Laurdan GP values measured at the PM of MDA-MB-231, Figure S6: Laurdan GP values measured at the PM of MCF-7 cells after EPC3 treatment, Figure S7: Analysis of Laurdan GP values measured at the PM of MCF-7 cells, Figure S8: sFCS measurements in giant plasma membrane vesicles (GPMV), Table S1: Di-4-ANEPPDHQ GP values (mean and standard deviation) measured at the PM of MDA-MB-231, Table S2: Di-4-ANEPPDHQ GP values (mean and standard deviation) measured at the PM of MCF-7, Table S3: Laurdan GP values (mean and standard deviation) measured at the PM of MDA-MB-231, Table S4: Laurdan GP values (mean and standard deviation) measured at the PM of MCF-7 cells after EPC3 treatment, Table S5: Diffusion coefficients of FPV-HA-EGFP measured via sFCS, at different time points after treatment with EPC3.

Author Contributions: Conceptualization, R.T. and S.C.; Investigation, R.T., T.S., A.P., D.P., and V.U.; Formal Analysis, R.T.; T.S., A.P., D.P., V.U., and S.C.; Writing–Original Draft Preparation, R.T. and S.C.; Writing–Review and Editing, A.P. and A.M.; Software, S.C.; Supervision, R.T. and S.C.; Funding Acquisition, A.M. and S.C. All authors have read and agreed to the published version of the manuscript.

Conflicts of Interest: The authors declare no conflict of interest.

References

1. Jaffres, P.A.; Gajate, C.; Bouchet, A.M.; Couthon-Gourves, H.; Chantome, A.; Potier-Cartereau, M.; Besson, P.; Bougnoux, P.; Mollinedo, F.; Vandier, C. Alkyl ether lipids, ion channels and lipid raft reorganization in cancer therapy. *Pharmacol. Ther.* **2016**, *165*, 114–131. [CrossRef]

2. Rios-Marco, P.; Marco, C.; Galvez, X.; Jimenez-Lopez, J.M.; Carrasco, M.P. Alkylphospholipids: An update on molecular mechanisms and clinical relevance. *Biochim. Biophys. Acta Biomembr.* **2017**, *1859*, 1657–1667. [CrossRef]

3. Dietrich, C.; Bagatolli, L.A.; Volovyk, Z.N.; Thompson, N.L.; Levi, M.; Jacobson, K.; Gratton, E. Lipid rafts reconstituted in model membranes. *Biophys. J.* **2001**, *80*, 1417–1428. [CrossRef]

4. Lingwood, D.; Simons, K. Lipid rafts as a membrane-organizing principle. *Science* **2010**, *327*, 46–50. [CrossRef] [PubMed]

5. Simons, K.; Toomre, D. Lipid rafts and signal transduction. *Nat. Rev. Mol. Cell Biol.* **2000**, *1*, 31–39. [CrossRef] [PubMed]

6. Mollinedo, F.; Gajate, C. Lipid rafts as major platforms for signaling regulation in cancer. *Adv. Biol. Regul.* **2015**, *57*, 130–146. [CrossRef] [PubMed]

7. Sezgin, E.; Levental, I.; Mayor, S.; Eggeling, C. The mystery of membrane organization: Composition, regulation and roles of lipid rafts. *Nat. Rev. Mol. Cell Biol.* **2017**, *18*, 361–374. [CrossRef] [PubMed]

8. Mouritsen, O.G. The liquid-ordered state comes of age. *Biochim. Biophys. Acta* **2010**, *1798*, 1286–1288. [CrossRef] [PubMed]

9. Silvius, J.R. Partitioning of membrane molecules between raft and non-raft domains: Insights from model-membrane studies. *Biochim. Biophys. Acta* **2005**, *1746*, 193–202. [CrossRef]

10. van der Goot, F.G.; Harder, T. Raft membrane domains: From a liquid-ordered membrane phase to a site of pathogen attack. *Semin. Immunol.* **2001**, *13*, 89–97. [CrossRef]

11. Ausili, A.; Martinez-Valera, P.; Torrecillas, A.; Gomez-Murcia, V.; de Godos, A.M.; Corbalan-Garcia, S.; Teruel, J.A.; Gomez Fernandez, J.C. Anticancer agent edelfosine exhibits a high affinity for cholesterol and disorganizes liquid-ordered membrane structures. *Langmuir* **2018**, *34*, 8333–8346. [CrossRef] [PubMed]

12. Wnetrzak, A.; Lipiec, E.; Latka, K.; Kwiatek, W.; Dynarowicz-Latka, P. Affinity of alkylphosphocholines to biological membrane of prostate cancer: Studies in natural and model systems. *J. Membr. Biol.* **2014**, *247*, 581–589. [CrossRef] [PubMed]

13. Castro, B.M.; Fedorov, A.; Hornillos, V.; Delgado, J.; Acuna, A.U.; Mollinedo, F.; Prieto, M. Edelfosine and miltefosine effects on lipid raft properties: Membrane biophysics in cell death by antitumor lipids. *J. Phys. Chem. B* **2013**, *117*, 7929–7940. [CrossRef] [PubMed]

14. Heczkova, B.; Slotte, J.P. Effect of anti-tumor ether lipids on ordered domains in model membranes. *FEBS Lett.* **2006**, *580*, 2471–2476. [CrossRef] [PubMed]

15. Wnetrzak, A.; Latka, K.; Makyla-Juzak, K.; Zemla, J.; Dynarowicz-Latka, P. The influence of an antitumor lipid-erucylphosphocholine—On artificial lipid raft system modeled as langmuir monolayer. *Mol. Membr. Biol.* **2015**, *32*, 189–197. [CrossRef] [PubMed]

16. Tanovska, M.; Rahmani, M.; Vladimirova Mihaleva, L.; Berger, M.; Neshev, D.; Momchilova, A.; Tzoneva, R. An ellipsometric study of interaction of anti-cancer agent erufosine on lipid model systems. *AIP Conf. Proc.* **2019**, *2075*, 170011.

17. Ries, J.; Chiantia, S.; Schwille, P. Accurate determination of membrane dynamics with line-scan fcs. *Biophys. J.* **2009**, *96*, 1999–2008. [CrossRef]

18. Chiantia, S.; Ries, J.; Chwastek, G.; Carrer, D.; Li, Z.; Bittman, R.; Schwille, P. Role of ceramide in membrane protein organization investigated by combined afm and fcs. *Biochim. Biophys. Acta* **2008**, *1778*, 1356–1364. [CrossRef]

19. Dunsing, V.; Mayer, M.; Liebsch, F.; Multhaup, G.; Chiantia, S. Direct evidence of amyloid precursor-like protein 1 trans interactions in cell-cell adhesion platforms investigated via fluorescence fluctuation spectroscopy. *Mol. Biol. Cell* **2017**, *28*, 3609–3620. [CrossRef]

20. Dunsing, V.; Chiantia, S. A fluorescence fluctuation spectroscopy assay of protein-protein interactions at cell-cell contacts. *J. Vis. Exp.* **2018**. [CrossRef]

21. Dunsing, V.; Luckner, M.; Zuhlke, B.; Petazzi, R.A.; Herrmann, A.; Chiantia, S. Optimal fluorescent protein tags for quantifying protein oligomerization in living cells. *Sci. Rep.* **2018**, *8*, 10634. [CrossRef]

22. Chiantia, S.; Ries, J.; Schwille, P. Fluorescence correlation spectroscopy in membrane structure elucidation. *Biochim. Biophys. Acta* **2009**, *1788*, 225–233. [CrossRef] [PubMed]

23. Chiantia, S.; Kahya, N.; Ries, J.; Schwille, P. Effects of ceramide on liquid-ordered domains investigated by simultaneous afm and fcs. *Biophys. J.* **2006**, *90*, 4500–4508. [CrossRef]

24. Kiessling, V.; Yang, S.T.; Tamm, L.K. Supported lipid bilayers as models for studying membrane domains. *Curr. Top. Membr.* **2015**, *75*, 1–23. [PubMed]

25. Amaro, M.; Reina, F.; Hof, M.; Eggeling, C.; Sezgin, E. Laurdan and di-4-aneppdhq probe different properties of the membrane. *J. Phys. D Appl. Phys.* **2017**, *50*, 134004. [CrossRef] [PubMed]

26. Owen, D.M.; Rentero, C.; Magenau, A.; Abu-Siniyeh, A.; Gaus, K. Quantitative imaging of membrane lipid order in cells and organisms. *Nat. Protoc.* **2011**, *7*, 24–35. [CrossRef]

27. Carter, R.E.; Sorkin, A. Endocytosis of functional epidermal growth factor receptor-green fluorescent protein chimera. *J. Biol. Chem.* **1998**, *273*, 35000–35007. [CrossRef]

28. Engel, S.; Scolari, S.; Thaa, B.; Krebs, N.; Korte, T.; Herrmann, A.; Veit, M. Flim-fret and frap reveal association of influenza virus haemagglutinin with membrane rafts. *Biochem. J.* **2010**, *425*, 567–573. [CrossRef]

29. Visco, I.; Chiantia, S.; Schwille, P. Asymmetric supported lipid bilayer formation via methyl-beta-cyclodextrin mediated lipid exchange: Influence of asymmetry on lipid dynamics and phase behavior. *Langmuir* **2014**, *30*, 7475–7484. [CrossRef]

30. Hofer, C.T.; Di Lella, S.; Dahmani, I.; Jungnick, N.; Bordag, N.; Bobone, S.; Huang, Q.; Keller, S.; Herrmann, A.; Chiantia, S. Structural determinants of the interaction between influenza a virus matrix protein m1 and lipid membranes. *Biochim. Biophys. Acta Biomembr.* **2019**, *1861*, 1123–1134. [CrossRef]

31. Stoyanova, T.; Uzunova, V.; Popova, D.; Hadzhilazova, M.; Berger, M.R.; Momchilova, A.; Toshkova, R.; Tzoneva, R. Effect of erufosine on mda-mb 231 breast cancer cells. *J. Oncol. Res. Forecast* **2018**, *1*, 105.

32. Pankov, R.; Markovska, T.; Antonov, P.; Ivanova, L.; Momchilova, A. The plasma membrane lipid composition affects fusion between cells and model membranes. *Chem. Biol. Interact.* **2006**, *164*, 167–173. [CrossRef] [PubMed]

33. Bligh, E.G.; Dyer, W.J. A rapid method of total lipid extraction and purification. *Can. J. Biochem. Physiol.* **1959**, *37*, 911–917. [CrossRef] [PubMed]

34. Kahovcova, J.; Odavic, R. A simple method for the quantitative analysis of phospholipids separated by thin layer chromatography. *J. Chromatogr.* **1969**, *40*, 90–96. [CrossRef]

35. Nikolova-Karakashian, M.N.; Petkova, H.; Koumanov, K.S. Influence of cholesterol on sphingomyelin metabolism and hemileaflet fluidity of rat liver plasma membranes. *Biochimie* **1992**, *74*, 153–159. [CrossRef]

36. Petrasek, Z.; Schwille, P. Precise measurement of diffusion coefficients using scanning fluorescence correlation spectroscopy. *Biophys. J.* **2008**, *94*, 1437–1448. [CrossRef]

37. Ries, J.; Schwille, P. Studying slow membrane dynamics with continuous wave scanning fluorescence correlation spectroscopy. *Biophys. J.* **2006**, *91*, 1915–1924. [CrossRef]

38. Dorlich, R.M.; Chen, Q.; Niklas Hedde, P.; Schuster, V.; Hippler, M.; Wesslowski, J.; Davidson, G.; Nienhaus, G.U. Dual-color dual-focus line-scanning fcs for quantitative analysis of receptor-ligand interactions in living specimens. *Sci. Rep.* **2015**, *5*, 10149. [CrossRef]

39. Chiantia, S.; Ries, J.; Kahya, N.; Schwille, P. Combined afm and two-focus sfcs study of raft-exhibiting model membranes. *ChemPhysChem* **2006**, *7*, 2409–2418. [CrossRef]

40. Veatch, S.L.; Keller, S.L. Seeing spots: Complex phase behavior in simple membranes. *Biochim. Biophys. Acta* **2005**, *1746*, 172–185. [CrossRef]

41. Sengupta, P.; Baird, B.; Holowka, D. Lipid rafts, fluid/fluid phase separation, and their relevance to plasma membrane structure and function. *Semin. Cell Dev. Biol.* **2007**, *18*, 583–590. [CrossRef]

42. Gomide, A.B.; Thome, C.H.; dos Santos, G.A.; Ferreira, G.A.; Faca, V.M.; Rego, E.M.; Greene, L.J.; Stabeli, R.G.; Ciancaglini, P.; Itri, R. Disrupting membrane raft domains by alkylphospholipids. *Biochim. Biophys. Acta* **2013**, *1828*, 1384–1389. [CrossRef] [PubMed]

43. Boggs, K.; Rock, C.O.; Jackowski, S. The antiproliferative effect of hexadecylphosphocholine toward hl60 cells is prevented by exogenous lysophosphatidylcholine. *Biochim. Biophys. Acta* **1998**, *1389*, 1–12. [CrossRef]

44. Jimenez-Lopez, J.M.; Rios-Marco, P.; Marco, C.; Segovia, J.L.; Carrasco, M.P. Alterations in the homeostasis of phospholipids and cholesterol by antitumor alkylphospholipids. *Lipids Health Dis.* **2010**, *9*, 33. [CrossRef] [PubMed]

45. Wieder, T.; Orfanos, C.E.; Geilen, C.C. Induction of ceramide-mediated apoptosis by the anticancer phospholipid analog, hexadecylphosphocholine. *J. Biol. Chem.* **1998**, *273*, 11025–11031. [CrossRef] [PubMed]

46. Geilen, C.C.; Wieder, T.; Reutter, W. Hexadecylphosphocholine inhibits translocation of ctp:Choline-phosphate cytidylyltransferase in madin-darby canine kidney cells. *J. Biol. Chem.* **1992**, *267*, 6719–6724.

47. Marco, C.; Jimenez-Lopez, J.M.; Rios-Marco, P.; Segovia, J.L.; Carrasco, M.P. Hexadecylphosphocholine alters nonvesicular cholesterol traffic from the plasma membrane to the endoplasmic reticulum and inhibits the synthesis of sphingomyelin in hepg2 cells. *Int. J. Biochem. Cell Biol.* **2009**, *41*, 1296–1303. [CrossRef]

48. Colombini, M. Membrane channels formed by ceramide. In *Sphingolipids: Basic Science and Drug Development*; Springer: Vienna, Austria, 2013; pp. 109–126.

49. Birge, R.B.; Boeltz, S.; Kumar, S.; Carlson, J.; Wanderley, J.; Calianese, D.; Barcinski, M.; Brekken, R.A.; Huang, X.; Hutchins, J.T.T.; et al. Phosphatidylserine is a global immunosuppressive signal in efferocytosis, infectious disease, and cancer. *Cell Death Differ.* **2016**, *23*, 962–978. [CrossRef]

50. Danilo, C.; Gutierrez-Pajares, J.L.; Mainieri, M.A.; Mercier, I.; Lisanti, M.P.; Frank, P.G. Scavenger receptor class b type i regulates cellular cholesterol metabolism and cell signaling associated with breast cancer development. *Breast Cancer Res.* **2013**, *15*, R87. [CrossRef]

51. Antalis, C.J.; Uchida, A.; Buhman, K.K.; Siddiqui, R.A. Migration of mda-mb-231 breast cancer cells depends on the availability of exogenous lipids and cholesterol esterification. *Clin. Exp. Metastasis* **2011**, *28*, 733–741. [CrossRef]

52. Awad, A.B.; Fink, C.S.; Williams, H.; Kim, U. In vitro and in vivo (scid mice) effects of phytosterols on the growth and dissemination of human prostate cancer pc-3 cells. *Eur. J. Cancer Prev.* **2001**, *10*, 507–513. [CrossRef] [PubMed]

53. Carrasco, M.P.; Jimenez-Lopez, J.M.; Rios-Marco, P.; Segovia, J.L.; Marco, C. Disruption of cellular cholesterol transport and homeostasis as a novel mechanism of action of membrane-targeted alkylphospholipid analogues. *Br. J. Pharmacol.* **2010**, *160*, 355–366. [CrossRef] [PubMed]

54. Ait Slimane, T.; Hoekstra, D. Sphingolipid trafficking and protein sorting in epithelial cells. *FEBS Lett.* **2002**, *529*, 54–59. [CrossRef]

55. Abramcyzk, H.; Surmacki, J.; Kopec, M.; Olejnik, A.K.; Lubecka-Pietruszewska, K.; Fabianowska-Majewska, K. The role of lipid droplets and adipocytes in cancer. Raman imaging of cell cultures: Mcf10a, mcf7, and mda-mb-231 compared to adipocytes in cancerous human breast tissue. *Analyst* **2015**, *140*, 2224–2235. [CrossRef] [PubMed]

56. de Gonzalo-Calvo, D.; Lopez-Vilaro, L.; Nasarre, L.; Perez-Olabarria, M.; Vazquez, T.; Escuin, D.; Badimon, L.; Barnadas, A.; Lerma, E.; Llorente-Cortes, V. Intratumor cholesteryl ester accumulation is associated with human breast cancer proliferation and aggressive potential: A molecular and clinicopathological study. *BMC Cancer* **2015**, *15*, 460. [CrossRef]

57. Bozza, P.T.; Viola, J.P. Lipid droplets in inflammation and cancer. *Prostaglandins Leukot. Essent. Fatty Acids* **2010**, *82*, 243–250. [CrossRef] [PubMed]

58. Rysman, E.; Brusselmans, K.; Scheys, K.; Timmermans, L.; Derua, R.; Munck, S.; Van Veldhoven, P.P.; Waltregny, D.; Daniels, V.W.; Machiels, J.J.; et al. De novo lipogenesis protects cancer cells from free radicals and chemotherapeutics by promoting membrane lipid saturation. *Cancer Res.* **2010**, *70*, 8117–8126. [CrossRef]

59. Wang, R.F.; Zhang, L.H.; Shan, L.H.; Sun, W.G.; Chai, C.C.; Wu, H.M.; Ibla, J.C.; Wang, L.F.; Liu, J.R. Effects of the fibroblast activation protein on the invasion and migration of gastric cancer. *Exp. Mol. Pathol.* **2013**, *95*, 350–356. [CrossRef]

60. Li, Y.C.; Park, M.J.; Ye, S.K.; Kim, C.W.; Kim, Y.N. Elevated levels of cholesterol-rich lipid rafts in cancer cells are correlated with apoptosis sensitivity induced by cholesterol-depleting agents. *Am. J. Pathol.* **2006**, *168*, 1107–1118; quiz 1404–1405. [CrossRef]

61. Petit, K.; Suwalsky, M.; Colina, J.R.; Aguilar, L.F.; Jemiola-Rzeminska, M.; Strzalka, K. In vitro effects of the antitumor drug miltefosine on human erythrocytes and molecular models of its membrane. *Biochim. Biophys. Acta Biomembr.* **2019**, *1861*, 17–25. [CrossRef]

62. Pehlivanova, V.; Uzunova, V.; Tsoneva, I.; Berger, M.R.; Ugrinova, I.; Tzoneva, R. Effect of erufosine on the reorganization of cytoskeleton and cell death in adherent tumor and non-tumorigenic cells. *Biotechnol. Biotechnol. Equip.* **2013**, *27*, 3695–3699. [CrossRef]

63. Stoyanova, T.; Uzunova, V.; Popova, D.; Hadzhilazova, M.; Berger, M.R.; Momchilova, A.; Toshkova, R.; Tzoneva, R. The treatment of breast cancer cells with erufosine leads to actin cytoskeleton reorganization, inhibition of cell motility, cell cycle arrest and apoptosis. *Compt. Rend. Acad. Bulg. Sci.* **2018**. accepted for publication.

64. Mazeres, S.; Fereidouni, F.; Joly, E. Using spectral decomposition of the signals from laurdan-derived probes to evaluate the physical state of membranes in live cells. *F1000Res* **2017**, *6*, 763. [CrossRef] [PubMed]

65. Bag, N.; Huang, S.; Wohland, T. Plasma membrane organization of epidermal growth factor receptor in resting and ligand-bound states. *Biophys. J.* **2015**, *109*, 1925–1936. [CrossRef] [PubMed]

66. Takeda, M.; Leser, G.P.; Russell, C.J.; Lamb, R.A. Influenza virus hemagglutinin concentrates in lipid raft microdomains for efficient viral fusion. *Proc. Natl. Acad. Sci. USA* **2003**, *100*, 14610–14617. [CrossRef] [PubMed]

67. Scheiffele, P.; Rietveld, A.; Wilk, T.; Simons, K. Influenza viruses select ordered lipid domains during budding from the plasma membrane. *J. Biol. Chem.* **1999**, *274*, 2038–2044. [CrossRef]

68. Shvartsman, D.E.; Kotler, M.; Tall, R.D.; Roth, M.G.; Henis, Y.I. Differently anchored influenza hemagglutinin mutants display distinct interaction dynamics with mutual rafts. *J. Cell Biol.* **2003**, *163*, 879–888. [CrossRef]

69. Beloribi-Djefaflia, S.; Vasseur, S.; Guillaumond, F. Lipid metabolic reprogramming in cancer cells. *Oncogenesis* **2016**, *5*, e189. [CrossRef]

70. Ollila, S.; Hyvonen, M.T.; Vattulainen, I. Polyunsaturation in lipid membranes: Dynamic properties and lateral pressure profiles. *J. Phys. Chem. B* **2007**, *111*, 3139–3150. [CrossRef]

71. Kostadinova, A.; Topouzova-Hristova, T.; Momchilova, A.; Tzoneva, R.; Berger, M.R. Antitumor lipids—Structure, functions, and medical applications. *Adv. Protein Chem. Struct. Biol.* **2015**, *101*, 27–66.

SUPPLEMENTARY INFORMATION

Tzoneva R., Stoyanova T. et al.
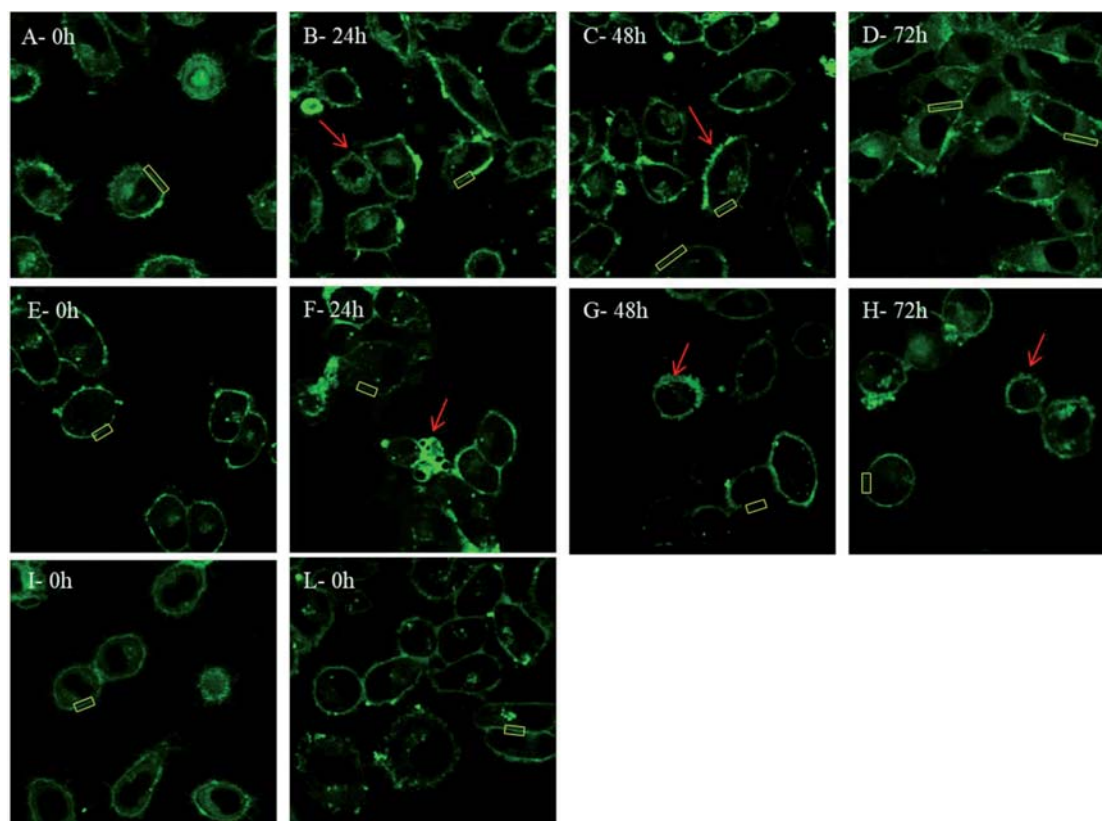
Figure S1. Typical fluorescence microscopy images of cells samples used in this work. Confocal microscopy images of MDA-MB 231 (**A-D**, **I**) and MCF-7 cells (**E-H**, **L**). Cells were labelled with Di-4-ANEPPDHQ (**A-H**) or with Laurdan (**I** and **L**). Samples are shown before treatment (**A**, **E**, **I** and **L**) and after treatment with IC_{75} EPC3 (24h: **B** and **F**; 48h: **C** and **G**; 72h: **D** and **H**). The yellow rectangles represent examples of ROIs selected for general polarization analysis. Red arrows indicate examples of morphological alterations in the plasma membrane of treated cells. These regions were in general not included in further analysis. All images are 106 μm x 106 μm.
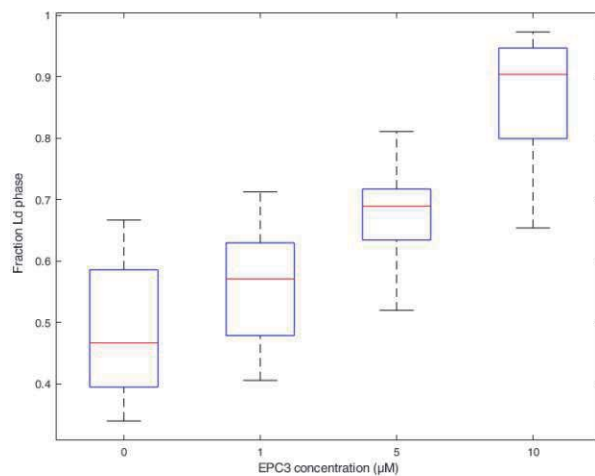
Figure S2. Variation of ordered phase surface extension in response to EPC3 treatment. Confocal fluorescence microscopy images of EggPC/bSM/Chol 4/4/2 molar ratio SLBs were acquired in the presence of 0, 1, 5 and 10 μM EPC3 (see Figure 1 A-D of the main text). Rhod-DOPE (0.1 mol%) was used to label the L_d phase. ROIs were selected to exclude e.g. bilayer defects and were filtered using a median filter. Subsequently, ROIs were binarized using a threshold that ensured a net separation into two phases and minimal pixel noise. The ratio between the number of pixels containing high intensity (corresponding to the L_d phase) and the total amount of pixels in the ROI is represented as box plot. A total amount of 16-26 images were analyzed for each EPC3 concentration.
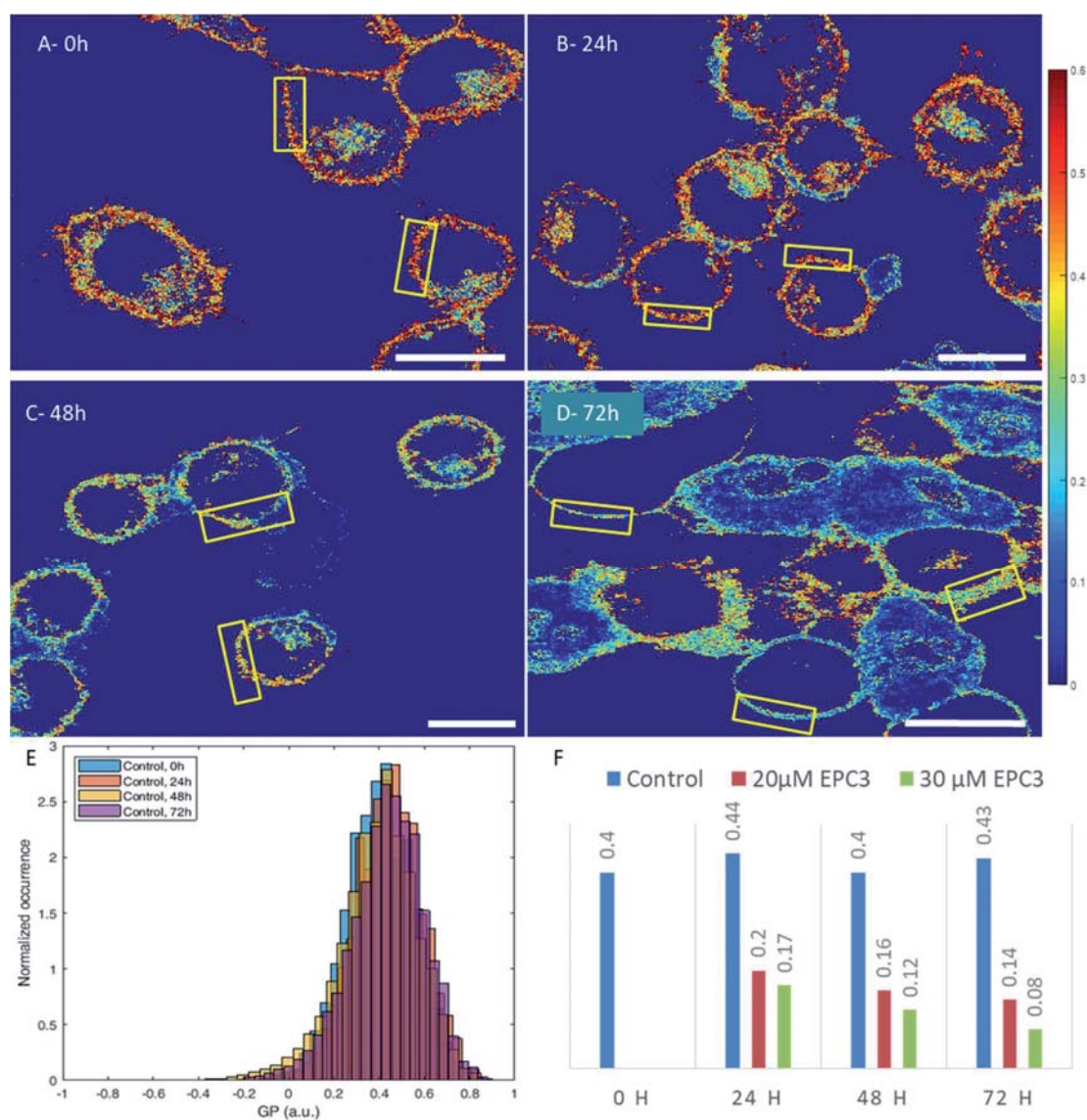
Figure S3. Analysis of Di-4-ANEPPDHQ GP values measured at the PM of MDA-MB-231. (**A-D**) Representative GP images of MDA-MB-231 cells labeled with Di-4-ANEPPDHQ and treated with IC_{75} EPC3, after 0, 24, 48 and 72h. Yellow rectangles represent examples of ROIs selected for GP quantification. (**E**) GP values for all the control samples at different time points (see Fig. 3 in the main text), including the data acquired before the beginning of the EPC3 treatment (Control, 0h). (**F**) Average values of the normalized histograms shown in Fig. 3 and in Table S1, as a function of treatment time.

Table S1. Di-4-ANEPPDHQ GP values (mean and standard deviation) measured at the PM of MDA-MB-231.

	Mean	Std. dev.
Control 0h	**0.40**	**0.15**
Control 24h	**0.44**	**0.15**
IC50 24h	**0.20**	**0.22**
IC75 24h	**0.17**	**0.24**
Control 48h	**0.40**	**0.17**
IC50 48h	**0.16**	**0.22**
IC75 48h	**0.12**	**0.26**
Control 72h	**0.43**	**0.17**
IC50 72h	**0.14**	**0.23**
IC75 72h	**0.08**	**0.22**
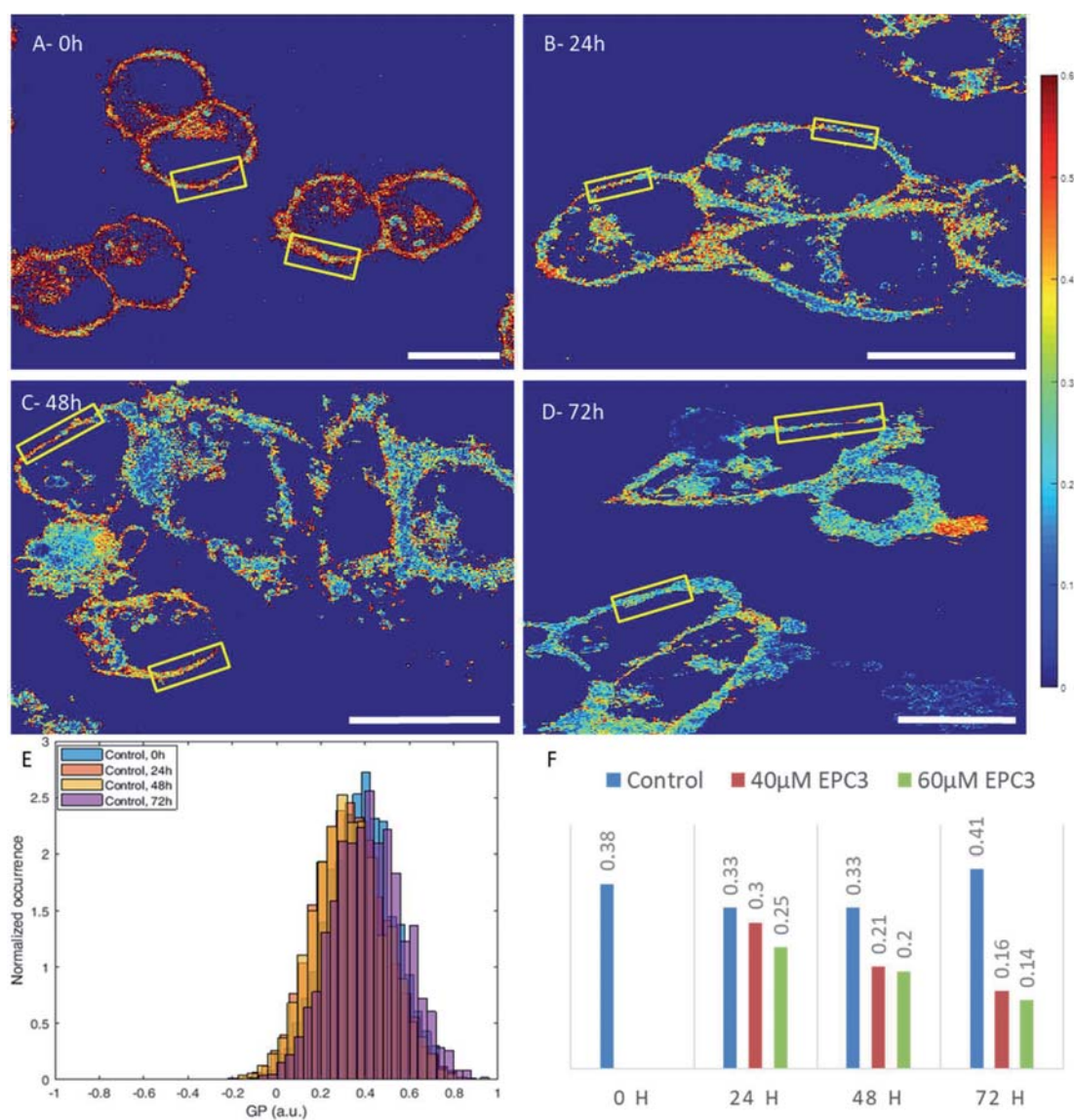
Figure S4. Analysis of Di-4-ANEPPDHQ GP values measured at the PM of MCF-7. (**A-D**) Representative GP images of MCF-7 cells labeled with Di-4-ANEPPDHQ and treated with IC$_{75}$ EPC3, after 0, 24, 48 and 72h. Yellow rectangles represent examples of ROIs selected for GP quantification. (**E**) GP values for all the control samples at different time points (see Fig. 4 in the main text), including the data acquired before the beginning of the EPC3 treatment (Control, 0h). (**F**) Average values of the normalized histograms shown in Fig. 4 and in Table S2, as a function of treatment time.

Table S2. Di-4-ANEPPDHQ GP values (mean and standard deviation) measured at the PM of MCF-7.

	Mean	Std. dev.
Control 0h	**0.38**	**0.16**
Control 24h	**0.33**	**0.16**
IC50 24h	**0.30**	**0.19**
IC75 24h	**0.25**	**0.20**
Control 48h	**0.33**	**0.16**
IC50 48h	**0.21**	**0.24**
IC75 48h	**0.20**	**0.23**
Control 72h	**0.41**	**0.16**
IC50 72h	**0.16**	**0.24**
IC75 72h	**0.14**	**0.23**
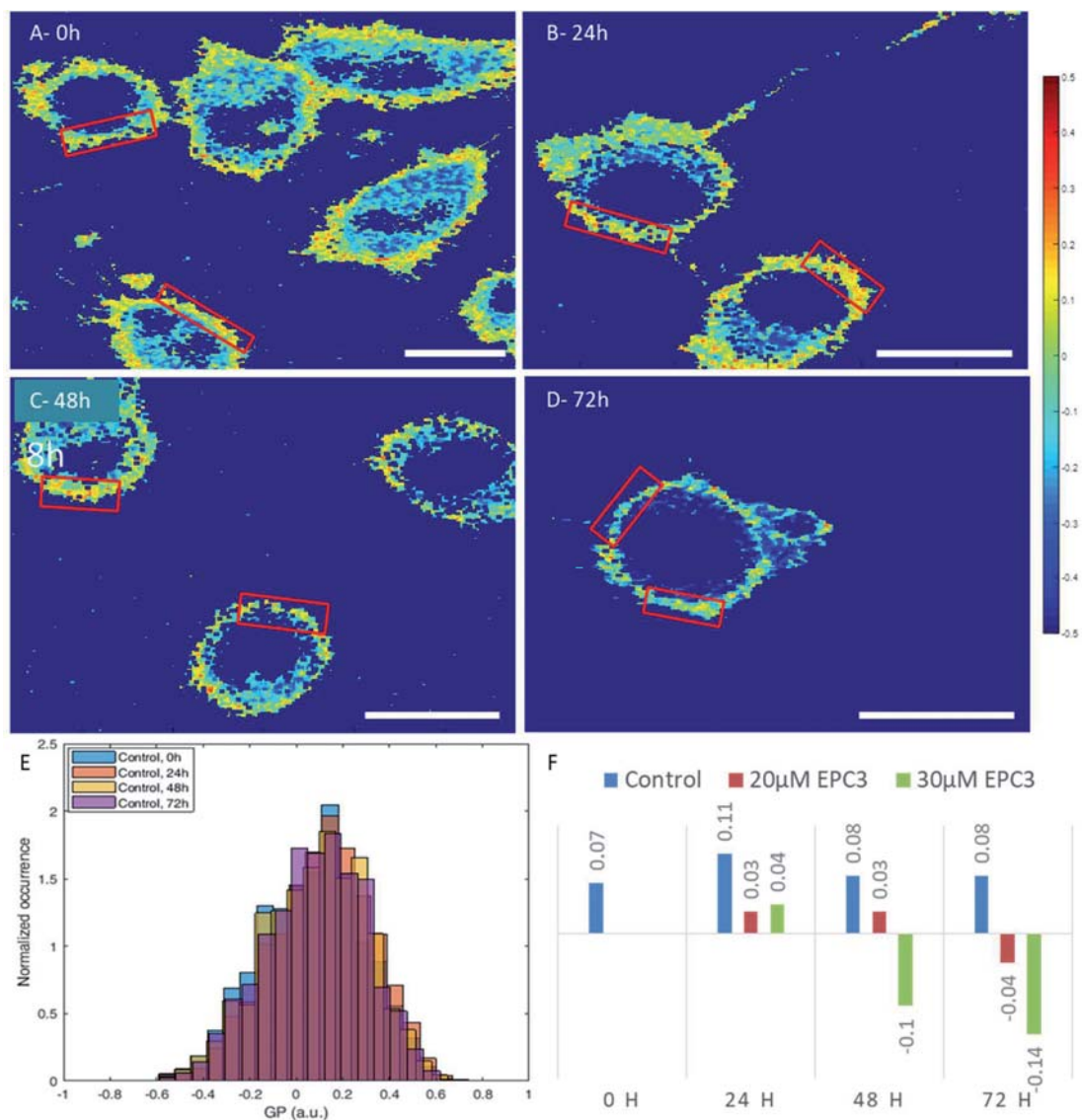
Figure S5. Analysis of Laurdan GP values measured at the PM of MDA-MB-231. (**A-D**) Representative GP images of MDA-MB-231 cells labeled with Laurdan and treated with IC_{75} EPC3, after 0, 24, 48 and 72h. Red rectangles represent examples of ROIs selected for GP quantification. (**E**) GP values for all the control samples at different time points (see Fig. 5 in the main text), including the data acquired before the beginning of the EPC3 treatment (Control, 0h). (**F**) Average values of the normalized histograms shown in Fig. 5 and in Table S3, as a function of treatment time.

Table S3. Laurdan GP values (mean and standard deviation) measured at the PM of MDA-MB-231.

	Mean	Std. dev.
Control 0h	**0.07**	**0.22**
Control 24h	**0.11**	**0.22**
IC50 24h	**0.03**	**0.24**
IC75 24h	**0.04**	**0.23**
Control 48h	**0.08**	**0.22**
IC50 48h	**0.03**	**0.23**
IC75 48h	**-0.10**	**0.24**
Control 72h	**0.08**	**0.21**
IC50 72h	**-0.04**	**0.24**
IC75 72h	**-0.14**	**0.24**
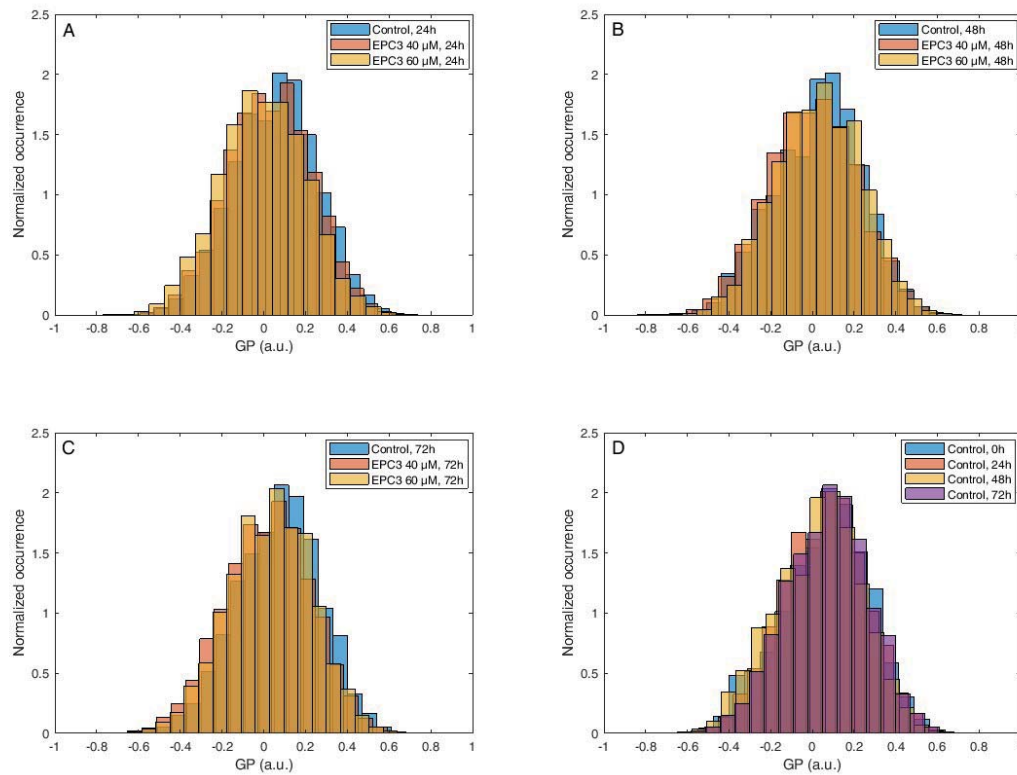
Figure S6. Laurdan GP values measured at the PM of MCF-7 cells after EPC3 treatment. (**A-C**) normalized histograms of GP values measured in pixels belonging to the PM of MCF-7 cells labelled with Laurdan. Cells were treated with 40 μM (orange bars) or 60 μM (yellow bars) EPC3. GP values measured in cells not treated with EPC3 are shown as blue bars. Fluorescence intensity values were acquired 24 h (**A**), 48 h (**B**) and 72 h (**C**) after the addition of EPC3. (**D**) GP values for all the control samples at different time points, including the data acquired before the beginning of the EPC3 treatment (Control, 0h). For each condition, GP values were pooled from ca. 50 ROIs selected at the PM of distinct cells, in two independent experiments. The total number of calculated GP values (and measured pixels) for each experimental condition was between ca. 10000 and 30000. Measurements were performed at RT.
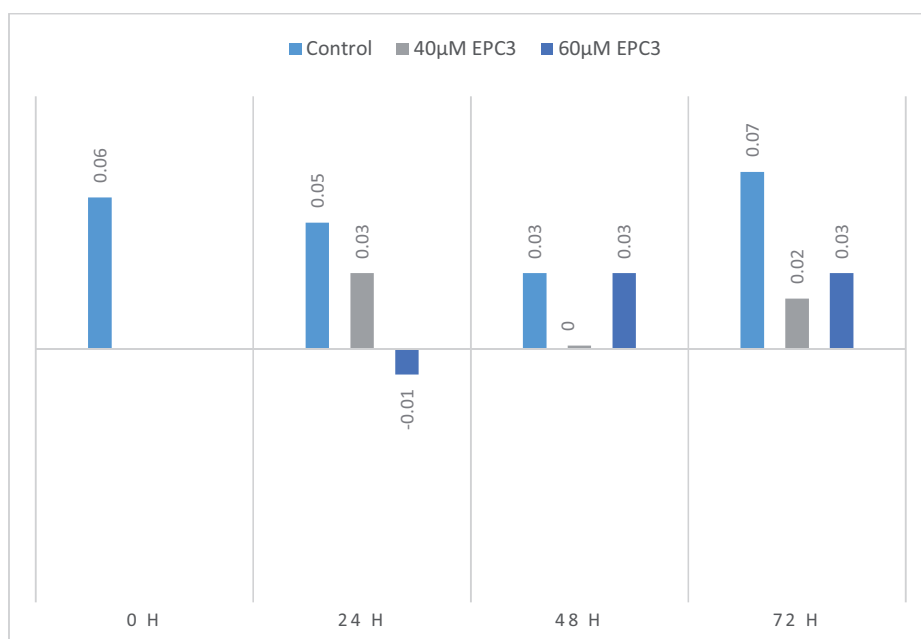
Figure S7. Analysis of Laurdan GP values measured at the PM of MCF-7 cells. Average values of the normalized histograms shown in Fig. S6 and in Table S4, as a function of treatment time.

Table S4. Laurdan GP values (mean and standard deviation) measured at the PM of MCF-7 cells after EPC3 treatment.

	Mean	SD
Control 0h	**0.06**	**0.21**
Control 24h	**0.05**	**0.20**
IC50 24h	**0.03**	**0.20**
IC75 24h	**-0.01**	**0.21**
Control 48h	**0.03**	**0.21**
IC50 48h	**0.00**	**0.21**
IC75 48h	**0.03**	**0.20**
Control 72h	**0.07**	**0.20**
IC50 72h	**0.02**	**0.21**
IC75 72h	**0.03**	**0.20**
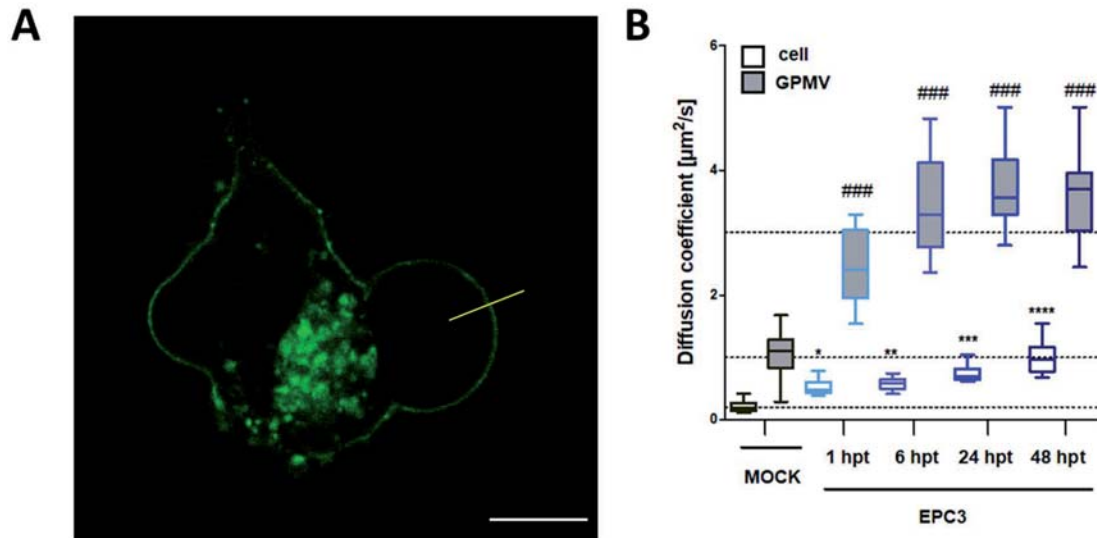
Figure S8. sFCS measurements in giant plasma membrane vesicles (GPMV). MDA-MB-231 cells were seeded on 35-mm dishes (CellVis, Mountain View, CA) with optical glass bottom. After 24 h, cells were transfected as described in Par. 2.9 of the main text. After 16 h, cells were treated with medium containing 30 μM EPC3 (IC$_{75}$) for 1 h, 6 h, and 24 h. After EPC3-treatment, GPMVs were produced following the *N*-ethylmaleimide (NEM) protocol (1). Briefly, cells were washed twice with GPMV buffer (10 mM HEPES, 150 mM NaCl, 2 mM CaCl2, pH 7.4) and then incubated in NEM-GPMV-Buffer (2 mM NEM, 10 mM HEPES, 150 mM NaCl, 2 mM CaCl2, pH 7.4) for 1 h at 37°C. Afterwards, sFCS measurements at the cell PM or in GPMVs were performed as described in Par. 2.9. To minimize out-of-focus movement or drift, GPMVs still attached to cells were selected for analysis.

(A) Representative image of GPMVs originating from a MDA-MB-231 cell expressing FPV-HA-EGFP. The yellow line indicates a typical scanning path used for sFCS measurements. Scale bar is 10 μm. (**B**) Box plots of diffusion coefficients D of FPV-HA-EGFP, after different amounts of hours post EPC3 treatment (hpt). The value of D significantly increases in the PM (from 0.21 ± 0.08 μm²/s to 1.0 ± 0.3 μm²/s), and in GPMVs (from 1.1 ± 0.3 μm²/s to 3.7 ± 0.6 μm²/s). Each group includes measurements of 20 to 26 cells or GPMVs. All measurements were performed at RT. Statistical tests were performed using one-way ANOVA followed by post-hoc Student's t-test with Bonferroni multiple comparison test. *$p < 0.01$ vs MOCK - cell, **$p < 0.005$ vs MOCK - cell, ***$p < 0.001$ vs MOCK - cell, #$p < 0.01$ vs MOCK - GPMV, ##$p < 0.005$ vs MOCK - GPMV, ###$p < 0.001$ vs MOCK - GPMV

Table S5. Diffusion coefficients of FPV-HA-EGFP measured via sFCS, at different time points after treatment with EPC3 (see Fig. S8).

	Number of examined cells/GPMVs	Diffusion coefficient (mean ± SD) [$\mu m^2/s$]	
		Cell PM	GPMV
MOCK	**20/26**	**0.21 ± 0.08**	**1.1 ± 0.3**
EPC3 1 hpt	**26/24**	**0.52 ± 0.11**	**2.5 ± 0.6**
EPC3 6 hpt	**20/20**	**0.65 ± 0.10**	**3.5 ± 0.8**
EPC3 24 hpt	**20/24**	**0.75 ± 0.12**	**3.7 ± 0.6**
EPC3 48 hpt	**20/24**	**1.0 ± 0.3**	**3.6 ± 0.7**

1.   **Sezgin E, Kaiser HJ, Baumgart T, Schwille P, Simons K, Levental I.** 2012. Elucidating membrane structure and protein behavior using giant plasma membrane vesicles. Nat Protoc **7:**1042-1051.

3.3 Publication III: Influenza A virus infection alters lipid packing and surface electrostatic potential of the host plasma membrane

Influenza A virus infection alters lipid packing and surface electrostatic potential of the host plasma membrane

Annett Petrich [1] and Salvatore Chiantia [1,*]

[1] University of Potsdam, Institute of Biochemistry and Biology, Karl-Liebknecht-Str. 24-25, 14476 Potsdam, Germany

* Correspondence: chiantia@uni-potsdam.de

Abstract: The pathogenesis of influenza A viruses (IAVs) is influenced by several factors, including IAV strain origin and reassortment, tissue tropism and host type. While such factors were mostly investigated in the context of virus entry, fusion and replication, little is known about the viral-induced changes to the host lipid membranes which might be relevant in the context of virion assembly. In this work, we applied several biophysical fluorescence microscope techniques (i.e., Förster energy resonance transfer, generalized polarization imaging and scanning fluorescence correlation spectroscopy) to quantify the effect of infection by two IAV strains of different origin on the plasma membrane (PM) of avian and human cell lines. We found that IAV infection affects the membrane charge of the inner leaflet of the PM. Moreover, we showed that IAV infection impacts lipid-lipid interactions by decreasing membrane fluidity and increasing lipid packing. Because of such alterations, diffusive dynamics of membrane-associated proteins are hindered. Taken together, our results indicate that the infection of avian and human cell lines with IAV strains of different origins had similar effects on the biophysical properties of the PM.

Keywords: fluorescence microscopy, spectral imaging, quantitative microscopy, fluorescence correlation spectroscopy, fluorescence resonance energy transfer, biosensors, plasma membrane, membrane fluidity, lipid packing, influenza A virus

1. Introduction

Influenza A virus (IAV) is an enveloped, negative-sense RNA virus that belongs to the Orthomyxoviridae family [1, 2]. This pathogen poses a significant threat to both humans and animals and can cause widespread infections resulting in significant morbidity and mortality [2, 3]. Apart from the commonly occurring seasonal IAV subtypes H1N1 and H3N2, there has been a recent rise in human infections caused by different avian influenza viruses such as H5Nx, H7N9, and H9N2, as well as swine influenza viruses [2, 3]. Several studies have revealed that IAV infection can alter the lipid metabolism in various hosts, impacting IAV replication, viral envelope lipid composition and potentially contributing to pathogenicity [1, 4-9]. These alterations have been also linked to inflammatory responses in host organisms [1, 8]. Additionally, some avian IAV strains have been found to trigger a more intense inflammatory response in humans compared to human(-adapted) strains [10-12]. Therefore, investigating the connection between lipid metabolism, physical properties of cellular membranes and IAV infection is crucial for understanding the pathogenic mechanisms of IAV and developing targeted antiviral treatments.

In general, lipids and cellular membranes play a crucial role in various stages of the IAV life cycle, such as virus-host receptor interaction, membrane fusion, nuclear transport, virion assembly and budding [11, 13-17]. Several studies have proposed that IAV assembles and buds from specific lipid domains within the apical plasma membrane

(PM), which are enriched in cholesterol and sphingolipids [15, 16, 18-21]. This hypothesis is supported by lipidome analyses conducted on purified influenza viral envelopes, which were shown to contain higher levels of certain sphingolipid species and cholesterol, thus potentially increasing the bilayer structural order in comparison to the host-cell membrane [5, 19, 21, 22]. Furthermore, removing cholesterol from the viral envelope destabilized the viral membrane and morphology, leading to a decrease in virus infectivity [23, 24]. Of note, a previous study found that three egg-grown IAV strains with varying pathogenicity exhibited a modified glycerophospholipid (GPL) composition compared to non-infected allantoic fluid (NAF) or mammalian cells [5]. Specifically, highly pathogenic IAV strains were found to contain higher fractions of sphingomyelin (SM) and saturated fatty acids compared to the other IAV strains and NAF [5].

On the other hand, it is also well established that IAV structural proteins participate in specific lipid-protein interactions in infected cells. For example, the spike proteins hemagglutinin (HA) and neuraminidase (NA) are transported to the PM via cholesterol-/sphingomyelin-rich vesicles [13, 14, 17, 18, 20, 25, 26] and their lateral organization might be indirectly influenced by lipids [27, 28] or specifically depend on ordered lipid-protein domains [20, 29, 30]. The cytoplasmic tail of HA possesses multiple basic residues which interact with phosphoinositides (e.g., PIP2), modulating protein clustering and membrane association [31, 32]. Additionally, several studies have investigated the interplay between lipids and the IAV matrix protein 2 (M2) [30, 33-40]. It has been proposed that M2 is transported to the apical PM independently from HA and NA through its interaction with the phosphatidylserine (PS)-conjugated microtubule-associated protein 1 light chain 3 protein (LC3-II) [37, 41-43]. Thus, the interaction between M2 and the IAV matrix protein 1 (M1) might be supported by a local enrichment of PS at the virus assembly site [44-46]. Moreover, previous studies have indicated that M2-M2 interactions are enhanced in cholesterol-enriched membranes [35, 39, 40].

These findings emphasize the crucial role of a controlled lipid metabolism in multiple stages of IAV infection, which appears to be influenced by both the origin of the IAV strain and the host type [1, 4-11, 14, 17, 47]. While previous studies have primarily investigated virus entry, fusion, and replication, a comprehensive analysis of how the host environment and IAV strain origin impact virus assembly and the PM environment in general is still lacking. Previous lipidomic studies focused mainly on the analysis of purified influenza virions [5, 19, 21, 22] and only few analyzed the lipidome of whole (non-)infected mammalian cells [6, 7, 9, 22]. A small number of studies observed no significant difference in the lipidome of whole cells after infection compared to non-infected cells whereas others reported IAV-mediated induction of sphingomyelin, cholesterol and fatty acid biosynthesis [6, 7, 9, 22].

In light of these contrasting results, we directly investigated in this work the physical properties of the PM lipid bilayer, comparing infected and non-infected cells. To this aim, we used avian and human IAV strains, as well as two cell lines. The previously observed increase of the transport of cholesterol-/sphingolipid-rich vesicles [48] and GPL-conjugated LC3-positive vesicles [37, 41-43] to the PM and their subsequent fusion with the PM might have an impact on membrane organization, composition, fluidity and membrane protein dynamics. For this reason, we used a fluorescence membrane charge sensor (MCS) to monitor changes in the electrostatic potential at the inner leaflet of the membrane [49]. Second, we quantified the influence of IAV infection on PM fluidity by using solvatochromic dyes (Laurdan and Di-4ANEPPDHQ) which are influenced by lipid packing, membrane hydration and lipid composition [50, 51]. Finally, we applied scanning fluorescence spectroscopy (sFCS) to monitor the dynamics of different membrane-associated proteins [52-55]. Our findings indicate that infection by either IAV strains might modulate the lipid composition of the PM and lipid-lipid interactions in both cell models. These changes in membrane properties have a direct effect also on membrane protein dynamics.

2. Materials and Methods

2.1. Plasmids

The plasmid for FRET analysis, MCS+ [49], was acquired from Addgene (gift from Katharina Gaus, Addgene plasmid #90412). All plasmids for sFCS analysis encoded the monomeric enhanced green fluorescent protein (mEGFP) which was fused to the C-terminus of a myristoylated and palmitoylated peptide (mp-mEGFP), avian influenza A/FPV/Rostock/1934 virus hemagglutinin (HA-mEGFP, Addgene plasmid #127810), or to the N-terminus of a glycosylphosphatidylinositol (GPI)-anchor (GPI-mEGFP, Addgene plasmid #182866) and were previously described [42, 56]. A schematic overview of the localization of each construct within the PM is provided Figure S1A and F.

2.2. Cell culture, transfection and infection

Madin-Darby canine kidney type II (MDCK II) cells (ECACC 00062107, European Collection of Authenticated Cell Cultures, Porton Down, UK), chicken embryonic fibroblast cell line DF1 (ATCC number: CRL–12203, kindly provided by Andreas Herrmann, Humboldt University Berlin, Germany) and human embryonic kidney (HEK) cells from the 293T line (CRL-3216TM, purchased from ATCC, Kielpin Lomianki, Poland) were maintained in phenol red-free, high glucose Dulbecco's modified Eagle's medium (DMEM) supplemented with 2 mM L-glutamine, 100 U/mL penicillin, 100 µg/mL streptomycin and 10% fetal bovine serum in a humidified incubator at 37°C and 5% CO_2 atmosphere. Cells were passaged every 2–4 days, until passage 15. All cell culture products were purchased from PAN-Biotech (Aidenbach, Germany).

For imaging experiments, 35-mm dishes (CellVis, Mountain View, CA, USA) with an optical glass bottom (#1.5 glass, 0.16–0.19 mm) were coated with 0.01% (w/v) poly-L-lysine (molecular weight [MW] 150,000–300,000 Da, Sigma-Aldrich, Munich, Germany) for four hours at 37°C and rinsed three times with Dulbecco's phosphate-buffered saline containing Mg^{2+}/Ca^{2+} (DPBS+/+; PAN-Biotech, Aidenbach, Germany) before cell seeding. Cells were seeded 24 h prior to transfection and infection at a density of 6×10^5 cells per dish.

For FRET and sFCS measurements, cells were transfected four hours prior infection with Turbofect® according to the manufacturer's protocol (Thermo Fisher Scientific, Waltham, MA, USA) by using 100 ng pDNA per dish for the membrane-associated proteins (mp-mEGFP and GPI-mEGFP) and the FRET-sensor (MCS+) or 600 ng pDNA per dish for the transmembrane glycoprotein, HA-mEGFP. Briefly, pDNA was pre-incubated with 2 µL of reagent in a final volume of 50 µL serum-free medium and was added dropwise to cells after incubation for 20 min at room temperature.

Before single-round infections with the avian influenza A/FPV/Rostock/1934 virus mutant 1 (FPV, H7N1, kind gift from Michael Veit, Free University Berlin [57]) and the human influenza A/WSN/1933 virus (WSN, H1N1, kind gift from Andreas Herrmann, Humboldt Universität zu Berlin, Germany), cells were washed three times with DPBS+/+ and then infected with a multiplicity of infection (MOI) 5 in DMEM containing 0.2 % (w/v) Bovine Serum Albumin (BSA; Sigma Aldrich, Taufkirchen, Germany), 2 mM L-glutamine, 100 U/mL penicillin, and 100 µg/mL streptomycin. Cells were first incubated for 15 min on ice and then for 45 min in a humidified incubator at 37°C and 5% CO_2 atmosphere. Afterwards, cells were rinsed three times with DPBS+/+ and fresh infection medium was added. Cells were further maintained under standard growth conditions until the measurements (~ 16 hours post infection (hpi)). This time point has been chosen in agreement with previous studies (monitoring infection after 12, 18 and 24 h [7]) and also with our results showing that M1 is efficiently recruited to the PM after ca. 16 hours [46]. Virus propagation and titration were performed in MDCK II cells as previously described [46].

2.3. Alteration of PM properties to obtain control samples

For FRET measurements, cells were treated with lipid vesicles containing the anionic phospholipid 1,2-dioleoyl-sn-glycero-3-phospho-L-serine (DOPS, purchased from Avanti Polar Lipids, Inc., Alabaster, AL, USA) to increase the concentration of negative-charged lipids at the PM and, thus, function as positive control [49]. Lipids were dissolved in chloroform at the concentration of 1 mM, dried on the walls of a glass vials under nitrogen gas and stored at -20°C until use. Prior to each experiment, the lipid film was rehydrated with DPBS without Ca^{2+}/Mg^{2+} (DPBS$_{-/-}$) to a final concentration of 0.1 mM and vigorously vortexed until multilamellar vesicles (MLV) were formed. The MLV suspension was then sonicated to clarity in a bath sonicator to form small unilamellar vesicles (SUVs). DOPS vesicles were added to the cells after three washing steps with DPBS$_{-/-}$ and incubated for 30 min at room temperature. Afterwards, cells were washed with DPBS$_{-/-}$ and fresh culture medium was added before starting the measurement.

For GP measurements, cells were treated with 10 mM methyl-beta cyclodextrin (MbCD; Sigma-Aldrich, Darmstadt, Germany) in serum-free DMEM after three washing steps with DPBS$_{+/+}$ to obtain a control sample featuring an increase in membrane fluidity, consequent to cholesterol depletion. After incubation for four hours in a humidified incubator at 37°C and 5% CO_2 atmosphere, cells were washed three times with DPBS$_{+/+}$ before labelling with a fluorophore.

2.4. Membrane labelling with Laurdan and Di-4-ANEPPDHQ

The membrane probes Di-4-ANEPPDHQ and Laurdan (6-dodecanyl-2-dimethylaminonaphtalene) were obtained from Molecular Probes (Eugene, OR, USA) and dissolved in ethanol and dimethyl sulfoxide (DMSO, Sigma-Aldrich, Darmstadt, Germany) at the desired concentrations, respectively. Aliquots of 2 mM stock solutions were stored at -20°C until use. Before each experiment, membrane probes were diluted in serum-free and phenol red-free DMEM to a final concentration of 1 µM for Di-4-ANEPPDHQ and 5 µM for Laurdan (the final concentration of DMSO was kept below 0.5% v/v). The probes were added to the cells after three washing steps with DPBS$_{+/+}$ and incubated for 10 min at room temperature. Afterwards, cells were washed twice with DPBS$_{+/+}$ and fresh serum-free and phenol red-free DMEM were added to the cells before imaging.

2.5. Confocal spectral imaging

Spectral imaging was performed on a Zeiss LSM 780 system (Carl Zeiss Microscopy GmbH, Oberkochen, Germany) equipped with a Plan-Apochromat 40×/1.2 Korr DIC M27 water immersion objective and a 32-channel gallium arsenide phosphide (GaAsP) detector array. The excitation sources were a 405 nm diode laser (for Laurdan) and a 488 nm Argon laser (for Di-4-ANEPPDQH and the FRET-sensor). Images were collected with detection ranges between for 419 and 610 nm for Laurdan and 499 and 695 nm for Di-4-ANEPPDQH and FRET-sensor in 8.9 nm increments after passing 405/625 nm or 488 nm dichroic mirrors, respectively. Laser power was adjusted so that no pixel saturation occurred. For image acquisition, ten frames were taken with a frame resolution of 128 x 128 pixels, a pixel dwell time of 50.4 µs and a pinhole size of 1 AU to reduce out-of-focus fluorescence. All measurements were performed at room temperature (22 ± 1°C) and images were acquired at the equatorial plane of the cell.

2.6. FRET analysis

Confocal spectral images were analyzed as previously described [42, 49, 58]. To quantify the FRET signal, several regions of interest (ROIs) were manually defined at the PM of several cells and emission spectra were computed from the mean normalized fluorescence intensities over all pixels of each ROI, after the application of an intensity threshold (set as 1/5 of the maximum intensity over all wavelengths). Additionally, the

normalized pixel intensity values within the ROIs were used to calculate the red-green intensity ratio (RG ratio). The red spectral range was set 601-619 nm and the green from 512-539 nm. Hence, the RG ratio is defined as:

$$RG\ ratio = \frac{\sum_{601\ nm}^{619\ nm} I}{\sum_{512\ nm}^{539\ nm} I}. \tag{1}$$

RG ratio values were then either plotted as RG ratio maps or used for the normalized occurrence histograms of all selected pixels. The RG ratio distributions for these samples range from 0 to ca. 1, corresponding to low to high FRET levels. A schematic overview of the FRET analysis is provided in Figure S1 A-B.

All calculations were performed using a custom-written MATLAB code (The MathWorks, Natick, MA, USA). The mean normalized intensity spectra were visualized by using GraphPad Prism vs. 9.0.0 (GraphPad Software, LCC, San Diego, CA).

2.7. GP index analysis

Spectral GP measurements were analyzed as previously described [42, 54, 58]. Briefly, an average fluorescence intensity image over 10 frames was calculated before defining ROIs at the PM. After the application of an intensity threshold (set as 1/5 of the maximum intensity over all wavelengths), pixel intensities of each channel were used to calculate the average fluorescence intensity spectrum over all pixels within this mask. Moreover, the generalized polarization (GP) index was calculated from a pixel-wise analysis and the obtained values were used to obtain the GP map, the normalized occurrence histograms of all selected pixels and to compute the average GP value over the entire ROI. For the calculation of the GP values, the wavelengths relative to ordered and disordered phases were previously identified for each probe, by measuring standard giant unilamellar vesicles (GUVs, Figure S1E). In this study, spectral ranges of 420-450 nm (with enhanced emission from ordered bilayers) and 520-560 nm (showing enhanced emission for disordered bilayers) were set for Laurdan. 545-585 nm and 625-690 nm were chosen for Di-4-ANEPPDQH. The sum of the normalized intensity values for each range (I_o and I_d, respectively) was then used for the GP index calculation as followed:

$$GP\ index = \frac{\sum I_o - \sum I_d}{\sum I_o + \sum I_d}. \tag{2}$$

The GP index ranges from -1.0 (very fluid) to 1.0 (gel-like). A schematic overview of the GP index analysis is provided in Figure S1C-E.

All measurements were analyzed with custom-written MATLAB code (The MathWorks, Natick, MA, USA). The mean normalized intensity spectra were visualized by using GraphPad Prism vs. 9.0.0 (GraphPad Software, LCC, San Diego, CA).

2.8. sFCS analysis

Scanning FCS experiments were performed on a Zeiss LSM780 system (Carl Zeiss Microscopy GmbH, Oberkochen, Germany) as previously described [54, 56, 59]. Briefly, the samples were excited with 488 nm Argon laser (≈3 µW) through a Plan-Apochromat 40×/1.2 Korr DIC M27 water immersion objective. The fluorescence signal was collected between 499 and 600 nm with a 32-channel GaAsP detector array after passing through a 488 nm dichroic mirror. The pinhole size was restricted to an airy unit of one to minimize out-of-focus signal. Line scans of 256 × 1 pixels and pixel size ≈ 80 nm were acquired perpendicular to the PM with a scan time of 472.73 µs. Typically, 400,000 lines were acquired in photon counting mode. All measurements were performed at 22 ± 1°C.

Prior to each experiment, the confocal volume was calibrated by performing a series of point FCS measurements with a 30 nM Alexa Fluor® 488 solution (AF488, Thermo Fischer, Waltham, MA, USA) at the same excitation power and beam path used for sFCS

measurements. For that, the fluorescence signal was optimized at first by adjusting the collar ring of the objective and the pinhole position to the maximal count rate. Then, FCS measurements (15 repetitions of 10 s) at five different positions were performed and the data was fitted using a 3D diffusion model including a triplet contribution in order to calculate the structure parameter S (ratio of the vertical and lateral dimension of the confocal volume, typically between 6 and 8) and the diffusion time τ_d (usually, $\approx 30 \pm 2$ μs). The measured average diffusion time and a previously determined diffusion coefficient ($D_{488} = 435 \, \mu m^2 s^{-1}$) [60] were used to calculate the waist ω_0 of the confocal volume (usually, $\approx 230 \pm 10$ nm).

Scanning FCS data were exported as TIFF files, imported and analyzed in MATLAB (The MathWorks, Natick, MA, USA) using a custom code as previously described [46, 54, 56]. Briefly, all scanning lines were aligned and divided into blocks in which the lines were fitted with a Gaussian function in order to define the membrane position. Subsequently, pixels of each line were integrated to provide the membrane fluorescence time series $F(t)$. Photobleaching was corrected by a two-component exponential fit function [61]. Afterwards, the normalized autocorrelation function (ACF) was calculated using the following Equations (3) and (4):

$$G(\tau) = \frac{\langle \delta F(t) \delta F(t+\tau) \rangle}{\langle F(t) \rangle^2} \quad (3)$$

where

$$\delta F = F(t) - \langle F(t) \rangle. \quad (4)$$

The ACF was calculated segment wise (each ca. 20 s long) and segments with extreme alterations were removed before averaging the ACFs. Finally, a two-dimensional diffusion fitting model and the structure parameter S from the calibration were used to analyze the ACF [62], as described in Equation (5):

$$G(\tau) = \frac{1}{N} \left(1 + \frac{\tau}{\tau_D} \right)^{-\frac{1}{2}} \left(1 + \frac{\tau}{\tau_D S^2} \right)^{-\frac{1}{2}} \quad (5)$$

where τ_D represents the diffusion time and N the number of particles. The diffusion coefficient D was then calculated using the waist ω_0 from the calibration as follows:

$$D = \frac{\omega_0^2}{4\tau_D} \quad (6)$$

A schematic overview of the sFCS analysis is provided in Figure S1G.

2.9. Statistical analysis

Data from at least two independent experiments were pooled, analyzed and visualized using a self-written R script (R Foundation for Statistical Computing, Vienna, Austria) built from common packages (*rstatix*, *fBasics*, *ggplot2* and *ggpubr*). Data is displayed as box plots with single data points corresponding to measurements in single cells. Median values and whiskers ranging from minimum to maximum values are displayed. The corresponding descriptive statistics for each plot are summarized in supplementary tables (see supplementary material). The *p* values are provided in each graph and figure captions. Statistical significance was tested by using D'Agostino-Pearson normality test followed by one-way ANOVA analysis and Tukey's multiple comparisons test.

3. Results

3.1. Infection increases the negative surface charge of the inner leaflet of the PM

Previous studies have shown that the viral proteins HA and M1 can modulate the clustering of PIP2 in the PM [31, 32]. Moreover, it was reported that the apical transport of M2 is carried out via PS-conjugated LC3-positive vesicles [41-43, 63]. Both observations could have an impact on the membrane composition and, specifically, the amount and lateral organization of anionic lipids.

First, we investigated to what extent the infection induced apoptosis which, in turn, could lead to PS flipping to the outer leaflet of the membrane, as it was reported for late infection states [64, 65]. Trans-bilayer rearrangement of PS might in fact influence the quantification of membrane charge distribution [66, 67]. We have therefore characterized the state of the cells using PI and Annexin V to determine cell viability and apopto-sis-induced PS flipping to the outer leaflet of the PM [64, 67]. Infection status and total cell numbers were determined via immunofluorescence and Hoechst 33342 staining, re-spectively (Figure S2, Table S1). We used H_2O_2/Saponine-treated cells as positive control for apoptosis and cell death [68, 69]. The FPV infection efficiencies in HEK293T and DF1 samples were 81.9 ± 4.9 % and 64.7 ± 8.3 % (mean ± SD). The values for WSN were 90.6 ± 3.6 % and 83.1 ± 14.7 % (mean ± SD) (Figure S2A-B, E). We observed no significant in-duction of apoptosis or PS translocation 16 h after infection with FPV or WSN, in either cell line (Figure S2A-D).

Next, we used a fluorescence membrane charge sensor (MCS+) to monitor changes of the electrostatic potential at the inner leaflet of the membrane [49] in non-infected (MOCK), FPV-/WSN-infected and DOPS-SUV-treated HEK293T and DF1 cells (Figure 1).

FRET measurements to quantify the membrane potential were carried-out via spec-tral imaging, instead of the standard, filter-based method [49]. The spectral imaging ap-proach and detection in the photon-counting mode were previously shown to provide more information and to improve the accuracy and sensitivity of the measurements [70, 71]. For the FRET analysis, ROIs at the equatorial plane of the cells were chosen and the RG ratio quantified. High RG ratio values correspond to a relative higher fluorescence emission peak in the longer-wavelength region (i.e., more efficient FRET between the MCS+ domains) and, therefore, a higher negative membrane potential at the inner leaflet of the membrane. We used DOPS-treated cells as a positive control, since it was shown that DOPS is quickly internalized and transported to the inner leaflet of the PM with a half time of a few minutes [72, 73]. The sensor MCS+ was expressed with similar effi-ciency in all cell lines and differently treated samples (data not shown). For both cell lines, we observed an increase of the second emission maximum upon virus infection or DOPS-SUV-treatment (Figure 1A), which resulted in ~2-fold higher RG ratio values (Figure 1B-C and S3, Table S2). Interestingly, no significant differences between IAV strains or cell types were detectable. In summary, these findings indicate a significant increase of the available negative charge at the inner leaflet of the PM in FPV- and WSN-infected cells, independent of their host cell type.
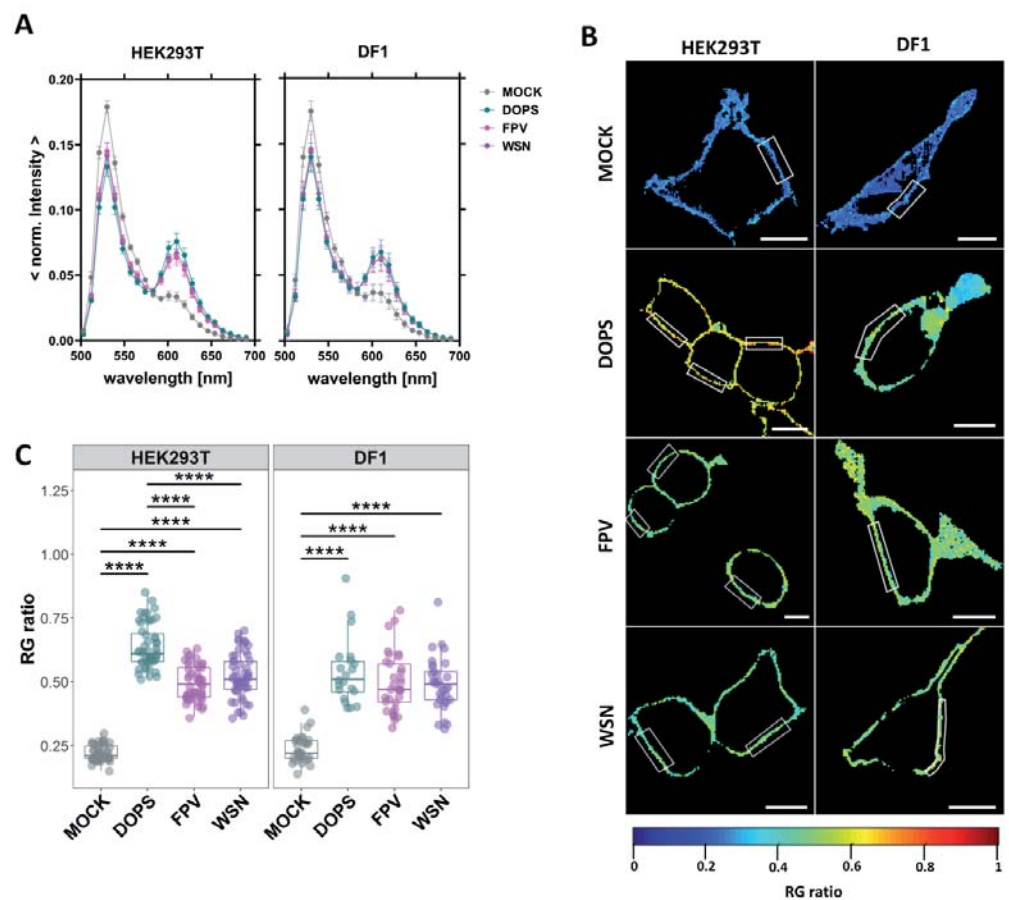
Figure 1: Increase of negative surface charge at the inner leaflet of the PM in infected cells. HEK293T and DF1 cells were either: non-infected (MOCK), treated with DOPS-SUV (DOPS, positive control), infected with FPV or with WSN influenza A strains. All cells were expressing the FRET-sensor MCS+ and emission spectrum images (22 spectral channels from 499 nm to 695 nm) were acquired 16 hpi using 488 nm excitation. **(A)** Average normalized emission spectra of all the selected regions of interest (ROI) at the equatorial plane of HEK293T and DF1 cells expressing MCS+, following the indicated treatment. Data are represented as mean ± SD from 50-55 HEK293T cells and 21-33 DF1 cells. **(B)** Representative ratiometric FRET images (RG ratio, pseudo-colored as indicated by the color scale) of HEK293T and DF1 cells expressing MCS+. White rectangles represent examples of ROIs at the PM selected for FRET quantification. Scale bars represent 10 μm. **(C)** RG ratio derived from the average intensity spectra of each cell type for the indicated treatment. Data from two separate experiments were pooled, plotted and analyzed using one-way ANOVA Tukey´s multiple comparison test (**** p < 0.0001). Each data point represents the average value measured for a ROI at the PM in one cell (Table S2).

3.2. IAV infection increases lipid packing in the plasma membrane lipid bilayer

Multiple studies have shown that the membrane of influenza A virions contains high levels of sphingolipids and cholesterol, a modified GPL composition and is more ordered compared to the host cell membrane [5, 7, 19, 21, 22, 74, 75]. Little is known about alterations in the physical properties (e.g., order, lipid packing) of the host cell membrane. Therefore, we investigated the effect of IAV infection on membrane order directly in the PM of living cells, using solvatochromic probes (i.e., Laurdan and Di-4ANEPPDHQ). The spectroscopic properties of these dyes depend on the local membrane environment [50, 51]. Specifically, their emission spectra exhibit a blue-shift when they localize in an ordered, more apolar environment, such as a liquid-ordered phase or a "lipid-raft" domain [50, 51]. This shift can be quantified by calculating the GP value, which involves a ratiometric analysis of the fluorescence intensity in two spectral regions [58]. Higher GP values indicate a higher fluorescence intensity in the short-

er-wavelength region, which corresponds to a higher degree of membrane order and li-
pid packing [51].
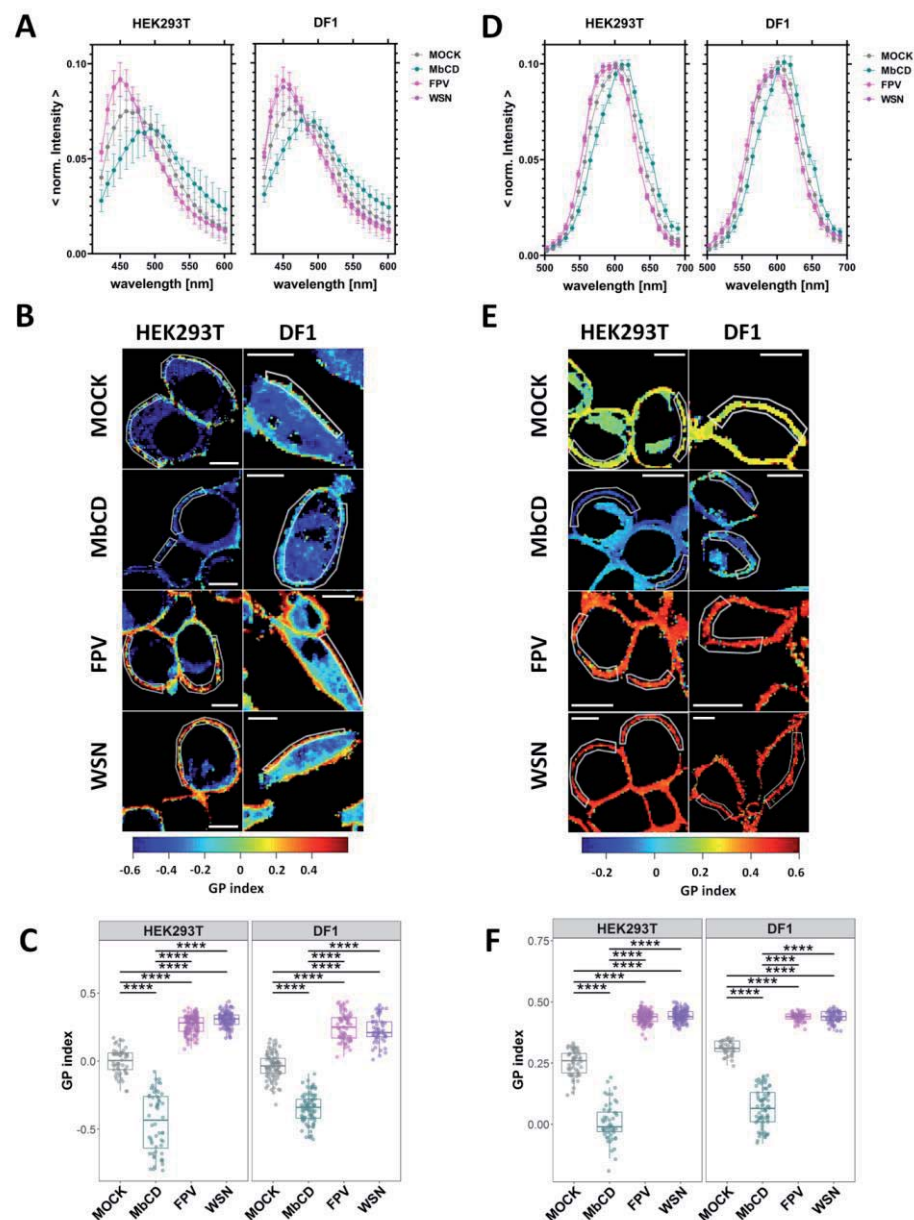
Figure 2: Increase of lipid packing of the PM upon IAV infection. HEK293T and DF1 cells were
either: non-infected (MOCK), treated with methyl-β-cyclodextrin (MbCD), infected with FPV or
with WSN influenza A strains. All cells were labelled with the solvatochromic probes Laurdan
(A-C) and Di-4-ANEPPDHQ **(D-F)**, and then imaged 16 hpi. Averaged normalized fluorescence
emission spectra of all selected regions of interest (ROI) at the equatorial plane of HEK293T and
DF1 cells stained with Laurdan **(A)** or Di-4-ANEPPDHQ **(D),** for the indicated treatment. Data are
represented as mean ± SD of 52-110 cells stained with Laurdan and 36-127 cells stained with
Di-4-ANEPPDHQ (Table S3 and S4). Representative ratiometric GP images (GP index, pseu-
do-colored as indicated by the color scale) of HEK293T and DF1 cells stained with Laurdan **(B)** or
Di-4-ANEPPDHQ **(E)**. White lines represent examples of ROIs at the PM selected for GP index
quantification. Scale bars represent 10 μm. GP index derived from the average intensity spectra
from Laurdan- **(C)** or Di-4-ANEPPDHQ-stained **(F)** cells for each cell type and indicated treatment.
Data from three separate experiments were pooled, plotted and analyzed using one-way ANOVA
Tukey´s multiple comparison test (**** $p < 0.0001$). Each data point represents the average value
measured for a ROI at the PM in one cell (Tables S3 and S4).

We used GUVs with varying lipid compositions as reference for the behavior of each dye in solid ordered gel (L$_\beta$) phase and liquid-disordered (L$_d$) phase membranes. With such reference samples, we could reliably test our experimental conditions, the GP analysis pipeline, and the phasor approach (Figure S1E and S4). DLPC GUVs (consisting of a bilayer in the L$_d$ phase) were significantly distinguishable from DPPC GUVs (bilayer in the L$_\beta$ phase), using either Laurdan or Di-4-ANEPPDHQ. In agreement with previous reports, the spectral shift of Di-4-ANEPPDHQ is less dramatic than that observed for Laurdan [50, 58, 76-78].

The investigation of changes in lipid packing was carried out in non-infected cells (MOCK), FPV- and WSN-infected cells and MbCD-treated cells (Figure 2, S5-S6, Table S3-S4). MbCD-treated cells were used as control, since it is known that cholesterol depletion reduces membrane order [58, 67]. In all cases, PM regions at the equatorial plane of the cells were chosen and the GP index was quantified from the spectral information of each pixel. We observed in both cell lines a shift in fluorescence emission towards the shorter-wavelength region upon FPV- and WSN-infection (Figure 2A, D). This shift was less pronounced in Di-4-ANEPPDHQ- stained cells, in agreement with control experiments in GUVs (Figure S4).

MbCD-treated cells showed as expected, for all cell types, a red-shifted spectrum [58, 67]. Moreover, the alternative representation via phasor plots showed a clear "clockwise" shift (see also Figure S4C) for infected cells (Figure S5), confirming stronger lipid-lipid interactions in these samples. Finally, our data indicate that the observed PM ordering effect consequent to IAV infection does not depend on IAV strain, cell type (Figure 2C and F, S5-S6, Table S3 and S4), or degree of labelling (data not shown).

3.3. IAV infection reduces membrane protein dynamics

Next, we aimed to determine whether the changes induced by IAV infection in the context of PM physical properties (see previous paragraphs) and lipid composition [6, 7, 9, 22] have an effect on the diffusive dynamics of trans-membrane proteins. Therefore, we quantified the in-plane diffusion of three membrane(-associated) proteins: i) a model for a protein associated to the inner leaflet of the PM (mp-mEGFP), ii) a model for a protein associated to the outer leaflet of the PM (GPI-mEGFP) and iii) a model of a trans-membrane protein (HA-mEGFP). Measurements were carried out in non-infected and FPV-/WSN-infected (16 hpi) HEK293T and DF1 cells. Quantification of the diffusion dynamics of the fluorescently labelled proteins was performed via sFCS measurements perpendicular to the membrane, at the equatorial plane of the cells. Representative cell images and ACFs obtained in HEK293T cells are shown in Figures S7 and S8, respectively.

Quantitative analysis of the ACFs indicated that both membrane-associated proteins diffuse in the PM of non-infected cells with a diffusion coefficient (D) of $\approx$ 1.1 $\mu m^2/s$, while the transmembrane protein exhibit slower dynamics (D $\approx$ 0.4 $\mu m^2/s$, Figure 3, Table S5). Both results are in line with previous experiments [46, 56, 79]. In FPV- and WSN-infected cells, we observed a decrease of diffusive dynamics for both mp-mEGFP (2.05-fold change $\pm$ 0.24) and GPI-mEGFP (1.81-fold change $\pm$ 0.15), for both cell lines. A decrease of mobility for the model transmembrane protein, HA-mEGFP, was also observed, albeit smaller (1.37-fold $\pm$ 0.23) and only in avian DF1 cells infected with either IAV strain.
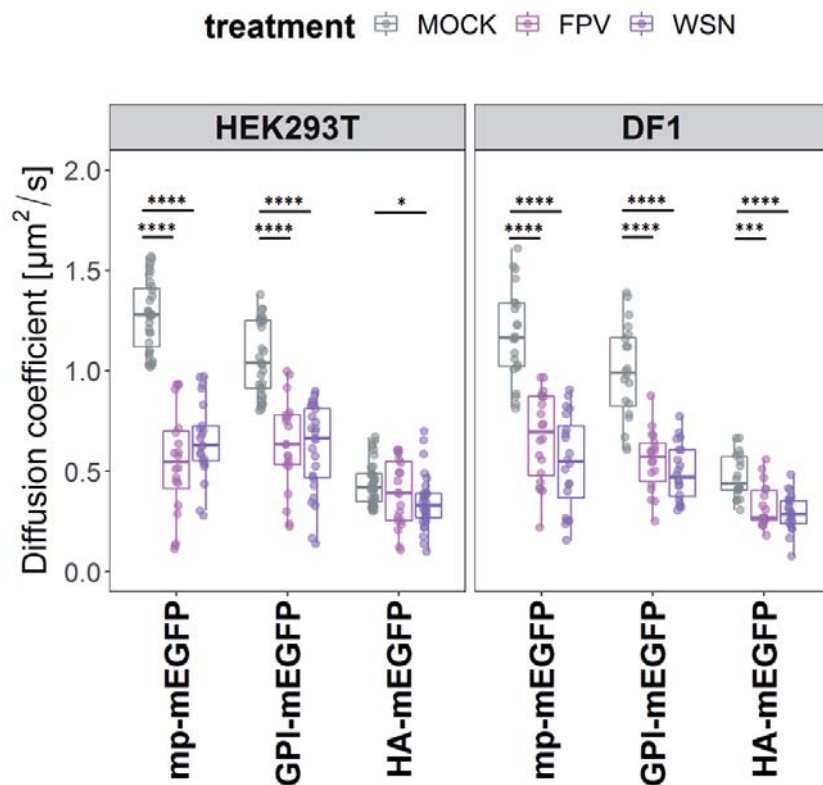
Figure 3: Decrease of membrane protein diffusion upon IAV-infection. Quantitative analysis of protein diffusion via fluorescence correlation spectroscopy (sFCS) in non-infected (MOCK) and FPV-/WSN-infected HEK293T and DF1 cells expressing three model proteins labelled with green fluorescent proteins (mEGFPs) and associated to the plasma membrane (PM). Specifically, we investigated: i) a construct anchored to the inner-leaflet of the PM via a myristoylated and palmitoylated (mp) peptide (mp-mEGFP), ii) a construct anchored to the outer-leaflet of the PM via a glycosylphosphatidylinositol (GPI) anchor (GPI-mEGFP) and iii) one representative transmembrane protein, i.e. the influenza envelope protein hemagglutinin (HA-mEGFP). Measurements were performed 16 hpi. The box plots show the diffusion coefficients calculated from sFCS diffusion times. Data from three separate experiments were plotted and analyzed using one-way ANOVA Tukey´s multiple comparison test (* $p < 0.05$, *** $p < 0.001$, **** $p < 0.0001$). Each data point represents the value measured at the PM in one cell (Table S5).

4. Discussion

Previous studies have shown that IAV infection induces changes in the lipid metabolism of infected cells [6, 7, 9]. Therefore, the concentration of specific lipids in cellular membranes might change as a consequence of infection [6, 7, 9]. For example, an IAV-induced increase in saturated lipids [5-7], cholesterol/sphingolipids [6, 7, 9] or anionic lipids [7, 9] might significantly alter the physical properties of the PM, including local order of the lipid bilayer and its surface charge at the inner leaflet side. Such alterations, in turn, might affect protein-protein and protein-lipid interactions [80]. Here, we have quantified the effect of IAV infection on the properties of the PM and, specifically, its fluidity, structural order, and surface charge.

One finding of this study is the enhancement of the negative surface electrostatic potential at the inner leaflet of the PM, upon IAV infection, as demonstrated using a FRET-based membrane charge sensor. The simplest explanation for this result is an increase of the local concentration of anionic lipids in the inner leaflet. This idea is supported by the fact that the concentration of, e.g., PS in the membranes of infected cells or in the viral envelope was shown to be higher than in non-infected cells [5, 7, 9, 21]. On the other hand, it must be kept in mind that our results might also be compatible with the

electrostatic potential being altered by, e.g., changes in cytoplasm ionic strength/composition or, more likely, alterations in lipid/protein lateral organization [31, 44]. In the latter case, it is reasonable that clustering of negative lipids or unbinding of positively charged proteins interacting with anionic lipids might alter the (local) effective electrostatic potential. In any case, such an increase in the amount or "availability" of anionic lipids at the inner leaflet might indeed relate to the organization of several viral components. For instance, it was shown that M1 is recruited by M2 to the PM and that M1 co-clusters with PS as well as with PIP2 [32, 44, 46]. Similar observations were made in the case of HA and both proteins contain polybasic residues which play a role in their interaction with anionic lipids and membrane localization [31, 44, 45]. Additionally, viral protein transport occurs via LC3, a protein that interacts with anionic lipids, especially in IAV-infected cells [41-43]. Finally, also genome packing is regulated by anionic lipids at the PM (i.e., PIP2) interacting with viral RNA and the IAV nucleoprotein NP [81].

Overall, these observations suggest that alterations in the local concentration of anionic lipid at the inner leaflet or, more in general, alterations of the negative electrostatic potential of infected cells might modulate viral assembly and release. Our results show for the first time that such alterations are indeed directly observable at the PM of infected cells, independent of IAV strain or cell type. Of note, this might be a general phenomenon, common also to other viral infections. For example, reduction in PS and PIP2 levels in mammalian cells hinders the recruitment of VP40 protein to the PM and its oligomerization, thereby inhibiting Ebola virus/Marburg virus assembly and egress (reviewed in [82]). Rearrangements of lipids at the PM, such as PIP2 and cholesterol, were also observed during the assembly of the human immunodeficiency virus (HIV) Gag protein (reviewed in [82]).

Another finding reported in this work is the enhancement of lipid-lipid interactions in the PM of infected cells. Specifically, we have used Laurdan and Di-4-ANEPPDHQ to quantify the impact of IAV infection on membrane fluidity and lipid packing. These two fluorophores are commonly used to probe membrane order [50, 51, 58, 78] and are influenced, each in a specific way, by several factors including: cholesterol content (in connection to glycerol backbone dynamics), membrane hydration (in connection to lipid internal motions and hydrogen bond network dynamics) [77, 83] and lipid phase behavior [50, 78]. Furthermore, it was reported that while Laurdan is a reliable probe for membrane order, Di-4-ANEPPDHQ is influenced by cholesterol and membrane potential [50]. Interestingly, our results indicate that both probes report similar alterations in the PM of IAV-infected cells. Taking into account also previous lipidomic analyses [6, 7, 9], the simplest explanation for these data is indeed an increase in the (local) concentration of cholesterol and/or saturated lipids (including e.g., sphingolipids). Of interest, this interpretation is compatible with our results regarding the possible increase of negatively charged lipids: on one hand, an increase in cholesterol can be accompanied by higher levels of the anionic lipid PIP2 in cellular membranes (reviewed in [84]); on the other hand, a recent report linked the presence of PS to enhanced interleaflet coupling in model membranes and, as a consequence, an increase in membrane stiffness [85]. Furthermore, an increase in PM cholesterol concentration might, at least, partially explain the enhanced M2 clustering (see Figure S2, and compared to transfected cells [46]) which is, in fact, modulated by cholesterol [35, 39, 40]. This issue is the object of current studies in our laboratory.

As a consequence of the altered lipid composition and increased structural order, the diffusive dynamics of membrane components might be hindered. The in-plane mobility of transmembrane proteins is tightly connected to their function [86] and affects several cellular processes [87]. To study membrane dynamics in infected cells, we used two model fluorescent proteins associating with the inner leaflet of the PM (mp-mEGFP) or to its outer leaflet (GPI-mEGFP). Both markers diffused significantly slower after infection, in agreement with the increased membrane order that was detected upon infection, via e.g. Laurdan-based assays. This effect was even stronger at later infection time

points (data not shown). The decreased fluidity of both leaflets might be due to alterations of either local lipid composition (i.e., restricted to one specific leaflet and transmitted to the other leaflet through enhanced interleaflet coupling [85, 88]) or general bilayer composition (e.g. cholesterol concentration, affecting both leaflets [88]). Interestingly, the effect of infection on the diffusion dynamics of HA was less pronounced than for the other test proteins. This could be due to the fact that the diffusive dynamics of transmembrane proteins are determined also by other factors, such as interaction with the cytoskeleton, rather than just lipid bilayer viscosity [89-91]. Moreover, in the case of HA, it might be possible that this protein is enriched in specific domains [27, 30, 92] with a local lipid composition which is not significantly altered during infection. Nevertheless, our findings indicate that the diffusive dynamics of membrane-associated proteins are hindered in general by the decrease in membrane fluidity and/or increase in lipid packing. In general, such alterations in the membrane order parameters might originate from an overall re-organization of the membrane components or might be caused by the presence of, e.g., locally-ordered membrane domains [11] from which the virus can efficiently assemble and bud.

Although our study focuses on the consequences of the increased lipid-lipid interactions in the PM of infected cells, it is interesting to speculate about the possible mechanisms leading to, e.g., alterations in membrane compositions during IAV infection. So far, the viral proteins NA and M2 have been reported to directly alter the fatty acid metabolism of host cells [93]. Also, it appears that HA and NA are transported to the PM via cholesterol-/sphingomyelin-rich vesicles that might alter the composition of the target membrane [13, 15, 18, 20, 21, 25]. Of interest, enrichment of cholesterol and saturated ordered-inducing lipids at the PM (or, specifically, at the budding site) might be important for the environmental stability of the virus and virus morphology [23, 24, 94, 95].

5. Conclusions

In this study, we provide evidence for IAV-induced alterations of PM dynamics and structural organization in infected cells. To the best of our knowledge, we demonstrate for the first time that IAV infection induces a decrease in membrane fluidity, an increase in lipid packing and an enhancement of the negative electrostatic potential at the PM inner leaflet (probably caused by increased local concentrations of anionic lipids). Moreover, our study highlights the potential of combined biophysical methods to investigate membrane properties at the single cell level, from multiple points of view, with the aim of better understanding virus-host interactions. These techniques can also be utilized in future studies to explore the effects of specific agents targeting lipid metabolism and host cell PM properties on virus egress and replication. Additionally, it might be possible to shed light on the role of specific viral proteins that influence membrane physical properties during virus assembly.

Supplementary Materials: The following supporting information can be downloaded at: www.mdpi.com/xxx/s1, Supporting Materials and Methods, Table S1: Overview of the Annexin V, cell viability and infection status analysis for HEK293T and DF1 cells, Table S2: Overview of the RG ratio from the FRET analysis for HEK293T and DF1 cells, Table S3: Overview of the GP index analysis with Laurdan for HEK293T and DF1 cells, Table S4: Overview of the GP index analysis with Di-4-ANEPPDHQ for HEK293T and DF1 cells, Table S5: Overview of the diffusion coefficient values [μm²/s] from the sFCS analysis for HEK293T and DF1 cells, Figure S1: Schematic overview of the experimental setup for the analysis of the enrichment of negatively charged lipids at the inner leaflet of the PM via FRET (A-B), changes in membrane fluidity via GP index (C-E), and diffusion time of PM-associated peptids/proteins using sFCS (F-G), Figure S2: No induction of apoptosis or PS flip upon FPV or WSN infection in human and avian cells, Figure S3: Quantification of the RG ratio from the FRET measurements at the PM of HEK293T and DF1 cells, Figure S4: GP and spectral phasor analysis of Laurdan and Di-4-ANEPPDHQ labelled GUVs, Figure S5: Spectral phasor analysis of Laurdan and Di-4-ANEPPDHQ labelled HEK293T and DF1 cells, Figure S6: Quantification of the GP index from the membrane fluidity measurements at the PM of HEK293T and DF1

cells with Laurdan and Di-4-ANEPPDHQ, Figure S7: Representative confocal fluorescence images of HEK293T cells expressing mEGFP-tagged proteins, Figure S8: Examples of autocorrelation functions, Data S1: Excel sheet including data for Figure 1A, Figure 1C, Figure 2A, . Figure 2C, Figure 2D, Figure 2F, Figure 3, Figure S2C-E, Figure S4A.

Author Contributions: Conceptualization, A.P.; methodology, A.P.; software, A.P. and S.C.; validation, A.P.; investigation, A.P.; writing—original draft preparation, A.P.; writing—review and editing, S.C.; visualization, A.P.; supervision, S.C.; project administration, S.C.; Funding Acquisition, S.C. All authors have read and agreed to the published version of the manuscript.

Institutional Review Board Statement: Not applicable.

Informed Consent Statement: Not applicable.

Data Availability Statement: The datasets analyzed during the current study are included the Supplementary Materials.

Code Availability Statement: MATLAB custom-written codes are available from the corresponding author upon reasonable request.

Conflicts of Interest: The authors declare no conflict of interest.

Supporting citations

References **[49, 58, 96-102]** appear in the supplementary material.

References

1. Tam, Vincent C.; Quehenberger, O.; Oshansky, Christine M.; Suen, R.; Armando, Aaron M.; Treuting, Piper M.; Thomas, Paul G.; Dennis, Edward A.; Aderem, A., Lipidomic Profiling of Influenza Infection Identifies Mediators that Induce and Resolve Inflammation. *Cell* **2013,** 154, (1), 213-227.

2. Taubenberger, J. K.; Kash, J. C., Influenza virus evolution, host adaptation, and pandemic formation. *Cell Host Microbe* **2010,** 7, (6), 440-451.

3. Schrauwen, E. J. A.; Fouchier, R. A. M., Host adaptation and transmission of influenza A viruses in mammals. *Emerg Microbes Infect* **2014,** 3, (1), 1-10.

4. Cui, L.; Zheng, D.; Lee, Y. H.; Chan, T. K.; Kumar, Y.; Ho, W. E.; Chen, J. Z.; Tannenbaum, S. R.; Ong, C. N., Metabolomics Investigation Reveals Metabolite Mediators Associated with Acute Lung Injury and Repair in a Murine Model of Influenza Pneumonia. *Sci Rep* **2016,** 6, 26076.

5. Ivanova, P. T.; Myers, D. S.; Milne, S. B.; McClaren, J. L.; Thomas, P. G.; Brown, H. A., Lipid composition of viral envelope of three strains of influenza virus - not all viruses are created equal. *ACS Infect Dis* **2015,** 1, (9), 399-452.

6. Lin, S.; Liu, N.; Yang, Z.; Song, W.; Wang, P.; Chen, H.; Lucio, M.; Schmitt-Kopplin, P.; Chen, G.; Cai, Z., GC/MS-based metabolomics reveals fatty acid biosynthesis and cholesterol metabolism in cell lines infected with influenza A virus. *Talanta* **2010,** 83, (1), 262-8.

7. Tanner, L. B.; Chng, C.; Guan, X. L.; Lei, Z.; Rozen, S. G.; Wenk, M. R., Lipidomics identifies a requirement for peroxisomal function during influenza virus replication [S]. *Journal of Lipid Research* **2014,** 55, (7), 1357-1365.

8. Tisoncik-Go, J.; Gasper, D. J.; Kyle, J. E.; Eisfeld, A. J.; Selinger, C.; Hatta, M.; Morrison, J.; Korth, M. J.; Zink, E. M.; Kim, Y. M.; Schepmoes, A. A.; Nicora, C. D.; Purvine, S. O.; Weitz, K. K.; Peng, X.; Green, R. R.; Tilton, S. C.; Webb-Robertson, B. J.; Waters, K. M.; Metz, T. O.; Smith, R. D.; Kawaoka, Y.; Suresh, M.; Josset, L.; Katze, M. G., Integrated Omics Analysis of Pathogenic Host Responses during Pandemic H1N1 Influenza Virus Infection: The Crucial Role of Lipid Metabolism. *Cell Host Microbe* **2016,** 19, (2), 254-66.

9. Woods, P. S.; Doolittle, L. M.; Rosas, L. E.; Joseph, L. M.; Calomeni, E. P.; Davis, I. C., Lethal H1N1 influenza A virus infection alters the murine alveolar type II cell surfactant lipidome. *American Journal of Physiology-Lung Cellular and Molecular Physiology* **2016,** 311, (6), L1160-L1169.

10. Knepper, J.; Schierhorn, K. L.; Becher, A.; Budt, M.; Tönnies, M.; Bauer, T. T.; Schneider, P.; Neudecker, J.; Rückert, J. C.; Gruber, A. D.; Suttorp, N.; Schweiger, B.; Hippenstiel, S.; Hocke, A. C.; Wolff, T., The novel human influenza A(H7N9) virus is naturally adapted to efficient growth in human lung tissue. *mBio* **2013,** 4, (5), e00601-13.

11. Li, Y.-J.; Chen, C.-Y.; Yang, J.-H.; Chiu, Y.-F., Modulating cholesterol-rich lipid rafts to disrupt influenza A virus infection. *Frontiers in Immunology* **2022,** 13.

12. Wang, D.; Zhu, W.; Yang, L.; Shu, Y., The Epidemiology, Virology, and Pathogenicity of Human Infections with Avian Influenza Viruses. *Cold Spring Harb Perspect Med* **2021,** 11, (4).

13. Audi, A.; Soudani, N.; Dbaibo, G.; Zaraket, H., Depletion of Host and Viral Sphingomyelin Impairs Influenza Virus Infection. *Front Microbiol* **2020,** 11, 612.

14. Hidari, K. I. P. J.; Suzuki, Y.; Suzuki, T., Suppression of the Biosynthesis of Cellular Sphingolipids Results in the Inhibition of the Maturation of Influenza Virus Particles in MDCK Cells. *Biological and Pharmaceutical Bulletin* **2006,** 29, (8), 1575-1579.

15. Ohkura, T.; Momose, F.; Ichikawa, R.; Takeuchi, K.; Morikawa, Y., Influenza A virus hemagglutinin and neuraminidase mutually accelerate their apical targeting through clustering of lipid rafts. *J Virol* **2014,** 88, (17), 10039-55.

16. Rossman, J. S.; Lamb, R. A., Influenza virus assembly and budding. *Virology* **2011,** 411, (2), 229-36.

17. Tafesse, F. G.; Sanyal, S.; Ashour, J.; Guimaraes, C. P.; Hermansson, M.; Somerharju, P.; Ploegh, H. L., Intact sphingomyelin biosynthetic pathway is essential for intracellular transport of influenza virus glycoproteins. *Proc Natl Acad Sci U S A* **2013,** 110, (16), 6406-11.

18. Sato, R.; Okura, T.; Kawahara, M.; Takizawa, N.; Momose, F.; Morikawa, Y., Apical Trafficking Pathways of Influenza A Virus HA and NA via Rab17- and Rab23-Positive Compartments. *Front Microbiol* **2019,** 10, 1857.

19. Scheiffele, P.; Rietveld, A.; Wilk, T.; Simons, K., Influenza viruses select ordered lipid domains during budding from the plasma membrane. *J Biol Chem* **1999,** 274, (4), 2038-44.

20. Veit, M.; Thaa, B., Association of influenza virus proteins with membrane rafts. *Adv Virol* **2011,** 2011, 370606.

21. Zhang, J.; Pekosz, A.; Lamb, R. A., Influenza virus assembly and lipid raft microdomains: a role for the cytoplasmic tails of the spike glycoproteins. *Journal of virology* **2000,** 74, (10), 4634-4644.

22. Gerl, M. J.; Sampaio, J. L.; Urban, S.; Kalvodova, L.; Verbavatz, J. M.; Binnington, B.; Lindemann, D.; Lingwood, C. A.; Shevchenko, A.; Schroeder, C.; Simons, K., Quantitative analysis of the lipidomes of the influenza virus envelope and MDCK cell apical membrane. *J Cell Biol* **2012,** 196, (2), 213-21.

23. Barman, S.; Nayak, D. P., Lipid raft disruption by cholesterol depletion enhances influenza A virus budding from MDCK cells. *Journal of virology* **2007,** 81, (22), 12169-12178.

24. Rossman, J. S.; Jing, X.; Leser, G. P.; Balannik, V.; Pinto, L. H.; Lamb, R. A., Influenza virus m2 ion channel protein is necessary for filamentous virion formation. *Journal of virology* **2010,** 84, (10), 5078-5088.

25. Barman, S.; Nayak, D. P., Analysis of the transmembrane domain of influenza virus neuraminidase, a type II transmembrane glycoprotein, for apical sorting and raft association. *J Virol* **2000,** 74, (14), 6538-45.

26. Engel, S.; de Vries, M.; Herrmann, A.; Veit, M., Mutation of a raft-targeting signal in the transmembrane region retards transport of influenza virus hemagglutinin through the Golgi. *FEBS Lett* **2012,** 586, (3), 277-82.

27. Wilson, Robert L.; Frisz, Jessica F.; Klitzing, Haley A.; Zimmerberg, J.; Weber, Peter K.; Kraft, Mary L., Hemagglutinin Clusters in the Plasma Membrane Are Not Enriched with Cholesterol and Sphingolipids. *Biophysical Journal* **2015,** 108, (7), 1652-1659.

28. Leser, G. P.; Lamb, R. A., Lateral Organization of Influenza Virus Proteins in the Budozone Region of the Plasma Membrane. *J Virol* **2017,** 91, (9), e02104-16.

29. Leser, G. P.; Lamb, R. A., Influenza virus assembly and budding in raft-derived microdomains: a quantitative analysis of the surface distribution of HA, NA and M2 proteins. *Virology* **2005,** 342, (2), 215-27.

30. Veit, M.; Engel, S.; Thaa, B.; Scolari, S.; Herrmann, A., Lipid domain association of influenza virus proteins detected by dynamic fluorescence microscopy techniques. *Cell Microbiol* **2013,** 15, (2), 179-89.

31. Curthoys, N. M.; Mlodzianoski, M. J.; Parent, M.; Butler, M. B.; Raut, P.; Wallace, J.; Lilieholm, J.; Mehmood, K.; Maginnis, M. S.; Waters, H.; Busse, B.; Zimmerberg, J.; Hess, S. T., Influenza Hemagglutinin Modulates Phosphatidylinositol 4,5-Bisphosphate Membrane Clustering. *Biophys J* **2019,** 116, (5), 893-909.

32. Raut, P.; Obeng, B.; Waters, H.; Zimmerberg, J.; Gosse, J. A.; Hess, S. T., Phosphatidylinositol 4,5-Bisphosphate Mediates the Co-Distribution of Influenza A Hemagglutinin and Matrix Protein M1 at the Plasma Membrane. *Viruses* **2022,** 14, (11).

33. Ekanayake, E. V.; Fu, R.; Cross, Timothy A., Structural Influences: Cholesterol, Drug, and Proton Binding to Full-Length Influenza A M2 Protein. *Biophysical Journal* **2016,** 110, (6), 1391-1399.

34. Elkins, M. R.; Williams, J. K.; Gelenter, M. D.; Dai, P.; Kwon, B.; Sergeyev, I. V.; Pentelute, B. L.; Hong, M., Cholesterol-binding site of the influenza M2 protein in lipid bilayers from solid-state NMR. *Proc Natl Acad Sci U S A* **2017,** 114, (49), 12946-12951.

35. Georgieva, E. R.; Borbat, P. P.; Norman, H. D.; Freed, J. H., Mechanism of influenza A M2 transmembrane domain assembly in lipid membranes. *Sci Rep* **2015,** 5, 11757-11757.

36. Kuroki, T.; Hatta, T.; Natsume, T.; Sakai, N.; Yagi, A.; Kato, K.; Nagata, K.; Kawaguchi, A., ARHGAP1 Transported with Influenza Viral Genome Ensures Integrity of Viral Particle Surface through Efficient Budozone Formation. *mBio* **2022**, 13, (3), e0072122.

37. Manzoor, R.; Igarashi, M.; Takada, A., Influenza A Virus M2 Protein: Roles from Ingress to Egress. *Int J Mol Sci* **2017**, 18, (12), 2649.

38. Martyna, A.; Bahsoun, B.; Madsen, J. J.; Jackson, F.; Badham, M. D.; Voth, G. A.; Rossman, J. S., Cholesterol Alters the Orientation and Activity of the Influenza Virus M2 Amphipathic Helix in the Membrane. *J Phys Chem B* **2020**, 124, (31), 6738-6747.

39. Paulino, J.; Pang, X.; Hung, I.; Zhou, H. X.; Cross, T. A., Influenza A M2 Channel Clustering at High Protein/Lipid Ratios: Viral Budding Implications. *Biophys J* **2019**, 116, (6), 1075-1084.

40. Sutherland, M.; Tran, N.; Hong, M., Clustering of tetrameric influenza M2 peptides in lipid bilayers investigated by (19)F solid-state NMR. *Biochim Biophys Acta Biomembr* **2022**, 1864, (7), 183909.

41. Beale, R.; Wise, H.; Stuart, A.; Ravenhill, B. J.; Digard, P.; Randow, F., A LC3-interacting motif in the influenza A virus M2 protein is required to subvert autophagy and maintain virion stability. *Cell Host Microbe* **2014**, 15, (2), 239-47.

42. Dunsing, V.; Petrich, A.; Chiantia, S., Multicolor fluorescence fluctuation spectroscopy in living cells via spectral detection. *Elife* **2021**, 10.

43. Durgan, J.; Florey, O., Many roads lead to CASM: Diverse stimuli of noncanonical autophagy share a unifying molecular mechanism. *Sci Adv* **2022**, 8, (43), eabo1274.

44. Bobone, S.; Hilsch, M.; Storm, J.; Dunsing, V.; Herrmann, A.; Chiantia, S., Phosphatidylserine Lateral Organization Influences the Interaction of Influenza Virus Matrix Protein 1 with Lipid Membranes. *Journal of virology* **2017**, 91, (12), e00267-17.

45. Kordyukova, L. V.; Shtykova, E. V.; Baratova, L. A.; Svergun, D. I.; Batishchev, O. V., Matrix proteins of enveloped viruses: a case study of Influenza A virus M1 protein. *J Biomol Struct Dyn* **2019**, 37, (3), 671-690.

46. Petrich, A.; Dunsing, V.; Bobone, S.; Chiantia, S., Influenza A M2 recruits M1 to the plasma membrane: A fluorescence fluctuation microscopy study. *Biophysical Journal* **2021**, 120, (24), 5478-5490.

47. Zhou, Y.; Pu, J.; Wu, Y., The Role of Lipid Metabolism in Influenza A Virus Infection. *Pathogens* **2021**, 10, (3).

48. Kawaguchi, A.; Hirohama, M.; Harada, Y.; Osari, S.; Nagata, K., Influenza Virus Induces Cholesterol-Enriched Endocytic Recycling Compartments for Budozone Formation via Cell Cycle-Independent Centrosome Maturation. *PLoS pathogens* **2015**, 11, e1005284.

49. Ma, Y.; Yamamoto, Y.; Nicovich, P. R.; Goyette, J.; Rossy, J.; Gooding, J. J.; Gaus, K., A FRET sensor enables quantitative measurements of membrane charges in live cells. *Nature Biotechnology* **2017**, 35, (4), 363-370.

50. Amaro, M.; Reina, F.; Hof, M.; Eggeling, C.; Sezgin, E., Laurdan and Di-4-ANEPPDHQ probe different properties of the membrane. *Journal of Physics D: Applied Physics* **2017**, 50, (13), 134004.

51. Owen, D. M.; Rentero, C.; Magenau, A.; Abu-Siniyeh, A.; Gaus, K., Quantitative imaging of membrane lipid order in cells and organisms. *Nat Protoc* **2011**, 7, (1), 24-35.

734   52.   Chiantia, S.; Ries, J.; Schwille, P., Fluorescence correlation spectroscopy in membrane
735   structure elucidation. *Biochim Biophys Acta* **2009,** 1788, (1), 225-33.

736   53.   Dunsing, V.; Chiantia, S., A Fluorescence Fluctuation Spectroscopy Assay of Protein-Protein
737   Interactions at Cell-Cell Contacts. *JoVE* **2018**, (142), e58582.

738   54.   Tzoneva, R.; Stoyanova, T.; Petrich, A.; Popova, D.; Uzunova, V.; Momchilova, A.; Chiantia, S.,
739   Effect of Erufosine on Membrane Lipid Order in Breast Cancer Cell Models. *Biomolecules* **2020,**
740   10, (5), 802.

741   55.   Yang, G.-S.; Wagenknecht-Wiesner, A.; Yin, B.; Suresh, P.; London, E.; A. Baird, B.; Bag, N.,
742   Lipid Driven Inter-leaflet Coupling of Plasma Membrane Order Regulates FcεRI Signaling in
743   Mast Cells. *bioRxiv* **2022**, 2022.11.24.517890.

744   56.   Dunsing, V.; Luckner, M.; Zühlke, B.; Petazzi, R. A.; Herrmann, A.; Chiantia, S., Optimal
745   fluorescent protein tags for quantifying protein oligomerization in living cells. *Sci Rep* **2018,** 8,
746   (1), 10634-10634.

747   57.   Wagner, R.; Gabriel, G.; Schlesner, M.; Alex, N.; Herwig, A.; Werner, O.; Klenk, H.-D.,
748   Protease activation mutants elicit protective immunity against highly pathogenic avian
749   influenza viruses of subtype H7 in chickens and mice. *Emerg Microbes Infect* **2013,** 2, (2), e7-e7.

750   58.   Sezgin, E.; Waithe, D.; Bernardino de la Serna, J.; Eggeling, C., Spectral imaging to measure
751   heterogeneity in membrane lipid packing. *Chemphyschem* **2015,** 16, (7), 1387-94.

752   59.   Petrich, A.; Koikkarah Aji, A.; Dunsing, V.; Chiantia, S., Benchmarking of novel green
753   fluorescent proteins for the quantification of protein oligomerization in living cells. *bioRxiv*
754   **2023**, 2023.02.07.527542.

755   60.   Petrášek, Z.; Schwille, P., Precise Measurement of Diffusion Coefficients using Scanning
756   Fluorescence Correlation Spectroscopy. *Biophysical Journal* **2008,** 94, (4), 1437-1448.

757   61.   Ries, J.; Chiantia, S.; Schwille, P., Accurate determination of membrane dynamics with
758   line-scan FCS. *Biophysical journal* **2009,** 96, (5), 1999-2008.

759   62.   Ries, J.; Schwille, P., Studying Slow Membrane Dynamics with Continuous Wave Scanning
760   Fluorescence Correlation Spectroscopy. *Biophysical Journal* **2006,** 91, (5), 1915-1924.

761   63.   Liu, S.; Mok, B. W.-Y.; Deng, S.; Liu, H.; Wang, P.; Song, W.; Chen, P.; Huang, X.; Zheng, M.;
762   Lau, S.-Y.; Cremin, C. J.; Tam, C.-Y.; Li, B.; Jiang, L.; Chen, Y.; Yuen, K.-Y.; Chen, H.,
763   Mammalian cells use the autophagy process to restrict avian influenza virus replication. *Cell*
764   *Reports* **2021,** 35, (10).

765   64.   Chaurio, R. A.; Janko, C.; Muñoz, L. E.; Frey, B.; Herrmann, M.; Gaipl, U. S., Phospholipids:
766   Key Players in Apoptosis and Immune Regulation. In *Molecules*, 2009; Vol. 14, pp 4892-4914.

767   65.   Gui, R.; Chen, Q., Molecular Events Involved in Influenza A Virus-Induced Cell Death. *Front*
768   *Microbiol* **2021,** 12, 797789.

769   66.   Bailey, R. W.; Nguyen, T.; Robertson, L.; Gibbons, E.; Nelson, J.; Christensen, R. E.; Bell, J. P.;
770   Judd, A. M.; Bell, J. D., Sequence of Physical Changes to the Cell Membrane During
771   Glucocorticoid-Induced Apoptosis in S49 Lymphoma Cells. *Biophysical Journal* **2009,** 96, (7),
772   2709-2718.

773   67.   Darwich, Z.; Klymchenko, A. S.; Kucherak, O. A.; Richert, L.; Mély, Y., Detection of apoptosis
774   through the lipid order of the outer plasma membrane leaflet. *Biochim Biophys Acta* **2012,** 1818,
775   (12), 3048-54.

68. Tochigi, M.; Inoue, T.; Suzuki-Karasaki, M.; Ochiai, T.; Ra, C.; Suzuki-Karasaki, Y., Hydrogen peroxide induces cell death in human TRAIL-resistant melanoma through intracellular superoxide generation. *Int J Oncol* **2013**, 42, (3), 863-72.

69. Wu, C. A.; Yang, Y. W., Induction of cell death by saponin and antigen delivery. *Pharm Res* **2004**, 21, (2), 271-7.

70. Leavesley, S. J.; Britain, A. L.; Cichon, L. K.; Nikolaev, V. O.; Rich, T. C., Assessing FRET using spectral techniques. *Cytometry Part A* **2013**, 83, (10), 898-912.

71. Pokorna, S.; Ventura, A. E.; Santos, T. C. B.; Hof, M.; Prieto, M.; Futerman, A. H.; Silva, L. C., Laurdan in live cell imaging: Effect of acquisition settings, cell culture conditions and data analysis on generalized polarization measurements. *J Photochem Photobiol B* **2022**, 228, 112404.

72. Fellmann, P.; Hervé, P.; Pomorski, T.; Müller, P.; Geldwerth, D.; Herrmann, A.; Devaux, P. F., Transmembrane movement of diether phospholipids in human erythrocytes and human fibroblasts. *Biochemistry* **2000**, 39, (17), 4994-5003.

73. Herrera, S. A.; Grifell-Junyent, M.; Pomorski, T. G., NBD-lipid Uptake Assay for Mammalian Cell Lines. *Bio-protocol* **2022**, 12, (4), e4330.

74. Klenk, H. D.; Rott, R.; Becht, H., On the structure of the influenza virus envelope. *Virology* **1972**, 47, (3), 579-91.

75. Landsberger, F. R.; Lenard, J.; Paxton, J.; Compans, R. W., Spin-labeled electron spin resonance study of the lipid-containing membrane of influenza virus. *Proc Natl Acad Sci U S A* **1971**, 68, (10), 2579-83.

76. Golfetto, O.; Hinde, E.; Gratton, E., The Laurdan spectral phasor method to explore membrane micro-heterogeneity and lipid domains in live cells. *Methods Mol Biol* **2015**, 1232, 273-90.

77. Jin, L.; Millard, A. C.; Wuskell, J. P.; Dong, X.; Wu, D.; Clark, H. A.; Loew, L. M., Characterization and application of a new optical probe for membrane lipid domains. *Biophys J* **2006**, 90, (7), 2563-75.

78. Sezgin, E.; Sadowski, T.; Simons, K., Measuring lipid packing of model and cellular membranes with environment sensitive probes. *Langmuir* **2014**, 30, (27), 8160-6.

79. Dunsing, V.; Mayer, M.; Liebsch, F.; Multhaup, G.; Chiantia, S., Direct evidence of amyloid precursor-like protein 1 trans interactions in cell-cell adhesion platforms investigated via fluorescence fluctuation spectroscopy. *Mol Biol Cell* **2017**, 28, (25), 3609-3620.

80. Goyette, J.; Gaus, K., Mechanisms of protein nanoscale clustering. *Current Opinion in Cell Biology* **2017**, 44, 86-92.

81. Kakisaka, M.; Yamada, K.; Yamaji-Hasegawa, A.; Kobayashi, T.; Aida, Y., Intrinsically disordered region of influenza A NP regulates viral genome packaging via interactions with viral RNA and host PI(4,5)P2. *Virology* **2016**, 496, 116-126.

82. Motsa, B. B.; Stahelin, R. V., Lipid-protein interactions in virus assembly and budding from the host cell plasma membrane. *Biochem Soc Trans* **2021**, 49, (4), 1633-1641.

83. Orlikowska-Rzeznik, H.; Krok, E.; Chattopadhyay, M.; Lester, A.; Piatkowski, L., Laurdan Discerns Lipid Membrane Hydration and Cholesterol Content. *The Journal of Physical Chemistry B* **2023**, 127, (15), 3382-3391.

84. Doole, F. T.; Gupta, S.; Kumarage, T.; Ashkar, R.; Brown, M. F., Biophysics of Membrane Stiffening by Cholesterol and Phosphatidylinositol 4,5-bisphosphate (PIP2). *Adv Exp Med Biol* **2023,** 1422, 61-85.

85. Frewein, M. P. K.; Piller, P.; Semeraro, E. F.; Czakkel, O.; Gerelli, Y.; Porcar, L.; Pabst, G., Distributing aminophospholipids asymmetrically across leaflets causes anomalous membrane stiffening. *Biophysical Journal* **2023,** 122, (12), 2445-2455.

86. Maynard, S. A.; Triller, A., Inhibitory Receptor Diffusion Dynamics. *Frontiers in Molecular Neuroscience* **2019,** 12.

87. Alenghat, F. J.; Golan, D. E., Membrane protein dynamics and functional implications in mammalian cells. *Curr Top Membr* **2013,** 72, 89-120.

88. Sarmento, M. J.; Hof, M.; Šachl, R., Interleaflet Coupling of Lipid Nanodomains - Insights From in vitro Systems. *Front Cell Dev Biol* **2020,** 8, 284.

89. Bag, N.; Huang, S.; Wohland, T., Plasma Membrane Organization of Epidermal Growth Factor Receptor in Resting and Ligand-Bound States. *Biophysical Journal* **2015,** 109, (9), 1925-1936.

90. Gudheti, M. V.; Curthoys, N. M.; Gould, T. J.; Kim, D.; Gunewardene, M. S.; Gabor, K. A.; Gosse, J. A.; Kim, C. H.; Zimmerberg, J.; Hess, S. T., Actin mediates the nanoscale membrane organization of the clustered membrane protein influenza hemagglutinin. *Biophys J* **2013,** 104, (10), 2182-92.

91. Huang, S.; Lim, S. Y.; Gupta, A.; Bag, N.; Wohland, T., Plasma membrane organization and dynamics is probe and cell line dependent. *Biochim Biophys Acta Biomembr* **2017,** 1859, (9 Pt A), 1483-1492.

92. Frisz, J. F.; Lou, K.; Klitzing, H. A.; Hanafin, W. P.; Lizunov, V.; Wilson, R. L.; Carpenter, K. J.; Kim, R.; Hutcheon, I. D.; Zimmerberg, J.; Weber, P. K.; Kraft, M. L., Direct chemical evidence for sphingolipid domains in the plasma membranes of fibroblasts. *Proc Natl Acad Sci U S A* **2013,** 110, (8), E613-22.

93. Chua, S.; Cui, J.; Engelberg, D.; Lim, L. H. K., A Review and Meta-Analysis of Influenza Interactome Studies. *Front Microbiol* **2022,** 13, 869406.

94. Bajimaya, S.; Frankl, T.; Hayashi, T.; Takimoto, T., Cholesterol is required for stability and infectivity of influenza A and respiratory syncytial viruses. *Virology* **2017,** 510, 234-241.

95. Zeng, L.; Li, J.; Lv, M.; Li, Z.; Yao, L.; Gao, J.; Wu, Q.; Wang, Z.; Yang, X.; Tang, G.; Qu, G.; Jiang, G., Environmental Stability and Transmissibility of Enveloped Viruses at Varied Animate and Inanimate Interfaces. *Environment & Health* **2023,** 1, (1), 15-31.

96. Angelova, M. I.; Dimitrov, D. S., Liposome electroformation. *Faraday Discussions of the Chemical Society* **1986,** 81, (0), 303-311.

97. Stein, H.; Spindler, S.; Bonakdar, N.; Wang, C.; Sandoghdar, V., Production of Isolated Giant Unilamellar Vesicles under High Salt Concentrations. *Front Physiol* **2017,** 8, 63.

98. Malacrida, L.; Astrada, S.; Briva, A.; Bollati-Fogolín, M.; Gratton, E.; Bagatolli, L. A., Spectral phasor analysis of LAURDAN fluorescence in live A549 lung cells to study the hydration and time evolution of intracellular lamellar body-like structures. *Biochim Biophys Acta* **2016,** 1858, (11), 2625-2635.

99. Klymchenko, A. S.; Kreder, R., Fluorescent probes for lipid rafts: from model membranes to living cells. *Chem Biol* **2014,** 21, (1), 97-113.

100. Bondelli, G.; Sardar, S.; Chiaravalli, G.; Vurro, V.; Paternò, G. M.; Lanzani, G.; D'Andrea, C., Shedding Light on Thermally Induced Optocapacitance at the Organic Biointerface. *J Phys Chem B* **2021,** 125, (38), 10748-10758.

101. Gunther, G.; Malacrida, L.; Jameson, D. M.; Gratton, E.; Sánchez, S. A., LAURDAN since Weber: The Quest for Visualizing Membrane Heterogeneity. *Acc Chem Res* **2021,** 54, (4), 976-987.

102. Yu, L.; Lei, Y.; Ma, Y.; Liu, M.; Zheng, J.; Dan, D.; Gao, P., A Comprehensive Review of Fluorescence Correlation Spectroscopy. *Frontiers in Physics* **2021,** 9.

Supplementary Material

1. Materials and Methods

1.1 Cell Surface immunofluorescence and Annexin V/PI staining.

To assess the infection status (i.e., infected vs. non-infected), cells were washed three times with DPBS$_{+/+}$ 16hpi, before adding the primary antibody, monoclonal mouse anti-influenza A M2, clone 14C2 (#ab5416, Abcam, Cambridge, UK), with a dilution of 1:200 in 0.2 % (w/v) BSA in DMEM. Cells were incubated for one hour in a humidified incubator at 37°C and 5% CO_2 atmosphere. After three washing steps with DPBS$_{+/+}$, cells were incubated with 1:1000 diluted secondary antibody (goat anti-mouse AlexaFluor® 647-conjugated; Thermo Fisher Scientific, Waltham, MA, USA) for one hour in a humidified incubator at 37°C and 5% CO_2 atmosphere. Cells were subsequently washed three times with DPBS$_{+/+}$ and stained with 7 mM AlexaFluor® 488-labelled Annexin V, 2 µg/mL propidium iodide (PI) and 2 µg/mL Hoechst 33342 for 15 min at room temperature, to assess cellular integrity and the exposure of PS. All probes were purchased from Thermo Fisher Scientific (Waltham, MA, USA). Afterwards, cells were washed once more with DPBS$_{+/+}$ and analysed using a Zeiss LSM 780 system (Carl Zeiss Microscopy GmbH, Oberkochen, Germany). Confocal fluorescence images were acquired with a Plan-Apochromat 40×/1.2 Korr DIC M27 water immersion objective and an image resolution of 512 x 512 pixels. Samples were excited with a 405 nm diode laser (Hoechst 33342), a 488 nm Argon laser (Annexin V), a 561 nm diode laser (PI) and 633 diode laser (M2). Fluorescence was observed between 415 – 502 nm (Hoechst 33342), 490 – 570 nm (Annexin V), 588 – 650 nm (PI) and 650 – 735 nm (M2), after passing a 405/505c dichroic mirror or 488/561/633 dichroic mirror. Finally, all cells were counted and classified via ImageJ (http://imagej.nih.gov/ij/) to calculate the amounts of Annexin V-positive cells (%), cell viability (%) and infection status (%).

Non-infected (MOCK) cells functioned as negative control for the infection status and cells treated with 8 µM H_2O_2/0.1% Saponine for 10 min in a humidified incubator at 37°C and 5% CO_2 atmosphere, were used as positive control for PS externalization (Annexin V) and cell death (PI).

1.2 Giant unilamellar vesicles preparation.

Giant unilamellar vesicles (GUVs) were produced using the electroformation method [1, 2] and were used for microscopic visualization of the GP index and Phasor analysis in L_o and L_d membranes. These measurements served as reference points for the solvatochromic probes described below. We used the following lipids (purchased from Avanti Polar Lipids, Inc., Alabaster, AL, USA): 1,2-dipalmitoyl-sn-glycero-3-phosphocholine (DPPC) as main component of the solid ordered gel (L_β) phase, and 1,2-dilauroyl-sn-glycero-3-phosphocholine (DLPC) as main component of the L_d phase. Briefly, 4 µl of a 2.5 mg/mL lipid solution were homogeneous spread onto two parallel Pt wires mounted in a custom-made cylindrical Teflon chamber and the chloroform was evaporated under a nitrogen stream for five minutes at room temperature. Then, the chamber was filled with a 50 mM sucrose solution in deionized water and the wires were placed in the solution and connected to a voltage generator (AC generator FG 250 D, H-Tronic, Hirschau, Germany). GUV formation was induced by applying a sinusoidal electric field with an amplitude (peak-to-peak) of 2 V and a frequency of 10 Hz for 1 h at room temperature (DLPC) or above the specific transition temperature at 70 °C (DPPC). The fission of GUVs from the wires surface was facilitated by lowering the frequency to 2 Hz and the voltage to 1.3 V for at least 30 minutes. Subsequently, the GUVs were gently mixed 1:1 with 40 mOsm/kg PBS, stained with 4 µM of probes and imaged in a previously coated (0.1 mg/ml

bovine serum albumin in 40 mOsm/kg PBS, pH 7.4) 8 well ibidi® glass bottom µ-slide (ibidi GmbH, Gräfelfing, Germany).

1.3 Spectral phasor analysis

The fluorescence emission spectra from each pixel of the ROIs within spectral images were transformed into the phasor coordinates ($g(\lambda)$ and $s(\lambda)$) as following:

$$x\ coordinate = g(\lambda) = \frac{\sum_\lambda I(\lambda) \cos\left(\frac{2\pi n(\lambda-\lambda_{min})}{\lambda_{max}-\lambda_{min}}\right)}{\sum_\lambda I(\lambda)} \tag{1}$$

$$y\ coordinate = s(\lambda) = \frac{\sum_\lambda I(\lambda) \sin\left(\frac{2\pi n(\lambda-\lambda_{min})}{\lambda_{max}-\lambda_{min}}\right)}{\sum_\lambda I(\lambda)} \tag{2}$$

The coordinates $g(\lambda)$ and $s(\lambda)$ represent the real and imaginary component of the Fourier transformation, respectively. $I(\lambda)$ is the intensity for each wavelength and n is the harmonic number. We restricted our analysis to the first harmonic ($n = 1$) and the conclusions of the analysis remained qualitatively similar setting n=2. The x- and y-coordinates were then plotted in the four-quadrant spectral phasor plot as previously described [3]. The coordinates $g(\lambda)$ and $s(\lambda)$ take values between 1 to -1. The angular position in the phasor plot is proportional to the center of mass and the phasor radius is inversely proportional to the full width at half maximum (FWHM) of the emission spectrum. The advantage of the phasor approach is that small spectral shifts of Laurdan/ Di-4-ANEPPDHQ emission from labelled cells (caused by small changes in the lipid microenvironment) can be more easily resolved. Moreover, the phasor analysis takes into account the entire spectrum (rather than specific wavelengths or intervals) and it is model-free.

All measurements were analyzed with custom-written MATLAB code (The MathWorks, Natick, MA, USA). A schematic overview of the spectral phasor analysis is provided in Figure S1E and representative analysis for GUVs in Figure S4.

2. Tables

Table S1: Overview of the Annexin V, cell viability and infection status analysis for HEK293T and DF1 cells.
Data correspond to Figure S2. n: number of images, iqr: interquartile range, sd: standard deviation, se: standard error of the mean, ci: confidence interval.

cell type	treatment	n	median	iqr	mean	sd	se	ci
% Annexin V								
HEK293T	MOCK	16	1.1	1.9	1.4	1.6	0.4	0.8
HEK293T	H_2O_2-Saponine	15	86.4	10.8	86.7	7.2	1.9	4.0
HEK293T	FPV	15	1.7	1.5	2.2	2.0	0.5	1.1
HEK293T	WSN	15	0.9	1.4	1.0	0.9	0.2	0.5
DF1	MOCK	18	3.9	6.3	3.9	3.8	0.9	1.9
DF1	H_2O_2-Saponine	15	100.0	0.0	100.0	0.0	0.0	0.0
DF1	FPV	15	0.0	7.5	3.8	5.2	1.3	2.9
DF1	WSN	15	0.0	9.6	4.5	5.1	1.3	2.8
% cell viability								
HEK293T	MOCK	16	99.6	1.8	98.9	1.7	0.4	0.9
HEK293T	H_2O_2-Saponine	15	0.0	0.0	0.0	0.0	0.0	0.0
HEK293T	FPV	15	100.0	0.0	99.9	0.3	0.1	0.2
HEK293T	WSN	15	99.1	1.4	99.0	0.9	0.2	0.5
DF1	MOCK	18	98.5	5.8	96.7	3.9	0.9	2.0
DF1	H_2O_2-Saponine	15	0.0	0.0	0.0	0.0	0.0	0.0
DF1	FPV	15	100.0	0.0	98.6	3.8	1.0	2.1
DF1	WSN	15	100.0	9.6	94.6	6.7	1.7	3.7
% infected cells								
HEK293T	MOCK	16	0.0	0.0	0.0	0.0	0.0	0.0
HEK293T	H_2O_2-Saponine	15	0.0	0.0	0.0	0.0	0.0	0.0
HEK293T	FPV	15	82.9	7.3	81.9	4.9	1.3	2.7
HEK293T	WSN	15	90.5	3.8	90.6	3.6	0.9	2.0
DF1	MOCK	18	0.0	0.0	0.0	0.0	0.0	0.0
DF1	H_2O_2-Saponine	15	0.0	0.0	0.0	0.0	0.0	0.0
DF1	FPV	15	63.6	12.5	64.8	8.3	2.2	4.6
DF1	WSN	15	84.6	20.2	83.1	14.7	3.8	8.1

Table S2: Overview of the RG ratio values from the FRET analysis for HEK293T and DF1 cells. Data correspond to Figure 1 of the main manuscript. n: number of cells, iqr: interquartile range, sd: standard deviation, se: standard error of the mean, ci: confidence interval.

cell type	treatment	n	median	iqr	mean	sd	se	ci
HEK293T	MOCK	50	0.21	0.05	0.22	0.03	0.00	0.01
HEK293T	DOPS	55	0.61	0.11	0.64	0.08	0.01	0.02
HEK293T	FPV	51	0.49	0.12	0.49	0.07	0.01	0.02
HEK293T	WSN	53	0.51	0.11	0.53	0.09	0.01	0.02
DF1	MOCK	33	0.22	0.07	0.24	0.05	0.01	0.02
DF1	DOPS	21	0.51	0.12	0.54	0.13	0.03	0.06
DF1	FPV	33	0.47	0.15	0.50	0.12	0.02	0.04
DF1	WSN	33	0.49	0.11	0.49	0.10	0.02	0.04

Table S3: Overview of the GP index values from the analysis with Laurdan for HEK293T and DF1 cells. Data correspond to Figure 2 of the main manuscript. n: number of cells, iqr: interquartile range, sd: standard deviation, se: standard error of the mean, ci: confidence interval.

cell type	treatment	n	median	iqr	mean	sd	se	ci
HEK293T	MOCK	52	0.01	0.12	0.00	0.09	0.01	0.03
HEK293T	MbCD	56	-0.44	0.38	-0.45	0.22	0.03	0.06
HEK293T	FPV	103	0.28	0.10	0.27	0.07	0.01	0.01
HEK293T	WSN	110	0.31	0.07	0.31	0.05	0.01	0.01
DF1	MOCK	86	-0.04	0.11	-0.04	0.10	0.01	0.02
DF1	MbCD	87	-0.34	0.14	-0.35	0.11	0.01	0.02
DF1	FPV	61	0.25	0.15	0.25	0.10	0.01	0.03
DF1	WSN	57	0.21	0.11	0.23	0.10	0.01	0.03

Table S4: Overview of the GP index values from the analysis with Di-4-ANEPPDHQ for HEK293T and DF1 cells. Data correspond to Figure 2 of the main manuscript. n: number of cells, iqr: interquartile range, sd: standard deviation, se: standard error of the mean, ci: confidence interval.

cell type	treatment	n	median	iqr	mean	sd	se	ci
HEK293T	MOCK	53	0.26	0.08	0.25	0.05	0.01	0.01
HEK293T	MbCD	53	-0.01	0.08	0.01	0.08	0.01	0.02
HEK293T	FPV	116	0.44	0.03	0.44	0.02	0.00	0.00
HEK293T	WSN	127	0.44	0.03	0.44	0.02	0.00	0.00
DF1	MOCK	36	0.31	0.04	0.31	0.03	0.01	0.01
DF1	MbCD	76	0.07	0.12	0.07	0.08	0.01	0.02
DF1	FPV	51	0.44	0.02	0.44	0.02	0.00	0.01
DF1	WSN	63	0.44	0.04	0.44	0.02	0.00	0.01

Table S5 Overview of the diffusion coefficient values [μm²/s] from the sFCS analysis for HEK293T and DF1 cells. Data correspond to Figure 3 of the main manuscript. n: number of cells, iqr: interquartile range, sd: standard deviation, se: standard error of the mean, ci: confidence interval.

protein	cell type	treatment	n	median	iqr	mean	sd	se	ci
mp-mEGFP	HEK293T	MOCK	31	1.28	0.29	1.28	0.17	0.03	0.06
mp-mEGFP	HEK293T	FPV	20	0.55	0.29	0.55	0.26	0.06	0.12
mp-mEGFP	HEK293T	WSN	21	0.63	0.18	0.65	0.19	0.04	0.09
GPI-mEGFP	HEK293T	MOCK	29	1.04	0.34	1.06	0.18	0.03	0.07
GPI-mEGFP	HEK293T	FPV	20	0.64	0.25	0.63	0.23	0.05	0.11
GPI-mEGFP	HEK293T	WSN	25	0.66	0.34	0.61	0.22	0.04	0.09
HA-mEGFP	HEK293T	MOCK	36	0.42	0.14	0.44	0.11	0.02	0.04
HA-mEGFP	HEK293T	FPV	20	0.39	0.29	0.39	0.17	0.04	0.08
HA-mEGFP	HEK293T	WSN	30	0.33	0.12	0.35	0.14	0.03	0.05
mp-mEGFP	DF1	MOCK	22	1.17	0.32	1.18	0.23	0.05	0.10
mp-mEGFP	DF1	FPV	20	0.70	0.39	0.67	0.22	0.05	0.10
mp-mEGFP	DF1	WSN	20	0.55	0.36	0.55	0.24	0.05	0.11
GPI-mEGFP	DF1	MOCK	20	0.99	0.34	0.99	0.24	0.05	0.11
GPI-mEGFP	DF1	FPV	18	0.57	0.19	0.55	0.15	0.04	0.08
GPI-mEGFP	DF1	WSN	20	0.47	0.23	0.49	0.14	0.03	0.07
HA-mEGFP	DF1	MOCK	18	0.44	0.17	0.48	0.11	0.03	0.06
HA-mEGFP	DF1	FPV	18	0.27	0.15	0.33	0.11	0.03	0.05
HA-mEGFP	DF1	WSN	22	0.29	0.11	0.29	0.09	0.02	0.04

3. Figures
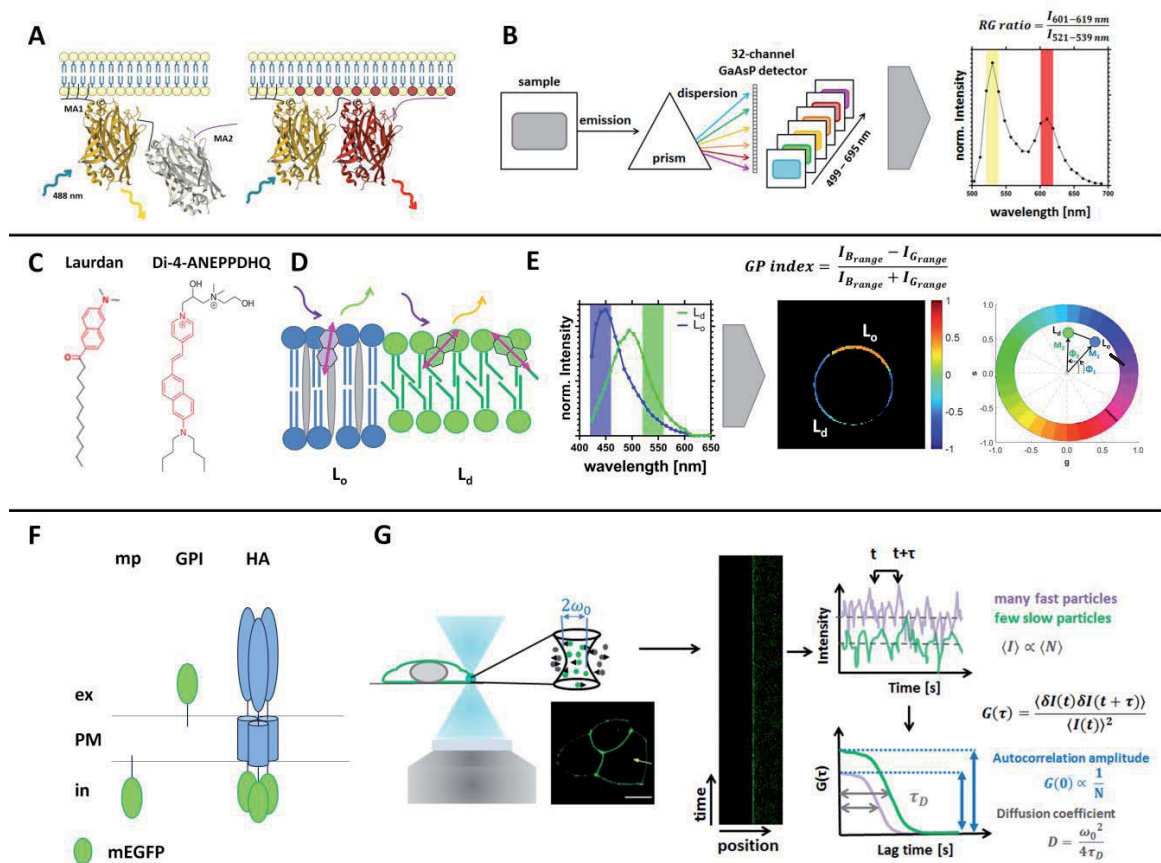
Figure S1: Overview of experimental approaches used in this study. Schematic overview of the experimental setup for the analysis of the enrichment of negatively charged lipids at the inner leaflet of the PM via FRET (A-B), changes in membrane fluidity via GP index (C-E), and dynamics of PM-associated proteins using sFCS (F-G). **(A)** Cartoon of the strategy used to study the effective electrostatic potential of the inner leaflet of the plasma membrane (PM). The lipid charge FRET-sensor (MCS+) contains two membrane attachment (MA) units and two fluorescent proteins (FPs, Venus and mCherry). MA1 is linked to the N-terminus of the FP Venus and consists of two palmitoylation and one myristoylation sites with the LCK10 sequence (MGCVCSSNPE), which allows a permanent binding to the PM via hydrophobic interactions. MA2 (purple) is linked to the C-terminus of the FP mCherry and contains a polybasic sequence (ARFGRRRRRRIRFRWVIM) which associates to negatively charged lipids at the inner leaflet of the PM. The FRET efficiency is then low when MA2 is separated from the PM (left panel) and high upon association of MA2 to the PM (right panel). Adapted from [4]. **(B)** Schematic illustration of the spectral FRET imaging analysis. The fluorescence emission from the sample upon illumination with laser light (488 nm) is dispersed (using a prism or other device) and guided onto a 32-channel GaAsP detector. Each channel records the signal at different wavelengths (499-695 nm), with a bin width of 8.9 nm. The signals are then used to visualize the emission spectrum for each pixel in the image. The intensity ratio (RG ratio) is then calculated from the spectrum values at each pixel (and averaged for all the pixels in a ROI and for different ROIs, if needed). Adapted from [5]. **(C)** Chemical structures of the solvatochromic probes Laurdan and Di-4-ANEPPDHQ used for the determination of the membrane fluidity at the PM, with the fluorophores highlighted in red. Parts in red highlight the fluorophore in the different probes. Taken from [6]. **(D)** Working principle of the solvatochromic probe Laurdan for lipid bilayers, presented as a mix of lipid ordered (L_o, blue, with cholesterol in grey) and lipid disordered (L_d, green) phases. Magenta arrows represent the orientation of Laurdan in the membrane. The interaction with the local environment leads to a spectral shift. The emission is shifted towards shorter wavelengths when the probe is in the L_o phase and towards longer in the L_d phase. Adapted from [7, 8]. **(E)** The emission signals of the spectral imaging (as shown in panel B) were then used to visualize the emission spectrum for each image. Representative fluorescence spectra for Laurdan in the L_o (blue) and L_d (green) phases of lipid bilayers. Intensity shifts between the L_o and L_d phases region can be quantified through a generalized polarization (GP) index.

Figure S1 (continued): GP value range from −1.0 (very fluid) to 1.0 (very gel-like) and are calculated for each image pixel in order to obtain a membrane "fluidity" map. The emission spectra are alternatively used to obtain a phasor plot. Spectral phasor plots represent the spectra as vectors of modulation (M) and phase angle (Φ), which are related to the spectral width and emission maximum (λ_{max}). The phase angle moves counterclockwise with increasing $\lambda_{max.}$ An increase in spectral width shifts the phasor closer to the center. Single dots represent exemplificative phasor values for a fluid membrane (L_d, green) and a rigid membrane (L_o, blue). Adapted from [7, 8]. **(F)** Overview of the different proteins used to study the dynamics of membrane components via sFCS. Monomeric membrane associated constructs consisting of a myristoylated and palmitoylated (mp) peptide or glycosylphosphatidylinositol (GPI)-anchor linked to the monomeric fluorescent protein mEGFP are used to probe the diffusion behavior in the inner and outer leaflet of the PM, respectively. As a model of transmembrane protein, we selected the trimeric hemagglutinin (HA) receptor from IAV, which is C-terminal linked to mEGFP. **(G)** Schematic principle of a confocal based sFCS setup. The focused laser beam scans the sample perpendicular to the PM (scan line is shown as kymograph), where mEGFP-linked proteins diffuse in and out of the confocal volume, giving rise to fluorescence fluctuations. From the resulting intensity trace, the autocorrelation function ($G(\tau)$), which represents the self-similarity of the signal, is calculated and fitted to a two-dimensional diffusion model in order to obtain diffusion time (τ_D, half-maximum decay of $G(\tau)$) and the concentration of the diffusing particles (N, from the ACF value at time zero). An increase of τ_D is associated with slower diffusive dynamics and a decrease of the ACF amplitude corresponds to an increase of N. Adapted from [9].
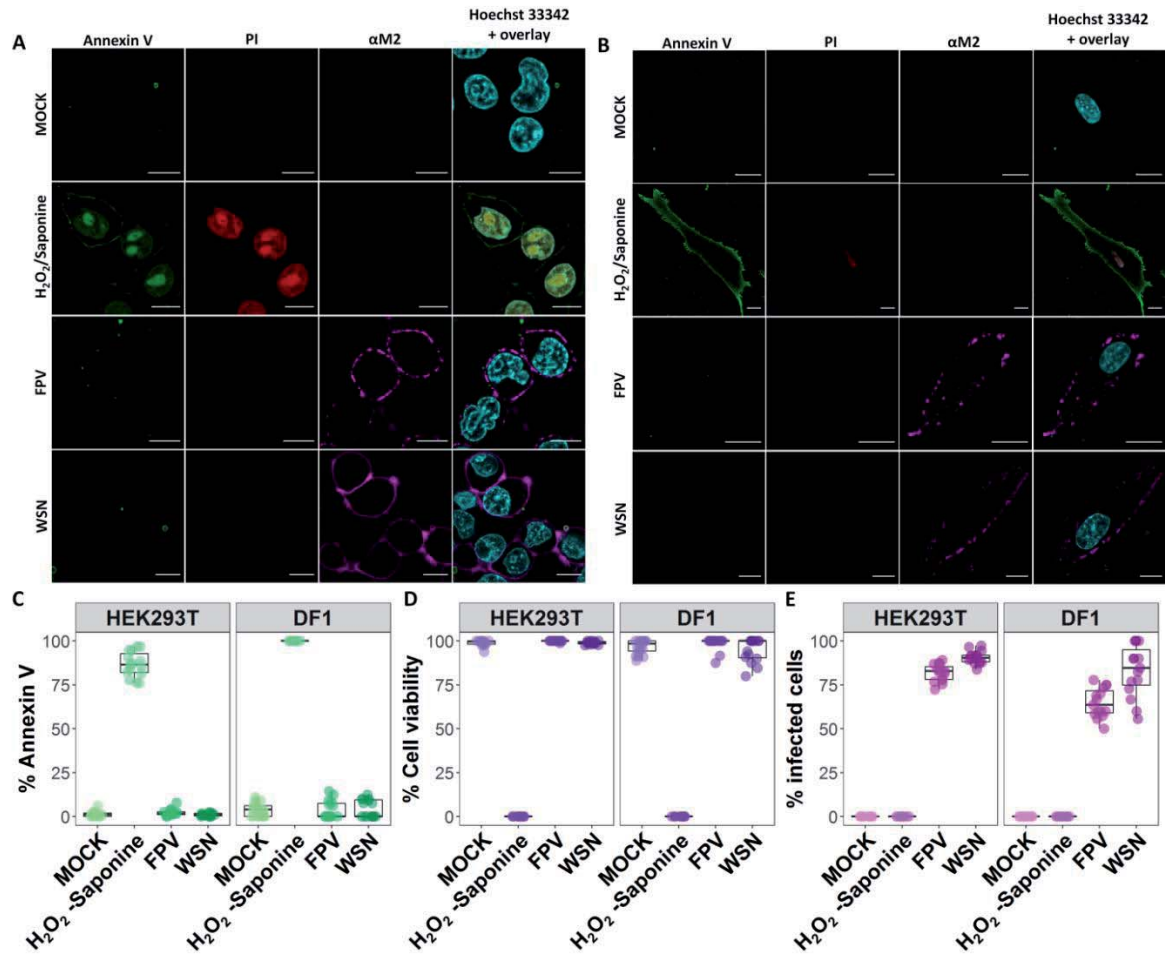
Figure S2: Early-stage IAV infection does not impact cell viability and PS trans-leaflet organization in the investigated cell models. HEK293T and DF1 cells were either: non-infected (MOCK), treated with 8 μM H_2O_2/0.1% Saponine (positive control), infected with FPV or infected with WSN. Samples were co-stained 16 hpi with Annexin V-AF488, propidium iodide (PI), anti-M2-AF647 (αM2) and Hoechst 33342. Representative confocal scanning microscope images of co-stained HEK293T cells **(A)** and DF1 cells **(B)**. Apoptotic cells exposing PS in the outer leaflet of the PM were visualized with Annexin V (green), dead/non-viable cells with PI (red), infected cells with αM2 (magenta) and the cell nucleus with Hoechst 33342 (cyan). Scale bars: 10 μm. Box plot with single data points of two independent experiments show the percentages of apoptotic (Annexin V-positive) cells **(C)**, the percentages of viable (Annexin V-/PI-negative) cells **(D)** and the percentage of infected (αM2-positive) cells **(E)**, which were calculated in relation to the total amount of cells (Hoechst 33342-positive). Quantitative information and statistical description are summarized in Table S1. For each condition, 15 to 18 images were manually analyzed, including in total more than 830 HEK293T cells and more than 150 DF1 cells per treatment.-
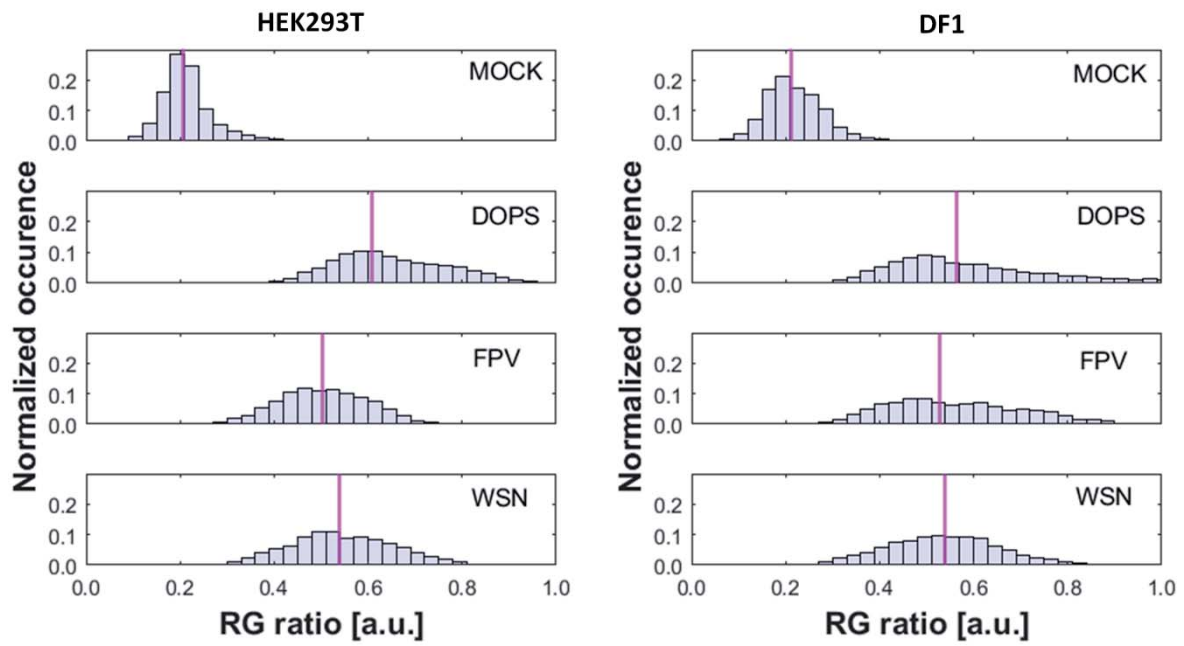
Figure S3: Quantification of the RG ratio from FRET measurements at the PM of HEK293T and DF1 cells. HEK293T and DF1 cells were either: non-infected (MOCK), treated with DOPS-SUVs (positive control), infected with FPV or WSN. All cells were expressing the FRET-sensor MCS+ and emission spectrum images were acquired 16 hpi. The obtained RG ratio values from each pixel in all ROIs selected at the PM of 50-55 HEK293T cells and 21-33 DF1 cells (Table S2) for all conditions were pooled and represented as normalized histogram showing the median value (magenta). Data correspond to the analyzed cells in Figure 1 of the main manuscript.
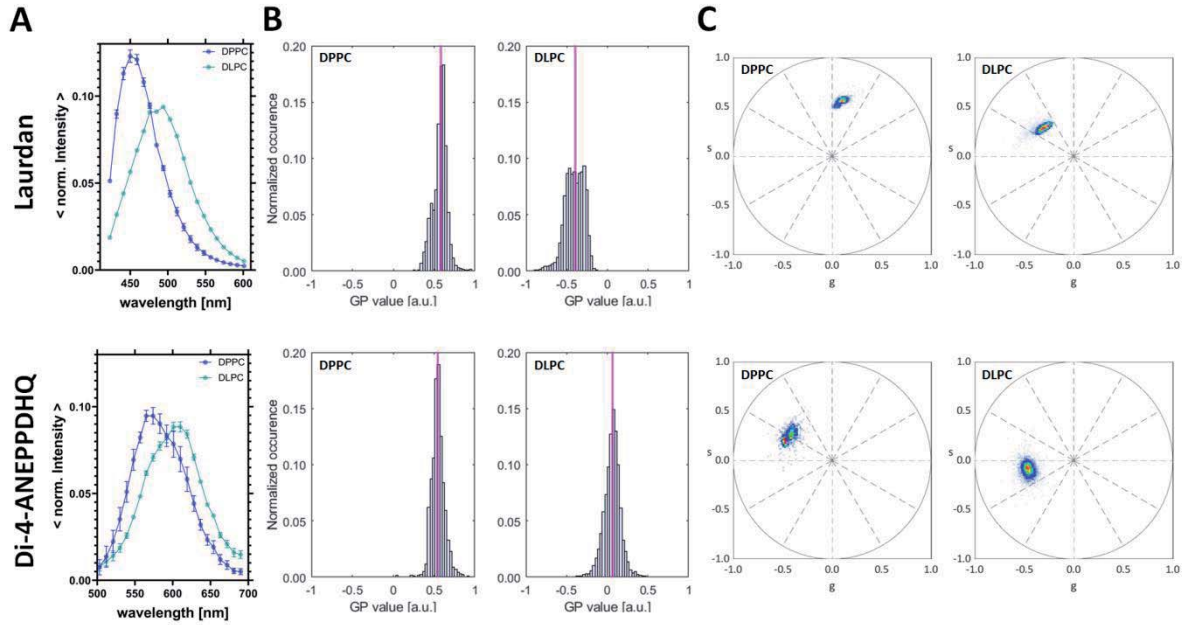
Figure S4: GP and spectral phasor analysis of GUVs labelled with Laurdan and Di-4-ANEPPDHQ. In order to acquire reference points for the GP and phasor analysis of infected cells, GUVs with extremely different lipid bilayer environments (solid ordered DPPC and liquid disordered DLPC) were prepared. These samples were then stained with Laurdan or Di-4-ANEPPDHQ and imaged with the same acquisition parameters used for the analysis of infected cells. For this analysis, 15 DLPC GUVs and 10 DPPC GUVs were analyzed for each dye. **(A)** Averaged normalized intensity spectra of all selected ROIs in the two types of GUVs. Data are represented as mean ± SD. **(B)** The obtained pixel-wise GP values of all ROIs GUVs were pooled and represented as normalized histogram, with the median value highlighted in magenta. The median values for DPPC were 0.58 (Laurdan) and 0.55 (Di-4-ANEPPDHQ). For DLPC they were -0.40 (Laurdan) and 0.07 (Di-4-ANEPPDQ). **(C)** Spectral phasor plots are obtained as described in Paragraph 1.3. Each point in the plot corresponds to s and g coordinates calculated from the pixel-wise spectrum of each ROI in a GUV. In the presence of a more ordered lipid environment, the point cloud shifts "clockwise" in the plot.
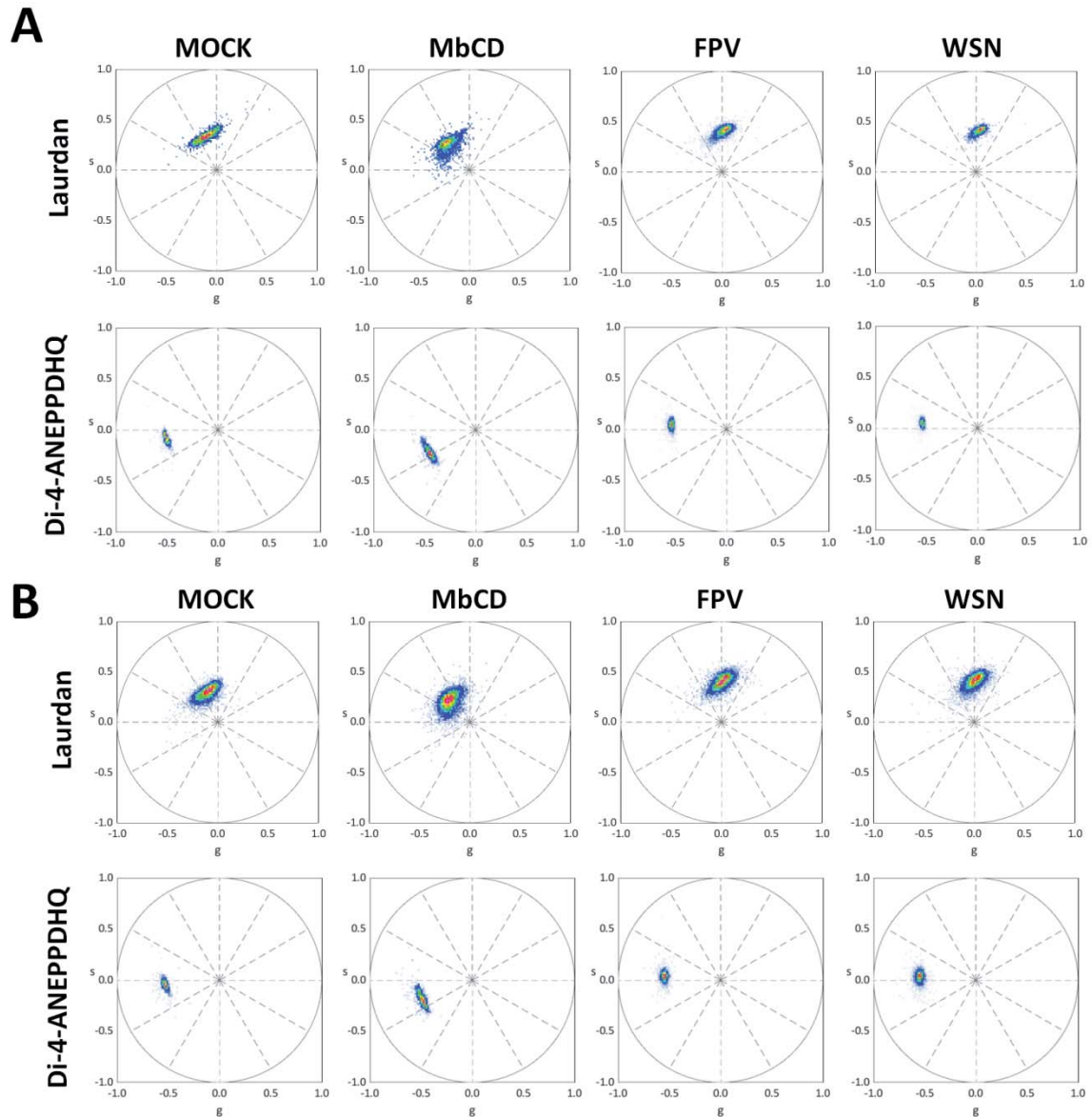
Figure S5: Spectral phasor analysis of Laurdan- and Di-4-ANEPPDHQ-labelled HEK293T and DF1 cells. HEK293T **(A)** and DF1 **(B)** cells were either: non-infected (MOCK), treated with methyl-β-cyclodextrin (MbCD), infected with FPV or infected with WSN. All cells were labelled with Laurdan and Di-4-ANEPPDHQ and emission spectrum images were acquired 16 hpi. For this analysis, 52-110 Laurdan-stained cells and 36-127 Di-4-ANEPPDHQ-stained cells were selected (Table S3 and S4) Spectral phasor plots are obtained as described in Paragraph 1.3. Each point in the plot corresponds to s and g coordinates calculated from the pixel-wise spectrum of each selected ROI. Data correspond to the analyzed cells in Figure 2 of the main manuscript.
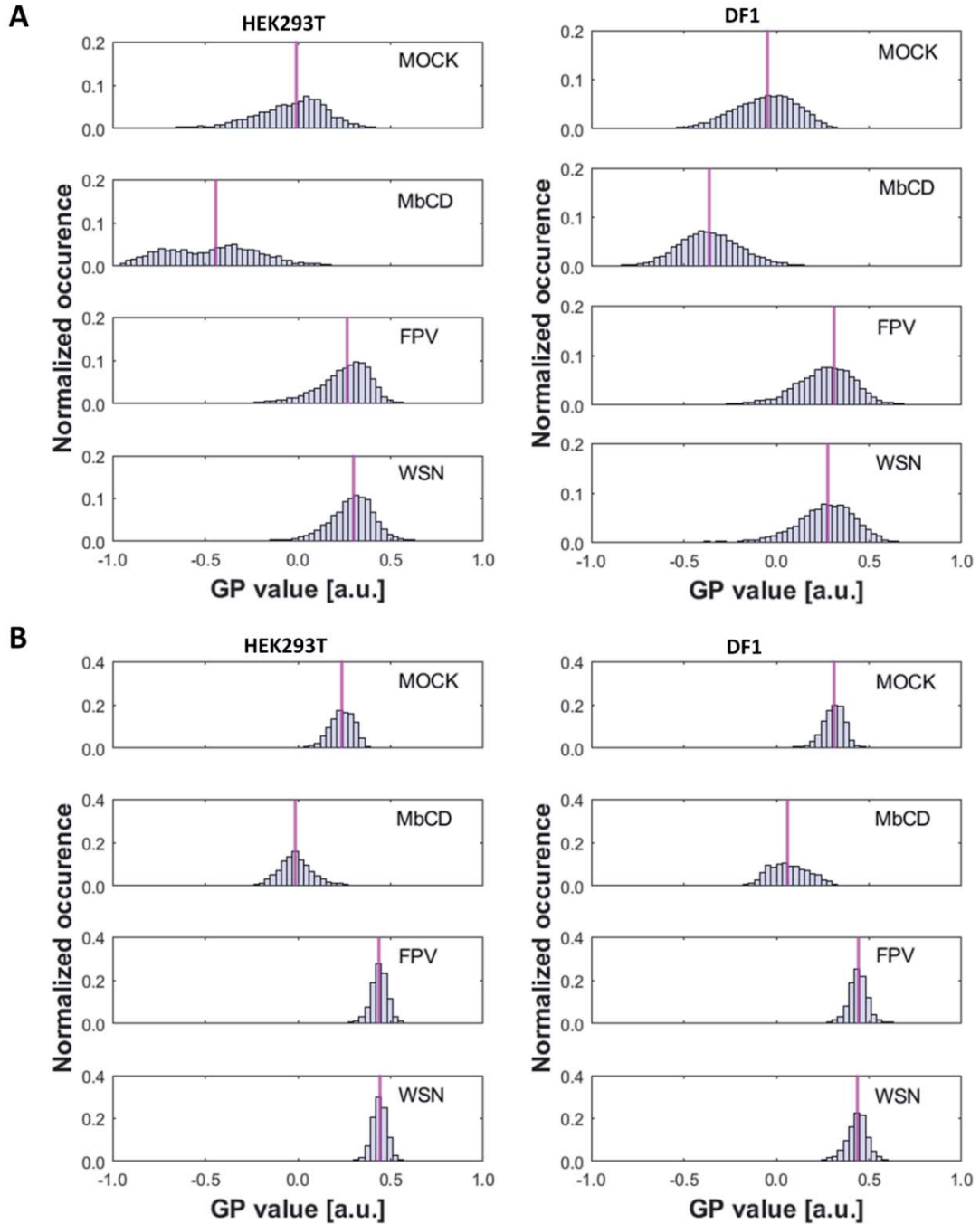
Figure S6: Quantification of the GP index from membrane fluidity measurements at the PM of HEK293T and DF1 cells. HEK293T and DF1 cells were either: non-infected (MOCK), treated with methyl-β-cyclodextrin (MbCD), infected with FPV or infected with WSN. All cells were labelled with Laurdan **(A)** and Di-4-ANEPPDHQ **(B)** and emission spectrum images were acquired 16 hpi. For this analysis, 52-110 Laurdan stained cells and 36-127 Di-4-ANEPPDHQ cells were selected (Table S3 and S4). Obtained pixel-wise GP values from all selected PM ROIs were pooled for each condition and represented as normalized histogram showing the median value (magenta). Descriptive statistics are summarized in Table S3-S4.Data correspond to the analyzed cells in Figure 2 of the main manuscript.
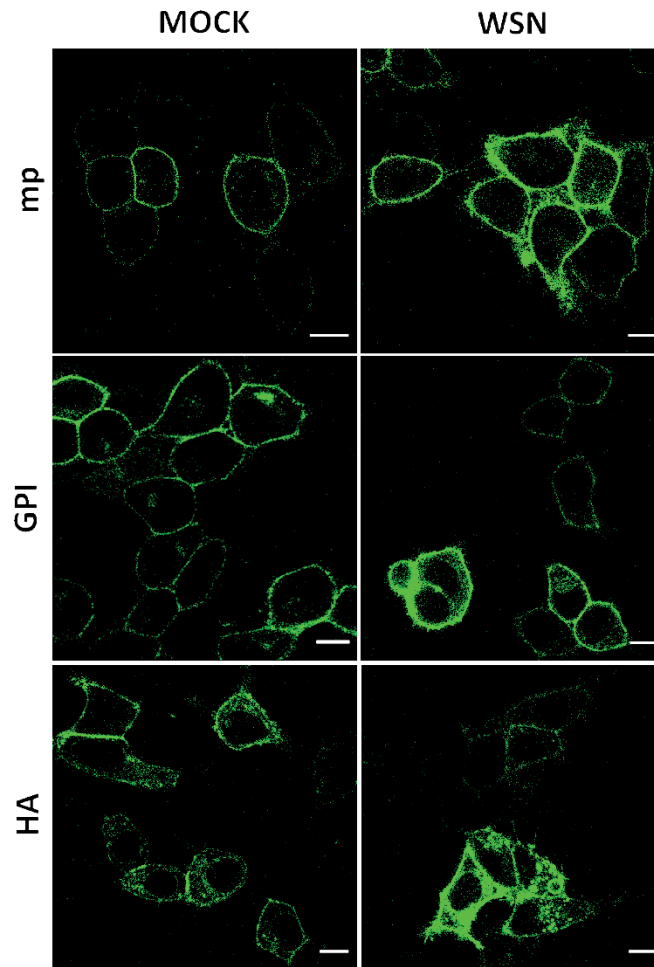
Figure S7: Representative confocal fluorescence images of HEK293T cells expressing mEGFP-tagged proteins. HEK293T cells were transfected with mp-mEGFP, GPI-mEGFP or HA-mEGFP. After four hours, cells were infected with WSN or treated with simple medium (MOCK). The images acquired after 16 hours indicate no major differences in the fluorescence protein appearance between infected and non-infected cells. Cells with very high expression levels could be seen more often following infection, but those cells were not selected for further analysis. Cells with expression levels similar to those observed in MOCK samples were selected instead. Similar results were obtained for cells infected with FPV (data not shown). Scale bars represent 10 μm.
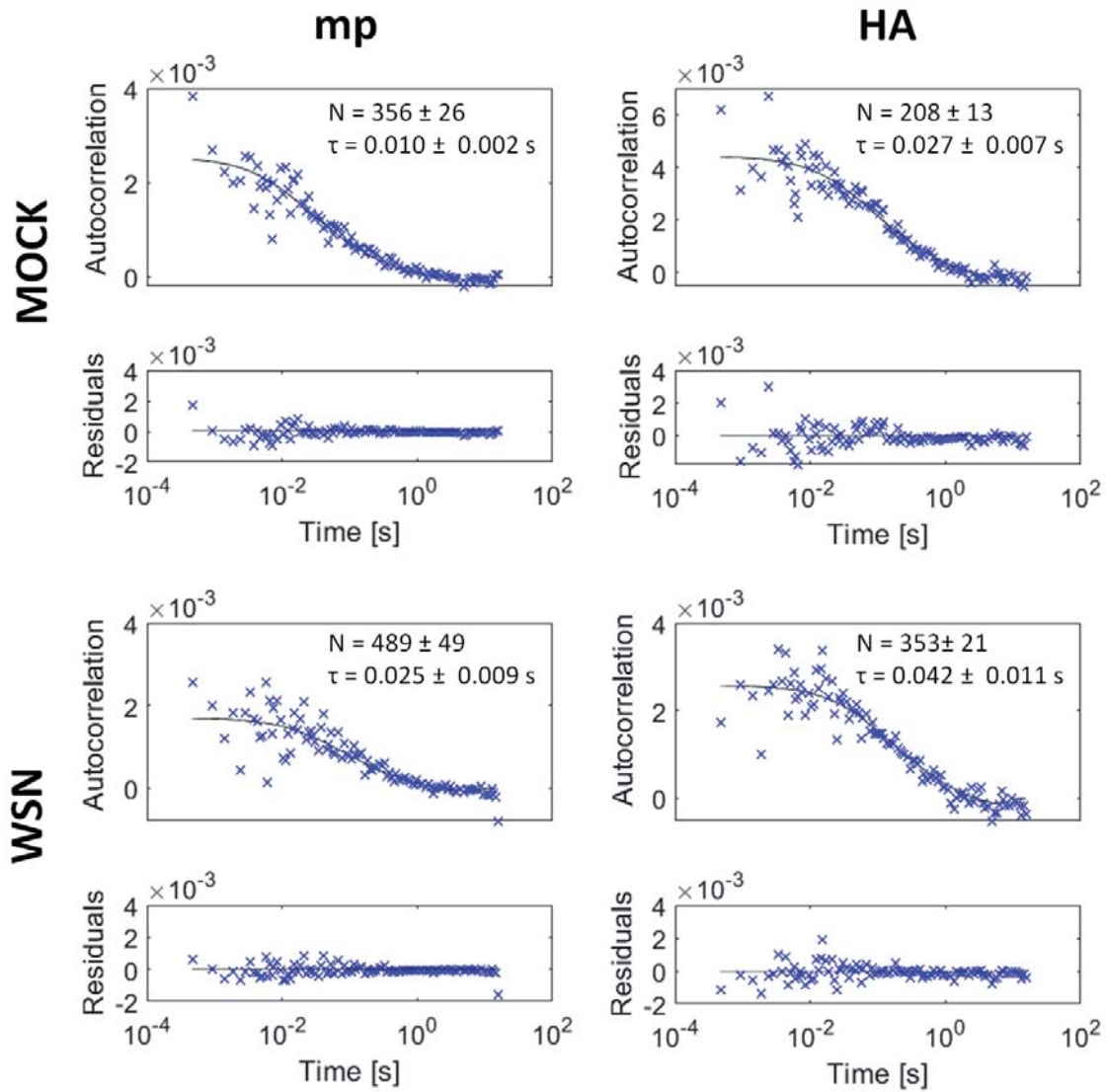
Figure S8: Examples of autocorrelation functions. Representative sFCS autocorrelation functions and fit curves obtained for non-infected (MOCK) and WSN-infected HEK293T cells expressing mp-mEGFP and HA-mEGFP. Fit curves (solid line) were obtained by fitting a two-dimensional diffusion model to the data, as described in the main text (Methods section). Data correspond to Figure 3 of the main manuscript. Similar data were obtained for DF1 cells (data not shown).

4. References

1. Angelova, M. I.; Dimitrov, D. S., Liposome electroformation. *Faraday Discussions of the Chemical Society* **1986,** 81, (0), 303-311.

2. Stein, H.; Spindler, S.; Bonakdar, N.; Wang, C.; Sandoghdar, V., Production of Isolated Giant Unilamellar Vesicles under High Salt Concentrations. *Front Physiol* **2017,** 8, 63.

3. Malacrida, L.; Astrada, S.; Briva, A.; Bollati-Fogolín, M.; Gratton, E.; Bagatolli, L. A., Spectral phasor analysis of LAURDAN fluorescence in live A549 lung cells to study the hydration and time evolution of intracellular lamellar body-like structures. *Biochim Biophys Acta* **2016,** 1858, (11), 2625-2635.

4. Ma, Y.; Yamamoto, Y.; Nicovich, P. R.; Goyette, J.; Rossy, J.; Gooding, J. J.; Gaus, K., A FRET sensor enables quantitative measurements of membrane charges in live cells. *Nature Biotechnology* **2017,** 35, (4), 363-370.

5. Sezgin, E.; Waithe, D.; Bernardino de la Serna, J.; Eggeling, C., Spectral imaging to measure heterogeneity in membrane lipid packing. *Chemphyschem* **2015,** 16, (7), 1387-94.

6. Klymchenko, A. S.; Kreder, R., Fluorescent probes for lipid rafts: from model membranes to living cells. *Chem Biol* **2014,** 21, (1), 97-113.

7. Bondelli, G.; Sardar, S.; Chiaravalli, G.; Vurro, V.; Paternò, G. M.; Lanzani, G.; D'Andrea, C., Shedding Light on Thermally Induced Optocapacitance at the Organic Biointerface. *J Phys Chem B* **2021,** 125, (38), 10748-10758.

8. Gunther, G.; Malacrida, L.; Jameson, D. M.; Gratton, E.; Sánchez, S. A., LAURDAN since Weber: The Quest for Visualizing Membrane Heterogeneity. *Acc Chem Res* **2021,** 54, (4), 976-987.

9. Yu, L.; Lei, Y.; Ma, Y.; Liu, M.; Zheng, J.; Dan, D.; Gao, P., A Comprehensive Review of Fluorescence Correlation Spectroscopy. *Frontiers in Physics* **2021,** 9.

3.4 Publication IV: Influenza A M2 recruits M1 to the plasma membrane: A fluorescence fluctuation microscopy study

Influenza A M2 recruits M1 to the plasma membrane: A fluorescence fluctuation microscopy study

Annett Petrich,[1] Valentin Dunsing,[1] Sara Bobone,[2] and Salvatore Chiantia[1,*]

[1]University of Potsdam, Institute of Biochemistry and Biology, Potsdam, Germany and [2]University of Rome Tor Vergata, Department of Chemical Science and Technologies, Roma, Italy

ABSTRACT   Influenza A virus (IAV) is a respiratory pathogen that causes seasonal epidemics with significant mortality. One of the most abundant proteins in IAV particles is the matrix protein 1 (M1), which is essential for the virus structural stability. M1 organizes virion assembly and budding at the plasma membrane (PM), where it interacts with other viral components. The recruitment of M1 to the PM as well as its interaction with the other viral envelope proteins (hemagglutinin [HA], neuraminidase, matrix protein 2 [M2]) is controversially discussed in previous studies. Therefore, we used fluorescence fluctuation microscopy techniques (i.e., scanning fluorescence cross-correlation spectroscopy and number and brightness) to quantify the oligomeric state of M1 and its interactions with other viral proteins in co-transfected as well as infected cells. Our results indicate that M1 is recruited to the PM by M2, as a consequence of the strong interaction between the two proteins. In contrast, only a weak interaction between M1 and HA was observed. M1-HA interaction occurred only in the event that M1 was already bound to the PM. We therefore conclude that M2 initiates the assembly of IAV by recruiting M1 to the PM, possibly allowing its further interaction with other viral proteins.

SIGNIFICANCE   Influenza A virus (IAV) is a pathogen responsible for epidemics and occasional pandemics and, therefore, is a significant burden on health systems. To develop innovative therapeutic approaches, a deeper understanding of the viral replication cycle is needed. For example, during the formation of new virions in infected cells, several viral components must assemble at the plasma membrane, but the molecular interactions involved in this process are not clearly understood. In this work, we use quantitative fluorescence microscopy methods to monitor the interplay between several viral proteins in live cell models. Our results underline the importance of the interactions between two specific proteins (M1 and M2) and shed light on the first steps in IAV assembly.

INTRODUCTION

Influenza A viruses (IAVs) belong to the family of the Orthomyxoviridae. These pathogens represent a substantial global health burden, being associated with significant morbidity and mortality through frequent epidemics and several pandemics (1,2). IAV is enveloped by a lipid bilayer that is derived from the host cell membrane and contains two integral transmembrane glycoproteins (i.e., hemagglutinin [HA] and neuraminidase [NA]) and one transmembrane protein with a proton-selective ion channel activity (i.e., the matrix protein 2 [M2]) (3,4). The envelope protein HA is a homotrimeric type I transmembrane glycoprotein and is the major surface protein of IAV particles (5–7). HA plays a ma-

jor role in viral entry by mediating the attachment of the virus to cell surface sialic acid molecules, membrane fusion after internalization, and the release of viral genome into target cells (5–8). The surface protein NA is a homotetrameric type II transmembrane glycoprotein that facilitates the release of newly synthesized virus particles from the infected cells by enzymatic cleavage of the cell surface receptor molecules (5–8). Additionally, a small amount of homotetrameric M2 molecules are embedded in the viral envelope (approximately 16–20 molecules in a virus, compared with circa [ca.] 300–400 HA and 50 NA copies) (6,7). M2 is a type III transmembrane protein that functions as proton channel activated by acidic pH and is important for genome unpacking during virus entry (7–9). Moreover, it was shown that M2 is connected to virus morphology, production of infectious virus particles, and membrane scission (9–13). All the three envelope proteins are transported from the *trans*-Golgi network to the apical plasma membrane

(PM) via the secretory pathway (8,9,14). Both glycoproteins, HA and NA, are supposed to be enriched in lipid "raft" microdomains at the virion budding site, whereas M2 was suggested to localize to the edges of such domains (8,14–16).

The luminal side of the viral envelope is coated with the matrix protein 1 (M1), which forms the viral nucleocapsid in close contact with the lipid membrane (17–20), binds the viral ribonucleoproteins (vRNPs) (4,21), and is supposed to interact with viral surface proteins (10,11,22–24). Moreover, M1 is the most abundant, highly conserved protein in IAV particles and is important for several processes during viral replication, including the regulation of capsid disassembly, virus budding, and morphogenesis (3,8,25). Interestingly, M1 lacks an apical transport signal, implying that the membrane localization of M1 in infected cells might be due to piggyback transport with HA, NA, M2, or vRNPs (26,27). For this reason, various hypotheses regarding the association of M1 to the PM have been proposed over the years. First, several studies established that M1 associates with negatively charged lipids in model membranes (17–20,28,29). Nevertheless, such interactions appear not to be sufficient for the actual association of M1 to the PM in non-infected cells (i.e., in cells expressing M1 as the only viral protein) (17,27). Accordingly, M1 was proposed to interact with the cytoplasmic tails of HA and NA during their apical transport (22–24,30,31), as well as with the cytoplasmic tails of M2 at the assembly site (10,11,27). Interactions between M1 and HA, NA, or M2 have been investigated via bulk biochemistry methods (e.g., by altered detergent solubility (22,24), increased membrane association (31) of M1 in the presence of HA or NA, or co-immunoprecipitation of M1 in the presence of M2 (10,11,32)). Nevertheless, no clear consensus has been reached regarding the role of HA, NA, or M2 in recruiting M1 to the PM and its subsequent incorporation into virions (11,33–37). In conclusion, the molecular mechanisms involved in M1-driven IAV assembly are not fully understood and the specific interactions between M1 and other viral surface proteins have not yet been quantified directly in living cells.

To obtain quantitative information on how protein-protein interactions (e.g., M1-M1 or M1-HA) occur in the native cellular environment, minimally invasive approaches (e.g., fluorescence fluctuation spectroscopy) are needed (38). Here, we apply number and brightness (N&B) and cross-correlation N&B (ccN&B) as well as scanning fluorescence correlation spectroscopy (sFCS) and scanning fluorescence cross-correlation spectroscopy (sFCCS) analysis in living cells to quantify oligomeric state, concentration, and diffusion dynamics of the viral envelope proteins (HA, NA, M2) and M1, as well as their interactions. Our results suggest the presence of a strong interaction between M1 and M2, leading to the recruitment of M1 to the PM in an M2 concentration-dependent manner. We further hypothesize that the interaction between M1 and HA occurs in a subse-

quent step. Finally, we provide the first experimental evidence of a possible M2-binding site within the N-terminal domain of M1.

MATERIALS AND METHODS

Plasmids and cloning

The plasmids for the transcription and translation of influenza virus RNAs and proteins of the influenza A/FPV/Rostock/1934 virus (H7N1; FPV) mutant 1 were obtained from Michael Veit (Free University, Berlin, Germany), and previously described (39,40). The plasmids encoding the fluorescence proteins (FPs) monomeric EGFP (mEGFP) or mCherry2 linked to a myristoylated and palmitoylated peptide (mp-mEGFP, mp-mCherry2, mp-2x-mEGFP), and the plasmids for cytosolic expression of mEGFP, 2x-mEGFP were previously described (41) and are available on Addgene (Watertown, MA, USA). The plasmids encoding the FP heterodimer mCherry2-mEGFP linked to a myristoylated and palmitoylated peptide (mp-mCherry2-mEGFP), and M2 of FPV with mCherry2 fused to the extracellular terminus of M2 (mCherry2-M2) were previously described (42). Further information regarding other plasmids and constructs used in this work is provided in the supporting material.

Cell culture and virus infection

Human embryonic kidney (HEK) cells from the 293T line (CRL-3216TM, purchased from ATCC, Kielpin Lomianki, Poland), and Madin-Darby canine kidney type II (MDCK II) cells (ECACC 00062107, European Collection of Authenticated Cell Cultures, Porton Down, UK) were cultured in phenol red-free Dulbecco's modified Eagle's medium (DMEM) with 10% fetal bovine serum, 2 mM L-glutamine, 100 U/mL penicillin, and 100 μg/mL streptomycin at 37°C and 5% CO_2. Cells were passaged every 2–3 days when they reached nearly 80% confluence in tissue culture flask, no more than 15 times. All solutions, buffers, and media used for cell culture were purchased from PAN-Biotech (Aidenbach, Germany).

For immunostaining experiments, dishes were coated with a 0.01% (w/v) poly-L-lysine solution (molecular weight [MW] 150,000–300,000 Da, Sigma-Aldrich, Munich, Germany) before cell seeding.

Information regarding virus propagation, titration and infection is provided in the supporting material.

Immunofluorescence

Transfected and infected cells were fixed at the indicated time points with 4% (w/v) paraformaldehyde (Sigma-Aldrich, Taufkirchen, Germany) in DPBS+/+. After 15 min, cells were washed three times Dulbecco's phosphate-buffered saline with Mg^{2+}/Ca^{2+} (DPBS +/+, PANBiotech, Aidenbach, Germany). Permeabilization was performed with 0.1% (v/v) Triton X-100 (Sigma-Aldrich, Taufkirchen, Germany) for 10 min, and subsequently washed three times with DPBS+/+. Afterward, cells were incubated with 2% (w/v) bovine serum albumin (BSA, Sigma-Aldrich, Taufkirchen, Germany) in DPBS+/+ for 1 h at room temperature. Primary antibody (monoclonal mouse anti-influenza A M2, clone 14C2 (#ab5416, abcam, Cambridge, UK), monoclonal mouse anti-influenza A H7 (#3HI7, HyTest Ltd, Turku, Finland), clone monoclonal mouse anti-influenza A N1, clone #2F10E12G1 (#AB_2860298, SinoBiological, Eschborn, Germany), monoclonal mouse anti-influenza nucleoprotein, clone A1 (#MAB8257, Millipore trademark of Merck KGaA, Darmstadt, Germany) were diluted 1:200 or 1:1000 in 0.2% (w/v) BSA in DPBS+/+, and incubated overnight at 4°C. After three washing steps with DPBS+/+, cells were incubated with the 1:1000 diluted secondary antibodies (goat anti-mouse Alexa Fluor 488 conjugated (AF488) or Alexa Fluor 568 conjugated

(AF568); Thermo Fisher Scientific, Waltham, MA, USA) for 1 h at room temperature. Cells were subsequently washed three times with DPBS+/+.

Confocal microscopy imaging

Microscopy measurements were performed on a Zeiss LSM780 system (Carl Zeiss, Oberkochen, Germany) using a Plan-Apochromat 40×/1.2 Korr DIC M27 water immersion objective and a 32-channel GaAsP detector array. To decrease out-of-focus light, a pinhole with size corresponding to one Airy unit (~39 μm) was used. Samples were excited with a 488-nm argon laser and a 561-nm diode laser. Fluorescence was detected between 499 and 552 nm (mEGFP, AF488) and between 570 and 695 nm (AF568), after passing through an MBS 488/561-nm dichroic mirror. For multicolor measurements, fluorophores were excited and detected sequentially for different regions of the spectrum. Confocal imaging was performed with a frame size of 512 × 512 pixels.

Further information regarding setup calibration, sF(C)CS, (cc)N&B, bidirectional plasmids, and multimerization analysis is provided in the supporting material. A schematic overview of the sFCCS and ccN&B analysis is shown in Fig. S1.

Statistical analysis

Data from at least three independent experiments were pooled and visualized by using GraphPad Prism vs. 9.0.0 (GraphPad Software, LCC, San Diego, CA, USA) or R (R Foundation for Statistical Computing, Vienna, Austria) packages *ggplot2* (43), *ggpubr* (44), and *cowplot* (45). If not otherwise indicated, data were displayed as box plots with single data points corresponding to measurements in single cells. Median values and whiskers ranging from minimum to maximum values are displayed. Quantities in the main text are given as median $\pm$ interquartile range (IQR). Sample sizes and p values are given in each graph and figure captions, respectively. Statistical significance was tested by using D'Agostino-Pearson normality test followed by the one-way ANOVA analysis and the Bonferroni's multiple comparisons test.

Code availability

MATLAB custom-written code is available from the corresponding author upon reasonable request.

Data availability

The datasets analyzed during the current study are available from the corresponding author upon reasonable request.

RESULTS

M1 is recruited to the PM by M2 but not by HA or NA

Previous studies have shown that the intracellular localization of the influenza A matrix protein M1 varies between transfected and infected cells (15,27). As a starting point for our investigations, we have therefore characterized the behavior of an M1-mEGFP fluorescent construct derived from the avian IAV strain FPV directly in living HEK293T cells. Protein localization was monitored via confocal microscopy either (1) when expressed by itself, (2) in the presence of all other viral proteins (i.e., via the
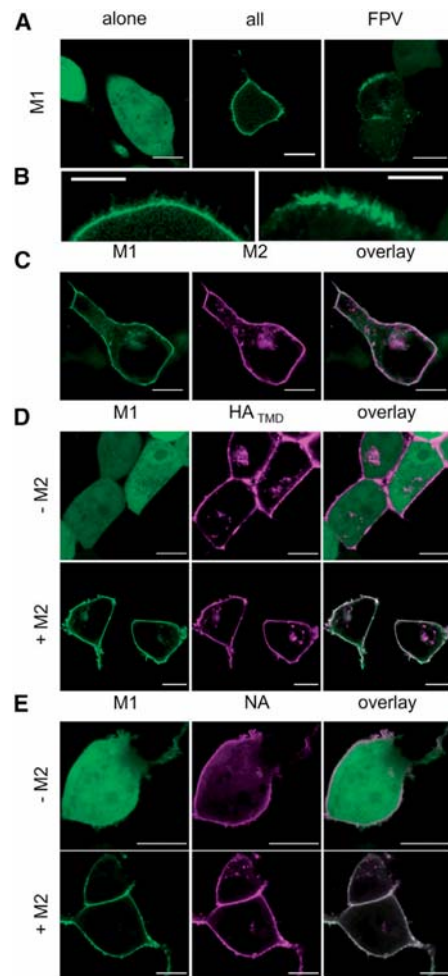
FIGURE 1 Membrane recruitment of IAV matrix protein 1 (M1) in co-transfected and infected cells. (A and B) Representative confocal fluorescence images of HEK293T cells expressing M1-mEGFP (*green*) from the influenza A/FPV/Rostock/1934 strain (FPV) alone (A, *left*). The same construct was also observed in cells co-transfected with the reverse genetic plasmid system of FPV and unlabeled M2, here labeled "all" (A, *middle*; B, *left*) and in cells infected with FPV (A, *right*; B, *left*). (C) Representative confocal fluorescence images of HEK293T cells co-expressing M1-mEGFP (*green*) and the FPV M2 (mCherry2-M2, *magenta*). The right panels show the two channels merged in a single image. (D) Representative confocal fluorescence images of HEK293T cells co-expressing M1-mEGFP (*green*) and the hemagglutinin (mCherry2-HA_{TMD}, *magenta*) in the absence (*upper panels*) or in the presence (*lower panels*) of unlabeled M2. (E) Representative confocal fluorescence images of HEK293T cells co-expressing M1-mEGFP (*green*) and the neuraminidase (NA-mCherry2, *magenta*) in the absence (*upper panels*) or in the presence (*lower panels*) of unlabeled M2. Scale bars represent 10 μm.

reverse genetic plasmid system and unlabeled M2 termed here as "all"), or (3) in FPV-infected cells (Fig. 1, A and B).

Expression of M1-mEGFP alone indicated a homogenous distribution of M1 through the cytosol and the nucleus (Fig. 1 A), whereas mEGFP-M1 (i.e., mEGFP fused at the N terminus) formed large, bright aggregates in the cytosolic region in close proximity to the nucleus (data not shown). The localization of M1-mEGFP was similar to what was

previously described for unlabeled M1 (46,47). Therefore, this construct was used for all further experiments. Upon co-transfection of all other IAV (unlabeled) proteins, a distinct enrichment of M1-mEGFP at the PM was detectable, with the protein being homogeneously distributed (Fig. 1 A). A statistical analysis of the frequency of such an occurrence is not trivial since the number of cells effectively transfected with all nine plasmids is unknown. Nevertheless, a control experiment suggests that most of the successfully transfected cells express several fluorescently tagged proteins at the same time (Fig. S2). Also, the probability that a cell expressing M1-mEGFP does not express any other viral protein is estimated to be very low (i.e., $< \sim 1\%$ for a six-plasmid system approximation; Fig. S2 B). Therefore, we conclude that the observed enrichment of M1 at the PM is probably due to the presence of at least one other viral protein.

Notably, we observed filamentous structures originating from the PM (Fig. 1 B, *left*; Fig. S3 A) that were not present when M1 was substituted by the membrane-anchored mp-mEGFP (Fig. S3 A). Cells infected with FPV showed heterogeneous M1 binding to the PM and formation of clusters in almost every cell (i.e., > ca. 90%) at 24 hpi (Fig. 1 A), as previously observed also for unlabeled M1 (15,16). M1-enriched structures at the PM resembling ruffles were even more evident, compared with the case of the reverse genetic plasmid system (Fig. 1 B, *right*; Fig. S3 A). The effectiveness of IAV infection was confirmed via immunofluorescence detection of expressed nucleoprotein (ca. 90% of infected cells, data not shown).

In order to determine whether M1 localization is determined by the presence of other viral proteins at the PM as previously suggested (15,16), M1-mEGFP was co-expressed with either mCherry2-M2, mCherry2-HA$_{TMD}$, or NA-mCherry2 (Fig. 1, C–E). It is worth noting that these viral proteins are labeled at the extracellular side (so to preserve possible interactions with intracellular M1) and strongly localize at the PM, similarly to their non-fluorescent counterparts (48,49). Fluorescence microscopy imaging indicated the absence of M1-mEGFP localization at the PM in cells co-expressing this protein with mCherry2-HA$_{TMD}$, NA-mCherry2 constructs (Fig. 1, D and E) or unlabeled HA or NA (Fig. S4 A). On the other hand, upon co-expression of M1-mEGFP with mCherry2-M2, clear colocalization of both proteins at the PM was observed (Fig. 1 C). Unequivocal association of M1-mEGFP to the PM was observed in ca. one-quarter of the examined cells and appeared qualitatively correlated with the amount of mCherry2-M2 at the PM (Figs. S4, B and C). A quantitative analysis of the correlation between the concentrations of the two proteins at the PM is presented in the following paragraphs.

The membrane distribution of M1-mEGFP was macroscopically homogeneous and no filamentous structures or clustering of M1-mEGFP at the PM were detectable. M2-induced binding of M1-mEGFP to the PM was qualitatively

not further influenced by co-expression of mCherry2-HA$_{TMD}$ or NA-mCherry2 (Fig 1, D and E).

In conclusion, M2 seems to be necessary for the recruitment of M1 to the PM. Also, the lateral organization of this protein on the lipid membrane is influenced by the presence of other viral proteins, as observed in infected cells.

M1 multimeric state at the PM ranges from dimers to large multimers

In order to quantify the concentration-dependent oligomerization of M1, N&B analysis was carried out in infected as well as co-transfected cells (Fig. 2). This approach was applied in the past to quantify protein multimerization as a function of local concentration and cellular localization (50,51). Compared with other methods based on fluorescence fluctuation analysis, N&B provides more representative results in samples characterized by spatial inhomogeneities and slow dynamics (52). The amount of fluorescence signal detected for an individual independent protein complex (e.g., a protein dimer) in the unit of time is indicated by the molecular brightness. This parameter is directly connected to the number of fluorophores within such a complex and, therefore, to the multimeric state of the fusion-labeled protein. Specifically, the multimerization can be quantified by normalization of the measured brightness values with the molecular brightness of a monomeric and dimeric reference (see section, "materials and methods") (41). To avoid possible interactions between the ectodomain of viral proteins and the solid substrate, we performed all measurements at the equatorial plane of cells rather than the basal membrane (which is often analyzed in the context of N&B studies). Our data show that protein oligomerization can be reproducibly quantified for both PM regions, without substantial differences (Fig. S5).

The fluorescent construct M1-mEGFP described in the previous paragraph was expressed in HEK293T cells either (1) in the presence of unlabeled M2; (2) concurrently with the reverse genetic plasmid system and unlabeled M2, named hereafter "all"; (3) concurrently with FPV infection; or (4) alone (Fig. 2).

The results shown in Fig. 2, A and B indicate that, upon co-expression of M2, M1-mEGFP does not form large complexes, compared with the cases in which other viral proteins are present (i.e., in the case of the reverse genetic plasmid system or of infection). In the latter cases, higher intensity and brightness values are in fact observed at the PM. The average intensity and molecular brightness values were calculated at each pixel of regions of interest (ROIs) (including, e.g., the PM or cytosolic regions) and represented as two-dimensional histograms (Fig. S6, representative example of data from Fig. 2, A and B). The brightness values of M1-mEGFP within each cell were usually symmetrically distributed around their average values for
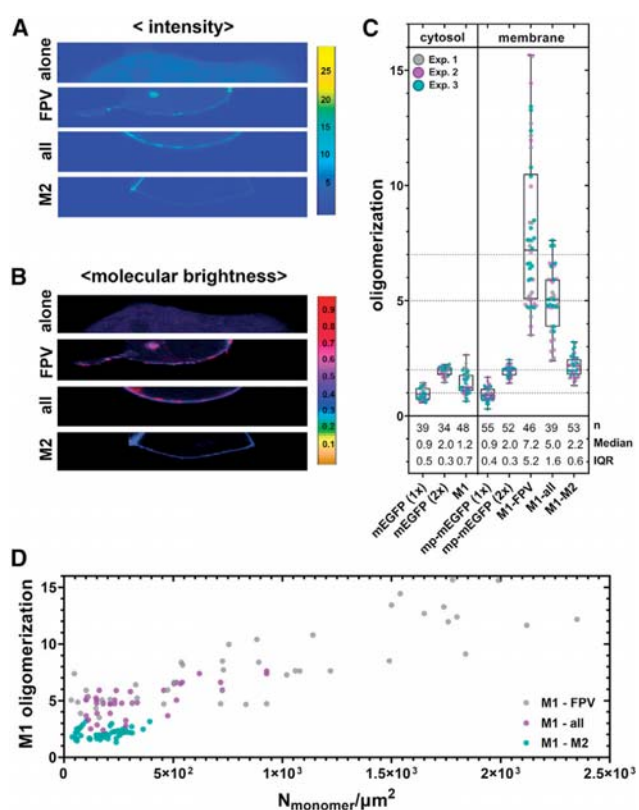
FIGURE 2 M1 oligomerizes in a concentration-dependent manner. N&B analysis of M1-mEGFP in cells expressing only M1-mEGFP, infected with FPV, co-transfected cells expressing unlabeled M2 and the reverse genetic plasmid system for all other FPV proteins ("all"), or co-transfected cells expressing unlabeled M2. Oligomerization and surface concentration values were obtained as described in the section "materials and methods." (A) Representative average intensity maps of M1-mEGFP in HEK293T cells. The average intensity map is visualized via color scale with units photon counts/dwell time. (B) Representative brightness-intensity maps corresponding to the images represented in (A). The images show pixel brightness as pixel color (counts/dwell time per molecule) and mean photon count rate as pixel intensity. (C) (Left) Box plot of single data points from three independent experiments showing the normalized brightness (i.e., oligomerization) for M1-mEGFP and the corresponding controls; i.e., cytosolic monomer mEGFP(1x), cytosolic dimer mEGFP(2x) in the cytosol of HEK293T cells. (C) (Right) Box plot of single data points from three independent experiments showing the oligomerization of M1-mEGFP at the PM of infected (M1-FPV) or co-transfected (M1-all, M1-M2) cells. Oligomerization values for PM-anchored controls are also shown: monomer mp-mEGFP(1x), dimer mp-mEGFP(2x). Median values and whiskers ranging from minimum to maximum values are displayed. Sample size, median, and IQR are indicated at the bottom. Horizontal dotted lines corresponding to oligomerization values 1, 2, 5, and 7 are shown as guide to the eye. (D) M1-mEGFP oligomerization as a function of surface concentration at the PM (in $N_{monomer}/\mu m^2$). The number of measured cells were: M1-FPV (n = 46), M1-all (n = 39), and M1-M2 (n = 53).

co-transfected cells expressing unlabeled M2, but slightly skewed toward large values in infected cells or cells transfected with the plasmid set "all." The brightness values of such distributions were then normalized using the corresponding monomer and dimer controls (Fig. 2 C). The analysis of cells expressing only M1 indicated that M1-mEGFP

in the cytosol has a normalized brightness between 1 and 2 (1.2 ± 0.7, median ± IQR, n = 48 cells). For comparison, the oligomerization state of cytosolic control monomers (mEGFP) and dimers (mEGFP-mEGFP) is also shown. It is worth noting that N&B analysis provides an average oligomerization value in the case of mixtures of different multimeric species (51). Therefore, the measured normalized brightness for cytosolic M1-mEGFP suggests that the protein is present as a mixture of, e.g., monomers (ca. 80%, assuming a fluorescence probability $p_f = 0.7$) and dimers (ca. 20%) at the observed concentrations. M1-mEGFP oligomerization slightly increased upon binding to the PM in the presence of unlabeled M2 (2.2 ± 0.6, median ± IQR, n = 53 cells). M1-mEGFP oligomeric state increased significantly upon co-transfection with all other viral proteins ("all," 5.0 ± 1.6, median ± IQR, n = 39 cells), or upon infection (7.2 ± 5.2, median ± IQR, n = 46 cells). For comparison, the oligomeric state of control monomers (mp-mEGFP) and dimers (mp-mEGFP-mEGFP) is also shown. Additionally, M1-mEGFP showed a significant concentration-dependent oligomerization behavior in concurrently infected cells and in transfected cells expressing all other viral proteins (Fig. 2 D). On the other hand, the oligomerization of M1-mEGFP in co-transfected cells expressing unlabeled M2 seemed to be independent from concentration and stable around values corresponding, on average, to M1-mEGFP dimers. As is also evident from Fig. 2 D, higher concentrations of M1-mEGFP at the PM were observed in general in infected cells, as well as in co-transfected cells expressing all other viral proteins.

Of note, it must be considered that, in infected cells, M1 concentration and oligomerization are underestimated, due to the co-expression of viral unlabeled M1, which might take part in the formation of complexes with M1-mEGFP. Since N&B analysis accounts only for labeled proteins, complexes containing both labeled and unlabeled species will effectively appear as smaller oligomers. Additionally, it is also possible that a precise determination of the multimeric state might be hindered by high protein concentrations at the PM, especially for very large multimers.

In summary, M1-mEGFP forms up to dimers in the cytoplasm or at the PM, upon co-expression of M2. The oligomerization of membrane-bound M1-mEGFP increases dramatically as a function of local concentration in infected cells and, to a minor extent, in cells expressing all other viral proteins via a reverse genetic plasmid system.

HA and NA do not induce M1 oligomerization

The interaction of M1 with other viral membrane proteins (HA, NA, and M2) is controversially discussed in previous studies (10,11,22–24,30,31,35,36).

To clarify this issue, we performed two-color sFCCS analysis in HEK293T cells expressing M1-mEGFP in combination with (1) mCherry2-M2, (2) mCherry2-HA_{TMD} and
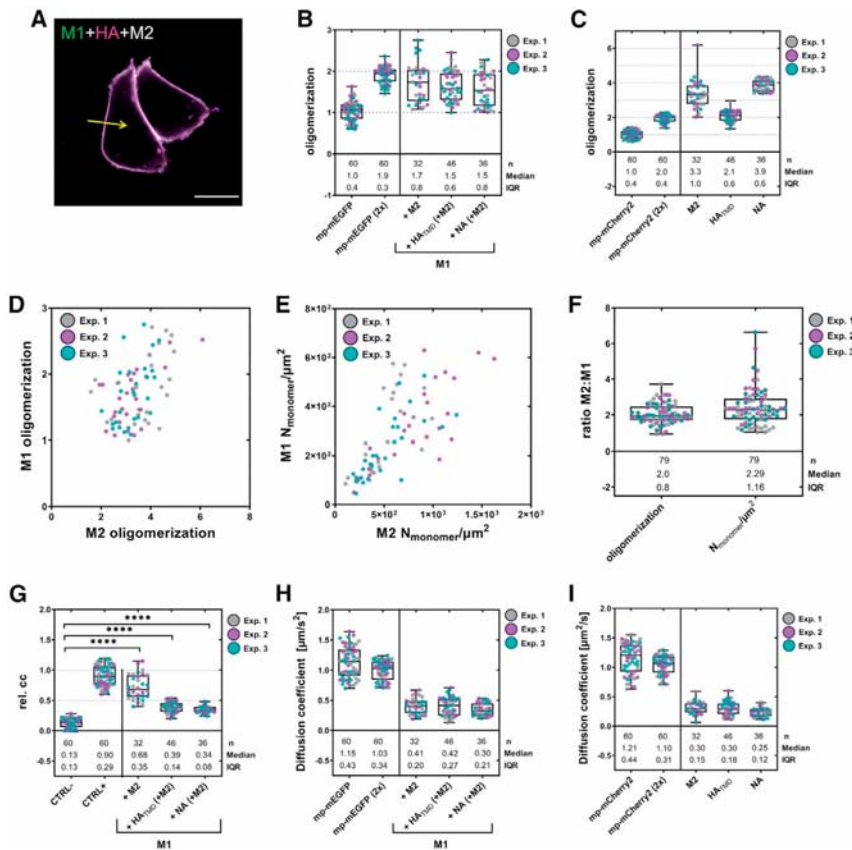
FIGURE 3 M2 interacts with M1 in a concentration-dependent manner. sFCCS of M1-mEGFP in HEK293T cells co-expressing mCherry2-M2, mCherry2-HA$_{TMD}$/M2-untagged, and NA-mCherry2/M2-untagged. Oligomerization, surface concentration (N$_{monomer}$/µm^2), cross-correlation, and diffusion coefficient (µm^2/s) values were obtained as described in the section, "materials and methods." (*A*) Representative confocal fluorescence image of HEK293T cells co-expressing M1-mEGFP (*green*), mCherry2-HA$_{TMD}$ (*magenta*), M2-untagged. Yellow arrow indicates the scanning path used for sFCCS. Scale bar represents 10 µm. (*B*) Box plot with single data points from three independent experiments shows the oligomerization of the controls monomer mp-mEGFP(1x) and dimer mp-mEGFP(2x), and M1-mEGFP co-expressed with mCherry2-M2, mCherry2-HA$_{TMD}$/M2-untagged, and NA-mCherry2/M2-untagged. Median values and whiskers ranging from minimum to maximum values are displayed. Sample size, median, and IQR are indicated in the graph. (*C*) Box plot with single data points from three independent experiments shows the oligomerization of the controls monomer mp-mCherry2(1x) and dimer mp-mCherry2(2x), and the viral surface proteins mCherry2-M2, mCherry2-HA$_{TMD}$, and NA-mCherry2 for the same samples described for (*B*). Median values and whiskers ranging from minimum to maximum values are displayed. Sample size, median, and IQR are indicated in the graph. (*D* and *E*) Scatter plots show the oligomerization of M1-mEGFP as a function of the oligomerization of mCherry2-M2 (*D*), and the surface concentration of M1-mEGFP as a function of the surface concentration of mCherry2-M2 (*E*). (*F*) Box plot with single data points from three independent

experiments shows the ratio of the oligomerization, and the surface concentration of M2:M1. Median values and whiskers ranging from minimum to maximum values are displayed. Sample size, median, and IQR are indicated in the graph. (*G*) Box plot with single data points from three independent experiments shows the rel. cc for the controls negative control mp-mEGFP(1x)/mp-Cherry2 and positive control mp-mCherry2-mEGFP, and between M1-mEGFP and mCherry2-M2, mCherry2-HA$_{TMD}$, or NA-mCherry2. Cells expressing mCherry2-HA$_{TMD}$ and NA-mCherry2 also expressed unlabeled M2. Median values and whiskers ranging from minimum to maximum values are displayed. Sample size, median, and IQR are indicated in the graph. Statistical significance was determined using one-way ANOVA multiple comparison test; ****$p < 0.0001$ compared with the negative control (CTRL−). (*H*) Box plot with single data points from three independent experiments shows the diffusion coefficient of the controls monomer mp-mEGFP(1x) and dimer: mp-mEGFP(2x), and M1-mEGFP co-expressed with mCherry2-M2, mCherry2-HA$_{TMD}$/M2-untagged, and NA-mCherry2/M2-untagged. Median values and whiskers ranging from minimum to maximum values are displayed. Sample size, median, and IQR are indicated in the graph. (*I*) Box plot with single data points from three independent experiments shows the diffusion coefficient of the controls monomer mp-mCherry2(1x) and dimer mp-mCherry2(2x), and the viral surface proteins mCherry2-M2, mCherry2-HA$_{TMD}$, and NA-mCherry2 for the same samples described for (*H*). Median values and whiskers ranging from minimum to maximum values are displayed. Sample size, median, and IQR are indicated in the graph.

unlabeled M2, or (3) NA-mCherry2 and unlabeled M2. As shown for example in Fig. 3 *A* for the case of co-transfected cells expressing M1-mEGFP, mCherry2-HA$_{TMD}$, and unlabeled M2, M1 partitions strongly at the PM in all cases. For sFCCS measurements, the confocal detection volume is scanned in a linear fashion perpendicularly to the PM, as illustrated by the yellow arrow. Following the calculation of autocorrelation functions (ACFs) and cross-correlation functions (CCFs) (Fig. S7), this approach allows the quantification of the interactions between two differently labeled proteins by calculating the relative cross-correlation (rel. cc); i.e., a measure of the relative abundance of molecular hetero-complexes. Furthermore, from the analysis of the

ACF, sFCCS provides quantitative information about diffusion dynamics and, similar to N&B analysis, the average oligomerization state of the monitored proteins.

Our results suggest that M1 forms monomers and dimers at the PM, upon co-expression of M2 (1.7 ± 0.8, median ± IQR, n = 32 cells), confirming the results of the N&B experiments (Fig. 3 *B*). For comparison, the oligomerization state of control monomers (mp-mEGFP) and dimers (mp-mEGFP-mEGFP) is also shown. Further, the oligomerization of M1 is not significantly altered by additionally co-expressing the IAV glycoproteins, mCherry2-HA$_{TMD}$ (1.5 ± 0.6, median ± IQR, n = 46 cells), or NA-mCherry2 (1.5 ± 0.8, median ± IQR, n = 36 cells). To verify whether the FP fused to viral

glycoproteins alters their quaternary structure, the molecular brightness of mCherry2-HA$_{TMD}$ and NA-mCherry2 was also analyzed and compared with the corresponding controls (Fig. 3 C). The HA transmembrane domain construct mCherry2-HA$_{TMD}$ formed in average dimers (2.1 $\pm$ 0.6, median $\pm$ IQR, n = 46 cells), and NA–mCherry2 formed in average tetramers (3.9 $\pm$ 0.6, median $\pm$ IQR, n = 36 cells). Both oligomeric states are consistent with those obtained in earlier studies (53,54). The average oligomerization state of mCherry2-M2 (3.3 $\pm$ 1.0, median $\pm$ IQR, n = 32 cells) indicated that M2 might be present as a mixture of, e.g., dimers and tetramers on the PM, which is consistent with previous results (55). Surprisingly, for all the examined IAV proteins, we observed that their average oligomerization state was not strongly influenced by their local concentration (Fig. S8).

It is worth noting that the mCherry2-M2 construct (i.e., with mCherry2 fused to the N terminus of M2) was newly designed to monitor M1:M2 interactions while avoiding steric hindrance at the cytosolic side of M2. In order to determine whether this fluorescent M2 construct behaves as expected (especially in the context of M1-M2 interactions), we used an alternative strategy to simultaneously express untagged M2 and a membrane marker (mp-mCherry2) via a bi-directional vector system (indicated as M2 $\leftrightarrow$ mp-mCherry2) (56). The measured concentration of mp-mCherry2 can be used to estimate the amount of unlabeled M2 in the PM (see section, "materials and methods" in supporting material, Fig. S9). The correct expression of M2 at the PM was validated by immunofluorescence (Fig. S9 C). No significant difference in the oligomeric state of M1-mEGFP as a function of the surface concentration of M2 between both plasmid constructs (i.e., bi-directional M2 and mCherry2-M2) was observed (Fig. S9 D). Therefore, only the mCherry2-M2 construct was used for further investigations of M1-M2 interaction.

Notably, the oligomerization of M1-mEGFP was consistently independent from the concentration of mCherry2-M2 at the PM (Fig. S9 D) but correlated with the oligomerization state of mCherry2-M2 (Fig. 3 D). Also, the concentration of M1-mEGFP at the PM increased with increasing mCherry2-M2 concentration (Fig. 3 E). As shown in Fig. 3 F, we could finally estimate that both M1-mEGFP concentration at the PM and oligomerization are ca. half of what is observed for mCherry2-M2 (M2:M1$_{oligo.state}$: 2.0 $\pm$ 0.8, and M2:M1$_{surface conc.}$: 2.29 $\pm$ 1.16, median $\pm$ IQR).

In summary, our results suggest that M1 binds to the PM as dimer upon co-expression of M2. M1-M1 and M1-lipid interactions did not appear to be modulated by the presence of HA or NA.

M1 strongly interacts with M2 but only weakly associates to HA or NA

Direct information regarding the formation of protein hetero-complexes at the PM can be derived by the analysis of ACFs and CCFs obtained via sFCCS (see previous paragraph). We therefore calculated the rel. cc as a measure of the hetero-interactions between M1-mEGFP and either mCherry2-M2, mCherry2-HA$_{TMD}$, or NA-mCherry2 (Fig. 3 G, and S3). Two interacting molecules diffusing together through the observation volume as a complex will give rise to a positive rel. cc that can be quantified by the amplitude of the cross-correlation curve (Fig. S7 B). Low rel. cc indicates the absence of interaction between the observed proteins (see, e.g., Fig. S7 A). However, due to incomplete maturation of the fluorescent proteins and the partial overlap of the confocal volumes in both channels, the maximum achievable rel. cc value is lower than 1. For example, a tandem of mp-mCherry2-mEGFP used here as a positive control for rel. cc displayed a rel. cc of 0.90 $\pm$ 0.29 (median $\pm$ IQR, n = 60 cells). As expected, we detected a very low rel. cc (0.13 $\pm$ 0.13, median $\pm$ IQR, n = 60 cells) in negative control experiments (i.e., in samples of co-transfected cells expressing mp-mEGFP and mp-mCherry2). As shown in Fig. 3 G, a rel. cc of 0.7 $\pm$ 0.4 (median $\pm$ IQR, n = 32 cells) was measured for M1-mEGFP and mCherry2-M2. This value is significantly higher than the negative control and close (ca. 80%) to that obtained for the positive control, suggesting very strong association of M1-mEGFP with mCherry2-M2. Assuming a very simple scenario consisting, e.g., of M1 dimers, M2 tetramers, and 2:4 M1-M2 complexes, all detectable with p_f = 1, ca. 80% of M1 molecules appear to be in complex with M2.

On the other hand, the obtained rel. cc values for M1-mEGFP with either mCherry2-HA$_{TMD}$, or NA-mCherry2 (rel. cc(M1,HA$_{TMD}$) = 0.39 $\pm$ 0.14, n = 46 cells; rel. cc(M1,NA) = 0.34 $\pm$ 0.08, n = 36 cells, median $\pm$ IQR) were lower but still significantly higher than the negative control. It is worth noting that such measurements could only be performed in the presence of unlabeled M2 since, without this third protein, no localization of M1-mEGFP at the PM could be observed (see previous paragraphs). The observed rel. cc values indicate a weak interaction between M1-mEGFP and the glycoproteins mCherry2-HA$_{TMD}$, and NA-mCherry2. In the simple approximation of p_f = 1 and constant multimerization, independently from the participation in complexes, ca. 40% of M1 molecules appear to be associated with the viral glycoproteins. To further investigate this issue, we also quantified the interaction between M1 and the glycoproteins in infected cells. To this aim, we performed ccN&B in cells infected with FPV and, additionally, co-transfected with M1-mEGFP and either mCherry2-HA$_{TMD}$ or NA-mCherry2 plasmids. Similar to sFCCS, ccN&B can be used to quantify the rel. cc between different FPs, especially in samples characterized by slow dynamics (52). sFCCS measurements of M1-mEGFP in infected cells did not provide reproducible results (data not shown). As shown in Fig. S10, the rel. cc values determined by ccN&B in infected cells for

M1-mEGFP and mCherry2-HA$_{TMD}$ (rel. cc(M1,HA$_{TMD}$) = 0.31 ± 0.10, n = 21 cells, median ± IQR), as well as for M1-mEGFP and NA-mCherry2 (rel. cc(M1,NA) = 0.28 ± 0.08, n = 22 cells, median ± IQR) were roughly comparable with the rel. cc values obtained in non-infected cells, as measured via sFCCS (Fig. 3 G). A more precise quantification is complicated in this case by the presence of non-fluorescent viral proteins and unknown stoichiometry of the investigated molecular complexes.

Finally, we quantified protein dynamics by fitting a two-dimensional diffusion model to the ACF data (Figs. 3, H, I, and S7). Knowing the size of the observation volume, it is possible to obtain diffusion coefficients of the proteins (D in μm/s^2, see section, "materials and methods"). Protein diffusion depends in general on the size of the protein complex and on protein-membrane interactions. The diffusion coefficients measured for M1-mEGFP at the PM (D = 0.3–0.4 μm/s^2, Fig. 3 H) were lower than those of the monomer control (D = 1.1 ± 0.4 μm/s^2, median ± IQR, n = 60), and similar to the diffusion coefficient of the IAV integral surface proteins mCherry2-M2, mCherry2-HA$_{TMD}$, and NA-mCherry2 (indicated in Fig. 3 I).

Taken together, our data indicate that M1 strongly interacts with M2. On the other hand, a relatively small amount of complexes containing M1 together with HA or NA was detected.

Non-specific M1 recruitment to the PM is sufficient for the establishment of M1-HA interaction

To investigate the origin of the interaction between M1 and HA (or NA) that was observed in cells additionally expressing M2, we artificially induced M1 binding to the PM. These experiments were performed to test the hypothesis that M1 is recruited (by M2) to the PM, where it can then interact with other membrane proteins (independently from the specific protein that first induced M1-PM binding).

Specifically, we designed two M1 constructs in which the protein was modified by myristoylation and palmitoylation (mp-M1-mEGFP) and, additionally, with a poly-lysine motif (mp-KrΦ-M1-mEGFP), as shown in Fig. 4 A. The underlying idea is that the additional targeting sequences direct M1 specifically to lipid ordered raft domains (myristoyl-palmitoyl anchor (57)) or to regions containing acidic lipids (poly-lysine motif) in the PM, as supported by previous studies (27,58–60). M1 localization within specialized PM domains might indeed be relevant, since the viral envelope proteins HA and NA were previously reported to localize in lipid rafts, whereas M2 was observed at the edges between ordered and disordered domains (7,14).

First, we verified the sub-localization of the two new constructs in transfected HEK293T cells. Both mp-M1-mEGFP and mp-KrΦ-M1-mEGFP were efficiently trafficked to the PM (Fig. 4 B). Next, we examined the rel. cc between these
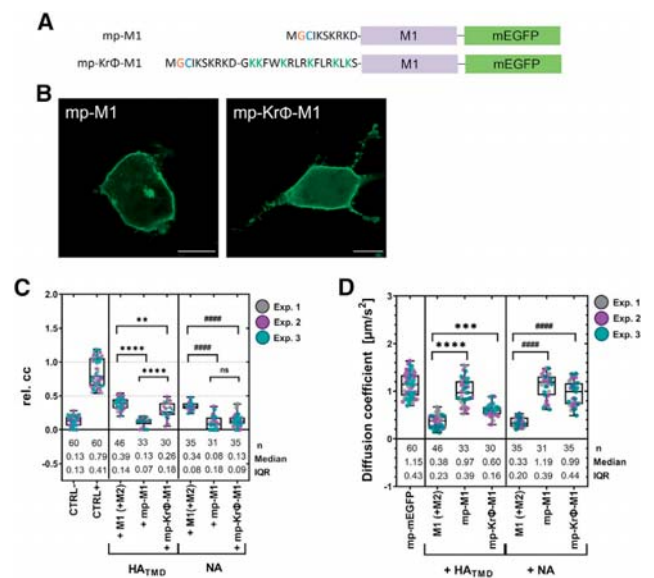
FIGURE 4 HA interacts with a membrane-associated M1 construct. (A) Schematic diagram of M1 constructs with N-terminal PM-targeting sequences. One construct has a myristoylation (orange) and palmitoylation (blue) motif (mp-M1-mEGFP), and the other has an additional poly-lysine motif (green letters, mp-KrΦ-M1-mEGFP). (B) Representative M1 subcellular localization images in transfected HEK293T cells expressing mp-M1-mEGFP (left side), or mp-KrΦ-M1-mEGFP (right side). Scale bars represent 10 μm. (C) Box plot with single data points from three independent experiments shows the cross-correlation for the controls negative control mp-mEGFP (1x)/mp-mCherry2 (1x) and positive control mp-mCherry2-mEGFP), and between M1-mEGFP (or mp-M1-mEGFP, or mp-KrΦ-M1-mEGFP) and mCherry2-HA$_{TMD}$, or NA-mCherry2. Median values and whiskers ranging from minimum to maximum values are displayed. Sample size, median, and IQR are indicated in the graph. Statistical significance was determined using one-way ANOVA multiple comparison test; **p < 0.01, ****p < 0.0001 compared with M1-mEGFP/mCherry2-HA$_{TMD}$; ####p < 0.0001 compared with M1-mEGFP/NA-mCherry2; ns, not significant. (D) Box plot with single data points from three independent experiments shows the diffusion coefficient of the monomer control (mp-mEGFP), and M1-mEGFP, mp-M1-mEGFP, and mp-KrΦ-M1-mEGFP co-expressed with mCherry2-HA$_{TMD}$, or NA-mCherry2. Median values and whiskers ranging from minimum to maximum values are displayed. Sample size, median, and IQR are indicated in the graph. Statistical significance was determined using one-way ANOVA multiple comparison test; ***p < 0.001, ****p < 0.0001 compared with M1-mEGFP/mCherry2-HA$_{TMD}$; ####p < 0.0001 compared with M1-mEGFP/NA-mCherry2.

two constructs and mCherry2-HA$_{TMD}$, as well as NA-mCherry2 (Fig. 4 C), in co-transfected cells. The obtained rel. cc values (indicated in Fig. 4 C) for mp-M1-mEGFP with mCherry2-HA$_{TMD}$ or NA-mCherry2, as well as mp-KrΦ-M1-mEGFP with NA-mCherry2, were similar to those of the negative rel. cc control. These results indicate that NA-mCherry2 does not significantly interact with any of the modified membrane-associated M1 constructs. Also, mCherry2-HA$_{TMD}$ does not seem to interact with the supposedly lipid raft-associated mp-M1-mEGFP. In contrast, a reproducible interaction between mp-KrΦ-M1-mEGFP and mCherry2-HA$_{TMD}$ (rel. cc(mp-KrΦ-M1,HA$_{TMD}$) = 0.26 ± 0.18, n = 30 cells, median ± IQR) was observed.

Notably, the rel. cc value observed in this case was significantly lower than the one obtained in the context of the interaction between (wild-type) M1-mEGFP and mCherry2-HA$_{TMD}$, in the presence of M2. Next, we calculated the surface concentration of each protein and plotted the cross-correlation values against the surface concentration, as well as the ratio of the concentration between the protein pairs (Fig. S11). This analysis was performed to exclude that the obtained rel. cc values are influenced by the surface concentration of the proteins or the expression ratio between the proteins. No concentration dependency of the rel. cc for all pairs was observed.

Finally, we quantified the diffusion dynamics of the examined protein constructs (Fig. 4 *D*). The obtained diffusion coefficient values (shown in Fig. 4 *D*) for mp-M1-mEGFP in the presence of mCherry2-HA$_{TMD}$ or NA-mCherry2 were similar to those of the monomer control (mp-mEGFP). A similar observation was made for mp-KrΦ-M1-mEGFP in the presence of NA-mCherry2. The fact that these M1 constructs diffuse as fast as a lipid-anchored protein (rather than a membrane-spanning protein; see Fig. 3 *I*) suggests the absence of significant interactions/co-diffusion of M1 with mCherry2-HA$_{TMD}$ or NA-mCherry2. For comparison, the diffusion coefficients of M1-mEGFP in the presence of M2 and one glycoprotein are also reported in Fig. 4 *D* (D = 0.38 ± 0.23 μm/s^2, median ± IQR, n = 46, when co-expressed, e.g., with mCherry2-HA$_{TMD}$). This result is comparable with the diffusion coefficient of mCherry2-M2 (D = 0.30 ± 0.15 μm/s^2, median ± IQR, n = 46; Fig. 3 *I*). Interestingly, the diffusion coefficient for mp-KrΦ-M1-mEGFP (D = 0.60 ± 0.16 μm/s^2, median ± IQR, n = 32) co-expressed with mCherry2-HA$_{TMD}$ was slightly lower than that measured for the monomer control, although still higher than the one measured for M1-mEGFP in the presence of unlabeled M2. It is also worth noting that the distribution of diffusion coefficient values for the above-mentioned sample appears to slightly deviate from a normal distribution (Kolmogorov-Smirnov test *p* = 0.0356). The reason for this deviation is not clear at this point but one possible cause might be the occasional presence of cytosolic signal (see, e.g., Fig. 4 *B*) weakly interfering with measurements at the PM.

In conclusion, NA-mCherry2 does not exhibit significant cross-correlation or co-diffusion with neither of the "artificially" PM-associated M1 proteins. In contrast, mCherry2-HA$_{TMD}$ appears to interact with M1 depending on the specific way in which the latter is anchored to the PM.

A potential M2-binding site is located in the N domain (aa 1–67) of M1

An interaction site for M2 has not yet been identified within M1. Therefore, we created different M1 constructs for the expression of specific protein subdomains, in order to locate

a potential M2-binding site (Fig. 5 *A*). The truncated M1 constructs encoded (1) the N- and M domains (NM1, amino acids [aa] 1–164), (2) the N-terminal domain including the linker region (NM1, aa 1–86), (3) only the N domain (NM1, aa 1–67), or (4) the M1 C domain (CM1, aa 165–252). A mEGFP was fused to the C-terminal site of each M1 variant. Moreover, a well-conserved amino acid sequence in the cytoplasmic C-terminal tail of M2 at positions 71 and 73 was previously shown as an interaction site for M1 (10). Hence, we generated a substitution mutant of M2 (M2$_{mut}$) in which the triplet sequence (71-SMR-73) was replaced by alanine (Fig. 5 *A*).

To verify whether the truncated M1-mEGFP constructs are altered in their subcellular localization, we observed
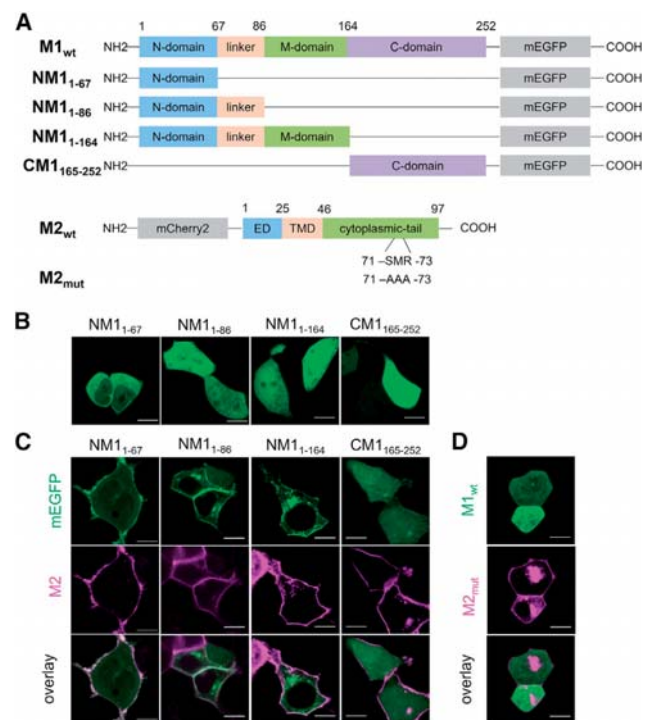
FIGURE 5 M2-binding site on M1 is located in the N-terminal domain. (*A*) Schematic diagram of different M1 and M2 expression constructs. On top, M1 constructs showing the wild type and the truncated M1 variants with their domains: N-terminal domain (N domain, aa 1–67, *blue*), linker region (*orange*, aa 68–86), middle domain (M domain, aa 87–164, *green*), and C-terminal domain (C domain, aa 165–252, *purple*). An mEGFP was fused to the C terminus of each protein construct. On the bottom, M2 constructs showing the wild type and the M2 mutant (71-SMR-73 was replaced by three alanine) with their domains: ectodomain (ED, aa 1–25, *blue*), transmembrane domain (TMD, aa 26–46, *orange*), cytoplasmic tail (cyto-tail, aa 47–97, *green*). Each construct had an mCherry2 fused to the N-terminal site of M2. (*B*) Representative confocal fluorescence images of HEK293T cells expressing truncated M1-mEGFP variants: NM1$_{1-67}$, NM1$_{1-86}$, NM1$_{1-164}$, and CM1$_{165-252}$. (*C*) Representative confocal fluorescence images of HEK293T cells expressing truncated M1-mEGFP variants: NM1$_{1-67}$, NM1$_{1-86}$, NM1$_{1-164}$, and CM1$_{165-252}$ (*green*) in the presence of wild-type mCherry2-M2 (*magenta*). (*D*) Representative confocal fluorescence images of HEK293T cells expressing wild-type M1-mEGFP (*green*) with mCherry2-M2 mutant (M2$_{mut}$, *magenta*). Scale bars represent 10 μm.

them in HEK293T in the absence of mCherry2-M2. All truncated M1-mEGFP variants showed a similar subcellular localization to the wild-type M1-mEGFP (Figs. 1 *A* and 5 *B*). Next, all truncated M1-mEGFP constructs were co-expressed with mCherry2-M2 in HEK293T cells. All N-terminal M1 variants were recruited to the PM, whereas the C-terminal M1 construct still showed a homogeneous distribution in the cytoplasm (Fig. 5 *C*). The percentages of cells with M1 at the PM for the NM1 variants were similar to those observed for the M1 wild type in co-expression with mCherry2-M2 (Fig. S4 *C*). These results indicated that the M2-binding site might be pinpointed to the N-terminal domain of M1 and, specifically, to the aa 1–67. Furthermore, no recruitment of M1 wild type was observed upon a co-expression with the mCherry2-M2mut (Fig. 5 *D*). Based on this result, we could confirm that the recruitment of M1 to PM occurred via a specific interaction of M1 with the amino acid sequence (71-SMR-73) on M2.

DISCUSSION

The role of M1 in IAV assembly is of fundamental importance, as it is now understood that this protein connects together the viral envelope, its membrane proteins (HA, NA, and M2), and the genome (61). It has been suggested that interactions of M1 with the viral glycoproteins (e.g., HA) drive M1 localization to the PM of infected cells (10,11,22–24), but other studies reported conflicting data regarding the interaction of M1 with HA and NA (30,31,35,36). Such findings are mostly based on biochemistry approaches providing indirect interaction data (7,62).

Therefore, in order to quantify protein-protein interactions directly at the PM of living cells, we performed fluorescence fluctuation spectroscopy experiments under physiological conditions. Such experimental approaches (i.e., sF(C)CS and (cc)N&B) provide information regarding the oligomeric state, surface concentration, hetero-interactions, and dynamics in complex biological systems (51,52,63–66).

To this aim, we selected HEK293T cells as a cellular model because they are often used for reverse genetic virus production (39,40,67) and were shown to be appropriate for IAV protein expression (17,41,42). Additionally, we produced and tested several fluorescent IAV protein constructs. Of note, the fluorescent NA construct designed in this study allowed for the first time the investigation of the interaction between this IAV glycoprotein and other viral proteins directly in living cells. It is worth noting that incorporating fluorescent fusion tags might have an impact in general on the localization, function, and conformation of the protein of interest (68,69). For example, our control experiments showed that the cellular distribution of M1 with an mEGFP fused to its C terminus was similar to that of unlabeled M1 (46,47), whereas an N-terminally fused mEGFP M1 variant seemed to have transport failures, which are probably

caused by steric hindrance between fluorophore and signal peptide (47). On the other hand, the fluorescent constructs used to investigate the viral envelope proteins (HA, NA, and M2) were all localized at the PM, similar to the corresponding non-fluorescent proteins (48,49), and yielded the expected oligomerization state (41,42,53,54). For example, our results are compatible with the presence of NA tetramers and mixtures of M2 dimers and tetramers (Fig. 3 *C*), in agreement with previous data (55,70). Furthermore, we also demonstrated that the protein-protein interactions investigated here (e.g., between M1-mEGFP and mCherry2-M2) are specific and analogous to those observed in other contexts (10), as shown by mutagenesis experiments (Fig. 5 *D*) and using unlabeled interaction partners (Fig. S1).

In order to identify the minimum requirement for M1 association to the PM, we observed cells expressing different combinations of viral proteins. First, we confirmed that M1 does not bind to the PM in the absence of other viral proteins, despite the strong lipid-protein interactions previously observed in model membrane systems (17–20). Surprisingly, we did not observe any recruitment of M1 to the PM in the presence of HA or NA (Fig. 1). It is worth noting that several studies proposed that M1 interacts with the cytoplasmic tails of HA or NA (23,30,71–74), but our direct observations in living cells strongly suggest that the two IAV glycoproteins are not able to recruit M1 to the PM by themselves. It is unlikely that the lack of interaction might be a simple consequence of the presence of fluorescent labels, since HA and NA are labeled at the extracellular side. Also, the same M1-mEGFP strongly associates with the PM in the presence of M2. This result is in agreement with previous studies indicating that M1-M2 interactions affect M1 localization and drive virus assembly (10,11,27,75,76). For the first time, we could provide direct experimental evidence that the M2-binding region is located within the first 67 aa of M1 (Fig. 5). Also, thanks to the application of quantitative fluorescence microscopy methods, we could additionally prove that M1 and M2 do not simply colocalize at the PM but rather form complexes. This conclusion is supported by the similar diffusion dynamics observed for M1 and M2 (i.e., diffusion coefficients typical of transmembrane proteins rather than membrane-associated proteins; Fig. 3 *H*) and by the significant degree of cross-correlation between the signals of the two proteins (Fig. 3 *G*). Due to the lack of strong intracellular colocalization (Figs. 1 *C* and 5 *C*), we hypothesize that M1 diffuses freely in the cytoplasm and M1-M2 interaction occurs directly at the PM. M1-M2 complexes appear to consist, on average, of one or two M1 and two to four M2 molecules (Fig. 3). Assuming that each M2 monomer has a binding site for M1, the observed 1:2 stoichiometry suggests that the M1 binding might be limited, for example, by steric constraints or competition with other binding partners of M2 (e.g., LC3 (42)). Furthermore, in the simple approximation of M1

dimers, M2 tetramers, and 2:4 M1-M2 complexes being associated with the PM, our cross-correlation measurements indicate that ca. 80% of M1 is indeed complexed to M2. The remaining amount of PM-associated M1 might interact with, e.g., acidic lipids at the PM (19,20), but, of note, we never observed any significant degree of M1 localization at the PM in the absence of M2. This finding puts forward the hypothesis that M2-M1 complex formation might facilitate the interaction of M1 with other membrane components. This mechanism might also explain previous findings indicating the presence of HA and M1 in the same membrane fractions (22,23) or within the same region in the PM (15). Accordingly, we have observed that, in the presence of M2 (i.e., M1 being efficiently recruited to the PM), there is a significant (although modest) interaction between M1 and the glycoproteins HA or NA (Fig. 3 G). On one hand, it is possible that, e.g., M1-HA interactions are not direct but, rather, mediated by M2 (15). Alternatively, it is possible that, while M2 is needed for the initial recruitment of M1 to the PM, M1-M2 interactions are not long lived and can be partially replaced, for example, by M1-HA interactions. In this case, M2 might induce interactions between M1 and other membrane components by, e.g., increasing M1 local concentration in specific PM regions or stabilizing a certain geometric configuration of M1. However, based on control experiments monitoring M1-HA/NA interactions as a function of local protein concentration (Fig. S11), a prominent role of concentration seems unlikely. To evaluate whether M2 is strictly needed for HA-M1 interactions, we performed sFCCS experiments in which M1 was artificially anchored to the PM (Fig. 4). In this case, depending on the specific lipid anchor, we were also able to observe M1-HA interactions in the absence of M2, thus indicating that (1) the latter protein is not always required as a bridge between M1 and IAV glycoproteins, and (2) the lipid environment plays a role in the establishment of interactions among IAV proteins. Of interest, it was shown that HA is associated with specific lipids, such as phosphatidylinositol 4,5-bisphosphate (PI(4,5)P2) (14,49) and this observation might provide a molecular mechanism explaining our observation of non-negligible M1-HA interactions, in the event that M1 was artificially anchored to the membrane via lipidation and, additionally, a polybasic motif. The degree of association between HA and mp-KrΦ-M1-mEGFP appeared to be between that observed for wild-type M1 and that observed for mp-M1-mEGFP, as supported by the observation of intermediate cross-correlation values (Fig. 4 C) and diffusion dynamics (Fig. 4 D).

The observation that one single IAV membrane protein (i.e., M2) is sufficient for the recruitment of M1 to the PM prompted us to investigate whether M1-M2 interaction is also sufficient for the initiation of the large-scale M1 multimerization associated with IAV assembly (17). Our experiments clearly demonstrate that this is not the case, since

M1 remains, on average, mostly dimeric when bound to the PM in the presence of M2 (Fig. 2 C). On the other hand, in the presence of all the other viral proteins, M1 formed larger multimers (up to 5–10 monomers). This effect does not seem to be a direct consequence of the presence of HA or NA alone (Fig. 3 B) and is even stronger in infected cells. It is worth noting that the formation of very large multimers of M1-mEGFP in infected cells might be partially due to (1) higher M1 concentrations at the PM or (2) the presence of unlabeled M1 molecules that more efficiently support protein-protein interactions. It was in fact reported that fluorescent viral proteins might not be able to oligomerize on a very large scale (65). Alternatively, other viral proteins or altered lipid metabolism (and, consequently, modification of PM composition) in infected cells might play a role, and these possibilities are currently under investigation.

In conclusion, our study sheds light on the very first steps in IAV assembly. According to our results, the main role of M2 in this context is to recruit M1 to specific regions of the PM. This is in agreement with previously proposed models according to which M2 chaperones M1 to the PM (77) and, specifically, to interface regions between raft and non-raft domains (14,16) or domains enriched in negatively charged lipids (17). In further steps, M1 can then interact with lipids and other viral proteins, and such interactions might be involved in the formation of larger protein complexes, eventually leading to IAV capsid assembly.

SUPPORTING MATERIAL

Supporting material can be found online at https://doi.org/10.1016/j.bpj.2021.11.023.

AUTHOR CONTRIBUTIONS

Research Planning, A.P. and S.C; Investigation, A.P.; Data Analysis, A.P.; Writing – Original Draft Preparation, A.P. and S.C.; Writing – Review & Editing, V.D. and S.B.; Software, V.D. and S.C.; Supervision, S.C.; Funding Acquisition, S.C.

ACKNOWLEDGMENTS

SUPPORTING CITATIONS

References (78–86) appear in the supporting material.

REFERENCES

1. Davlin, S., L. Blanton, …, L. Brammer. 2016. Influenza activity - United States, 2015-16 season and composition of the 2016-17 influenza vaccine. *Morb. Mortal. Wkly. Rep.* 65:567–575.

2. Taubenberger, J. K., and D. M. Morens. 2009. Pandemic influenza–including a risk assessment of H5N1. *Rev. Sci. Tech.* 28:187–202.

3. Bouvier, N. M., and P. Palese. 2008. The biology of influenza viruses. *Vaccine.* 26 (*Suppl 4*):D49–D53.

4. Taubenberger, J. K., and J. C. Kash. 2010. Influenza virus evolution, host adaptation, and pandemic formation. *Cell Host Microbe.* 7:440–451.

5. Mostafa, A., E. M. Abdelwhab, …, S. Pleschka. 2018. Zoonotic potential of influenza A viruses: a comprehensive overview. *Viruses.* 10:497.

6. Samji, T. 2009. Influenza A: understanding the viral life cycle. *Yale J. Biol. Med.* 82:153–159.

7. Veit, M., and B. Thaa. 2011. Association of influenza virus proteins with membrane rafts. *Adv. Virol.* 2011:370606.

8. Dou, D., R. Revol, …, R. Daniels. 2018. Influenza A virus cell entry, replication, virion assembly and movement. *Front. Immunol.* 9:1581.

9. Manzoor, R., M. Igarashi, and A. Takada. 2017. Influenza A virus M2 protein: roles from ingress to egress. *Int. J. Mol. Sci.* 18:2649.

10. Chen, B. J., G. P. Leser, …, R. A. Lamb. 2008. The influenza virus M2 protein cytoplasmic tail interacts with the M1 protein and influences virus assembly at the site of virus budding. *J. Virol.* 82:10059–10070.

11. McCown, M. F., and A. Pekosz. 2006. Distinct domains of the influenza a virus M2 protein cytoplasmic tail mediate binding to the M1 protein and facilitate infectious virus production. *J. Virol.* 80:8178–8189.

12. Rossman, J. S., X. Jing, …, R. A. Lamb. 2010. Influenza virus M2 ion channel protein is necessary for filamentous virion formation. *J. Virol.* 84:5078–5088.

13. Rossman, J. S., X. Jing, …, R. A. Lamb. 2010. Influenza virus M2 protein mediates ESCRT-independent membrane scission. *Cell.* 142:902–913.

14. Veit, M., S. Engel, …, A. Herrmann. 2013. Lipid domain association of influenza virus proteins detected by dynamic fluorescence microscopy techniques. *Cell Microbiol.* 15:179–189.

15. Leser, G. P., and R. A. Lamb. 2017. Lateral organization of influenza virus proteins in the budozone region of the plasma membrane. *J. Virol.* 91:e02104–16.

16. Rossman, J. S., and R. A. Lamb. 2011. Influenza virus assembly and budding. *Virology.* 411:229–236.

17. Bobone, S., M. Hilsch, …, S. Chiantia. 2017. Phosphatidylserine lateral organization influences the interaction of influenza virus matrix protein 1 with lipid membranes. *J. Virol.* 91:e00267–00217.

18. Dahmani, I., K. Ludwig, and S. Chiantia. 2019. Influenza A matrix protein M1 induces lipid membrane deformation via protein multimerization. *Biosci. Rep.* 39:BSR20191024.

19. Hilsch, M., B. Goldenbogen, …, S. Chiantia. 2014. Influenza A matrix protein M1 multimerizes upon binding to lipid membranes. *Biophys. J.* 107:912–923.

20. Höfer, C. T., S. Di Lella, …, S. Chiantia. 2019. Structural determinants of the interaction between influenza A virus matrix protein M1 and lipid membranes. *Biochim. Biophys. Acta Biomembr.* 1861:1123–1134.

21. Noton, S. L., E. Medcalf, …, P. Digard. 2007. Identification of the domains of the influenza A virus M1 matrix protein required for NP binding, oligomerization and incorporation into virions. *J. Gen. Virol.* 88:2280–2290.

22. Barman, S., A. Ali, …, D. P. Nayak. 2001. Transport of viral proteins to the apical membranes and interaction of matrix protein with glycoproteins in the assembly of influenza viruses. *Virus Res.* 77:61–69.

23. Jin, H., G. P. Leser, …, R. A. Lamb. 1997. Influenza virus hemagglutinin and neuraminidase cytoplasmic tails control particle shape. *EMBO J.* 16:1236–1247.

24. Zhang, J., A. Pekosz, and R. A. Lamb. 2000. Influenza virus assembly and lipid raft microdomains: a role for the cytoplasmic tails of the spike glycoproteins. *J. Virol.* 74:4634–4644.

25. Darapaneni, V. 2015. Large-scale analysis of influenza A virus sequences reveals universally conserved residues of matrix proteins. *Am. J. Curr. Microbiol.* 3:1–13.

26. Nayak, D. P., R. A. Balogun, …, S. Barman. 2009. Influenza virus morphogenesis and budding. *Virus Res.* 143:147–161.

27. Wang, D., A. Harmon, …, F. Li. 2010. The lack of an inherent membrane targeting signal is responsible for the failure of the matrix (M1) protein of influenza A virus to bud into virus-like particles. *J. Virol.* 84:4673.

28. Ruigrok, R. W., A. Barge, …, G. R. Whittaker. 2000. Membrane interaction of influenza virus M1 protein. *Virology.* 267:289–298.

29. Baudin, F., I. Petit, …, R. W. Ruigrok. 2001. In vitro dissection of the membrane and RNP binding activities of influenza virus M1 protein. *Virology.* 281:102–108.

30. Ali, A., R. T. Avalos, …, D. P. Nayak. 2000. Influenza virus assembly: effect of influenza virus glycoproteins on the membrane association of M1 protein. *J. Virol.* 74:8709–8719.

31. Enami, M., and K. Enami. 1996. Influenza virus hemagglutinin and neuraminidase glycoproteins stimulate the membrane association of the matrix protein. *J. Virol.* 70:6653–6657.

32. Su, W.-C., W.-Y. Yu, …, M. M. C. Lai. 2018. Ubiquitination of the cytoplasmic domain of influenza A virus M2 protein is crucial for production of infectious virus particles. *J. Virol.* 92:e01972–01917.

33. García-Sastre, A., and P. Palese. 1995. The cytoplasmic tail of the neuraminidase protein of influenza A virus does not play an important role in the packaging of this protein into viral envelopes. *Virus Res.* 37:37–47.

34. Jin, H., G. P. Leser, and R. A. Lamb. 1994. The influenza virus hemagglutinin cytoplasmic tail is not essential for virus assembly or infectivity. *EMBO J.* 13:5504–5515.

35. Kretzschmar, E., M. Bui, and J. K. Rose. 1996. Membrane association of influenza virus matrix protein does not require specific hydrophobic domains or the viral glycoproteins. *Virology.* 220:37–45.

36. Zhang, J., and R. A. Lamb. 1996. Characterization of the membrane association of the influenza virus matrix protein in living cells. *Virology.* 225:255–266.

37. Chen, B. J., G. P. Leser, …, R. A. Lamb. 2007. Influenza virus hemagglutinin and neuraminidase, but not the matrix protein, are required for assembly and budding of plasmid-derived virus-like particles. *J. Virol.* 81:7111–7123.

38. Dunsing, V., and S. Chiantia. 2018. A fluorescence fluctuation spectroscopy assay of protein-protein interactions at cell-cell contacts. *J. Vis. Exp.* https://doi.org/10.3791/58582.

39. Wagner, R., G. Gabriel, …, H.-D. Klenk. 2013. Protease activation mutants elicit protective immunity against highly pathogenic avian influenza viruses of subtype H7 in chickens and mice. *Emerg. Microbes Infect.* 2:e7.

40. Wagner, R., A. Herwig, …, H. D. Klenk. 2005. Acylation-mediated membrane anchoring of avian influenza virus hemagglutinin is essential for fusion pore formation and virus infectivity. *J. Virol.* 79:6449.

41. Dunsing, V., M. Luckner, …, S. Chiantia. 2018. Optimal fluorescent protein tags for quantifying protein oligomerization in living cells. *Sci. Rep.* 8:10634.

42. Dunsing, V., A. Petrich, and S. Chiantia. 2020. Multi-color fluorescence fluctuation spectroscopy in living cells via spectral detection. *eLife.* 10:e69687. https://doi.org/10.7554/eLife.69687.

43. Wickham, H. 2016. ggplot2 - Elegant Graphics for Data Analysis. Springer International Publishing.

44. Kassambara, A. 2020. ggpubr: 'ggplot2' based publication ready plots. R package version 0.4.0. https://CRAN.R-project.org/package=ggpubr.

45. Wilke, C. O. 2020. Cowplot: streamlined plot theme and plot annotations for 'ggplot2'. R package version 1.1.0. https://CRAN.R-project.org/package=cowplot.

46. Das, S. C., S. Watanabe, …, Y. Kawaoka. 2012. The highly conserved arginine residues at positions 76 through 78 of influenza A virus matrix protein M1 play an important role in viral replication by affecting the intracellular localization of M1. *J. Virol.* 86:1522–1530.

47. Thaa, B., A. Herrmann, and M. Veit. 2009. The polybasic region is not essential for membrane binding of the matrix protein M1 of influenza virus. *Virology.* 383:150–155.

48. Chlanda, P., O. Schraidt, …, J. A. Briggs. 2015. Structural analysis of the roles of influenza A virus membrane-associated proteins in assembly and morphology. *J. Virol.* 89:8957–8966.

49. Curthoys, N. M., M. J. Mlodzianoski, …, S. T. Hess. 2019. Influenza hemagglutinin modulates phosphatidylinositol 4,5-bisphosphate membrane clustering. *Biophys. J.* 116:893–909.

50. Digman, M. A., R. Dalal, …, E. Gratton. 2008. Mapping the number of molecules and brightness in the laser scanning microscope. *Biophys. J.* 94:2320–2332.

51. Petazzi, R. A., A. K. Aji, and S. Chiantia. 2020. Chapter one - fluorescence microscopy methods for the study of protein oligomerization. *In* Progress in Molecular Biology and Translational Science. J. Giraldo and F. Ciruela, eds. Academic Press, pp. 1–41.

52. Dunsing, V., M. Mayer, …, S. Chiantia. 2017. Direct evidence of amyloid precursor-like protein 1 trans interactions in cell-cell adhesion platforms investigated via fluorescence fluctuation spectroscopy. *Mol. Biol. Cell.* 28:3609–3620.

53. Scolari, S., S. Engel, …, A. Herrmann. 2009. Lateral distribution of the transmembrane domain of influenza virus hemagglutinin revealed by time-resolved fluorescence imaging. *J. Biol. Chem.* 284:15708–15716.

54. Varghese, J. N., W. G. Laver, and P. M. Colman. 1983. Structure of the influenza virus glycoprotein antigen neuraminidase at 2.9 Å resolution. *Nature.* 303:35–40.

55. Georgieva, E. R., P. P. Borbat, …, J. H. Freed. 2015. Mechanism of influenza A M2 transmembrane domain assembly in lipid membranes. *Sci. Rep.* 5:11757.

56. Orekhova, A. S., P. S. Sverdlova, …, P. M. Rubtsov. 2011. [Novel bidirectional promoter from human genome]. *Mol. Biol. (Mosk).* 45:486–495.

57. Sengupta, P., A. Y. Seo, …, J. Lippincott-Schwartz. 2019. A lipid-based partitioning mechanism for selective incorporation of proteins into membranes of HIV particles. *Nat. Cell Biol.* 21:452–461.

58. Gao, X., and J. Zhang. 2008. Spatiotemporal analysis of differential Akt regulation in plasma membrane microdomains. *Mol. Biol. Cell.* 19:4366–4373.

59. Zacharias, D. A., J. D. Violin, …, R. Y. Tsien. 2002. Partitioning of lipid-modified monomeric GFPs into membrane microdomains of live cells. *Science.* 296:913.

60. Yeung, T., M. Terebiznik, …, S. Grinstein. 2006. Receptor activation alters inner surface potential during phagocytosis. *Science.* 313:347.

61. Nayak, D. P., E. K. Hui, and S. Barman. 2004. Assembly and budding of influenza virus. *Virus Res.* 106:147–165.

62. Zhao, H., and P. Lappalainen. 2012. A simple guide to biochemical approaches for analyzing protein-lipid interactions. *Mol. Biol. Cell.* 23:2823–2830.

63. Dawes, M. L., C. Soeller, and S. Scholpp. 2020. Studying molecular interactions in the intact organism: fluorescence correlation spectroscopy in the living zebrafish embryo. *Histochem. Cell Biol.* 154:507–519.

64. Langowski, J. 2008. Protein-protein interactions determined by fluorescence correlation spectroscopy. *Methods Cell Biol.* 85:471–484.

65. Petazzi, R. A., A. A. Koikkarah, …, S. Chiantia. 2020. Detection of envelope glycoprotein assembly from old-world hantaviruses in the Golgi apparatus of living cells. *J. Virol.* 95:e01238-20.

66. Tzoneva, R., T. Stoyanova, …, S. Chiantia. 2020. Effect of erufosine on membrane lipid order in breast cancer cell models. *Biomolecules.* 10:802.

67. Hoffmann, E., G. Neumann, …, R. G. Webster. 2000. A DNA transfection system for generation of influenza A virus from eight plasmids. *Proc. Natl. Acad. Sci. U S A.* 97:6108–6113.

68. Rana, M. S., X. Wang, and A. Banerjee. 2018. An improved strategy for fluorescent tagging of membrane proteins for overexpression and purification in mammalian cells. *Biochemistry.* 57:6741–6751.

69. Snapp, E. 2005. Design and use of fluorescent fusion proteins in cell biology. *Curr. Protoc. Cell Biol.* 21:21.4.1–21.4.13.

70. Cristian, L., J. D. Lear, and W. F. DeGrado. 2003. Use of thiol-disulfide equilibria to measure the energetics of assembly of transmembrane helices in phospholipid bilayers. *Proc. Natl. Acad. Sci. U S A.* 100:14772–14777.

71. Barman, S., L. Adhikary, …, D. P. Nayak. 2004. Role of transmembrane domain and cytoplasmic tail amino acid sequences of influenza a virus neuraminidase in raft association and virus budding. *J. Virol.* 78:5258–5269.

72. Zhang, J., G. P. Leser, …, R. A. Lamb. 2000. The cytoplasmic tails of the influenza virus spike glycoproteins are required for normal genome packaging. *Virology.* 269:325–334.

73. Melkonian, K. A., A. G. Ostermeyer, …, D. A. Brown. 1999. Role of lipid modifications in targeting proteins to detergent-resistant membrane rafts. Many raft proteins are acylated, while few are prenylated. *J. Biol. Chem.* 274:3910–3917.

74. Tatulian, S. A., and L. K. Tamm. 2000. Secondary structure, orientation, oligomerization, and lipid interactions of the transmembrane domain of influenza hemagglutinin. *Biochemistry.* 39:496–507.

75. Iwatsuki-Horimoto, K., T. Horimoto, …, Y. Kawaoka. 2006. The cytoplasmic tail of the influenza A virus M2 protein plays a role in viral assembly. *J. Virol.* 80:5233–5240.

76. McCown, M. F., and A. Pekosz. 2005. The influenza A virus M2 cytoplasmic tail is required for infectious virus production and efficient genome packaging. *J. Virol.* 79:3595–3605.

77. Zebedee, S. L., and R. A. Lamb. 1989. Growth restriction of influenza A virus by M2 protein antibody is genetically linked to the M1 protein. *Proc. Natl. Acad. Sci. U S A.* 86:1061–1065.

78. Baer, A., and K. Kehn-Hall. 2014. Viral concentration determination through plaque assays: using traditional and novel overlay systems. *J. Vis. Exp.* https://doi.org/10.3791/52065.

79. Petrášek, Z., and P. Schwille. 2008. Precise measurement of diffusion coefficients using scanning fluorescence correlation spectroscopy. *Biophys. J.* 94:1437–1448.

80. Bacia, K., S. A. Kim, and P. Schwille. 2006. Fluorescence cross-correlation spectroscopy in living cells. *Nat. Methods.* 3:83–89.

81. Schneider, F., D. Waithe, …, E. Sezgin. 2017. Diffusion of lipids and GPI-anchored proteins in actin-free plasma membrane vesicles measured by STED-FCS. *Mol. Biol. Cell.* 28:1507–1518.

82. Ries, J., and P. Schwille. 2006. Studying slow membrane dynamics with continuous wave scanning fluorescence correlation spectroscopy. *Biophys. J.* 91:1915–1924.

83. Ries, J., S. Chiantia, and P. Schwille. 2009. Accurate determination of membrane dynamics with line-scan FCS. *Biophys. J.* 96:1999–2008.

84. Linkert, M., C. T. Rueden, …, J. R. Swedlow. 2010. Metadata matters: access to image data in the real world. *J. Cell Biol.* 189:777–782.

85. Trullo, A., V. Corti, …, M. Zamai. 2013. Application limits and data correction in number of molecules and brightness analysis. *Microsc. Res. Tech.* 76:1135–1146.

86. Chen, Y., J. Johnson, …, J. D. Mueller. 2010. Chapter 16 - observing protein interactions and their stoichiometry in living cells by brightness analysis of fluorescence fluctuation experiments. *In* Methods in Enzymology. N. G. Walter, ed. Academic Press, pp. 345–363.

Supplemental information

Influenza A M2 recruits M1 to the plasma membrane: A fluorescence fluctuation microscopy study

Annett Petrich, Valentin Dunsing, Sara Bobone, and Salvatore Chiantia

Supplemental Information

Supplemental Materials and Methods

Plasmids and cloning.

For the cloning of all following constructs, standard PCRs with custom-designed primers were performed, followed by digestion with FastDigest restriction enzymes and ligation with T4-DNA-Ligase according to the manufacturer's instructions. All enzymes and reagents were purchased from Thermo Fisher Scientific (Waltham, MA, USA) and primers were acquired from Sigma Aldrich trademark of Merck KGaA (Darmstadt, Germany). The correctness of each construct was verified by Sanger sequencing (LGC Genomics GmbH, Berlin, Germany).

The original plasmid encoding Influenza A/FPV/Rostock/1934 matrix protein 1 (M1) with EYFP fused to the N-terminus or C-terminus of M1 (EYFP-M1, M1-EYFP) was a kind gift of Michael Veit (Free University, Berlin, Germany) (1). A monomeric variant of EGFP, containing the A206K mutation (2), was inserted into both M1 constructs by digestion of mEGFP-C1 (gift from Michael Davidson, Addgene plasmid #54759) with AgeI and BsrGI. The modification of M1-mEGFP with an N-terminal mp-signal (amino acids MGCIKSKRKDNLNDDEPV, mp-M1-mEGFP) or an N-terminal mp-signal with an additional polybasic sequence (amino acids MGCIKSKRKDGKKFWKRLRKFLRKLKS, mp-KrΦ-M1-mEGFP) were introduced by PCR with primers encoding the additional amino acids. For the construction of mp-M1-mEGFP and mp-KrΦ-M1-mEGFP, the PCR products were subcloned into mEGFP-N1 (gift from Michael Davidson, Addgene plasmid #54767) with XhoI and EcoRI. The truncated M1 sequences encoding the M1 N-terminus (NM1, amino acids 1–67; 1-86; 1-164) or the M1 C-terminus (CM1, amino acids 165–252) were amplified from the plasmid M1-mEGFP, and subcloned into mEGFP-N1 by using the restriction endonucleases XhoI and EcoRI, yielding plasmids NM1(1-67)-mEGFP, NM1(1-86)-mEGFP, NM1(1-164)-mEGFP, and CM1(165-252)-mEGFP.

An untagged FPV M2 construct was cloned by amplifying M2 sequence from FPV-M2-EYFP (a kind gift from Michael Veit), and cloned into pcDNA3.1+ (Thermo Fisher Scientific, Waltham, MA, USA , #V79020) via restriction with HindIII and EcoRI. The plasmid for bi-directional expression was a gift from Katja Arndt (University of Potsdam, Potsdam, Germany) and

contains the two promoters TTC31 and CCDC142, allowing for simultaneous expression of the encoded genes (3). For the calibration of the relative expression level, mp-EGFP and mp-mCherry2 were amplified and cloned into the two expression cassettes flanked by restriction sites BamHI/EcoRI and SacI/KpnI respectively, to obtain mp-mEGFP $\leftrightarrow$ mp-mCherry2. A construct with mp-mCherry2 and mp-mEGFP cloned into BamHI/EcoRI and SacI/KpnI restriction sites, respectively, was also produced (mp-mCherry2 $\leftrightarrow$ mp-mEGFP). Unlabeled M2 sequence was amplified and separately cloned into the BamHI/EcoRI cassette to produce M2 $\leftrightarrow$ mp-mCherry2. Site-directed mutagenesis in order to replace the amino acids of the M1-binding site in M2 (amino acids 71–73, SMR) by alanine residues was performed by two-step overlap-extension PCR of the plasmid mCherry2-M2, yielding the plasmid mCherry2-M2$_{mut}$. The plasmid mCardinal-M2 was cloned based on the previously described mCherry2-M2 (4) by using mCardinal-C1 (gift from Michael Davidson, Addgene plasmid #54590).

The FPV HA constructs HA$_{wt}$-mCherry2 and mCherry2-HA$_{TMD}$ were cloned based on the previously described HA$_{wt}$-mEGFP (5) and mEGFP-HA$_{TMD}$ (5) plasmids. HA$_{wt}$-mEGFP contains the full-length HA protein fused to mEGFP at the (intracellular) C-terminus, whereas in mEGFP -HA$_{TMD}$ a large part of the extracellular domain of HA is replaced by mEGFP. To clone mCherry2-HA$_{TMD}$ and HA$_{wt}$-mCherry2, the mEGFP-HA$_{TMD}$, HA$_{wt}$-mEGFP, and mCherry2-C1 plasmids (5) were digested with AgeI and BsrGI to replace mEGFP with mCherry2. The plasmids PA-mTurqouise, NP-mCherry2 and mEYFP-HA$_{TMD}$ were a kind gift from Andreas Herrmann (Humboldt University Berlin, Germany) (6).

The FPV NA construct was cloned by amplifying NA sequence from pHH21-NA (7), and cloned into pcDNA3.1+ (Thermo Fisher Scientific, Waltham, MA, USA , #V79020) via restriction with NheI and AflII. To clone NA-mCherry2, mCherry2 was amplified from mCherry2-C1, and the obtained insert was ligated into NA-pcDNA3.1+ by digestion with NotI and XbaI. The construct contains full-length NA fused to mCherry2 at the extracellular side. The plasmid mApple-NA was derived from PMT-mApple (a kind gift from Thorsten Wohland, National University of Singapore, Singapore).

Virus propagation and titration.

For virus propagation, confluent MDCK II cells were infected with the avian influenza FPV virus mutant 1 (kind gift from Michael Veit, Free University Berlin (8)) at multiplicity of infection (MOI) 0.01 in DMEM with 0.2 % (w/v) Bovine Serum Albumin (BSA; Sigma Aldrich, Taufkirchen, Germany), 2 mM L-glutamine, 100 U/mL penicillin, and 100 µg/mL streptomycin and incubated at 37 °C. After one hour, virus inoculum was removed and the cells were washed twice with Dulbecco's phosphate-buffered saline with Mg^{2+}/Ca^{2+} (DPBS+/+; PAN-Biotech, Aidenbach, Germany). Fresh infection medium with 0.1 µg/mL TPCK-treated trypsin (Sigma Aldrich, Taufkirchen, Germany) was added to the cells and incubated for 2-3 days at 37 °C. Upon visual observation of a cytopathic effect, the supernatant was harvested and cellular debris was removed by centrifugation (3000 × g for 30 min at 4 °C). Virus aliquots were stored at -80 °C.

To measure the plaque-forming units (PFU) of the suspension, MDCK II cells were grown in six-well plates until full confluency was reached. The cells were infected with serial 10-fold dilutions of the virus containing supernatant and incubated for one hour at 37°C. Virus inoculum was then removed and replaced by SeaPlaque agarose overlay medium (1x Minimum Essential Medium (PAN-Biotech, Aidenbach, Germany), 0.9 % (w/v) SeaPlaque Agarose (Biozym Scientific GmbH, Hessisch Oldendorf, Germany), 0.2 % (w/v) BSA, 2 mM L-glutamine, 100 U/mL penicillin, and 100 µg/mL streptomycin). After three days of incubation at 37 °C and 5 % CO_2, agarose overlay medium was removed, cells were fixated with 10 % (w/v) formaldehyde (Sigma Aldrich, Taufkirchen, Germany) for one hour and PFU was determined by crystal violet staining (0.05 % (w/v) crystal violet (Sigma Aldrich, Taufkirchen, Germany), 1 % (w/v) formaldehyde, 1 % (v/v) methanol in 1 x PBS) (9).

Transfection and virus infection.

Cells were seeded in 35-mm dishes (CellVis, Mountain View, CA, USA) with an optical glass bottom (#1.5 glass, 0.16–0.19 mm) at a density of 6 × 10^5 cells per dish. After 24 h, cells were transfected with Turbofect® according to the manufacturer's instructions (Thermo Fisher Scientific, Waltham, MA, USA) by using 200 ng pDNA per dish for the controls or 600 - 1200 ng pDNA per dish for IAV proteins. Briefly, plasmids were incubated for 20 min with 3 µL Turbofect diluted in 50 µL serum-free medium, and then added dropwise to the cells.

When needed, cells were co-transfected with the reverse genetic plasmid set of FPV excluding segment 7 (encoding M). Instead, M1-mEGFP and M2-untagged were used. This co-transfection procedure is referred to in what follows as "all".

In some cases, cells were infected with a MOI 5 with IAV FPV mutant 1 in infection medium at 5 h post-transfection, first on ice for 15 min and then at 37°C for 45 min. Samples were then rinsed with DPBS+/+ and typically observed 12 to 16 h after infection.

Confocal microscopy system and setup calibration for fluorescence fluctuation spectroscopy.

All fluorescence fluctuation spectroscopy measurements were performed on a Zeiss LSM780 system (Carl Zeiss, Oberkochen, Germany) using a Plan-Apochromat 40×/1.2 Korr DIC M27 water immersion objective and a 32-channel GaAsP detector array. Samples were excited with a 488 nm Argon laser (AlexaFluor®488, [AF488], mEGFP) and a 561 nm diode laser (Alexa Fluor® 568, [AF568], mCherry2). For measurements with 488 nm excitation, fluorescence was detected between 499 and 552 nm; for 561 nm excitation, between 570 and 695 nm, after passing through a 488/561 nm dichroic mirror (for two color measurements) or 488 nm dichroic mirror (for one color measurements). All measurements with more than one fluorescent species were recorded sequentially to minimize signal cross-talk. To decrease out-of-focus light, a pinhole with size corresponding to one airy unit (~39 µm) was used. All measurements were performed at room temperature (22 ± 1 °C).

At the beginning of each measurement day, the focal volume was calibrated by performing a series of point FCS measurements with AF488 (Thermo Fischer, Waltham, MA, USA) dissolved in water at 30 nM, at the same laser power, with the same dichroic mirror and pinhole size. Beforehand, the signal was optimized by adjusting the collar ring of the objective and the pinhole position to the maximal count rate for AF488. Then, ten measurements at different locations were taken, each consisting of 15 repetitions of 10 s, and the data were fitted using a three-dimensional diffusion model including a triplet contribution. The structure parameter S (defined as the ratio between the vertical and lateral dimension of the theoretical confocal ellipsoid) was typically around 5 to 9, and the diffusion time τ_d around 35 to 40 µs. The waist ω_0 was calculated from the measured average diffusion time ($\tau_{d,AF488}$) and previously determined diffusion coefficient D of the

used dye at room temperature (D_{AF488}= 435 $\mu m^2 s^{-1}$) (10), according to the following equation:

$$\omega_0 = \sqrt{4\tau_{d,AF488}D_{AF488}} \qquad (1)$$

Typical values were 200–250 nm. All measurements were performed at room temperature.

Scanning fluorescence (cross-) correlation spectroscopy.

sFCS and sFCCS were used to probe slow diffusive dynamics in lipid membranes as previously described (5, 11-15) with few modifications. Briefly, a line scan of 256 × 1 pixels (pixel size 80 nm) was performed perpendicular to the membrane with 945.45 μs scan time. Typically, 250,000 lines were acquired (total scan time 3 min) in photon counting mode alternating two different excitation wavelengths. Laser powers were adjusted to keep photobleaching below 20 %. Typical values were ~4.7 μW (488 nm) and ~10 μW (561 nm). Scanning data were exported as TIFF files, imported and analyzed in MATLAB (The MathWorks, Natick, MA, USA) using custom-written code. The analysis started with an alignment of all lines as kymographs and then a division into blocks of 1000 lines. In each block, lines were summed up column-wise and the position along the line with maximum fluorescence was determined. This position defines the membrane localization in each block and is used to align all lines to a common origin. Then, all aligned line scans were averaged over time and fitted with a Gaussian function summed to a sigmoidal function (modelling intra-cellular background signal). The pixels corresponding to the membrane were defined as pixels within ± 2.5σ of the peak. To clearly identify the signal originating from the PM, we restricted our analysis to cells in which the surface concentration of the analyzed FP was > 100 monomers/μm^2. In each line, these pixels were integrated, providing the membrane fluorescence time series *F(t)*. In order to correct for depletion due to photobleaching, the fluorescence time series was fitted with a two-component exponential function and a correction was applied (16). Then, auto-correlation functions (ACFs; g= green channel, r =red channel), and cross-correlation function (CCF) were calculated as follows, using a multiple tau algorithm:

$$G_i(\tau) = \frac{<\delta F_i(t)\delta F_i(t+\tau)>}{<F_i(t)>^2}, \qquad (2)$$

$$G_{cross}(\tau) = \frac{<\delta F_g(t)\delta F_r(t+\tau)>}{<F_g(t)> <F_r(t)>}, \tag{3}$$

where $\delta F_i = F_i(t) - <F_i(t)>$ and $i = g, r$.

To avoid artefacts caused by long-term instabilities or single bright events, CFs were calculated segment-wise (20 segments) and then averaged. Segments showing clear distortions (typically less than 25% of all segments) were manually removed (12). Furthermore, a model for two-dimensional diffusion in the membrane and a Gaussian confocal volume geometry was fitted to the ACFs and CCF (15):

$$G(\tau) = \frac{1}{N}\left(1 + \frac{\tau}{\tau_d}\right)^{-1/2}\left(1 + \frac{1}{S^2\tau_d}\right)^{-1/2}. \tag{4}$$

Here, the particle number N and diffusion time τ_d were obtained from the fit. Moreover, diffusion coefficients were calculated using the calibrated waist ω_0 of the focal volume, $D = \omega_0^2/4\tau_d$. The apparent molecular brightness ε was calculated by dividing the mean count rate detected for each species i, $< F_i(t) >$, by the particle number N_i determined from the fit:

$$\varepsilon_i = \frac{<F_i(t)>}{N_i}. \tag{5}$$

Relative cross-correlation values were calculated from the amplitudes of ACFs and CCFs:

$$rel.\,cc = max\left\{\frac{G_{cross}(0)}{G_g(0)}, \frac{G_{cross}(0)}{G_r(0)}\right\}, \tag{6}$$

where $G_{cross}(0)$ is the amplitude of the CCF and $G_i(0)$ is the amplitude of the ACF in the i-th channel (g = green, r = red) (12).

To analyze concentration-dependent oligomerization, the surface concentration was calculated according to the following equations:

$$N_{monomer,protein} = \frac{<I_{protein}>}{<\varepsilon_{monomer,i}>}, \tag{7}$$

$$surface\ concentration = \frac{N_{monomer,protein}}{p_{f,i}\pi\omega_0^2 S}, \tag{8}$$

where $< I_{protein} >$ is the average fluorescence intensity of the protein of interest within a single cell measurement, $\varepsilon_{monomer,i}$ is the average molecular brightness of the monomer

control for the corresponding fluorescence species i, and $p_{f,i}$ is the probability factor described below in "Brightness calibration and fluorophore maturation". For all SF(C)CS experiments, p_f values in Eq. 8 have been set to 0.7 and 0.6 for mEGFP and mCherry2 respectively, as previously determined (5). By using the effective detection area ($A_{eff} = \pi\omega_0^2 S$), the surface concentration for a protein of interest in expressed in monomeric units per µm^2.

(Cross-Correlation) Number and Brightness.

(cc)N&B experiments were performed as previously described (5, 12, 13, 18, 19) with few modifications. Briefly, an image stack was acquired over time at a fixed position in the sample, typically consisting of 100 frames. Images of 128 x 512 pixels were acquired by using a pixel size of 70 nm, and 6.3 µs dwell time and alternating two different excitation wavelengths. Laser powers were maintained low enough to keep bleaching below 20 % of the initial fluorescence signal (typically ~3 µW for 488 nm, and ~5 µW for 561 nm). CZI image output files were imported into MATLAB using the Bioformats package (20), and analyzed using a self-written MATLAB script implementing the equations from Digman et al. (21) for the specific case of photon-counting detectors, thus obtaining the molecular brightness and number as a function of pixel position. Before further analysis, pixels corresponding to regions of interest (ROI) were selected manually in an image map. To clearly identify the signal originating from the PM, we restricted our analysis to cells in which the surface concentration of the analyzed FP was > 100 monomers/µm². Next, to correct for lateral drift during the acquisition, frames were aligned to the first frame by maximizing the spatial correlation between sub-selections in consecutive frames, averaged over both channels, as a function of arbitrary translations (22). Finally, brightness-intensity maps were obtained (see e.g. Figure 2 B). These maps show the pixel brightness with a color code in units of counts/dwell time/molecule. The average fluorescence count rate (counts/dwell time) is represented as pixel intensity.

Corrections for bleaching, minor cell movements and specific detector response were performed as described in (12, 19). The calculation of the multimerization state from apparent brightness values is described below in the paragraph "Brightness calibration and fluorophore maturation".

Finally, for two color measurements, the cross variance $\sigma_{cc}^2 = <(I_g - <I_g>)(I_r - <I_r>)>$ was calculated for each pixel (18). In order to obtain a ccN&B analogue of Eq. 6, we defined:

$$N_{cc} = \frac{\sigma_{cc}^2}{\varepsilon_g \varepsilon_r}, \tag{9}$$

where ε_i is the channel brightness ($i = g, r$) calculated as usual as $\frac{\sigma_i^2}{<I_i>} - 1$.

The relative cross-correlation values were calculated in analogy to Eq. 6 from the particle numbers for each channel N_i ($i = g, r$; $N_i = \frac{<I_i>}{\varepsilon_i}$), and the apparent number of complexes N_{cc}:

$$rel.cc. = max\left\{ \frac{N_{cc}}{N_g}, \frac{N_{cc}}{N_r} \right\}. \tag{10}$$

To analyze concentration-dependent oligomerization, the surface concentration was calculated according Eqs. 7 and 8, using p_f values determined daily.

Brightness calibration and fluorophore maturation

The molecular brightness, i.e. the photon count rate per molecule, is used as a measure for the oligomeric state of protein complexes. This quantity is often based on the assumption that all fluorophores within an oligomer are fluorescent. However, fluorescent proteins (FPs) can undergo dark state transitions or be in a non-mature, non-fluorescent state (23). To quantify the amount of non-fluorescent FPs, we consider all these processes together in a single parameter, the apparent fluorescence probability (p_f), i.e. the probability of a FP to emit a fluorescence signal. We used the median of the normalized FP homo-dimer brightness ε_{dimer} to determine the probability p_f for each FP species i:

$$p_{f,i} = \frac{<\varepsilon_{i,dimer}>}{<\varepsilon_{i,monomer}>} - 1. \tag{11}$$

(11)

An estimate of the oligomeric state is determined by normalizing the molecular brightness ε_i by the average molecular brightness $\varepsilon_{i,mono}$ of the corresponding monomeric reference and, subsequently, using the previously determined values of $p_{f,i}$ for species i (5):

$$\text{Oligomerization} = \frac{1}{p_{f,i}}\left(\frac{\varepsilon_i}{<\varepsilon_{i,monomer}>} - 1\right) + 1. \tag{12}$$

We applied this transformation to every brightness data point of both (cc)N&B and sF(C)CS measurements, obtaining then the true oligomeric size of the complexes. The p_f was determined daily.

Calibration of bi-directional plasmids

We examined bi-directional plasmids with either i) mp-mEGFP upstream and mp-mCherry2 downstream of the bi-directional promoter region (mp-mEGFP $\leftrightarrow$ mp-mCherry2) or ii) mp-mCherry2 upstream and mp-mEGFP downstream of the bi-directional promoter region (mp-mCherry2 $\leftrightarrow$ mp-mEGFP). sFCS measurements were independently performed at the membrane of transfected HEK293T cells (Figure S1 A) to calculate the concentrations of each FP, for each bidirectional plasmid. The box plot (Figure S1 B) with the single data points for each experiment shows the relative expression ratio, defined as the ratio between the measured amounts of FPs (downstream and upstream of the promoter region). Each FP amount is quantified as the number of molecules detected in the confocal volume, provided by sFCCS. The average of the measured relative expression ratios (4.16) was then used to estimate the concentration of M2 for the experiments in which the M2 $\leftrightarrow$ mCherry2 construct was used for transfection. For the sake of simplicity, all three proteins are assumed to mature with similar efficiency.

Quantification of the plasmid composition

Cells were co-transfected with six different fluorescent proteins constructs (PA-mTurquoise, M1-mEGFP, mEYFP-HA$_{TMD}$, NA-mApple, NP-mCherry2, and mCardinal-M2). For the acquisition of reference spectra, cells were transfected with only one plasmid. Imaging was performed on a Zeiss LSM780 system (Carl Zeiss, Oberkochen, Germany) using a 40x, 1.2 NA water immersion objective operating in the "lambda mode". Samples were excited with a 405 nm laser (mTurquoise), 488 nm Argon laser (mEGFP, mEYFP) and a 561 nm diode laser (mCardinal, mCherry2, mApple). To split excitation and emission light, 405/505 nm and 488/561 nm dichroic mirrors were used. Fluorescence was detected in spectral channels of 8.9 nm (26 channels between 459 nm and 690 nm) on a 32 channel GaAsP array detector operating in photon counting mode. Afterwards, a reference spectrum from each individual FP was defined by using the "Automatic Component Extraction (ACE)" function of the

''Linear Unmixing'' module of the ZEN software. These reference spectra were then used to separate the fluorophore channels in cells expressing all six plasmids.

Quantification of the PM convexity

Cells were transfected with (i) mp-mEGFP ("control") or M1-mEGFP together with either (ii) mCherry2-M2 ("M1-M2") or (iii) the recombinant virus plasmid set without M1 ("M1-all"). A fourth sample consisted of cells transfected with M1-mEGFP and, 4 h post-transfection, infected with FPV ("M1-FPV"). Cells were imaged after 16 h and analyzed with ImageJ (http://imagej.nih.gov/ij/). First, we generated a binary mask of the cell: the fluorescence images were subjected to Gaussian filtering (radius = 1 pixel) and segmented by applying Otsu threshold (Image → Adjust → Threshold). Next, single outlier pixels were removed (Process → Noise → Remove Outliers), the inner regions of cells were filled (Process → Binary → Fill Holes) and outlines of the final objects were generated (Process → Binary → Outline). The binary outline masks were thus used for the following shape descriptive analysis. We calculated the convexity (also called roughness) of the cells by using the ImageJ plugin "shape-filter" (https://imagej.net/plugins/shape-filter). This parameter measures local irregularities in contour shapes by comparing the perimeter of the cell´s convex hull enclosing the cell to the perimeter of the cell itself:

$$convexity = \frac{perimeter\ of\ convex\ hull}{perimeter}.$$

(13)

A value significantly below one indicates the presence of an irregular boundary.

Supplemental Figures
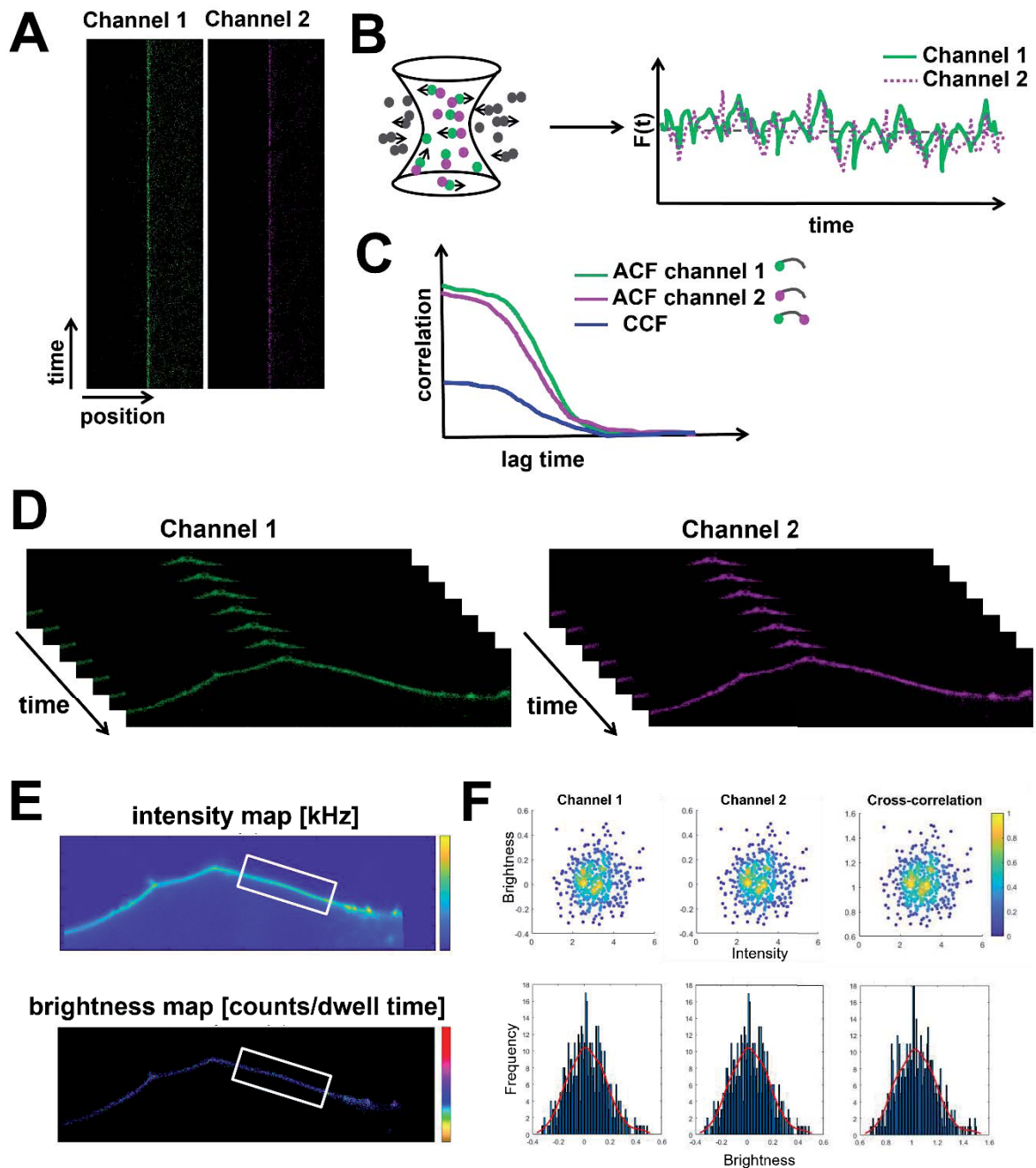
Figure S1: Schematic representation of scanning fluorescence cross-correlation spectroscopy (sFCCS) and cross-correlation Number and Brightness analysis (ccN&B) in cells. A: sFCCS measurements are performed by scanning a line perpendicular to the cell membrane in two spectral channels (channel 1, green and channel 2, magenta). Scan lines (represented here as kymographs) are aligned, and membrane pixels are summed. B: sFCCS provides the average number and transit time of fluorescent molecules diffusing through the confocal observation volume. C: Auto-correlation functions (ACFs) of each fluorophore species are calculated from the time-intensity trace, $F_i(t)$ (B), and are represented here in green and magenta. The interaction between two different types of molecules diffusing through the observation volume is determined by calculating the cross-correlation function (CCF) between the two intensity traces. The CCF is represented in blue. D: ccN&B acquisition results in a three-dimensional (x-y-time) image stack. E: Intensity maps and brightness maps of the image stack are obtained from moment analysis of the image stacks and are used to define a region of interest (ROI, white rectangle) around the cell membrane. F: Channel and cross-correlation brightness ($\varepsilon 1$, $\varepsilon 2$, and Bcc) values are calculated and represented for each pixel. The results are then visualized as scatter plot (brightness as a function of intensity) and as histograms, pooling all selected pixels.
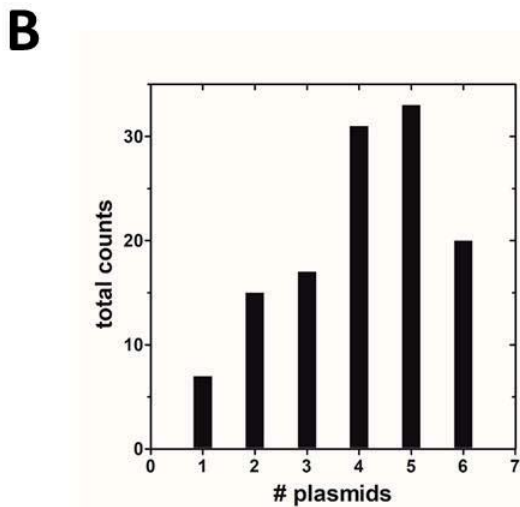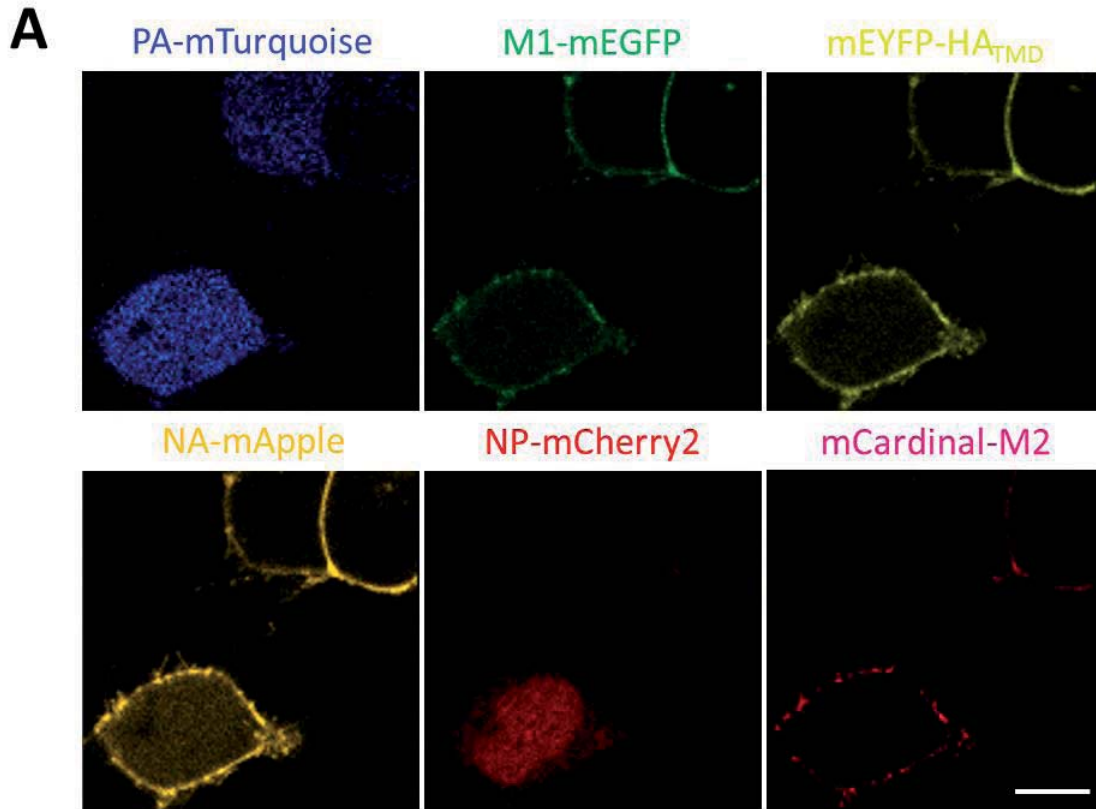
Figure S2: Quantification of the plasmid expression for six different fusion proteins. HEK293T cells were transfected with PA-mTurquoise, M1-mEGFP, mEYFP-HA$_{TMD}$, NA-mApple, NP-mCherry2, and mCardinal-M2. After 16 h, samples were imaged using spectral decomposition with channels of 8.9 nm width (26 channels between 459 nm and 690 nm) on a 32 channel GaAsP array detector operating in photon counting mode. A: Representative confocal fluorescence images of HEK293T cells expressing six fusion proteins. Scale bar: 10 μm. B: Quantification of the plasmid expression of each fusion protein in co-transfected HEK293T cells (n = 123). Transfection of the 6 plasmids was performed as described in Material and Methods and in the SI paragraph **"**Quantification of the plasmid composition**"**. The bar plot shows the frequency of the distinct fluorescent proteins observed per cell. According to our results, the majority of visible (i.e. fluorescent) cells expressed > 4 fluorescent constructs (B). The probability to find a fluorescent cell transfected with only one plasmid was circa 5%. The probability of finding a fluorescent cell expressing only M1-mEGFP in these conditions is circa 5%/6=0.8%.
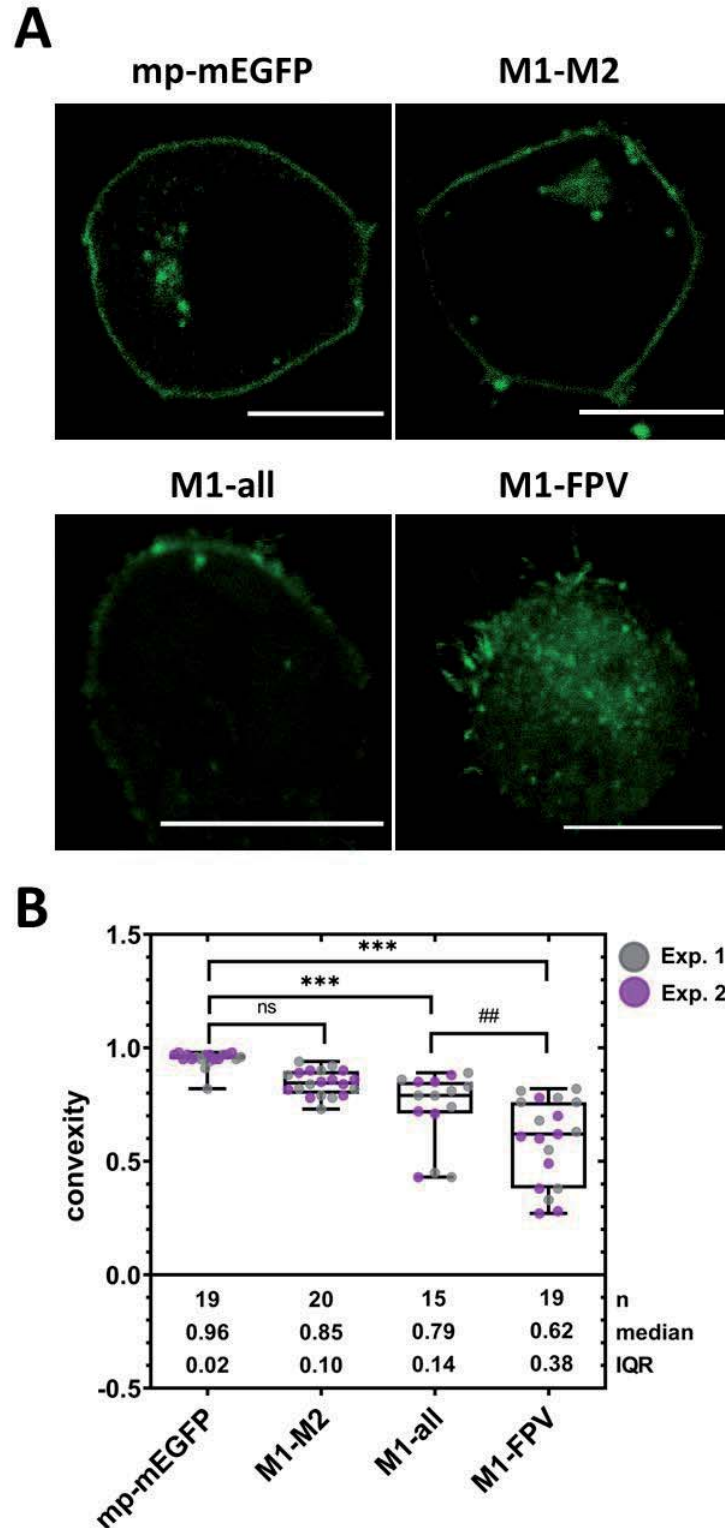
Figure S3: Shape descriptive analysis of transfected/infected HEK293T cells. A: Representative confocal fluorescence images of HEK293T cells expressing (i) mp-mEGFP, (ii) M1-mEGFP and unlabeled M2, (iii) M1-mEGFP and the recombinant virus plasmid set (except for segment M, "all") and unlabeled-M2, (iv) M1-mEGFP infected with FPV. A total of 73 images were used for the shape descriptive analysis as described in the SI paragraph "Quantification of the PM convexity". Scale bar: 10 µm. B: Boxplot with single data points (each representing a cell) from two independent experiments shows the convexity of the cell shapes. Cell convexity was calculated by using the ImageJ plugin "shape-filter". Median values and whiskers ranging from minimum to maximum values are displayed. Sample size, median, and interquartile range (IQR) are indicated in the graph. Statistical significance was determined using one-way ANOVA multiple comparison test (ns indicates not significant, *** indicates $p < 0.001$ compared to mp-mEGFP; ## indicates $p < 0.01$ compared to M1-all). The convexity

(also called roughness) of each cell was calculated to quantify local irregularities in contour shapes. The convexity values of M1-all (0.79 ± 0.14, median ± IQR, n = 15 cells) and M1-FPV cells (0.62 ± 0.38, median ± IQR, n = 19 cells) were significantly lower than that measured for control cells expressing mp-mEGFP (0.96 ± 0.02, median ± IQR, n = 19 cells). Cells from the M1-M2 sample (0.85 ± 0.10, median ± IQR, n = 20 cells) showed no significant difference compared to the control. Moreover, M1-FPV cells displayed a significant lower convexity compared to M1-all cells. The higher variance observed in M1-all and M1-FPV cells could be attributed to different expression levels of the respective plasmids and different infection stages/health conditions of the examined cells.

A

M1-mEGFP αHA-AF568 overlay

M1-mEGFP αNA-AF568 overlay

B

M1-mEGFP

mCherry2-M2

overlay

C

% M1 membrane localization

	$M1_{wt}$	$M1_{wt}$ + HA	$M1_{wt}$ + NA	$M1_{wt}$	$NM1_{1-67}$	$NM1_{1-86}$	$NM1_{1-164}$	$CM1_{165-252}$	$M1_{wt}$ + $M2_{mut}$
n_{images}	10	10	10	14	11	11	12	10	10
n_{cells}	583	412	410	717	469	405	437	472	406
Median	0	0	0	28	25	27	26	0	0
IQR	0	0	0	8	8	8	11	0	0

+ M2
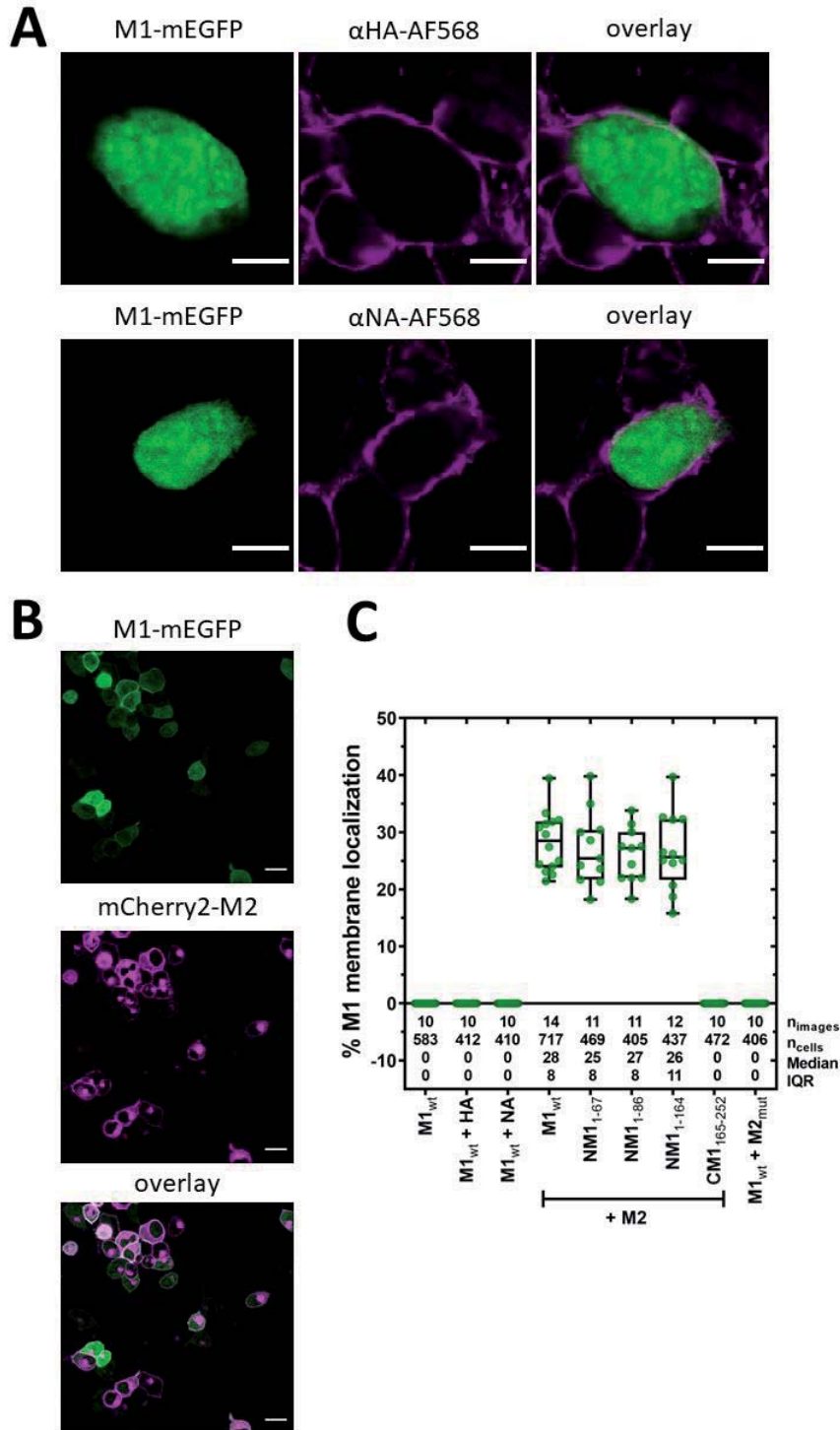
Figure S4: Immunofluorescence visualization and quantification of membrane-bound M1 in co-transfected cells. A: Representative confocal fluorescence images of $M1_{wt}$-mEGFP and HA-untagged (upper panel) as well as $M1_{wt}$-mEGFP and NA-untagged (lower panel) co-transfected HEK293T cells after immunofluorescence staining with α-HA-AF568 (magenta) or α-NA-AF568 (magenta). Scale bars are 10 μm. B: Representative confocal fluorescence overview images of $M1_{wt}$-mEGFP and mCherry2-M2 in co-transfected HEK293T cells. Such images were used for the quantification analysis of the recruitment of M1 to the PM. Scale bars represent 10 μm. C: Box Plot with single data points (corresponding to single cells) shows the percentage of HEK293T cells displaying M1 localization at the PM. Median values and whiskers ranging from minimum to maximum values are displayed. Sample size, median, and interquartile range (IQR) are indicated in the graph. No recruitment of M1 to the PM was observed in the presence of HA, NA or $M2_{mut}$. In the presence of M2, all the truncated M1-constructs encoding the N-terminal domains were significantly recruited to the PM, whereas the M1 construct encoding only the C-terminal domain showed no membrane localization.
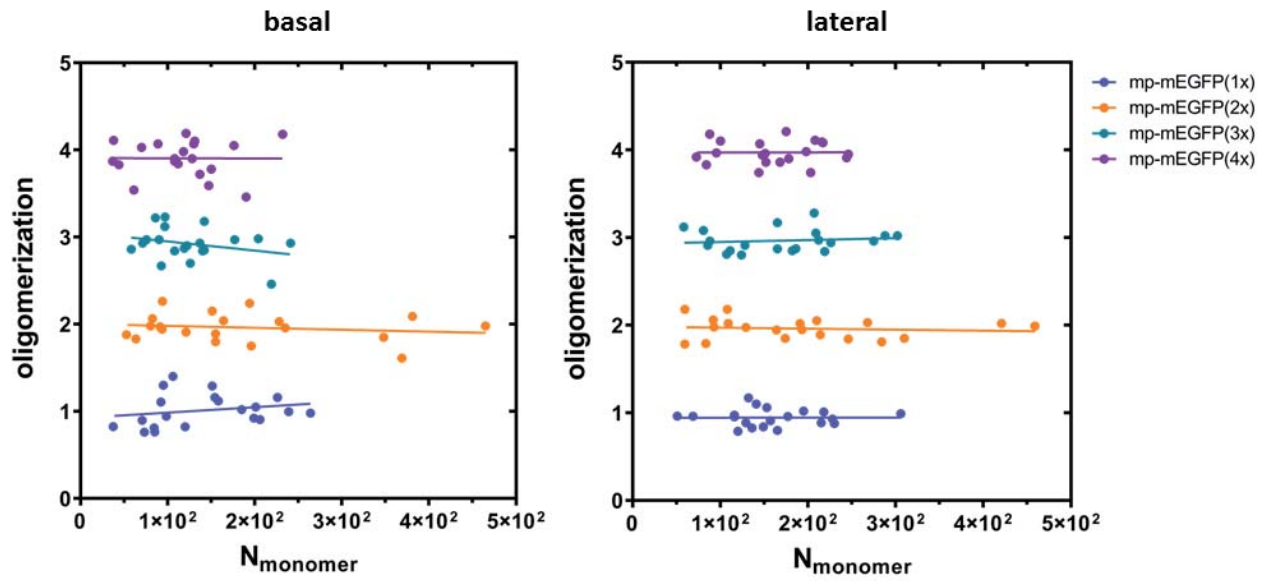
Figure S5: Comparison of the oligomerization state of oligomeric membrane constructs measured at the basal and lateral membrane in HEK293T cells via N&B. Oligomerization as a function of the estimated monomer numbers ($N_{monomer}$) for membrane-localized FP constructs (mp-mEGFP(1x) in blue, mp-mEGFP(2x) in yellow, mp-mEGFP(3x) in cyan, mp-mEGFP(4x) in magenta). Values were obtained from N&B measurements at the basal membrane (left panel) and lateral membrane (right panel). Solid lines represent a linear regression fit as guide to the eye. Data are pooled from two independent experiments. The monomer numbers were calculated as ratio between average fluorescence intensity and average monomer brightness. The data show that N&B measurements provide reliable multimerization data for concentrations up to at least ca. 10^3 monomers / μm^2 in the described experimental conditions (ca. $5*10^2$ monomers in the confocal volume).
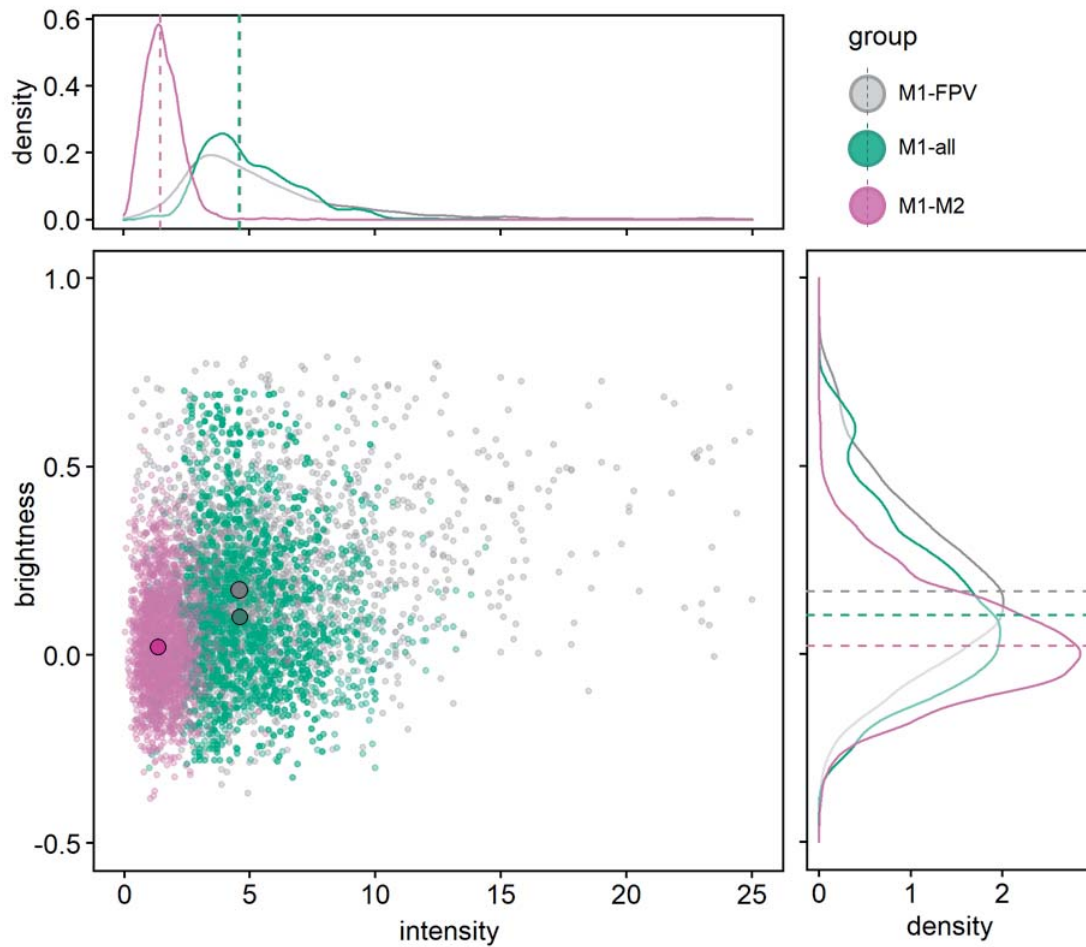
Figure S6: Higher oligomeric states of M1 in infected cells. Representative distribution of brightness (counts/dwell time per molecule) and fluorescence intensity (photon counts/dwell time) values for all the pixels within a ROI in an exemplary HEK293T cell expressing i) M1-mEGFP and M2-untagged (magenta), ii) co-transfected cells expressing M1-mEGFP, unlabeled M2 and the reverse genetic plasmid system for all other FPV proteins ("all", green), or iii) M1-mEGFP in FPV infected cells (grey). The brightness-intensity medians are indicated in the graph (large dots with black border line). The sub-panels show the frequency distribution of measured brightness values (right side, solid line), and the frequency distribution of measured intensity values (top side, solid line). The median values of all curves in both sub-panels are shown by the dashed line. Represented data correspond to M1-mEGFP expression at the PM shown in Figure 2 A and B.
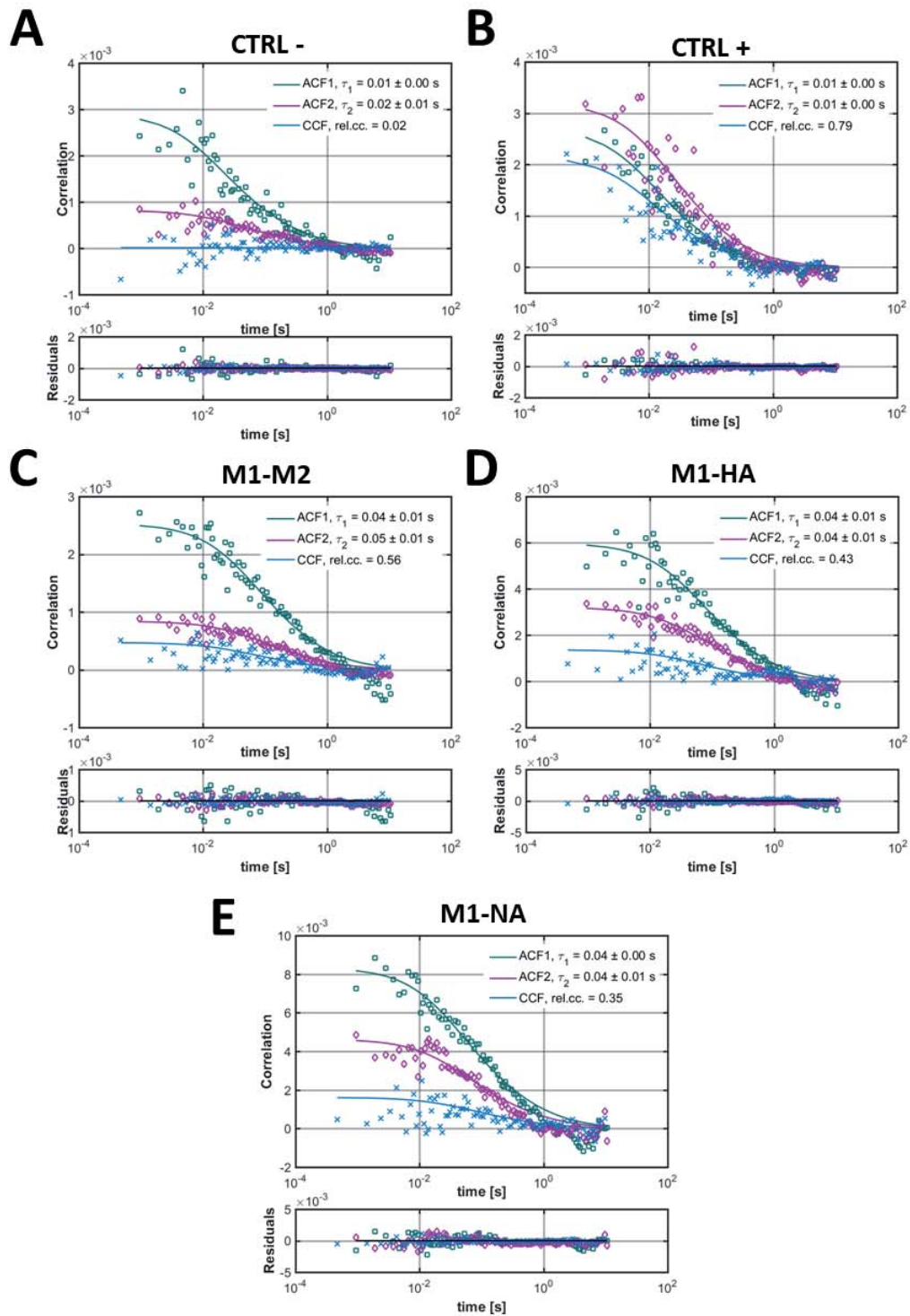
Figure S7: M1 cross-correlates strongly with M2 and weakly with the glycoproteins HA and NA. Representative auto-correlation functions (ACFs, mEGFP: green, mCherry2: magenta) and cross-correlation functions (CCFs, blue) obtained from sFCCS measurements on the PM of living HEK 293T cells co-expressing mp-mEGFP/mp-Cherry2 (A, cross-correlation negative control), mp-mCherry2-mEGFP (B, cross-correlation positive control), M1-mEGFP/mCherry2-M2 (C), M1-mEGFP/mCherry2-HA$_{TMD}$ (D), M1-mEGFP/NA-mCherry2 (E). Solid thick lines show fits of a two-dimensional diffusion model to the CFs.
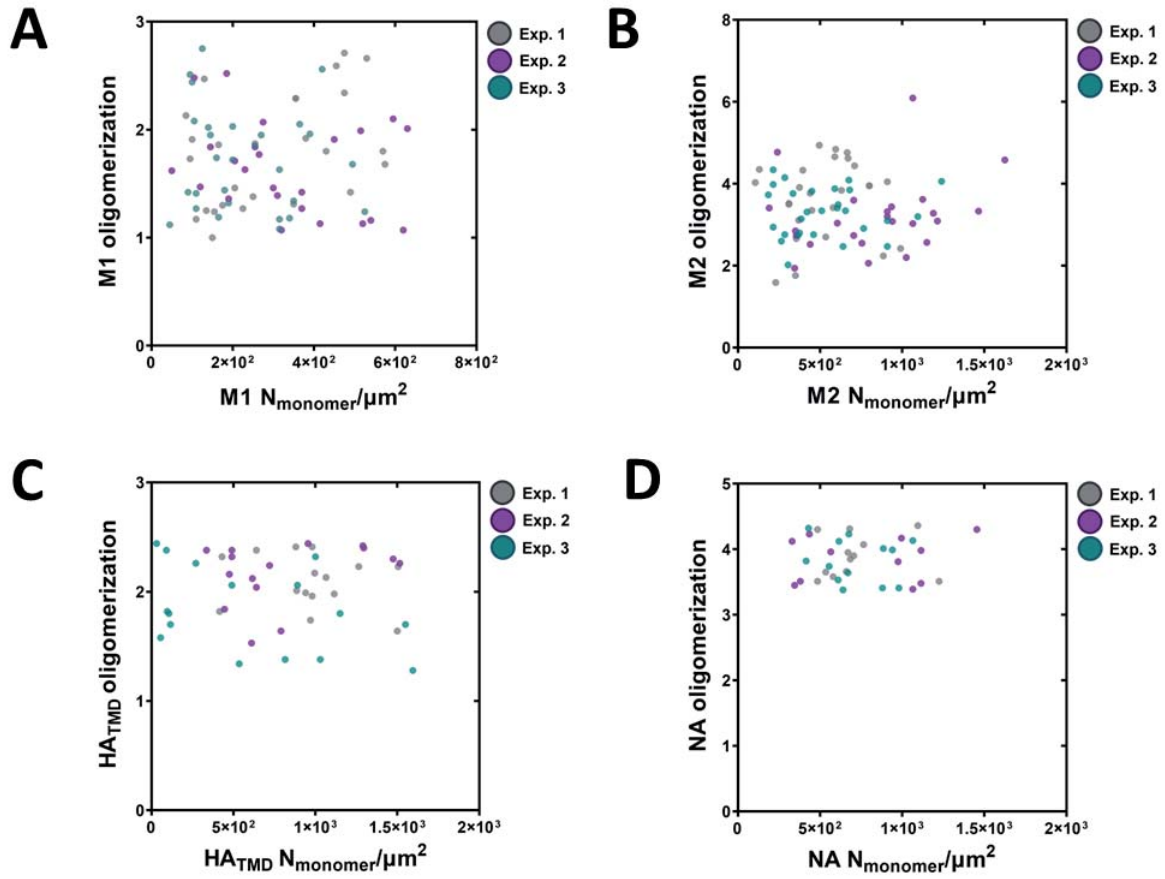
Figure S8: Oligomerization of viral proteins is independent from surface concentration at the PM. Scatter plots show oligomerization as a function of surface concentration for M1-mEGFP (A), mCherry2-M2 (B), mCherry2-HA$_{TMD}$ (C), and NA-mCherry2 (D). Values are obtained from sFCCS measurements. Data are pooled from three independent experiments and refer to the data shown Figure 3 of the main manuscript.
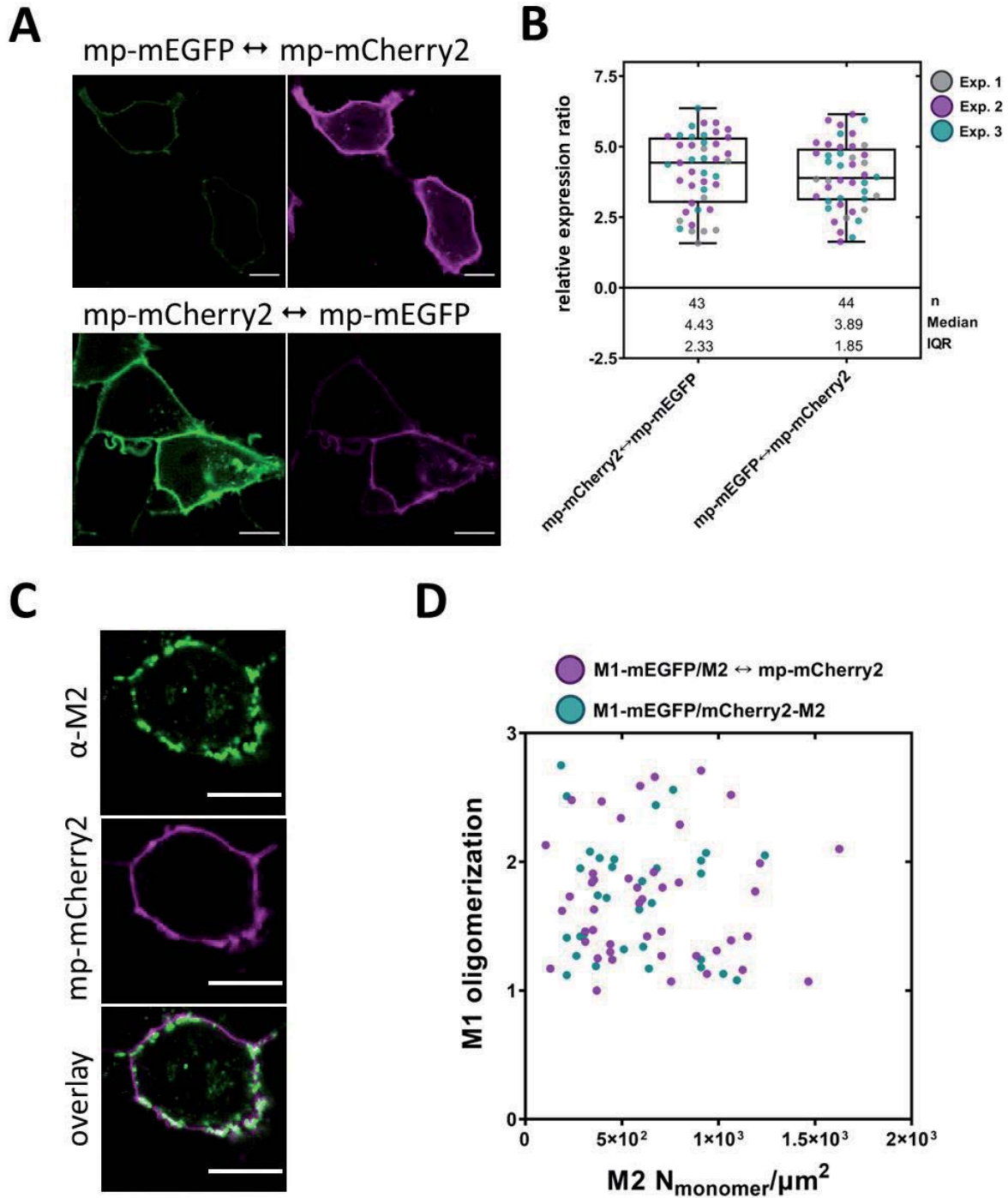
Figure S9: Expression and calibration of bi-directional plasmids. A: Representative confocal fluorescence images of the mp-mEGFP ↔ mp-mCherry2 and mp-mCherry2 ↔ mp-mEGFP constructs (mEGFP in green, mCherry2 in magenta) expressed in HEK293T cells. Scale bars represent 10 µm. B: Box plot with single cell data points from three independent experiments shows the relative expression ratios between the surface concentrations of downstream and upstream fluorescent proteins expressed in HEK293T cells. Concentration values were measured using sFCCS at the PM. Median values and whiskers ranging from minimum to maximum values are displayed. Sample size, median, and IQR are indicated in the graph. C: Representative confocal fluorescence images of the M2↔ mp-mCherry2 construct expressed in HEK293T cells after an immunofluorescence staining with α-M2-AF488 (green). Scale bars represent 10 µm. D: M1-mEGFP oligomerization as a function of the estimated M2 surface concentration for the bi-directional M2 ↔ mp-mCherry2 construct, as well as mCherry2-M2. Values are obtained from sFCCS measurements. Data are pooled from three independent experiments.
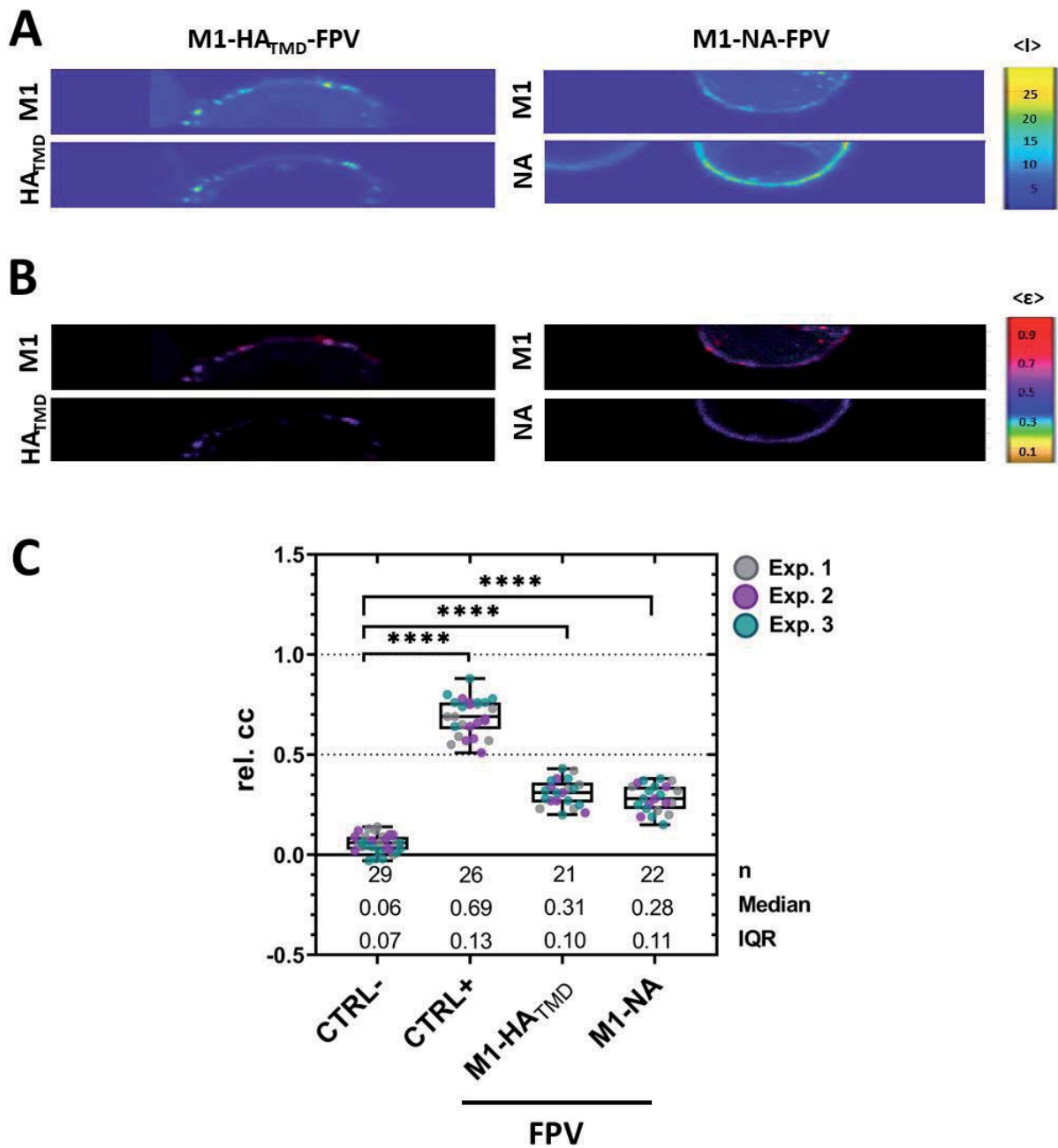
Figure S10: Weak interaction between M1 and HA$_{TMD}$ or NA in infected cells. Cross-correlation Number and Brightness (ccN&B) analysis for M1-mEGFP co-transfected with mCherry2-HA$_{TMD}$ or NA-mCherry2 in FPV infected cells. Average intensity as well as molecular brightness maps and rel. cc values were obtained as described in the Methods section. A: Representative average intensity maps of M1-mEGFP (top) in infected HEK293T cells co-expressing mCherry2-HA$_{TMD}$ (bottom, left) or NA-mCherry2 (bottom, right). The average intensity map is visualized via color scale with the unit counts/dwell time. B: representative brightness-intensity maps of M1-mEGFP (top) and mCherry2-HA$_{TMD}$ (bottom, left) or NA-mCherry2 (bottom, right), corresponding to the panels shown in (A). The image shows pixel brightness as pixel color (counts/dwell time/molecule), and mean photon count rate as pixel intensity. C: Box plot with single data points from three independent experiments shows the rel. cc of the controls (negative control: mp-mEGFP(1x)/mp-Cherry2(1x), and positive control: mp-mCherry2-mEGFP), and M1-mEGFP co-expressed with mCherry2-HA$_{TMD}$, and NA-mCherry2. Median values and whiskers ranging from minimum to maximum values are displayed. Sample size, median, and IQR are indicated in the graph. Statistical significance was determined using one-way ANOVA multiple comparison test (**** indicates $p < 0.0001$ compared to the negative control (CTRL-)).
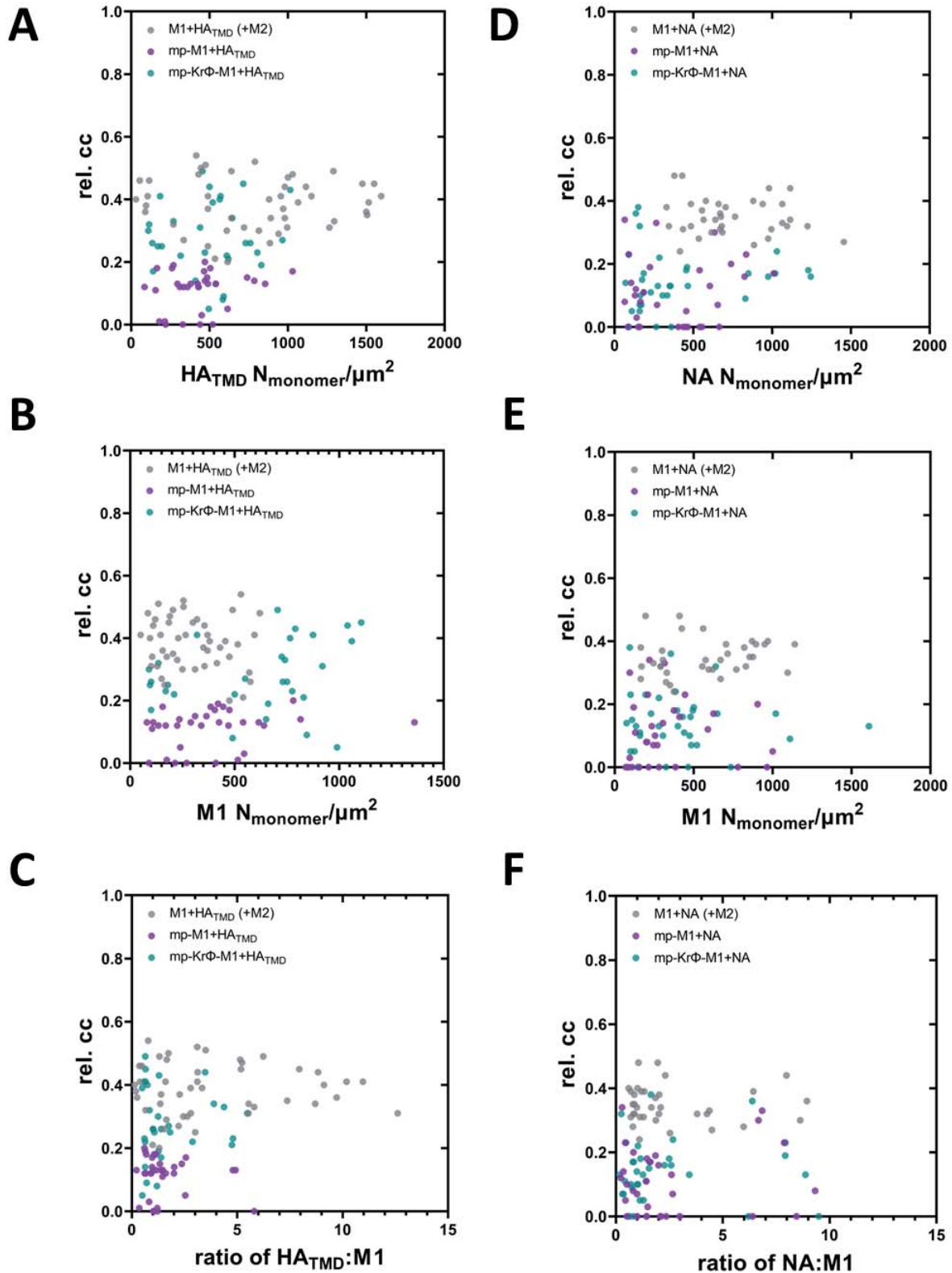
Figure S11: Cross-correlation between M1 and HA (or NA) is independent from surface concentration at the PM. A-C: Scatter plots show the rel. cc between different M1 constructs and mCherry2-HA$_{TMD}$, as a function of the surface concentration of mCherry2-HA$_{TMD}$ (A), each of the M1-mEGFP constructs (B), and the expression ratio of mCherry2-HA$_{TMD}$:M1-mEGFP constructs (C). D-F: Scatter plots show the rel. cc between different M1 constructs and NA-mCherry2, as a function of the surface concentration of NA-mCherry2 (D), each of the M1-mEGFP constructs (E), and the expression ratio of NA-mCherry2:M1-mEGFP constructs (F). Solid lines represent a linear regression fit, shown here as guide to the eye. Values are obtained from sFCCS measurements. Data are pooled from three independent experiments and are related to the data shown in Figure 4.

Supporting References

1. Thaa, B., A. Herrmann, and M. Veit. 2009. The polybasic region is not essential for membrane binding of the matrix protein M1 of influenza virus. Virology 383:150-155.
2. Zacharias, D. A., J. D. Violin, A. C. Newton, and R. Y. Tsien. 2002. Partitioning of Lipid-Modified Monomeric GFPs into Membrane Microdomains of Live Cells. Science 296:913.
3. Orekhova, A. S., P. S. Sverdlova, P. V. Spirin, O. G. Leonova, V. I. Popenko, V. S. Prasolov, and P. M. Rubtsov. 2011. [Novel bidirectional promoter from human genome]. Mol Biol (Mosk) 45:486-495.
4. Dunsing, V., A. Petrich, and S. Chiantia. 2020. Multi-color fluorescence fluctuation spectroscopy in living cells via spectral detection. bioRxiv:2020.2012.2018.423407.
5. Dunsing, V., M. Luckner, B. Zühlke, R. A. Petazzi, A. Herrmann, and S. Chiantia. 2018. Optimal fluorescent protein tags for quantifying protein oligomerization in living cells. Scientific reports 8:10634-10634.
6. Scolari, S., S. Engel, N. Krebs, A. P. Plazzo, R. F. M. De Almeida, M. Prieto, M. Veit, and A. Herrmann. 2009. Lateral distribution of the transmembrane domain of influenza virus hemagglutinin revealed by time-resolved fluorescence imaging. The Journal of biological chemistry 284:15708-15716.
7. Wagner, R., A. Herwig, N. Azzouz, and H. D. Klenk. 2005. Acylation-Mediated Membrane Anchoring of Avian Influenza Virus Hemagglutinin Is Essential for Fusion Pore Formation and Virus Infectivity. Journal of Virology 79:6449.
8. Wagner, R., G. Gabriel, M. Schlesner, N. Alex, A. Herwig, O. Werner, and H.-D. Klenk. 2013. Protease activation mutants elicit protective immunity against highly pathogenic avian influenza viruses of subtype H7 in chickens and mice. Emerg Microbes Infect 2:e7-e7.
9. Baer, A., and K. Kehn-Hall. 2014. Viral concentration determination through plaque assays: using traditional and novel overlay systems. J. Vis. Exp. https://doi.org/10.3791/52065.
10. Petrášek, Z., and P. Schwille. 2008. Precise Measurement of Diffusion Coefficients using Scanning Fluorescence Correlation Spectroscopy. Biophysical Journal 94:1437-1448.
11. Bacia, K., S. A. Kim, and P. Schwille. 2006. Fluorescence cross-correlation spectroscopy in living cells. Nature Methods 3:83-89.
12. Dunsing, V., and S. Chiantia. 2018. A Fluorescence Fluctuation Spectroscopy Assay of Protein-Protein Interactions at Cell-Cell Contacts. J. Vis. Exp. https://doi.org/10.3791/58582.
13. Dunsing, V., M. Mayer, F. Liebsch, G. Multhaup, and S. Chiantia. 2017. Direct evidence of amyloid precursor-like protein 1 trans interactions in cell-cell adhesion platforms investigated via fluorescence fluctuation spectroscopy. Mol Biol Cell 28:3609-3620.
14. Schneider, F., D. Waithe, M. P. Clausen, S. Galiani, T. Koller, G. Ozhan, C. Eggeling, and E. Sezgin. 2017. Diffusion of lipids and GPI-anchored proteins in actin-free plasma membrane vesicles measured by STED-FCS. Molecular biology of the cell 28:1507-1518.
15. Ries, J., and P. Schwille. 2006. Studying Slow Membrane Dynamics with Continuous Wave Scanning Fluorescence Correlation Spectroscopy. Biophysical Journal 91:1915-1924.

16. Ries, J., S. Chiantia, and P. Schwille. 2009. Accurate determination of membrane dynamics with line-scan FCS. Biophysical journal 96:1999-2008.

17. Dunsing, V., M. Luckner, B. Zuhlke, R. A. Petazzi, A. Herrmann, and S. Chiantia. 2018. Optimal fluorescent protein tags for quantifying protein oligomerization in living cells. Sci Rep 8:10634.

18. Digman, M. A., P. W. Wiseman, C. Choi, A. R. Horwitz, and E. Gratton. 2009. Stoichiometry of molecular complexes at adhesions in living cells. Proceedings of the National Academy of Sciences of the United States of America 106:2170-2175.

19. Petazzi, R. A., A. A. Koikkarah, N. D. Tischler, and S. Chiantia. 2020. Detection of Envelope Glycoprotein Assembly from Old-World Hantaviruses in the Golgi Apparatus of Living Cells. J Virol. 95:e01238-20.

20. Linkert, M., C. T. Rueden, C. Allan, J.-M. Burel, W. Moore, A. Patterson, B. Loranger, J. Moore, C. Neves, D. MacDonald, A. Tarkowska, C. Sticco, E. Hill, M. Rossner, K. W. Eliceiri, and J. R. Swedlow. 2010. Metadata matters: access to image data in the real world. Journal of Cell Biology 189:777-782.

21. Digman, M. A., R. Dalal, A. F. Horwitz, and E. Gratton. 2008. Mapping the number of molecules and brightness in the laser scanning microscope. Biophys J 94:2320-2332.

22. Trullo, A., V. Corti, E. Arza, V. R. Caiolfa, and M. Zamai. 2013. Application limits and data correction in number of molecules and brightness analysis. Microscopy Research and Technique 76:1135-1146.

23. Chen, Y., J. Johnson, P. Macdonald, B. Wu, and J. D. Mueller. 2010. Chapter 16 - Observing Protein Interactions and Their Stoichiometry in Living Cells by Brightness Analysis of Fluorescence Fluctuation Experiments. In Methods in Enzymology. N. G. Walter, editor. Academic Press. 345-363.

3.5 Publication V: Multicolor fluorescence fluctuation spectroscopy in living cells via spectral detection

Multicolor fluorescence fluctuation spectroscopy in living cells via spectral detection

Valentin Dunsing*, Annett Petrich, Salvatore Chiantia*

Universität Potsdam, Institute of Biochemistry and Biology, Potsdam, Germany

Abstract Signaling pathways in biological systems rely on specific interactions between multiple biomolecules. Fluorescence fluctuation spectroscopy provides a powerful toolbox to quantify such interactions directly in living cells. Cross-correlation analysis of spectrally separated fluctuations provides information about intermolecular interactions but is usually limited to two fluorophore species. Here, we present scanning fluorescence spectral correlation spectroscopy (SFSCS), a versatile approach that can be implemented on commercial confocal microscopes, allowing the investigation of interactions between multiple protein species at the plasma membrane. We demonstrate that SFSCS enables cross-talk-free cross-correlation, diffusion, and oligomerization analysis of up to four protein species labeled with strongly overlapping fluorophores. As an example, we investigate the interactions of influenza A virus (IAV) matrix protein 2 with two cellular host factors simultaneously. We furthermore apply raster spectral image correlation spectroscopy for the simultaneous analysis of up to four species and determine the stoichiometry of ternary IAV polymerase complexes in the cell nucleus.

*For correspondence:
valentin.dunsing@gmx.de (VD);
chiantia@uni-potsdam.de (SC)

Competing interest: The authors declare that no competing interests exist.

Introduction

Living cells rely on transport and interaction of biomolecules to perform their diverse functions. To investigate the underlying molecular processes in the native cellular environment, minimally invasive techniques are needed. Fluorescence fluctuation spectroscopy (FFS) approaches provide a powerful toolbox that fulfills this aim (*Jameson et al., 2009*; *Weidemann et al., 2014*; *Petazzi et al., 2020*). FFS takes advantage of inherent molecular dynamics present in biological systems, for example, diffusion, to obtain molecular parameters from fluctuations of the signal emitted by an ensemble of fluorescent molecules. More in detail, the temporal evolution of such fluctuations allows the quantification of intracellular dynamics. In addition, concentration and oligomerization state of molecular complexes can be determined by analyzing the magnitude of fluctuations. Finally, hetero-interactions of different molecular species can be detected by cross-correlation analysis of fluctuations emitted by spectrally separated fluorophores (*Schwille et al., 1997*). Over the last two decades, several experimental FFS schemes such as raster image (cross-) correlation spectroscopy (RI(C)CS) (*Digman et al., 2005*; *Digman et al., 2009b*), (cross-correlation) Number&Brightness analysis (*Digman et al., 2008*; *Digman et al., 2009a*), and imaging FCS (*Krieger et al., 2015*) have been developed, extending the concept of traditional single-point fluorescence (cross-) correlation spectroscopy (F(C)CS) (*Magde et al., 1972*). A further interesting example of FFS analysis relevant in the field of cell biology is represented by scanning F(C)CS (SF(C)CS). Using a scan path perpendicular to the plasma membrane (PM), this technique provides enhanced stability and the ability to probe slow membrane dynamics (*Ries and Schwille, 2006*), protein interactions (*Ries et al., 2009b*; *Dunsing et al., 2017*), and oligomerization (*Dunsing et al., 2018*) at the PM of cells.

FFS studies are conventionally limited to the analysis of two spectrally distinguished species due to (i) broad emission spectra of fluorophores with consequent cross-talk artifacts and (ii) limited overlap

of detection/excitation geometries for labels with large spectral separation. Generally, only a few fluorescence-based methods are available to detect ternary or higher order interactions of proteins (*Galperin et al., 2004*; *Sun et al., 2010*; *Hur et al., 2016*). First in vitro approaches to perform FCS on more than two species exploited quantum dots (*Burkhardt et al., 2005*) or fluorescent dyes with different Stokes shifts excited with a single laser line in one- (*Hwang et al., 2006*) or two-photon excitation (*Heinze et al., 2004*; *Ridgeway et al., 2012a*), coupled with detection on two or more single photon counting detectors. Following an alternative conceptual approach, it was shown in vitro that two spectrally strongly overlapping fluorophore species can be discriminated in FCS by applying statistical filtering of detected photons based on spectrally resolved (fluorescence spectral correlation spectroscopy [FSCS]; *Benda et al., 2014*) or fluorescence lifetime (fluorescence lifetime correlation spectroscopy [FLCS]; *Böhmer et al., 2002*; *Kapusta et al., 2007*; *Ghosh et al., 2018*) detection. Such framework allows the minimization of cross-talk artifacts in FCCS measurements performed in living cells (*Padilla-Parra et al., 2011*). Recently, three-species implementations of RICCS and FCCS were successfully demonstrated for the first time in living cells. Schrimpf et al. presented raster spectral image correlation spectroscopy (RSICS), a powerful combination of RICS with spectral detection and statistical filtering based on the emission spectra of mEGFP, mVenus, and mCherry fluorophores (*Schrimpf et al., 2018*). Stefl et al. developed single-color fluorescence lifetime cross-correlation spectroscopy (sc-FLCCS), taking advantage of several GFP variants characterized by short or long fluorescence lifetimes (*Štefl et al., 2020*). Using this elegant approach, three-species FCCS measurements could be performed in yeast cells, with just two excitation lines.

Here, we explore the full potential of FSCS and RSICS. In particular, we present scanning fluorescence spectral correlation spectroscopy (SFSCS), combining SFCS and FSCS. We show that SFSCS enables cross-talk-free SFCCS measurements of two protein species at the PM of living cells tagged with strongly overlapping fluorophores in the green or red regions of the visible spectrum, excited with a single excitation line. This approach results in correct estimates of protein diffusion dynamics, oligomerization, and interactions between both species. Further, we extend our approach to the analysis of three or four interacting partners: by performing cross-correlation measurements on different fluorescent protein (FP) hetero-oligomers, we demonstrate that up to four FP species can be simultaneously analyzed. We then apply this scheme to simultaneously investigate the interaction of influenza A virus (IAV) matrix protein 2 (M2) with two cellular host factors, the tetraspanin CD9 and the autophagosome protein LC3, co-expressed in the same cell. Finally, we extend RSICS for the detection of four molecular species and quantify, for the first time directly in living cells, the complete stoichiometry of ternary IAV polymerase complexes assembling in the nucleus, using three-species fluorescence correlation and brightness analysis.

Results

Cross-talk-free SFSCS analysis of membrane-associated proteins using FPs with strongly overlapping emission spectra and a single excitation wavelength

To test the suitability of SFSCS to quantify interactions between membrane proteins tagged with strongly spectrally overlapping fluorophores, we investigated HEK 293T cells co-expressing myristoylated and palmitoylated mEGFP (mp-mEGFP) and mp-mEYFP. These monomeric FPs are anchored independently to the inner leaflet of the PM and their emission maxima are only ca. 20 nm apart (*Figure 1—figure supplement 1*). The signal originating from the two fluorophores was decomposed using spectral filters (*Figure 1—figure supplement 2A*) based on the emission spectra detected on cells expressing mp-mEGFP and mp-mEYFP separately (*Figure 1—figure supplement 1*). We then calculated autocorrelation functions (ACFs) and the cross-correlation function (CCF) for signal fluctuations assigned to each fluorophore species. Representative CFs for a typical measurement are shown in *Figure 1A*, indicating absence of interactions and negligible cross-talk between the two FPs. In contrast, we observed substantial CCFs when analyzing measurements on cells expressing mp-mEYFP-mEGFP heterodimers (*Figure 1—figure supplement 3A*). Overall, we obtained a relative cross-correlation (rel.cc.) of 0.72 ± 0.12 (mean ± SD, n = 22 cells) in the latter sample compared to a vanishing rel.cc. of 0.02 ± 0.04 (mean ± SD, n = 34 cells) in the negative control (*Figure 1B*). Comparison of two types of linker peptides (short flexible or long rigid) between mEGFP and mEYFP

165
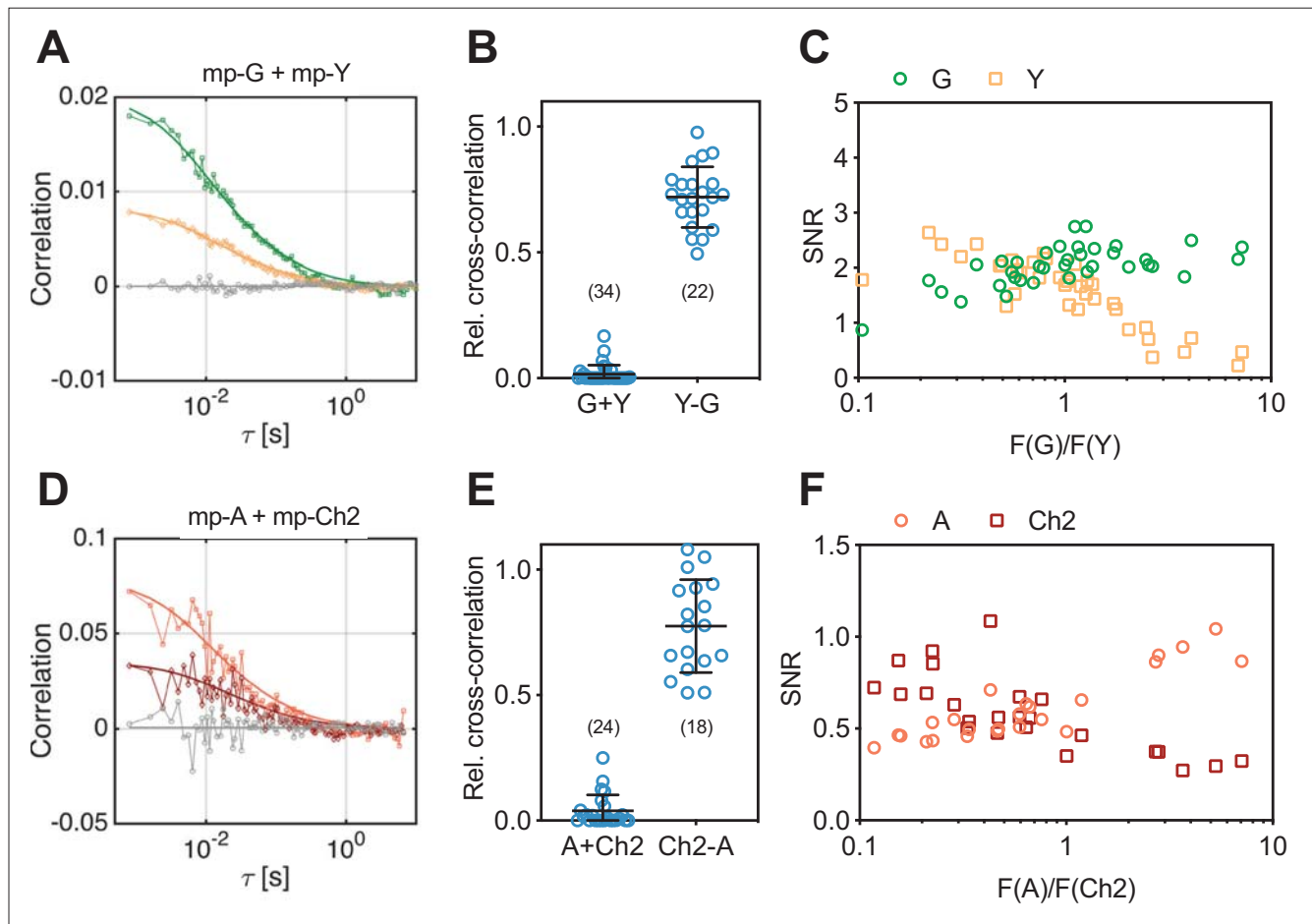
Figure 1. Cross-correlation and signal-to-noise ratio (SNR) analysis for two-species scanning fluorescence spectral correlation spectroscopy (SFSCS) measurements at the plasma membrane (PM) of HEK 293T cells, performed with fluorescent proteins (FPs) showing strongly overlapping emission spectra. (**A**) Representative correlation functions (CFs) (green: autocorrelation function [ACF] for mEGFP ['G']; yellow: ACF for mEYFP ['Y'] gray: cross-correlation function [CCF] calculated for both fluorophore species) obtained from SFSCS measurements on the PM of HEK 293T cells co-expressing mp-mEGFP and mp-mEYFP. Solid thick lines show fits of a two-dimensional diffusion model to the CFs. (**B**) Relative cross-correlation values obtained from SFSCS measurements described in (**A**) ('G + Y') or on HEK 293T cells expressing mp-mEYFP-mEGFP heterodimers ('Y-G'). (**C**) SNR of ACFs for mEGFP (green) and mEYFP (yellow), obtained from SFSCS measurements described in (**A**), plotted as a function of the average ratio of detected mEGFP and mEYFP fluorescence. (**D**) Representative CFs (light red: ACF for mApple ['A']; dark red: ACF for mCherry2 ['Ch2']; gray: CCF calculated for both fluorophores) obtained from SFSCS measurements on the PM of HEK 293T cells co-expressing mp-mApple and mp-mCherry2. Solid thick lines show fits of a two-dimensional diffusion model to the CFs. (**E**) Relative cross-correlation values obtained from SFSCS measurements described in (**D**) ('A + Ch2') or on HEK 293T cells expressing mp-mCherry2-mApple heterodimers ('Ch2-A'). (**F**) SNR of ACFs for mApple (light red) and mCherry2 (dark red), obtained from SFSCS measurements described in (**D**), plotted as a function of the average ratio of detected mApple and mCherry2 fluorescence. Data are pooled from three (**B**) or two (**E**) independent experiments each. The number of cells measured is given in parentheses. Error bars represent mean ± SD.

The online version of this article includes the following source data and figure supplement(s) for figure 1:

Source data 1. Relative cross-correlation and signal-to-noise ratios for two-species scanning fluorescence correlation spectroscopy measurements.

Figure supplement 1. Fluorescent protein (FP) emission spectra.

Figure supplement 2. Spectral filters for two-species scanning fluorescence spectral correlation spectroscopy (SFSCS).

Figure supplement 3. Scanning fluorescence spectral correlation spectroscopy (SFSCS) on fluorescent protein (FP) heterodimers.

showed that the linker length slightly affected rel.cc. values obtained for heterodimers (*Figure 1—figure supplement 3C*). FPs linked by a short peptide displayed lower rel.cc., probably due to fluorescence resonance energy transfer (FRET), as previously reported (*Foo et al., 2012*). Therefore, unless otherwise noted, similar long rigid linkers were inserted in all constructs used in this study that contain multiple FPs (see *Supplementary file 1a*).

166

Overlapping fluorescence emission from different species detected in the same channels provides unwanted background signal and thus reduces the signal-to-noise ratio (SNR) of the CFs (*Schrimpf et al., 2018*). To assess to which extent the SNR depends on the relative concentration of mEGFP and mEYFP fluorophores, we compared it between measurements on cells with different relative expression levels of the two membrane constructs (*Figure 1C*). While the SNR of mEGFP ACFs was only moderately affected by the presence of mEYFP signal (i.e., SNR ranging from ca. 2.5 to 1.0, with 90% to 10% of the signal originating from mEGFP), the ACFs measured for mEYFP showed strong noise when mEGFP was present in much higher amount (i.e., SNR ranging from 2.5 to 0.2, with 90% to 10% of the signal originating from mEYFP).

Next, we tested whether the same approach can be used for FPs with overlapping emission in the red region of the visible spectrum, which generally suffer from reduced SNR in FFS applications (*Dunsing et al., 2018*; *Foust et al., 2019*). Therefore, we performed SFSCS measurements on HEK 293T cells co-expressing mp-mCherry2 and mp-mApple. Also, the emission spectra of these FPs are shifted by less than 20 nm (*Figure 1—figure supplement 1*, spectral filters are shown in *Figure 1—figure supplement 2B*). Correlation analysis resulted generally in noisier CFs (*Figure 1D*) compared to mEGFP and mEYFP. Nevertheless, a consistently negligible rel.cc. of 0.04 ± 0.06 (mean ± SD, n = 24 cells) was observed. In contrast, a high rel.cc. of 0.78 ± 0.19 (mean ± SD, n = 18 cells) was obtained on cells expressing mp-mCherry2-mApple heterodimers (*Figure 1E*, *Figure 1—figure supplement 3B*). SNR analysis confirmed lower SNRs of the CFs obtained for red FPs (*Figure 1F*) compared to mEGFP and mEYFP, with values for mApple depending more weakly on the relative fluorescence signal than mCherry2 (i.e., ca. twofold change for mApple vs. ca. fourfold change for mCherry2, when the relative abundance changed from 90% to 10%).
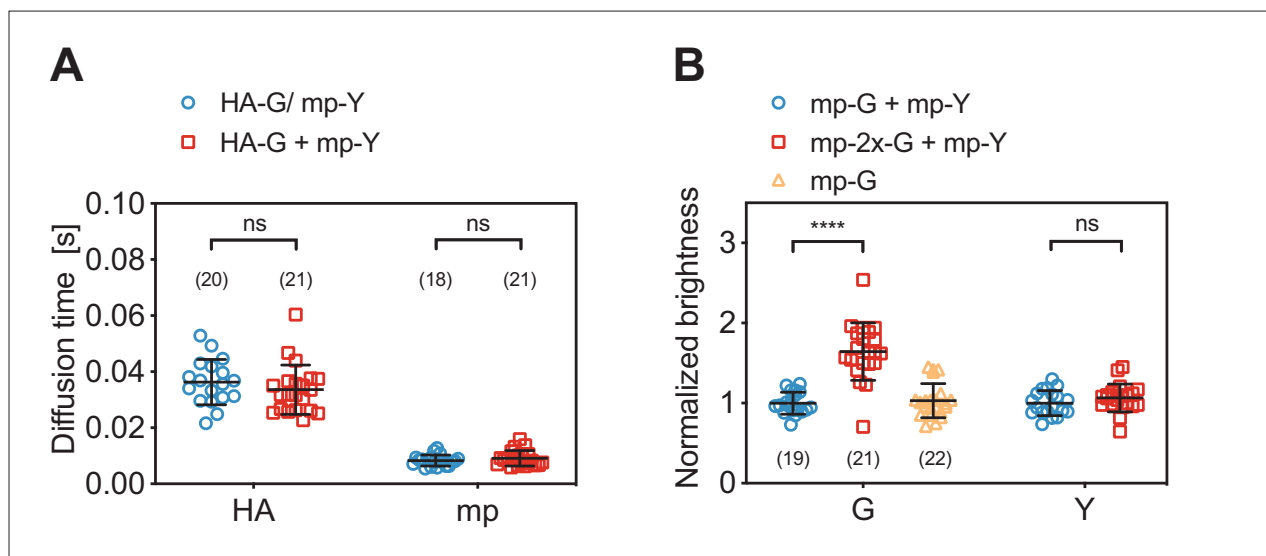
Figure 2. Diffusion and molecular brightness analysis for two-species scanning fluorescence spectral correlation spectroscopy (SFSCS) measurements at the plasma membrane (PM) of HEK 293T cells. (**A**) Diffusion times obtained from SFSCS measurements on HEK 293T cells expressing either influenza A virus (IAV) HA-mEGFP or mp-mEYFP separately (blue), or co-expressing both fusion proteins (red). (**B**) Normalized molecular brightness values obtained from SFSCS measurements on HEK 293T cells co-expressing mp-mEGFP and mp-mEYFP (blue), mp-2x-mEGFP and mp-mEYFP (red), or expressing mp-mEGFP alone (yellow). Normalized brightness values were calculated by dividing molecular brightness values detected in each SFSCS measurement by the average brightness obtained for mEGFP and mEYFP in cells co-expressing mp-mEGFP and mp-mEYFP. Data are pooled from two independent experiments for each sample. The number of cells measured is given in parentheses. Error bars represent mean ± SD. Statistical significance was determined using Welch's corrected two-tailed Student's *t*-test (****p<0.0001, ns: not significant).

The online version of this article includes the following source data and figure supplement(s) for figure 2:

Source data 1. Diffusion times and normalized molecular brightness values for two-species scanning fluorescence correlation spectroscopy measurements.

Figure supplement 1. Relative cross-correlation obtained from two-species scanning fluorescence spectral correlation spectroscopy (SFSCS) measurements.

167

We furthermore verified that SFSCS analysis results in correct estimates of protein diffusion dynamics. To this aim, we co-expressed mEGFP-tagged IAV hemagglutinin spike transmembrane protein (HA-mEGFP) and mp-mEYFP. We then compared the diffusion times measured by SFSCS to the values obtained on cells expressing each of the two constructs separately (*Figure 2A*). For HA-mEGFP, an average diffusion time of 34 ± 9 ms (mean ± SD, n = 21 cells) was determined in cells expressing both proteins. This value was comparable to that measured for HA-mEGFP expressed separately (36 ± 8 ms, mean ± SD, n = 18 cells). For mp-mEYFP, diffusion times of 9 ± 3 ms and 8 ± 2 ms were measured in samples expressing both proteins or just mp-mEYFP, respectively. In addition to diffusion analysis, we also analyzed the cross-correlation of HA-mEGFP and mp-mEYFP signal for two-species measurements, resulting in negligible rel.cc. values (*Figure 2—figure supplement 1*). Hence, SFSCS yielded correct estimates of diffusion dynamics and allowed to distinguish faster and slower diffusing protein species tagged with spectrally strongly overlapping FPs.

Finally, we evaluated the capability of SFSCS to precisely determine the molecular brightness as a measure of protein oligomerization. We compared the molecular brightness values for mEGFP and mEYFP in samples co-expressing monomeric FP constructs mp-mEGFP and mp-mEYFP with the values obtained for cells co-expressing mp-2x-mEGFP homodimers and mp-mEYFP (*Figure 2B*). From SFSCS analysis of measurements in the latter sample, we obtained a normalized molecular brightness of 1.64 ± 0.36 (mean ± SD, n = 21 cells) for mp-2x-mEGFP, relative to the brightness determined in the monomer sample (n = 19 cells). This value is in agreement with our previous quantification of the relative brightness of mEGFP homodimers, corresponding to a fluorescence probability (p_f) of ca. 60–75% for mEGFP (*Dunsing et al., 2018*). The p_f is an empirical, FP-specific parameter that was previously characterized for multiple FPs (*Dunsing et al., 2018*). It quantifies the fraction of non-fluorescent FPs due to photophysical processes, such as transitions to long-lived dark states, or slow FP maturation and needs to be taken into account to correctly determine the oligomerization state of FP tagged protein complexes. As a reference for the absolute brightness, we also determined the relative molecular brightness of mEGFP in cells expressing mp-mEGFP alone, yielding a value of 1.03 ± 0.21 (mean ± SD, n = 22 cells). Additionally, the brightness values determined for mEYFP in both two-species samples were similar, with a relative ratio of 1.07 ± 0.18, as expected. This confirms that reliable brightness values were obtained and that dimeric and monomeric species can be correctly identified.

In summary, these results demonstrate that SFSCS analysis of fluorescence fluctuations successfully separates the contributions of FPs exhibiting strongly overlapping emission spectra, yielding correct quantitative estimates of protein oligomerization and diffusion dynamics.

Simultaneous cross-correlation and brightness analysis for three spectrally overlapping FPs at the PM

In the previous section, we showed that SFSCS enables cross-talk-free cross-correlation analysis of two fluorescent species excited with a single laser line, even in the case of strongly overlapping emission spectra. To explore the full potential of SFSCS, we extended the approach to systems containing three spectrally overlapping fluorophores. We excited mEGFP, mEYFP, and mCherry2 with 488 nm and 561 nm lines simultaneously and detected their fluorescence in 23 spectral bins in the range of 491–695 nm. We measured individual emission spectra (*Figure 1—figure supplement 1*) for single-species samples to calculate three-species spectral filters (*Figure 3—figure supplement 1*), which we then used to decompose the signal detected in cells expressing multiple FPs into the contribution of each species.

As a first step, we performed three-species SFSCS measurements on HEK 293T cells co-expressing mp-mEYFP with either (i) mp-mEGFP and mp-mCherry2 (mp-G+ mp-Y + mp-Ch2) or (ii) mp-mCherry2-mEGFP heterodimers (mp-Ch2-G + mp-Y). Additionally, we tested a sample with cells expressing mp-mEYFP-mCherry2-mEGFP heterotrimers (mp-Y-Ch2-G). We then calculated ACFs for all three FP species and CCFs for all fluorophore combinations, respectively. In the first sample (mp-G + mp-Y + mp-Ch2), in which all three FPs are anchored independently to the PM, we obtained CCFs fluctuating around zero for all fluorophore combinations, as expected (*Figure 3A*). In the second sample (mp-Ch2-G + mp-Y), a substantial cross-correlation was detected between mEGFP and mCherry2, whereas the other two combinations resulted in CCFs fluctuating around zero (*Figure 3B*). In the heterotrimer sample, CCFs with low level of noise and amplitudes significantly above zero were successfully obtained for all three fluorophore combinations (*Figure 3C*). From the amplitude ratios

168
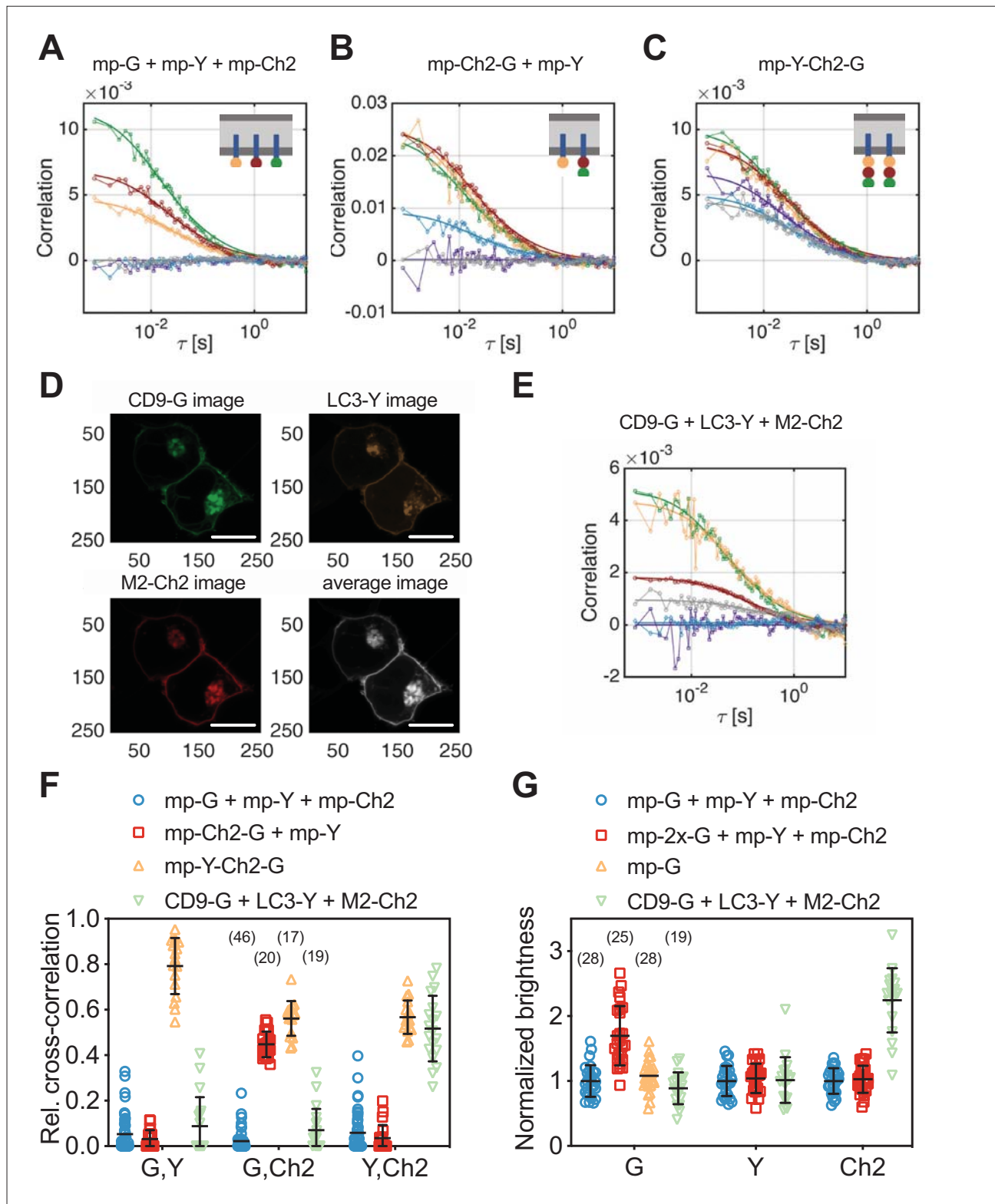
Figure 3. Cross-correlation and molecular brightness analysis for three-species scanning fluorescence spectral correlation spectroscopy (SFSCS) measurements on fluorescent protein (FP) hetero-oligomers and influenza A virus (IAV) M2 at the plasma membrane (PM) of HEK 293T cells. (**A–C**) Representative correlation functions (CFs) (green/yellow/red: autocorrelation functions [ACFs] for mEGFP ['G']/mEYFP ['Y']/mCherry2 ['Ch2']; purple/blue/gray: cross-correlation functions [CCFs] calculated for the pairs mEGFP and mEYFP/mEGFP and mCherry2/mEYFP and mCherry2) obtained from

Figure 3 continued on next page

169

Figure 3 continued

three-species SFSCS measurements on HEK 293T cells co-expressing mp-mEGFP, mp-mEYFP, and mCherry2 (**A**), mp-mCherry2-mEGFP heterodimers and mp-mEYFP (**B**), or expressing mp-mEYFP-mCherry2-mEGFP heterotrimers (**C**), as illustrated in insets. Solid thick lines show fits of a two-dimensional diffusion model to the CFs. (**D**) Representative fluorescence images of HEK 293T cells co-expressing CD9-mEGFP, LC3-mEYFP, and IAV protein M2-mCh2. Spectral filtering and decomposition were performed to obtain a single image for each species. Scale bars are 5 μm. (**E**) Representative CFs (green/yellow/red: ACFs for mEGFP/mEYFP/mCherry2; purple/blue/gray: CCFs calculated for the pairs mEGFP and mEYFP/mEGFP and mCherry2/ mEYFP and mCherry2) obtained from three-species SFSCS measurements on HEK 293T cells co-expressing CD9-mEGFP, LC3-mEYFP, and M2-mCh2. Solid thick lines show fits of a two-dimensional diffusion model to the CFs. (**F**) Relative cross-correlation values obtained from three-species SFSCS measurements described in (**A–C**) and (**E**). (**G**) Normalized molecular brightness values obtained from three-species SFSCS measurements on HEK 293T cells co-expressing mp-mEGFP, mp-mEYFP, and mp-mCherry2 (blue), mp-2x-mEGFP, mp-mEYFP, and mp-mCherry2 (red), CD9-mEGFP, LC3-mEYFP, and M2-mCh2 (green), or expressing mp-mEGFP alone (yellow). Normalized brightness values were calculated by dividing the molecular brightness values detected in each SFSCS measurement by the average brightness obtained for mEGFP, mEYFP, and mCherry2 in cells co-expressing mp-mEGFP, mp-mEYFP, and mp-mCherry2. Data are pooled from two independent experiments for each sample. The number of cells measured is given in parentheses. Error bars represent mean ± SD.

The online version of this article includes the following source data and figure supplement(s) for figure 3:

Source data 1. Relative cross-correlation and normalized molecular brightness values for three-species scanning fluorescence correlation spectroscopy measurements.

Figure supplement 1. Spectral filters for three-species scanning fluorescence spectral correlation spectroscopy (SFSCS).

Figure supplement 2. Relative cross-correlation (rel.cc.) for three-species scanning fluorescence spectral correlation spectroscopy (SFSCS) analyzed using different fitting algorithms.

Figure supplement 3. Noise analysis of three-species scanning fluorescence spectral correlation spectroscopy (SFSCS) measurements.

Figure supplement 4. Membrane recruitment of LC3 in M2-expressing cells.

of the ACFs and CCFs, we then calculated rel.cc. values for all measurements (*Figure 3F*). Low rel.cc. values were obtained for all fluorophore combinations that were not expected to show interactions, for example, 0.05 ± 0.08 (mean ± SD, n = 46 cells) between mEGFP and mEYFP signal in the first sample. It is worth noting that these values, albeit consistently negligible, appear to depend on the specific fitting procedure (see *Figure 3—figure supplement 2* and Materials and methods for details). For mEGFP and mCherry2, similar rel.cc. values of 0.45 ± 0.06 (mean ± SD, n = 20 cells) and 0.56 ± 0.08 (mean ± SD, n = 17 cells) were observed in cells expressing mp-mCherry2-mEGFP heterodimers or mp-mEYFP-mCherry2-mEGFP heterotrimers. The minor difference could be attributed, for example, to different linker peptides (i.e., long rigid linker between FPs in heterotrimers and a short flexible linker in heterodimers), increasing the degree of FRET between mEGFP and mCherry2 in heterodimers and reducing the cross-correlation. The heterotrimer sample showed high rel.cc. values also for the other two fluorophore combinations: mEGFP and mEYFP (rel.cc.$_{G,Y}$ = 0.79 ± 0.12) or mCherry2 and mEYFP (rel.cc.$_{Y,Ch2}$ = 0.57 ± 0.07).

In addition to cross-correlation analysis, we performed molecular brightness measurements on samples containing three FP species. In particular, we compared molecular brightness values obtained by SFSCS on HEK 293T cells co-expressing homodimeric mp-2x-mEGFP, mp-mEYFP, and mp-mCherry2 (mp-2x-G + mp-Y + mp-Ch2) to the values measured on cells co-expressing the three monomeric constructs mp-mEGFP, mp-mEYFP, and mp-mCherry2 (mp-G + mp-Y + mp-Ch2). Whereas similar brightness values were obtained for mEYFP and mCherry2 in both samples, for example, relative brightness of 1.04 ± 0.23 for mEYFP and 1.03 ± 0.21 for mCherry2 (mean ± SD, n = 25 cells/n = 28 cells), a higher brightness of 1.70 ± 0.46 was measured for mEGFP in the first sample (*Figure 3G*). This value corresponds to a p_f of ca. 70% for mEGFP, as expected (*Dunsing et al., 2018*). To confirm that absolute brightness values are not influenced by the spectral decomposition, we also determined the brightness of mEGFP in cells expressing mp-mEGFP alone (*Figure 3G*), resulting in values close to 1 (1.08 ± 0.23, mean ± SD, n = 28 cells).

The IAV protein M2 interacts strongly with LC3 but not with CD9

Having demonstrated the capability of SFSCS to successfully quantify protein interactions and oligomerization, even in the case of three FPs with overlapping emission spectra, we applied this approach in a biologically relevant context. In more detail, we investigated the interaction of IAV channel protein M2 with the cellular host factors CD9 and LC3. CD9 belongs to the family of tetraspanins and is supposedly involved in virus entry and virion assembly (*Florin and Lang, 2018*; *Hantak et al.,*

2019; *Dahmane et al., 2019*). The autophagy marker protein LC3 was recently shown to be recruited to the PM in IAV-infected cells (see also *Figure 3—figure supplement 4A,B*), promoting filamentous budding and virion stability, thus indicating a role of LC3 in virus assembly (*Beale et al., 2014*). To detect hetero-interactions between CD9, LC3, and M2, we co-expressed the fluorescent fusion proteins CD9-mEGFP, LC3-mEYFP, and M2-mCherry2 (i.e., M2 carrying an mCherry2 tag at the extracellular terminus) in HEK 293T cells (*Figure 3D*) and performed three-species SFSCS measurements at the PM (*Figure 3E*).

We then calculated rel.cc. values to quantify pair-wise interactions of the three proteins (*Figure 3F*). The obtained rel.cc. values for CD9-mEGFP with LC3-mEYFP or M2-mCherry2 (rel.cc.$_{CD9-G,LC3-Y}$ = 0.09 ± 0.13, rel.cc.$_{CD9-G,M2-Ch2}$ = 0.07 ± 0.09, mean ± SD, n = 19 cells) were similar to those of the negative cross-correlation control (i.e., cells co-expressing mp-mEGFP, mp-mEYFP, and mp-mCherry2, see previous paragraph). In contrast, we detected a substantial rel.cc. of 0.52 ± 0.14 for LC3-mEYFP and M2-mCherry2. This value was close (ca. 90% on average) to that obtained for this fluorophore combination in measurements on FP heterotrimers, suggesting very strong association of LC3-mEYFP with M2-mCherry2. We furthermore analyzed the molecular brightness for each species, normalized to the monomeric references (*Figure 3G*). While CD9-mEGFP and LC3-mEYFP showed normalized brightness values close to 1 (B_{CD9-G} = 0.89 ± 0.25, B_{LC3-Y} = 1.02 ± 0.35), suggesting that both proteins are monomers, we observed significantly higher relative brightness values for M2-mCherry2 (B_{M2-Ch2} = 2.24 ± 0.49). Assuming a p_f of ca. 60% for mCherry2 (*Dunsing et al., 2018*), the determined relative brightness corresponds to an oligomerization state of ε_{M2-Ch2} = 3.1 ± 0.8, that is, formation of M2 dimers to tetramers at the PM.

SFSCS allows simultaneous analysis of protein-protein interactions for four spectrally overlapping FP species

Having demonstrated robust three-species cross-correlation analysis, we aimed to further explore the limits of SFSCS. We investigated therefore whether SFSCS can discriminate differential interactions between four species using the spectral emission patterns of mEGFP, mEYFP, mApple, and mCherry2 for spectral decomposition (*Figure 1—figure supplement 1*, *Figure 4—figure supplement 1*). As a proof of concept, we performed four-species measurements on three different samples: (i) cells co-expressing all four FPs independently as membrane-anchored proteins (mp-G + mp-Y + mp-A + mp-Ch2), (ii) cells co-expressing mp-mCherry2-mEGFP heterodimers, mp-mEYFP, and mp-mApple (mp-Ch2-G + mp-Y + mp-A), and (iii) cells expressing mp-mEYFP-mCherry2-mEGFP-mApple heterotetramers (mp-Y-Ch2-G-A). We then calculated four ACFs, six CCFs, and rel.cc. values from the amplitude ratios of the ACFs and CCFs. For all fluorophore species, ACFs with amplitudes significantly above zero were obtained. ACFs calculated for mEGFP and mEYFP were characterized by a higher SNR compared to those for the red FPs mApple and, in particular, mCherry2 (*Figure 4A–C*). Nevertheless, reasonable diffusion time values could be determined for all species, showing the largest variation for mCherry2 (*Figure 4—figure supplement 2*).

Noise levels of the CCFs were moderate (*Figure 4D–F*), yet allowing robust fitting and estimation of cross-correlation amplitudes. Based on the determined rel.cc. values (*Figure 4G*), the different samples could successfully be discriminated. In the first sample (mp-G + mp-Y + mp-A + mp-Ch2), negligible to very low values were obtained, that is, at maximum 0.11 ± 0.11 (mean ± SD, n = 12 cells) for mApple and mCherry2. In the second sample (mp-Ch2-G + mp-Y + mp-A), similarly low rel.cc. values were obtained for all fluorophore combinations, for example, 0.10 ± 0.10 (mean ± SD, n = 13 cells) for mApple and mCherry2, with the exception of mEGFP and mCherry2, showing an average value of 0.55 ± 0.13. For the hetero-tetramer sample, high rel.cc. values were measured for all fluorophore combinations, ranging from 0.42 ± 0.07 (mean ± SD, n = 15 cells) for mEGFP and mApple to 0.78 ± 0.08 for mEGFP and mEYFP. Notably, a significant rel.cc. of 0.53 ± 0.10 was also determined for mApple and mCherry2 signals, that is, from the CCFs exhibiting the lowest SNR.

RSICS can be extended to simultaneous detection of four fluorophore species

Having identified a set of FPs that is compatible with four-species SFSCS, we aimed to extend the recently presented RSICS method (*Schrimpf et al., 2018*) to applications with four fluorophore species being detected simultaneously. To test the effectiveness of this approach, we carried out

171
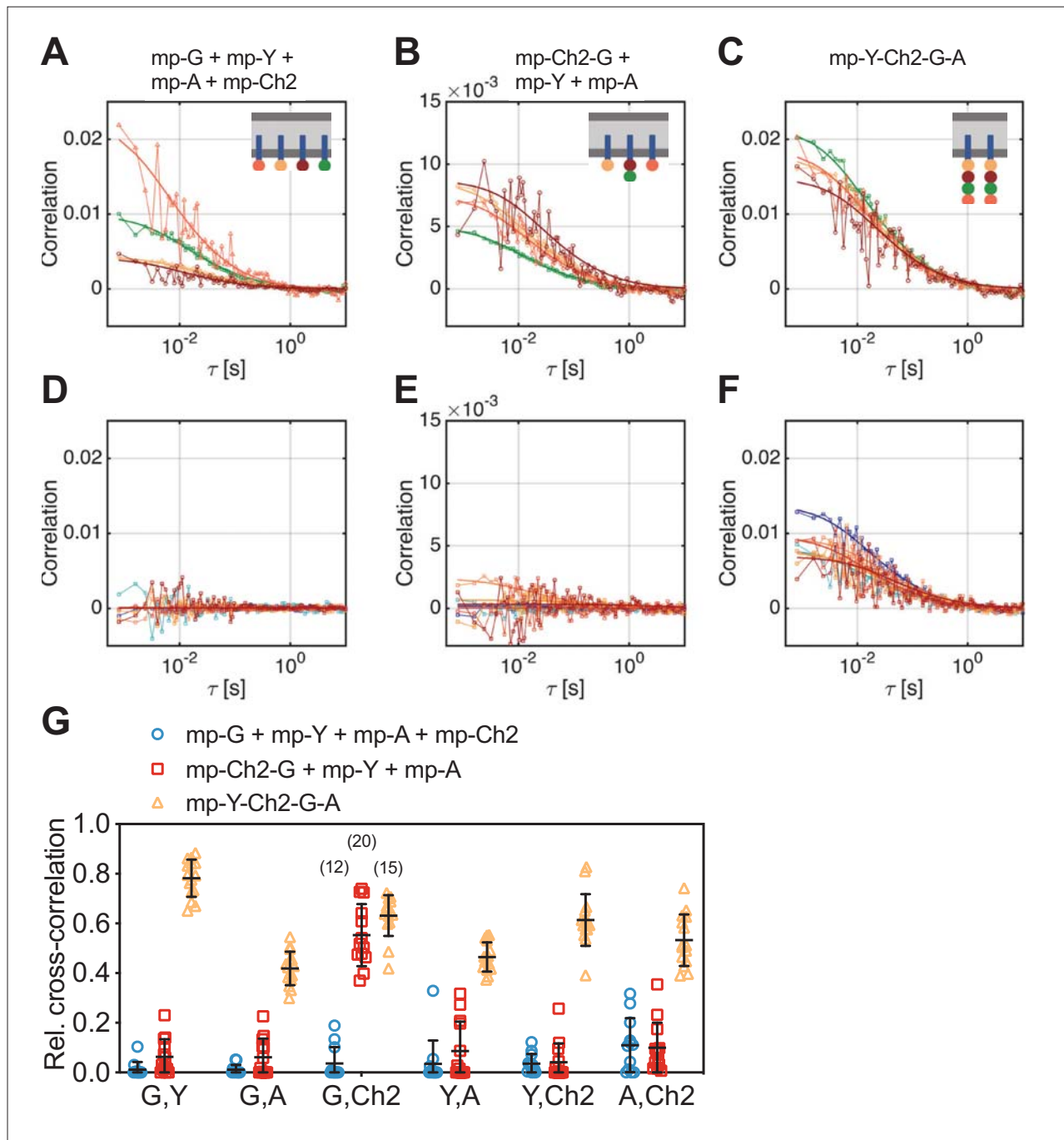
Figure 4. Cross-correlation analysis for four-species scanning fluorescence spectral correlation spectroscopy (SFSCS) measurements on fluorescent protein (FP) hetero-oligomers in HEK 293T cells. (**A–C**) Representative autocorrelation functions (ACFs) (green/yellow/orange/red for mEGFP ['G']/ mEYFP ['Y']/mApple ['A']/mCherry2 ['Ch2']) obtained from four-species SFSCS measurements on HEK 293T cells co-expressing mp-mEGFP, mp-mEYFP, mp-mApple, and mp-mCherry2 (**A**), mp-mCherry2-mEGFP heterodimers, mp-mEYFP, and mp-mApple (**B**), or expressing mp-mEYFP-mCherry2-mEGFP-mApple hetero-tetramers (**C**), as illustrated in insets. Solid thick lines show fits of a two-dimensional diffusion model to the correlation functions (CFs). (**D–F**) SFSCS cross-correlation functions (CCFs) (dark blue/ light blue/orange/yellow/red/dark red for CCFs calculated for mEGFP and mEYFP/mEGFP and mApple/mEGFP and mCherry2/mEYFP and mApple/mEYFP and mCherry2/mApple and mCherry2) from measurements described in (**A–C**) (CCFs in (**D**)/(**E**)/(**F**)) corresponding to ACFs shown in (**A**)/(**B**)/(**C**). Solid thick lines show fits of a two-dimensional diffusion model to the CFs. (**G**) Relative cross-correlation values obtained from four-species SFSCS measurements described in (**A–C**). Data are pooled from two independent experiments. The number of cells measured is given in parentheses. Error bars represent mean ± SD.

Figure 4 continued on next page

172

Figure 4 continued

The online version of this article includes the following source data and figure supplement(s) for figure 4:

Source data 1. Relative cross-correlation values for four-species scanning fluorescence correlation spectroscopy measurements.

Figure supplement 1. Spectral filters for four-species scanning fluorescence spectral correlation spectroscopy (SFSCS).

Figure supplement 2. Diffusion dynamics of four-species scanning fluorescence spectral correlation spectroscopy (SFSCS) measurements.

measurements in the cytoplasm of living A549 cells co-expressing mEGFP, mEYFP, mApple, and mCherry2 in several configurations, similar to the SFSCS experiments presented in the previous paragraph. In more detail, we performed four-species RSICS measurements on the following three samples: (i) cells co-expressing free mEGFP, mEYFP, mApple, and mCherry2 (1x-G + 1x-Y + 1x-A + 1x-Ch2), (ii) cells co-expressing mCherry2-mEGFP and mEYFP-mApple heterodimers (Ch2-G + Y -A), and (iii) cells expressing mEYFP-mCherry2-mEGFP-mApple hetero-tetramers (Y-Ch2-G-A). Representative CFs obtained following RSICS analysis with arbitrary region selection (*Hendrix et al., 2016*) are shown in *Figure 5*. In all samples, ACFs with amplitudes significantly above zero were obtained, with the highest noise level detected for mCherry2 (*Figure 5A, C and E*). A three-dimensional diffusion model could be successfully fitted to all detected ACFs.

Detected CCFs showed the expected pattern: all six CCFs were indistinguishable from noise for the first sample with four independent FPs (*Figure 5B*), whereas large CCF amplitudes were obtained for the pairs mEGFP and mCherry2, as well as mEYFP and mApple in the second sample (Ch2-G + Y- A) (*Figure 5D*). Also, significantly large amplitudes were observed for all six CCFs for the hetero-tetramer sample, albeit with different levels of noise. For example, the lowest SNR was observed in CCFs for mApple and mCherry2 (*Figure 5F*).

From the amplitude ratios of ACFs and CCFs, we determined rel.cc. values (*Figure 5G*). This analysis resulted in negligible values for the first sample (1x-G + 1x-Y + 1x-A + 1x-Ch2): for example, rel. $cc._{G,Ch2} = 0.03 \pm 0.05$ (mean ± SD, n = 21 cells). For the second sample (Ch2-G + Y -A), values significantly above zero, that is, rel.cc.$_{G,Ch2} = 0.46 \pm 0.09$ (mean ± SD, n = 23 cells) and rel.cc.$_{Y,A} = 0.30 \pm 0.10$, were only observed for two fluorophore pairs. For the third sample, cells expressing mEYFP-mCherry2-mEGFP-mApple hetero-tetramers (Y-Ch2-G-A), rel.cc. values significantly above zero were obtained for all FP pairs, ranging from rel.cc.$_{A,Ch2} = 0.31 \pm 0.11$ (mean ± SD, n = 20 cells) to rel.cc.$_{G,Y} = 0.60 \pm 0.05$. Notably, rel.cc. values obtained for the FP species correlating in the second sample (Ch2-G + Y -A) were similar for the third sample (Y-Ch2-G-A): for example, rel.cc.$_{G,Ch2} = 0.45 \pm 0.07$ and rel.cc.$_{Y,A} = 0.41 \pm 0.06$. The lower rel.cc. value measured for mEYFP and mApple in heterodimers (Ch2-G + Y -A) could be attributed to different linker sequences (long rigid linker in heterodimers vs. mCherry2-mEGFP and three long rigid linkers as spacer in hetero-tetramers [Y-Ch2-G-A]), possibly affecting FRET between neighboring FPs.

Finally, we analyzed the diffusion dynamics of FP fusion proteins as determined from the spatial dependence of the ACFs for the four fluorophore species. Diffusion coefficients (D) obtained for mCherry2 showed the highest variation (*Figure 5H*), reflecting the reduced SNR for this fluorophore. Nevertheless, similar average D values were determined for different fluorophore species coupled as hetero-oligomers, for example, $D_G = 19.4 \pm 3.4$ μm^2/s and $D_{Ch2} = 20 \pm 11$ μm^2/s (mean ± SD, n = 23 cells) for mEGFP-mCherry2 heterodimers, and $D_G = 11.2 \pm 2.5$ μm^2/s, $D_Y = 11.6 \pm 2.6$ μm^2/s, $D_A = 12.8 \pm 3.2$ μm^2/s, $D_{Ch2} = 12.6 \pm 5.0$ μm^2/s (mean ± SD, n = 20 cells) for hetero-tetramers.

Cross-correlation and molecular brightness analysis via three-species RSICS provide stoichiometry of IAV polymerase complex assembly

To test the versatility of three-species RSICS, we quantified intracellular protein interactions and stoichiometries in a biologically relevant context. As an example, we focused on the assembly of the IAV polymerase complex (PC), consisting of the three subunits polymerase acidic protein (PA), polymerase basic protein 1 (PB1), and 2 (PB2). A previous investigation using FCCS suggested an assembly model in which PA and PB1 form heterodimers in the cytoplasm of cells. These are imported into the nucleus and appear to interact with PB2 to form heterotrimeric complexes (*Huet et al., 2010*). Nevertheless, the previous analysis could only be performed between two of the three subunits at the same time. Also, the stoichiometry of the complex was reported only for one of the three subunits, that is, PA protein dimerization. Here, we labeled all three subunits using FP fusion constructs and co-expressed

173
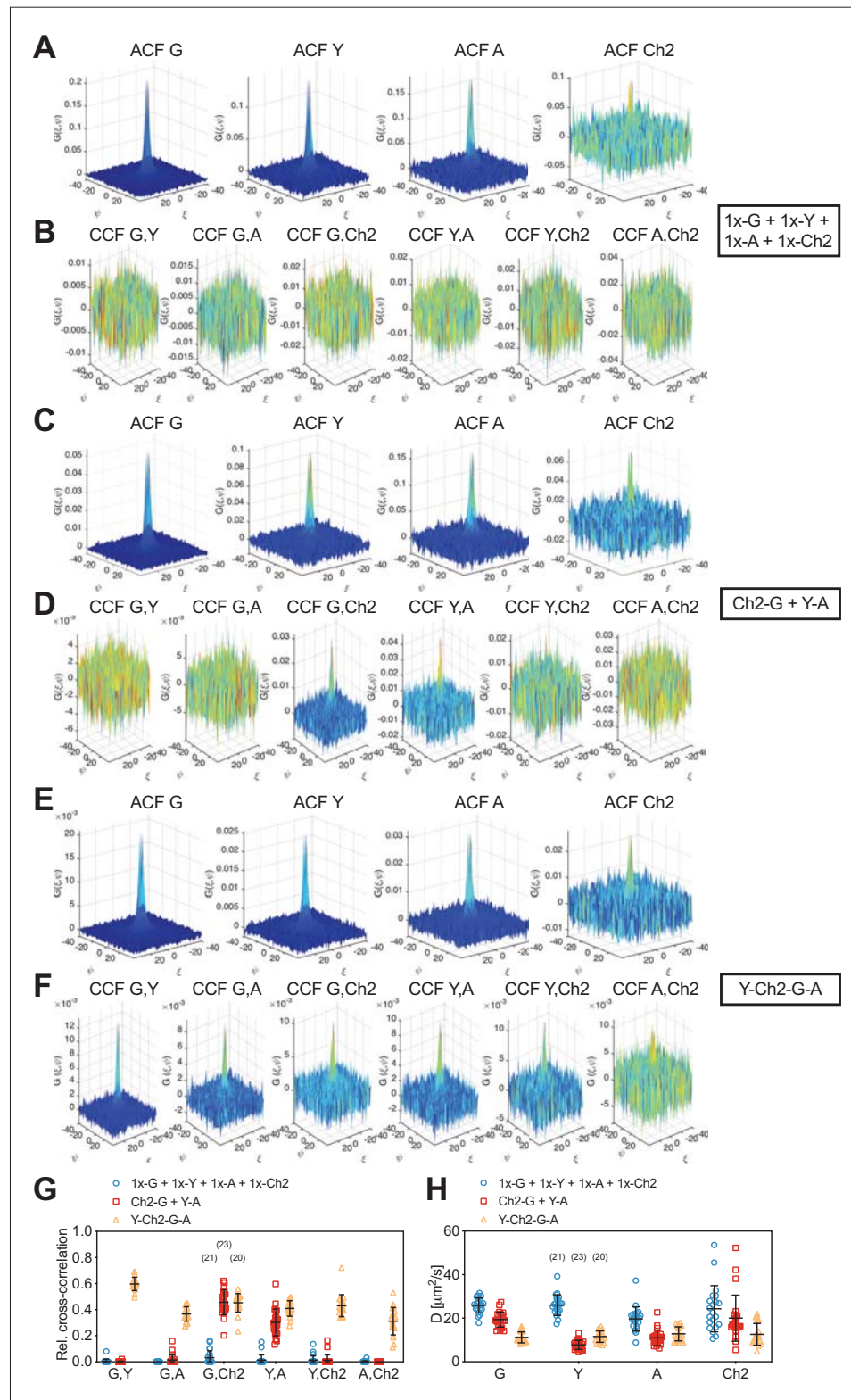
Figure 5. Cross-correlation analysis for four-species raster spectral image correlation spectroscopy (RSICS) measurements on fluorescent protein (FP) hetero-oligomers expressed in cytoplasm of A549 cells. (**A–F**) Representative RSICS spatial autocorrelation functions (ACFs) (**A, C, E**) and cross-correlation functions (CCFs) (**B, D, F**) obtained from four-species RSICS measurements on A549 cells. Cells were co-expressing mEGFP ('G'),

Figure 5 continued on next page

174

Figure 5 continued

mEYFP ('Y'), mApple ('A'), mCherry2 ('Ch2') (**A, B**), mCherry2-mEGFP and mEYFP-mApple heterodimers (**C, D**), or mEYFP-mCherry2-mEGFP-mApple hetero-tetramers (**E, F**). (**G, H**) Relative cross-correlation values (**G**) and diffusion coefficients (**H**) obtained from four-species RSICS measurements described in (**A–F**). Data are pooled from two independent experiments. The number of cells measured is given in parentheses. Error bars represent mean ± SD.

The online version of this article includes the following source data and figure supplement(s) for figure 5:

Source data 1. Relative cross-correlation values and diffusion coefficients for four-species raster spectral image correlation spectroscopy measurements.

Figure supplement 1. Fluorescent protein (FP) emission spectra.

Figure supplement 2. Fluorescent protein (FP) emission spectra at different pH values.

PA-mEYFP, PB1-mEGFP, and PB2-mCherry2 in A549 cells. We then performed three-species RSICS measurements in the cell nucleus, where all three proteins are enriched (***Figure 6A***). RSICS analysis was performed on an arbitrarily shaped homogeneous region of interest in the nucleus. We then calculated RSICS ACFs (***Figure 6B***), CCFs (***Figure 6C***), and rel.cc. values (***Figure 6D***) for the three fluorophore combinations. The determined rel.cc. values were compared to the values obtained on negative controls (i.e., cells co-expressing free mEGFP, mEYFP, and mCherry) and positive controls (i.e., cells expressing mEYFP-mCherry2-mEGFP heterotrimers) (***Figure 6D***).

For the polymerase sample, high rel.cc. values were observed for all combinations: rel.cc.$_{PB1-G,PA-Y}$ = 0.93 ± 0.18 (mean ± SD, n = 53 cells), rel.cc.$_{PB1-G,PB2-Ch2}$ = 0.47 ± 0.14, rel.cc.$_{PA-Y,PB2-Ch2}$ = 0.39 ± 0.14. For the positive control, similar values were observed for mEGFP and mCherry2, rel.cc.$_{G,Ch2}$ = 0.48 ± 0.11 (mean ± SD, n = 46 cells), whereas the values were higher than that measured for PCs for mEYFP and mCherry2, rel.cc.$_{Y,Ch2}$ = 0.53 ± 0.11, and lower for mEGFP and mEYFP, rel.cc.$_{G,Y}$ = 0.65 ± 0.10. The lower average rel.cc. between PA-mEYFP and PB2-mCherry2 compared to the positive control indicates the presence of a minor fraction of non-interacting PA and PB2. These proteins could be present in the nucleus in unbound form when expressed in higher amount than PB1 since both PA and PB2 localize in the nucleus individually and were previously shown not to interact when both present without PB1 (***Huet et al., 2010***). This explanation is supported by the correlation between rel.cc.$_{PA-Y,PB2-Ch2}$ and the relative abundance of PB1-mEGFP (***Figure 6—figure supplement 1A***). Also, the observation that PB1 is only transported to the nucleus in complex with PA is confirmed by the lower concentration of PB1-mEGFP compared to PA-mEYFP in the nuclei of all measured cells (***Figure 6—figure supplement 1A***). Thus, the fraction of PB1-mEGFP bound to PA-mEYFP should be as high as the positive control, for a 1:1 stoichiometry. The observation of higher rel.cc. between mEGFP and mEYFP for the polymerase subunits indicates higher order interactions, that is, higher stoichiometry than 1:1 (***Kaliszewski et al., 2018***).

To quantify the stoichiometry of the PC directly, we analyzed the molecular brightness of RSICS measurements for all three fluorophore species. We normalized the obtained values to the average values determined by RSICS on cells co-expressing monomeric mEGFP, mEYFP, and mCherry2, measured on the same day. To test whether RSICS can be used to obtain reliable brightness/oligo-merization values for all fluorophore species, we first performed control experiments on cells co-expressing either (i) 2x-mEGFP homodimers with mEYFP and mCherry monomers (2x-G + 1x-Y + 1x-Ch2) or (ii) the three homodimers 2x-mEGFP, 2x-mEYFP, and 2x-mCherry2 (2x-G + 2x-Y + 2x-Ch2). In the first sample, we observed an increased relative brightness of 1.67 ± 0.38 (mean ± SD, n = 34 cells) for mEGFP, whereas values around 1 were obtained for mEYFP and mCherry2. This confirmed the presence of mEGFP dimers as well as mEYFP and mCherry2 monomers in this control sample, as expected (***Figure 6E***). In the sample containing all three homodimers, increased relative brightness values were observed for all fluorophore species: 1.75 ± 0.37 (mean ± SD, n = 39 cells) for mEGFP, 1.77 ± 0.33 for mEYFP, and 1.61 ± 0.29 for mCherry2 (see ***Supplementary file 1b*** for data on day-to-day variations). These values indicate successful determination of the dimeric state of all three FP homodimers and are in good agreement with previous brightness measurements on homodimers of mEGFP, mEYFP, and mCherry2, corresponding to p_f values of 60–75% (***Dunsing et al., 2018***). Next, we proceeded with the analysis of PC oligomerization. For each polymerase subunit, relative brightness values close to the values of homodimers were observed. Assuming p_f values of 75, 77, and 61% (as calculated from the determined relative brightness values of homodimers) for mEGFP, mEYFP, and
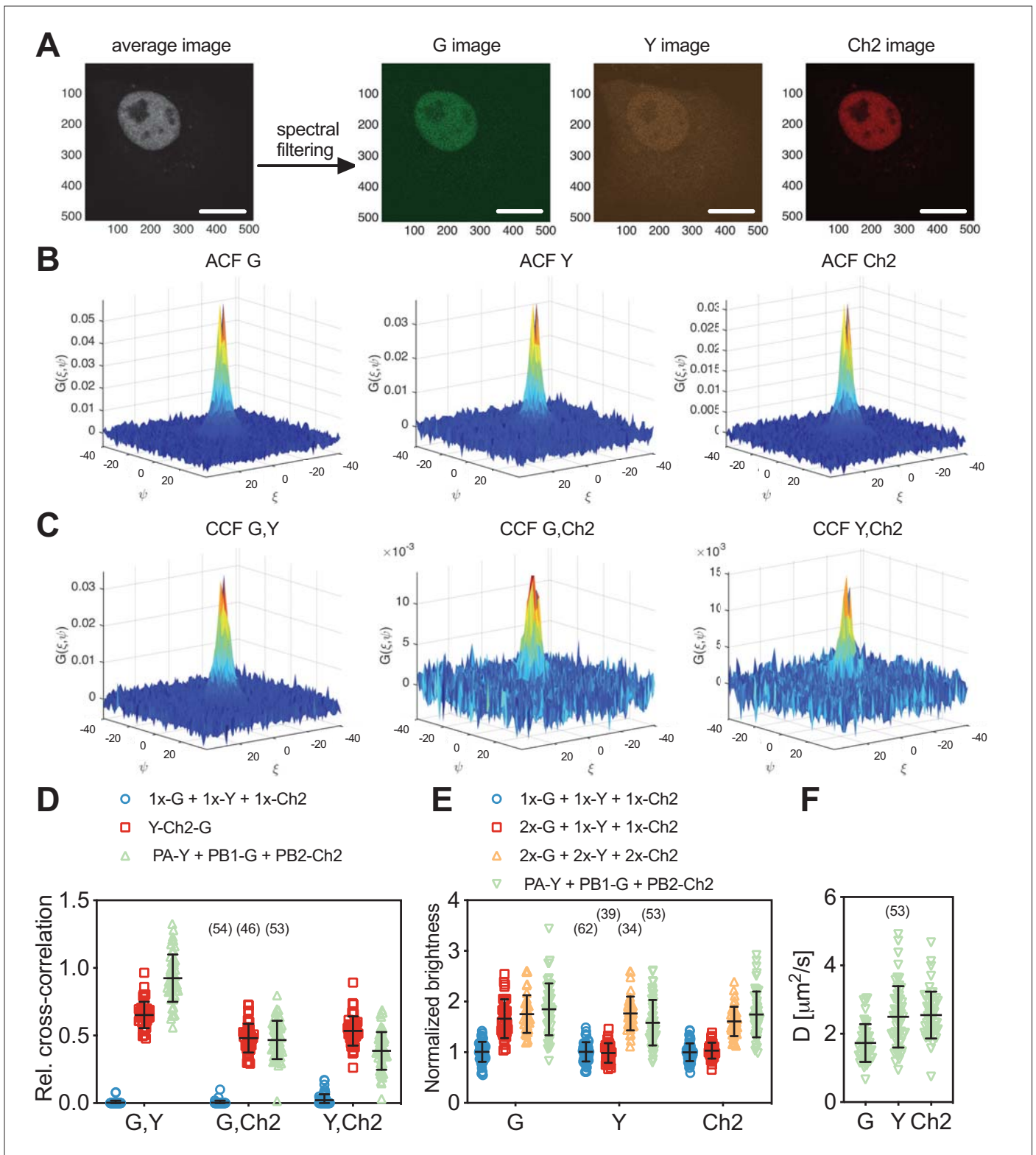
Figure 6. Three-species raster spectral image correlation spectroscopy (RSICS) measurements on influenza A virus (IAV) polymerase complex (PC) and fluorescent protein (FP) hetero-oligomers in the nucleus of A549 cells. (**A**) Representative fluorescence image (left) of A549 cells co-expressing FP-tagged IAV PC proteins PA-mEYFP, PB1-mEGFP, and PB2-mCherry2. Spectral filtering and decomposition result in a single image for each species (right), denoted with 'Y,' 'G,' and 'Ch2.' Scale bars are 10 μm. (**B, C**) Representative RSICS spatial autocorrelation functions (ACFs) (**B**) and cross-

Figure 6 continued on next page

Figure 6 continued

correlation functions (CCFs) (**C**) obtained from three-species RSICS measurements on A549 cells co-expressing PA-mEYFP, PB1-mEGFP, and PB2-mCherry2. (**D**) Relative cross-correlation values obtained from three-species RSICS measurements on A549 cells co-expressing mEGFP, mEYFP, and mCherry2 (blue), PA-mEYFP, PB1-mEGFP, PB2-mCherry2 (green), or expressing mEYFP-mCherry2-mEGFP heterotrimers (red). Data are pooled from four independent experiments. (**E**) Normalized molecular brightness values obtained from three-species RSICS measurements on A549 cells co-expressing mEGFP, mEYFP, and mCherry2 (blue), 2x-mEGFP, mEYFP, and mCherry2 (red), 2x-mEGFP, 2x-mEYFP, 2x-mCherry2 (yellow), or PA-mEYFP, PB1-mEGFP, and PB2-mCherry2 (green). Data are pooled from three (2x-mEGFP + mEYFP + mCherry2, 2x-mEGFP + 2x-mEYFP + 2x-mCherry2), four (PA-mEYFP + PB1-mEGFP + PB2-mCherry2), or five (mEGFP + mEYFP + mCherry2) independent experiments. (**F**) Diffusion coefficients obtained from three-species RSICS measurements on A549 cells co-expressing PA-mEYFP, PB1-mEGFP, and PB2-mCherry2. Data are pooled from four independent experiments. For (**D**–**F**), the number of cells measured is given in parentheses. Error bars represent mean ± SD.

The online version of this article includes the following source data and figure supplement(s) for figure 6:

Source data 1. Relative cross-correlation, normalized molecular brightness values, and diffusion coefficients for three-species raster spectral image correlation spectroscopy measurements on influenza A virus complex and fluorescent protein hetero-oligomers in the nucleus of A549 cells.

Figure supplement 1. Cross-correlation and diffusion analysis for three-species raster spectral image correlation spectroscopy (RSICS) measurements on influenza A virus (IAV) polymerase complex as a function of relative protein concentration.

mCherry2, respectively, p_f corrected normalized brightness values of ε_{PB1-G} = 2.1 ± 0.7 (mean ± SD, n = 53 cells), ε_{PA-Y} = 1.8 ± 0.6, and $\varepsilon_{PB2-Ch2}$ = 2.2 ± 0.7 were obtained (see Materials and methods for details). These results suggest a 2:2:2 stoichiometry of the IAV PC subunits. Finally, we analyzed the diffusion dynamics of PCs via RSICS (*Figure 6F*). The average D measured for PB1-mEGFP, D_{PB1-G} = 1.7 ± 0.6 μm^2/s (mean ± SD, n = 53 cells), was ca. 30% lower than the diffusion coefficients determined for PA-mEYFP- and PB2-mCherry2 (D_{PA-Y} = 2.5 ± 0.9 μm^2/s and $D_{PB2-Ch2}$ = 2.6 ± 0.7 μm^2/s). This observation is compatible with the above-mentioned presence of a minor fraction of unbound (and thus faster diffusing) PA and PB2 (likely in cells with a lower amount of PB1). A more detailed analysis of the data confirmed this interpretation: the molecular brightness and diffusion coefficient of PA-mEYFP depended on the relative concentration of PB1-mEGFP and PA-mEYFP. Lower brightness and higher diffusion coefficients were obtained in cells where PA-mEYFP was present at much higher concentrations than PB1-mEGFP (*Figure 6—figure supplement 1B,C*).
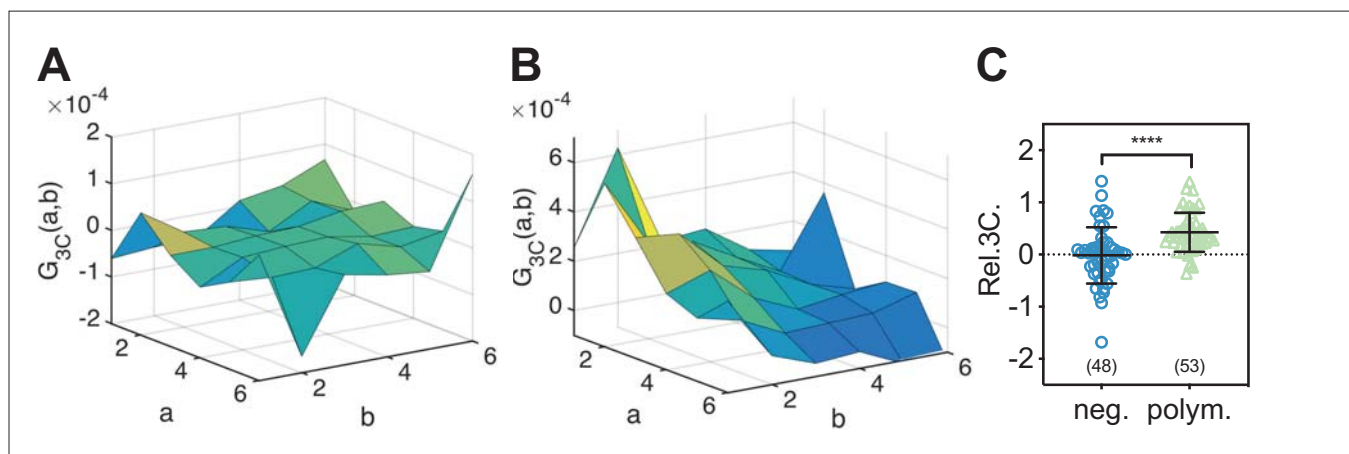
Figure 7. Triple raster image correlation spectroscopy (TRICS) reveals the formation of ternary influenza A virus (IAV) polymerase hetero-complexes in the nucleus of A549 cells. (**A, B**) Representative triple-correlation functions (3CFs) obtained from TRICS measurements on A549 cells co-expressing mEGFP, mEYFP, and mCherry2 ('neg.') (**A**) or co-expressing PA-mEYFP, PB1-mEGFP, and PB2-mCherry2 ('polym.') (**B**). The axes *a* and *b* indicate shifts in the x and y direction, respectively, across the three detection channels, as described in Materials and methods. (**C**) Relative triple-correlation (rel.3C.) values obtained from the measurements described in (**A, B**). The number of cells measured is given in parentheses. Error bars represent mean ± SD. Statistical significance was determined using Welch's corrected two-tailed Student's *t*-test (****p<0.0001).

The online version of this article includes the following source code for figure 7:

Source data 1. Relative triple correlation values for triple raster image correlation spectroscopy analysis of influenza A virus polymerase complex in the nucleus of A549 cells.

Triple raster image correlation spectroscopy (TRICS) analysis provides direct evidence for assembly of ternary IAV polymerase complexes

To directly confirm that IAV PC subunits form ternary complexes in the cell nucleus, we implemented a triple-correlation analysis (TRICS) to detect coincident fluctuations of the signal emitted by mEGFP-, mEYFP-, and mCherry2-tagged proteins. A similar analysis has previously been presented for three-channel FCS measurements (e.g., fluorescence triple-correlation spectroscopy [*Ridgeway et al., 2012a*], triple-color coincidence analysis [*Heinze et al., 2004*]), but was so far limited to in vitro systems such as purified proteins (*Ridgeway et al., 2012a*) or DNA oligonucleotides (*Heinze et al., 2004*) labeled with organic dyes. We performed TRICS on data obtained on cells co-expressing PC subunits PA-mEYFP, PB1-mEGFP, and PB2-mCherry2 or cells co-expressing free mEGFP, mEYFP, and mCherry as a negative triple-correlation control. To evaluate ternary complex formation, we quantified the relative triple-correlation (rel.3C., see Materials and methods) for both samples from the amplitudes of the ACFs and triple-correlation functions (3CFs). *Figure 7A and B* show representative 3CFs for the negative control and the PC sample, respectively. For the negative control, we obtained rel.3C. values fluctuating around zero (*Figure 7C*), rel.3C. = -0.02 ± 0.54 (mean ± SD, n = 49 cells). In contrast, significantly higher, positive rel.3C. values were obtained for the polymerase samples, rel.3C. = 0.43 ± 0.38 (mean ± SD, n = 53 cells). The detection of ternary complexes is limited by non-fluorescent FPs, that is, only a fraction of ternary complexes present in a sample will emit coincident signals for all three FP species. In addition, imperfect overlap of the detection volumes for each channel will further reduce the fraction of ternary complexes that can be detected by TRICS. We therefore performed an approximate calculation of the expected rel.3C. value for a sample containing 100% ternary complexes assuming a p_f of 0.7 for each FP species and estimating the reduction due to imperfect overlap from the pair-wise rel.cc. values detected on the positive cross-correlation control (see Appendix 1, Section A1.3 for details). For a 2:2:2 stoichiometry, we obtained an estimated rel.3C. of 0.48, that is, only slightly higher than the average value determined experimentally for IAV PCs. Thus, we estimate that around 90% of PC subunits undergo ternary complex formation in the cell nucleus when all subunits are present.

Discussion

In this work, we combine FFS techniques with spectral detection to perform multicolor studies of protein interactions and dynamics in living cells. In particular, we present SFSCS, a combination of FSCS (*Benda et al., 2014*) and lateral scanning FCS (*Ries and Schwille, 2006*). We show that SFSCS allows cross-talk-free measurements of protein interactions and diffusion dynamics at the PM of cells and demonstrate that it is capable of detecting three or four species simultaneously. Furthermore, we extend RSICS (*Schrimpf et al., 2018*) to investigate four fluorophore species and apply this approach to determine the stoichiometry of higher order protein complexes assembling in the cell nucleus. Notably, the technical approaches can be carried out on a standard confocal microscope, equipped with a spectral photon counting detector system.

In the first part, we present two-species SFSCS using a single excitation wavelength and strongly overlapping fluorophores. Compared to the conventional implementation of FCCS with two excitation lasers and two detectors, two-species SFSCS has substantial advantages, similar to the recently presented sc-FLCCS (*Štefl et al., 2020*). Since it requires a single excitation line and is compatible with spectrally strongly overlapping FPs, it circumvents optical limitations such as imperfect overlap of the observation volumes. This is evident from higher rel.cc. values of 70–80% measured for mEGFP and mEYFP coupled in FP hetero-oligomers compared to 45–60% observed for mEGFP and mCherry2. Rel.cc. values around 70% are to be expected for the examined FP tandems even in the case of single-wavelength excitation, given that the p_f for such fluorophores is indeed around 0.7 (*Foo et al., 2012*; *Dunsing et al., 2018*) (see also SI, paragraph 1). On the other hand, in three- and four species measurements discussed below, FP pairs requiring two excitation wavelengths display the typical reduction of the rel.cc. due to imperfect optical volume overlap. For combinations of green and red FPs, rel.cc. values below 60% were also observed with single-wavelength excitation (*Foo et al., 2012*; *Shi et al., 2009*), indicating that overlap of both excitation and detection volumes (the latter requiring FPs with similar emission spectra) is required to maximize the achievable cross-correlation (*Foo et al., 2012*). Notably, two-species SFSCS can not only successfully discriminate between mEGFP

178

and mEYFP, but is also applicable when using the red FPs mApple and mCherry2. These two FPs were successfully used in several FFS studies (*Dunsing et al., 2018*; *Foust et al., 2019*; *Sankaran et al., 2021*), providing the best compromise between brightness, maturation, and photostability among available red FPs, which generally suffer from reduced SNR compared to FPs emitting in the green or yellow part of the optical spectrum (*Dunsing et al., 2017*; *Dunsing et al., 2018*; *Cranfill et al., 2016*).

In comparison to sc-FLCCS, it may be more robust to discriminate fluorophores based on spectra rather than lifetimes, which can be strongly affected by FRET (*Štefl et al., 2020*). The emission spectra of the FPs utilized in this study did not depend on cell lines or subcellular localization (*Figure 5—figure supplement 1*) and showed no (mEGFP, mEYFP) or little (mApple, mCherry2) variation with pH over a range of 5.0–9.2 (*Figure 5—figure supplement 2*). For red FPs, specifically mApple, a red shift appeared at more acidic pH, in agreement with previous studies (*Hendrix et al., 2008*). This aspect should be considered for specific applications, for example, RSICS in the cytoplasm containing acidic compartments such as lysosomes. Generally, spectral approaches require accurate detection of photons in each spectral bin. A previous study using the same detection system reported intrinsic cross-talk between adjacent spectral bins (*Foust et al., 2019*). However, since the methodology presented here is based on temporal (SFSCS) or spatial (RSICS) correlation (both excluding the correlation at zero time or spatial lag), this issue can be neglected in our analysis.

A major limitation of SFSCS is the reduced SNR of the CFs (see *Figure 1*, *Figure 3—figure supplement 3*) caused by the statistical filtering of the signal emitted by spectrally overlapping fluorophore species (see, e.g., *Figure 4—figure supplement 1*). This limitation applies to all FFS methods that discriminate different fluorophore species based on spectral (e.g., FSCS [*Benda et al., 2014*], RSICS [*Schrimpf et al., 2018*]) or lifetime patterns (e.g., sc-FLCCS [*Štefl et al., 2020*]). The increase in noise depends on the spectral (or lifetime) overlap of different species and is more prominent for species that completely lack 'pure' channels, that is, detection channels in which the majority of photons can be univocally assigned to a single species (*Schrimpf et al., 2018*). In sc-FLCCS, this issue particularly compromises the SNR of short lifetime species (*Štefl et al., 2020*) since photons of longer lifetime species are detected in all 'short lifetime' channels at substantial relative numbers. In these conditions, sc-FLCCS could not provide reliable results with sixfold (or higher) difference in relative protein abundance, even though the lower abundant protein was tagged with the brighter, longer lifetime FP (*Štefl et al., 2020*). Similarly in SFSCS, CFs corresponding to mEYFP or mCherry2 were most prone to noise (*Figure 1C and F*) since all channels that contain, for example, mEYFP signal also contain mEGFP signal (*Figure 1—figure supplement 1*). In our experiments, cross-talk-free SFSCS analysis with two species excited with a single excitation wavelength could be performed for relative intensity levels as low as 1:10 (mEGFP/mEYFP) or 1:5 (mApple/mCherry2). In this range, SFSCS not only enabled the quantification of protein interactions via cross-correlation analysis, but also yielded correct estimates of protein diffusion dynamics and oligomerization at the PM. An improvement of the allowed relative concentration range can be achieved by using brighter or more photostable fluorophores, for example, organic dyes, compensating for reduced SNR due to statistical filtering. Alternatively, FP tags could be selected based on proteins' oligomerization state. For example, monomeric proteins exhibiting low molecular brightness should be tagged with fluorophores that are less prone to noise. It should be noted that the limitation of reduced SNR due to excess signal from another species also applies to conventional dual-color FCCS: bleed-through from green to red channels can be corrected on average, but reduces the SNR in red channels (*Bacia et al., 2012*), unless more sophisticated schemes such as pulsed interleaved excitation (*Müller et al., 2005*; *Hendrix et al., 2013*) are applied.

Having demonstrated that two-species SFSCS is feasible with a single excitation wavelength in the green (mEGFP, mEYFP) or red (mApple, mCherry2) part of the visible spectrum, we finally implemented three- and four-species SFSCS as well as four-species RSICS. These extensions do not further compromise the SNR of CFs detected for mEGFP and mEYFP (see *Figure 3—figure supplement 3A,B*), but may additionally reduce the SNR of CFs corresponding to red FPs (in particular when mEGFP and/or mEYFP concentration is much higher than that of red FPs, *Figure 3—figure supplement 3C*). For this reason, three- and four-species analysis was restricted to cells with relative average intensity levels of 1:5 or less between species with adjacent emission spectra. In this range, the increase in noise due to statistical filtering was moderate, benefitting from the fairly large spectral separation of green/yellow and red emission (*Figure 3—figure supplement 3*). In addition, the higher molecular brightness of mApple (compared to mCherry2) compensated for the larger overlap

179

of this FP with the tail of mEYFP emission. The excitation power for red FPs was generally limited by the lower photostability of mApple, which could be responsible for consistently lower rel.cc. values of mEGFP or mEYFP with mApple than with mCherry2. Nevertheless, four-species SFSCS and RSICS could successfully resolve different combinations of strongly overlapping FP hetero-oligomers, for example, a mixture of mEGFP-mCherry2 and mEYFP-mApple heterodimers, at the PM or in the cytoplasm of cells. To explore the interaction of four different FP-tagged proteins, four-species FFS may substantially reduce the experimental effort because all pair-wise interactions can be quantified in a single measurement (instead of six separate conventional two-species FCCS measurements). Yet, weak interaction of proteins, that is, a low amount of hetero-complexes compared to a high amount of unbound proteins, may not be detectable due to the large noise of the CCF in this case. The SNR might be further compromised by slow FP maturation or dark FP states, limiting the amount of complexes that simultaneously emit fluorescence of all bound FP species (*Dunsing et al., 2018*). Ultimately, the mentioned limitations currently restrict SFSCS and RSICS to four FP species. The approaches would thus strongly benefit from a multiparametric analysis. For instance, combining spectral and lifetime detection schemes would provide additional contrast for photons detected in the same spectral bin. This improvement could expand the range of detectable relative concentrations or might allow further multiplexing of FFS.

Conventional two-color scanning FCCS has been previously applied to quantify receptor-ligand interactions in living zebrafish embryos (*Ries et al., 2009b*) and CRISPR/Cas9 edited cell lines to study such interactions at endogenous protein level (*Eckert et al., 2020*). SFSCS is thus directly applicable in the complex environment of living multicellular organisms. In this context, spectral information could be further exploited to separate low signal levels of endogenously expressed, fluorescently tagged proteins from autofluorescence background.

As a first biological application of SFSCS, we investigated the interaction of IAV matrix protein M2 with two cellular host factors: the tetraspanin CD9 and the autophagosome protein LC3. We observed strong association of LC3 with M2, and consequent recruitment of LC3 to the PM (*Figure 3—figure supplement 4*), in agreement with previous in vitro and localization studies (*Beale et al., 2014*). Interestingly, molecular brightness analysis reported oligomerization (dimers to tetramers) of M2, but indicated a monomeric state of LC3 at the PM, that is, binding of LC3 to M2 in an apparent stoichiometry of 1:2 to 1:4. However, each M2 monomer provides a binding site for LC3 in the cytoplasmic tail (*Claridge et al., 2020*). A more detailed analysis of our data showed that in the analyzed cells (i.e., cells showing clear membrane recruitment of LC3, *Figure 3—figure supplement 4A*,B), the PM concentration of LC3 was on average only 30% compared to that of M2 (*Figure 3—figure supplement 4C*), although both proteins were expressed in comparable amounts in the sample in general. This suggests that not all potential binding sites in the cytoplasmic tail of M2 may be available to fluorescently tagged LC3, either due to binding of endogenous LC3, other cellular host factors, or steric hindrance. In contrast to the case of LC3, we did not detect significant binding of M2 with the tetraspanin CD9, a protein that was previously shown to be incorporated into IAV virions and supposedly plays a functional role during the infection process (*Shaw et al., 2008*; *Hutchinson, 2014*). Of note, we cannot exclude the possibility that the FP tag at the C-terminus of CD9 might hamper interactions with M2, in the specific case of M2-CD9 interaction being mediated by the C-terminal cytoplasmic tails of the two proteins. In future studies, the approach presented here may be used to further elucidate the complex interaction network of viral proteins, for example, matrix protein 1 (M1) (*Hilsch et al., 2014*), M2, HA, and neuraminidase, cellular host factors, and PM lipids (*Bobone et al., 2017*) during the assembly process of IAV at the PM of living cells (*Rossman and Lamb, 2011*).

Finally, we demonstrated that RSICS allows the quantification of the stoichiometry of higher order molecular complexes, based on molecular brightness analysis for each FP species. As example of an application in a biological context, we determined the stoichiometry of the IAV PC. Our data provide strong evidence for a 2:2:2 stoichiometry of the PC subunits PA, PB1, and PB2, that is, dimerization of heterotrimeric PCs. Such interactions were previously proposed based on experiments in solution using X-ray crystallography and cryo-electron microscopy (*Fan et al., 2019*), co-immunoprecipitation assays (*Jorba et al., 2008*; *Nilsson-Payant et al., 2018*), as well as single-channel brightness analysis of FCCS data (for the PA subunit) (*Huet et al., 2010*). Intermolecular interactions in the PC are hypothesized to be required for the initiation of vRNA synthesis during replication of the viral genome (*Fan et al., 2019*; *Chen et al., 2019*). The results presented here provide the first quantification of

180

these interactions in living cells and a direct estimate of the stoichiometry of PCs in the cell nucleus. The formation of ternary PC complexes in these samples could be extrapolated from the observed high rel.cc. values for all three pair combinations, indicating very low amounts of unbound PA, PB1, or PB2 and higher order interactions (see Appendix 1, Section A1.1 for additional details). Furthermore, this observation could also be directly confirmed by performing, for the first time in living cells, a triple-correlation analysis (TRICS), indicating the presence of a considerable amount of PA-PB1-PB2 complexes. It is worth noting though that the detection of coincident triple fluctuations is prone to considerable noise and thus still limited to molecular complexes present at low concentration and characterized by high molecular brightness for each fluorophore species (*Ridgeway et al., 2012a*; *Ridgeway et al., 2012b*).

Of note, the RSICS approach presented here provides for the first time simultaneous information on molecular interactions, molecular brightness (and thus stoichiometry), diffusion dynamics, and concentration for all three complex subunits. This specific feature opens the possibility of a more in-depth analysis. For example, it is possible to quantify the relative cross-correlation of two subunits, e.g. PA and PB2, as a function of the relative concentration of the third subunit, for example, PB1 (*Figure 6—figure supplement 1A*). Similarly, molecular brightness and diffusion coefficients can be analyzed as a function of the abundance of each subunit (*Figure 6—figure supplement 1B,C*). With this approach, it is therefore possible to distinguish specific molecular mechanisms, such as inefficient PA-PB2 interactions in the presence of low PB1 concentration or efficient heterotrimer dimerization when all subunits are present at similar concentrations. The employed experimental scheme offers a powerful tool for future studies, exploring, for example, interaction of the PC with cellular host factors or the development of inhibitors that could interfere with the assembly process of the complex, as a promising therapeutic target for antiviral drugs (*Massari et al., 2021*).

Limitations

We summarize in this section the main instrumental, conceptual, and sample-related limitations and requirements connected to the multicolor FFS approach employed in this work.

Instrumental limitations

To perform multicolor FFS, a spectral photon counting detector system is required. Alternatively, the same conceptual approach can be implemented based on detection of fluorophore lifetimes rather than emission spectra (*Štefl et al., 2020*). For both approaches, two excitation wavelengths are currently required for three- and four-species detection. As a consequence, the overlap of excitation volumes of the two laser lines might be limited, thus reducing the maximum achievable rel.cc., as previously discussed for standard FCCS (*Foo et al., 2012*). For the instrumentation utilized in the present work, the time resolution for SFSCS was limited to 0.5 ms. However, RSICS can be applied to detect faster dynamics, as demonstrated by experiments on cytoplasmic proteins.

Conceptual limitations

FFS approaches generally require the proteins of interest to diffuse and thus cannot be applied in the case of immobile or strongly clustered targets (*Ciccotosto et al., 2013*). The statistical filtering of spectrally overlapping FP emission leads to increased noise of CFs. FPs lacking 'pure' channels, for example, mEYFP when co-expressed with mEGFP, are most compromised. As a consequence, the approach provides reliable results only in a certain range of relative protein abundance. For the presented three- and four-species SFSCS and RSICS experiments, relative signals were limited to 1:5 (i.e., range of 1:5 to 5:1). The given ratios characterize the minimum acceptable signal ratio for spectrally neighboring fluorescent species, for the FPs utilized in this work. The set of FPs may be optimized for specific applications. The increase in noise as a result of filtering may prevent detection of weak protein interactions due to the low SNR of CCFs in this case. Furthermore, detection of co-fluctuations of three FP species based on triple correlation is prone to considerable noise and thus limited to detection of molecular complexes present at low concentrations or characterized by high molecular brightness, as discussed previously for in vitro studies (*Ridgeway et al., 2012a*).

Sample-related limitations

To apply multicolor FFS, multiple FP species (e.g., FP-tagged proteins of interest) have to be expressed in the same cell, in relative amounts compatible with the ranges given above. Since tagging of proteins of interest with FPs is required (or other labels such as organic dyes, if the labeling ratio can be precisely determined), potential hindrance of protein interactions by the tags should be carefully evaluated. Typical measures consist in, for example, testing different positions for the tag in the protein of interest, trying different linkers with varying length and flexibility, using tags with smaller sizes, or bio-orthogonal labeling (*Huang et al., 2014*; *Işbilir et al., 2021*). The emission spectra of most FPs are typically well-defined, but might depend on physicochemical conditions (e.g., mApple showed red-shifted emission at more acidic pH). Differences between calibrated and actual spectra could induce errors in filtering and cause residual cross-talk between different FP species (*Schrimpf et al., 2018*). Therefore, the same optical components (e.g., filters, beam splitters) and experimental conditions (e.g., laser powers, sample media, dishes) should be used to calibrate the spectra. Due to lower photostability and quantum yield, red FPs suffer from reduced SNR and, thus, larger variation of parameter estimates compared to green FPs. This is most evident for mCherry2 in four-species applications. In addition, molecular brightness and cross-correlation analysis are compromised by FP maturation. Slow maturation will lead to an increased fraction of dark states, increasing the noise of CCFs and reducing the dynamic range for brightness analysis of protein oligomers (*Dunsing et al., 2018*; *Foo et al., 2012*). Cross-correlation analysis may be further affected by FRET between different FP species, potentially reducing experimental rel.cc. values (*Foo et al., 2012*). This should be carefully evaluated, for example, by analyzing molecular brightness values relative to monomeric references, for both the proteins of interest and FP-hetero-oligomers used to calibrate the maximum achievable rel.cc. FRET artifacts can be minimized using appropriate linkers, for example, rigid linker peptides, as presented here.

Conclusions

In summary, we present here three-species and, for the first time, four-species measurements of protein interactions and diffusion dynamics in living cells. This is achieved by combining and extending existing FFS techniques with spectrally resolved detection. The presented approaches provide a powerful toolbox to investigate complex protein interaction networks in living cells and organisms.

Materials and methods

Cell culture and sample preparation

Human embryonic kidney (HEK) cells from the 293T line (purchased from ATCC, Manassas, VA; CRL-3216TM) and human epithelial lung cells A549 (ATCC, CCL-185TM) were cultured in Dulbecco's modified Eagle medium (DMEM) with the addition of fetal bovine serum (10%), L-glutamine (2 mM), penicillin (100 U/mL), and streptomycin (100 µg/mL). Mycoplasma contamination tests and morphology tests were performed every 3 months and 2 weeks, respectively. Cells were passaged every 3–5 days, no more than 15 times. All solutions, buffers, and media used for cell culture were purchased from PAN-Biotech (Aidenbach, Germany).

For microscopy experiments, 3×10^5 (HEK) or 4×10^5 (A549) cells were seeded in 35 mm #1.5 optical glass-bottom dishes (CellVis, Mountain View, CA) 24 hr before transfection. Cells were transfected 16–24 hr prior to the experiment using between 50 ng and 150 ng plasmid per dish with Turbofect (HEK) or Lipofectamin3000 (A549) according to the manufacturer's instructions (Thermo Fisher Scientific, Waltham, MA). Briefly, plasmids were incubated for 20 min with 3 µl Turbofect diluted in 50 µl serum-free medium, or 15 min with 2 µl P3000 and 2 µl Lipofectamine3000 diluted in 100 µl serum-free medium, and then added dropwise to the cells. For spectral imaging at different pH values, culture medium was exchanged with buffer containing 140 mM NaCl, 2.5 mM KCl, 1.8 mM CaCl$_2$, 1.0 mM MgCl$_2$, and 20 mM HEPES with pH ranging from 5.0 to 9.2.

Plasmids and cloning

The plasmids encoding FPs linked to a myristoylated and palmitoylated peptide (mp-mEGFP, mp-mEYFP, mp-mCherry2, mp-2x-mEGFP), the full-length IAV A/chicken/FPV/Rostock/1934 hemagglutinin (HA) construct HA-mEGFP, and the plasmids for cytosolic expression of mEGFP, mEYFP,

mCherry2, 2x-mEGFP, 2x-mEYFP, 2x-mCherry2, and mCherry2-mEGFP heterodimers were previously described (*Dunsing et al., 2018*) and are available on Addgene.

For the cloning of all following constructs, standard PCRs with custom-designed primers were performed, followed by digestion with fast digest restriction enzymes and ligation with T4-DNA-Ligase according to the manufacturer's instructions. All enzymes and reagents were purchased from Thermo Fisher Scientific.

To obtain mp-mEGFP-mEYFP, a mp-mEGFP_pcDNA3.1+ vector was first generated by amplifying mp-mEGFP insert from the respective plasmid, and inserting it into pcDNA3.1+ vector (obtained from Thermo Fisher Scientific) by digestion with NheI and AflII. Afterwards, mEYFP was amplified from mp-mEYFP and inserted into mp-mEGFP_pcDNA3.1+ using digestion with AflII and KpnI. To clone mp-mEYFP-(L)-mEGFP (a plasmid encoding for mp-mEYFP-mEGFP heterodimers with a long rigid linker peptide [L] between FPs), a mp-mEYFP-(L)_pcDNA3.1+ construct was first generated by amplifying mp-mEYFP from the respective plasmid with primers encoding for the rigid linker (see *Supplementary file 1a* for linker peptide sequences) and inserting it into pcDNA3.1+ vector by digestion with NheI and AflII. Then, mEGFP was inserted from mEGFP-(L)_pcDNA3.1+ (see below) by digestion with KpnI and BamHI. To generate mp-mEYFP-(L)-mCherry2-(L)-mEGFP, a mp-mEYFP-(L)-mCherry2-(L) construct was first cloned by amplifying mCherry2 from a mCherry2-C1 vector (a gift from Michael Davidson, Addgene plasmid # 54563) and inserting it into mp-mEYFP-(L)_pcDNA3.1+ by digestion with AflII and KpnI. Subsequently, mEGFP was inserted from mEGFP-(L)_pcDNA3.1+ (see below) using KpnI and BamHI restriction. The mp-mEYFP-(L)-mCherry2-(L)-mEGFP-(L)-mApple plasmid was generated by inserting an mEGFP-(L)-mApple cassette into mp-mEYFP-(L)-mCherry2-(L) by digestion with KpnI and EcoRI. The mEGFP-(L)-mApple construct was cloned beforehand by amplifying mApple from PMT-mApple (*Sankaran et al., 2021*) (a kind gift from Thorsten Wohland) and inserting it into mEGFP-(L)_pcDNA3.1+ by digestion with BamHI and EcoRI. The mEGFP-(L)_pcDNA3.1+ plasmid was obtained by amplifying mEGFP from an mEGFP-N1 vector (a gift from Michael Davidson, Addgene plasmid #54767) (using a primer encoding a long rigid linker sequence) and inserting it into a pcDNA3.1+ vector by KpnI and BamHI restriction. The mApple_pcDNA3.1+ plasmid was generated by amplifying mApple from PMT-mApple and inserting it into pcDNA3.1+ vector by digestion with KpnI and BamHI. The mp-mApple plasmid was generated by amplifying mApple from PMT-mApple and inserting it into mp-mCherry2 by digestion with AgeI and BsrGI. To clone mp-mCherry2-(L)-mApple, mp-mCherry2-(L)_pcDNA3.1+ plasmid was first generated by amplifying mp-mCherry2 (using a primer encoding a long rigid linker sequence) and inserting it into pcDNA3.1+ using NheI and KpnI restriction. Afterwards, mApple was amplified from PMT-mApple and inserted into mp-mCherry2-(L)_pcDNA3.1+ by digestion with KpnI and EcoRI. The mp-mCherry2-mEGFP plasmid was cloned by inserting mp from mp-mEGFP into mCherry2-mEGFP using digestion with NheI and AgeI. The plasmids mEYFP-(L)-mApple, mEYFP-(L)-mCherry2-(L)-mEGFP, and mEYFP-(L)-mCherry2-(L)-mEGFP-(L)-mApple were generated by amplifying the respective insert from mp-mEYFP-(L)-mApple, mp-mEYFP-(L)-mCherry2-(L)-mEGFP, or mp-mEYFP-(L)-mCherry2-(L)-mEGFP-(L)-mApple and inserting it into pcDNA3.1+ vector by digestion with NheI and XbaI. The mp-mEYFP-(L)-mApple construct was cloned beforehand by inserting mApple from mEGFP-(L)-mApple into mp-mEYFP-(L)_pcDNA3.1+ using restriction by BamHI and EcoRI.

The CD9-mEGFP plasmid was cloned by amplifying CD9 from pCMV3-CD9 (obtained from SinoBiological #HG11029-UT, encoding human CD9) and inserting into mEGFP-C1 vector using restriction by HindIII and BamHI. The LC3-mEYFP plasmid was generated by inserting mEYFP from mEYFP-C1 vector into pmRFP-LC3 (*Kimura et al., 2007*) (a gift from Tamotsu Yoshimori, Addgene plasmid #21075, encoding rat LC3) using digestion with NheI and BglII. Plasmid M2-mCherry2 (mCherry2 fused to the extracellular terminus of matrix protein 2 from influenza A/chicken/FPV/Rostock/1934) was cloned by inserting mCherry2 from an mCherry2-C1 vector into mEYFP-FPV-M2 (a kind gift from Michael Veit) using restriction by AgeI and BsrGI. Plasmids encoding IAV polymerase subunits PA-mEYFP, PB1-mEGFP, and PB2-mCherry2 (from influenza A/human/WSN/1933) were a kind gift from Andreas Herrmann.

The plasmids GPI-mEYFP and GPI-EGFP were a kind gift from Roland Schwarzer. GPI-mEGFP was cloned by amplifying mEGFP from an mEGFP-N1 vector and inserting it into GPI-EGFP using digestion with AgeI and BsrGI. To generate GPI-mApple and GPI-mCherry2, mApple and mCherry2 inserts

183

were amplified from PMT-mApple and mCherry2-C1, respectively, and inserted into GPI-mEYFP using restriction by AgeI and BsrGI.

All plasmids generated in this work will be made available on Addgene.

Confocal microscopy system

SFSCS and RSICS were performed on a Zeiss LSM880 system (Carl Zeiss, Oberkochen, Germany) using a 40×, 1.2 NA water immersion objective. For two-species measurements, samples were excited with a 488 nm argon laser (mEGFP, mEYFP) or a 561 nm diode laser (mCherry2, mApple). For three- and four-species measurements, both laser lines were used. To split excitation and emission light, 488 nm (for two-species measurements with mEGFP and mEYFP) or 488/561 nm (for measurements including mCherry2 and mApple) dichroic mirrors were used. Fluorescence was detected in spectral channels of 8.9 nm (15 channels between 491 nm and 624 nm for two-species measurements on mEGFP, mEYFP; 14 channels between 571 nm and 695 nm for two-species measurements on mCherry2, mApple; 23 channels between 491 nm and 695 nm for three- and four-species measurements) on a 32-channel GaAsP array detector operating in photon counting mode. All measurements were performed at room temperature.

Scanning fluorescence spectral correlation spectroscopy (SFSCS)

Data acquisition

For SFSCS measurements, line scans of 256 × 1 pixels (pixel size 80 nm) was performed perpendicular to the PM with 403.20 µs scan time. This time resolution is sufficient to reliably detect the diffusion dynamics observed in the samples described in this work (i.e., diffusion times ~6–60 ms). Typically, 450,000–600,000 lines were acquired (total scan time ca. 2.5–4 min). Laser powers were adjusted to keep photobleaching below 50% at maximum for all species (average signal decays were ca. 10% for mEGFP, 30% for mEYFP, 40% for mApple, and 20% for mCherry2). Typical excitation powers were ca. 5.6 µW (488 nm) and ca. 5.9 µW (561 nm). Spectral scanning data were exported as TIFF files (one file per three spectral channels), imported, and analyzed in MATLAB (The MathWorks, Natick, MA) using custom-written code (*Dunsing and Chiantia, 2021*).

Data analysis

SFSCS analysis followed the scanning FCS scheme described previously (*Ries and Schwille, 2006*; *Dunsing and Chiantia, 2018*), combined with spectral decomposition of the fluorescence signal by applying the mathematical framework of FLCS and FSCS (*Benda et al., 2014*; *Böhmer et al., 2002*). Briefly, all scan lines were aligned as kymographs and divided in blocks of 1000 lines. In each block, lines were summed up column-wise and across all spectral channels, and the lateral position with maximum fluorescence was determined. This position defines the membrane position in each block and was used to align all lines to a common origin. Then, all aligned line scans were averaged over time and fitted with a Gaussian function. The pixels corresponding to the PM were defined as pixels within ±2.5 SD of the peak. In each line and spectral channel, these pixels were integrated, providing membrane fluorescence time series $F^k(t)$ in each spectral channel k (m channels in total). These time series were then temporally binned with a binning factor of 2 and subsequently transformed into the contributions $F_i(t)$ of each fluorophore species i (i.e., one fluorescence time series for each species) by applying the spectral filtering algorithm presented by *Benda et al., 2014*:

$$F_i(t) = \sum_{k=1}^{m} f_i^k F^k(t).$$

Spectral filter functions f_i^k were calculated based on reference emission spectra p_i^k that were determined for each individual species i from single species measurements performed on each day using the same acquisition settings:

$$f_i^k = \left(\left[\hat{M}^T D \hat{M} \right]^{-1} \hat{M} D \right)_{ik}.$$

Here, $\hat{M}$ is a matrix with elements $M_{ki} = p_i^k$ and D is a diagonal matrix, $D = diag \left[1/ \left\langle F^k(t) \right\rangle \right]$.

In order to correct for depletion due to photobleaching, a two-component exponential function was fitted to the fluorescence time series for each spectral species, $F_i(t)$, and a correction formula

was applied (*Dunsing and Chiantia, 2018*; *Ries et al., 2009a*). Finally, ACFs and pair-wise CCFs of fluorescence time series of species i and j were calculated as follows using a multiple tau algorithm:

$$G_{i,j}\left(\tau\right) = \frac{\langle \delta F_i(t) \delta F_j(t+\tau)\rangle}{\langle F_i(t)\rangle \langle F_j(t)\rangle},$$

where $\delta F_i\left(t\right) = F_i\left(t\right) - \langle F_i\left(t\right)\rangle$.

To avoid artifacts caused by long-term instabilities or single bright events, CFs were calculated segment-wise (10–20 segments) and then averaged. Segments showing clear distortions (typically less than 25% of all segments) were manually removed from the analysis (*Dunsing and Chiantia, 2018*).

A model for two-dimensional diffusion in the membrane and Gaussian focal volume geometry (*Ries and Schwille, 2006*) was fitted to all CFs:

$$G\left(\tau\right) = \frac{1}{N}\left(1 + \frac{\tau}{\tau_d}\right)^{-1/2}\left(1 + \frac{\tau}{\tau_d S^2}\right)^{-1/2}$$

To ensure convergence of the fit for all samples (i.e., ACFs and CCFs of correlated and uncorrelated data), positive initial fit values for the particle number N and thus $G\left(\tau\right)$ were used. In the case of uncorrelated data, that is, for CFs fluctuating around zero, this constraint can generate low, but positive correlation amplitudes due to noise. This issue can be circumvented, if needed, by selecting adaptive initial values, for example, obtaining the initial amplitude value from averaging the first points of the CFs (see *Figure 3—figure supplement 2*).

To calibrate the focal volume, point FCS measurements with Alexa Fluor 488 (Thermo Fisher Scientific) dissolved in water at 20 nM were performed at the same laser power. The structure parameter S was fixed to the average value determined in calibration measurements (typically between 4 and 8).

From the amplitudes of ACFs and CCFs, rel.cc. values were calculated for all cross-correlation combinations:

$$rel.cc._{i,j} = max\left\{\frac{G_{i,j}(0)}{G_i(0)}, \frac{G_{i,j}(0)}{G_j(0)}\right\},$$

where $G_{i,j}(0)$ is the amplitude of the CCF of species i and j, and $G_i(0)$ the amplitude of the ACF of species i. The molecular brightness was calculated by dividing the mean count rate detected for each species i by the particle number N_i determined from the fit: $B_i = \frac{\langle F_i(t)\rangle}{N_i}$. From this value, an estimate of the oligomeric state ε_i was determined by normalizing B_i by the average molecular brightness $B_{i,1}$ of the corresponding monomeric reference, and, subsequently, by the fluorescence probability $p_{f,i}$ for species i: $\varepsilon_i = \frac{\frac{B_i}{B_{i,1}} - 1}{p_{f,i}} + 1$, as previously derived (*Dunsing et al., 2018*). The p_f was previously characterized for several FPs (for example, ca. 60% for mCherry2) (*Dunsing et al., 2018*).

The SNR of the ACFs was calculated by dividing ACF values by their variance and summing over all points of the ACF. The variance of each point of the ACF was calculated in the multiple tau algorithm (*Wohland et al., 2001*).

To ensure statistical robustness of the SFSCS analysis and sufficient SNR, the analysis was restricted to cells expressing all fluorophore species in comparable amounts, that is, relative average signal intensities of less than 1:10 (mEGFP/mEYFP) or 1:5 (mApple/mCherry2, three- and four-species measurements).

Raster spectral image correlation spectroscopy (RSICS)
Data acquisition

RSICS measurements were performed as previously described (*Ziegler et al., 2020*). Briefly, 200–400 frames of 256 × 256 pixels were acquired with 50 nm pixel size (i.e., a scan area of 12.83 × 12.83 μm² through the midplane of cells), 2.05 μs or 4.10 μs pixel dwell time, 1.23 ms or 2.46 ms line, and 314.57 ms or 629.14 ms frame time (corresponding to ca. 2 min total acquisition time per measurement). Samples were excited at ca. 5.6 μW (488 nm) and 4.6 μW (561 nm) excitation powers, respectively. Laser powers were chosen to maximize the signal emitted by each fluorophore species but keeping photobleaching below 50% at maximum for all species (average signal decays were ca. 10% for mEGFP, 15% for mEYFP, 40% for mApple, and 25% for mCherry2). Typical counts per molecule were ca. 25 kHz for mEGFP (G), 15–20 kHz for mEYFP (Y), 20–30 kHz for mApple (A), and 5–10 kHz

185

for mCherry2 (Ch2). To obtain reference emission spectra for each individual fluorophore species, four image stacks of 25 frames were acquired at the same imaging settings on single-species samples on each day.

Data analysis

RSICS analysis followed the implementation introduced recently (*Schrimpf et al., 2018*), which is based on applying the mathematical framework of FLCS and FSCS (*Benda et al., 2014*; *Böhmer et al., 2002*) to RICS. Four-dimensional image stacks $I(x, y, t, k)$ (time-lapse images acquired in k spectral channels) were imported in MATLAB (The MathWorks) from CZI image files using the Bioformats package (*Linkert et al., 2010*) and further analyzed using custom-written code (*Dunsing and Chiantia, 2021*). First, average reference emission spectra were calculated for each individual fluorophore species from single-species measurements. Four-dimensional image stacks were then decomposed into three-dimensional image stacks $I_i(x, y, t)$ for each species i using the spectral filtering algorithm presented by *Schrimpf et al., 2018* (following the mathematical framework given in the SFSCS section). Cross-correlation RICS analysis was performed in the arbitrary region RICS framework (*Hendrix et al., 2016*). To this aim, a polygonal region of interest (ROI) was selected in the time- and channel-averaged image frame containing a homogeneous region in the cytoplasm (four-species measurements on FP constructs) or nucleus (three-species measurements on polymerase complex and related controls) of cells. This approach allowed excluding visible intracellular organelles or pixels in the extracellular space, but to include all pixels containing signal from the nucleus of cells. In some cells, nucleus and cytoplasm could not be clearly distinguished. In these cases, all pixels were selected and minor brightness differences between cytoplasm and nucleus, previously found to be ca. 10% (*Dunsing et al., 2018*), were neglected. Image stacks were further processed with a high-pass filter (with a moving four-frame window) to remove slow signal variations and spatial inhomogeneities. Afterwards, RICS spatial ACFs and pair-wise CCFs were calculated for each image stack and all combinations of species i, j (e.g., G and Y, G and Ch2, Y and Ch2 for three species), respectively (*Schrimpf et al., 2018*; *Hendrix et al., 2016*):

$$G_i(\xi, \psi) = \frac{\langle \delta I_i(x,y) \delta I_i(x+\xi, y+\psi) \rangle}{\langle I_i(x,y) \rangle^2},$$

$$G_{i,j}(\xi, \psi) = \frac{\langle \delta I_i(x,y) \delta I_j(x+\xi, y+\psi) \rangle}{\langle I_i(x,y) \rangle \langle I_j(x,y) \rangle},$$

where $\delta I_i(x, y) = I_i(x, y) - \langle I_i(x, y) \rangle$.

ACF amplitudes were corrected as described in *Hendrix et al., 2016* to account for the effect of the high-pass filter. A three-dimensional normal diffusion RICS fit model (*Digman et al., 2005*; *Digman et al., 2009b*) for Gaussian focal volume geometry (with particle number N, diffusion coefficient D, waist ω_0, and structure parameter S as free fit parameters) was then fitted to both ACFs and CCFs:

$$G(\xi, \psi) = \frac{1}{N} \left(1 + \frac{4D|(\xi-\xi_0)\tau_p + \psi\tau_l|}{\omega_0^2}\right)^{-1} \left(1 + \frac{4D|(\xi-\xi_0)\tau_p + \psi\tau_l|}{\omega_0^2 S^2}\right) exp\left(-\frac{\delta s^2 \left((\xi-\xi_0)^2 + \psi^2\right)}{\omega_0^2 + 4D|(\xi-\xi_0)\tau_p + \psi\tau_l|}\right),$$

where τ_p, τ_l denote the pixel dwell and line time and δs the pixel size. The free parameter ξ_0 (starting value = 13 pixels) was used to determine which CCFs were too noisy (i.e., $\xi_0 > 4$ pixels) to obtain meaningful parameters (typically in the absence of interaction). For ACF analysis, ξ_0 was set to 0. To remove shot noise contributions, the correlation at zero lag time was omitted from the analysis.

From the fit amplitudes of the ACFs and CCFs, rel.cc. values were calculated:

$$rel.cc._{i,j} = max\left\{\frac{G_{i,j}(0,0)}{G_i(0,0)}, \frac{G_{i,j}(0,0)}{G_j(0,0)}\right\},$$

where $G_{i,j}(0,0)$ is the amplitude of the CCF of species i and j, and $G_i(0,0)$ the ACF amplitude of species i. In the case of non-meaningful convergence of the fit to the CCFs (i.e., $\xi_0 > 4$ pixels), the rel.cc. was simply set to 0. To ensure statistical robustness of the RSICS analysis and sufficient SNR, the analysis was restricted to cells expressing all fluorophore species in comparable amounts, that is, relative average signal intensities of less than 1:6 for all species (in all RSICS experiments). The molecular brightness of species i was calculated by dividing the average count rate in the ROI by the particle

number determined from the fit to the ACF: $B_i = \frac{\langle I_i(t) \rangle}{N_i}$. From this value, an estimate of the oligomeric state ε_i was determined by normalizing B_i by the average molecular brightness $B_{i,1}$ of the corresponding monomeric reference, and, subsequently, by the fluorescence probability $p_{f,i}$ for species i: $\varepsilon_i = \frac{\frac{B_i}{B_{i,1}} - 1}{p_{f,i}} + 1$, as previously derived (**Dunsing et al., 2018**). The p_f was calculated from the obtained molecular brightness $B_{i,2}$ of FP homodimers of species i: $p_f = \frac{B_{i,2}}{B_{i,1}} - 1$ (**Dunsing et al., 2018**).

TRICS analysis

TRICS was performed using three-dimensional RSICS image stacks $I_i(x, y, t)$ detected for three species i. First, the spatial 3CF was calculated:

where ξ_1, ξ_2 denote spatial lags along lines and ψ_1, ψ_2 along columns of the image stacks. Contributions from δI triplets containing at least two intensity values from the same pixel position were not included in the calculation in order to avoid shot-noise artifacts (since all channels are detected here by the same detector). From the resulting four-dimensional matrix, a two-dimensional representation was calculated by introducing coordinates a, b for the effective spatial shift between signal fluctuations evaluated for the two-species combinations:

$$a = ceil\left(\sqrt{\xi_1^2 + \xi_2^2}\right),$$

$$b = ceil\left(\sqrt{\psi_1^2 + \psi_2^2}\right).$$

The four-dimensional triple-correlation matrix was transformed into a two-dimensional representation $G_{3C}(a,b)$ by rounding up a and b to integer values and averaging all points with the same rounded spatial shift. For example, for a one-pixel shift along a line in one FP channel and a one-pixel shift along a column in the third FP channel (i.e., $\xi_1 = 1, \psi_1 = 0, \xi_2 = 0, \psi_2 = 1$, $a = b = 1$. $G_{3C}(1,1)$ also includes in its averaged value the other seven correlation values corresponding, for example, to $(\xi_1 = 0, \psi_1 = 1, \xi_2 = 1, \psi_2 = 0)$, $(\xi_1 = 1, \psi_1 = 0, \xi_2 = 0, \psi_2 = -1)$, etc. As a further example, $G_{3C}(2,0)$ includes and averages only the two correlation values corresponding to $\psi_1 = \psi_2 = 0$ (i.e., no shift along columns) and $\xi_1 = -\xi_2 = \pm 1$ (i.e., a one-pixel shift along a line, in opposite directions for the two channels). Note that the combinations $(\psi_1 = \psi_2 = 0, \xi_1 = \pm 2, \xi_2 = 0)$ and $(c\psi_1 = \psi_2 = 0, \xi)$ would also result in $a = 2$ and $b = 0$, but these values were not included since they refer to a correlation between identical pixel positions (e.g., $\xi_2 = 0, \psi_2 = 0$) between two FP channels and would be influenced by shot-noise artifacts (see above).

To determine the triple-correlation amplitude $G_{3C}(0,0)$, the closest points (e.g., $G_{3C}(1,1)$, $G_{3C}(1,2)$, $G_{3C}(2,1)$, $G_{3C}(2,2)$, $G_{3C}(3,0)$) of the two-dimensional triple correlation were averaged as an (slightly underestimated) approximation of the amplitude value at (0,0). Note that we chose not to include $G_{3C}(2,0)$ because this point is the average of only two possible spatial shift combinations, resulting in large statistical noise. Also, the point $G_{3C}(0,3)$ was not included since it refers to shifts along columns (i.e., the slow scanning direction), which, in turn, are characterized by a steeper decrease in amplitude. Finally, for best visualization, G_{3C} is plotted for a and b values ≥ 1 (see **Figure 7** and **Appendix 1—figure 2**).

To account for reduction of the triple-correlation amplitude due to the high-pass filter, an empirical correction was applied based on simulated triple-correlation amplitudes with different sizes F of the moving window (see Appendix 1, Section A1.2 and **Appendix 1—figure 1**). Notably, applying this empirical correction to the auto- and cross-correlation amplitudes confirmed the previously introduced correction formula (see **Appendix 1—figure 1**), $G_{corr}(\xi, \psi) = \frac{F}{F-1} G(\xi, \psi)$ (**Hendrix et al., 2016**). The triple-correlation amplitude is related to the number of triple complexes N_{3C} (**Heinze et al., 2004**; **Palmer and Thompson, 1987**):

where N_i is the total number of proteins detected for species i. In analogy to the rel.cc., a relative triple correlation rel.3C. is defined, quantifying the fraction of triple complexes relative to the total number of proteins of the species that is present in the lowest concentration:

$$rel.3C. = max\left\{\frac{N_{3C}}{N_1}, \frac{N_{3C}}{N_2}, \frac{N_{3C}}{N_3}\right\} = \frac{3}{4} \frac{G_{3C}(0,0)}{G_1(0,0) G_2(0,0) G_3(0,0)} max\{G_1(0,0), G_2(0,0), G_3(0,0)\}$$

Statistical analyses

All data are displayed as scatter dot plots indicating mean values and SDs. Sample size is given in parentheses in each graph. Statistical significance was tested using Welch's corrected two-tailed Student's t-test in GraphPad Prism 7.0 (GraphPad Software) and p-values are given in figure captions.

Acknowledgements

Additional information

Funding

Author contributions

Valentin Dunsing, Conceptualization, Data curation, Formal analysis, Investigation, Methodology, Project administration, Resources, Software, Visualization, Writing - original draft, Writing – review and editing; Annett Petrich, Investigation, Resources, Writing – review and editing; Salvatore Chiantia, Conceptualization, Formal analysis, Funding acquisition, Methodology, Project administration, Resources, Software, Supervision, Visualization, Writing - original draft, Writing – review and editing

Author ORCIDs

Valentin Dunsing http://orcid.org/0000-0003-2482-1498
Annett Petrich http://orcid.org/0000-0002-2372-826X
Salvatore Chiantia http://orcid.org/0000-0003-0791-967X

Decision letter and Author response

Decision letter https://doi.org/10.7554/69687.sa1
Author response https://doi.org/10.7554/69687.sa2

Additional files

Supplementary files

• Supplementary file 1. Linker sequences for fluorescent protein (FP) hetero-oligomer constructs and day-to-day variability of molecular brightness values obtained three-species raster spectral image correlation spectrosopcy (RSICS). (a): Linker sequences of FP hetero-oligomer constructs. (b): Day-to-day variability of molecular brightness values obtained from three-species RSICS measurements.

• Transparent reporting form

Data availability

All data generated or analysed during this study are included in the manuscript and supporting files. Source data files have been provided for Figures 1-7. The analysis software is freely available on GitHub: https://github.com/VaDu8989/SpectralFFS.

References

Bacia K, Petrášek Z, Schwille P. 2012. Correcting for spectral cross-talk in dual-color fluorescence cross-correlation spectroscopy. *Chemphyschem* **13**: 1221–1231. DOI: https://doi.org/10.1002/cphc.201100801, PMID: 22344749

Beale R, Wise H, Stuart A, Ravenhill BJ, Digard P, Randow F. 2014. A LC3-interacting motif in the influenza A virus M2 protein is required to subvert autophagy and maintain virion stability. *Cell Host & Microbe* **15**: 239–247. DOI: https://doi.org/10.1016/j.chom.2014.01.006, PMID: 24528869

Benda A, Kapusta P, Hof M, Gaus K. 2014. Fluorescence spectral correlation spectroscopy (FSCS) for probes with highly overlapping emission spectra. *Optics Express* **22**: 2973–2988. DOI: https://doi.org/10.1364/OE.22.002973, PMID: 24663589

Bobone S, Hilsch M, Storm J, Dunsing V, Herrmann A, Chiantia S. 2017. Phosphatidylserine lateral organization influences the interaction of influenza virus matrix protein 1 with lipid membranes. *Journal of Virology* **91**: e00267-17. DOI: https://doi.org/10.1128/JVI.00267-17, PMID: 28356535

Böhmer M, Wahl M, Rahn HJ, Erdmann R, Enderlein J. 2002. Time-resolved fluorescence correlation spectroscopy. *Chemical Physics Letters* **353**: 439–445. DOI: https://doi.org/10.1016/S0009-2614(02)00044-1

Burkhardt M, Heinze KG, Schwille P. 2005. Four-color fluorescence correlation spectroscopy realized in a grating-based detection platform. *Optics Letters* **30**: 2266–2268. DOI: https://doi.org/10.1364/ol.30.002266, PMID: 16190439

Chen K-Y, Santos Afonso ED, Enouf V, Isel C, Naffakh N. 2019. Influenza virus polymerase subunits co-evolve to ensure proper levels of dimerization of the heterotrimer. *PLOS Pathogens* **15**: e1008034. DOI: https://doi.org/10.1371/journal.ppat.1008034, PMID: 31581279

Ciccotosto GD, Kozer N, Chow TTY, Chon JWM, Clayton AHA. 2013. Aggregation distributions on cells determined by photobleaching image correlation spectroscopy. *Biophysical Journal* **104**: 1056–1064. DOI: https://doi.org/10.1016/j.bpj.2013.01.009, PMID: 23473488

Claridge JK, Mohd-Kipli F, Florea A, Gate T, Schnell JR. 2020. Ph-dependent secondary structure propensity of the influenza A virus m2 cytoplasmic tail. *Biomolecular NMR Assignments* **14**: 157–161. DOI: https://doi.org/10.1007/s12104-020-09937-8, PMID: 32157574

Cranfill PJ, Sell BR, Baird MA, Allen JR, Lavagnino Z, de Gruiter HM, Kremers GJ, Davidson MW, Ustione A, Piston DW. 2016. Quantitative assessment of fluorescent proteins. *Nature Methods* **13**: 557–562. DOI: https://doi.org/10.1038/nmeth.3891, PMID: 27240257

Dahmane S, Doucet C, Le Gall A, Chamontin C, Dosset P, Murcy F, Fernandez L, Salas D, Rubinstein E, Mougel M, Nollmann M, Milhiet PE. 2019. Nanoscale organization of tetraspanins during HIV-1 budding by correlative DSTORM/AFM. *Nanoscale* **11**: 6036–6044. DOI: https://doi.org/10.1039/c8nr07269h, PMID: 30869094

Digman MA, Brown CM, Sengupta P, Wiseman PW, Horwitz AR, Gratton E. 2005. Measuring fast dynamics in solutions and cells with a laser scanning microscope. *Biophysical Journal* **89**: 1317–1327. DOI: https://doi.org/10.1529/biophysj.105.062836, PMID: 15908582

Digman MA, Dalal R, Horwitz AF, Gratton E. 2008. Mapping the number of molecules and brightness in the laser scanning microscope. *Biophysical Journal* **94**: 2320–2332. DOI: https://doi.org/10.1529/biophysj.107.114645, PMID: 18096627

Digman MA, Wiseman PW, Choi C, Horwitz AR, Gratton E. 2009a. Stoichiometry of molecular complexes at adhesions in living cells. *PNAS* **106**: 2170–2175. DOI: https://doi.org/10.1073/pnas.0806036106, PMID: 19168634

Digman MA, Wiseman PW, Horwitz AR, Gratton E. 2009b. Detecting protein complexes in living cells from laser scanning confocal image sequences by the Cross correlation raster image spectroscopy method. *Biophysical Journal* **96**: 707–716. DOI: https://doi.org/10.1016/j.bpj.2008.09.051, PMID: 19167315

Dunsing V, Mayer M, Liebsch F, Multhaup G, Chiantia S. 2017. Direct evidence of amyloid precursor-like protein 1 trans interactions in cell-cell adhesion platforms investigated via fluorescence fluctuation spectroscopy. *Molecular Biology of the Cell* **28**: 3609–3620. DOI: https://doi.org/10.1091/mbc.E17-07-0459, PMID: 29021345

Dunsing V, Chiantia S. 2018. A fluorescence fluctuation spectroscopy assay of protein-protein interactions at cell-cell contacts. *Journal of Visualized Experiments* **1**: e58582. DOI: https://doi.org/10.3791/58582

Dunsing V, Luckner M, Zühlke B, Petazzi RA, Herrmann A, Chiantia S. 2018. Optimal fluorescent protein tags for quantifying protein oligomerization in living cells. *Scientific Reports* **8**: 10634. DOI: https://doi.org/10.1038/s41598-018-28858-0, PMID: 30006597

Dunsing V, Chiantia S. 2021. SpectralFFS. 8942980. Github. https://github.com/VaDu8989/SpectralFFS

Eckert AF, Gao P, Wesslowski J, Wang X, Rath J, Nienhaus K, Davidson G, Nienhaus GU. 2020. Measuring ligand-cell surface receptor affinities with axial line-scanning fluorescence correlation spectroscopy. *eLife* **9**: e55286. DOI: https://doi.org/10.7554/eLife.55286, PMID: 32441251

Fan H, Walker AP, Carrique L, Keown JR, Serna Martin I, Karia D, Sharps J, Hengrung N, Pardon E, Steyaert J, Grimes JM, Fodor E. 2019. Structures of Influenza a virus RNA polymerase offer insight into viral genome replication. *Nature* **573**: 287–290. DOI: https://doi.org/10.1038/s41586-019-1530-7, PMID: 31485076

Florin L, Lang T. 2018. Tetraspanin assemblies in virus infection. *Frontiers in Immunology* **9**: 1140. DOI: https://doi.org/10.3389/fimmu.2018.01140, PMID: 29887866

Foo YH, Naredi-Rainer N, Lamb DC, Ahmed S, Wohland T. 2012. Factors affecting the quantification of biomolecular interactions by fluorescence cross-correlation spectroscopy. *Biophysical Journal* **102**: 1174–1183. DOI: https://doi.org/10.1016/j.bpj.2012.01.040, PMID: 22404940

189

Foust DJ, Godin AG, Ustione A, Wiseman PW, Piston DW. 2019. Two-color spatial cumulant analysis detects heteromeric interactions between membrane proteins. *Biophysical Journal* **117**: 1764–1777. DOI: https://doi.org/10.1016/j.bpj.2019.09.028, PMID: 31606123

Galperin E, Verkhusha VV, Sorkin A. 2004. Three-chromophore fret Microscopy to analyze multiprotein interactions in living cells. *Nature Methods* **1**: 209–217. DOI: https://doi.org/10.1038/nmeth720, PMID: 15782196

Ghosh A, Karedla N, Thiele JC, Gregor I, Enderlein J. 2018. Fluorescence Lifetime Correlation Spectroscopy: Basics and applications. *Methods* **140–141**: 32–39. DOI: https://doi.org/10.1016/j.ymeth.2018.02.009, PMID: 29454862

Hantak MP, Qing E, Earnest JT, Gallagher T. 2019. Tetraspanins: Architects of viral entry and exit platforms. *Journal of Virology* **93**: e01429-17. DOI: https://doi.org/10.1128/JVI.01429-17, PMID: 30567993

Heinze KG, Jahnz M, Schwille P. 2004. Triple-color coincidence analysis: One step further in following higher order molecular complex formation. *Biophysical Journal* **86**: 506–516. DOI: https://doi.org/10.1016/S0006-3495(04)74129-6, PMID: 14695295

Hendrix J, Flors C, Dedecker P, Hofkens J, Engelborghs Y. 2008. Dark states in monomeric red fluorescent proteins studied by fluorescence correlation and single molecule spectroscopy. *Biophysical Journal* **94**: 4103–4113. DOI: https://doi.org/10.1529/biophysj.107.123596, PMID: 18234806

Hendrix J, Schrimpf W, Höller M, Lamb DC. 2013. Pulsed interleaved excitation fluctuation imaging. *Biophysical Journal* **105**: 848–861. DOI: https://doi.org/10.1016/j.bpj.2013.05.059, PMID: 23972837

Hendrix J, Dekens T, Schrimpf W, Lamb DC. 2016. Arbitrary-region raster image correlation spectroscopy. *Biophysical Journal* **111**: 1785–1796. DOI: https://doi.org/10.1016/j.bpj.2016.09.012, PMID: 27760364

Hilsch M, Goldenbogen B, Sieben C, Höfer CT, Rabe JP, Klipp E, Herrmann A, Chiantia S. 2014. Influenza A matrix protein m1 multimerizes upon binding to lipid membranes. *Biophysical Journal* **107**: 912–923. DOI: https://doi.org/10.1016/j.bpj.2014.06.042, PMID: 25140426

Huang L, Pike D, Sleat DE, Nanda V, Lobel P. 2014. Potential pitfalls and solutions for use of fluorescent fusion proteins to study the lysosome. *PLOS ONE* **9**: e88893. DOI: https://doi.org/10.1371/journal.pone.0088893, PMID: 24586430

Huet S, Avilov SV, Ferbitz L, Daigle N, Cusack S, Ellenberg J. 2010. Nuclear import and assembly of influenza a virus RNA polymerase studied in live cells by fluorescence cross-correlation spectroscopy. *Journal of Virology* **84**: 1254–1264. DOI: https://doi.org/10.1128/JVI.01533-09, PMID: 19906916

Hur KH, Chen Y, Mueller JD. 2016. Characterization of ternary protein systems in vivo with tricolor heterospecies partition analysis. *Biophysical Journal* **110**: 1158–1167. DOI: https://doi.org/10.1016/j.bpj.2016.01.009, PMID: 26958892

Hutchinson EC. 2014. Conserved and host-specific features of influenza virion architecture. *Nature Communications* **5**: 1–11. DOI: https://doi.org/10.1038/ncomms7446

Hwang LC, Gösch M, Lasser T, Wohland T. 2006. Simultaneous multicolor fluorescence cross-correlation spectroscopy to detect higher order molecular interactions using single wavelength laser excitation. *Biophysical Journal* **91**: 715–727. DOI: https://doi.org/10.1529/biophysj.105.074120, PMID: 16632502

Işbilir A, Serfling R, Möller J, Thomas R, De Faveri C, Zabel U, Scarselli M, Beck-Sickinger AG, Bock A, Coin I, Lohse MJ, Annibale P. 2021. Determination of G-protein-coupled receptor oligomerization by molecular brightness analyses in single cells. *Nature Protocols* **16**: 1419–1451. DOI: https://doi.org/10.1038/s41596-020-00458-1, PMID: 33514946

Jameson DM, Ross JA, Albanesi JP. 2009. Fluorescence fluctuation spectroscopy: Ushering in a new age of enlightenment for cellular dynamics. *Biophysical Reviews* **1**: 105–118. DOI: https://doi.org/10.1007/s12551-009-0013-8, PMID: 21547245

Jorba N, Area E, Ortín J. 2008. Oligomerization of the influenza virus polymerase complex in vivo. *The Journal of General Virology* **89**: 520–524. DOI: https://doi.org/10.1099/vir.0.83387-0, PMID: 18198383

Kaliszewski MJ, Shi X, Hou Y, Lingerak R, Kim S, Mallory P, Smith AW. 2018. Quantifying membrane protein oligomerization with fluorescence cross-correlation spectroscopy. *Methods* **140**: 40–51. DOI: https://doi.org/10.1016/j.ymeth.2018.02.002, PMID: 29448037

Kapusta P, Wahl M, Benda A, Hof M, Enderlein J. 2007. Fluorescence lifetime correlation spectroscopy. *Journal of Fluorescence* **17**: 43–48. DOI: https://doi.org/10.1007/s10895-006-0145-1, PMID: 17171439

Kim SA, Heinze KG, Bacia K, Waxham MN, Schwille P. 2005. Two-photon cross-correlation analysis of intracellular reactions with variable stoichiometry. *Biophysical Journal* **88**: 4319–4336. DOI: https://doi.org/10.1529/biophysj.104.055319, PMID: 15792970

Kimura S, Noda T, Yoshimori T. 2007. Dissection of the autophagosome maturation process by a novel reporter protein, tandem fluorescent-tagged LC3. *Autophagy* **3**: 452–460. DOI: https://doi.org/10.4161/auto.4451, PMID: 17534139

Krieger JW, Singh AP, Bag N, Garbe CS, Saunders TE, Langowski J, Wohland T. 2015. Imaging Fluorescence (cross-) correlation spectroscopy in live cells and organisms. *Nature Protocols* **10**: 1948–1974. DOI: https://doi.org/10.1038/nprot.2015.100, PMID: 26540588

Linkert M, Rueden CT, Allan C, Burel J-M, Moore W, Patterson A, Loranger B, Moore J, Neves C, Macdonald D, Tarkowska A, Sticco C, Hill E, Rossner M, Eliceiri KW, Swedlow JR. 2010. Metadata matters: Access to image data in the real world. *The Journal of Cell Biology* **189**: 777–782. DOI: https://doi.org/10.1083/jcb.201004104, PMID: 20513764

190

Magde D, Elson E, Webb WW. 1972. Thermodynamic Fluctuations in a Reacting System—Measurement by Fluorescence Correlation Spectroscopy. *Physical Review Letters* **29**: 705–708. DOI: https://doi.org/10.1103/PhysRevLett.29.705

Massari S, Desantis J, Nizi MG, Cecchetti V, Tabarrini O. 2021. Inhibition of Influenza Virus Polymerase by Interfering with Its Protein-Protein Interactions. *ACS Infectious Diseases* **7**: 1332–1350. DOI: https://doi.org/10.1021/acsinfecdis.0c00552, PMID: 33044059

Müller BK, Zaychikov E, Bräuchle C, Lamb DC. 2005. Pulsed interleaved excitation. *Biophysical Journal* **89**: 3508–3522. DOI: https://doi.org/10.1529/biophysj.105.064766, PMID: 16113120

Nilsson-Payant BE, Sharps J, Hengrung N, Fodor E. 2018. The Surface-Exposed PA51-72-Loop of the Influenza A Virus Polymerase Is Required for Viral Genome Replication. *Journal of Virology* **92**: e00687-18. DOI: https://doi.org/10.1128/JVI.00687-18, PMID: 29875249

Padilla-Parra S, Audugé N, Coppey-Moisan M, Tramier M. 2011. Dual-color fluorescence lifetime correlation spectroscopy to quantify protein-protein interactions in live cell. *Microscopy Research and Technique* **74**: 788–793. DOI: https://doi.org/10.1002/jemt.21015, PMID: 21618649

Palmer AG, Thompson NL. 1987. Molecular aggregation characterized by high order autocorrelation in fluorescence correlation spectroscopy. *Biophysical Journal* **52**: 257–270. DOI: https://doi.org/10.1016/S0006-3495(87)83213-7, PMID: 3663831

Petazzi RA, Aji AK, Chiantia S. 2020. Fluorescence microscopy methods for the study of protein oligomerization. *Progress in Molecular Biology and Translational Science* **169**: 1–41. DOI: https://doi.org/10.1016/bs.pmbts.2019.12.001, PMID: 31952683

Ridgeway WK, Millar DP, Williamson JR. 2012a. Quantitation of ten 30S ribosomal assembly intermediates using fluorescence triple correlation spectroscopy. *PNAS* **109**: 13614–13619. DOI: https://doi.org/10.1073/pnas.1204620109, PMID: 22869699

Ridgeway WK, Millar DP, Williamson JR. 2012b. The Spectroscopic Basis of Fluorescence Triple Correlation Spectroscopy. *The Journal of Physical Chemistry. B* **116**: 1908–1919. DOI: https://doi.org/10.1021/jp208605z, PMID: 22229664

Ries J, Schwille P. 2006. Studying slow membrane dynamics with continuous wave scanning fluorescence correlation spectroscopy. *Biophysical Journal* **91**: 1915–1924. DOI: https://doi.org/10.1529/biophysj.106.082297, PMID: 16782786

Ries J, Chiantia S, Schwille P. 2009a. Accurate determination of membrane dynamics with line-scan FCS. *Biophysical Journal* **96**: 1999–2008. DOI: https://doi.org/10.1016/j.bpj.2008.12.3888, PMID: 19254560

Ries J, Yu SR, Burkhardt M, Brand M, Schwille P. 2009b. Modular scanning FCS quantifies receptor-ligand interactions in living multicellular organisms. *Nature Methods* **6**: 643–645. DOI: https://doi.org/10.1038/nmeth.1355, PMID: 19648917

Rossman JS, Lamb RA. 2011. Influenza virus assembly and budding. *Virology* **411**: 229–236. DOI: https://doi.org/10.1016/j.virol.2010.12.003, PMID: 21237476

Sankaran J, Balasubramanian H, Tang WH, Ng XW, Röllin A, Wohland T. 2021. Simultaneous Spatiotemporal Super-Resolution and Multi-Parametric Fluorescence Microscopy. *Nature Communications* **12**: 1748. DOI: https://doi.org/10.1038/s41467-021-22002-9, PMID: 33741958

Schrimpf W, Lemmens V, Smisdom N, Ameloot M, Lamb DC, Hendrix J. 2018. Crosstalk-free multicolor rics using spectral weighting. *Methods* **140–141**: 97–111. DOI: https://doi.org/10.1016/j.ymeth.2018.01.022, PMID: 29408283

Schwille P, Meyer-Almes FJ, Rigler R. 1997. Dual-color fluorescence cross-correlation spectroscopy for multicomponent diffusional analysis in solution. *Biophysical Journal* **72**: 1878–1886. DOI: https://doi.org/10.1016/S0006-3495(97)78833-7, PMID: 9083691

Shaw ML, Stone KL, Colangelo CM, Gulcicek EE, Palese P. 2008. Cellular proteins in influenza virus particles. *PLOS Pathogens* **4**: e1000085. DOI: https://doi.org/10.1371/journal.ppat.1000085, PMID: 18535660

Shi X, Foo YH, Sudhaharan T, Chong SW, Korzh V, Ahmed S, Wohland T. 2009. Determination of dissociation constants in living zebrafish embryos with single wavelength fluorescence cross-correlation spectroscopy. *Biophysical Journal* **97**: 678–686. DOI: https://doi.org/10.1016/j.bpj.2009.05.006, PMID: 19619483

Štefl M, Herbst K, Rübsam M, Benda A, Knop M. 2020. Single-Color Fluorescence Lifetime Cross-Correlation Spectroscopy In Vivo. *Biophysical Journal* **119**: 1359–1370. DOI: https://doi.org/10.1016/j.bpj.2020.06.039, PMID: 32919495

Sun Y, Wallrabe H, Booker CF, Day RN, Periasamy A. 2010. Three-Color Spectral FRET Microscopy Localizes Three Interacting Proteins in Living Cells. *Biophysical Journal* **99**: 1274–1283. DOI: https://doi.org/10.1016/j.bpj.2010.06.004, PMID: 20713013

Weidemann T, Mücksch J, Schwille P. 2014. Fluorescence fluctuation microscopy: a diversified arsenal of methods to investigate molecular dynamics inside cells. *Current Opinion in Structural Biology* **28**: 69–76. DOI: https://doi.org/10.1016/j.sbi.2014.07.008, PMID: 25126766

Wohland T, Rigler R, Vogel H. 2001. The standard deviation in fluorescence correlation spectroscopy. *Biophysical Journal* **80**: 2987–2999. DOI: https://doi.org/10.1016/S0006-3495(01)76264-9, PMID: 11371471

Ziegler M, Yserentant K, Middel V, Dunsing V, Gralak A, Pakari K, Bargstedt J, Kern C, Chiantia S, Strähle U, Herten DP, Wombacher R. 2020. A Chemical Strategy to Control Protein Networks in Vivo. *bioRxiv*. DOI: https://doi.org/10.1101/2020.04.08.031427

191

Appendix 1

A1.1 Is pair-wise cross-correlation analysis sufficient to detect ternary interactions?

Generally, pair-wise cross-correlation analysis can only detect pair-wise interactions between fluorescently tagged protein species. To understand whether this analysis is sufficient to indicate the presence of heterotrimeric protein complexes for the specific case reported in this work, we investigated brightness and rel.cc. data obtained by RSICS measurements of IAV PC proteins in more detail.

For all three protein species (PA-mEYFP, PB1-mEGFP, PB2-mCherry2, referred here simply as A, B, and C), normalized brightness values close to the values of FP-homodimers were observed in this work. As a simple approximation, we assume therefore that each species, independently of its participation in hetero-complexes, is either (i) exclusively dimeric or (ii) present as a well-defined mixture of monomers and homotrimers. For the latter case, the fraction of monomers ($f_{1,i}$) and trimers ($f_{3,i}$) for each species i can be calculated from the average molecular brightness $\langle \varepsilon \rangle_i$:

$$f_{1,i} = \frac{1}{1 + \frac{\varepsilon_{1,i}\left(\varepsilon_{1,i} - \langle \varepsilon \rangle_i\right)}{\varepsilon_{3,i}\left(\langle \varepsilon \rangle_i - \varepsilon_{3,i}\right)}}$$

$$f_{3,i} = \frac{1}{1 + \frac{\varepsilon_{3,i}\left(\langle \varepsilon \rangle_i - \varepsilon_{3,i}\right)}{\varepsilon_{1,i}\left(\varepsilon_{1,i} - \langle \varepsilon \rangle_i\right)}}$$

where $\varepsilon_{1,i}$ and $\varepsilon_{3,i}$ denote the molecular brightness of monomers and trimers, respectively.

We then calculate the maximum rel.cc. amplitudes that can be expected in the presence of optimal pair-wise interactions, while still assuming a negligible concentration of complexes containing A, B, and C.

Generally, the ACF and CCF amplitudes for multiple populations (i.e., complexes of species i and j with variable stoichiometry) are calculated as follows (*Kim et al., 2005*):

where $\varepsilon_{k,i}$ and $\varepsilon_{k,j}$ denote the molecular brightness of species i and j (assumed here to be the same for all species) for population k , present at a concentration C_k in the effective volume V_{eff}.

For the sake of simplicity, we discuss here only two simple possible scenarios for the two mixtures discussed above (i.e., each PC protein being present exclusively as homodimers or as a mixture of monomers and homotrimers), in the absence of complexes containing all three PC subunits:

1. Homodimers interacting with homodimers of the other species (i.e., AA-BB, AA-CC, BB-CC).
2. Monomers and oligomers interacting (exclusively) with monomers or oligomers of the other species (i.e., A-B, A-C, B-C, AAA-BBB, AAA-CCC, BBB-CCC).

The two scenarios evaluated here correspond to configurations with the highest possible pair-wise correlations (in the absence of complexes containing A, B, and C), still compatible with an average oligomerization value of 2.

For the two scenarios, we calculate ACF and CCF amplitudes according to the formulas given above, assuming the same total concentration for all species and replacing the concentrations by the derived relative fractions of monomers and oligomers. For each scenario, we determine rel.cc. values from the ratio of CCF and ACF amplitudes. Finally, we extend our calculations by considering incomplete maturation of FP tags based on the fluorescence probability P_f For simplicity, we assume the same P_f for each FP species, in agreement with the similar P_f values of ca. 60–75% observed here for mEGFP, mEYFP, and mCherry2. We use a binomial model for the relative occurrence of different subpopulations in each species (*Dunsing et al., 2018*). For example, actual trimers give rise to a fraction f_k of fluorescent trimers (k = 3), dimers (k = 2), or monomers (k = 1) with a relative occupancy of $f_k = \binom{3}{k} p_f^k (1 - p_f)^{3-k}$ and brightness $k\varepsilon_1$.

The obtained rel.cc. values for all models are given in *Appendix 1—table 1* for = 1 or P_f = 0.7. For comparison, we also calculated rel.cc. values of the positive control, that is, the maximum

192

pair-wise rel.cc. for 1:1 stoichiometry heterodimers (A-B/A-C/B-C) or 1:1:1 stoichiometry heterotrimers (A-B-C), resulting in values of 1 (for P_f = 1) and 0.7 (for P_f = 0.7). Experimentally, this control would also account for suboptimal overlap of the detection volumes for each FP combination, which we neglected here for simplicity. In the absence of ternary hetero-interactions, the determined rel.cc. values are at maximum 59% of the rel.cc. of the positive control (i.e., 0.59 for P_f = 0.7 for scenario 1). Higher normalized values (up to 1.19, see *Appendix 1—table 1*) can be obtained only in the presence of hetero-complexes involving all three PC subunits, which we calculated for comparison for the two mixtures (i.e., AA-BB-CC, or A-B-C in mixtures with AAA-BBB-CCC) and both P_f values.

Appendix 1—table 1. Relative cross-correlation (rel.cc.) values (here, same for all channel combinations) for pair-wise or ternary interactions of three-species mixtures.
Values in brackets for p_f = 0.7 give rel.cc. values normalized to that of the positive control (i.e., the pair-wise rel.cc. for 1:1 stoichiometry).

| Binding model	p_f = 1	p_f = 0.7
Pair-wise interactions of dimers (e.g., AA-BB, AA-CC, BB-CC)	0.50	0.41 (0.59)
Pair-wise interactions of monomers and homotrimers (e.g., A-B, A-C, B-C, AAA-BBB, AAA-CCC, BBB-CCC)	0.5	0.40 (0.57)
Positive control (A-B/A-C/B-C or A-B-C)	1.0	0.7 (1.0)
Ternary interactions of dimers (e.g., AA-BB-CC)	1.0	0.83 (1.19)
Ternary interactions of monomers and trimers (e.g., A-B-C, AAA-BBB-CCC)	1.0	0.80 (1.14)

Of note, in our experiments, rel.cc.values > 0.7 (relative to the positive control) were observed for all pair-wise interactions between PC subunits (detected average pair-wise rel.cc. values normalized to the positive control were 0.71 for B-C, 0.97 for A-C, and 1.43 for A-B, see *Figure 6D*). As shown based on the different binding models, such high pair-wise rel.cc. values are only possible if ternary complexes are present. Thus, by combining molecular brightness and cross-correlation analysis, we conclude that PC proteins form a substantial amount of ternary complexes in the nucleus of cells.

A1.2 TRICS analysis of simulated three-species RICS data

To evaluate the performance of TRICS, we first analyzed simulated RICS data. We ran Monte Carlo simulations of three-species RICS for either (i) three independently diffusing species A, B, C or (ii) a heterotrimeric species (e.g., A-B-C complexes). Two-dimensional diffusion and image acquisition was simulated with the following parameters: diffusion coefficient D = 1 μm²/s (set to be the same for all species), N = 1000 particles (for each species), waist ω_0 =0.2 μm, pixel size δs=0.05 μm, pixel dwell time τ_p =2 μs, 256 × 256 pixels, 100 frames. RICS ACFs, CCFs, and the TRICS 3CF were calculated. To correct for the reduction of the triple correlation due to the high-pass filter (with filter size of F frames), an empirical correction was applied. To this aim, the variance and third central moment of a series of 10^5 random numbers, sampled from a Poissonian distribution (with mean f_0 = 10), were calculated within windows with variable size ΔF (*Appendix 1—figure 1*). The empirical function $f_i\left(\Delta F\right) = f_0\left(\frac{\Delta F-1}{\Delta F}\right)^{b_i}$ was fitted to the variance (i = 2) and third central moment (i = 3). For the variance and third central moment, b_2 = 1.0 and b_3 = 3.4 were obtained, respectively. Thus, the reduction of variance and third central moment for a given value F can be corrected using the factor $\left(\frac{\Delta F}{\Delta F-1}\right)^{b_i}$. For the variance, the determined value b_2 is in agreement with a previously discussed correction (*Hendrix et al., 2016*), which was used here to correct experimental ACFs and CCFs. To test whether 3CFs can be effectively corrected with the obtained $\left(\frac{\Delta F}{\Delta F-1}\right)^{b_3}$ factor, 3CFs were calculated with variable F (in the range 2–16) and the amplitude values determined without or with the correction. In the latter case, fairly constant 3CF amplitudes were obtained, agreeing with the 3CF amplitude calculated without the high-pass filter (data not shown). Exemplary 3CFs for the two simulated scenarios are shown in *Appendix 1—figure 2*. As expected, the rel.3C. values are close to 100 % in the case of heterotrimers and 0% in the case of independently diffusing monomers. The slight underestimation of the rel.3C. for heterotrimers is likely due to the approximated interpolation of the amplitude value from only the first five points of the 3CF.
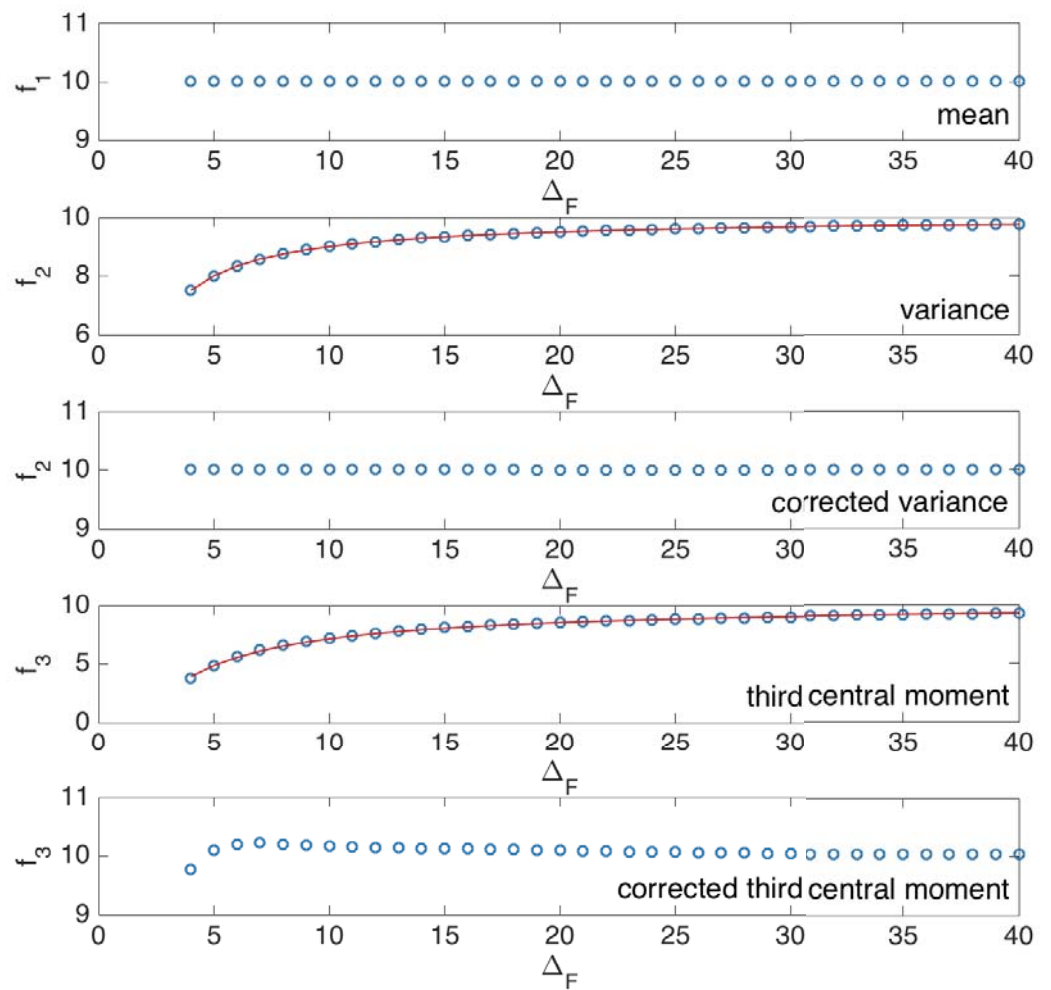
Appendix 1—figure 1. Effect of high-pass filter on calculation of variance and third central moment of random numbers sampled from a Poissonian probability distribution. Variance (f_2, blue circles) and third central moment (f_3, blue circles) were calculated with a moving average (window size ΔF) for a set of 10^5 random numbers drawn from a Poissonian distribution with average 10. An empirical function (red solid line) of the form $f_i\left(\Delta F\right) = f_0\left(\frac{\Delta F - 1}{\Delta F}\right)^{b_i}$ was fitted to the variance (f_2) and third central moment (f_3), and used to correct for the undersampling effect. The corresponding values after applying the empirical correction are shown as blue circles in the panels labeled as 'corrected.'

194
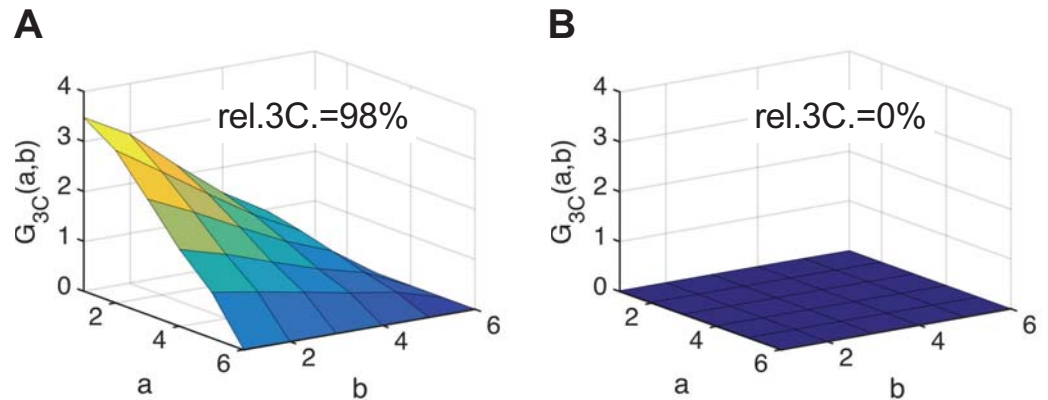
Appendix 1—figure 2. Triple raster image correlation spectroscopy (TRICS) analysis of simulated three-species RICS data. (**A, B**) Two-dimensional representation of the triple-correlation function (3CF) calculated for simulated TRICS data (with a four-frame high-pass filter) for (**A**) ternary hetero-complexes or (**B**) the same number of particles per species diffusing as independent monomers. From a linear interpolation of G_{3C} to (0,0) (using the first point $G_{3C}(1,1)$ and the average of the four points $G_{3C}(1,2)$, $G_{3C}(2,1)$, $G_{3C}(2,2)$, $G_{3C}(3,0)$) an approximate value of the 3CF amplitude was determined and corrected with the correction factor discussed in Section A1.1. The obtained value and the autocorrelation function (ACF) amplitude value (also corrected for the decay induced by the high-pass filter) were used to calculate the relative triple-correlation value rel.3C. (given as inset).

A1.3 Relative triple correlation for ternary complexes of fluorescently tagged proteins

The rel.3C. is a measure of the relative amount of ternary complexes in a system containing three fluorescently tagged protein species. Incomplete maturation or non-fluorescent photophysical states of FP tags will reduce the amount of detectable ternary complexes. To quantify the maximum rel.3C. that can be expected in an experiment, we calculate rel.3C. values for ternary complexes of (i) 1:1:1 or (ii) 2:2:2 stoichiometry, under the assumption that each fluorescent protein can be detected with a probability P_f For simplicity, we assume the same P_f and molecular brightness ε for all three fluorophore species. Generally, the ACF and 3CF amplitudes for fully formed ternary complexes (i.e., in the absence of partially formed complexes) of concentration c composed of species 1, 2, and 3 with variable stoichiometry $l:m:n$ are calculated as follows (***Kim et al., 2005***):

$$G_1(0,0) = \frac{c\left(\sum_{i=1}^{l}(i\varepsilon)^2\binom{l}{i}p_f^i(1-p_f)^{l-i}\right)}{V_{eff}\left(c\sum_{i=1}^{l}i\varepsilon\binom{l}{i}p_f^i(1-p_f)^{l-i}\right)^2}$$

(analogously $G_2(0,0)$, $G_3(0,0)$ with upper index m,n),

$$G_{3C}(0,0) = \frac{c\left(\sum_{i=1}^{l}(i\varepsilon)^2\binom{l}{i}p_f^i(1-p_f)^{l-i}\right)\left(\sum_{j=1}^{m}(j\varepsilon)^2\binom{m}{j}p_f^j(1-p_f)^{m-j}\right)\left(\sum_{k=1}^{n}(k\varepsilon)^2\binom{n}{k}p_f^k(1-p_f)^{n-k}\right)}{V_{eff}\left(c\sum_{i=1}^{l}i\varepsilon\binom{l}{i}p_f^i(1-p_f)^{l-i}\right)\left(c\sum_{j=1}^{m}j\varepsilon\binom{m}{j}p_f^j(1-p_f)^{m-j}\right)\left(c\sum_{k=1}^{n}k\varepsilon\binom{n}{k}p_f^k(1-p_f)^{n-k}\right)}$$

From these amplitudes, the rel.3C. can be calculated (see Materials and methods). We obtain rel.3C. = p_f^2 = 0.49 (1:1:1 stoichiometry) and rel.3C. = $4p_f^2/(p_f+1)^2 \approx 0.68$ (2:2:2 stoichiometry) for $p_f = 0.7$. Due to imperfect optical overlap, experimentally detectable rel.3C. values will be lower than these values. To estimate the fraction of ternary complexes than can be detected, we compare experimental rel.cc. values obtained for all FP combinations on a positive control (FP

195

heterotrimers) in pair-wise cross-correlation analysis with the expected value of rel.cc. = 0.7 for p_f = 0.7 (see Section A1.1). The average rel.cc. value of 0.65 detected for mEGFP and mEYFP signal (see *Figure 6D*) was close to the expected value, hence, almost all complexes containing fluorescent mEGFP and mEYFP were detectable. On the other hand, rel.cc. values for mEGFP and mCherry2 (0.48)/mEYFP and mCherry2 (0.53) were ca. 70% of the expected value (*Figure 6D*). Hence, we estimate that ca. 70% of complexes carrying an mCherry2 tag and an mEGFP or mEYFP tag are detectable due to nonoptimal overlap of excitation/detection volumes. We can therefore assume that for the case of ternary complexes ca. 70% of all fully fluorescent ternary complexes that are present in the sample are optically detectable. The expected experimental rel.3C. values are thus approximately 0.34 and 0.48 for complete binding in 1:1:1 and 2:2:2 stoichiometry, respectively.

196

Supplementary

Multicolor fluorescence fluctuation spectroscopy in living cells via spectral detection

Valentin Dunsing, Annett Petrich, Salvatore Chiantia
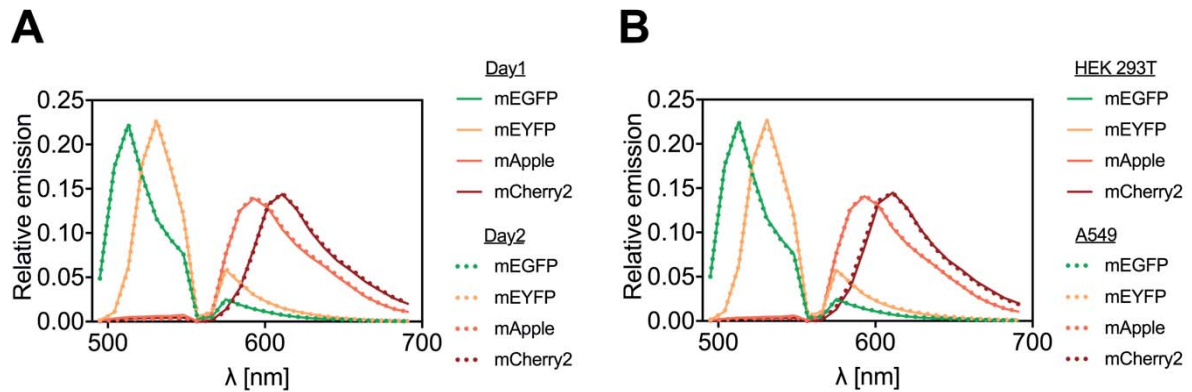
Supplementary Figure S1. FP emission spectra. (A) Average emission spectra of mp-mEGFP, mp-mEYFP, mp-mApple, mp-mCherry2 measured by spectral imaging (23 spectral channels from 491 nm to 695 nm) with 488 nm and 561 nm excitation on HEK 293T cells expressing each FP individually. Spectra are shown for two different days (day1: solid line, day2: dotted line) and averaged over four cells each. For each cell, 25 frames were acquired and pixels corresponding to the PM semi-manually segmented in the average image (manual selection followed by removal of pixels with intensities below 25% of the maximum pixel intensity in the selected region). **(B)** Average emission spectra measured on HEK 293T cell samples (solid line) described in (A), or on A549 cells expressing cytosolic mEGFP, mEYFP, mApple, mCherry2 (dotted line). Spectra measured on four cells each were averaged over three (HEK 293T) or two (A549) days. For A549 cells, a homogeneous ROI in the cytosol was manually selected.
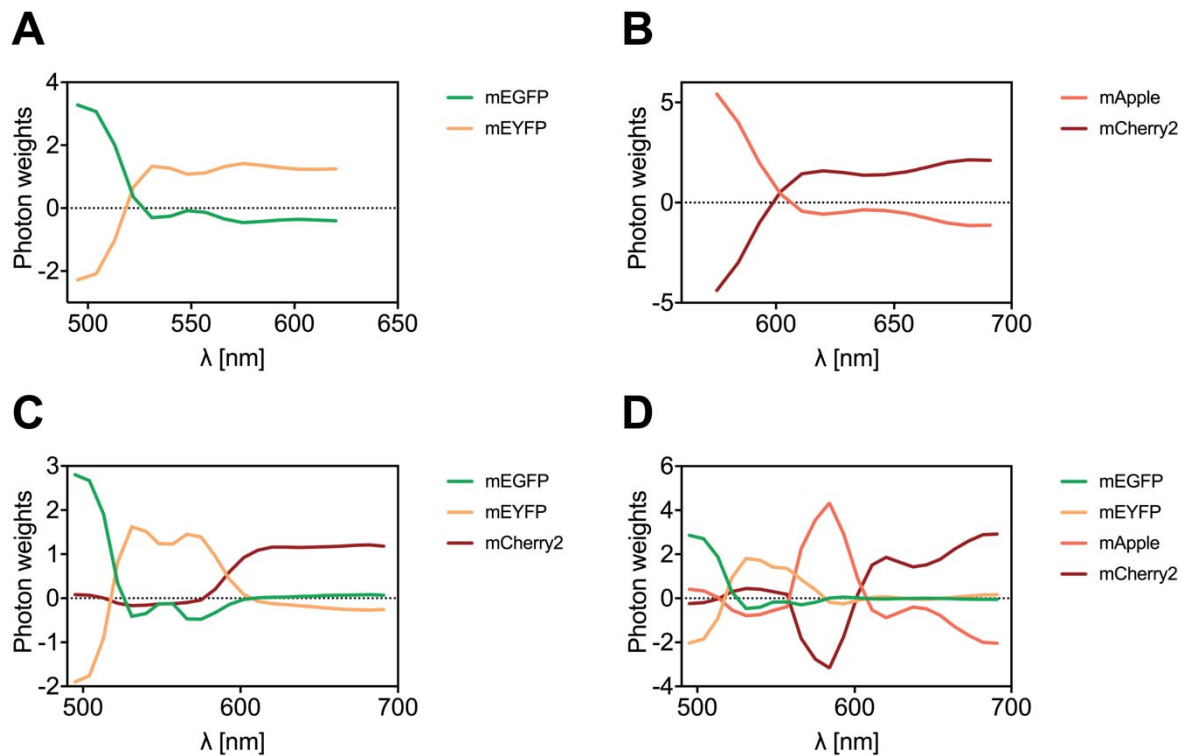
Supplementary Figure S2. Spectral filters for two-, three-, and four-species SFSCS. (A-D) Photon weights calculated in spectral decomposition of SFSCS data acquired on HEK 293T cells expressing mp-mEYFP-mEGFP (A), mp-mCherry2-mApple (B), mp-mEYFP-mCherry2-mEGFP (C), mp-mEYFP-mCherry2-mEGFP-mApple (D). Shown are average photon weights from five SFSCS acquisitions each.
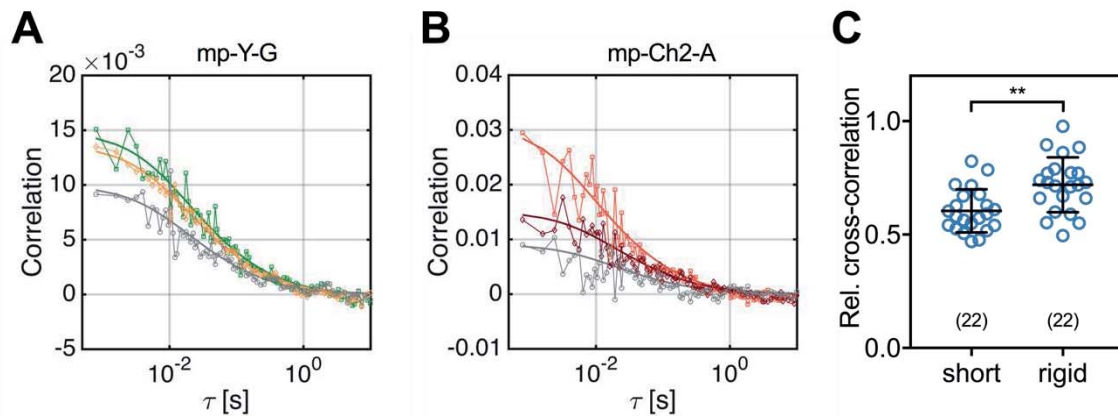
Supplementary Figure S3. SFSCS on FP hetero-dimers. (A) Representative CFs (green: ACF for mEGFP ("G"), yellow: ACF for mEYFP ("Y"), grey: CCF calculated between both fluorophore signals) obtained from SFSCS measurements on the PM of living HEK 293T cells expressing mp-mEYFP-mEGFP hetero-dimers. Solid thick lines show fits of a two-dimensional diffusion model to the CFs. **(B)** Representative CFs (light red: ACF for mApple ("A"), dark red: ACF for mCherry2 ("Ch2), grey: CCF calculated between both fluorophore signals) obtained from SFSCS measurements on the PM of living HEK 293T cells expressing mp-mCherry2-mApple hetero-dimers. Solid thick lines show fits of a two-dimensional diffusion model to the CFs. **(C)** Relative cross-correlation values obtained from SFSCS measurements on HEK 293T cells expressing mp-mEYFP-mEGFP (rigid linker between the two FPs, see Table S1) or mp-mEGFP-mEYFP (short linker between the two FPs, see Table S1) hetero-dimers. Data are pooled from three independent experiments each. The number of cells measured is given in parentheses. Error bars represent mean±SD. Statistical significance was determined using Welch's corrected two-tailed student's t-test (**$P<0.05$).
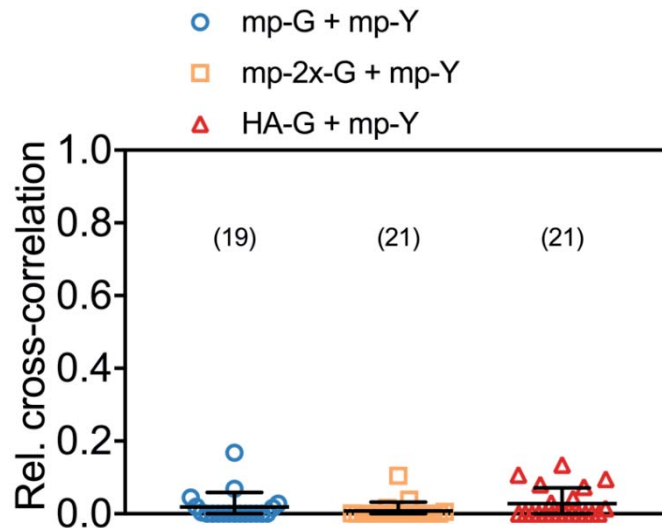
Supplementary Figure S4. Relative cross-correlation obtained from two-species SFSCS measurements described in Fig.2 of the main text. The number of cells measured is given in parentheses. Error bars represent mean±SD.
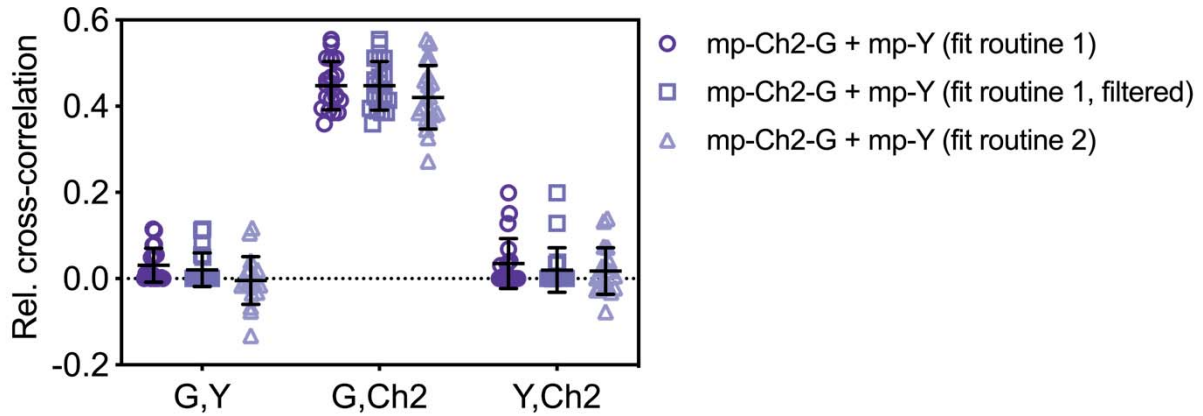
Supplementary Figure S5. Relative cross-correlation for three-species SFSCS described in Fig.3, analyzed using different fitting algorithms. CCFs obtained from measurements on cells co-expressing mp-mCherry2-mEGFP hetero-dimers and mp-mEYFP were fitted using as start parameter for the amplitude either a positive value (same for all CCFs, fit routine 1), or the average of the first five points of each CCF (fit routine 2). For non-correlated data (e.g. G,Y and Y,Ch2 combinations), the second fit routine may converge to negative fit amplitudes, resulting in a distribution of rel.cc. values scattered around 0. Fit routine 1 always converged to positive amplitude values, producing low but positive rel.cc. values. Filtering based on the cross-correlation diffusion time (fit routine 1, filtered) removes some of the residual positive rel.cc. in non-correlated data. Here a threshold value of five times the maximum of the two diffusion times obtained from ACFs for each respective FP combination was chosen. For correlated data, e.g. G,Ch2, both fit routines converged to comparable positive values.
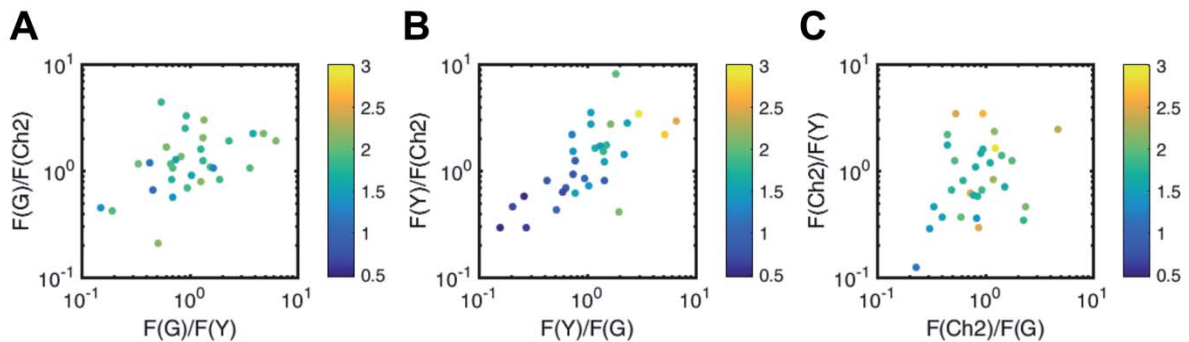
Supplementary Figure S6. Noise analysis of three-species SFSCS measurements described in Fig.3. SNR (color coded) of ACFs for mEGFP (A), mEYFP (B), and mCherry2 (C) channels obtained from SFSCS measurements on HEK 293T cells co-expressing mp-mEGFP, mp-mEYFP, and mp-mCherry2, as a function of their signal relative to that of the other two FP species. Data was pooled from two independent experiments in which 31 cells were measured in total.

A   **B**   **C**
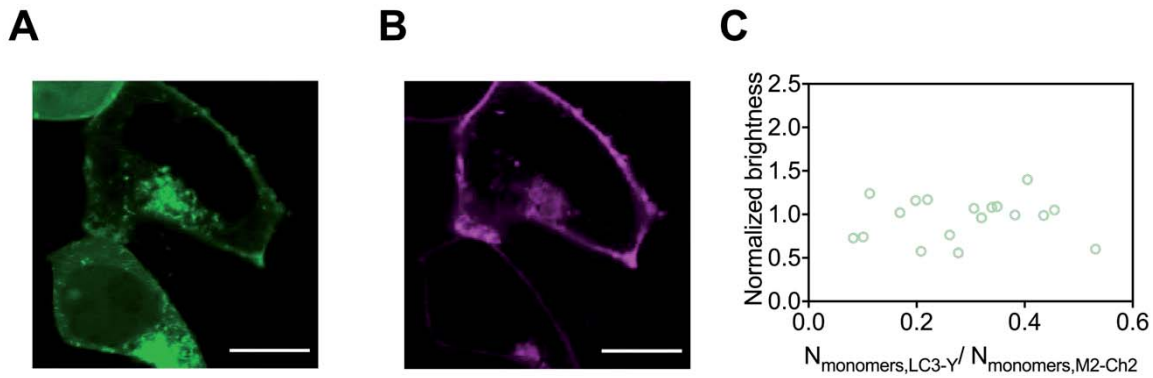
Supplementary Figure S7. Membrane recruitment of LC3 in M2 expressing cells. (A,B) Fluorescence images of LC3-mEYFP (A) and M2-mCherry2 (B) excited with either 488 nm (A) or 561 nm (B) excitation. LC3 is recruited to the PM in cells showing higher expression of M2 (top cell) relative to M2, but remains in the cytosol in cells expressing only low levels of M2 compared to LC3 (bottom cell). Scale bars are 10 μm. **(C)** Molecular brightness of LC3-mEYFP obtained from three-species SFSCS measurements shown in Fig.3, as a function of the ratio of LC3-mEYFP to M2-mCherry2 expression at the PM, in units of protein monomers. The number of monomers was calculated by dividing the signal detected for LC3-mEYFP/M2-mCherry2 in SFSCS measurements by the average molecular brightness detected for mEYFP and mCherry2 fluorophores in the monomeric reference sample (cells co-expressing mp-mEGFP, mp-mEYFP, and mp-mCherry2, Fig.3).
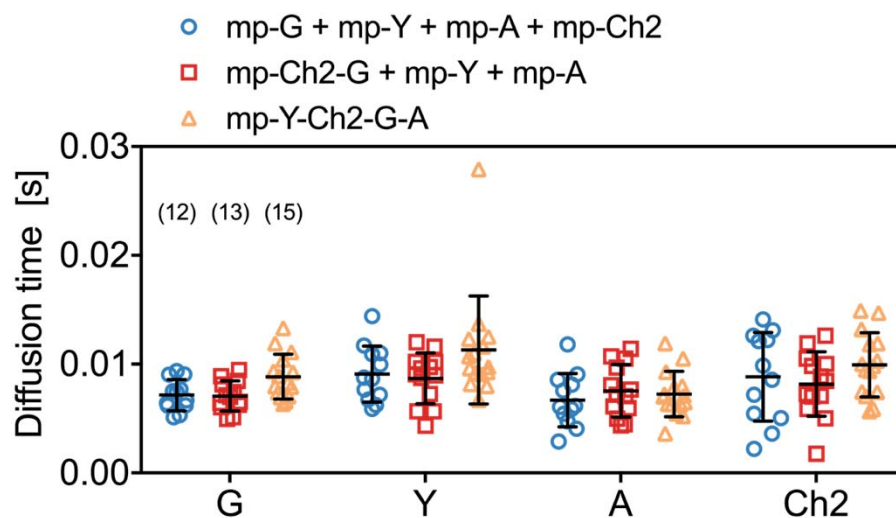
Supplementary Figure S8. Diffusion dynamics of four-species SFSCS measurements. Diffusion times obtained from four-species SFSCS measurements on HEK 293T cells co-expressing mp-mEGFP, mp-mEYFP, mp-mApple, and mCherry2 (blue), mp-mCherry2-mEGFP hetero-dimers, mp-mEYFP, and mp-mApple (red), or expressing mp-mEYFP-mCherry2-mEGFP-mApple hetero-tetramers (yellow). The four FP species are denoted with "G", "Y", "A", "Ch2". Data are pooled from two independent experiments. The number of cells measured is given in parentheses. Error bars represent mean±SD.
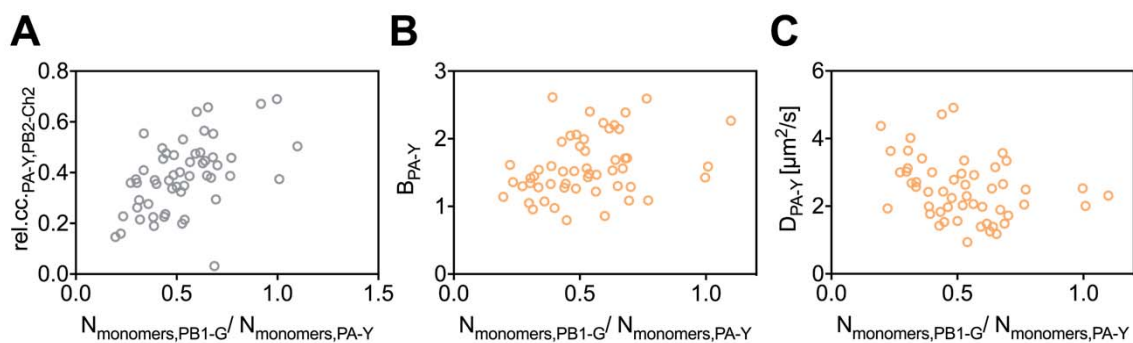
Supplementary Figure S9. Cross-correlation and diffusion analysis for three-species RSICS measurements on IAV polymerase complex as a function of relative protein concentration. (A-C) Relative cross-correlation for PA-mEYFP and PB2-mCherry2 (A), normalized molecular brightness (B) and diffusion coefficient (C) detected for PA-mEYFP, obtained from three-species RSICS measurements on A549 cells co-expressing PA-mEYFP, PB1-mEGFP, and PB2-mCherry2. Data are plotted as a function of the ratio of PB1-mEGFP to PA-mEYFP, in units of protein monomers, and pooled from four independent experiments (n=53 cells). The number of monomers was calculated by dividing the signal detected for PB1-mEGFP and PA-mEYFP in SFSCS measurements by the average molecular brightness detected for mEGFP and mEYFP fluorophores in the monomeric reference sample (cells co-expressing mp-mEGFP, mp-mEYFP, and mp-mCherry2, Fig.6)
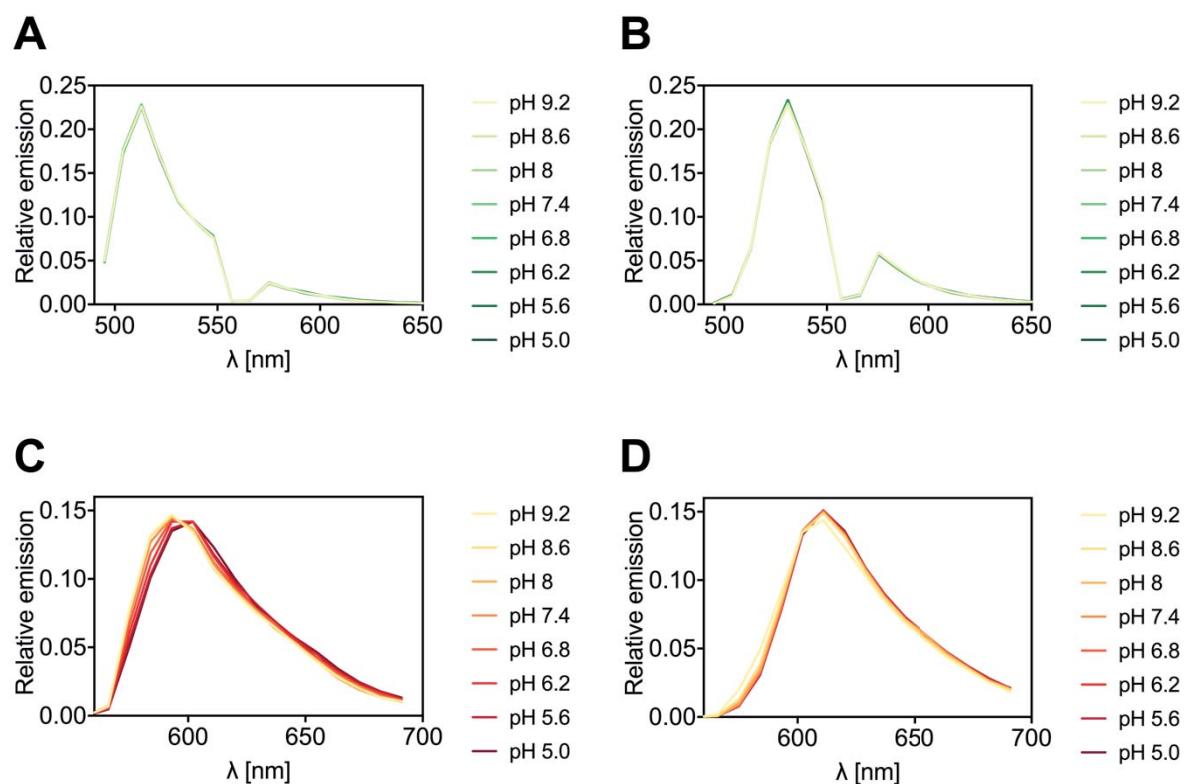
Supplementary Figure S10. FP emission spectra at different pH values. (A-D) Average emission spectra of GPI-mEGFP (A), GPI-mEYFP (B), GPI-mApple (C), and GPI-mCherry2 (D) measured by spectral imaging (23 spectral channels from 491 nm to 695 nm) using 488 nm and 561 nm excitation on HEK 293T cells supplemented with buffer at different pH values, ranging from pH 5.0 to pH 9.2. At each pH value, ca. 10-20 cells were imaged for five frames. To obtain average emission spectra, pixels corresponding to the PM were semi-manually segmented (manual selection followed by removal of pixels with intensities below 25% of the maximum pixel intensity in the selected region) and detected spectra averaged over all pixels and cells measured at each pH.

Supplementary Table S1. Linker sequences of FP hetero-oligomer constructs.

Plasmid	Linker sequence between FPs
mp-mEGFP-mEYFP	LK
mp-mEYFP-mEGFP	PPAAAPPVLSLVP
mp-mCherry2-mEGFP	SGLRSRG
mp-mEYFP-mCherry2-mEGFP	1st: PPAAAPPVLSLVP, 2nd: PPAAAPPVVP
mp-mEYFP-mCherry2-mEGFP-mApple	1st: PPAAAPPVLSLVP, 2nd: PPAAAPPVVP, 3rd: PPAAAPPVDP
mp-mCherry2-mApple	PPAAAPPVVP
mCherry2-mEGFP	SGLRSRG
mEYFP-mApple	PPAAAPPVLSLVPSS
mEYFP-mCherry2-mEGFP	1st: PPAAAPPVLSLVP, 2nd: PPAAAPPVVP
mEYFP-mCherry2-mEGFP-mApple	1st: PPAAAPPVLSLVP, 2nd: PPAAAPPVVP, 3rd: PPAAAPPVDP

Supplementary Table S2. Day-to-day variability of molecular brightness values obtained from three-species RSICS measurements. Normalized brightness values for 2x-mEGFP, 2x-mEYFP, and 2x-mCherry2 were obtained by normalization to the average brightness values detected for free monomers, on the same day.

Date		Normalized brightness			Absolute brightness [kHz]		
	Sample	2x-G	2x-Y	2x-Ch2	1x-G	1x-Y	1x-Ch2
16.06.20	mean	1.59	1.77	1.58	21.9	14.5	6.30
	median	1.62	1.79	1.51	21.8	14.4	6.29
	SD	0.23	0.22	0.20	3.1	1.7	0.71
	n	9	9	9	14	14	14
14.10.20	mean	1.82	1.78	1.67	17.8	12.5	6.62
	median	1.79	1.71	1.67	17.5	12.3	6.61
	SD	0.44	0.38	0.34	3.8	2.8	1.21
	n	14	14	14	14	14	14
10.07.20	mean	1.78	1.76	1.57	17.4	11.6	5.88
	median	1.66	1.77	1.54	17.6	12.1	5.88
	SD	0.37	0.36	0.29	2.0	1.5	0.58
	n	16	16	16	14	14	14

Supplementary References

1. Kim, S.A., K.G. Heinze, K. Bacia, M.N. Waxham, and P. Schwille. 2005. Two-Photon Cross-Correlation Analysis of Intracellular Reactions with Variable Stoichiometry. *Biophys. J.* 88:4319–4336.
2. Dunsing, V., M. Luckner, B. Zühlke, R.A. Petazzi, A. Herrmann, and S. Chiantia. 2018. Optimal fluorescent protein tags for quantifying protein oligomerization in living cells. *Sci. Rep.* 8:10634.
3. Hendrix, J., T. Dekens, W. Schrimpf, and D.C. Lamb. 2016. Arbitrary-Region Raster Image Correlation Spectroscopy. *Biophys. J.* 111:1785–1796.

4 Discussion and Outlook

In the current work, quantitative biophysical fluorescence microscopy techniques were utilized to examine cell membrane properties, biomolecule interactions and dynamics across diverse biological scenarios. Initially, a systematic evaluation of green FPs was carried out in living cells via FFS techniques, encompassing different experimental setups (e.g. pH conditions). This study has shown that the fluorescence properties of green FPs are impacted differently with varying pH conditions and excitation powers, thus biasing the quantification of protein oligomerization. Therefore, it is crucial to consider these variables when planning such experiments to ensure accurate and reliable results. Secondly, a combination of different fluorescence microscopy methods (i.e., membrane charge FRET, GP imaging and sFCS) was applied to quantify the effect of EPC3-treatment and IAV infection on membrane properties. The results imply that EPC3 disrupts lipid–lipid interactions in biomembranes and modulates lipid composition in cancer cell membranes, which could lead to an induction of apoptosis in cancer cells. Furthermore, it is shown that IAV infection modified the lipid organization and lipid-lipid-packing at the assembly site in living cells, which are crucial for virion morphology and stability. Finally, various FFS techniques were utilized to gather crucial insights about protein-protein interactions occurring at the initial stages of IAV assembly. The findings suggested that the translocation of M1 to the assembly site occurs via a strong interaction with M2, aided possibly via the non-canonical autophagy pathway.

4.1 The choice of fluorescent protein tags affects molecular brightness analysis in living cells

Quantifying the oligomeric state of protein complexes and characterizing their spatial distribution are crucial for understanding the functional roles of PPIs studied in their native cellular environment and to observe dysregulations in diseases (155-157). FFS microscopy techniques, such as N&B and FCS, have emerged as powerful tools for studying protein complex dynamics in living cells (5, 9, 18, 157, 158). FP tags are commonly used to track protein complexes in living cells (159, 160). However, the accuracy of oligomerization studies can be influenced by different tags due to alterations in their brightness, photophysical properties and maturation time, which are governed by experimental configurations (i.e., excitation source and power, duration time) and local environment (i.e., pH and ion composition) (32, 138, 141, 145, 160-162). Intracellular compartments, such as the ER and the Golgi network, expose proteins to varied pH environments during their maturation and trafficking (144, 146). Therefore, a systematic analysis of fluorescence properties from FPs is essential in ensuring accurate quantifications in diverse intracellular compartments.

In the present work, several green FPs (mEGFP, mNeonGreen (mNG), mGreenLantern (mGL) and Gamillus) were investigated to affirm their suitability for FFS under different pH conditions (Chapter 3.1). To rule out potential artefacts arising from a particular expression

system, two subcellular localizations (cytoplasm and PM) and cell lines (HEK293T and CHO-K1) were compared. Previous studies have indicated that the novel green FPs mNG, mGL, and Gamillus exhibit superior brightness and faster maturation than mEGFP (143, 145, 161). Additionally, it has been demonstrated that Gamillus displays a low sensitivity to acidity compared to mEGFP (161). These findings suggest that these FPs are promising candidates for quantitative FFS studies in different cell compartments. It is noteworthy, that these observations about FP properties were obtained using different microscope setups. Hence, it is relevant to systematically compare FPs using specific conditions and approaches resembling actual FFS experiments, such as N&B and sFCS. For accurate oligomerization studies via FFS, these FPs should possess high photostability to ensure continuous illumination, high molecular brightness to achieve a sufficient signal-to-noise ratio (SNR) for single molecule fluctuation detection, and high p_f values to reach a high dynamic range (32). The recently developed FP Gamillus exhibited higher molecular brightness compared to mEGFP at the PM in both cell lines, irrespective of pH conditions, laser power or FFS method. However, Gamillus suffered from strong initial bleaching when excited with high excitation power or under less basic conditions (pH $\leq$ 7.4). The highest photostability was observed for mEGFP followed by mNG and very low photostability for mGL under all pH conditions. A comprehensive comparison of these observations with previous reports is challenging due to the fact that distinct experimental conditions and configurations often lead to varying apparent photochemical responses. For instance, mEGFP exhibited inferior photostability compared to mNG under widefield illumination, whereas it displayed superior photostability under laser illumination and no discernible disparity in photostability using a spinning disk confocal microscope (145, 160). However, photostabilities observed for mEGFP and mGL at pH 7.4 are in line with prior reports (143, 145, 163). Contrary results were reported for Gamillus, which showed significantly higher photostability under acidic environments and widefield illumination (161). Similar to Gamillus, mGL and mNG showed also higher molecular brightness values than mEGFP. Moreover, the molecular brightness of mEGFP, mGL and mNG were not significantly affected by pH changes. These observations were unexpected since previous studies showed that the molecular brightness of mNG increased proportionally with pH and that the molecular brightness of mEGFP decreased at low pH due the induction of flickering by (de)protonation processes under high laser power (138, 162, 164, 165). A reduction in molecular brightness due such light-induced photochemical process was only observed with high laser power at acidic pH (Figure S1A). A previous work suggested that a fast maturation of FPs will lead in higher p_f values (32). This was observed specifically for mGL, which demonstrated higher p_f values ($\geq$ 80%) than the other FPs at neutral pH conditions for both FFS techniques and cell types. Moreover, mEGFP exhibited the highest p_f value under acidic conditions and Gamillus under alkaline conditions. Nevertheless, dark state fractions up to 45% were observed depending on FP and pH environment, which was similar to previous reports (32, 155, 162). An ideal fluorescent fraction for the determination of protein oligomerization would be $\geq$ 60 % in order to have a maximal dynamic range (32, 133). Otherwise, a reduction in fluorescent fractions may result in an underestimation of protein oligomerization, because the molecular brightness per FP would only slightly increase (32, 133). For example, it has been demonstrated that a mCherry tetramer with a p_f value of ~ 40% exhibits only a

twofold increase in brightness compared to a monomer, leading to its classification as a dimer (32). It is worth noting that high p_f values are also desirable for an accurate quantification of the protein concentration, which would otherwise result in an underestimation of the actual protein concentration. Hence, the p_f value was introduced as a FP specific correction factor for dark states for the quantification of protein oligomerization (32) and concentration (Chapter 3.4). Interestingly, similar to the current study, it was previously demonstrated that the molecular brightness and the p_f value of various FPs are consistent across different cell types and temperatures as well as FFS techniques (32). These findings indicate that the p_f value is an inherent photophysical property of the FPs, that can be applied as a correction factor to other methods in future studies. Notable, fluorescence intensity and molecular brightness of red FPs such as mCherry (166, 167) and mCherry2 (Figure S1B; Chapter 3.5) did not change considerably over a wide pH range whereas YFP variants showed more complex light-induced photochemical processes, which can result in a higher variability of p_f value between used FFS techniques, microscope setups, cell types and intracellular localization (32, 168).

In addition to pH, other cell environmental factors may also affect the quantification of protein oligomerization/concentration and must be considered when selecting an appropriate FP for FFS analysis in specific compartments. For instance, disulfide bond formation can occur in oxidizing environments like the eukaryotic secretory pathway and mitochondrial inner membrane space, resulting in the oligomerization of FPs with two cysteine residues, such as GFP-derived FPs (144, 169). This is consistent with a prior study that employed stepwise photobleaching analysis and discovered higher oligomeric states of mEGFP in the ER and Golgi, but not at the PM (170). Typically, superfold GFP (sfGFP) or DsRed family members such as mCherry do not contain cysteines (144, 169). Additionally, certain FPs such as Tag-RFP and mKate2 possess N-glycosylation sites (169). These sites can alter protein folding and potentially introduce steric hindrance by obstructing protein interaction sites, or interfere with the glycosylation quality control machinery, disrupt ER homeostasis, or even reduce the protein's half-life (144, 169). Normally, GFP and DsRed variants do not comprise N-glycosylation sites (169). Furthermore, some FPs are obligate oligomers (i.e., tdTomato and DsRed) and others oligomerize in a concentration dependent-manner (i.e., EGFP and Tag-RFP), which was previously shown for FPs linked to membrane proteins (144, 169, 171). A single mutation (A206K) was shown to prevent dimerization at the interface of the ß-barrel (144, 172). Additionally, some FPs (i.e., TagRFP, mFruit FPs) have a tendency to be sticky and can aggregate into bright puncta, leading to a disruption of organelles in the secretory pathway (144, 169). Some red FPs have been demonstrated to exhibit a high portion of uncomplete chromophore formation, which emit in green instead in red (144, 173). Such FPs are not suitable for general imaging or PPI quantification via FFS techniques in specific intracellular compartments.

Evaluation of FPs, as shown in this work (Chapter 3.1) and in prior studies with various FPs (32, 155, 174), are also important to select correct FP pairs for single molecule FRET (smFRET) analysis (163, 175-177) or for multi-color FFS studies (32). Based on these studies, the FP pair mEGFP and mCherry2 were selected for the influenza PPI studies of IAV

proteins via two-color FFS (Chapter 3.4) and for the spectral FFS study, the FPs mEGFP, mEYFP, mApple and mCherry2 (Chapter 3.5).

Nonetheless, it is crucial to consider that the intracellular localization and PPIs can be altered by the linkage of the FPs to the protein of interest (POI) and the relatively high molecular mass (~27 kDa) of FPs (18, 178, 179). Consequently, they can impact protein oligomerization and overall protein function (18, 178-181). Genetically encoded self-labelling tags, such as HALO-, SNAP-, or CLIP-tag, allow the attachment of diverse organic dyes to a POI, but their molecular size are similar (~30 kDa) or negligible smaller (~19 kDa) than FPs and need an additional labelling step (181, 182). The labelling efficiency and kinetic of such tags depends on the labelling substrates (i.e., chloroalkane-PEG (CA) and benzylguanine (BG)) and their modifications with (non-)fluorescent agents as well as on the protein/tag localization (intra-/extracellular) and cell environmental (183, 184). SNAP-tags were shown to exhibit slower labelling kinetics, lower labelling efficiency (30 - 80 %), and higher off-target labelling compare to HALO-tags ($\geq$ 90 % labelling efficiency) (182-184). The organic fluorophores exhibit higher brightness and photostability than FPs that makes them attractive for super-resolution fluorescence imaging approaches and FFS studies, but their fluorescence probabilities have to be well characterized (18, 178, 180-182). Other groups of site-specific protein labelling with a significant smaller size are tetracysteine-tags and noncanonical amino acid (ncAA) (18, 182). Tetracysteine-tags contain a short amino acid group (CCXXCC, in which X denotes any amino acid) linked to a POI and reacts with bisarsenical fluorophores such as the fluorescein arsenical hairpin (FlAsH) and resorufin arsenical hairpin (ReAsH) (182, 185). These probes are membrane permeable with a fast labelling kinetic and efficiency, but displayed high off-targeting labelling and low photostability (185, 186). A previous FCS study demonstrated that FlAsH contains high fractions of long-lived triplet states in solution, which can alter the quantification of protein oligomerization and concentration (187). Moreover, their similar sequence limits their application to target proteins with comparable cellular abundances or protein complexes due to competition (186). Therefore, targeting sequence and biaresenical fluorophores were optimized over the last decade (185, 186). Nonetheless, the length and conformational flexibility of the targeting sequence can impact the labelling efficiency and potentially lead to undesired disulfide bond formations (186). There is currently a lack of comprehensive studies on the various tetracysteine tags for *in cellula* FFS studies in different cellular compartments. A minimal invasive technique with less to none perturbation nature is the genetically incorporation of functionalized ncAAs with a chemically reactive group into the POI followed by the conjugation of small organic fluorophores by fast and specific bioorthogonal click chemistry (18, 178, 181, 188). To utilize this method for modifying a POI, the codon at the desired position must be replaced with an alternative codon that specifies the ncAA such as suppressing stop codons (typically UAG) (178, 188). A successful incorporation of ncAAs into POIs relies on the co-expression of bioorthogonal tRNAs that recognizes these codons and corresponding aminoacyl-tRNA synthetases (aaRSs) to conjugate the ncAA to the tRNA (178, 188). This new approach has been demonstrated to be suitable for several fluorescence microscopy techniques (i.e., stimulated emission depletion microscopy (STED), single molecule localization microscopy (SMLM) and smFRET) (178, 188). Nevertheless, possible drawbacks of this labelling strategy are that efficiency varies strongly with the different

tRNA/aaRS pairs, the targeting codon and its position in the POI, the fluorescent dyes, cell line and cellular localization (i.e., cell surface ~ 90% and intracellular 30-40 %) (178, 181, 188). Moreover, this technology can be challenging for live cell imaging due its toxicity and slow labeling reaction compare to HALO-tags etc. (184). Therefore, more systematically studies are required for live cell FFS studies.

4.2 High-throughput biophysical fluorescence microscopy approaches unravel the impact of biological processes on membrane properties

Previous research has demonstrated that lipid metabolism is altered in cancer cells (147, 148) and IAV infected cells (154, 189-191), which contributes to their pathogenicity (64, 147-149, 190, 192-194). As a result, the concentration of certain lipids (i.e., anionic and saturated lipids, cholesterol and sphingomyelin) in cellular membranes might be changed, which, in turn, could modify the biophysical characteristics of cellular membranes (i.e., lipid membrane order and membrane charge) and affect protein-protein as well as protein-lipid interactions (148, 195-197). Exploring the biophysical properties of cellular membranes is crucial in understanding the effectiveness of potential therapeutic agents and to develop targeted therapies that disrupt disease progression by identifying specific lipid changes and their underlying mechanisms. In this study a biophysical analysis pipeline was implemented to investigate the mechanism of action of the antineoplastic drug EPC3 (Chapter 3.2) and the influence of IAV infection (Chapter 3.3) on the PM properties.

4.2.1 EPC3 modulates lipid-lipid interactions in cellular membranes

First, membrane models, which mimic the outer leaflet of the PM, were used in combination with phase sensing fluorescent probes to investigate the effect of EPC3 on lipid-lipid interaction. This approach allowed the quantification of L_d phase and L_o phase surface coverage, as well as the diffusive dynamics in both phases. It was demonstrated that as the concentration of EPC3 increased, the proportion of the L_d-phase increased while the proportion of the L_o-phase decreased inside the SBLs. Additionally, the lipid diffusive dynamics in both phases were observed to increase. These findings suggested that EPC3 can effectively incorporate into the lipid bilayer, destabilizing the Lo phase and fluidizing the lipid bilayer. Similar observations have been reported in previous studies for other APLs in various membrane models, indicating their ability to accumulate in the membrane and increase membrane tension by lowering the liquid-to-gel transition temperature, potentially leading to membrane destabilization and rupture (198-202). It has been proposed that saturated APLs tend to partition at the boundary between L_o and L_d phases (200). Additionally, it was noted that the enthalpy effect during the transition was more pronounced in models with higher cholesterol content, implying that APLs must be located within the hydrophobic region of the phospholipid (199). Interestingly, strong attractive interactions were observed between some APLs and cholesterol, unlike phosphatidylcholines (PCs), which exhibited weak interactions with a tendency for compo-

nent separation (203). Furthermore, certain APLs demonstrated a stronger interaction with unsaturated PC than to saturated ones, which is noteworthy considering that cancer cell membranes typically contain higher levels of unsaturated phospholipids compared to healthy cells (203). These findings suggest that the lipid composition of healthy cell membranes could serve as a natural barrier against APL incorporation into normal cells, while the disruption or reduction of L_o domains induced by APLs may contribute to their toxicity towards cancer cells by selectively affecting crucial proteins within these raft domains in the PM (200, 203).

Next, the impact of EPC3 on the levels of major lipid species in cellular membranes of two breast cancer cell models was assessed using thin-layer chromatography and gas chromatography. To further evaluate the impact of EPC3 on PM fluidity in both breast cancer cell lines, two fluorescent probes, Laurdan and Di-4-ANEPPDHQ, were employed. Furthermore, changes in membrane dynamics were investigated by measuring two model transmembrane proteins via sFCS. It was shown that EPC3 treatment leads to decreased levels of sphingomyelin, cholesterol, and PC in the cellular membranes of breast cancer cells, while simultaneously increasing the levels of PS. It is worth noting that hormone-dependent breast cancer cell line MCF-7 exhibited lower levels of cholesterol compared to the highly invasive, metastatic breast cancer cell line MDA-MB-231. Furthermore, treatment with EPC3 resulted in a time-dependent increase in membrane fluidity and enhanced diffusion dynamics of transmembrane proteins in the PM in a cytoskeleton independent manner for both cell lines. Notably, this fluidizing effect was more pronounced and faster in MDA-MB-231 cells than in MCF-7 cells. These observations suggest that EPC3 can modify the biophysical properties of the PM in breast cancer cells through two distinct mechanisms. Firstly, EPC3 directly influences lipid-lipid interactions, potentially by affecting cholesterol interactions with other lipids or by altering the bilayer's internal electric dipole potential. Secondly, EPC3 induces changes in lipid metabolism and cell membrane composition, which could further enhance membrane fluidity and dynamics, working synergistically with the initial effect.

The regulation of ceramide and sphingomyelin content in cellular membranes is essential for numerous cellular functions, including maintaining cell integrity, promoting cell proliferation and differentiation, ensuring cell survival, and regulating signaling pathways (i.e., intrinsic and extrinsic apoptosis pathways) (204-208). Previous research has indicated that multidrug-resistant (MDR) cancer cells exhibit decreased levels of ceramide, which could be attributed to the upregulation of sphingomyelin synthesis or the inhibition of sphingomyelinase-mediated conversion of sphingomyelin to ceramide within the cell membrane (208). In this case, increase in sphingomyelin levels leads to more rigid PMs, which are less permeable for anticancer drugs; uncontrolled cell proliferation, resistance to apoptosis and immune response escape (208, 209). Consequently, there is growing interest in disrupting sphingomyelin synthesis to elevate ceramide and sphingosine levels. This elevation can promote apoptosis through various mechanisms such as recruiting, aggregating and activating the Fas/CD95 and TNF-related apoptosis-inducing ligand (TRIAL) receptors in the PM and modulating the mitochondrial membrane permeability, thereby releasing cytochrome C and subsequent activating caspases (205, 207, 208, 210). Previous studies have demonstrated that EPC3 and other APLs have the ability to induce apoptosis in various cancer cell lines through the accumulation of Fas/CD95 receptors and procaspase 8 in the PM, resulting to the formation of the death

inducing signal complex (DISC); the recruitment of TRAIL receptors to the PM, thereby connecting the receptors with the mitochondrial signaling cascade and activating caspases (151, 208, 211-215). Edelfosine and EPC3 have been shown also to release cytochrome C from the mitochondrial membrane (214). These findings suggest that APLs potentially induce a decrease in sphingomyelin levels and an increase in ceramide, aligning with the observations of the present study. Moreover, it was previously shown that cancer cells exhibit elevated levels of PC compared to healthy cells, which has been associated with enhanced cell proliferation, survival, malignant transformation, cancer progression, and manifestation of more aggressive cancer phenotypes (216). Additionally, PC depletion and inhibition of the PC synthesis by anticancer drugs such as APLs were shown to induce apoptosis (214, 216, 217). Since PC serves as precursor for the sphingomyelin synthesis, a decrease of PC levels correlates with a reduction sphingomyelin and an accumulation of ceramide, thereby inducing the previously mentioned processes (214, 216). In addition, a decrease in PC levels may indicate an increase in phosphatidylserine (PS) synthase, the enzyme responsible for converting PC to PS (197). This increase in PS synthesis would result in higher levels of PS in cellular membranes (197), as observed in the current study. This hypothesis is supported by a recent study that demonstrated APLs inhibiting PS uptake (218). Moreover, several studies have shown PS levels at the outer leaflet of the PM can be increased by radiation, external electric fields, and certain chemotherapeutic agents such as APLs (211, 218-221). Importantly, these elevated levels of PS can be effectively targeted using PS-targeting antibodies and peptides to induce cytotoxicity in cancer cells (220, 221).

Cholesterol, a vital component of cell membranes, plays a critical role in various cellular processes, including biomolecule interactions, cell signaling, membrane fluidity, permeability, formation and maintenance of lipid rafts (222-224). Lipid rafts serve as platforms for the recruitment of receptors and activation of various signaling molecules, including receptor tyrosine kinases, which promote cell survival, proliferation, and angiogenesis (208, 223, 225, 226). Additionally, cholesterol metabolites, such as oxysterols, have been shown to modulate key signaling pathways involved in cancer cell growth and survival (223, 225). Cancer cells often exhibit dysregulated cholesterol metabolism, characterized by increased *de novo* cholesterol synthesis and enhanced uptake of exogenous cholesterol (223, 225). This dysregulation is mediated by the upregulation of key enzymes involved in cholesterol biosynthesis and the overexpression of cholesterol transporters, which contribute to the elevated cholesterol levels observed in cancer cells (223, 225). Moreover, studies have shown that highly invasive/metastatic cancer cells (i.e., MDA-MB-231 cells) and MDR cancer cells exhibit higher cholesterol levels compared to their non-invasive and drug-sensitive counterparts (208, 223, 227), aligning with the observation in the current study. Elevated cholesterol levels in MDR cells have been associated with decreased membrane fluidity and permeability, altered lipid raft composition, and enhanced efflux pump activity, which collectively contribute to drug resistance by limiting drug accumulation and promoting cell survival (208, 227). Over the years, researchers have explored various strategies to target cholesterol synthesis and uptake. Cholesterol depletion agents such as methyl-ß-cyclodextrin (MbCD) have the ability to deplete cholesterol from cellular membranes, thereby disrupt lipid rafts (222, 227, 228). This disruption leads to the dissociation of signaling molecules and receptors from lipid rafts, alter-

ing their localization and inhibiting downstream signaling events (222, 227, 228). These alterations affect multiple pathways involved in cancer cell survival, proliferation, migration and invasiveness (222, 228). Notable, it was suggested that MbCD can also affect non-raft domains (35, 229), cause an extraction of sphingomyelin (107, 112, 230) and increase membrane permeability (35, 227). These additional actions can contribute to the modulation of signaling cascades and are likely to influence the previously mentioned processes. Nevertheless, caution must be taken due some MbCD disadvantages: (i) an effective treatment seems to rely on cancer cells having higher surface cholesterol levels, and (ii) MbCD displays cytotoxic effects depending on its concentration and the cancer type (227, 228). Extensive research has underscored the significant potential of statins as anti-cancer agents (223, 227, 228). Statins inhibit the enzyme HMG-CoA reductase, a key enzyme in cholesterol synthesis, thereby reducing intracellular cholesterol levels (227, 228). Therefore, statins were shown to impair cancer cell survival by initiation of cell apoptosis, inhibit cell proliferation by induction of cell cycle arrest, reduce angiogenesis and invasiveness through modulation of receptor expression and signal molecule localization in the PM, leading to tumor growth inhibition (223, 228, 231). However, it is noteworthy that a substantial number of patients can develop intolerance to statin, and the efficacy of statins can vary depending on the cancer type, as MDA-MB-231 cells have been found to be sensitive to statin, whereas MCF-7 cells exhibit statin-resistance (223, 227, 232). APLs exhibit a high affinity for cholesterol in lipid rafts, where they accumulate and subsequently induce lipid domain disruption and increase membrane fluidity as previously seen in model membranes (214, 224, 227, 233-236). Moreover, previous studies have revealed that APLs can be internalized through clathrin-independent, raft-mediated endocytosis or unknown lipid transporter, and subsequently interact with lipid rafts of various cellular membranes such as ER and mitochondrial membranes (214, 224). As a result of these interactions, APLs have inhibited the transport of surface cholesterol to the ER, leading to an accumulation of cholesterol in the PM and depletion of cholesterol in the ER membrane (214, 237). This disruption hinders the esterification process of cholesterol in the ER and cause a dysregulation of the cholesterol synthesis (214, 237). The accumulation of APLs in mitochondrial membranes has been observed to result in mitochondrial swelling, increased membrane permeability, inhibition of mitochondrial respiration, and a decrease in transmembrane potential (224). These effects collectively contribute to the induction of cell apoptosis (224). Additionally, prior research has revealed that APLs can reduce the cellular cholesterol levels through mechanisms such as cholesterol depletion effects similar to those of MbCD and ABCA1-mediated cholesterol efflux into the extracellular space (218, 238), thereby initializing the same process as observed for MbCD and statins. These findings are consistent with the observations of the current study. Moreover, the observed reduction in sphingomyelin and cholesterol levels, along with the increase in PS levels induced by APLs, lead to an increase in membrane fluidity (239). This alteration in lipid-lipid interactions is in line with the findings of the present work.

Overall, this study provided valuable insights in the molecular mechanism of action of EPC3, utilizing a combination of biophysical methods to explore cellular membrane properties. In particular, EPC3 induced alterations in cellular lipid composition in cellular membranes and significantly increased PM fluidity, with a more pronounced effect observed in highly inva-

sive breast cancer cells. These findings suggest that when used in combination with other anticancer drugs, EPC3 has the potential to enhance treatment outcomes, particularly for highly invasive and MDR tumors.

4.2.2 *IAV infection leads to alterations in lipid-lipid interactions and modifies the intracellular membrane charge of the PM*

To investigate the effect of IAV infection on the inner surface electrostatic potential of the PM, a FRET-based membrane charge sensor was utilized. The results in this study demonstrated for the first time that IAV infection led to an increase in the negative electrostatic potential of the PM inner surface. This observed change might be attributed to a local enrichment of anionic lipids on the inner surface of the PM, which is consistent with previous research, showing higher concentrations of PS in cellular membranes of infected cells and within the viral envelope compared to non-infected cells (127, 154, 191, 240). Interestingly, Woods *et al.* have shown elevated levels of specific phosphatidylinositol (PI) lipids and decrease of PC levels in cellular membranes of infected alveolar type II (AEC-II) cells (191). These variations in phospholipid levels may be indicative of specific mechanisms employed by IAV to manipulate phospholipid metabolism and host cell membranes (191). In addition, M2 directly interacts with LC3-II, leading to the inhibition of autophagosome-lysosome fusion and causing a re-localization of the autophagosomes to the PM (Chapter 3.5) (99, 106). Subsequently, this autophagosomes fuse with the PM, enabling the insertion of these proteins and other vesicular components (e.g., PE, PS, different phosphoinositides) into the PM (Chapter 3.5) (99, 106). Liu *et al.* have provided evidence demonstrating that the levels of LC3-II, in conjunction with M2, significantly increase during infection (241). These alterations have the potential to further increase the local concentration of anionic lipids within the inner leaflet of the PM. However, it is important to consider that the observed changes could be also influenced by alterations in cytoplasmic ionic strength/composition or changes in lipid/protein organization (117, 129, 242-244). Specifically, there are two factors that can contribute to the alteration of membrane properties: a decrease in cytosolic cation concentration and the dissociation of proteins containing polybasic amino acid sequences (243). These changes can lead to a reduction in the ion shield effect, which affects the overall charge distribution across the membrane (243). Additionally, the clustering of negatively charged lipids can potentially modify the local zeta potential of the membrane (117, 129, 243, 244). The enhanced abundance or availability of anionic lipids on the inner surface of the PM could have implications for the organization of viral components. For instance, studies have indicated that M1 forms clusters with PS when recruited to the PM by M2 in IAV infected cells (Chapter 3.4) (129) as well as with phosphatidylinositol 4,5-biphosphate (PIP2) in co-transfected cells (244). Furthermore, Curthoys *et al.* proposed that an expression of HA results in reduced mobility of PIP2 and in re-localization of PIP2 to the center of HA clusters (117), which might crucial for its interaction with the cytoskeleton (119) and with M1 (244). Interestingly, Kakisaka *et al.* have shown that the localization of NP to the inner leaflet of the PM is controlled by the level of PIP2 in the PM (245). This effect was facilitated by direct interaction between the intrinsi-

cally disordered region 2 (IDR2) of NP, viral RNAs (vRNAs), and PIP2, which plays a fundamental role in viral genome packaging (245). These findings strongly suggest that an IAV infection promotes lipid rearrangement at the inner surface of the PM, leading to accumulation of anionic lipids in confined areas, regardless of IAV strain or cell type. These lipid alterations could play a critical role in viral assembly and egress, a phenomenon that may not be exclusive to IAV but could also occur during the assembly of other enveloped viruses that bud from the PM. For instance, the human immunodeficiency virus (HIV) Gag protein was shown to interact with PIP2 on the inner surface of the PM (246, 247). This interaction could trigger the assembly of Gag proteins, which in turn can induce the formation of PIP2/cholesterol-enriched domains without trapping phosphatidylethanolamine (PE) and sphingomyelin (246, 247). This specific lipid rearrangement would result in a more anionic inner leaflet (246, 247). This unique combination of lipids could then promote the recruitment and assembly of more Gag proteins at the specific lipid microdomains of the budding side, thereby enhancing HIV assembly and egress (246, 247). These findings are supported by the fact that a depletion or delocalization of PIP2 disrupts the targeting of Gag to the PM and severely impairs the budding of HIV (248). Furthermore, studies have demonstrated that a decrease in PS and PIP2 levels in mammalian cells can inhibit the recruitment and oligomerization of viral protein 40 (VP40) at the PM, effectively blocking the assembly and egress of Ebola virus and Marburg virus (249-252). Similar effects have also been observed for the matrix (M) protein of Nipah virus and measles virus (253). Notably, the binding of VP40 and M proteins to the PM has been demonstrated to provoke clustering of PS and PIP2 at cholesterol-enriched nanodomains (253, 254). Interestingly, the expression of VP40 and Gag proteins has been shown to expose PS on the outer leaflet of the PM (252, 255), further highlighting the intricate interplay between viral proteins and lipid components in the assembly and release of these viruses. Taken together, the findings suggest that targeting the biosynthesis of anionic lipids or modulating the trafficking of specific anionic lipids, such as through inhibiting uptake, efflux, or flip-flop mechanisms, could serve as potential therapeutic strategies to mitigate the spread of IAV (248, 250-253).

To further investigate the effects of IAV infection on biophysical membrane properties, two commonly used membrane environmental sensing probes, namely Laurdan and Di-4-ANEPPDHQ, were employed as previously used in Chapter 3.2 (46-48, 51). These probes can provide complementary information about lipid packing and membrane fluidity (46-48, 51). Additional, two PM markers, mp-mEGFP for the inner leaflet and GPI-mEGFP for the outer leaflet, were used to quantify membrane dynamics via sFCS (35, 44, 45). The results in this study demonstrated that IAV infection enhanced lipid-lipid-interactions in the PM. This was caused by an increase in lipid packing and a reduction in the fluidity of the PM, as observed for both environmental sensing probes. Consequently, the diffuse dynamics of both PM leaflet markers were significantly slower after infection. These observations suggest that the local enrichment of cholesterol and/or saturated lipids such as sphingolipids may be responsible for these changes, either by altering local lipid composition within one specific leaflet and transmitting it to the other leaflet through enhanced interleaflet coupling (256, 257), or by affecting the general bilayer composition such as cholesterol concentration in both leaflets (257). This assumption is further supported by previous studies. In particular, Tanner *et al.* have shown

that IAV infection results in a decrease in ester-linked PC species levels and elevation in sphingomyelin levels within cellular membranes of A549 lung cells (154). This could potentially be attributed to the depletion of cellular choline stores, which may be utilized for sphingomyelin synthesis (258). Previous studies provided further evidence that sphingomyelin plays a crucial role for the transport of newly synthesized HA and NA proteins from the Golgi apparatus to the PM and virus egress (107, 152). These observations are consistent with previous research, showing higher concentrations of sphingomyelin and reduction of PC levels in the viral envelope compared to non-infected cells (154, 240, 259). Additionally, Lin *et al.* reported that IAV infection mediates an enrichment of cholesterol within cellular membranes of A549 cells (189), which is consistent with the previously observed higher cholesterol levels within viral membranes compared to non-infected cells (259, 260). Cholesterol has been found to play a significant role for the apical transport of viral glycoproteins, HA and NA (261). Kawaguchi *et al.* proposed that these cholesterol-enriched vesicles subsequently fuse with the PM, resulting in the accumulation of sphingomyelin, crucial for the formation of the budding zone and for the stability of the viral envelop (262, 263). Fusion of such cholesterol/sphingomyelin-enriched vesicles with the PM could further increase membrane rigidity and reduces membrane dynamics. Additionally, prior research has demonstrated a significant clustering of M2 in cholesterol-enriched membranes, and that the insertion of the M2 amphipathic helix has a profound impact on the lipid order of the inner leaflet of the PM (264-266), which would support the findings in the current study and preliminary results from M1-M2 co-transfected HEK293T cells treated with cholesterol small unilamellar vesicles (SUVs) (Figure S2A). Interestingly, a recent study conducted by Loshkareva *et al.* proposed that the adsorption of M1 to raft-forming GUVs could potentially initiate phase separation and vesicle formation (242). This phenomenon is believed to be facilitated by the presence of an amphipathic helix within the M1 structure (242, 267). Moreover, IAV-induced modulations of phospholipid synthesis (154, 189, 191) and phospholipid rearrangements (117, 129, 244) could cause a phospholipid imbalance inside the membrane leaflets and destabilizing the PM (242, 268), which was recently shown to be compensated by cholesterol rearrangements across both leaflets of the PM (268). It is worth mentioning that cholesterol enrichment can be accompanied by increased levels of PIP2 (269) and that an incorporation of PS into cholesterol/sphingomyelin domains enhances interleaflet coupling, leading to an increase in membrane stiffness (256). These findings strongly suggest that an IAV infection alters lipid-lipid interactions at both PM, leading to a reduction in membrane fluidity and dynamic, regardless of IAV strain or cell type. In general, such alterations in the membrane order parameters might originate from an overall re-organization of the membrane components or might be caused by the presence of, e.g., locally-ordered membrane domains (250) from which the virus can efficiently assemble and bud. Moreover, these findings underscore the crucial involvement of cholesterol and sphingolipids in multiple stages of IAV infection, as well as their impact on the properties of the PM. Notably, the viral envelope proteins HA, NA, and M2 as well as the core protein M1 are likely to be the primary factors influencing these effects (117, 242, 244, 261, 262, 264). This phenomenon may not be unique to IAV but could also occur during the assembly of other enveloped viruses that bud from the PM (e.g., HIV and Ebola virus) (246, 270-273). Therefore, compounds which inhibit cholesterol/sphingomyelin lipid biosynthesis or modulate the traffic of such lipids (i.e., uptake and efflux) are promising therapeutic strate-

gies to reduce influenza A virion spread (107, 152, 250, 263, 274, 275). For instance, inhibition of sphingomyelin syntheses, which would lead to an increase of ceramide levels, were shown to impair viral protein transport, virus uptake and egress (107, 152). Additional, reduction of cholesterol levels via cholesterol depletion agents (e.g., MbCD), inhibiting of cholesterol synthesis (e.g., statins), or modulating the expression levels of key regulators of the cholesterol homeostasis (e.g. Annexin A6) have been demonstrated to hinder viral protein transport, virus entry and budding (250, 261, 263, 276). However, as previously mentioned (Chapter 4.1), such compounds can have moderate-to-severe side effects and patients can develop intolerances to specific agents (e.g. statins). Therefore, future studies should focus on investigating the efficacy and action of newly designed agents against IAV infection. Promising candidates are APLs, which were shown to significantly impair HIV production (277-279).

In summary, this study provides compelling evidence of IAV-induced alterations in the organization and dynamics of the PM. The results indicate that IAV infection leads to decreased membrane fluidity, increased lipid packing, and an enhancement of the negative electrostatic potential at the inner surface of the PM. The latter is likely attributed to increased local concentrations of anionic lipids. Given the pivotal role of various lipid species in different stages of the IAV life cycle, targeting them therapeutically holds promise for combatting IAV infections.

4.2.3   Conclusion and Outlook

Both studies highlight the potential of combining biophysical methods in investigating membrane properties in order to gain a better understanding of virus-host interactions and the molecular mechanisms of action of lipid-targeting drugs on various diseases, and to characterize cancer cell types. Furthermore, these approaches would provide insights into the role of specific viral proteins that influence membrane physical properties during virus assembly. Notably, the fluorescence microscopy approaches in comjunction with the implemented semi-automatic analysis pipeline offer a valuable, fast screening tool at a single-cell level. Especially, the FRET membrane charge sensor offered several advantages over the commonly used intensity-based measurements (e.g., lactadherin C2 domain linked to a FP senses PS) (243). Firstly, it is stably linked with the inner leaflet of the PM, leading to a reduction of cytosolic signals and an improvement of the signal-to-noise ratio (243). Additionally, the sensor employs an identical number of donor and acceptor molecules, enabling ratiometric measurements that do not rely on sensor concentration (243). This permits cell-to-cell comparisons, the detection and quantification of the negatively charged membrane domains (243). Moreover, the use of multiple probes, such as Laurdan and Di-4-ANEPPDHQ, enables cross-validation of the obtained membrane fluidity measurements. This approach enhances the reliability of the findings by reducing the potential bias or limitations associated with a single probe. Both probes are influenced, each in a specific way, by several factors including: cholesterol content (in connection to glycerol backbone dynamics), membrane hydration (in connection to lipid internal motions and hydrogen bond network dynamics) (280, 281) and phase

behavior (46, 48). Furthermore, it was reported that while Laurdan is a reliable probe for membrane order, Di-4-ANEPPDHQ is influenced by cholesterol and membrane potential (46). However, both probes have their drawbacks. Laurdan, in particular, exhibits fast initial photobleaching and has a higher tendency to penetrate into the cytosol, which can result in the labeling of intracellular structures (48, 282). This renders the selection of regions of interest more challenging and less accurate, while also generally increasing the variability in observed GP values. Therefore, Laurdan should be substituted by the newly designed Laurdan derivate Pro12A to overcome these limitations (282, 283). Di-4-ANEPPDHQ, on the other hand, displays complex photophysics (46, 48). In particular, Di-4-ANEPPDHQ was demonstrated to be less sensitive to Lo phase and could possible attenutate the order of Lo membranes (46, 48, 49). To investigate changes in the biophysical properties of the PM at nano-scale level using live cell super-resolution techniques, it is recommended to replace both probes with recently developed Nile Red analogues (283-286). These analogues exhibit on/off switching characteristics, or permit long-term acquisition through higher photostablity or transiently binding features (284, 285). Furthermore, the model-free spectral phasor analysis can be improved by incorporating the phasor image and additional quantitative analysis tools, such as the calculation of pixel fractions of each phase (55, 287). Additionally, several model membrane proteins were used in these current studies to quantify membrane dynamics. The GPI-anchored protein (GPI-mEGFP) and the mp-lipidated protein (mp-mEGFP) are ideal candidates for observing dynamic membrane alterations at the PM in both directions, increase and reduction in diffusive dynamics (Chapter 3.3) (44, 45, 55, 287), whereas both model transmembrane proteins were better suitable for the detection of increased membrane dynamics (Chapter 3.2) (44). One possible explanation for this phenomenon is that the diffusive dynamics of transmembrane proteins are not solely determined by lipid bilayer viscosity, but by other factors including their interaction with the cytoskeleton or protein crowding (43, 44, 112, 116, 119, 158, 288). To unravel the impact of the cytoskeleton on such measurements, the analysis could be improved by incorporating additional controls: (i) utilizing cytoskeleton-free GPMVs (Chapter 3.2) (289), and (ii) treating cells with compounds like latrunculin A to induce actin cytoskeleton depolymerization (44). Another possible explanation for the limited suitability of the model transmembrane proteins could be the slow diffusive dynamics exhibited by these proteins, which are already in the range of the temporal resolution limit of confocal sFCS analysis (290-292). Combination of sFCS with super-resolution techniques such as scanning stimulated emission depletion (sSTED)-FCS (291, 293-295) and others (reviewed in (296)) would simultaneously improve the spatiotemporal resolution. For example, sSTED-FCS was previously used to study the mobility of the HIV proteins and at the assembly site in lymphocytes and in the viral envelope (293, 294), as well as the spatiotemporal heterogeneity of fluorescent lipid analogues in the PM (291).

To gain a better understanding how each viral protein alter the structural organization of specific lipid species in nanodomains of the assembly site, constructs of the viral proteins and of several lipid sensors linked to photoconvertible and photoactivatable FPs were generated for future studies using photoactivation localization microscopy (PALM). For example, this approach were shown to be suitable for studying co-clustering of HA, M1 and lipid sensor for PIP2, as well as the impact of the quaternary ammonium compound cetylpyridinium chloride,

which is an modulator of the structural membrane organization and associations of PIP2-binding proteins, on the assembly of HA and M1 in the PM (117, 244). This method can also be expanded to investigate structural membrane organizations of other diseases. For cancer diseases, it is important to determine: (i) the magnitude, variety, and interaction between different lipid domains, (ii) the degree to which nanometric rafts merge into submicrometric domains under specific conditions, and (iii) whether there is a correlation between lipid domains of both PM leaflets (227). Considering the significant impact of membrane tension alterations on cancer cell migration and invasion (297), as well as various stages of the viral life cycles (298-300), mechanosensitive fluorescent probes, namely Flippers, should be included in future studies (301). Such probes can detect alterations in membrane tension resulting from lipid-packing changes in different cellular compartments and membrane domains (301). Furthermore, recent studies have demonstrated the significance of PM viscosity in drug resistance among cancer cells, primarily influenced by changes in the lipid composition of the PM (302). Therefore, it is advisable to incorporate measurements of membrane viscosity into the analysis pipeline using techniques such as the fluorescent molecular rotor BODIPY2 (302). By considering both membrane tension and membrane viscosity, in addition to membrane fluidity and dynamic analysis, a comprehensive cross-validation of the results can be achieved. There are limited number of lipodome studies on IAV-infected mammalian cells, with a primarily focus on specific lipid metabolites of whole cells (154, 189, 191). These studies often utilized laboratory-adapted IAV strains, cancer cell lines, or non-human cell models (154, 189, 191). Consequently, the existing studies lack detailed information on IAV-induced alterations in lipid composition and organization within specific cellular membranes in their natural environment. Therefore, it is essential to utilize more comprehensive lipidomics analysis techniques on primary cells and/or human lung tissue infected with various strains of IAV at different infection stages, as well as transfected with individual viral proteins. Techniques such as matrix-assisted laser desorption/ionization (MALDI)-mass spectrometry (MS) imaging or nano secondary ion mass spectrometry (nanoSIMS) can be used to analyze lipid composition and organization at the PM (303-305). Additionally, classical MS analysis can be conducted on isolated cell compartments to obtain the lipid profile of each specific compartment (306).

4.3   Combination of FFS approaches reveal insights into IAV protein-protein interactions at the assembly site and in the nucleus

Influenza virus proteins interact with each other and with host proteins to carry out essential functions during viral replication (6). Studying these interactions can provide valuable insights into the molecular mechanisms of viral replication and virus-host interactions (7). This knowledge is essential in the development of antiviral strategies that target these interactions and disrupt viral replication (7).

Most IAV PPI studies based on classical approaches, such as co-immunoprecipitation followed by Western blot analysis, yeast 2-hybrid systems and affinity purification of epitope-tagged viral proteins combined with MS (43, 125, 307). However, each technique has certain limitations that should be considered. These limitations include the need for purified proteins,

the possibility of artifacts caused by overexpression, the potential for false positive or false negative PPIs, difficulties in detecting proteins in subcellular compartments or membranes, as well as the inability to detect weak or transient interactions (1-3). Moreover, these techniques do not permit detection of PPIs in living cells (2, 18). Consequently, several studies reported conflicting data, leading to uncertainty in this area (125, 307). In the past decades, various imaging techniques have been used to analyze PPIs in living cells, including BiFC, FRET, and FFS (2, 18, 43). These approaches enable direct observation of the spatial and temporal aspects of such protein interactions (2, 18, 43). BiFC offers several advantages for studying protein-protein interactions. It can detect weak and transient interactions due to the irreversible assembly of FP units (1, 18). Additionally, BiFC is compatible with a wide range of FPs, including photoactivatable and photoconvertible FPs, making it suitable for integration with techniques like SMLM (18). Furthermore, BiFC can be paired with FRET to observe interactions involving three proteins within a complex (18). BiFC has been used in previous studies to demonstrate the capability of Gag proteins from various HIV strains to co-assemble and mutually enhance their functionality (308). Additionally, Hemerka *et al.* utilized BiFC to provide evidence of a direct interaction between IAV PA and both PB1 and PB2 (309). However, it is important to consider that BiFC data may be prone to false positives due to the intrinsic binding affinity of the FP units (1, 18). The irreversible nature of FP complementation also limits the ability to perform time-dependent studies (18). On the other hand, FRET has the ability to quantify dynamic changes of protein complexes with single-molecule resolution continuously in living cells (1, 2). However, there are certain drawbacks associated with FRET. One limitation is the inability to compare dissociation constant values or FRET efficiencies across different protein pairs, even if they are linked to the same FP pair (103). Furthermore, variations in maturation time, quantum yields, and detection efficiencies between the two different FPs can have a detrimental impact on their fluorescence probability consequently affecting the accuracy of FRET efficiencies (18). In case of membrane associated proteins, FRET events can occur by random collision of both FP through their restriction to lateral movement (43). FRET efficiency is directly proportional to the concentration of the acceptor. The combination of FRET with fluorescence lifetime imaging microscopy (FLIM) can overcome some limitations. FLIM-FRET eliminates the need for corrections related to signal bleed-through, is less affected by photobleaching, and is independent from FP concentration, thereby making it a more robust and quantitative approach (18, 310). Previous studies have utilized this approach to demonstrate that HA clusters with lipid raft markers and with M2 in a cytoskeleton-dependent manner (311-313), as well as to monitor HIV protein assembly (314). However, it is important to consider that fluorescence lifetime can be influenced by various environmental factors, including pH and the presence of ions, which can pose challenges when studying PPIs in different cellular compartments (310). Moreover, due to the necessity of short distances ($\leq$ 6nm) and specific orientation between the FPs, they must be positioned, for instance, at the same membrane leaflet site of the proteins (43). This positioning might be in close proximity to protein binding sites thereby potentially hinder PPIs, making this approach not suitable for the PPI investigations of the current studies (Chapter 3.4 and Chapter 3.5).

The current work presents an alternative approach that overcomes the limitations of previous techniques. Various FFS techniques were utilized to investigate protein self-assembly and protein complex assembly. The latter technique detects correlated number fluctuations resulting from the co-diffusion of protein complexes within a diffraction-limited focal volume (5, 22, 23, 315). For instance, sFCCS is well suited for studying interactions of proteins that are evenly distributed, including membrane proteins that do not exist in spatially resolvable clusters, whereas ccN&B also allows the analysis of PPIs in clusters (5, 22, 23, 289, 315). For example, in the case of sFCCS, the membrane signal is gathered throughout the scanning direction, and the combined contributions from several pixels are obtained at each time point (22, 23, 315). As a result, the cross-correlation analysis is not compromised by larger distances between FPs or any potential optical shifts in the observation volumes during scanning (18, 22, 23, 289, 315). The cross-correlation analysis remains robust as long as the diffusion times are significantly longer than the time needed to obtain the signal in one line (18, 22, 23, 289, 315). Consequently, for studying PPIs between IAV transmembrane proteins (HA, NA, and M2) and IAV M1 proteins as well as host factors at the initial steps of IAV assembly, FPs can be positioned on opposite sides of the PM studies (Chapter 3.4 and Chapter 3.5). The implementation of FFS assays has enabled the development of a model for the early stages of IAV assembly. The observations have provided evidence that M2 is transported to the PM as consequence of its strong interaction with LC3-II-postive vesicle (Chapter 3.5). Once associated with the PM, M2 plays a crucial role in facilitating the recruitment of M1 to specific regions of the PM through direct interaction, irrespective of the IAV strain (Chapter 3.4, Figure S2C). Subsequently, M1 interacts with the viral glycoproteins HA and NA (Chapter 3.4). This proposed model aligns with previous studies that have demonstrated the ability of M2 to trigger non-canonical autophagy, and subsequently block the formation of the autolysosome by directly interacting with LC3-II (316-318). This interaction leads to a re-direction of LC3-II positive vesicles to the PM, and fusion between these vesicles and the PM (241, 316-318). Furthermore, previous observations have emphasized that the interaction between M1 and M2 directs M1 to the interface region between raft and non-raft domains at the PM or to regions enriched with anionic phospholipids, which is crucial for driving virus assembly (43, 75, 122, 129, 319-323). This interaction may be facilitated by phosphorylation events occurring at the protein binding sites or electrostatic interactions (323-327). Moreover, previous reports have shown that the cytoplasmic tails of HA and NA facilitate the association of M1 with lipid rafts at the PM in infected cells (328-330). It was previously shown that M2 may serve as a mediator between the viral glycoproteins and M1, which might be influenced by the lipid environmental, such as the re-organization of PIP2 towards HA cluster (113, 117, 242, 244, 313, 330-332). These interactions are believed to be involved in the formation of larger protein complexes and ultimately contribute to IAV capsid assembly. However, it is important to note that contradictory results have been observed for different cell lines and infection statuses. Thus, further investigations are needed to clarify these interactions. Additionally, primarily results showed that M1 and M2 co-cluster upon treatment with cholesterol in cells (Figure 2B). The oligomerization of M2 has been reported to be dependent on protein/lipid molar ratios and cholesterol levels (264, 265). Furthermore, M2 tetramers were found to be more tightly packed in membrane regions with higher cholesterol content, particularly in the highly

curved region of the neck of viral budding (333). Therefore, future studies should further investigate the role of cholesterol for M1-M2 interactions.

Nevertheless, it is important to consider several limitations of the FFS approaches used. Firstly, these approaches typically rely on protein diffusion, making them unsuitable for studying immobile or very slow diffusive protein complexes (334). In the present study, this issue was encountered with all investigated viral proteins in infected cells, as they formed viral protein clusters (Chapter 3.4). The sFCCS measurements in these clusters suffered from significant initial photobleaching, which could not be corrected using standard algorithms (i.e., multiexponential function algorithm (20)) and thus were not suitable for PPI analysis. In contrast, ccN&B analysis proved to be more appropriate for detecting PPI between viral proteins in infected cells. To reduce potential photobleaching, it may be beneficial to introduce short pauses between each frame (32). However, slow dynamics need long acquisition times of several minutes, which may not be feasible in highly dynamic systems. This can be challenging due to the limitations imposed by cell movement. To address this issue in the present work, a previously developed image alignment algorithm was employed to correct for lateral cell movement (32). Another limitation to consider is the presence of stronger background fluorescence in cellular systems. This can introduce bias in the Gaussian fit utilized in sF(C)CS analysis for the definition of the membrane signals, subsequently affecting FFS parameters such as particle number, molecular brightness, and diffusion time. For instance, background signal from the cytosol may lead to an increase in the number of particles detected, as well as a decrease in diffusion time and molecular brightness. Hence, it is essential to interpret the values obtained from such measurements with caution. To minimize potential sources of error, it may be beneficial to incorporate a background correction step into the analysis pipeline in future studies.

Next, molecular brightness analysis of sF(C)CS and (cc)N&B data only provides average values for all molecular species. Hence, this analysis is suitable for characterizing a uniform group of particles with identical molecular brightness, but it lacks the ability to distinguish more intricate scenarios, such as mixtures of particles exhibiting different oligomeric states. In this case, relying solely on the average molecular brightness value does not provide an accurate representation of the actual molecular composition of the sample. To address this limitation, various techniques incorporating advanced statistical analysis have been developed. The recently developed enhanced N&B approach was utilized to investigate the dynamics of ligand-binding dependent receptor oligomerization (335, 336). This method employs circular shifting of the analysis window per time frame, enabling the determination of brightness distribution per pixel rather than just an average value (335, 336). Another extension of the N&B approach allows the determination of association constants at the equilibrium state by fitting an empirical model to the obtained brightness values as a function of protein concentration (or number) normalized to the focal volume (18, 337). This approach is particularly useful for detecting concentration-dependent protein oligomerization (18, 337), as demonstrated in the present study where it was successfully used to monitor M1 oligomerization in infected cells (Chapter 3.4). Another technique that can be employed is the amplitude distribution analysis of fluorescence fluctuations using photon counting histograms (PCH) (338, 339). This method captures the brightness distribution and has the advantage of being able to resolve even mon-

omer-dimer mixtures, unlike FCS (134, 338). Additionally, higher order moment analysis of photon count distributions, such as (time-integrated) fluorescence cumulant analysis ((TI)FCA), provides further statistical criteria for predicting oligomer species ratios (340, 341). However, it is important to note that these methods require longer acquisition times to achieve a sufficient SNR and lower concentrations compared to FCS and N&B measurements, which may not be achievable in overexpressing living cells (335, 339, 342).

Finally, traditional FFS methods were limited to studying PPIs with only two chromatically separable fluorescent proteins (FPs), making it difficult to study more complex interactions involving multiple partners (343-345). However, recent advancements have introduced two new approaches: (i) three-color RSICS, which uses statistical filtering of spectral information to separate fluorescence signals during spatial correlation analysis (344), and (ii) single-color fluorescence lifetime cross-correlation spectroscopy (sc-FLCCS), which takes advantage of GFP variants with different fluorescence lifetimes (345). In this study, two FFS techniques, FSCS (346) and sFCS (21), were combined to enable multi-color studies of PPIs at the PM (Chapter 3.5). Additionally, FSFS approaches were extended to four-color analysis and their potential for multiple protein complex analysis was explored (Chapter 3.5). It was demonstrated that SFSCS and RSICS enabled a cross-talk free analysis of up to four FP species simultaneously in living cells. These methods provided accurate estimations of protein concentration, diffusive dynamics, oligomerization (and thus stoichiometry), and protein interactions of multiple species. Importantly, these methods can be employed on a conventional confocal laser scanning microscope with a spectral photon counting detector system, and have recently been transferred to a camera-based microscope system (343). Therefore, these approaches represent a powerful tool for studying complex protein interaction networks in living cells, as exemplified by the two biological examples presented in this study. Specifically, the three-color SFSCS analysis of the interaction between IAV M2 and two host factors, LC3-II and CD9, at the PM revealed a strong interaction between LC3-II and M2, consistent with previous reports (316). However, no interaction between CD9 and M2 or LC3-II was detected. Shaw *et al.* provided evidence of CD9 incorporation into influenza virions (347), suggesting that tetraspanin-enriched microdomains may interact with lipid raft domains to mediate virus budding (347, 348). However, recent reports indicate that the interaction between NA and tetraspanin CD81, rather than CD9, facilitates this effect (349). Next, to investigate the IAV polymerase complex PC, the stoichiometry of its subunits PA, PB1, and PB2 in the cell nucleus was determined using three-color RSICS. The results strongly support a 2:2:2 stoichiometry, indicating that the heterotrimeric PC dimerizes inside the nucleus. This model aligns with previous findings from X-ray crystallography and cryo-electron microscopy experiments (350). It was suggested that PA and PB1 form heterodimers in the cytosol and are transported together into the nucleus, where they interact with PB2 to form the heterotrimeric polymerase complex (6, 95, 96). The dimerization of this complex is crucial for viral genome replication and transcription (6, 350). In conclusion, the experimental approaches employed in this study provide a powerful tool for future investigations. For example, they can be used to explore the interaction between viral proteins and cellular host factors or PM lipids at different stages of the IAV life cycle. Thus, these methods can aid in the development of inhibitors that target

the assembly process of such protein complexes, offering a promising therapeutic strategy for antiviral drugs.

5 Supplemental material
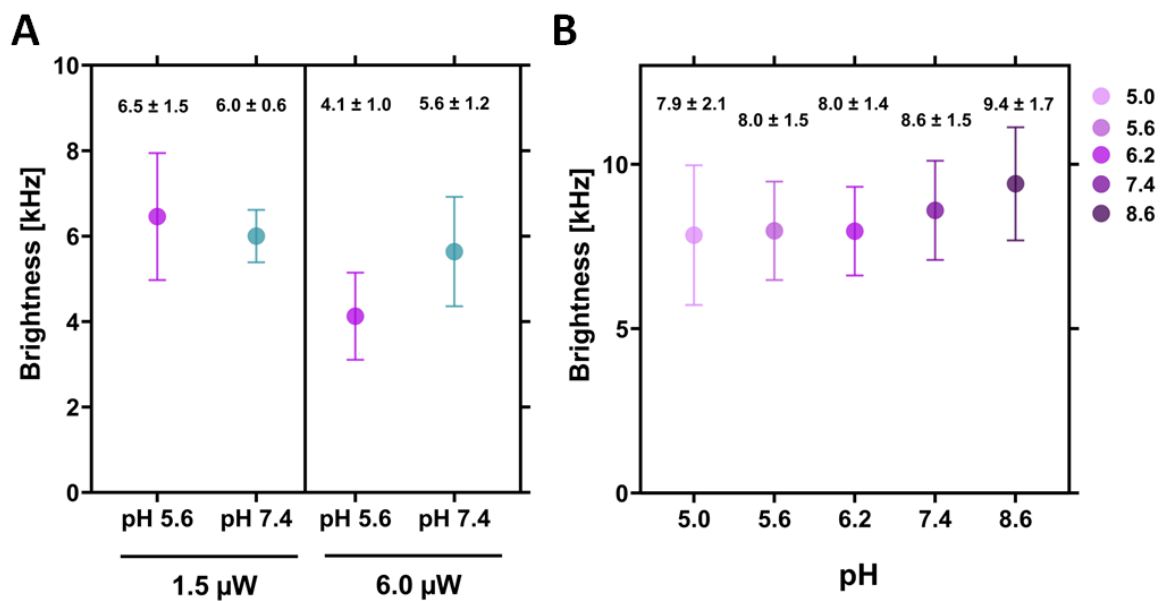
Figure S1 Comparison of molecular brightness for membrane-associated mEGFP and mCherry2, as obtained from sFCS measurements in HEK293T cells under different excitation powers and pH conditions.
A) Average molecular brightness of GPI-mEGFP measured under two different excitation powers and pH conditions. Data for each condition are collected from ten cells. The error bars represent the standard derivation. B) Average molecular brightness of GPI-mCherry2 measured under different pH conditions using a constant excitation power. Data for each condition are collected from 10-15 cells. The error bars represent the standard derivation.
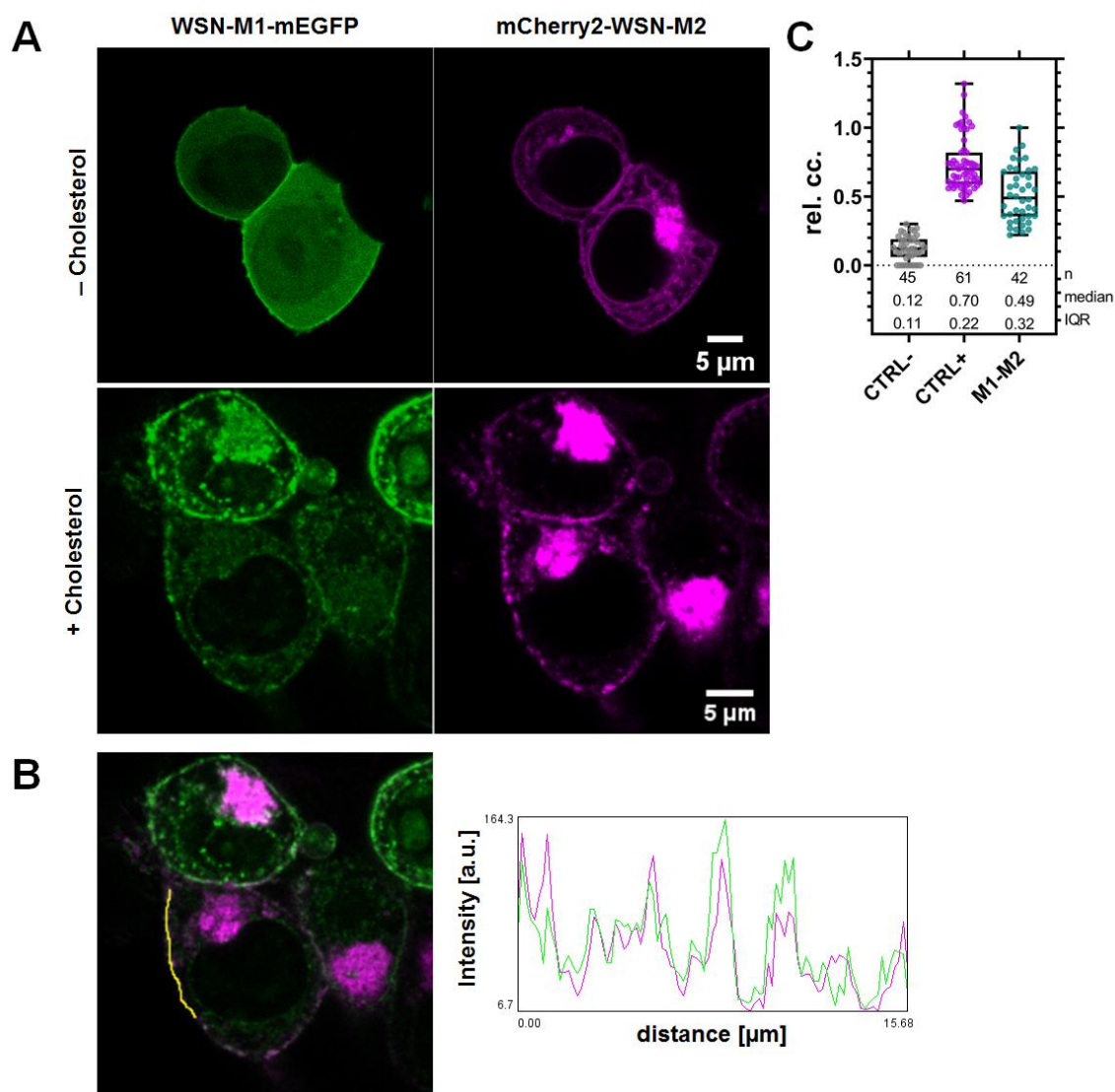
Figure S2 Treatment of IAV M1-M2 co-transfected HEK293T cells with cholesterol results in the co-clustering of both proteins. HEK293T cells were seeded on poly-L-lysine coated 35 mm glass dishes 24 h prior transfection with WSN-M1-mEGFP and mCherry2-WSN-M2 (for further details see Chapter 3.4). After ca. 16 hpt, cells were washed twice with DPBS without Ca^{2+} and Mg^{2+} (DPBS$_{-/-}$) and subsequently incubated with cholesterol small unilamellar vesicles (SUVs, final concentration ~ 0.5 mM in DPBS$_{-/-}$) or DPBS$_{-/-}$ for 30 min at room temperature. Afterwards, cells were washed twice with and imaged on the Zeiss LSM780 system. A) Representative confocal fluorescence images of HEK293T cells expressing WSN-M1-mEGFP (green) and mCherry2-WSN-M2 (magenta) with and without cholesterol treatment. B) Line intensity profile plot indicate the intensity distribution of both channels along the yellow line in the overlay image of HEK293T cells after cholesterol treatment. C) Box plot with single data points from three independent experiments shows the relative cross-correlation (rel. cc) for the controls negative control mp-mEGFP(1x)/mp-Cherry2 and positive control mp-mCherry2-mEGFP, and between WSN-M1-mEGFP and mCherry2-WSN-M2 without cholesterol treatment. Median values and whiskers ranging from minimum to maximum values are displayed. Sample size, median, and IQR are indicated in the graph.

6 Bibliography

1. Poluri, K. M., K. Gulati, and S. Sarkar. 2021. Experimental Methods for Determination of Protein–Protein Interactions. In Protein-Protein Interactions: Principles and Techniques: Volume I. K. M. Poluri, K. Gulati, and S. Sarkar, editors. Springer Singapore, Singapore. 197-264.
2. Syafrizayanti, C. Betzen, J. D. Hoheisel, and D. Kastelic. 2014. Methods for analyzing and quantifying protein-protein interaction. Expert Rev Proteomics 11:107-120.
3. Xing, S., N. Wallmeroth, K. W. Berendzen, and C. Grefen. 2016. Techniques for the Analysis of Protein-Protein Interactions in Vivo. Plant Physiol 171:727-758.
4. Chen, Y., J. D. Müller, K. M. Berland, and E. Gratton. 1999. Fluorescence fluctuation spectroscopy. Methods 19:234-252.
5. Yu, L., Y. Lei, Y. Ma, M. Liu, J. Zheng, D. Dan, and P. Gao. 2021. A Comprehensive Review of Fluorescence Correlation Spectroscopy. Frontiers in Physics 9.
6. Dou, D., R. Revol, H. Östbye, H. Wang, and R. Daniels. 2018. Influenza A Virus Cell Entry, Replication, Virion Assembly and Movement. Frontiers in Immunology 9:1581.
7. Heaton, N. S., N. Moshkina, R. Fenouil, T. J. Gardner, S. Aguirre, P. S. Shah, N. Zhao, L. Manganaro, J. F. Hultquist, J. Noel, D. Sachs, J. Hamilton, P. E. Leon, A. Chawdury, S. Tripathi, C. Melegari, L. Campisi, R. Hai, G. Metreveli, A. V. Gamarnik, A. García-Sastre, B. Greenbaum, V. Simon, A. Fernandez-Sesma, N. J. Krogan, L. C. F. Mulder, H. van Bakel, D. Tortorella, J. Taunton, P. Palese, and I. Marazzi. 2016. Targeting Viral Proteostasis Limits Influenza Virus, HIV, and Dengue Virus Infection. Immunity 44:46-58.
8. Jameson, D. M., J. A. Ross, and J. P. Albanesi. 2009. Fluorescence fluctuation spectroscopy: ushering in a new age of enlightenment for cellular dynamics. Biophysical Reviews 1:105-118.
9. Kitamura, A., and M. Kinjo. 2018. State-of-the-Art Fluorescence Fluctuation-Based Spectroscopic Techniques for the Study of Protein Aggregation. Int J Mol Sci 19.
10. Digman, M. A., and E. Gratton. 2012. Scanning image correlation spectroscopy. Bioessays 34:377-385.
11. Magde, D., E. Elson, and W. W. Webb. 1972. Thermodynamic Fluctuations in a Reacting System-Measurement by Fluorescence Correlation Spectroscopy. Physical Review Letters 29:705-708.
12. Elson, E. L., J. Schlessinger, D. E. Koppel, D. Axelrod, and W. W. Webb. 1976. Measurement of lateral transport on cell surfaces. Prog Clin Biol Res 9:137-147.
13. Schlessinger, J., D. E. Koppel, D. Axelrod, K. Jacobson, W. W. Webb, and E. L. Elson. 1976. Lateral transport on cell membranes: mobility of concanavalin A receptors on myoblasts. Proc Natl Acad Sci U S A 73:2409-2413.
14. Fahey, P. F., D. E. Koppel, L. S. Barak, D. E. Wolf, E. L. Elson, and W. W. Webb. 1977. Lateral diffusion in planar lipid bilayers. Science 195:305-306.
15. Chiantia, S., J. Ries, and P. Schwille. 2009. Fluorescence correlation spectroscopy in membrane structure elucidation. Biochim Biophys Acta 1788:225-233.
16. Krieger, J. W., A. P. Singh, N. Bag, C. S. Garbe, T. E. Saunders, J. Langowski, and T. Wohland. 2015. Imaging fluorescence (cross-) correlation spectroscopy in live cells and organisms. Nature Protocols 10:1948-1974.
17. Mütze, J., T. Ohrt, and P. Schwille. 2011. Fluorescence correlation spectroscopy in vivo. Laser & Photonics Reviews 5:52-67.

18. Petazzi, R. A., A. Koikkarah Aji, and S. Chiantia. 2020. Fluorescence microscopy methods for the study of protein oligomerization. Prog Mol Biol Transl Sci 169:1-41.
19. Petrásek, Z., and P. Schwille. 2008. Precise measurement of diffusion coefficients using scanning fluorescence correlation spectroscopy. Biophys J 94:1437-1448.
20. Ries, J., S. Chiantia, and P. Schwille. 2009. Accurate determination of membrane dynamics with line-scan FCS. Biophys J 96:1999-2008.
21. Ries, J., and P. Schwille. 2006. Studying slow membrane dynamics with continuous wave scanning fluorescence correlation spectroscopy. Biophys J 91:1915-1924.
22. Schwille, P., F. J. Meyer-Almes, and R. Rigler. 1997. Dual-color fluorescence cross-correlation spectroscopy for multicomponent diffusional analysis in solution. Biophys J 72:1878-1886.
23. Bacia, K., S. A. Kim, and P. Schwille. 2006. Fluorescence cross-correlation spectroscopy in living cells. Nature Methods 3:83-89.
24. Longfils, M., N. Smisdom, M. Ameloot, M. Rudemo, V. Lemmens, G. S. Fernández, M. Röding, N. Lorén, J. Hendrix, and A. Särkkä. 2019. Raster Image Correlation Spectroscopy Performance Evaluation. Biophys J 117:1900-1914.
25. Brown, C. M., R. B. Dalal, B. Hebert, M. A. Digman, A. R. Horwitz, and E. Gratton. 2008. Raster image correlation spectroscopy (RICS) for measuring fast protein dynamics and concentrations with a commercial laser scanning confocal microscope. J Microsc 229:78-91.
26. Digman, M. A., C. M. Brown, P. Sengupta, P. W. Wiseman, A. R. Horwitz, and E. Gratton. 2005. Measuring fast dynamics in solutions and cells with a laser scanning microscope. Biophys J 89:1317-1327.
27. Mikuni, S., J. Yamamoto, T. Horio, and M. Kinjo. 2017. Negative Correlation between the Diffusion Coefficient and Transcriptional Activity of the Glucocorticoid Receptor. Int J Mol Sci 18.
28. Digman, M. A., R. Dalal, A. F. Horwitz, and E. Gratton. 2008. Mapping the number of molecules and brightness in the laser scanning microscope. Biophys J 94:2320-2332.
29. Trullo, A., V. Corti, E. Arza, V. R. Caiolfa, and M. Zamai. 2013. Application limits and data correction in number of molecules and brightness analysis. Microsc Res Tech 76:1135-1146.
30. Fukushima, R., J. Yamamoto, H. Ishikawa, and M. Kinjo. 2018. Two-detector number and brightness analysis reveals spatio-temporal oligomerization of proteins in living cells. Methods 140-141:161-171.
31. Mieruszynski, S., C. Briggs, M. A. Digman, E. Gratton, and M. R. Jones. 2015. Live Cell Characterization of DNA Aggregation Delivered through Lipofection. Scientific Reports 5:10528.
32. Dunsing, V., M. Luckner, B. Zühlke, R. A. Petazzi, A. Herrmann, and S. Chiantia. 2018. Optimal fluorescent protein tags for quantifying protein oligomerization in living cells. Sci Rep 8:10634.
33. Adhyapak, P., and S. Kapoor. 2019. Membrane Dynamics in Health and Disease: Impact on Cellular Signalling. The Journal of Membrane Biology 252:213-226.
34. Levental, K. R., E. Malmberg, J. L. Symons, Y. Y. Fan, R. S. Chapkin, R. Ernst, and I. Levental. 2020. Lipidomic and biophysical homeostasis of mammalian membranes counteracts dietary lipid perturbations to maintain cellular fitness. Nat Commun 11:1339.
35. Sezgin, E., I. Levental, S. Mayor, and C. Eggeling. 2017. The mystery of membrane organization: composition, regulation and roles of lipid rafts. Nat Rev Mol Cell Biol 18:361-374.

36. Simons, K., and M. J. Gerl. 2010. Revitalizing membrane rafts: new tools and insights. Nature Reviews Molecular Cell Biology 11:688-699.

37. Zachowski, A. 1993. Phospholipids in animal eukaryotic membranes: transverse asymmetry and movement. Biochem J 294 (Pt 1):1-14.

38. Gunther, G., L. Malacrida, D. M. Jameson, E. Gratton, and S. A. Sánchez. 2021. LAURDAN since Weber: The Quest for Visualizing Membrane Heterogeneity. Acc Chem Res 54:976-987.

39. Bondelli, G., G. M. Paternò, and G. Lanzani. 2021. (INVITED) Fluorescent probes for optical investigation of the plasma membrane. Optical Materials: X 12:100085.

40. Sezgin, E. 2022. Giant plasma membrane vesicles to study plasma membrane structure and dynamics. Biochim Biophys Acta Biomembr 1864:183857.

41. Sych, T., C. O. Gurdap, L. Wedemann, and E. Sezgin. 2021. How Does Liquid-Liquid Phase Separation in Model Membranes Reflect Cell Membrane Heterogeneity? Membranes (Basel) 11.

42. Sezgin, E., and P. Schwille. 2011. Fluorescence techniques to study lipid dynamics. Cold Spring Harb Perspect Biol 3:a009803.

43. Veit, M., S. Engel, B. Thaa, S. Scolari, and A. Herrmann. 2013. Lipid domain association of influenza virus proteins detected by dynamic fluorescence microscopy techniques. Cell Microbiol 15:179-189.

44. Bag, N., S. Huang, and T. Wohland. 2015. Plasma Membrane Organization of Epidermal Growth Factor Receptor in Resting and Ligand-Bound States. Biophys J 109:1925-1936.

45. Yang, G.-S., A. Wagenknecht-Wiesner, B. Yin, P. Suresh, E. London, B. A. Baird, and N. Bag. 2022. Lipid Driven Inter-leaflet Coupling of Plasma Membrane Order Regulates FcεRI Signaling in Mast Cells. bioRxiv:2022.2011.2024.517890.

46. Amaro, M., F. Reina, M. Hof, C. Eggeling, and E. Sezgin. 2017. Laurdan and Di-4-ANEPPDHQ probe different properties of the membrane. J Phys D Appl Phys 50:134004.

47. Owen, D. M., C. Rentero, A. Magenau, A. Abu-Siniyeh, and K. Gaus. 2011. Quantitative imaging of membrane lipid order in cells and organisms. Nat Protoc 7:24-35.

48. Sezgin, E., T. Sadowski, and K. Simons. 2014. Measuring lipid packing of model and cellular membranes with environment sensitive probes. Langmuir 30:8160-8166.

49. Suhaj, A., D. Gowland, N. Bonini, D. M. Owen, and C. D. Lorenz. 2020. Laurdan and Di-4-ANEPPDHQ Influence the Properties of Lipid Membranes: A Classical Molecular Dynamics and Fluorescence Study. The Journal of Physical Chemistry B 124:11419-11430.

50. Pinto, S. N., F. Fernandes, A. Fedorov, A. H. Futerman, L. C. Silva, and M. Prieto. 2013. A combined fluorescence spectroscopy, confocal and 2-photon microscopy approach to re-evaluate the properties of sphingolipid domains. Biochim Biophys Acta 1828:2099-2110.

51. Sezgin, E., D. Waithe, J. Bernardino de la Serna, and C. Eggeling. 2015. Spectral imaging to measure heterogeneity in membrane lipid packing. Chemphyschem 16:1387-1394.

52. Leavesley, S. J., A. L. Britain, L. K. Cichon, V. O. Nikolaev, and T. C. Rich. 2013. Assessing FRET using spectral techniques. Cytometry A 83:898-912.

53. Pokorna, S., A. E. Ventura, T. C. B. Santos, M. Hof, M. Prieto, A. H. Futerman, and L. C. Silva. 2022. Laurdan in live cell imaging: Effect of acquisition settings, cell culture conditions and data analysis on generalized polarization measurements. J Photochem Photobiol B 228:112404.

54. Torrado, B., L. Malacrida, and S. Ranjit. 2022. Linear Combination Properties of the Phasor Space in Fluorescence Imaging. Sensors (Basel) 22.

55. Golfetto, O., E. Hinde, and E. Gratton. 2015. The Laurdan spectral phasor method to explore membrane micro-heterogeneity and lipid domains in live cells. Methods Mol Biol 1232:273-290.

56. Gounder, A. P., and A. C. M. Boon. 2019. Influenza Pathogenesis: The Effect of Host Factors on Severity of Disease. J Immunol 202:341-350.

57. Hause, B. M., M. Ducatez, E. A. Collin, Z. Ran, R. Liu, Z. Sheng, A. Armien, B. Kaplan, S. Chakravarty, A. D. Hoppe, R. J. Webby, R. R. Simonson, and F. Li. 2013. Isolation of a novel swine influenza virus from Oklahoma in 2011 which is distantly related to human influenza C viruses. PLoS Pathog 9:e1003176.

58. Herold, S., C. Becker, K. M. Ridge, and G. R. Budinger. 2015. Influenza virus-induced lung injury: pathogenesis and implications for treatment. Eur Respir J 45:1463-1478.

59. Jennings, L., Q. S. Huang, I. Barr, P. I. Lee, W. J. Kim, P. Buchy, M. Sanicas, B. A. Mungall, and J. Chen. 2018. Literature review of the epidemiology of influenza B disease in 15 countries in the Asia-Pacific region. Influenza Other Respir Viruses 12:383-411.

60. Sullivan, K. M. 1996. Health impact of influenza in the United States. Pharmacoeconomics 9 Suppl 3:26-33; discussion 50-23.

61. Hussain, M., H. D. Galvin, T. Y. Haw, A. N. Nutsford, and M. Husain. 2017. Drug resistance in influenza A virus: the epidemiology and management. Infect Drug Resist 10:121-134.

62. Paget, J., P. Spreeuwenberg, V. Charu, R. J. Taylor, A. D. Iuliano, J. Bresee, L. Simonsen, and C. Viboud. 2019. Global mortality associated with seasonal influenza epidemics: New burden estimates and predictors from the GLaMOR Project. J Glob Health 9:020421.

63. Sharabi, S., Y. Drori, M. Micheli, N. Friedman, S. Orzitzer, R. Bassal, A. Glatman-Freedman, T. Shohat, E. Mendelson, M. Hindiyeh, and M. Mandelboim. 2016. Epidemiological and Virological Characterization of Influenza B Virus Infections. PLoS One 11:e0161195.

64. Taubenberger, J. K., and J. C. Kash. 2010. Influenza virus evolution, host adaptation, and pandemic formation. Cell Host Microbe 7:440-451.

65. Sederdahl, B. K., and J. V. Williams. 2020. Epidemiology and Clinical Characteristics of Influenza C Virus. Viruses 12.

66. Taubenberger, J. K., and D. M. Morens. 2008. The pathology of influenza virus infections. Annu Rev Pathol 3:499-522.

67. Morens, D. M., and J. K. Taubenberger. 2011. Pandemic influenza: certain uncertainties. Rev Med Virol 21:262-284.

68. Wang, D., W. Zhu, L. Yang, and Y. Shu. 2021. The Epidemiology, Virology, and Pathogenicity of Human Infections with Avian Influenza Viruses. Cold Spring Harb Perspect Med 11.

69. Schrauwen, E. J., and R. A. Fouchier. 2014. Host adaptation and transmission of influenza A viruses in mammals. Emerg Microbes Infect 3:e9.

70. Sun, H., Y. Xiao, J. Liu, D. Wang, F. Li, C. Wang, C. Li, J. Zhu, J. Song, H. Sun, Z. Jiang, L. Liu, X. Zhang, K. Wei, D. Hou, J. Pu, Y. Sun, Q. Tong, Y. Bi, K. C. Chang, S. Liu, G. F. Gao, and J. Liu. 2020. Prevalent Eurasian avian-like H1N1 swine influenza virus with 2009 pandemic viral genes facilitating human infection. Proc Natl Acad Sci U S A 117:17204-17210.

71.   Mostafa, A., E. M. Abdelwhab, T. C. Mettenleiter, and S. Pleschka. 2018. Zoonotic Potential of Influenza A Viruses: A Comprehensive Overview. Viruses 10.

72.   Becker, T., H. Elbahesh, L. A. Reperant, G. F. Rimmelzwaan, and A. Osterhaus. 2021. Influenza Vaccines: Successes and Continuing Challenges. J Infect Dis 224:S405-S419.

73.   Bouvier, N. M., and P. Palese. 2008. The biology of influenza viruses. Vaccine 26 Suppl 4:D49-53.

74.   Calder, L. J., S. Wasilewski, J. A. Berriman, and P. B. Rosenthal. 2010. Structural organization of a filamentous influenza A virus. Proc Natl Acad Sci U S A 107:10685-10690.

75.   Rossman, J. S., and R. A. Lamb. 2011. Influenza virus assembly and budding. Virology 411:229-236.

76.   Samji, T. 2009. Influenza A: understanding the viral life cycle. Yale J Biol Med 82:153-159.

77.   Wu, N. C., and I. A. Wilson. 2020. Influenza Hemagglutinin Structures and Antibody Recognition. Cold Spring Harb Perspect Med 10.

78.   Lu, Y., J. P. Welsh, and J. R. Swartz. 2014. Production and stabilization of the trimeric influenza hemagglutinin stem domain for potentially broadly protective influenza vaccines. Proc Natl Acad Sci U S A 111:125-130.

79.   McAuley, J. L., B. P. Gilbertson, S. Trifkovic, L. E. Brown, and J. L. McKimm-Breschkin. 2019. Influenza Virus Neuraminidase Structure and Functions. Frontiers in Microbiology 10:39.

80.   Claridge, J. K., F. Mohd-Kipli, A. Florea, T. Gate, and J. R. Schnell. 2020. pH-dependent secondary structure propensity of the influenza A virus M2 cytoplasmic tail. Biomol NMR Assign 14:157-161.

81.   Du, R., Q. Cui, and L. Rong. 2021. Flu Universal Vaccines: New Tricks on an Old Virus. Virol Sin 36:13-24.

82.   Peukes, J., X. Xiong, S. Erlendsson, K. Qu, W. Wan, L. J. Calder, O. Schraidt, S. Kummer, S. M. V. Freund, H.-G. Kräusslich, and J. A. G. Briggs. 2020. The native structure of the assembled matrix protein 1 of influenza A virus. Nature 587:495-498.

83.   Zheng, W., and Y. J. Tao. 2013. Structure and assembly of the influenza A virus ribonucleoprotein complex. FEBS Lett 587:1206-1214.

84.   Moreira, E. A., Y. Yamauchi, and P. Matthias. 2021. How Influenza Virus Uses Host Cell Pathways during Uncoating. Cells 10.

85.   Chauhan, R. P., and M. L. Gordon. 2022. An overview of influenza A virus genes, protein functions, and replication cycle highlighting important updates. Virus Genes 58:255-269.

86.   Cohen, S., S. Au, and N. Panté. 2011. How viruses access the nucleus. Biochim Biophys Acta 1813:1634-1645.

87.   Whittaker, G. R., M. Kann, and A. Helenius. 2000. Viral entry into the nucleus. Annu Rev Cell Dev Biol 16:627-651.

88.   Matsuoka, Y., H. Matsumae, M. Katoh, A. J. Eisfeld, G. Neumann, T. Hase, S. Ghosh, J. E. Shoemaker, T. J. Lopes, T. Watanabe, S. Watanabe, S. Fukuyama, H. Kitano, and Y. Kawaoka. 2013. A comprehensive map of the influenza A virus replication cycle. BMC Syst Biol 7:97.

89.   Zhang, M., M. Liu, S. Bai, C. Zhao, Z. Li, J. Xu, and X. Zhang. 2021. Influenza A Virus–Host Specificity: An Ongoing Cross-Talk Between Viral and Host Factors. Frontiers in Microbiology 12:777885.

90.   Eisfeld, A. J., G. Neumann, and Y. Kawaoka. 2015. At the centre: influenza A virus ribonucleoproteins. Nat Rev Microbiol 13:28-41.

91.   Hutchinson, E. C., and E. Fodor. 2013. Transport of the influenza virus genome from nucleus to nucleus. Viruses 5:2424-2446.

92.   Zhu, Z., E. Fodor, and J. R. Keown. 2023. A structural understanding of influenza virus genome replication. Trends in Microbiology 31:308-319.

93.   Shapiro, G. I., T. Gurney, Jr., and R. M. Krug. 1987. Influenza virus gene expression: control mechanisms at early and late times of infection and nuclear-cytoplasmic transport of virus-specific RNAs. J Virol 61:764-773.

94.   Khaperskyy, D. A., and C. McCormick. 2015. Timing Is Everything: Coordinated Control of Host Shutoff by Influenza A Virus NS1 and PA-X Proteins. J Virol 89:6528-6531.

95.   Huet, S., V. Avilov Sergiy, L. Ferbitz, N. Daigle, S. Cusack, and J. Ellenberg. 2010. Nuclear Import and Assembly of Influenza A Virus RNA Polymerase Studied in Live Cells by Fluorescence Cross-Correlation Spectroscopy. Journal of Virology 84:1254-1264.

96.   Zheng, H., L. Ma, R. Gui, X. Lin, X. Ke, X. Jian, C. Ye, and Q. Chen. 2022. G Protein Subunit β1 Facilitates Influenza A Virus Replication by Promoting the Nuclear Import of PB2. J Virol 96:e0049422.

97.   Perez, D. R., and R. O. Donis. 1998. The matrix 1 protein of influenza A virus inhibits the transcriptase activity of a model influenza reporter genome in vivo. Virology 249:52-61.

98.   Watanabe, K., H. Handa, K. Mizumoto, and K. Nagata. 1996. Mechanism for inhibition of influenza virus RNA polymerase activity by matrix protein. J Virol 70:241-247.

99.   Manzoor, R., M. Igarashi, and A. Takada. 2017. Influenza A Virus M2 Protein: Roles from Ingress to Egress. Int J Mol Sci 18.

100.   Pohl, M. O., C. Lanz, and S. Stertz. 2016. Late stages of the influenza A virus replication cycle-a tight interplay between virus and host. J Gen Virol 97:2058-2072.

101.   Amorim, M. J. 2018. A Comprehensive Review on the Interaction Between the Host GTPase Rab11 and Influenza A Virus. Front Cell Dev Biol 6:176.

102.   Kerviel, A., A. Thomas, L. Chaloin, C. Favard, and D. Muriaux. 2013. Virus assembly and plasma membrane domains: which came first? Virus Res 171:332-340.

103.   Veit, M., and B. Thaa. 2011. Association of influenza virus proteins with membrane rafts. Adv Virol 2011:370606.

104.   Copeland, C. S., R. W. Doms, E. M. Bolzau, R. G. Webster, and A. Helenius. 1986. Assembly of influenza hemagglutinin trimers and its role in intracellular transport. J Cell Biol 103:1179-1191.

105.   da Silva, D. V., J. Nordholm, U. Madjo, A. Pfeiffer, and R. Daniels. 2013. Assembly of Subtype 1 Influenza Neuraminidase Is Driven by Both the Transmembrane and Head Domains. Journal of Biological Chemistry 288:644-653.

106.   Durgan, J., and O. Florey. 2022. Many roads lead to CASM: Diverse stimuli of noncanonical autophagy share a unifying molecular mechanism. Sci Adv 8:eabo1274.

107.   Audi, A., N. Soudani, G. Dbaibo, and H. Zaraket. 2020. Depletion of Host and Viral Sphingomyelin Impairs Influenza Virus Infection. Frontiers in Microbiology 11:612.

108.   Sato, R., T. Okura, M. Kawahara, N. Takizawa, F. Momose, and Y. Morikawa. 2019. Apical Trafficking Pathways of Influenza A Virus HA and NA via Rab17- and Rab23-Positive Compartments. Frontiers in Microbiology 10.

109.   Nayak, D. P., E. K. Hui, and S. Barman. 2004. Assembly and budding of influenza virus. Virus Res 106:147-165.

110. Ekanayake, E. V., R. Fu, and Timothy A. Cross. 2016. Structural Influences: Cholesterol, Drug, and Proton Binding to Full-Length Influenza A M2 Protein. Biophysical Journal 110:1391-1399.

111. Elkins, M. R., J. K. Williams, M. D. Gelenter, P. Dai, B. Kwon, I. V. Sergeyev, B. L. Pentelute, and M. Hong. 2017. Cholesterol-binding site of the influenza M2 protein in lipid bilayers from solid-state NMR. Proc Natl Acad Sci U S A 114:12946-12951.

112. Frisz, J. F., K. Lou, H. A. Klitzing, W. P. Hanafin, V. Lizunov, R. L. Wilson, K. J. Carpenter, R. Kim, I. D. Hutcheon, J. Zimmerberg, P. K. Weber, and M. L. Kraft. 2013. Direct chemical evidence for sphingolipid domains in the plasma membranes of fibroblasts. Proc Natl Acad Sci U S A 110:E613-622.

113. Kuroki, T., T. Hatta, T. Natsume, N. Sakai, A. Yagi, K. Kato, K. Nagata, and A. Kawaguchi. 2022. ARHGAP1 Transported with Influenza Viral Genome Ensures Integrity of Viral Particle Surface through Efficient Budozone Formation. mBio 13:e0072122.

114. Moreno-Pescador, G., C. D. Florentsen, H. Østbye, S. L. Sønder, T. L. Boye, E. L. Veje, A. K. Sonne, S. Semsey, J. Nylandsted, R. Daniels, and P. M. Bendix. 2019. Curvature- and Phase-Induced Protein Sorting Quantified in Transfected Cell-Derived Giant Vesicles. ACS Nano 13:6689-6701.

115. Thaa, B., I. Leventhal, A. Herrmann, and M. Veit. 2011. Intrinsic membrane association of the cytoplasmic tail of influenza virus M2 protein and lateral membrane sorting regulated by cholesterol binding and palmitoylation. Biochem J 437:389-397.

116. Wilson, Robert L., Jessica F. Frisz, Haley A. Klitzing, J. Zimmerberg, Peter K. Weber, and Mary L. Kraft. 2015. Hemagglutinin Clusters in the Plasma Membrane Are Not Enriched with Cholesterol and Sphingolipids. Biophysical Journal 108:1652-1659.

117. Curthoys, N. M., M. J. Mlodzianoski, M. Parent, M. B. Butler, P. Raut, J. Wallace, J. Lilieholm, K. Mehmood, M. S. Maginnis, H. Waters, B. Busse, J. Zimmerberg, and S. T. Hess. 2019. Influenza Hemagglutinin Modulates Phosphatidylinositol 4,5-Bisphosphate Membrane Clustering. Biophysical Journal 116:893-909.

118. Gambhir, A., G. Hangyás-Mihályné, I. Zaitseva, D. S. Cafiso, J. Wang, D. Murray, S. N. Pentyala, S. O. Smith, and S. McLaughlin. 2004. Electrostatic sequestration of PIP2 on phospholipid membranes by basic/aromatic regions of proteins. Biophys J 86:2188-2207.

119. Gudheti, M. V., N. M. Curthoys, T. J. Gould, D. Kim, M. S. Gunewardene, K. A. Gabor, J. A. Gosse, C. H. Kim, J. Zimmerberg, and S. T. Hess. 2013. Actin mediates the nanoscale membrane organization of the clustered membrane protein influenza hemagglutinin. Biophys J 104:2182-2192.

120. Heo, W. D., T. Inoue, W. S. Park, M. L. Kim, B. O. Park, T. J. Wandless, and T. Meyer. 2006. PI(3,4,5)P3 and PI(4,5)P2 lipids target proteins with polybasic clusters to the plasma membrane. Science 314:1458-1461.

121. Nayak, D. P., R. A. Balogun, H. Yamada, Z. H. Zhou, and S. Barman. 2009. Influenza virus morphogenesis and budding. Virus Res 143:147-161.

122. Wang, D., A. Harmon, J. Jin, D. H. Francis, J. Christopher-Hennings, E. Nelson, R. C. Montelaro, and F. Li. 2010. The lack of an inherent membrane targeting signal is responsible for the failure of the matrix (M1) protein of influenza A virus to bud into virus-like particles. J Virol 84:4673-4681.

123. García-Sastre, A., and P. Palese. 1995. The cytoplasmic tail of the neuraminidase protein of influenza A virus does not play an important role in the packaging of this protein into viral envelopes. Virus Res 37:37-47.

124. Jin, H., G. P. Leser, and R. A. Lamb. 1994. The influenza virus hemagglutinin cytoplasmic tail is not essential for virus assembly or infectivity. EMBO J 13:5504-5515.

125. Kordyukova, L. V., E. V. Shtykova, L. A. Baratova, D. I. Svergun, and O. V. Batishchev. 2019. Matrix proteins of enveloped viruses: a case study of Influenza A virus M1 protein. J Biomol Struct Dyn 37:671-690.

126. Kretzschmar, E., M. Bui, and J. K. Rose. 1996. Membrane association of influenza virus matrix protein does not require specific hydrophobic domains or the viral glycoproteins. Virology 220:37-45.

127. Zhang, J., G. P. Leser, A. Pekosz, and R. A. Lamb. 2000. The cytoplasmic tails of the influenza virus spike glycoproteins are required for normal genome packaging. Virology 269:325-334.

128. Kordyukova, L. V., P. V. Konarev, N. V. Fedorova, E. V. Shtykova, A. L. Ksenofontov, N. A. Loshkarev, L. A. Dadinova, T. A. Timofeeva, S. S. Abramchuk, A. V. Moiseenko, L. A. Baratova, D. I. Svergun, and O. V. Batishchev. 2021. The Cytoplasmic Tail of Influenza A Virus Hemagglutinin and Membrane Lipid Composition Change the Mode of M1 Protein Association with the Lipid Bilayer. Membranes (Basel) 11.

129. Bobone, S., M. Hilsch, J. Storm, V. Dunsing, A. Herrmann, and S. Chiantia. 2017. Phosphatidylserine Lateral Organization Influences the Interaction of Influenza Virus Matrix Protein 1 with Lipid Membranes. J Virol 91:e00267-00217.

130. Dahmani, I., K. Ludwig, and S. Chiantia. 2019. Influenza A matrix protein M1 induces lipid membrane deformation via protein multimerization. Biosci Rep 39:BSR20191024.

131. Hilsch, M., B. Goldenbogen, C. Sieben, Chris T. Höfer, Jürgen P. Rabe, E. Klipp, A. Herrmann, and S. Chiantia. 2014. Influenza A Matrix Protein M1 Multimerizes upon Binding to Lipid Membranes. Biophysical Journal 107:912-923.

132. Höfer, C. T., S. Di Lella, I. Dahmani, N. Jungnick, N. Bordag, S. Bobone, Q. Huang, S. Keller, A. Herrmann, and S. Chiantia. 2019. Structural determinants of the interaction between influenza A virus matrix protein M1 and lipid membranes. Biochim Biophys Acta Biomembr 1861:1123-1134.

133. Arant, R. J., and M. H. Ulbrich. 2014. Deciphering the subunit composition of multimeric proteins by counting photobleaching steps. Chemphyschem 15:600-605.

134. Hillesheim, L. N., Y. Chen, and J. D. Müller. 2006. Dual-color photon counting histogram analysis of mRFP1 and EGFP in living cells. Biophys J 91:4273-4284.

135. Kuzmanov, U., and A. Emili. 2013. Protein-protein interaction networks: probing disease mechanisms using model systems. Genome Med 5:37.

136. Godin, A. G., B. Rappaz, L. Potvin-Trottier, T. E. Kennedy, Y. De Koninck, and P. W. Wiseman. 2015. Spatial Intensity Distribution Analysis Reveals Abnormal Oligomerization of Proteins in Single Cells. Biophys J 109:710-721.

137. Chen, Y., L. N. Wei, and J. D. Müller. 2003. Probing protein oligomerization in living cells with fluorescence fluctuation spectroscopy. Proc Natl Acad Sci U S A 100:15492-15497.

138. Haupts, U., S. Maiti, P. Schwille, and W. W. Webb. 1998. Dynamics of fluorescence fluctuations in green fluorescent protein observed by fluorescence correlation spectroscopy. Proc Natl Acad Sci U S A 95:13573-13578.

139. Hendrix, J., C. Flors, P. Dedecker, J. Hofkens, and Y. Engelborghs. 2008. Dark states in monomeric red fluorescent proteins studied by fluorescence correlation and single molecule spectroscopy. Biophys J 94:4103-4113.

140. Hur, K. H., P. J. Macdonald, S. Berk, C. I. Angert, Y. Chen, and J. D. Mueller. 2014. Quantitative measurement of brightness from living cells in the presence of photodepletion. PLoS One 9:e97440.

141. Widengren, J., Ü. Mets, and R. Rigler. 1999. Photodynamic properties of green fluorescent proteins investigated by fluorescence correlation spectroscopy. Chemical Physics 250:171-186.

142. Balleza, E., J. M. Kim, and P. Cluzel. 2018. Systematic characterization of maturation time of fluorescent proteins in living cells. Nat Methods 15:47-51.

143. Campbell, B. C., E. M. Nabel, M. H. Murdock, C. Lao-Peregrin, P. Tsoulfas, M. G. Blackmore, F. S. Lee, C. Liston, H. Morishita, and G. A. Petsko. 2020. mGreenLantern: a bright monomeric fluorescent protein with rapid expression and cell filling properties for neuronal imaging. Proc Natl Acad Sci U S A 117:30710-30721.

144. Costantini, L. M., M. Baloban, M. L. Markwardt, M. A. Rizzo, F. Guo, V. V. Verkhusha, and E. L. Snapp. 2015. A palette of fluorescent proteins optimized for diverse cellular environments. Nat Commun 6:7670.

145. Shaner, N. C., G. G. Lambert, A. Chammas, Y. Ni, P. J. Cranfill, M. A. Baird, B. R. Sell, J. R. Allen, R. N. Day, M. Israelsson, M. W. Davidson, and J. Wang. 2013. A bright monomeric green fluorescent protein derived from Branchiostoma lanceolatum. Nat Methods 10:407-409.

146. Casey, J. R., S. Grinstein, and J. Orlowski. 2010. Sensors and regulators of intracellular pH. Nat Rev Mol Cell Biol 11:50-61.

147. Bian, X., R. Liu, Y. Meng, D. Xing, D. Xu, and Z. Lu. 2020. Lipid metabolism and cancer. Journal of Experimental Medicine 218:e20201606.

148. Fu, Y., T. Zou, X. Shen, P. J. Nelson, J. Li, C. Wu, J. Yang, Y. Zheng, C. Bruns, Y. Zhao, L. Qin, and Q. Dong. 2021. Lipid metabolism in cancer progression and therapeutic strategies. MedComm (2020) 2:27-59.

149. Ohno, M., T. Sekiya, N. Nomura, T. j. Daito, M. Shingai, and H. Kida. 2020. Influenza virus infection affects insulin signaling, fatty acid-metabolizing enzyme expressions, and the tricarboxylic acid cycle in mice. Scientific Reports 10:10879.

150. Schultz, D., K. Methling, M. Rothe, and M. Lalk. 2019. Eicosanoid Profile of Influenza A Virus Infected Pigs. Metabolites 9.

151. Pehlivanova, V., V. Uzunova, I. Tsoneva, M. R. Berger, I. Ugrinova, and R. Tzoneva. 2013. Effect of Erufosine on the Reorganization of Cytoskeleton and Cell Death in Adherent Tumor and Non-Tumorigenic Cells. Biotechnology & Biotechnological Equipment 27:3695-3699.

152. Tafesse, F. G., S. Sanyal, J. Ashour, C. P. Guimaraes, M. Hermansson, P. Somerharju, and H. L. Ploegh. 2013. Intact sphingomyelin biosynthetic pathway is essential for intracellular transport of influenza virus glycoproteins. Proc Natl Acad Sci U S A 110:6406-6411.

153. Verma, D. K., D. Gupta, and S. K. Lal. 2018. Host Lipid Rafts Play a Major Role in Binding and Endocytosis of Influenza A Virus. Viruses 10.

154. Tanner, L. B., C. Chng, X. L. Guan, Z. Lei, S. G. Rozen, and M. R. Wenk. 2014. Lipidomics identifies a requirement for peroxisomal function during influenza virus replication [S]. Journal of Lipid Research 55:1357-1365.

155. Balasubramanian, H., J. Sankaran, S. Pandey, C. J. H. Goh, and T. Wohland. 2022. The dependence of EGFR oligomerization on environment and structure: A camera-based N&B study. Biophys J 121:4452-4466.

156. Chen, H., X. Xie, and T. Y. Chen. 2021. Single-molecule microscopy for in-cell quantification of protein oligomeric stoichiometry. Curr Opin Struct Biol 66:112-118.

157. Royer, C. A. 2019. Characterizing proteins in their cellular environment: Examples of recent advances in quantitative fluorescence microscopy. Protein Science 28:1210-1221.

158. Weidemann, T., J. Mücksch, and P. Schwille. 2014. Fluorescence fluctuation microscopy: a diversified arsenal of methods to investigate molecular dynamics inside cells. Curr Opin Struct Biol 28:69-76.

159. Chen, Y., J. Johnson, P. Macdonald, B. Wu, and J. D. Mueller. 2010. Observing protein interactions and their stoichiometry in living cells by brightness analysis of fluorescence fluctuation experiments. Methods Enzymol 472:345-363.

160. Heppert, J. K., D. J. Dickinson, A. M. Pani, C. D. Higgins, A. Steward, J. Ahringer, J. R. Kuhn, and B. Goldstein. 2016. Comparative assessment of fluorescent proteins for in vivo imaging in an animal model system. Mol Biol Cell 27:3385-3394.

161. Shinoda, H., Y. Ma, R. Nakashima, K. Sakurai, T. Matsuda, and T. Nagai. 2018. Acid-Tolerant Monomeric GFP from Olindias formosa. Cell Chem Biol 25:330-338 e337.

162. Vámosi, G., N. Mücke, G. Müller, J. W. Krieger, U. Curth, J. Langowski, and K. Tóth. 2016. EGFP oligomers as natural fluorescence and hydrodynamic standards. Sci Rep 6:33022.

163. Lam, A. J., F. St-Pierre, Y. Gong, J. D. Marshall, P. J. Cranfill, M. A. Baird, M. R. McKeown, J. Wiedenmann, M. W. Davidson, M. J. Schnitzer, R. Y. Tsien, and M. Z. Lin. 2012. Improving FRET dynamic range with bright green and red fluorescent proteins. Nat Methods 9:1005-1012.

164. Liu, Y., H. R. Kim, and A. A. Heikal. 2006. Structural basis of fluorescence fluctuation dynamics of green fluorescent proteins in acidic environments. J Phys Chem B 110:24138-24146.

165. Steiert, F., E. P. Petrov, P. Schultz, P. Schwille, and T. Weidemann. 2018. Photophysical Behavior of mNeonGreen, an Evolutionarily Distant Green Fluorescent Protein. Biophys J 114:2419-2431.

166. Doherty, G. P., K. Bailey, and P. J. Lewis. 2010. Stage-specific fluorescence intensity of GFP and mCherry during sporulation In Bacillus Subtilis. BMC Research Notes 3:303.

167. Pinilla-Redondo, R., L. Riber, and S. J. Sørensen. 2018. Fluorescence Recovery Allows the Implementation of a Fluorescence Reporter Gene Platform Applicable for the Detection and Quantification of Horizontal Gene Transfer in Anoxic Environments. Appl Environ Microbiol 84.

168. Schwille, P., S. Kummer, A. A. Heikal, W. E. Moerner, and W. W. Webb. 2000. Fluorescence correlation spectroscopy reveals fast optical excitation-driven intramolecular dynamics of yellow fluorescent proteins. Proc Natl Acad Sci U S A 97:151-156.

169. Costantini, L. M., and E. L. Snapp. 2013. Fluorescent proteins in cellular organelles: serious pitfalls and some solutions. DNA Cell Biol 32:622-627.

170. Petazzi, R. A., A. Koikkarah Aji, N. D. Tischler, and S. Chiantia. 2020. Detection of Envelope Glycoprotein Assembly from Old-World Hantaviruses in the Golgi Apparatus of Living Cells. bioRxiv:2020.2006.2001.127639.

171. Shaner, N. C., P. A. Steinbach, and R. Y. Tsien. 2005. A guide to choosing fluorescent proteins. Nat Methods 2:905-909.

172. Zacharias, D. A., J. D. Violin, A. C. Newton, and R. Y. Tsien. 2002. Partitioning of lipid-modified monomeric GFPs into membrane microdomains of live cells. Science 296:913-916.

173. Morozova, K. S., K. D. Piatkevich, T. J. Gould, J. Zhang, J. Bewersdorf, and V. V. Verkhusha. 2010. Far-red fluorescent protein excitable with red lasers for flow cytometry and superresolution STED nanoscopy. Biophys J 99:L13-15.

174. Heesink, G., C. Caron, K. van Leijenhorst-Groener, R. Molenaar, T. W. J. Gadella, Jr., M. Claessens, and C. Blum. 2022. Quantification of Dark Protein Populations in Fluorescent Proteins by Two-Color Coincidence Detection and Nanophotonic Manipulation. J Phys Chem B 126:7906-7915.

175. Liu, B., S. N. Mavrova, J. van den Berg, S. K. Kristensen, L. Mantovanelli, L. M. Veenhoff, B. Poolman, and A. J. Boersma. 2018. Influence of Fluorescent Protein Maturation on FRET Measurements in Living Cells. ACS Sens 3:1735-1742.

176. McCullock, T. W., D. M. MacLean, and P. J. Kammermeier. 2020. Comparing the performance of mScarlet-I, mRuby3, and mCherry as FRET acceptors for mNeonGreen. PLoS One 15:e0219886.

177. Stoneman, M. R., and V. Raicu. 2023. Fluorescence-Based Detection of Proteins and Their Interactions in Live Cells. The Journal of Physical Chemistry B 127:4708-4721.

178. Müller, T. G., V. Sakin, and B. Müller. 2019. A Spotlight on Viruses-Application of Click Chemistry to Visualize Virus-Cell Interactions. Molecules 24.

179. Snapp, E. 2005. Design and use of fluorescent fusion proteins in cell biology. Curr Protoc Cell Biol Chapter 21:21 24 21-21 24 13.

180. Gautier, A., and A. G. Tebo. 2018. Fluorogenic Protein-Based Strategies for Detection, Actuation, and Sensing. Bioessays 40:e1800118.

181. Serfling, R., L. Seidel, A. Bock, M. J. Lohse, P. Annibale, and I. Coin. 2019. Quantitative Single-Residue Bioorthogonal Labeling of G Protein-Coupled Receptors in Live Cells. ACS Chem Biol 14:1141-1149.

182. Gruβmayer, K. S., K. Yserentant, and D. P. Herten. 2019. Photons in - numbers out: perspectives in quantitative fluorescence microscopy for in situ protein counting. Methods Appl Fluoresc 7:012003.

183. Erdmann, R. S., S. W. Baguley, J. H. Richens, R. F. Wissner, Z. Xi, E. S. Allgeyer, S. Zhong, A. D. Thompson, N. Lowe, R. Butler, J. Bewersdorf, J. E. Rothman, D. St Johnston, A. Schepartz, and D. Toomre. 2019. Labeling Strategies Matter for Super-Resolution Microscopy: A Comparison between HaloTags and SNAP-tags. Cell Chem Biol 26:584-592 e586.

184. Wilhelm, J., S. Kühn, M. Tarnawski, G. Gotthard, J. Tünnermann, T. Tänzer, J. Karpenko, N. Mertes, L. Xue, U. Uhrig, J. Reinstein, J. Hiblot, and K. Johnsson. 2021. Kinetic and Structural Characterization of the Self-Labeling Protein Tags HaloTag7, SNAP-tag, and CLIP-tag. Biochemistry 60:2560-2575.

185. Hoffmann, C., G. Gaietta, A. Zürn, S. R. Adams, S. Terrillon, M. H. Ellisman, R. Y. Tsien, and M. J. Lohse. 2010. Fluorescent labeling of tetracysteine-tagged proteins in intact cells. Nat Protoc 5:1666-1677.

186. Hecht, K. A., Y. Xiong, D. A. Barrack, N. R. Ford, G. Roesijadi, and T. C. Squier. 2018. Distance-Matched Tagging Sequence Optimizes Live-Cell Protein Labeling by a Biarsenical Fluorescent Reagent AsCy3_E. ACS Omega 3:2104-2110.

187. Fernandes, D. D., J. Bamrah, S. Kailasam, G.-N. W. Gomes, Y. Li, H.-J. Wieden, and C. C. Gradinaru. 2017. Characterization of Fluorescein Arsenical Hairpin (FlAsH) as a Probe for Single-Molecule Fluorescence Spectroscopy. Scientific Reports 7:13063.

188. Shimogawa, M., and E. J. Petersson. 2021. New strategies for fluorescently labeling proteins in the study of amyloids. Current Opinion in Chemical Biology 64:57-66.

189. Lin, S., N. Liu, Z. Yang, W. Song, P. Wang, H. Chen, M. Lucio, P. Schmitt-Kopplin, G. Chen, and Z. Cai. 2010. GC/MS-based metabolomics reveals fatty acid

biosynthesis and cholesterol metabolism in cell lines infected with influenza A virus. Talanta 83:262-268.

190. Tam, V. C., O. Quehenberger, C. M. Oshansky, R. Suen, A. M. Armando, P. M. Treuting, P. G. Thomas, E. A. Dennis, and A. Aderem. 2013. Lipidomic profiling of influenza infection identifies mediators that induce and resolve inflammation. Cell 154:213-227.

191. Woods, P. S., L. M. Doolittle, L. E. Rosas, L. M. Joseph, E. P. Calomeni, and I. C. Davis. 2016. Lethal H1N1 influenza A virus infection alters the murine alveolar type II cell surfactant lipidome. Am J Physiol Lung Cell Mol Physiol 311:L1160-L1169.

192. Cui, L., D. Zheng, Y. H. Lee, T. K. Chan, Y. Kumar, W. E. Ho, J. Z. Chen, S. R. Tannenbaum, and C. N. Ong. 2016. Metabolomics Investigation Reveals Metabolite Mediators Associated with Acute Lung Injury and Repair in a Murine Model of Influenza Pneumonia. Sci Rep 6:26076.

193. Knepper, J., K. L. Schierhorn, A. Becher, M. Budt, M. Tönnies, T. T. Bauer, P. Schneider, J. Neudecker, J. C. Rückert, A. D. Gruber, N. Suttorp, B. Schweiger, S. Hippenstiel, A. C. Hocke, and T. Wolff. 2013. The novel human influenza A(H7N9) virus is naturally adapted to efficient growth in human lung tissue. mBio 4:e00601-00613.

194. Tisoncik-Go, J., D. J. Gasper, J. E. Kyle, A. J. Eisfeld, C. Selinger, M. Hatta, J. Morrison, M. J. Korth, E. M. Zink, Y. M. Kim, A. A. Schepmoes, C. D. Nicora, S. O. Purvine, K. K. Weitz, X. Peng, R. R. Green, S. C. Tilton, B. J. Webb-Robertson, K. M. Waters, T. O. Metz, R. D. Smith, Y. Kawaoka, M. Suresh, L. Josset, and M. G. Katze. 2016. Integrated Omics Analysis of Pathogenic Host Responses during Pandemic H1N1 Influenza Virus Infection: The Crucial Role of Lipid Metabolism. Cell Host Microbe 19:254-266.

195. Beloribi-Djefaflia, S., S. Vasseur, and F. Guillaumond. 2016. Lipid metabolic reprogramming in cancer cells. Oncogenesis 5:e189.

196. Preta, G. 2020. New Insights Into Targeting Membrane Lipids for Cancer Therapy. Front Cell Dev Biol 8:571237.

197. Szlasa, W., I. Zendran, A. Zalesińska, M. Tarek, and J. Kulbacka. 2020. Lipid composition of the cancer cell membrane. J Bioenerg Biomembr 52:321-342.

198. Busto, J. V., J. Sot, F. M. Goñi, F. Mollinedo, and A. Alonso. 2007. Surface-active properties of the antitumour ether lipid 1-O-octadecyl-2-O-methyl-rac-glycero-3-phosphocholine (edelfosine). Biochim Biophys Acta 1768:1855-1860.

199. dos Santos, G. A., C. H. Thomé, G. A. Ferreira, J. S. Yoneda, T. M. Nobre, K. R. Daghastanli, P. S. Scheucher, H. L. Gimenes-Teixeira, M. G. Constantino, K. T. de Oliveira, V. M. Faça, R. P. Falcão, L. J. Greene, E. M. Rego, and P. Ciancaglini. 2010. Interaction of 10-(octyloxy) decyl-2-(trimethylammonium) ethyl phosphate with mimetic membranes and cytotoxic effect on leukemic cells. Biochim Biophys Acta 1798:1714-1723.

200. Gomide, A. B., C. H. Thomé, G. A. dos Santos, G. A. Ferreira, V. M. Faça, E. M. Rego, L. J. Greene, R. G. Stabeli, P. Ciancaglini, and R. Itri. 2013. Disrupting membrane raft domains by alkylphospholipids. Biochim Biophys Acta 1828:1384-1389.

201. Hąc-Wydro, K., P. Dynarowicz-Łątka, P. Wydro, and K. Bąk. 2011. Edelfosine disturbs the sphingomyelin-cholesterol model membrane system in a cholesterol-dependent way - the Langmuir monolayer study. Colloids Surf B Biointerfaces 88:635-640.

202. Więcek, A., P. Dynarowicz-Łątka, N. Vila-Romeu, M. Nieto-Suarez, and M. Flasiński. 2008. Interactions between an anticancer drug – edelfosine – and DPPC in

Langmuir monolayers. Colloids and Surfaces A: Physicochemical and Engineering Aspects 321:201-205.

203. Wnętrzak, A., K. Lątka, and P. Dynarowicz-Łątka. 2013. Interactions of alkylphosphocholines with model membranes-the Langmuir monolayer study. J Membr Biol 246:453-466.

204. Adada, M., C. Luberto, and D. Canals. 2016. Inhibitors of the sphingomyelin cycle: Sphingomyelin synthases and sphingomyelinases. Chem Phys Lipids 197:45-59.

205. Hannun, Y. A., and L. M. Obeid. 2008. Principles of bioactive lipid signalling: lessons from sphingolipids. Nat Rev Mol Cell Biol 9:139-150.

206. Li, R. Z., X. R. Wang, J. Wang, C. Xie, X. X. Wang, H. D. Pan, W. Y. Meng, T. L. Liang, J. X. Li, P. Y. Yan, Q. B. Wu, L. Liu, X. J. Yao, and E. L. Leung. 2022. The key role of sphingolipid metabolism in cancer: New therapeutic targets, diagnostic and prognostic values, and anti-tumor immunotherapy resistance. Front Oncol 12:941643.

207. Morad, S. A., and M. C. Cabot. 2013. Ceramide-orchestrated signalling in cancer cells. Nat Rev Cancer 13:51-65.

208. Zalba, S., and T. L. Ten Hagen. 2017. Cell membrane modulation as adjuvant in cancer therapy. Cancer Treat Rev 52:48-57.

209. Tallima, H., H. M. E. Azzazy, and R. El Ridi. 2021. Cell surface sphingomyelin: key role in cancer initiation, progression, and immune evasion. Lipids Health Dis 20:150.

210. Colombini, M. 2013. Membrane channels formed by ceramide. Handb Exp Pharmacol:109-126.

211. Abdik, H. 2022. Antineoplastic effects of erufosine on small cell and non-small cell lung cancer cells through induction of apoptosis and cell cycle arrest. Mol Biol Rep 49:2963-2971.

212. Avsar Abdik, E., H. Abdik, D. Turan, F. Sahin, M. R. Berger, and F. Kaleagasioglu. 2021. Dual Akt and Bcl-2 inhibition induces cell-type specific modulation of apoptotic and autophagic signaling in castration resistant prostate cancer cell lines. Mol Biol Rep 48:7755-7765.

213. Gajate, C., and F. Mollinedo. 2007. Edelfosine and perifosine induce selective apoptosis in multiple myeloma by recruitment of death receptors and downstream signaling molecules into lipid rafts. Blood 109:711-719.

214. Kostadinova, A., T. Topouzova-Hristova, A. Momchilova, R. Tzoneva, and M. R. Berger. 2015. Antitumor Lipids--Structure, Functions, and Medical Applications. Adv Protein Chem Struct Biol 101:27-66.

215. Stoyanova T, Uzunova V, Popova D, Hadzhilazova M, Berger MR, Momchilova A, Toshkova R, and T. R. 2018. Effect of Erufosine on MDA-MB 231 Breast Cancer Cells. J Oncol Res Forecast 1:1005.

216. Saito, R. F., L. N. S. Andrade, S. O. Bustos, and R. Chammas. 2022. Phosphatidylcholine-Derived Lipid Mediators: The Crosstalk Between Cancer Cells and Immune Cells. Front Immunol 13:768606.

217. Neto, X. A. d. O., A. C. S. Alves, R. A. D. Junior, R. P. Rodrigues, M. Lancellotti, W. P. Almeida, and D. F. Kawano. 2020. Molecular Docking Reveals the Binding Modes of Anticancer Alkylphospholipids and Lysophosphatidylcholine within the Catalytic Domain of Cytidine Triphosphate: Phosphocholine Cytidyltransferase. European Journal of Lipid Science and Technology 122:1900422.

218. Iacano, A. J., H. Lewis, J. E. Hazen, H. Andro, J. D. Smith, and K. Gulshan. 2019. Miltefosine increases macrophage cholesterol release and inhibits NLRP3-inflammasome assembly and IL-1β release. Sci Rep 9:11128.

219. Ansari, S. S., A. K. Sharma, H. Soni, D. M. Ali, B. Tews, R. König, H. Eibl, and M. R. Berger. 2018. Induction of ER and mitochondrial stress by the alkylphosphocholine erufosine in oral squamous cell carcinoma cells. Cell Death Dis 9:296.

220. Birge, R. B., S. Boeltz, S. Kumar, J. Carlson, J. Wanderley, D. Calianese, M. Barcinski, R. A. Brekken, X. Huang, J. T. Hutchins, B. Freimark, C. Empig, J. Mercer, A. J. Schroit, G. Schett, and M. Herrmann. 2016. Phosphatidylserine is a global immunosuppressive signal in efferocytosis, infectious disease, and cancer. Cell Death Differ 23:962-978.

221. Kaynak, A., H. W. Davis, A. B. Kogan, J. H. Lee, D. A. Narmoneva, and X. Qi. 2022. Phosphatidylserine: The Unique Dual-Role Biomarker for Cancer Imaging and Therapy. Cancers (Basel) 14.

222. Ding, X., W. Zhang, S. Li, and H. Yang. 2019. The role of cholesterol metabolism in cancer. Am J Cancer Res 9:219-227.

223. Halimi, H., and S. Farjadian. 2022. Cholesterol: An important actor on the cancer immune scene. Front Immunol 13:1057546.

224. Mollinedo, F., and C. Gajate. 2021. Mitochondrial Targeting Involving Cholesterol-Rich Lipid Rafts in the Mechanism of Action of the Antitumor Ether Lipid and Alkylphospholipid Analog Edelfosine. Pharmaceutics 13.

225. Huang, B., B. L. Song, and C. Xu. 2020. Cholesterol metabolism in cancer: mechanisms and therapeutic opportunities. Nat Metab 2:132-141.

226. Mollinedo, F., and C. Gajate. 2015. Lipid rafts as major platforms for signaling regulation in cancer. Adv Biol Regul 57:130-146.

227. Maja, M., and D. Tyteca. 2022. Alteration of cholesterol distribution at the plasma membrane of cancer cells: From evidence to pathophysiological implication and promising therapy strategy. Front Physiol 13:999883.

228. Gu, L., S. T. Saha, J. Thomas, and M. Kaur. 2019. Targeting cellular cholesterol for anticancer therapy. FEBS J 286:4192-4208.

229. Levitan, I. 2021. Evaluating membrane structure by Laurdan imaging: Disruption of lipid packing by oxidized lipids. Curr Top Membr 88:235-256.

230. Giocondi, M. C., P. E. Milhiet, P. Dosset, and C. Le Grimellec. 2004. Use of cyclodextrin for AFM monitoring of model raft formation. Biophys J 86:861-869.

231. Di Bello, E., C. Zwergel, A. Mai, and S. Valente. 2020. The Innovative Potential of Statins in Cancer: New Targets for New Therapies. Front Chem 8:516.

232. Tilija Pun, N., and C. H. Jeong. 2021. Statin as a Potential Chemotherapeutic Agent: Current Updates as a Monotherapy, Combination Therapy, and Treatment for Anti-Cancer Drug Resistance. Pharmaceuticals (Basel) 14.

233. Ausili, A., A. Torrecillas, F. J. Aranda, F. Mollinedo, C. Gajate, S. Corbalán-García, A. de Godos, and J. C. Gómez-Fernández. 2008. Edelfosine is incorporated into rafts and alters their organization. J Phys Chem B 112:11643-11654.

234. Carrasco, M. P., J. M. Jiménez-López, P. Ríos-Marco, J. L. Segovia, and C. Marco. 2010. Disruption of cellular cholesterol transport and homeostasis as a novel mechanism of action of membrane-targeted alkylphospholipid analogues. Br J Pharmacol 160:355-366.

235. Dynarowicz-Latka, P., and K. Hac-Wydro. 2014. Edelfosine in membrane environment - the Langmuir monolayer studies. Anticancer Agents Med Chem 14:499-508.

236. Zaremberg, V., C. Gajate, L. M. Cacharro, F. Mollinedo, and C. R. McMaster. 2005. Cytotoxicity of an anti-cancer lysophospholipid through selective modification of lipid raft composition. J Biol Chem 280:38047-38058.

237. Ríos-Marco, P., C. Marco, X. Gálvez, J. M. Jiménez-López, and M. P. Carrasco. 2017. Alkylphospholipids: An update on molecular mechanisms and clinical relevance. Biochim Biophys Acta Biomembr 1859:1657-1667.

238. Ríos-Marco, P., J. M. Jiménez-López, C. Marco, J. L. Segovia, and M. P. Carrasco. 2011. Antitumoral alkylphospholipids induce cholesterol efflux from the plasma membrane in HepG2 cells. J Pharmacol Exp Ther 336:866-873.

239. Petit, K., M. Suwalsky, J. R. Colina, L. F. Aguilar, M. Jemiola-Rzeminska, and K. Strzalka. 2019. In vitro effects of the antitumor drug miltefosine on human erythrocytes and molecular models of its membrane. Biochim Biophys Acta Biomembr 1861:17-25.

240. Ivanova, P. T., D. S. Myers, S. B. Milne, J. L. McClaren, P. G. Thomas, and H. A. Brown. 2015. Lipid composition of viral envelope of three strains of influenza virus - not all viruses are created equal. ACS Infect Dis 1:399-452.

241. Liu, S., B. W. Mok, S. Deng, H. Liu, P. Wang, W. Song, P. Chen, X. Huang, M. Zheng, S. Y. Lau, C. J. Cremin, C. Y. Tam, B. Li, L. Jiang, Y. Chen, K. Y. Yuen, and H. Chen. 2021. Mammalian cells use the autophagy process to restrict avian influenza virus replication. Cell Rep 35:109213.

242. Loshkareva, A. S., M. M. Popova, L. A. Shilova, N. V. Fedorova, T. A. Timofeeva, T. R. Galimzyanov, P. I. Kuzmin, D. G. Knyazev, and O. V. Batishchev. 2023. Influenza A Virus M1 Protein Non-Specifically Deforms Charged Lipid Membranes and Specifically Interacts with the Raft Boundary. Membranes (Basel) 13.

243. Ma, Y., Y. Yamamoto, P. R. Nicovich, J. Goyette, J. Rossy, J. J. Gooding, and K. Gaus. 2017. A FRET sensor enables quantitative measurements of membrane charges in live cells. Nat Biotechnol 35:363-370.

244. Raut, P., B. Obeng, H. Waters, J. Zimmerberg, J. A. Gosse, and S. T. Hess. 2022. Phosphatidylinositol 4,5-Bisphosphate Mediates the Co-Distribution of Influenza A Hemagglutinin and Matrix Protein M1 at the Plasma Membrane. Viruses 14.

245. Kakisaka, M., K. Yamada, A. Yamaji-Hasegawa, T. Kobayashi, and Y. Aida. 2016. Intrinsically disordered region of influenza A NP regulates viral genome packaging via interactions with viral RNA and host PI(4,5)P2. Virology 496:116-126.

246. Favard, C., J. Chojnacki, P. Merida, N. Yandrapalli, J. Mak, C. Eggeling, and D. Muriaux. 2019. HIV-1 Gag specifically restricts PI(4,5)P2 and cholesterol mobility in living cells creating a nanodomain platform for virus assembly. Sci Adv 5:eaaw8651.

247. Motsa, B. B., and R. V. Stahelin. 2021. Lipid-protein interactions in virus assembly and budding from the host cell plasma membrane. Biochem Soc Trans 49:1633-1641.

248. Lorizate, M., and H. G. Kräusslich. 2011. Role of lipids in virus replication. Cold Spring Harb Perspect Biol 3:a004820.

249. Amiar, S., M. L. Husby, K. J. Wijesinghe, S. Angel, N. Bhattarai, B. S. Gerstman, P. P. Chapagain, S. Li, and R. V. Stahelin. 2021. Lipid-specific oligomerization of the Marburg virus matrix protein VP40 is regulated by two distinct interfaces for virion assembly. J Biol Chem 296:100796.

250. Husby, M. L., S. Amiar, L. I. Prugar, E. A. David, C. B. Plescia, K. E. Huie, J. M. Brannan, J. M. Dye, E. Pienaar, and R. V. Stahelin. 2022. Phosphatidylserine clustering by the Ebola virus matrix protein is a critical step in viral budding. EMBO Rep 23:e51709.

251. Johnson, K. A., M. R. Budicini, S. Urata, N. Bhattarai, B. S. Gerstman, P. P. Chapagain, S. Li, and R. V. Stahelin. 2018. PI(4,5)P2 Binding Sites in the Ebola Virus Matrix Protein Modulate Assembly and Budding. bioRxiv:341248.

252. Johnson, K. A., G. J. Taghon, J. L. Scott, and R. V. Stahelin. 2016. The Ebola Virus matrix protein, VP40, requires phosphatidylinositol 4,5-bisphosphate (PI(4,5)P2) for extensive oligomerization at the plasma membrane and viral egress. Sci Rep 6:19125.

253. Norris, M. J., M. L. Husby, W. B. Kiosses, J. Yin, R. Saxena, L. J. Rennick, A. Heiner, S. S. Harkins, R. Pokhrel, S. L. Schendel, K. M. Hastie, S. Landeras-Bueno, Z. L. Salie, B. Lee, P. P. Chapagain, A. Maisner, W. P. Duprex, R. V. Stahelin, and E. O. Saphire. 2022. Measles and Nipah virus assembly: Specific lipid binding drives matrix polymerization. Sci Adv 8:eabn1440.

254. Husby, M. L., and R. V. Stahelin. 2021. Negative-sense RNA viruses: An underexplored platform for examining virus-host lipid interactions. Mol Biol Cell 32.

255. Adu-Gyamfi, E., K. A. Johnson, M. E. Fraser, J. L. Scott, S. P. Soni, K. R. Jones, M. A. Digman, E. Gratton, C. R. Tessier, and R. V. Stahelin. 2015. Host Cell Plasma Membrane Phosphatidylserine Regulates the Assembly and Budding of Ebola Virus. J Virol 89:9440-9453.

256. Frewein, M. P. K., P. Piller, E. F. Semeraro, O. Czakkel, Y. Gerelli, L. Porcar, and G. Pabst. 2023. Distributing aminophospholipids asymmetrically across leaflets causes anomalous membrane stiffening. Biophys J 122:2445-2455.

257. Sarmento, M. J., M. Hof, and R. Šachl. 2020. Interleaflet Coupling of Lipid Nanodomains - Insights From in vitro Systems. Front Cell Dev Biol 8:284.

258. Keshavarz, M., F. Solaymani-Mohammadi, H. Namdari, Y. Arjeini, M. J. Mousavi, and F. Rezaei. 2020. Metabolic host response and therapeutic approaches to influenza infection. Cell Mol Biol Lett 25:15.

259. Gerl, M. J., J. L. Sampaio, S. Urban, L. Kalvodova, J. M. Verbavatz, B. Binnington, D. Lindemann, C. A. Lingwood, A. Shevchenko, C. Schroeder, and K. Simons. 2012. Quantitative analysis of the lipidomes of the influenza virus envelope and MDCK cell apical membrane. J Cell Biol 196:213-221.

260. Zhang, J., A. Pekosz, and R. A. Lamb. 2000. Influenza virus assembly and lipid raft microdomains: a role for the cytoplasmic tails of the spike glycoproteins. J Virol 74:4634-4644.

261. Engel, S., M. de Vries, A. Herrmann, and M. Veit. 2012. Mutation of a raft-targeting signal in the transmembrane region retards transport of influenza virus hemagglutinin through the Golgi. FEBS Lett 586:277-282.

262. Kawaguchi, A., M. Hirohama, Y. Harada, S. Osari, and K. Nagata. 2015. Influenza Virus Induces Cholesterol-Enriched Endocytic Recycling Compartments for Budozone Formation via Cell Cycle-Independent Centrosome Maturation. PLoS Pathog 11:e1005284.

263. Zhou, Y., J. Pu, and Y. Wu. 2021. The Role of Lipid Metabolism in Influenza A Virus Infection. Pathogens 10.

264. Martyna, A., B. Bahsoun, J. J. Madsen, F. Jackson, M. D. Badham, G. A. Voth, and J. S. Rossman. 2020. Cholesterol Alters the Orientation and Activity of the Influenza Virus M2 Amphipathic Helix in the Membrane. J Phys Chem B 124:6738-6747.

265. Paulino, J., X. Pang, I. Hung, H. X. Zhou, and T. A. Cross. 2019. Influenza A M2 Channel Clustering at High Protein/Lipid Ratios: Viral Budding Implications. Biophys J 116:1075-1084.

266. Sutherland, M., N. Tran, and M. Hong. 2022. Clustering of tetrameric influenza M2 peptides in lipid bilayers investigated by (19)F solid-state NMR. Biochim Biophys Acta Biomembr 1864:183909.

267. Tsfasman, T., V. Kost, S. Markushin, V. Lotte, I. Koptiaeva, E. Bogacheva, L. Baratova, and V. Radyukhin. 2015. Amphipathic alpha-helices and putative

cholesterol binding domains of the influenza virus matrix M1 protein are crucial for virion structure organisation. Virus Res 210:114-118.

268. Doktorova, M., J. Symons, L. , X. Zhang, H.-Y. Wang, J. Schlegel, J. Lorent, H. , F. A. Heberle, E. Sezgin, E. Lyman, K. R. Levental, and I. Levental. 2023. Cell Membranes Sustain Phospholipid Imbalance Via Cholesterol Asymmetry. bioRxiv:2023.2007.2030.551157.

269. Doole, F. T., S. Gupta, T. Kumarage, R. Ashkar, and M. F. Brown. 2023. Biophysics of Membrane Stiffening by Cholesterol and Phosphatidylinositol 4,5-bisphosphate (PIP2). Adv Exp Med Biol 1422:61-85.

270. Miller, M. E., S. Adhikary, A. A. Kolokoltsov, and R. A. Davey. 2012. Ebolavirus requires acid sphingomyelinase activity and plasma membrane sphingomyelin for infection. J Virol 86:7473-7483.

271. Nieto-Garai, J. A., A. Arboleya, S. Otaegi, J. Chojnacki, J. Casas, G. Fabriàs, F. X. Contreras, H. G. Kräusslich, and M. Lorizate. 2021. Cholesterol in the Viral Membrane is a Molecular Switch Governing HIV-1 Env Clustering. Adv Sci (Weinh) 8:2003468.

272. Shrivastava-Ranjan, P., M. Flint, É. Bergeron, A. K. McElroy, P. Chatterjee, C. G. Albariño, S. T. Nichol, and C. F. Spiropoulou. 2018. Statins Suppress Ebola Virus Infectivity by Interfering with Glycoprotein Processing. mBio 9.

273. Yoo, S. W., A. A. Waheed, P. Deme, S. Tohumeken, R. Rais, M. D. Smith, C. DeMarino, P. A. Calabresi, F. Kashanchi, E. O. Freed, B. S. Slusher, and N. J. Haughey. 2023. Inhibition of neutral sphingomyelinase 2 impairs HIV-1 envelope formation and substantially delays or eliminates viral rebound. Proc Natl Acad Sci U S A 120:e2219543120.

274. Chua, S., J. Cui, D. Engelberg, and L. H. K. Lim. 2022. A Review and Meta-Analysis of Influenza Interactome Studies. Front Microbiol 13:869406.

275. Drews, K., M. P. Calgi, W. C. Harrison, C. M. Drews, P. Costa-Pinheiro, J. J. P. Shaw, K. A. Jobe, J. D. Han, T. E. Fox, J. M. White, and M. Kester. 2020. Glucosylceramide synthase maintains influenza virus entry and infection. PLoS One 15:e0228735.

276. Mehrbod, P., A. R. Omar, M. Hair-Bejo, A. Haghani, and A. Ideris. 2014. Mechanisms of action and efficacy of statins against influenza. Biomed Res Int 2014:872370.

277. Chugh, P., B. Bradel-Tretheway, C. M. Monteiro-Filho, V. Planelles, S. B. Maggirwar, S. Dewhurst, and B. Kim. 2008. Akt inhibitors as an HIV-1 infected macrophage-specific anti-viral therapy. Retrovirology 5:11.

278. Lucas, A., Y. Kim, O. Rivera-Pabon, S. Chae, D. H. Kim, and B. Kim. 2010. Targeting the PI3K/Akt cell survival pathway to induce cell death of HIV-1 infected macrophages with alkylphospholipid compounds. PLoS One 5.

279. Sami Saribas, A., S. Cicalese, T. M. Ahooyi, K. Khalili, S. Amini, and I. K. Sariyer. 2017. HIV-1 Nef is released in extracellular vesicles derived from astrocytes: evidence for Nef-mediated neurotoxicity. Cell Death Dis 8:e2542.

280. Jin, L., A. C. Millard, J. P. Wuskell, X. Dong, D. Wu, H. A. Clark, and L. M. Loew. 2006. Characterization and application of a new optical probe for membrane lipid domains. Biophys J 90:2563-2575.

281. Orlikowska-Rzeznik, H., E. Krok, M. Chattopadhyay, A. Lester, and L. Piatkowski. 2023. Laurdan Discerns Lipid Membrane Hydration and Cholesterol Content. J Phys Chem B 127:3382-3391.

282. Danylchuk, D. I., E. Sezgin, P. Chabert, and A. S. Klymchenko. 2020. Redesigning Solvatochromic Probe Laurdan for Imaging Lipid Order Selectively in Cell Plasma Membranes. Anal Chem 92:14798-14805.

283. Ragaller, F., L. Andronico, J. Sykora, W. Kulig, T. Rog, Y. B. Urem, Abhinav, D. I. Danylchuk, M. Hof, A. Klymchenko, M. Amaro, I. Vattulainen, and E. Sezgin. 2022. Dissecting the mechanisms of environment sensitivity of smart probes for quantitative assessment of membrane properties. Open Biol 12:220175.

284. Carravilla, P., A. Dasgupta, G. Zhurgenbayeva, D. I. Danylchuk, A. S. Klymchenko, E. Sezgin, and C. Eggeling. 2021. Long-term STED imaging of membrane packing and dynamics by exchangeable polarity-sensitive dyes. Biophys Rep (N Y) 1:None.

285. Danylchuk, D. I., S. Moon, K. Xu, and A. S. Klymchenko. 2019. Switchable Solvatochromic Probes for Live-Cell Super-resolution Imaging of Plasma Membrane Organization. Angew Chem Int Ed Engl 58:14920-14924.

286. Frawley, A. T., K. G. Leslie, V. Wycisk, S. Galiani, D. Shrestha, C. Eggeling, and H. L. Anderson. 2023. A Photoswitchable Solvatochromic Dye for Probing Membrane Ordering by RESOLFT Super-resolution Microscopy. Chemphyschem 24:e202300125.

287. Malacrida, L., S. Astrada, A. Briva, M. Bollati-Fogolín, E. Gratton, and L. A. Bagatolli. 2016. Spectral phasor analysis of LAURDAN fluorescence in live A549 lung cells to study the hydration and time evolution of intracellular lamellar body-like structures. Biochim Biophys Acta 1858:2625-2635.

288. Huang, S., S. Y. Lim, A. Gupta, N. Bag, and T. Wohland. 2017. Plasma membrane organization and dynamics is probe and cell line dependent. Biochim Biophys Acta Biomembr 1859:1483-1492.

289. Dunsing, V., M. Mayer, F. Liebsch, G. Multhaup, and S. Chiantia. 2017. Direct evidence of amyloid precursor-like protein 1 trans interactions in cell-cell adhesion platforms investigated via fluorescence fluctuation spectroscopy. Mol Biol Cell 28:3609-3620.

290. Eggeling, C., C. Ringemann, R. Medda, G. Schwarzmann, K. Sandhoff, S. Polyakova, V. N. Belov, B. Hein, C. von Middendorff, A. Schönle, and S. W. Hell. 2009. Direct observation of the nanoscale dynamics of membrane lipids in a living cell. Nature 457:1159-1162.

291. Honigmann, A., V. Mueller, H. Ta, A. Schoenle, E. Sezgin, S. W. Hell, and C. Eggeling. 2014. Scanning STED-FCS reveals spatiotemporal heterogeneity of lipid interaction in the plasma membrane of living cells. Nat Commun 5:5412.

292. Li, X., D. T. Luu, C. Maurel, and J. Lin. 2013. Probing plasma membrane dynamics at the single-molecule level. Trends Plant Sci 18:617-624.

293. Chojnacki, J., and C. Eggeling. 2021. Super-Resolution STED Microscopy-Based Mobility Studies of the Viral Env Protein at HIV-1 Assembly Sites of Fully Infected T-Cells. Viruses 13.

294. Chojnacki, J., D. Waithe, P. Carravilla, N. Huarte, S. Galiani, J. Enderlein, and C. Eggeling. 2017. Envelope glycoprotein mobility on HIV-1 particles depends on the virus maturation state. Nat Commun 8:545.

295. Sezgin, E., F. Schneider, S. Galiani, I. Urbančič, D. Waithe, B. C. Lagerholm, and C. Eggeling. 2019. Measuring nanoscale diffusion dynamics in cellular membranes with super-resolution STED-FCS. Nat Protoc 14:1054-1083.

296. Sankaran, J., and T. Wohland. 2023. Current capabilities and future perspectives of FCS: super-resolution microscopy, machine learning, and in vivo applications. Commun Biol 6:699.

297. Tsujita, K., R. Satow, S. Asada, Y. Nakamura, L. Arnes, K. Sako, Y. Fujita, K. Fukami, and T. Itoh. 2021. Homeostatic membrane tension constrains cancer cell dissemination by counteracting BAR protein assembly. Nat Commun 12:5930.

298. Ajjaji, D., K. Ben M'barek, B. Boson, M. Omrane, A. Gassama-Diagne, M. Blaud, F. Penin, E. Diaz, B. Ducos, F. L. Cosset, and A. R. Thiam. 2022. Hepatitis C virus core protein uses triacylglycerols to fold onto the endoplasmic reticulum membrane. Traffic 23:63-80.

299. Rahman, M. M., and S. J. Williams. 2021. Membrane tension may define the deadliest virus infection. Colloid Interface Sci Commun 40:100338.

300. Sengupta, P., and J. Lippincott-Schwartz. 2020. Revisiting Membrane Microdomains and Phase Separation: A Viral Perspective. Viruses 12.

301. Roffay, C., J. M. García-Arcos, P. Chapuis, J. López-Andarias, F. Schneider, A. Colom, C. Tomba, I. D. Meglio, V. Dunsing, S. Matile, A. Roux, and V. Mercier. 2023. Technical insights into fluorescence lifetime microscopy of mechanosensitive Flipper probes. bioRxiv:2022.2009.2028.509885.

302. Shimolina, L., A. Gulin, N. Ignatova, I. Druzhkova, M. Gubina, M. Lukina, L. Snopova, E. Zagaynova, M. K. Kuimova, and M. Shirmanova. 2021. The Role of Plasma Membrane Viscosity in the Response and Resistance of Cancer Cells to Oxaliplatin. Cancers (Basel) 13.

303. Kraft, M. L. 2016. Sphingolipid Organization in the Plasma Membrane and the Mechanisms That Influence It. Front Cell Dev Biol 4:154.

304. Niehaus, M., J. Soltwisch, M. E. Belov, and K. Dreisewerd. 2019. Transmission-mode MALDI-2 mass spectrometry imaging of cells and tissues at subcellular resolution. Nat Methods 16:925-931.

305. Zemski Berry, K. A., R. C. Murphy, B. Kosmider, and R. J. Mason. 2017. Lipidomic characterization and localization of phospholipids in the human lung. J Lipid Res 58:926-933.

306. Reglinski, K., L. Steinfort-Effelsberg, E. Sezgin, C. Klose, H. W. Platta, W. Girzalsky, C. Eggeling, and R. Erdmann. 2020. Fluidity and Lipid Composition of Membranes of Peroxisomes, Mitochondria and the ER From Oleic Acid-Induced Saccharomyces cerevisiae. Front Cell Dev Biol 8:574363.

307. Zhao, M., L. Wang, and S. Li. 2017. Influenza A Virus-Host Protein Interactions Control Viral Pathogenesis. Int J Mol Sci 18.

308. Boyko, V., M. Leavitt, R. Gorelick, W. Fu, O. Nikolaitchik, V. K. Pathak, K. Nagashima, and W. S. Hu. 2006. Coassembly and complementation of Gag proteins from HIV-1 and HIV-2, two distinct human pathogens. Mol Cell 23:281-287.

309. Hemerka, J. N., D. Wang, Y. Weng, W. Lu, R. S. Kaushik, J. Jin, A. F. Harmon, and F. Li. 2009. Detection and characterization of influenza A virus PA-PB2 interaction through a bimolecular fluorescence complementation assay. J Virol 83:3944-3955.

310. Broussard, J. A., and K. J. Green. 2017. Research Techniques Made Simple: Methodology and Applications of Förster Resonance Energy Transfer (FRET) Microscopy. J Invest Dermatol 137:e185-e191.

311. Engel, S., S. Scolari, B. Thaa, N. Krebs, T. Korte, A. Herrmann, and M. Veit. 2010. FLIM-FRET and FRAP reveal association of influenza virus haemagglutinin with membrane rafts. Biochem J 425:567-573.

312. Scolari, S., S. Engel, N. Krebs, A. P. Plazzo, R. F. De Almeida, M. Prieto, M. Veit, and A. Herrmann. 2009. Lateral distribution of the transmembrane domain of influenza virus hemagglutinin revealed by time-resolved fluorescence imaging. J Biol Chem 284:15708-15716.

313. Thaa, B., A. Herrmann, and M. Veit. 2010. Intrinsic cytoskeleton-dependent clustering of influenza virus M2 protein with hemagglutinin assessed by FLIM-FRET. J Virol 84:12445-12449.

314. Richert, L., P. Didier, H. de Rocquigny, and Y. Mély. 2015. Monitoring HIV-1 Protein Oligomerization by FLIM FRET Microscopy. In Advanced Time-Correlated Single Photon Counting Applications. W. Becker, editor. Springer International Publishing, Cham. 277-307.

315. Dunsing, V., and S. Chiantia. 2018. A Fluorescence Fluctuation Spectroscopy Assay of Protein-Protein Interactions at Cell-Cell Contacts. JoVE:e58582.

316. Beale, R., H. Wise, A. Stuart, B. J. Ravenhill, P. Digard, and F. Randow. 2014. A LC3-interacting motif in the influenza A virus M2 protein is required to subvert autophagy and maintain virion stability. Cell Host Microbe 15:239-247.

317. Fletcher, K., R. Ulferts, E. Jacquin, T. Veith, N. Gammoh, J. M. Arasteh, U. Mayer, S. R. Carding, T. Wileman, R. Beale, and O. Florey. 2018. The WD40 domain of ATG16L1 is required for its non-canonical role in lipidation of LC3 at single membranes. EMBO J 37.

318. Gannagé, M., D. Dormann, R. Albrecht, J. Dengjel, T. Torossi, P. C. Rämer, M. Lee, T. Strowig, F. Arrey, G. Conenello, M. Pypaert, J. Andersen, A. García-Sastre, and C. Münz. 2009. Matrix protein 2 of influenza A virus blocks autophagosome fusion with lysosomes. Cell Host Microbe 6:367-380.

319. Chen, B. J., G. P. Leser, D. Jackson, and R. A. Lamb. 2008. The influenza virus M2 protein cytoplasmic tail interacts with the M1 protein and influences virus assembly at the site of virus budding. Journal of virology 82:10059-10070.

320. Iwatsuki-Horimoto, K., T. Horimoto, T. Noda, M. Kiso, J. Maeda, S. Watanabe, Y. Muramoto, K. Fujii, and Y. Kawaoka. 2006. The cytoplasmic tail of the influenza A virus M2 protein plays a role in viral assembly. J Virol 80:5233-5240.

321. McCown, M. F., and A. Pekosz. 2005. The influenza A virus M2 cytoplasmic tail is required for infectious virus production and efficient genome packaging. J Virol 79:3595-3605.

322. McCown, M. F., and A. Pekosz. 2006. Distinct domains of the influenza a virus M2 protein cytoplasmic tail mediate binding to the M1 protein and facilitate infectious virus production. Journal of virology 80:8178-8189.

323. Zebedee, S. L., and R. A. Lamb. 1989. Growth restriction of influenza A virus by M2 protein antibody is genetically linked to the M1 protein. Proc Natl Acad Sci U S A 86:1061-1065.

324. Darapaneni, V. 2015. Large-scale Analysis of Influenza A Virus Sequences Reveals Universally Conserved Residues of Matrix Proteins. American Journal of Current Microbiology 3:1-13.

325. Kerviel, A., S. Dash, O. Moncorgé, B. Panthu, J. Prchal, D. Décimo, T. Ohlmann, B. Lina, C. Favard, E. Decroly, M. Ottmann, P. Roingeard, and D. Muriaux. 2016. Involvement of an Arginine Triplet in M1 Matrix Protein Interaction with Membranes and in M1 Recruitment into Virus-Like Particles of the Influenza A(H1N1)pdm09 Virus. PLoS One 11:e0165421.

326. Tan, C. S. H. 2011. Sequence, Structure, and Network Evolution of Protein Phosphorylation. Science Signaling 4:mr6.

327. Thomas, J. M., M. P. Stevens, N. Percy, and W. S. Barclay. 1998. Phosphorylation of the M2 protein of influenza A virus is not essential for virus viability. Virology 252:54-64.

328. Ali, A., R. T. Avalos, E. Ponimaskin, and D. P. Nayak. 2000. Influenza virus assembly: effect of influenza virus glycoproteins on the membrane association of M1 protein. Journal of virology 74:8709-8719.

329. Enami, M., and K. Enami. 1996. Influenza virus hemagglutinin and neuraminidase glycoproteins stimulate the membrane association of the matrix protein. Journal of virology 70:6653-6657.

330. Leser, G. P., and R. A. Lamb. 2017. Lateral Organization of Influenza Virus Proteins in the Budozone Region of the Plasma Membrane. J Virol 91.

331. Bedi, S., A. Haag, and A. Ono. 2020. A Glu-Glu-Tyr sequence in the cytoplasmic tail of the M2 protein renders IAV susceptible to restriction of HA-M2 association in primary human macrophages. bioRxiv:2020.2007.2001.183186.

332. Hu, B., S. Siche, L. Möller, and M. Veit. 2020. Amphipathic Helices of Cellular Proteins Can Replace the Helix in M2 of Influenza A Virus with Only Small Effects on Virus Replication. J Virol 94.

333. Kim, S. S., M. A. Upshur, K. Saotome, I. D. Sahu, R. M. McCarrick, J. B. Feix, G. A. Lorigan, and K. P. Howard. 2015. Cholesterol-Dependent Conformational Exchange of the C-Terminal Domain of the Influenza A M2 Protein. Biochemistry 54:7157-7167.

334. Ciccotosto, G. D., N. Kozer, T. T. Chow, J. W. Chon, and A. H. Clayton. 2013. Aggregation distributions on cells determined by photobleaching image correlation spectroscopy. Biophys J 104:1056-1064.

335. Cutrale, F., D. Rodriguez, V. Hortigüela, C. L. Chiu, J. Otterstrom, S. Mieruszynski, A. Seriola, E. Larrañaga, A. Raya, M. Lakadamyali, S. E. Fraser, E. Martinez, and S. Ojosnegros. 2019. Using enhanced number and brightness to measure protein oligomerization dynamics in live cells. Nat Protoc 14:616-638.

336. Ojosnegros, S., F. Cutrale, D. Rodríguez, J. J. Otterstrom, C. L. Chiu, V. Hortigüela, C. Tarantino, A. Seriola, S. Mieruszynski, E. Martínez, M. Lakadamyali, A. Raya, and S. E. Fraser. 2017. Eph-ephrin signaling modulated by polymerization and condensation of receptors. Proc Natl Acad Sci U S A 114:13188-13193.

337. Paul, M. D., R. Rainwater, Y. Zuo, L. Gu, and K. Hristova. 2021. Probing Membrane Protein Association Using Concentration-Dependent Number and Brightness. Angew Chem Int Ed Engl 60:6503-6508.

338. Chen, Y., J. D. Müller, P. T. So, and E. Gratton. 1999. The photon counting histogram in fluorescence fluctuation spectroscopy. Biophys J 77:553-567.

339. Scales, N., and P. S. Swain. 2019. Resolving fluorescent species by their brightness and diffusion using correlated photon-counting histograms. PLoS One 14:e0226063.

340. Müller, J. D. 2004. Cumulant analysis in fluorescence fluctuation spectroscopy. Biophys J 86:3981-3992.

341. Wu, B., and J. D. Müller. 2005. Time-integrated fluorescence cumulant analysis in fluorescence fluctuation spectroscopy. Biophys J 89:2721-2735.

342. Müller, J. D., Y. Chen, and E. Gratton. 2000. Resolving heterogeneity on the single molecular level with the photon-counting histogram. Biophys J 78:474-486.

343. Gandhi, S. A., M. A. Sanders, J. G. Granneman, and C. V. Kelly. 2023. Four-color fluorescence cross-correlation spectroscopy with one laser and one camera. Biomed Opt Express 14:3812-3827.

344. Schrimpf, W., V. Lemmens, N. Smisdom, M. Ameloot, D. C. Lamb, and J. Hendrix. 2018. Crosstalk-free multicolor RICS using spectral weighting. Methods 140-141:97-111.

345. Štefl, M., K. Herbst, M. Rübsam, A. Benda, and M. Knop. 2020. Single-Color Fluorescence Lifetime Cross-Correlation Spectroscopy In Vivo. Biophys J 119:1359-1370.

346. Benda, A., P. Kapusta, M. Hof, and K. Gaus. 2014. Fluorescence spectral correlation spectroscopy (FSCS) for probes with highly overlapping emission spectra. Opt Express 22:2973-2988.

347. Shaw, M. L., K. L. Stone, C. M. Colangelo, E. E. Gulcicek, and P. Palese. 2008. Cellular proteins in influenza virus particles. PLoS Pathog 4:e1000085.

348. He, J., E. Sun, M. V. Bujny, D. Kim, M. W. Davidson, and X. Zhuang. 2013. Dual function of CD81 in influenza virus uncoating and budding. PLoS Pathog 9:e1003701.

349. Tripathi, S., M. O. Pohl, Y. Zhou, A. Rodriguez-Frandsen, G. Wang, D. A. Stein, H. M. Moulton, P. DeJesus, J. Che, L. C. Mulder, E. Yángüez, D. Andenmatten, L. Pache, B. Manicassamy, R. A. Albrecht, M. G. Gonzalez, Q. Nguyen, A. Brass, S. Elledge, M. White, S. Shapira, N. Hacohen, A. Karlas, T. F. Meyer, M. Shales, A. Gatorano, J. R. Johnson, G. Jang, T. Johnson, E. Verschueren, D. Sanders, N. Krogan, M. Shaw, R. König, S. Stertz, A. García-Sastre, and S. K. Chanda. 2015. Meta- and Orthogonal Integration of Influenza "OMICs" Data Defines a Role for UBR4 in Virus Budding. Cell Host Microbe 18:723-735.

350. Fan, H., A. P. Walker, L. Carrique, J. R. Keown, I. Serna Martin, D. Karia, J. Sharps, N. Hengrung, E. Pardon, J. Steyaert, J. M. Grimes, and E. Fodor. 2019. Structures of influenza A virus RNA polymerase offer insight into viral genome replication. Nature 573:287-290.

Acknowledgments

Eigenständigkeitserklärung (Declaration)

Hiermit versichere ich, dass ich die vorliegende Arbeit mit dem Titel

Quantitative fluorescence microscopy methods to investigate molecular interactions and dynamics in living cells

nach den Grundsätzen zur Sicherung guter wissenschaftlicher Praxis der DFG, ohne unzulässige Hilfe Dritter und ohne Benutzung anderer als der angegeben Hilfsmittel angefertigt habe; die aus fremden Quellen direkt oder indirekt übernommenen Gedanken sind als solche kenntlich gemacht. Die Arbeit wurde bisher weder im Inland noch im Ausland in gleicher oder ähnlicher Form einer anderen Prüfungsbehörde vorgelegt.

Ich erkenne die Promotionsordnung der Mathematisch-Naturwissenschaftlichen Fakultät der Universität Potsdam.

Ort, Datum   Annett Petrich

I herewith declare that I have produced this thesis

Quantitative fluorescence microscopy methods to investigate molecular interactions and dynamics in living cells

according to the principles for ensuring good scientific practice of the DFG, without the prohibited assistance of third parties and without making use of aids other than those specified; notions taken over directly or indirectly from other sources have been identified as such. This thesis has not been previously presented in identical or similar form to any other german or foreign examination board.

I declare that I recognize the doctorate regulations of the "Mathematisch-Naturwissenschaftlichen Fakultät" of the "Universität Potsdam".

City, Date   Annett Petrich